Searches for Supersymmetry in di-Lepton Final States with the ATLAS Detector at $\sqrt{s} = 7$ TeV

Eirik Gramstad
Department of Physics
University of Oslo
Norway

Dissertation presented for the degree of
Philosophiae Doctor (PhD) in Physics

June 2013

Searches for Supersymmetry in di-Lepton Final States with the ATLAS Detector at $\sqrt{s} = 7$ TeV

Eirik Gramstad

Abstract

The Standard Model (SM) of particle physics has been shown to describe, to great precision, many of the phenomena observed in Nature. With the recent discovery of the Higgs boson even the last missing piece of the SM is confirmed experimentally. Nevertheless, the SM has its limitations. It does not contain an explanation of the dark matter and dark energy, proven to constitute most of our Universe, nor does it incorporate the gravitational force. The SM also contains several parameters whose values are not predicted by the theory and therefore need to be measured experimentally.

The need for developing an extension of the SM, in order to answer all its questions and puzzles, has occupied theorists for many decades already. One of the most believed theories is Supersymmetry (SUSY). It postulates that every SM particle has a supersymmetric partner, similar in all respect except $\frac{1}{2}$ difference in spin. As no such particles are yet discovered SUSY needs naturally to be a broken symmetry, making the SUSY particles somewhat heavier than their SM partners.

SUSY, with its large number of parameters, gives a wide spread in possible phenomenological models, utterly interesting for experimental particle physicists. One of the main topics of the ATLAS experiment at the Large Hadron Collider (LHC) is to reveal if Nature is indeed supersymmetric or not. This thesis concentrates in particular on the searches for direct slepton and gaugino production in final states with two leptons and missing transverse energy using the pp collision data collected by the ATLAS experiment during 2011 at a center of mass energy of 7 TeV.

However, before searching for the unknown one needs to understand what is known. The LHC operates at energies larger than any other particle physics experiment ever has done before. All SM processes, possibly serving as backgrounds to the searches for new physics, must therefore be properly understood. A comprehensive study regarding the estimation of the SM backgrounds to SUSY searches stemming from fake leptons, i.e. leptons from decays of heavy- and light-flavoured hadrons and conversion processes, using the Matrix Method, is covered in this thesis.

No excess of events above what was expected from the SM was observed, and upper limits on the cross-section and masses of new phenomena and particles have consequently been calculated, extending the existing limits.

Acknowledgments

First of all, I would like to give a big thank you to my supervisor Farid Ould-Saada for good support and invaluable help whenever it was needed. I have enjoyed all of the motivating discussions, thorough answers to my questions, and your cheering jokes, which you never seem to run out of. It has been an honour to collaborate with you! A special thank you also goes to my colleague Maiken Pedersen, who I have worked very closely with during this PhD period. We have had many valuable and illuminating discussions and it has been of great support to always have someone to share particularly analysis-specific ideas and problems with. Maiken has also been the main person responsible for the appearance of ROOT plots and LaTeX documents, which have significantly lifted our part of the ATLAS publications to a higher aesthetic level.

In general I would like to thank the whole group of experimental particle physics (EPF) at the University of Oslo for giving me an inclusive and stimulating work place for the last 5 years! Some of the most enjoyable happenings outside work have been the annual summer parties at Farid's place, private football matches and subsequent barbecue nights at CERN. I must also mention the EPF team, *The Running Couplings*, at *Holmenkollstafetten*, for which I have been the sporting manager.[1] The EPF group consists of about 20 active members, so it is quite impressive to gather a team of 15 people! I am also very thankful to the EPF group and the Department of Physics for offering up some extra funding, helping me to finish this thesis.

The lecturer of the *AST1100* course, *Introduction to Astrophysics*, at UiO in the autumn semester of 2004, Viggo Hansteen, also deserves to be acknowledged. Through his eye-opening lectures he made me realize, for the first time, that physics, and in particular particle physics, is really awesome!

My family and friends accompanying me in life outside the Physics Department have also been of great importance during this work. All my running mates in OSI and SK Vidar deserve a special thanks. They have joined me in running a massive amount of kilometers during the past years. For me, the best way to forget about issues such as code not compiling, distributions looking suspicious, seemingly unsolvable problems and nerve-racking deadlines is to go out for a run with good friends. Twenty minutes, and all your problems are gone! A thank you also goes to my parents. They have never pushed me in any particular direction regarding what to study and where to go, but always supported me in whatever I have chosen.

Last, but far from being least, a heartfelt thank you goes to my wife and best friend

[1] *Holmenkollstafetten* is a huge relay which is arranged in the streets of Oslo every year. The teams consist of a total of 15 different stages. *The Running Couplings* has achieved the following results in the class for companies having mixed teams, with $N_{boys} > N_{girls}$ from 2009 to 2012 (time used (h:mm:ss) with the place out of the total number of teams in parentheses): 2009: 1:19:14 (544/698), 2010: 1:14:59 (562/890), 2011: 1:17:32 (605/1109) and 2012: 1:15:11 (460/1323).

Marte Skogen Evje. I deeply appreciate your support, humour and kindness, and for extending my life in several new directions and dimensions. You are nothing more than a mixture of quarks and electrons, but you are surely an extremely nice and unique compound!

Oslo, June 2013
Eirik Gramstad

Contents

Introduction

The Standard Model (SM) of particle physics is a theory describing the world of particles and the interactions between them. During the last 60 years the SM has been under constant development, driven both by experimental observations and theoretical predictions. These two camps have very successfully worked together, and new ideas have emerged from either observations or from theoretical predictions of new particles or phenomena. This interplay is one of the most fascinating things in the history of particle physics. At several occasions a theory has predicted the existence of a new particle, and years later it has been discovered by experimentalists. The most obvious and current example of this is of course the recent discovery of the Higgs boson.

The development of the SM started in the mid nineteen sixties, when the electromagnetic and weak interactions were elegantly unified at a high energy, into one common *electroweak* theory. At low energies, however, the electroweak symmetry is spontaneously broken into the long-range electromagnetic force, with a massless photon (γ) as exchange boson, and the short-ranged weak interaction, mediated by the heavy gauge bosons $W^{\pm}$ and Z. The spontaneous symmetry breaking is postulated to happen through the so-called Brout-Englert-Higgs (BEH) mechanism, keeping the γ massless, while predicting the existence and masses of the $W^{\pm}$ and Z bosons in addition to the existence of a Higgs boson [1, 2, 3, 4, 5, 6]. The same formalism was also used to incorporate the fermion masses. Although neutral currents consistent with observations were discovered in 1973, close to 20 years passed before the UA1 and UA2 collaborations at CERN finally discovered the $W^{\pm}$ and Z bosons with masses consistent with the predictions [7, 8]. Roughly another three decades went, and on Thursday the 4^{th} of July 2012, it was officially announced by the ATLAS and CMS collaborations at the Large Hadron Collider that also a Higgs-like particle had been discovered! [9, 10]. The last missing piece of the SM was finally confirmed through direct observation, although the SM consistency had already made it a widely esteemed member of the SM particle-zoo for many years. The SM model of electroweak and strong interactions is introduced in Chapter 1.

One can get the impression that the theory of particle physics, with the recent discovery of the Higgs boson, is a closed case. There is nothing more to discover and everything is understood. However, despite the enormous success of the SM there are several shortcomings in the theory. First of all the Higgs boson is far from being the end of the story. The couplings to fermions, the spin, parity and charge conjugation of this new particle must be precisely measured. More and more results and measurements also tend to indicate that there must be something more, in addition to the SM. The SM describes very well Nature at the energy scales so far probed in particle physics experiments, but ceases to give a coherent and complete picture through all orders of magnitude in energy. For

instance at the energy scale where gravitation can no longer be neglected the SM totally fails, as it does not incorporate the gravitational force. The SM does also not explain dark matter and dark energy proved to constitute a large fraction of our Universe. The SM does also not predict the values or origin of many of its parameters, and thus they can only be measured experimentally, like for instance the underlying theory behind the Mexican-hat shaped scalar potential needed to achieve spontaneous symmetry breaking.

There are many indications, which will be discussed in Chapter 1, that there must be something more happening at energies above the weak scale, i.e. $\gtrsim 250$ GeV. Supersymmetry (SUSY) is maybe the most believed (and most beautiful) extension of the SM, which elegantly attempts to shed light on and cure many of the SM limitations. SUSY predicts the existence of a supersymmetric partner for every SM particle, identical in all respects except that the spins differ by $\frac{1}{2}$, and thus they should have been relatively easy to observe. The fact that none of these particles are yet discovered indicates that SUSY must be a broken symmetry, making the supersymmetric particles somewhat heavier than their SM partners. SUSY, which is discussed at the end of Chapter 1, is every experimental particle physicist's dream, as it reveals an almost infinite set of different phenomenological scenarios. This thesis addresses especially searches for supersymmetry in channels including electrons and muons. However, Appendix B also covers another extremely interesting channel, using the decay into $b\bar{b}$ of the lightest supersymmetric Higgs boson, whose existence, together with four other Higgs bosons, is predicted in most SUSY scenarios. All the numerous searches for supersymmetric particles, including a broad set of possible final states and signatures, performed using the data recorded at the LHC have so far been negative, although the optimism and motivation to continue developing the searches are still impeccable.

One of the main motivations for building the LHC and the two multi-purpose detectors, ATLAS and CMS, was indeed to coerce nature to reveal its supersymmetric characteristic. The ideas and phenomenological concepts behind proton-proton collisions described in Chapter 2 and the CERN infrastructure with the LHC collider and the particle detector, ATLAS, described in Chapter 3 are fundamental knowledge needed before any step into the analysis of particle physics data can be carried out.

The research project for this thesis has stretched through a unique and extremely stimulating period of the ATLAS experiment at the LHC. It started with the final commissioning of the LHC and the detectors, then continued by the unsuccessful start-up and subsequent one-year unplanned shutdown which eventually ended up with a step-wise increase in proton-proton collision energy. First at a relatively modest center of mass energy of 900 GeV in 2009, then at 7 and later 8 TeV between 2010 and 2012. The exploration of a completely new energy regime, using cutting-edge technology, has resulted a tremendously steep learning curve for the whole collaboration, thus the road-map for this thesis has also changed along the way. Some of the intermediate studies performed on the way towards high energy proton-proton collisions, including the ATLAS authorship qualification assignment, are presented in Chapter 4. This was personally an extremely important and valuable preparation for the more interesting analysis to come. For the qualification task I also had to learn both Perl and bit-operations, the latter lead to Appendix D.

Chapter 5-8 are devoted to the main subject of this thesis, the *Searches for Supersymmetry in di-Lepton Final States with the ATLAS Detector at* $\sqrt{s} = 7$ *TeV*, with a special emphasis on the estimation of the fake lepton background coming from decay of light- and

heavy-flavoured hadrons and conversion processes, discussed in particular in Chapter 7 and Appendix A. Chapter 5 introduces the relevant SUSY signals and corresponding SM backgrounds. Chapter 6 includes all the details regarding the technical implementations of the analysis and summarizes the data and MC samples used. The final analysis is presented in Chapter 8 with the statistical treatment and interpretation of the results. With the complexity of the analysis and rather chaotic conditions of the software and detectors there is no way one can carry out a complete analysis alone given the time constraints from conferences and publication deadlines. Each analysis is therefore a combination of many peoples' work. For the publications [11, 12], using 1 fb^{-1} and 4.7 fb^{-1} of 7 TeV data respectively, my colleague Maiken Pedersen and myself were the main responsible for the fake lepton estimates, using the Matrix Method (MM), within the SUSY two-lepton working group. The work with the MM involved a large part of the analysis including the selections of objects, understanding of the signal region composition, finding appropriate MC samples, which triggers to use and how to re-weight the MC accordingly, input and discussion of the other background determination techniques affecting the MM results, etc. Many, often time-consuming, meetings and discussions were therefore necessary in order to put all the various pieces together into a coherent analysis. The work with the MM was therefore extremely valuable when re-doing parts of the analysis for this thesis, as I had already touched upon many of the other branches of the full analysis.

The final results presented in this thesis are all in agreement with the published limits [12] except in the direct slepton channels, where the published limits are made performing a flavour-blind analysis, with a signal region including both the ee and $\mu\mu$ channels, but where one searches for a single lepton flavour only. The limits presented in this thesis are therefore much stronger than the ones published.

Thanks to the start-up of the LHC, the discovery of the Higgs boson and neutrinos reported to travel faster than the speed of light [13][2], to mention a few things, the field of particle physics has gotten plenty of attention in the media the last few years. This has given me a unique opportunity and plenty of occasions to spread the word of particle physics to pupils, students, teachers and other communities in Norway. I have found this extremely amusing, maturing and a great diversion from the every-day life as a experimental particle physicist. Some of my most memorable outreach moments are presented in Appendix C.

[2]This was found later not to be the case. This rather revolutionary results were caused by a loose optic fibre cable connecting a GPS receiver and a computer.

Chapter 1

The Standard Model of Elementary Particle Physics - and Beyond

The developments in theoretical physics, along with experimental results of the last 50-60 years, have led to a consistent combination of quantum mechanics and special relativity into a Quantum Field Theory (QFT). QFT sets the base for the Standard Model (SM) of particle physics, a theory which describes properties of point-like particles and the interactions between them, using only a few elementary assumptions. With the SM formalism one can calculate to great precision many observables in particle physics. The great success of the SM has been confirmed numerous times through history. At several occasions particles and couplings have been measured in experiments many years after they were predicted by the theory. During the last year the SM has again shown its perfection, since ATLAS and CMS experiments both seem to have discovered the long-awaited Higgs Boson, predicted by the SM almost 50 years ago.

It might seem like the SM is a complete theory describing all phenomena observed in nature. Unfortunately[1] there are still several experimental observations that the SM has no explanation for or totally fails to describe. For instance why there seems to be exactly three generations of matter or the puzzling fact that 95% of our Universe is built up of something that is so far completely unknown.

Sections 1.1-1.8 give a brief introduction into the mathematical description of the SM. However, since this is an experimentalist's work, a very detailed description will not be presented. I refer to [14] for a deeper dive into the full beauty of QFT. After introducing the SM formalism, some of its limitations, and possible solutions, will be introduced in Section 1.9. This finally sets the scene for Supersymmetry, a possible extension of the SM, which will be discussed in Section 1.10.

In the following, natural units are used everywhere, setting $\hbar = c = 1$. Lorentz indices are always denoted by Greek characters; $\mu, \nu \ldots = 0, 1, 2, 3$. Four-vectors for space-time coordinates and particle momenta have the following contravariant components,

$$x = x^\mu = (x^0, \vec{x}), \quad x^0 = t,$$
$$p = p^\mu = (p^0, \vec{p}), \quad p^0 = E = \sqrt{\vec{p}^2 + m^2},$$

[1] Or luckily from a particle physicists' view.

where m is the rest mass. Covariant four-vector components are related to the contravariant components according to

$$a_\mu = g_{\mu\nu} a^\nu,$$

with the metric tensor defined as

$$g_{\mu\nu} = \begin{pmatrix} 1 & 0 & 0 & 0 \\ 0 & -1 & 0 & 0 \\ 0 & 0 & -1 & 0 \\ 0 & 0 & 0 & -1 \end{pmatrix}.$$

The gamma matrices are widely used in the matematical formulation of the SM defined as

$$\gamma^0 = \begin{pmatrix} 1 & 0 & 0 & 0 \\ 0 & 1 & 0 & 0 \\ 0 & 0 & -1 & 0 \\ 0 & 0 & 0 & -1 \end{pmatrix} \quad \gamma^1 = \begin{pmatrix} 0 & 0 & 0 & 1 \\ 0 & 0 & 1 & 0 \\ 0 & -1 & 0 & 0 \\ -1 & 0 & 0 & 0 \end{pmatrix}$$

$$\gamma^2 = \begin{pmatrix} 0 & 0 & 0 & -i \\ 0 & 0 & i & 0 \\ 0 & i & 0 & 0 \\ -i & 0 & 0 & 0 \end{pmatrix} \quad \gamma^3 = \begin{pmatrix} 0 & 0 & 1 & 0 \\ 0 & 0 & 0 & -1 \\ -1 & 0 & 0 & 0 \\ 0 & 1 & 0 & 0 \end{pmatrix},$$

with their product defined as

$$\gamma^5 = i\gamma^0\gamma^1\gamma^2\gamma^3 = \begin{pmatrix} 0 & 0 & 1 & 0 \\ 0 & 0 & 0 & 1 \\ 1 & 0 & 0 & 0 \\ 0 & 1 & 0 & 0 \end{pmatrix}. \tag{1.1}$$

1.1 Building Blocks of Nature

Nature is built up by indivisible[2] particles. The fundamental forces in nature describe how these particles are created, how they decay and how they interact with each other. The particles are grouped according to if and how they interact with the various forces. This classification is comparable with the more familiar periodic table of elements, which groups the elements after their physical and chemical properties.

[2]The notion of indivisibility or elementarity is tied up with the scale at which phenomena/particles are observed. At the present energies, there are no indications that the particles of the SM have a structure. In this context they are therefore referred to as indivisible particles.

1.1.1 Forces

There are four fundamental forces in nature. The macroscopic electromagnetic and gravitational forces and the microscopic weak and strong forces. In particle physics the gravitational force is negligible due to the extremely small masses of the particles. In fact, the SM totally fails to include gravitation. There are several ideas on how to solve this, however, but that is out of the scope of this introduction. Each force is typically represented by a specific quantum number. The quantum number of the electromagnetic force is the electric charge, Q. The weak force has the weak isospin, T, while the strong force is connected to colour charge, C[3]. In particle physics forces are mediated by particles with integer spin, known as bosons. Each force has one or more mediating particles connected to it. The electromagnetic force is mediated by the photon (γ). The strong force is mediated by eight gluons carrying colour and the weak force is mediated by the heavy Z and $W^{\pm}$ bosons. Table 1.1 summarize the four forces and the properties of the mediating particles (gauge bosons) in the SM. The gravitational force, with the Graviton as a hypothetical mediator, is also included in the Table, although it is not a part of the SM (yet).

Force	mediator	strength	mass [GeV]	Q [e]	spin
strong	8 gluons	1	0	0	1
electromagnetic	photon (γ)	1/137	0	0	1
weak	$W^{\pm}$, Z	10^{-14}	80.4, 91.2	$\pm 1, 0$	1
gravitation	Graviton?	$\sim 10^{-40}$	?	0	2

Table 1.1: The force mediators in the SM, including the hypothetical mediator of the gravitational force, Graviton. The strength is relative to the strong force.

1.1.2 Particles

The particles that make up matter have half integer spin and are known as fermions. The fermions carry a set of quantum numbers and are grouped according to whether and how they interact with the various forces, summarized in Table 1.2. All fermions appear in three generations,where each generation is grouped into left- and right-handed chirality states, χ_L and ψ_R respectively, given by

$$\chi_L = \frac{1-\gamma_5}{2} f \quad \text{and} \quad \psi_R = \frac{1+\gamma_5}{2} f,$$

where f is a fermionic field[4] and γ_5 is the chirality operator defined in 1.1. The left-handed chirality states of fermions with identical hypercharge, Y, are combined into left-handed doublets representing the two weak isospin components with $T_3 = \pm\frac{1}{2}$ of an isospin state

[3]The term *colour* in this context has nothing to do with the visual perception of colour. The term is used simply because the abstract property of *colour charge* can take exactly three values, analoug to the well-known primary colours; red, green and blue.

[4]The field f is a Dirac spinor with four complex components.

Generation			Quantum numbers					
1^{st}	2^{nd}	3^{rd}	s	Q	T	T_3	Y	C
Leptons								
$\begin{pmatrix} \nu_e \\ e^- \end{pmatrix}_L$	$\begin{pmatrix} \nu_\mu \\ \mu^- \end{pmatrix}_L$	$\begin{pmatrix} \nu_\tau \\ \tau^- \end{pmatrix}_L$	$\frac{1}{2}$	0	$\frac{1}{2}$	$\frac{1}{2}$	-1	0
			$\frac{1}{2}$	-1	$\frac{1}{2}$	$-\frac{1}{2}$	-1	0
ν_R^e	ν_R^μ	ν_R^τ	$\frac{1}{2}$	0	0	0	0	0
e_R	μ_R	τ_R	$\frac{1}{2}$	-1	0	0	-2	0
Quarks								
$\begin{pmatrix} u \\ d \end{pmatrix}_L$	$\begin{pmatrix} c \\ s \end{pmatrix}_L$	$\begin{pmatrix} t \\ b \end{pmatrix}_L$	$\frac{1}{2}$	$\frac{2}{3}$	$\frac{1}{2}$	$\frac{1}{2}$	$\frac{1}{3}$	3
			$\frac{1}{2}$	$-\frac{1}{3}$	$\frac{1}{2}$	$-\frac{1}{2}$	$\frac{1}{3}$	3
u_R	c_R	t_R	$\frac{1}{2}$	$\frac{2}{3}$	0	0	$\frac{4}{3}$	3
d_R	s_R	b_R	$\frac{1}{2}$	$-\frac{1}{3}$	0	0	$-\frac{2}{3}$	3

Table 1.2: The three generations of fermions in the SM. The left-handed (L) particles are grouped into isospin doublets and the right-handed ones (R) are iso-singlets with isospin $T = 0$. The quantum numbers s, Q, T, T_3, Y and C represent the spin, electric charge, isospin, the third component of isospin, the weak hypercharge and colour charge respectively. To each fermion corresponds an antifermion with opposite additive quantum numbers.

$T = \frac{1}{2}$. The charges, T and Y, are related to the electric charge, Q, and the third component of the weak isospin (weak charge) through the Gellmann-Nishijima formula

$$Q = T_3 + \frac{Y}{2}. \tag{1.2}$$

The right-handed fields are isospin singlets since they have $T_3 = T = 0$. The left- and right-handed components are indicated in Table 1.2 by the subscripts L and R, respectively. The fermions that do not carry colour and therefore do not "feel" the strong force are called leptons and grouped to form colour singlets. The fermions that do interact strongly are known as quarks and come in three primary colours: red, green and blue. They appear therefore as colour triplets. In nature only colourless states are allowed, and quarks do therefore always group together to form bound colourless states with the following possibilities: (1) equal mixture of red, green and blue; (2) equal mixture of antired, antigreen and antiblue; and (3) equal mixture of colour and anticolour. These possibilities correspond to all hadron states of quarks so far observed in nature: baryons, antibaryons and mesons respectively. The most famous example of a baryon is the proton, which consists of two up quarks and one down quark. Another well-known state is the neutral pi-meson, π^0, built up of a mixture of up-antiup and down-antidown quarks. In general all hadron states made up of three quarks are called baryons and those consisting of quark-antiquark pairs are known as mesons.

1.1.2.1 Charge Parity and Time (CPT) Symmetries

The CPT symmetry of the SM refers to a fundamental symmetry of the laws of physics under the transformations involving simultaneous inversion of charge (C), parity (P) and time (T). These symmetries, however, are found to individually not be conserved. This implies that particles and antiparticles, as well as left- and right-handed particles interact differently. For a long time it was believed that the CP symmetry was a true symmetry of nature, but CP violation was discovered in 1964 when studying weak decays of neutral kaons [15]. The combined CPT symmetry, however, is still believed to be a completely conserved symmetry, in accordance with the amount of T violation observed in Kaon decays [16]. The C and P violations explain why the SM weak interaction, which will be discussed in Section 1.3.1, only interacts with left-handed and not right-handed particles.

1.2 Standard Model Formalism

From classical mechanics, a Lagrangian, L, is a function that describes the dynamics of a system. Classically it is defined as a function of generalized coordinates, q, and their time derivatives, $\dot{q}$,

$$L = T(\dot{q}) - U(q) = \frac{1}{2}m\dot{q}^2 - U(q),$$

where T is the kinetic energy and U the potential energy. The equation of motion follows from the Euler-Lagrange equation

$$\frac{d}{dt}\left(\frac{\partial L}{\partial \dot{q}}\right) - \frac{\partial L}{\partial q} = 0$$
$$\Rightarrow F = \frac{dU}{dq} = ma,$$

which is the well-known Newton's second law. In field theory one defines the Lagrangian density, $\mathscr{L}$, as a function of the fields, $\Phi(x_\alpha)$, and their space-time derivatives (or gradients)

$$\mathscr{L} = \mathscr{L}\left(\Phi(x_\alpha), \frac{\partial \Phi(x_\alpha)}{\partial x_\alpha}\right).$$

The integration over the three dimensional space gives L

$$L = \int \mathscr{L}\left(\Phi, \partial_\alpha \Phi\right) d^3x.$$

The Euler-Lagrange equation becomes

$$\partial_\alpha \left[\frac{\partial \mathscr{L}}{\partial\left(\partial_\alpha \Phi\right)}\right] - \frac{\partial \mathscr{L}}{\partial \Phi} = 0. \tag{1.3}$$

A fermionic field, f, of mass m is described by the Lagrangian density

$$\mathscr{L} = \bar{f}(x)(i\gamma^\mu \partial_\mu - m)f(x), \tag{1.4}$$

where $\bar{f} = f^\dagger \gamma^0$. Plugging this into Eq. 1.3 gives the famous Dirac equation for the field f

$$(i\gamma^\mu \partial_\mu - m)f(x) = 0.$$

This is the equation of motion for a free fermion of type f without interaction. The interactions are introduced in the SM by requiring the action, $S = \int \mathscr{L}\, d^4x$, to be invariant under local gauge transformations. In other words it is required that the action does not change by more than a total derivative under the local gauge transformation. In addition the equation of motion should stay unchanged. The simplest example in the SM is the invariance under a local U(1) transformation

$$U_1(x) = e^{i\alpha(x)}.$$

The field f and its derivatives transform as

$$f(x) \rightarrow e^{i\alpha(x)} f(x) \tag{1.5}$$
$$\partial_\mu f(x) \rightarrow e^{i\alpha(x)} \partial_\mu f(x) + i\partial_\mu \alpha(x) e^{i\alpha(x)} f(x). \tag{1.6}$$

The field itself, Eq. 1.5, is invariant, but the derivative is not because of the $\partial_\mu \alpha(x)$ term in the rightmost expression in Eq. 1.6. To achieve invariance the covariant derivative, D_μ, is introduced, replacing the ordinary derivative, ∂_μ, with

$$\partial_\mu \rightarrow D_\mu = \partial_\mu - ieA_\mu(x),$$

including a new field, $A_\mu(x)$. By requiring the covariant derivative to transform as the field f we get

$$\begin{aligned} D_\mu f(x) &= \left[\partial_\mu - ieA_\mu(x)\right] f(x) \\ &\rightarrow \left[\partial_\mu - ieA'_\mu(x)\right] e^{i\alpha(x)} f(x) \\ &= e^{i\alpha(x)} \left[\partial_\mu + i\partial_\mu \alpha(x) - ieA'_\mu(x)\right] f(x). \end{aligned} \tag{1.7}$$

One can easily see that if we require the field A_μ to transform like

$$A_\mu \rightarrow A'_\mu(x) = A_\mu + \frac{1}{e}\partial_\mu \alpha(x)$$

Eq. 1.7 stays invariant under the transformation. The $A_\mu(x)$ is known as a gauge field and enters the Lagrangian density through the field strength tensor, $F_{\mu\nu}$, defined from the commutator of the two covariant derivatives

$$F_{\mu\nu} = -\frac{1}{e}\left[D_\mu, D_\nu\right] = \partial_\mu A_\nu(x) - \partial_\nu A_\mu(x). \tag{1.8}$$

This demonstrates how the interactions are related to the commutator relations of the transformation group generators. The final Lagrangian density in Eq. 1.4 becomes

$$\mathscr{L}_{U(1)} = \bar{f}(x)(i\gamma^\mu \partial_\mu - m)f(x) + e\bar{f}(x)\gamma^\mu A_\mu f(x) - \frac{1}{4}F_{\mu\nu}F^{\mu\nu}. \tag{1.9}$$

The middle term includes an interaction between a fermion, f, with charge e and the gauge field $A_\mu(x)$, which itself is described by the rightmost term. In the SM the Lagrangian in Eq. 1.9 is referred to as the theory of Quantum Electrodynamics (QED), where the gauge field $A_\mu(x)$ represents the massless photon. The symmetry under the $\mathrm{U}(1)_{EM}$[5] describes the electromagnetic interaction.The transformation in Eq. 1.5 is a simple example of an Abelian symmetry, and the photon therefore does not have any self-interactions. The Abelian symmetry is, however, a special case of the $\mathrm{U}(1)_EM$, as will become clear when moving to the more general non-Abelian symmetry groups of the SM in Section 1.3.

1.3 The Gauge Groups of the Standard Model

The previous Section showed an example on how to introduce an interaction between a fermion and a gauge field by requiring the Lagrangian density to be invariant under a local $\mathrm{U}(1)_{EM}$ transformation. The full gauge group of the SM is $\mathrm{SU}(3)_C \times \mathrm{SU}(2)_L \times \mathrm{U}(1)_Y$. By requiring invariance of the Lagrangian density under the transformations of these gauge groups all the interactions of the fermions of the SM are derived.

[5]The subscript EM is used to distinguish this transformation, associated with the *electric charge* Q, from that of the electroweak theory, tied up with the *weak hypercharge* Y, described in the next Section.

1.3.1 The Electroweak Interaction - $SU(2)_L \times U(1)_Y$

The electroweak interaction is a unified description of two of the four fundamental forces in nature, electromagnetism and the weak interaction. This unification was first proposed by Sheldon Glashow in 1960 [17]. Later, in 1967 and 68, Weinberg and Salam, independently, combined the electroweak model with the BEH mechanism (to be discussed in Section 1.4.1), and constructed the SM more or less as we know it today [18, 19]. Glashow, Weinberg and Salam shared the Nobel Prize in Physics in 1979 for this work. The theory of electroweak interactions was fully established by experimental results on neutrino scattering by the Gargamelle collaboration [20, 21] and the discovery of the W and Z gauge bosons at CERN by the UA1 and UA2 experiments [7, 8] during the 1970-80's.

We follow the same lines as outlined in Section 1.2 when constructing the theory of electroweak interactions. The subgroup $SU(2)_L \times U(1)_Y$ acts on a field with the local gauge transformation

$$U(x) = e^{i\frac{Y}{2}\alpha(x) + iT\vec{\beta}(x)\vec{\sigma}}, \tag{1.10}$$

where weak isospin T and weak hypercharge Y for each fermion can be found in Table 1.2. We recognize the first term in the exponential from Section 1.2 with an additional factor $Y/2$, where Y is the weak hypercharge. The second term belongs to the SU(2) group including the weak isospin, T. The $\vec{\beta}(x)$ is an arbitrary three-dimensional function while the $\vec{\sigma}$ consists of the famous Pauli matrices

$$\sigma_x = \begin{pmatrix} 0 & 1 \\ 1 & 0 \end{pmatrix}, \ \sigma_y = \begin{pmatrix} 0 & -i \\ i & 0 \end{pmatrix}, \ \sigma_z = \begin{pmatrix} 1 & 0 \\ 0 & -1 \end{pmatrix},$$

which, when multiplied by 1/2, become the generators of the $SU(2)_L$ group, $\vec{J} = \vec{\sigma}/2$. Using Eq. 1.10 the field f transforms under local gauge transformations as

$$f(x) \rightarrow e^{i\frac{Y}{2}\alpha(x) + iT\vec{\beta}(x)\vec{\sigma}} f(x). \tag{1.11}$$

The covariant derivative introduced to make the electroweak Lagrangian invariant is

$$D_\mu = \partial_\mu + ig'\frac{Y}{2}B_\mu(x) + igT\vec{\sigma}\cdot\vec{W}_\mu(x),$$

where the gauge field B_μ (associated to the $U(1)_Y$ group) and the three gauge fields $\vec{W}_\mu$ (associated to the $SU(2)_L$ group) are introduced. From Table 1.2 one sees that there are only the left-handed fermions that have $T \neq 0$, and the transformation $SU(2)_L \times U(1)_Y$ therefore acts differently on the left- and right-handed fermions, as discussed in Section 1.1.2.1,

$$\chi_L \rightarrow \chi'_L = e^{i\frac{Y}{2}\alpha(\vec{x}) + iT\vec{\beta}(\vec{x})\vec{\sigma}}\chi_L$$
$$\psi_R \rightarrow \psi'_R = e^{i\frac{Y}{2}\alpha(\vec{x})}\psi_R.$$

The gauge fields B_μ and $\vec{W}_\mu$ are not physical fields but mix to form the fields, corresponding to the photon (A_μ), Z and $W^\pm$ gauge bosons

$$W^\pm_\mu = \frac{1}{\sqrt{2}}\left(W^1_\mu \mp iW^2_\mu\right) \tag{1.12}$$
$$A_\mu = B_\mu \cos\theta_W + W^3_\mu \sin\theta_W \tag{1.13}$$
$$Z_\mu = -B_\mu \sin\theta_W + W^3_\mu \cos\theta_W, \tag{1.14}$$

where θ_W is the experimentally determined weak mixing angle. The mixing angle relates the couplings g and g′ to e through

$$e = g \sin\theta_W = g' \cos\theta_W. \tag{1.15}$$

The full electroweak Lagrangian then becomes

$$\begin{aligned}\mathscr{L}_{EW} = \bar{\chi}_L \gamma^\mu \left[i\partial_\mu + g\frac{1}{2}\vec{\sigma}\cdot\vec{W}_\mu - g'\frac{Y}{2}B_\mu \right] \chi_L + \bar{\psi}_R \gamma^\mu \left[i\partial_\mu - g'\frac{Y}{2}B_\mu \right] \psi_R \\ - \frac{1}{4}B^{\mu\nu}B_{\mu\nu} - \frac{1}{4}\vec{W}^{\mu\nu}\vec{W}_{\mu\nu}.\end{aligned} \tag{1.16}$$

The first (second) term describes the interactions between the left-handed (right-handed) fermions and the gauge fields. The next to last term describes the kinetic energy of the B_μ field, $B_{\mu\nu} \equiv \partial_\mu B_\nu - \partial_\nu B_\mu$. The last term contains the kinetic energy and self coupling of the $\vec{W}_\mu$ fields,

$$\vec{W}_{\mu\nu} = \partial_\mu \vec{W}_\nu - \partial_\nu \vec{W}_\mu - g\vec{W}_\mu \times \vec{W}_\nu. \tag{1.17}$$

An important part missing in the Lagrangian are the mass terms of the fermions, which from experiments are known to all have non-zero masses. Simply adding a mass term, $m\bar{f}f$, to the Lagrangian would however mix the left- and right-handed fields and thus ruin the gauge invariance. We also know from experiments that the Z and W bosons are massive, but the Lagrangian does not contain any proper mass terms of the type $-m_W^2 W_\mu^+ W^{-\mu} - m_Z^2 Z_\mu^+ Z^{-\mu}$ either, as inclusion of such terms also would ruin gauge invariance. A method on how to include masses of the fermions and gauge bosons in the SM without destroying gauge invariance will be discussed in Section 1.4. First we will introduce the last gauge group of the SM, $\mathrm{SU}(3)_C$, from which the theory of strong interactions, Quantum Chromodynamics (QCD), originates.

1.3.2 The Strong Interaction - $\mathrm{SU}(3)_C$

The $\mathrm{SU}(3)_C$ group is connected to the strong force and acts only on fermions that carry colour (i.e. the quarks). Since $\mathrm{SU}(3)_C$ is a non-Abelian gauge group it contains also self-interactions of the gluons. The gauge transformation connected with the $\mathrm{SU}(3)_C$ group is

$$U(x) = e^{\,i\sum_{a=1}^{8} \alpha_a(x)\frac{\lambda_a}{2}}, \tag{1.18}$$

where the sum goes over all colour combinations. The λ_a-terms are the well-known 3×3 Gell-Mann matrices which form the 8 generators of the SU(3) group, $T_a = \frac{\lambda_a}{2}$, $a = 1, 2, 3, \ldots, 8$. The covariant derivative needed to make the Lagrangian invariant under an $\mathrm{SU}(3)_C$ transformation is

$$D_\mu = \partial_\mu + ig_s \sum_{a=1}^{8} \frac{\lambda_a}{2} G_\mu^a.$$

This expression contains the eight gluon fields, G^a_μ, of QCD. The resulting Lagrangian then becomes

$$\mathscr{L}_{QCD} = \bar{q}(i\gamma^\mu\partial_\mu - m)q - g_s(\bar{q}\gamma^\mu T_a q)G^a_\mu - \frac{1}{4}G^a_{\mu\nu}G^{\mu\nu}_a,$$

where $G_{\mu\nu}$ is the gluonic field strength tensor given by

$$G^a_{\mu\nu} = \partial_\mu G^a_\nu - \partial_\nu G^a_\mu - g^{abc}G^b_\mu G^c_\nu, \tag{1.19}$$

where the g^{abc} are known as the structure constants of the SU(3) group. This Lagrangian looks very similar to the one in Eq. 1.9 for the U(1) group. The differences are the coupling constant g_s, quark colour triplets q and the generators T_a. Another important difference is that the field tensor $G_{\mu\nu}$ in Eq. 1.19 not only contains a kinetic term but also includes self-interactions (rightmost term in Eq. 1.19). This is contrary to what was found in QED for the $A_\mu(x)$ field in Eq. 1.8. This means that the gluons themselves need to carry colour charge. Similar to the SU(2) group the Lagrangian does not contain any mass terms for the gluons, but this is not required since the gluon is found to be massless, contrary to the W and Z bosons that are massive.

Due to the non-Abelian nature of QCD the energy dependence of the strong coupling constant is totally opposite that of the electromagnetic coupling constant of QED, which is an Abelian theory. The strong coupling constant leads to *asymptotic freedom*, meaning that it becomes asymptotically weaker as the distance decreases. Consequently the coupling constant increases when the distance increases. When trying to tear apart two quarks (dissociating a meson into a quark and an antiquark for example) the energy of the coupling between them grows until it is favourable to create a new quark-antiquark pair from the binding energy. As a consequence, isolated quarks or gluons are never found in nature, but rather grouped together forming colourless states, as discussed in Section 1.1.2. This is known as *colour confinement* and has important consequences for particle physics experiments, as will be discussed in Chapter 2.

1.3.2.1 Quark Mixing

The left-handed quark weak eigenstates of $\mathrm{SU}(2)_L \times \mathrm{U}(1)_Y$ are not the same as the mass eigenstates of the $\mathrm{SU}(3)_C$ group. The weak quark eigenstates (denoted with a $'$) can be written as orthogonal combinations of the mass eigenstates

$$\begin{pmatrix} u' \\ c' \\ t' \end{pmatrix} = U_u \begin{pmatrix} u \\ c \\ t \end{pmatrix} \quad \text{and} \quad \begin{pmatrix} d' \\ s' \\ b' \end{pmatrix} = U_d \begin{pmatrix} d \\ s \\ b \end{pmatrix},$$

where U_u and U_d are unitary matrices. The relation between the eigenstates are expressed by the 3×3 **C**abibbo-**K**obayashi-**M**askawa (CKM) matrix [22, 23] defined as

$$V_{CKM} = U_u^\dagger U_d = \begin{pmatrix} V_{ud} & V_{us} & V_{ub} \\ V_{cd} & V_{cs} & V_{cb} \\ V_{td} & V_{ts} & V_{tb} \end{pmatrix}$$

The entries in the CKM matrix give the probability of a transition of an up-type to a down-type quark (or vice versa) and are determined by three angles (the Cabbibo angle, θ_C, being one of them) and one phase. The single phase is the only parameter that violates CP symmetry and the study of the elements in the CKM matrix is therefore important to achieve a better understanding of the CP violation in the SM, discussed in Section 1.1.2.1. Figure 1.1 illustrates a weak interaction where a down-type quark (s) goes over to an antiup-type quark (u) with the exchange of a W^- boson. The CKM element, V_{us}, corresponding to this interaction is measured to be 0.2166 ± 0.0005 [24]. Many similar processes are observed in nature and the study of these have given us better information on the sizes of each of the elements in the CKM matrix. For instance the well-known and measured nuclear beta decay rate allows the transition probability V_{ud} to be extracted. The elements along the diagonal are all found to be close to unity as they represent up-down transitions within one generation. The elements above and below the diagonal are much smaller, with the elements furthest away from the diagonal being the smallest [24].

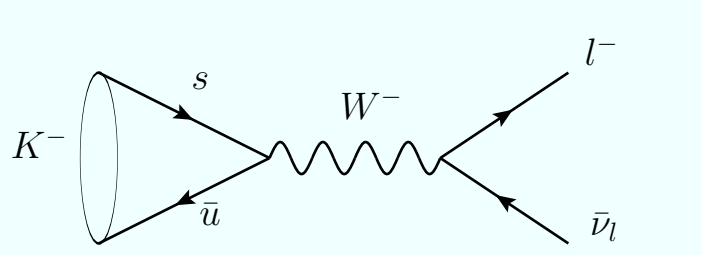

Figure 1.1: Kaon decay involving a transition of a strange quark to an antiup quark by emission of a W^-.

1.4 Spontaneous Symmetry Breaking

In the previous Sections, mass terms for the fermions and the W and Z bosons were shown to break the invariance of the Lagrangian density under gauge transformations. Since gauge invariance requires that $\mathrm{U}(1)_Y$ and $\mathrm{SU}(3)_C$ are to be exact symmetries, the photon and gluons are massless, as confirmed by experiments. The weak interaction, however, is short ranged and is valid only if the Z and W bosons are heavy. The strong force is also short ranged, but because of *colour confinement*, as discussed in Section 1.1.2, the $\mathrm{SU}(3)_C$ symmetry does not need to be broken. So in order to give masses to the Z and W bosons, and at the same time keeping the photon massless, the weak section of the electroweak symmetry must be broken.

In order to approach our goal of generating a mass for the gauge bosons we start by introducing a complex scalar field

$$\phi = \frac{\phi_1 + i\phi_2}{\sqrt{2}}, \tag{1.20}$$

described by the Lagrangian density

$$\mathscr{L} = (\partial_\mu \phi)^* (\partial^\mu \phi) - V(\phi), \tag{1.21}$$

with the potential defined as

$$V(\phi) = \mu^2\phi^*\phi + \lambda(\phi^*\phi)^2. \tag{1.22}$$

This Lagrangian is invariant under the global U(1) transformation. Substituting for the scalar field in Eq. 1.20 we get

$$\mathscr{L} = \frac{1}{2}\left(\partial_\mu\phi_1\right)^2 + \frac{1}{2}\left(\partial_\mu\phi_2\right)^2 - \frac{1}{2}\mu^2\left(\phi_1^2+\phi_2^2\right) - \frac{1}{4}\lambda\left(\phi_1^2+\phi_2^2\right)^2. \tag{1.23}$$

If we choose $\mu^2 > 0$ and $\lambda > 0$ the potential is a symmetric parabola with minimum at 0, and Eq. 1.23 simply describes a self interacting scalar field with mass μ, which is not what we want. We therefore consider the case when $\mu^2 < 0$ (keeping $\lambda > 0$) which gives a potential as shown in Figure 1.2. This potential has a continuous minimum in the ϕ_1, ϕ_2 plane of radius v given by $\phi_1^2 + \phi_2^2 = v^2$ with $v^2 = -\frac{\mu}{\lambda}$.

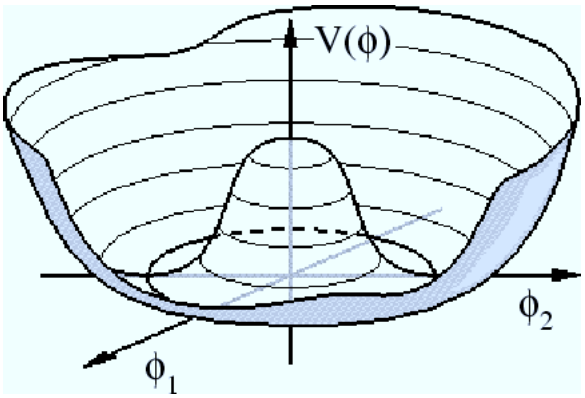

Figure 1.2: The potential $V(\phi) = \mu^2\phi^*\phi - \lambda(\phi^*\phi)^2$ with $\lambda > 0$ and $\mu^2 < 0$. It has a continuous minimum in the ϕ_1, ϕ_2 plane of radius v given by $\phi_1^2 + \phi_2^2 = v^2$ with $v^2 = -\frac{\mu}{\lambda}$.

plane of radius v given by $\phi_1^2 + \phi_2^2 = v^2$ with $v^2 = -\frac{\mu}{\lambda}$, obtained by minimizing V in Eq. 1.22. We choose a specific minimum with $\phi_1 = v$ and $\phi_2 = 0$ [6] and expand $\mathscr{L}$ about this value in terms of the fields η and ξ

$$\phi(x) = \frac{1}{\sqrt{2}}\left[v + \eta(x) + i\xi(x)\right]. \tag{1.24}$$

We substitute this into the Lagrangian in Eq. 1.21 and get

$$\mathscr{L}' = \frac{1}{2}(\partial_\mu\xi)^2 + \frac{1}{2}(\partial_\mu\eta)^2 + \mu^2\eta^2 + \text{const.} + \text{higher-order terms in}\,\eta\,\text{and}\,\xi$$

We see immediately that the η field, with kinetic term $\frac{1}{2}(\partial_\mu\eta)^2$, has a mass term, $\frac{1}{2}m_\eta^2\eta^2$, with $m_\eta = \sqrt{-2\mu^2}$. The higher-order terms in η and ξ represent the interactions of the fields with themselves. The first term is a kinetic term for the ξ field, but there is no corresponding mass term. This is known as a Goldstone boson. Generally, the Goldstone theorem states that massless scalars occur whenever a continuous symmetry of a physical system is spontaneously broken [25]. In our struggle towards a gauge theory of weak interactions with massive gauge bosons we also get massless Goldstone bosons, which never have been observed in any experiment. However, as will become clear later, the additional degrees of freedom from these massles Goldstone bosons are in fact needed in order to create the extra longitudinal polarization required when the W and Z bosons become massive.

[6] Which minimum we choose does not matter since any other choice always can be reached by rotation symmetry. In fact, nature also has to decide on one of the minima.

1.4.1 The BEH Mechanism

We now study the spontaneous symmetry breaking of a local U(1) symmetry. Just as in Section 1.2 we need the Lagrangian, Eq. 1.21, to be invariant under the U(1) transformation. Requiring this we end up with

$$\mathscr{L} = (\partial^\mu + ieA^\mu)\phi^*(\partial_\mu - ieA_\mu)\phi - \mu^2\phi^*\phi - \lambda(\phi^*\phi)^2 - \frac{1}{4}F_{\mu\nu}F^{\mu\nu}, \tag{1.25}$$

where we recognize the field strength tensor $F_{\mu\nu}$ from Eq. 1.8. With $\mu^2 > 0$ this Lagrangian becomes the QED Lagrangian for a charged scalar particle of mass μ in Eq. 1.9, except for the quartic term in ϕ. The previous Section showed, however, that we need to require $\mu^2 < 0$ in order to get spontaneous symmetry breaking. We repeat the same procedure by choosing a minimum and expand $\mathscr{L}$ about this minimum using the η and ξ fields (Eq. 1.24). The Lagrangian becomes then

$$\begin{aligned}\mathscr{L}' = &\frac{1}{2}(\partial_\mu\xi)^2 + \frac{1}{2}(\partial_\mu\eta)^2 - v^2\lambda\eta^2 + \frac{1}{2}e^2v^2A_\mu A^\mu \\ &- evA_\mu\partial^\mu\xi - \frac{1}{4}F_{\mu\nu}F^{\mu\nu} + \text{higher order terms}\end{aligned} \tag{1.26}$$

This Lagrangian contains a massless Goldstone boson, ξ, a massive scalar, η, with mass $m_\eta = \sqrt{2\lambda v^2}$, and a massive vector A_μ with mass, $m_A = ev$. So we seem to have managed to generate a massive gauge boson without disturbing gauge invariance, but we still have the unwanted Goldstone boson, ξ. Extra care must now be taken because of the bilinear term, $evA_\mu\partial^\mu\xi$, which introduces a coupling between the gauge field and the Goldstone boson. Since A_μ now has become massive, the degrees of freedom have raised from 2 to 3, but our procedure of translating field variables, as in Eq. 1.24, should not create a new degree of freedom. The only explanation to this must be that some of the fields in Eq. 1.26 are not physical particles. The task is then to find a particular gauge which eliminates one of the fields from the Lagrangian. If we write Eq. 1.24 to lowest order in ξ we get

$$\phi(x) = \frac{1}{\sqrt{2}}\left[v + \eta(x)\right]e^{i\frac{\xi}{v}},$$

which suggest that we should use a different set of real fields h, θ and A_μ, where

$$\begin{aligned}\phi(x) &\to \frac{1}{\sqrt{2}}\left[v + h(x)\right]e^{i\frac{\theta}{v}} \\ A_\mu &\to A_\mu + \frac{1}{ev}\partial_\mu\theta.\end{aligned}$$

Putting these into the original Lagrangian, Eq. 1.25, gives

$$\begin{aligned}\mathscr{L} = &\frac{1}{2}(\partial_\mu h)^2 - v^2\lambda h^2 + \frac{1}{2}e^2v^2A_\mu A^\mu - \lambda v h^3 - \frac{1}{4}\lambda h^4 \\ &+ \frac{1}{2}e^2A_\mu A^\mu h^2 + ve^2A_\mu A^\mu h - \frac{1}{4}F_{\mu\nu}F^{\mu\nu}.\end{aligned}$$

The Goldstone boson no longer appear in the Lagrangian and we are left with a massive gauge boson and a massive scalar h, known as the Higgs boson. The procedure on how to

turn the unwanted Goldstone boson into the longitudinal polarization of the new massive Higgs particle is known as the BEH mechanism[7].

1.4.2 Spontaneous Breaking of a Local SU(2) Gauge Symmetry

In the previous Section we introduced the BEH mechanism, but since what we really want is to give masses to the weak gauge bosons we have to repeat the procedure for an SU(2) gauge symmetry. Start again with the Lagrangian

$$\mathscr{L} = (\partial_\mu \phi)^\dagger (\partial^\mu \phi) - \mu^2 \phi^\dagger \phi - \lambda (\phi^\dagger \phi)^2, \tag{1.27}$$

where ϕ now is an SU(2) isospin doublet with weak hypercharge, $Y = 1$, consisting of four real scalar fields

$$\phi = \sqrt{\frac{1}{2}} \begin{pmatrix} \phi_1 + i\phi_2 \\ \phi_3 + i\phi_4 \end{pmatrix}. \tag{1.28}$$

We take the $\mathrm{SU}(2)_L \times \mathrm{U}(1)_Y$ local gauge transformation as in Eq. 1.11 and remove the term containing the weak hypercharge, Y, which belongs to the $\mathrm{U}(1)_Y$ gauge transformation,

$$\phi \rightarrow \phi' = e^{i\vec{\beta}(\vec{x})T\vec{\sigma}}\phi.$$

To ensure invariance under this transformation the ∂_μ is replaced with a proper covariant derivative

$$D_\mu = \partial_\mu + ig\frac{\vec{\sigma}}{2}\vec{W}_\mu,$$

where $\vec{W}_\mu$ are the three gauge fields transforming as

$$\vec{W}_\mu \rightarrow \vec{W}'_\mu = \vec{W}_\mu - \frac{1}{g}\partial_\mu \vec{\beta} - \vec{\beta} \times \vec{W}_\mu.$$

Putting this into the Lagrangian, Eq. 1.27, yields

$$\mathscr{L} = \left(\partial_\mu \phi + ig\frac{1}{2}\vec{\sigma} \cdot \vec{W}_\mu \phi\right)^\dagger \left(\partial^\mu \phi + ig\frac{1}{2}\vec{\sigma} \cdot \vec{W}^\mu \phi\right) - V(\phi) - \frac{1}{4}\vec{W}_{\mu\nu} \cdot \vec{W}^{\mu\nu}, \tag{1.29}$$

$V(\phi)$ being the Higgs potential defined in Eq. 1.22 and $W_{\mu\nu}$ as in Eq. 1.17. As we have seen several times already we need to choose $\mu^2 < 0$ and $\lambda > 0$ in order to achieve spontaneous symmetry breaking. The potential in Eq. 1.22 has its minimum value of $|\phi|$ for

$$\phi^\dagger \phi \equiv \frac{1}{2}\left(\phi_1^2 + \phi_2^2 + \phi_3^2 + \phi_4^2\right) = -\frac{\mu^2}{2\lambda}.$$

[7] BEH stands for Brout-Englert-Higgs. The mechanism is also called simply the Higgs mechanism, Englert-Brout-Higgs-Guralnik-Hagen-Kibble mechanism [26], Anderson-Higgs mechanism [27], Higgs-Kibble mechanism by Abdus Salam [28] and ABEGHHK'tH mechanism (for Anderson, Brout, Englert, Guralnik, Hagen, Higgs, Kibble and 't Hooft) by Peter Higgs [28].

Again we must expand $\phi(x)$ about a particular minimum, say

$$\phi_1 = \phi_2 = \phi_4 = 0, \quad \phi_3^2 = -\frac{\mu^2}{\lambda} = v^2,$$

which, substituting into Eq. 1.28, gives

$$\phi_0 = \sqrt{\frac{1}{2}} \begin{pmatrix} 0 \\ v \end{pmatrix}. \tag{1.30}$$

We now apply the BEH mechanism as discussed in the previous Section getting rid of all the unwanted Goldstone bosons. It turns out we can simply insert the expansion

$$\phi = \sqrt{\frac{1}{2}} \begin{pmatrix} 0 \\ v + h(x) \end{pmatrix} \tag{1.31}$$

into the Lagrangian in Eq. 1.29 and obtain the mass terms! For instance, let us have a look at what happens if we insert the ground state, ϕ_0, into the Lagrangian. The relevant term is

$$\begin{aligned} \left(ig\frac{1}{2}\vec{\sigma}\cdot\vec{W}_\mu\phi\right)^\dagger \left(ig\frac{1}{2}\vec{\sigma}\cdot\vec{W}^\mu\phi\right) &= \frac{g^2}{8}\left|\begin{pmatrix} W_\mu^3 & W_\mu^1 - iW_\mu^2 \\ W_\mu^1 - iW_\mu^2 & W_\mu^3 \end{pmatrix}\begin{pmatrix} 0 \\ v \end{pmatrix}\right|^2 \\ &= \frac{g^2v^2}{8}\left[W_\mu^1 W^{1\,\mu} + W_\mu^2 W^{2\,\mu} + W_\mu^3 W^{3\,\mu}\right]. \end{aligned}$$

which contains mass terms of type $\frac{1}{2}m_W^2 W_\mu W^\mu$ for the bosons with $m_W = \frac{1}{2}gv$. We have constructed a Lagrangian containing three massive gauge fields and one massive scalar h. The Goldstone bosons are "gauged away" and three of the four degrees of freedom of the scalar doublet field go into the longitudinal polarizations of the massive vector bosons. The last degree of freedom appears as an additional neutral scalar boson. This is yet another example of the BEH mechanism.

1.5 The Masses of The Gauge Bosons

Now we have all the tools to formulate the BEH mechanism so that the $W^\pm$ and Z become massive and the photon, A, remains massless. We need to add an $\mathrm{SU}(2)_L\times\mathrm{U}(1)_Y$ gauge invariant Lagrangian for the scalar field, ϕ, in Eq. 1.28. Based on Eq. 1.16 we construct the Lagrangian

$$\mathscr{L} = \left|\left(\partial_\mu - ig\frac{1}{2}\vec{\sigma}\cdot\vec{W}_\mu - ig'\frac{Y}{2}B_\mu\right)\phi\right|^2 - V(\phi) \tag{1.32}$$

where $|...|^2 = (...)^\dagger(...)$. Again we chose the potential, $V(\phi)$, as in Eq. 1.22 and require $\lambda > 0$ and $\mu^2 < 0$ to get spontaneous symmetry breaking. Now we want the photon to remain massless. This is in fact why we in the beginning choose the ϕ to be an isospin doublet of complex scalar fields with weak hypercharge, $Y = 1$. If the vacuum expectation

value of the ground state, ϕ_0, in Eq. 1.30, is kept invariant by some subgroup of gauge transformations the gauge bosons associated to this group will remain massless. The choice of ϕ_0 with $T = \frac{1}{2}$, $T_3 = -\frac{1}{2}$ and $Y = 1$ breaks the $\mathrm{SU}(2)_L \times \mathrm{U}(1)_Y$ gauge symmetry, but since ϕ_0, according to the formula in Eq. 1.2, has $Q = 0$ it remains unbroken under the U(1) gauge symmetry and the photon therefore remains massless. Let us see how to get the masses of the W and Z bosons. The relevant term in the Lagrangian, Eq. 1.32, is

$$\begin{aligned}
&\left| \left(-ig\frac{1}{2}\vec{\sigma}\cdot\vec{W}_\mu - ig'\frac{1}{2}B_\mu \right)\phi \right|^2 \\
&= \frac{1}{8}\left| \begin{pmatrix} gW_\mu^3 + g'B_\mu & g(W_\mu^1 - iW_\mu^2) \\ g(W_\mu^1 - iW_\mu^2) & -gW_\mu^3 + g'B_\mu \end{pmatrix} \begin{pmatrix} 0 \\ v \end{pmatrix} \right|^2 \\
&= \frac{1}{8}v^2 g^2 \left(W_\mu^1 W^{1\,\mu} + W_\mu^2 W^{2\,\mu} \right) + \frac{1}{8}v^2 \left(g'B_\mu - gW_\mu^3 \right)\left(g'B^\mu - gW^{3\,\mu} \right) \\
&= \left(\frac{1}{2}vg \right)^2 W_\mu^+ W^{-\,\mu} + \frac{1}{8}v^2 \begin{pmatrix} W_\mu^3 & B_\mu \end{pmatrix} \begin{pmatrix} g^2 & -gg' \\ -gg' & g'^2 \end{pmatrix} \begin{pmatrix} W^{3\,\mu} \\ B^\mu \end{pmatrix},
\end{aligned}$$

where we have used the expression for the physical W boson in Eq. 1.12. The first term contains a mass term for the W boson, $M_W^2 W^+ W^-$ where $M_W = \frac{1}{2}vg$. To get the masses of the Z and the photon we look at the second term

$$\frac{1}{8}v^2 \left(g^2 W_\mu^3 W^{3\,\mu} - 2gg' W_\mu^3 B^\mu + g'^2 B_\mu^2 \right) = \frac{1}{8}v^2 \left(gW_\mu^3 - g'B_\mu \right)^2 + 0 \left(g'W_\mu^3 - gB_\mu \right)^2 . \tag{1.33}$$

From the relation in Eq. 1.15 we know that $\frac{g'}{g} = \tan\theta_W$, using Eq. 1.14 and 1.13 we can express the physical fields as

$$\begin{aligned}
A_\mu &= \frac{g'W_\mu^3 - gB_\mu}{\sqrt{g^2 + g'^2}} \\
Z_\mu &= \frac{gW_\mu^3 - g'B_\mu}{\sqrt{g^2 + g'^2}}.
\end{aligned}$$

Looking at Eq. 1.33 the mass terms, $\frac{1}{2}M_Z^2 Z_\mu^2$ and $\frac{1}{2}M_A^2 A_\mu^2$, for the Z and the photon respectively, becomes

$$\begin{aligned}
M_A &= 0 \\
M_Z &= \frac{1}{2}\sqrt{g^2 + g'^2},
\end{aligned}$$

so the photon remains massless while the Z becomes massive, just as we wanted!

1.6 Fermion Masses

Fermions are also found experimentally to have non-zero masses. As already discussed, including mass terms of type $-m\bar{f}f$ in the Lagrangian would ruin gauge invariance.

Luckily we can use the Higgs field, as discussed in the previous Sections, to also generate masses of the fermions. Let us look at how to introduce masses for the down-type fermions by using the same isospin doublet that generated W and Z masses. We start with an $\mathrm{SU}(2)_L \times \mathrm{U}(1)_Y$ gauge invariant Lagrangian density of the form

$$\mathscr{L}_{m_{f(down)}} = -c_f \left(\bar{\chi}_L \phi \psi_R + \bar{\psi}_R \phi \chi_L \right), \tag{1.34}$$

where c_f is a free coupling parameter and ψ_R and χ_L represent the right-handed isospin singlets and left-handed isospin doublets respectively, listed in Table 1.2. We again spontaneously break the symmetry and substitute Eq. 1.31 into 1.34 and the Lagrangian becomes

$$\mathscr{L}'_{m_{f(down)}} = -\frac{c_f v}{\sqrt{2}} \left(\bar{f}_L \psi_R + \bar{\psi}_R f_L \right) - \frac{c_f}{\sqrt{2}} \left(\bar{f}_L \psi_R + \bar{\psi}_R f_L \right) h,$$

where f_L is the lower entry of the $\mathrm{SU}(2)_L$ doublet. Identifying $c_f v/\sqrt{2}$ in front of the $\left(\bar{f}_L \psi_R + \bar{\psi}_R f_L \right)$ as a mass term of the fermion, m_f, gives

$$c_f = \frac{m_f \sqrt{2}}{v}. \tag{1.35}$$

Applying this yields

$$\mathscr{L}'_{m_{f(down)}} = -m_f \bar{f} f - \frac{m_f}{v} \bar{f} f h,$$

using $\bar{f}_L \psi_R + \bar{\psi}_R f_L = \bar{f} f$. The first term above shows that after the spontaneous symmetry breaking we get one mass term for each fermion. In addition we get a term specifying the coupling between the fermion and the Higgs field, proportional to the fermion mass, m_f. The argument is exactly the same when generating masses for the up-type fermions only that the Higgs doublet is replaced by $\phi_c = -i\sigma_2 \phi^*$, which transforms identically to ϕ. This simple picture is slightly more complicated in the quark sector since the weak interaction operates on the mixed quark states as discussed in Section 1.3.2.1. It should be noted however that, since the value of c_f is not known, the BEH mechanism does not predict the masses of the fermions, as it did for the gauge bosons. The fermion mass terms are rather put in by hand in a gauge invariant way, using the same mechanism that predicted gauge boson masses, and do not come as a direct consequence of the spontaneous symmetry breaking.

1.7 The Higgs Mass

Last but not least the Higgs boson itself also has a mass, but its exact value is not predicted by the theory. From the Higgs potential in Eq. 1.22 we get the mass term, $\frac{1}{2} m_h^2 \phi^2$, with $m_h = \sqrt{2\lambda v^2}$. The v parameter is known from the masses of the W and Z through

$$M_W = \frac{1}{2} v g$$
$$M_Z = \frac{1}{2} v \sqrt{g^2 + g'^2},$$

and calculated to be $v \approx 246$ GeV. The value of λ is unknown in the theory, however, and the strongest constraints on the Higgs mass currently come from various experimental results as interpreted within the framework of the SM.[8]

1.8 The Full Standard Model Lagrangian

Putting together all the pieces of this Chapter we get the full SM Lagrangian describing the interactions and masses of all the elementary particles in nature with χ_L being a left-handed isospin doublet and ψ_R a right-handed isospin singlet.

$\mathscr{L}_{SM} =$	
$-\frac{1}{4}\vec{W}_{\mu\nu} \cdot \vec{W}^{\mu\nu} - \frac{1}{4} B_{\mu\nu} \cdot B^{\mu\nu}$	kinetic energies of W, Z and γ and the self-interactions of W, Z
$+\bar{\chi}_L \gamma^\mu \left(i\partial_\mu - g\frac{1}{2}\vec{\sigma} \cdot \vec{W}_\mu - g'\frac{Y}{2} B_\mu \right) \chi_L$	kinetic energy of the **left** handed fermions and their interactions with W, Z and γ
$+\bar{\psi}_R \gamma^\mu \left(i\partial_\mu - g'\frac{Y}{2} B_\mu \right) \psi_R$	kinetic energy of the **right** handed fermions and their interactions with Z and γ
$+ \left\lvert \left(i\partial_\mu - g\frac{1}{2}\vec{\sigma} \cdot \vec{W}_\mu - g'\frac{Y}{2} B_\mu \right) \phi \right\rvert^2 - V(\phi)$	masses and couplings of W, Z, γ and Higgs
$-\left(c_f \bar{\chi}_L \phi \psi_R + G'_f \bar{\chi}_L \phi_c \psi_R + \text{H.c.} \right)$	fermion masses and couplings to the Higgs

1.9 Problems with the Standard Model

The SM has been shown to describe to high accuracy all present results from precision measurements at high and low energies, spanning many orders of magnitude, including the tests at the level of quantum corrections [24]. Nevertheless, in spite of its impressive success, the SM is not regarded as a ultimate theory. It is rather considered as an effective theory, which works well up to energies around the electroweak energy scale of order v. The presence of the nineteen free parameters (particle masses, coupling constants, parameters of the CKM matrix, weak mixing angle, Higgs vacuum expectation value, etc.) which seemingly have nothing to do with the symmetries of the SM, may be regarded as one of the limitations of the theory. All these parameters can be measured using experiments and much effort has been put into doing so the last decades. Despite this, it is somewhat unsatisfactory to have a theory that contains many parameters that can only be determined experimentally. A more elegant theory would predict most of these

[8] Unless the new boson observed by ATLAS [9] and CMS [10] is the long-awaited SM Higgs, in which case its mass is around 126 GeV.

parameters. Another limitation, and probably most indispensable, is that the SM does not accommodate gravity.

The choice of the three symmetry groups $SU(3)_C \times SU(2)_L \times U(1)_Y$ discussed in the previous Sections is not motivated by any underlying fundamental theory. It gives a good match between experimental data and theory, and by construction, rather than consequence, it describes the three generations of fermions observed. Another issue within the SM is the unification of the three coupling constants α_1, α_2 and α_3 related to the $SU(3)_C$, $SU(2)_L$ and $U(1)_Y$ gauge groups respectively. With the measured value of $\sin^2\theta_W = 0.23116 \pm 0.000052$ [24] at the electroweak energy scale, the three coupling constants do not converge to a common unifying value at high energy when calculating the differential equations that describes their energy dependence, known as the Renormalization Group Equations (RGE). The evolution of the couplings as a function of energy is shown in Figure 1.3, based on current measurements. It is believed that some new physics should be present at a grand unification scale of order 10^{15} GeV from which there would be one coupling constant. This does not happen assuming SM only, however. Recent

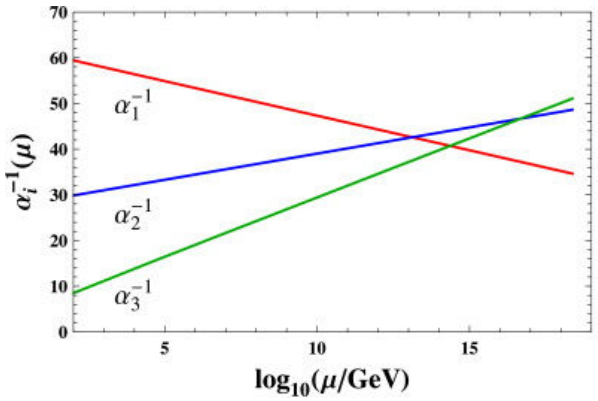

Figure 1.3: The running of the three gauge couplings α_1, α_2 and α_3 as a function of the energy in the SM. From Ref. [29]

cosmological studies have also shown that only 4% of the Universe consists of the well-known baryonic matter (quarks and leptons). There is strong evidence that there must exist a weakly interacting massive particle (WIMP) that does not couple (or at least very weakly) with ordinary matter. In the SM the neutrinos could serve as a candidate for dark matter, but they are found to be too light to account for all the missing mass. It seems like we therefore need a new theory which can predict the existence of such a particle in order be able to explain dark matter, which is responsible for about 25% of the total mass of the Universe. The rest is governed by the so-called dark energy which explains why the Universe's expansion accelerates.

During the last 30 years theorists have worked hard on constructing theoretical models which could give explanations to the experimentally determined values of the SM parameters and conform quantum physics with gravity. For an experimental researcher it is important that such new theories also predict departures from the SM. One such implication, which is one of the key subjects of the ATLAS experimental program [30, 31], is the prospect for supersymmetry (SUSY) to be a true symmetry of Nature and, as a consequence, the existence of supersymmetric particles.

SUSY in all its beauty is able to accommodate many of the issues raised above, but maybe the most intriguing feature of a SUSY theory is that it can explain the hierarchy problem of the SM.

1.9.1 The Hierarchy Problem

As was discussed in Section 1.7 the SM contains a parameter with the dimension of energy specifying the vacuum expectation value of the Higgs field, $v \approx 246$ GeV. This parameter sets the masses of many of the particles in the theory, among them the masses of the W and Higgs bosons given by

$$M_W = \frac{gv}{2} \text{ and } M_H = v\sqrt{2\lambda},$$

where g is the $\mathrm{SU}(2)_L$ weak gauge coupling constant and λ the strength of the Higgs self-interaction. These expressions give the mass at tree level (i.e. no loop correction) so the obvious question is; what happens if we include loops? When adding the higher order corrections to the Higgs boson mass we need to include all fermions and bosons that couple to the Higgs and contributes via loops like in Figure 1.4. Since the SM is not

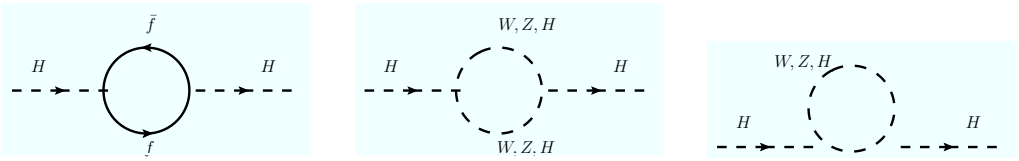

(a) Fermions (b) Bosons (c) Bosons

Figure 1.4: Loop corrections to the Higgs boson mass from fermion loops (a) and boson loops (b,c).

believed to be valid at all energy scales one needs to introduce a cut-off indicating the scale where new physics becomes important. At the very least, for instance, there must be some kind of new physics at the scale when quantum gravity becomes important (i.e. around the Planck scale, $M_P = 1/\sqrt{G_N} \simeq 1.2 \cdot 10^{19}$ GeV). Using an ultra-violet cut-off, Λ_{UV}, the correction to the Higgs boson mass from a loop like in Figure 1.4a including a fermion with repetition number N_f, becomes [32]

$$\Delta m_{H,f}^2 = N_f \frac{G_f^2}{8\pi^2}\left[-\Lambda_{UV}^2 + 6m_f^2 \ln\left(\frac{\Lambda_{UV}}{m_f}\right) - 2m_f^2\right] + \mathcal{O}(\frac{1}{\Lambda_{UV}^2}), \tag{1.36}$$

where G_f is the fermion Yukawa coupling defined in Eq. 1.35. The leading term clearly diverges quadratically, the higher Λ_{UV} the higher Higgs boson mass correction squared. This divergence could be removed by renormalization, but the other terms would still give large corrections if there exists new heavy particles below the Planck scale. Altogether, the Higgs boson mass is extremely sensitive to the heaviest particles to which it couples. Let us assume that there also exists a number of scalars, N_S, with masses m_S and with trilinear and quadrilinear couplings to the Higgs boson through the loops in Figure 1.5. Let these couplings be given by $v\lambda_S$ and λ_S respectively. This would contribute to the Higgs boson mass corrections by [32]

$$\begin{aligned}\Delta m_{H,S}^2 =& \frac{\lambda_S N_S}{16\pi^2}\left[\Lambda_{UV}^2 + 2m_S^2 \ln\left(\frac{\Lambda_{UV}}{m_S}\right)\right] \\ &- \frac{\lambda_S^2 N_S}{16\pi^2} v^2 \left[-1 + 2\ln\left(\frac{\Lambda_{UV}}{m_S}\right)\right] + \mathcal{O}(\frac{1}{\Lambda_{UV}^2}).\end{aligned} \tag{1.37}$$

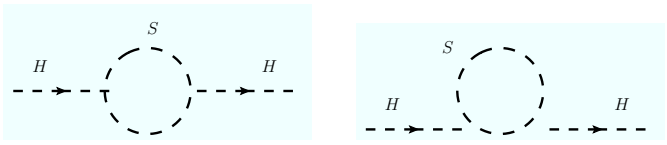

(a) Trilinear (b) Quadrilinear

Figure 1.5: Loop corrections to the Higgs boson mass from scalar loops.

Again the quadratic divergences are present, but if we assume that every fermion of the SM is accompanied by two scalars ($N_S = 2N_f$) with the couplings in such a way that $-\lambda_S = G_f^2$, the quadratic divergences cancel exactly. It might seem speculative to require the couplings to be so tightly related, but this can be achieved by imposing a new symmetry to the SM Lagrangian, as we will see in the next Section. If the mass differences between the scalars and the fermions are small, the total correction to the Higgs boson mass is reduced to [32]

$$\Delta m_{H,tot}^2 \simeq \frac{G_f^2 N_f}{4\pi^2}\left[(m_f^2 - m_S^2)\ln\left(\frac{\Lambda_{UV}}{m_s}\right) + 3m_f^2 \ln\left(\frac{m_S}{m_f}\right)\right] + \mathcal{O}(\frac{1}{\Lambda_{UV}^2}). \tag{1.38}$$

The quadratic divergences are canceled, and we are only left with the logarithmic divergence in the cut-off. If this imposed symmetry is an exact symmetry even the logarithmic divergences will disappear in Eq. 1.38. There is no evidence that such particles exist, however, and SUSY, which introduces such scalar particles, must therefore be a broken symmetry. On the other hand, if the symmetry is badly broken and the masses of the new scalars are much larger than the fermions the hierarchy problem would be reintroduced because the term $(m_f^2 - m_S^2)\ln(\Lambda_{UV}/m_s)$ will become large. Therefore, to keep the Higgs boson mass in the range of the electroweak symmetry breaking scale, $M_H = \mathcal{O}(100\text{ GeV})$, we need the mass difference between the SM particles and the new sparticles to not be much larger than the TeV scale, $m_S = \mathcal{O}(1\text{ TeV})$.

The above discussion only took into account the contribution from fermion loops, but one can do the same exercise including loops with W, Z and Higgs as in Figure 1.4b and c. The quadratic divergences from these loops are canceled by introducing fermionic partners to the W, Z and Higgs bosons, and adjust their couplings in a similar way as was done for the scalars above. All the quadratically divergent corrections to the Higgs boson mass would then be canceled.

1.10 Supersymmetry (SUSY)

The discussion in the previous Section suggests that a new symmetry, relating fermions and bosons, is required in order to solve the hierarchy problem of the SM. SUSY is such a symmetry, which states that each fermion has a scalar boson superpartner and each boson a fermionic superpartner. In other words, SUSY is a symmetry between particles whose spins differ by $\frac{1}{2}$. The rest of this Chapter is devoted to an introduction of SUSY. For a more thoroughly grounding to SUSY the reader is referred to Refs. [33, 34, 35].

1.10.1 Supermultiplets

A SUSY transformation turns a fermion state into a boson state and vice versa.

$$\hat{Q}|fermion\rangle = Q|boson\rangle \quad \text{and} \quad \hat{Q}|boson\rangle = Q|fermion\rangle$$

The Q operator responsible for these transformations clearly needs to carry spin $\frac{1}{2}$. The fermions and their bosonic counterparts are grouped together forming supermultiplets. Since Q commutes with the gauge transformations, all members of a supermultiplet are in the same representation of the gauge group and therefore have identical charge, weak isospin and colour. The only difference between the members of a supermultiplet is the spin.

The left- and right-handed fermions of the SM behave differently under weak interactions and they must therefore belong to different supermultiplets, which means they also need to have separate scalar partners. The supermultiplets containing a SM fermion and two scalars are therefore known as chiral supermultiplets. The spin-0 superpartners of the fermions are called **s**fermions (even though they are bosons) and are denoted in the same way as their fermionic counterpart, but with an additional tilde ($\sim$). For instance the superpartner of the electron is called **s**electron ($\tilde{e}$) and the superpartner of the top quark **s**top ($\tilde{t}$). On should, however, keep in mind that the left- and right-handed states of the SM particles in fact have separate scalar partners, being two different sparticles (e.g. $\tilde{e}_{\mathrm{L}}$and $\tilde{e}_{\mathrm{R}}$are the two superpartners of the left- and right-handed chirality states of the electron, respectively).

The Higgs boson is a complex scalar field and also resides in chiral supermultiplets with its fermionic counterparts, the higgs**ino**s.

The SM gauge bosons correspond to spin-1 vector fields and have fermionic superpartners called gaug**ino**s. Together they form vector supermultiplets. The superpartners of the $W^{\pm}$ and W^0 gauge bosons are the w**ino**s ($\tilde{W^{\pm}}$, $\tilde{W^0}$), the superpartner of the B boson is the b**ino** ($\tilde{B}$) and finally the gluon has a superpartner named glu**ino** ($\tilde{g}$).

1.10.2 The Minimal Supersymmetric Standard Model

The Minimal Supersymmetric Standard Model (MSSM) is constructed by extending the SM, adding a minimum of new particles when forming supermultiplets. Using Table 1.2 and knowing that the supermultiplets need to transform similarly under the gauge transformations makes it trivial to construct the supermultiplets of the MSSM. The only difficulty is the Higgs sector, where one could think of constructing a supermultiplet combining the Higgs scalar and the left-handed SU(2) doublets, since they transform similarly under the gauge transformations. This is not possible however, mainly because of the difference in lepton number between the Higgs boson and the leptons. The Higgs boson needs therefore to be accompanied by spin-$\frac{1}{2}$ higgs**ino**s to form a supermultiplet. The details of the MSSM Higgs sector will be discussed in more detail in Section 1.10.2.1. All the chiral supermultiplets in the MSSM for the first generation of fermions, with their gauge transformation properties and weak hypercharge, Y, are summarized in Table 1.3. The table can easily be extended to cover the two other generations (ignoring any possible mixing, as

will be discussed below). By convention, the chiral supermultiplets are expressed in terms of left-handed spinors only, and the Hermitian conjugate of the right-handed singlets are therefore used in Table 1.2.[9] In the notation, L and R subscripts on the scalars refer to the handedness of their SM partner, since the superpartners themselves carry spin 0.

Names	Notation	spin-0	spin$-\frac{1}{2}$	SU(3)$_C$	SU(2)$_L$	Y
Sleptons/Leptons	$\hat{L}$	$(\tilde{\nu}\ \tilde{e}_{\rm L})$	$(\nu\ e_L)$	**1**	**2**	-1
	$\hat{E}^c$	$\tilde{e}^*_{\rm R}$	$e^\dagger_R$	**1**	**1**	2
Squarks/Quarks	Q	$\left(\tilde{u}_{\rm L}\ \tilde{d}_{\rm L}\right)$	$(u_L\ d_L)$	**3**	**2**	$\frac{1}{3}$
	$\hat{U}^c$	$\tilde{u}^*_{\rm R}$	$u^\dagger_R$	$\bar{\mathbf{3}}$	**1**	$-\frac{4}{3}$
	$\hat{D}^c$	$\tilde{d}^*_{\rm R}$	$d^\dagger_R$	$\bar{\mathbf{3}}$	**1**	$\frac{2}{3}$
Higgs/Higgsinos	$\hat{H}_u$	$(h^+_u\ h^0_u)$	$\left(\tilde{h}^+_u\ \tilde{h}^0_u\right)$	**1**	**2**	1
	$\hat{H}_d$	$\left(h^0_d\ h^-_d\right)$	$\left(\tilde{h}^0_d\ \tilde{h}^-_d\right)$	**1**	$\mathbf{2}^*$	-1

Table 1.3: The chiral supermultiplets of the MSSM. The supermultiplets of the fermions are shown for the first generation only, but the Table can easily be extended to cover the two other generations.

The vector supermultiplets of the MSSM are constructed in the same way as the chiral supermultiplets and are shown in Table 1.4. As in the SM the **bino** and the neutral **wino** mix after electroweak symmetry breaking to form the **zino** ($\tilde{Z}$) and the **photino** ($\tilde{\gamma}$).

Names	Notation	spin$-\frac{1}{2}$	spin-1	SU(3)$_C$	SU(2)$_L$	Y
gluino/gluon	$\hat{G}$	$\tilde{g}$	g	**8**	**1**	0
winos/W boson	$\hat{W}$	$\tilde{W}^\pm$, $\tilde{W}^0$	$W^\pm$,W^0	**1**	**3**	0
bino/B boson	$\hat{B}$	$\tilde{B}$	B	**1**	**1**	0

Table 1.4: The vector supermultiplets of the MSSM with their gauge transformation properties and weak hypercharge, Y.

1.10.2.1 The Higgs Sector

In the SM the Higgs field consists of one left-handed scalar doublet given in Eq. 1.28. In the MSSM this doublet is promoted to a doublet of left-handed superfields

$$\Phi(x) = \begin{pmatrix} \phi_a(x) \\ \phi_b(x) \end{pmatrix} \rightarrow \hat{H}_u = \begin{pmatrix} h^+_u \\ h^0_u \end{pmatrix}.$$

[9] The Hermitian conjugate of any right-handed Weyl spinor is a left-handed Weyl spinor and vice versa.

This doublet carries weak hypercharge $Y = 1$, and gives mass to the up-type fermions. In the SM the right-handed charge conjugate of the Higgs field $\phi_c = -i\sigma_2\phi^*$ carries weak hypercharge $Y = -1$ and can give mass to the down-type fermions. Since the superpotential should be invariant under SUSY and gauge transformations it can only involve superfields, and not the conjugate superfields [32]. A second doublet is therefore needed

$$\hat{H}_d = \begin{pmatrix} h_d^0 \\ h_d^- \end{pmatrix},$$

carrying the same weak hypercharge as ϕ_c (i.e. $Y = -1$). This doublet can then give masses to the down-type fermions. Another reason for having two Higgs doublets in SUSY is to ensure that the anomalies originating from triangular fermionic loops involving axial-vector current coupling are not introduced. These anomalies would spoil the renormalizability of the theory and are not present in the SM because the sum of the hypercharges of all fermions in each generation cancel exactly. Applying SUSY, additional fermions are introduced through the higgsinos, and thus would contribute to the triangular loops [32]. By having two Higgs doublets with opposite hypercharge, however, the sum of the hypercharges would cancel, ensuring an anomaly-free theory. Including both Higgs doublets the potential becomes [32]

$$\begin{aligned} V_{Higgs} &= (\mu^2 + m_{H_u}^2)(|h_u^+|^2 + |h_u^0|^2) + (\mu^2 + m_{H_d}^2)(|h_d^0|^2 + |h_d^-|^2) \\ &\quad - [B\mu(h_u^+ h_d^- - h_u^0 h_d^0) + H.c.] \\ &\quad + \frac{1}{8}(g^2 + g'^2)(|h_d^0|^2 + |h_d^-|^2 - |h_u^+|^2 - |h_u^0|^2)^2 + \frac{1}{2}g^2|h_u^+ h_d^{0*} + h_u^0 h_d^{-*}|^2. \end{aligned} \tag{1.39}$$

The B-term is a scalar squared mass term coming from the soft SUSY breaking, to be discussed in Section 1.10.2.4. As in the SM we have the freedom to make $\mathrm{SU}(2)_L$ gauge transformations and can therefore rotate away possible vacuum expectation values for one of the weak isospin components of one of the scalar fields. We choose $\langle h_d^- \rangle = 0$ at the minimum of the potential. This condition, along with $\partial V_{Higgs}/\partial h_d^- = 0$, implies that $\langle h_u^+ \rangle = 0$. Applying $\langle h_u^+ \rangle = \langle h_d^- \rangle = 0$ in Eq. 1.39, we are left with

$$\begin{aligned} V_{Higgs} &= (\mu^2 + m_{H_u}^2)|h_u^0|^2 + (\mu^2 + m_{H_d}^2)|h_d^0|^2 + [B\mu(h_u^0 h_d^0) + H.c.] \\ &\quad + \frac{1}{8}(g^2 + g'^2)(|h_d^0|^2 - |h_u^0|^2)^2. \end{aligned} \tag{1.40}$$

Minimizing this potential, by requiring $\partial V_{Higgs}/\partial|h_u^0| = 0$ and $\partial V_{Higgs}/\partial|h_d^0| = 0$, gives two conditions necessary for spontaneous breaking of electroweak symmetry

$$\begin{aligned} B &= \frac{\left(m_{H_d}^2 - m_{H_u}^2\right)\tan 2\beta + M_Z^2 \sin 2\beta}{2\mu} \\ \mu^2 &= \frac{m_{H_u}^2 \sin^2\beta - m_{H_d}^2 \cos^2\beta}{\cos 2\beta} - \frac{M_Z^2}{2}. \end{aligned} \tag{1.41}$$

Here $\tan\beta$ is defined as the ratio of the vacuum expectation values, v_u and v_d, of the up- and down-part of the Higgs field respectively

$$\tan\beta \equiv \frac{v_u}{v_d}. \tag{1.42}$$

This parameter will become important when phenomenological consequences of the various supersymmetric models are discussed.

The Higgs Bosons

In the SM, with just one complex Higgs doublet, three of the four degrees of freedom gave masses to the three vector bosons, the $W^{\pm}$ and Z. The last degree of freedom gave rise to the Higgs boson. However, since the MSSM Higgs sector consist of two Higgs doublets, there are eight degrees of freedom. Therefore, in addition to give mass to the $W^{\pm}$ and Z bosons, three neutral spin zero bosons and a pair of charged scalars appear:

h^0	lightest Higgs
H^0	heavy CP-even Higgs
A^0	heavy CP-odd Higgs
$H^{\pm}$	charged Higgs.

The masses of the different Higgs bosons at tree-level are given by [32]

$$\begin{aligned} M^2_{H^{\pm}} &= B\mu\left(\cot\beta + \tan\beta\right) + M^2_W \\ M^2_{A^0} &= B\mu\left(\cot\beta + \tan\beta\right) \\ M^2_{h,H^0} &= \frac{1}{2}\left[\left(M^2_A + M^2_Z\right) \mp \sqrt{\left(M^2_A + M^2_Z\right)^2 - 4M^2_A M^2_Z \cos^2 2\beta}\right]. \end{aligned}$$

This states that $H^{\pm}$ is heavier than A^0 and $M_{H^0} > M_h$, thus the lightest Higgs is always h. The mass of h is predicted to be less than about 135 GeV [32]. Once we know the mass of A and $\tan\beta$ we can calculate all the other parameters in the Higgs sector except for the sign of μ^2. This means that by choosing/measuring the value of $\tan\beta$ and M_A, we can obtain the whole MSSM Higgs boson mass spectrum.

1.10.2.2 Mass Eigenstates

The spontaneous breaking of the $\mathrm{SU}(2)_L \times \mathrm{U}(1)_Y$ symmetry implies that states with the same quantum numbers will mix. This means that gauginos and higgsinos can not be the physical particles with definite mass, unless the mixing angle is found to be exactly 0. The neutral **higgsinos** mix with the neutral **wino** and **bino** to form four neutral gaugino mass eigenstates, known as the **neutralinos** ($\tilde{\chi}^0_1$,$\tilde{\chi}^0_2$,$\tilde{\chi}^0_3$,$\tilde{\chi}^0_4$). Also, the charged **higgsinos** mix with the charged **wino** to form two charged gauginos, named **charginos** ($\tilde{\chi}^{\pm}_1$,$\tilde{\chi}^{\pm}_2$). Since the $SU(3)_C$ symmetry is not broken the **gluino** does not mix and is therefore a mass eigenstate. The A^0 does not mix either because it is the only CP-odd particle in the theory. The first two generations sfermions have relatively small Yukawa couplings, thus their masses are much more similar than the masses of the third generation sfermions, which have significantly larger Yukawa couplings. The mixing of the first two generations sfermions is therefore often neglected. For the **s**quarks the $\tilde{t}_{\mathrm{L}}$ and $\tilde{t}_{\mathrm{R}}$ mix to form $\tilde{t}_1$ and $\tilde{t}_2$ mass eigenstates. Equivalently $\tilde{b}_{\mathrm{L}}$ and $\tilde{b}_{\mathrm{R}}$ mix to form $\tilde{b}_1$ and $\tilde{b}_2$. For the **s**leptons the $\tilde{\tau}_{\mathrm{L}}$ and $\tilde{\tau}_{\mathrm{R}}$ mix to form $\tilde{\tau}_1$ and $\tilde{\tau}_2$ mass eigenstates.

1.10.2.3 The Superpotential

Now all the ingredients are in place to construct an MSSM superpotential [34]

$$W_{MSSM} = \hat{U}^c \mathbf{y_u} \hat{Q} \hat{H}_u - \hat{D}^c \mathbf{y_d} \hat{Q} \hat{H}_d - \hat{E}^c \mathbf{y_e} \hat{L} \hat{H}_d + \mu \hat{H}_u \hat{H}_d. \tag{1.43}$$

The $\hat{U}^c$, $\hat{Q}$, $\hat{H}_u$, $\hat{D}^c$, $\hat{H}_d$, $\hat{E}^c$ and $\hat{L}$ are the superfields corresponding to the supermultiplets in Table 1.3 and 1.4. The $\mathbf{y_u}$, $\mathbf{y_d}$ and $\mathbf{y_e}$ are the 3×3 matrices in generation space containing the Yukawa couplings. In order to simplify the notation all the sums over the colour, weak isospin and family indices are neglected in Eq. 1.43.[10] The μ parameter is the one entering the Higgs potential in Eq. 1.39.

The superpotential in Eq. 1.43 is the absolute minimal one needs to construct a phenomenologically viable model. There are of course other terms one in principle could add to the superpotential that are still gauge invariant. The most general gauge invariant and renormalizable superpotential would, in addition to the terms in Eq. 1.43, include [34]

$$W_{\Delta L=1} = \frac{1}{2} \lambda^{ijk} \hat{L}_i \hat{L}_j \hat{E}^c_k + \lambda'^{ijk} \hat{L}_i \hat{Q}_j \hat{D}^c_k + \mu'^i \hat{L}_i \hat{H}_u \tag{1.44}$$

$$W_{\Delta B=1} = \frac{1}{2} \lambda''^{ijk} \hat{U}^c_i \hat{D}^c_j \hat{D}^c_k. \tag{1.45}$$

The $i, j, k \in \{1,2,3\}$ are now the index over generations. The $\hat{Q}_i$, $\hat{U}^c_i$ and $\hat{D}^c_i$ are the only parts carrying nonzero baryon number with $B = \frac{1}{3}, -\frac{1}{3}$ and $-\frac{1}{3}$ respectively. On the other hand L_i and $\hat{E}^c_i$ are the only parts carrying nonzero lepton number with $L = 1, -1$ respectively. It follows from this that the two expressions in Eq. 1.44 and 1.45 must violate lepton and baryon number respectively with 1 unit. Baryon- and lepton-number violating processes have never been seen experimentally, and there are strong constraints on this, especially from the non-observation of proton decays. It is therefore important to suppress these terms in the MSSM. In the SM such terms are absent because there exists no possible renormalizable terms which can be included in the Lagrangian that violate B or L. In order to fix this in the MSSM one can introduce a new symmetry called R-parity, defined as

$$P_R = (-1)^{3(B-L)+2s},$$

where B and L are the baryon and lepton numbers and s is the spin. It is important to note that R-parity is a multiplicative quantum number. From this it follows that all SM particles and the Higgs bosons have R-parity of $+1$ while all squarks, sleptons, gauginos and higgsinos have R-parity -1. First, this symmetry has the wanted consequence that the terms in Eq. 1.44 and 1.45 no longer are allowed in the superpotential. Second, this leads to several very interesting phenomenological consequences since every interaction vertex now needs to contain an even number of supersymmetric particles:

- the lightest supersymmetric particle (LSP) must be stable since there are no $P_R = -1$ states available for it to decay to. If it is neutral and only interacts weakly, it serves as a very good dark matter candidate.

[10] Including all the indices the $\hat{U}^c \mathbf{y_u} \hat{Q} \hat{H}_u$ would be $\hat{U}^{c\,ia} (\mathbf{y_u})^j_i \hat{Q}_{j\alpha a} (\hat{H}_u)_\beta \epsilon^{\alpha\beta}$ where $i \in \{1,2,3\}$ is a generation index, $a \in \{1,2,3\}$ is a colour index and $\{\alpha, \beta\} \in \{1,2\}$ are the weak isospin indices.

- in collider experiments, sparticles can only be produced in even numbers and each of them must eventually decay into a state that contains an odd number of LSPs. This means that every supersymmetric event must contain an even number of LSPs (i.e. at least two).

There exists also supersymmetric models where the R-parity is not conserved. Some of these models suggest that baryon number can only be violated in multiples of 3 units. This would allow the LSP to decay, but still forbid proton decays (violates B with 1 unit) or neutron-antineutron oscillations (violates B with 2 units). Another idea is that R-parity is an exact symmetry of the underlying superpotential, but happens to be broken by a scalar with $P_R = 1$. Introducing a new gauge-singlet chiral supermultiplet, where the scalar component gets a large vacuum expectation value, can then introduce L- and/or B-violating terms in the low-energy effective superpotential. A more detailed discussion of R-parity violating (RPV) SUSY can be found in [34]. In any case, if R-parity is violated at the energy scale available at LHC, it will necessitate very different search strategies than what is presented in this thesis. For an example of a study on searches for RPV SUSY the reader is referred to a paper published by ATLAS on searches for heavy resonances in the di-lepton final states [36].

1.10.2.4 Soft Supersymmetry Breaking

One of the most intriguing facts about the MSSM is that none of the superpartners are yet discovered. In an unbroken SUSY the superpartners should have masses identical to their SM counterparts. Obviously this can not be the case. For instance **s**leptons or **s**quarks with the same mass and couplings as their lepton or quark counterparts should have already been discovered if they existed. Clearly, SUSY must be a broken symmetry at the energy scale beyond those so far exploited in collider experiments. When constructing a SUSY breaking mechanism we should, however, bear in mind the motivation for introducing a symmetry between fermions and bosons; we want to cancel the quadratic divergences of the Higgs boson mass corrections. In order to preserve this feature the supersymmetric particles should not achieve a mass much larger than 1 TeV after the breaking. Also, the couplings need to stay nearly the same in order to sustain the cancellations in Eq. 1.37. This kind of breaking is therefore referred to as *soft* SUSY breaking, with a parameter $m_{soft} = \mathcal{O}(1\text{ TeV})$ indicating the mass scale of the superpartners. The part of the Lagrangian which governs the soft breaking is generally referred to as the soft SUSY-breaking Lagrangian, $\mathscr{L}_{soft}$, and contains all allowed terms that do not introduce quadratic divergences in the theory. This means in other words all gauge- and Lorentz-invariant terms of dimension two and three.

The SUSY breaking terms in the Lagrangian involve only supersymmetric particles, since the SM particles already acquire their mass through the BEH mechanism of Section 1.4.1. Since no convincing mechanism of SUSY breaking is so far observed, an effective Lagrangian is constructed where all possible supersymmetric mass breaking terms are added. These terms set m_{soft} to an appropriate size as well as conserving the gauge invariance of the theory. In this general form a total of 124 free parameters (including the parameters of the SM) are introduced [33]. Once we understand the mechanism underlying SUSY breaking it will be possible to reduce the number of free parameters drastically, as the 124 free parameters at the electroweak scale are assumed to take on

simplified forms at a given (usually high) energy scale. Until then, theoretical models of the breaking mechanisms based on well-motivated assumptions of physics at high energy scales are constructed. From these models interesting phenomenological scenarios can be constructed.

The underlying SUSY breaking is assumed to be spontaneous. Also, in order to achieve phenomenologically acceptable models, any tree-level approach to a spontaneous SUSY breaking at the TeV scale is ruled out, since this leads to experimentally excluded patterns of MSSM particle masses. Therefore the breaking presumably takes place in a hidden sector. Exactly how the breaking is transmitted to the superpartners is specified in the parameters of $\mathscr{L}_{soft}$. All the parameters in $\mathscr{L}_{soft}$ receive radiative corrections and are therefore scale-dependent, satisfying known RGEs. The communication from the hidden to the visible sector is believed to happen via suppressed interactions involving a third set of fields, the mediator or messenger fields. The result is the effective soft SUSY breaking Lagrangian in the observable sector. In two of the most commonly used models of soft SUSY breaking the transmissions are mediated by either gravitational interactions (SUGRA) or by gauge interactions (GMSB).

Gravity-Mediated Supersymmetry Breaking

Gravity-mediated SUSY breaking, or supergravity (SUGRA), was one of the first models trying to describe the soft SUSY breaking mechanism. Since all particles have gravitational interactions it is quite natural to imagine gravity to be the only interaction shared by both the hidden and observable sectors. The simplest model constructed is known as minimal supergravity (mSUGRA). Within the mSUGRA framework local SUSY is assumed to be spontaneously broken in the hidden sector and mediated to observables by Planck-suppressed non-renormalizable terms (which need to be specified when constructing a model). As we know from Section 1.4 any spontaneous broken symmetry will introduce a massless Goldstone particle. In the supersymmetric case this will be a massless fermion (since the supersymmetry generators are spinors), known as the Goldstino, $\tilde{G}$. The BEH mechanism states that the degree of freedom from this massless particle will become the longitudinal component of a corresponding massive gauge field. In mSUGRA this generates a mass to the gravit**ino** (the superpartner of the graviton), $m_{\tilde{G}} = M_m^2/M_P$ (M_m being the scale of the messenger sector and M_P the Planck mass) [37]. In mSUGRA the general soft SUSY breaking Lagrangian is simplified to only depend on the following five parameters at the GUT scale:

m_0: a common mass for all scalar particles (1.46)

$m_{\frac{1}{2}}$: a common gaugino mass (1.47)

A_0: the trilinear Higgs-fermion-fermion coupling

$\tan\beta$: the ratio of the vacuum expectation value of the up and down Higgs doublets

$sgn(\mu)$: the sign of the higgsino mass parameter.

The complete MSSM particle spectrum can be determined from a given set of the parameters above by using known RGEs as shown in Figure 1.6. The mSUGRA model is very commonly used to produce benchmark points in searches for SUSY, even though the model is believed to be too simple to describe the SUSY actually realized in Nature. Despite

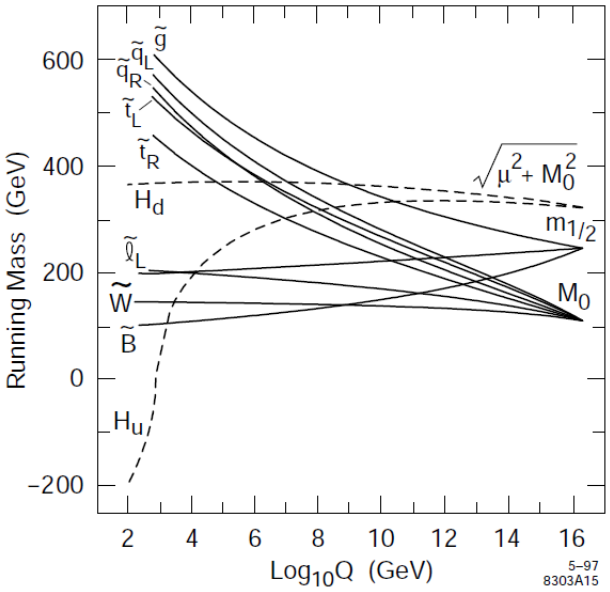

Figure 1.6: The evolution of the soft SUSY breaking mass terms from GUT scale down to the electroweak scale using known RGEs within the mSUGRA model. From Ref. [38].

its simplicity mSUGRA can give a relatively rich variety of different phenomenologies, making it very suitable to test many different searches for SUSY.

Gauge-Mediated Supersymmetry Breaking (GMSB)

In GMSB the ordinary gauge interactions are responsible for the appearance of the soft SUSY breaking terms in the MSSM Lagrangian. In order to achieve this, a new set of chiral supermultiplets are introduced (called messenger fields). They couple both to the source of the SUSY breaking (in the hidden sector), as well as to the sfermions and gauginos, through the ordinary $SU(3)_C \times SU(2)_L \times U(1)_Y$ gauge boson interactions. In order to preserve the unification of the gauge couplings at a higher energy scale the messenger particles should belong to a larger gauge group, such as e.g. SU(5). In GMSB the following six parameters fully describe the model at the GUT scale:

F_m: scale of SUSY breaking
M_m: the mass of the messenger scale
N_5: the number of messenger supermultiplets
$\tan\beta$: the ratio of the vacuum expectation value of the up and down Higgs doublets
$sgn(\mu)$: the sign of the higgsino mass parameter
C_{grav}: couplings for decays into gravitino.

There is still gravitational communication between the visible and hidden sector in the GMSB model, but compared with the gauge interactions it is now relatively small. Nevertheless the coupling of the GMSB scenario to gravity introduces local SUSY breaking (as in mSUGRA), which again leads to the creation of a massive gravitino. However, due to the relatively small value of M_m in many GMSB models, the gravitino will often be the lightest supersymmetric particle ($m_{\tilde{G}} = M_m^2/M_P$). Because of the very weak coupling, specified by C_{grav}, between the gravitino and the other sparticles, the next to lightest supersymmetric particle might also have a considerably long lifetime. These features give GMSB models a rather interesting and distinct phenomenology.

1.10.3 SUSY - a Solution to Everything?

The last few Sections have introduced the concepts of SUSY, with the motivation of describing some of the problems and unsatisfactory parts of the SM, as discussed in Section 1.9. The main motivation, however, of introducing a symmetry between fermions and bosons, was to solve the hierarchy problem introduced in Section 1.9.1. Since no supersymmetric particles are so far discovered SUSY must be a broken symmetry in Nature. The mechanism behind the breaking of SUSY is not yet known, but several theories predict the existence of a model with only a few free parameters which are able to theoretically explain all of the 124 free parameters of the MSSM at the electroweak scale. By also assuming that R-parity is conserved in nature SUSY exhibits a perfect candidate to constitute dark matter, i.e. the lightest supersymmetric particle.

Because of the supersymmetric particles that now enter the renormalization group equations, the evolution of the three gauge couplings changes. It is shown that with today's precisely measured value of the weak mixing angle, the coupling constants do indeed unite at a common energy if taking into account the MSSM particle spectrum [29]. This is illustrated in Figure 1.7. An explanation of the origin of the Mexican hat potential,

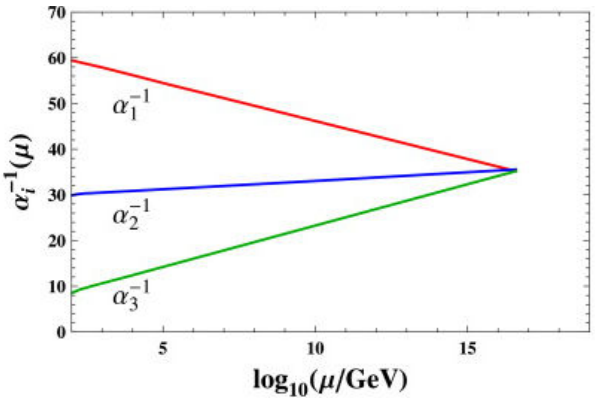

Figure 1.7: The running of the three gauge couplings α_1, α_2 and α_3 as a function of the energy including the supersymmetric particles predicted in the MSSM. It is believed that some new physics should be present at a grand unification scale from which there would be one coupling constant. From Ref. [29].

in Figure 1.2, needed to achieve spontaneous symmetry breaking of the electroweak theory (i.e. why is $\mu^2 < 0$?) might also also be governed by SUSY. Because of the relatively large top quark mass the μ^2 parameter, defined to be positive at the GUT scale, turns negative at the weak scale when the RGEs, which determine the evolution as a function of energy, is calculated within the mSUGRA model [33].

It seems like SUSY (and MSSM) is an extremely successful theory in explaining the problems of the SM, there is only one problem; although huge efforts has been put into it, supersymmetric particles have never been seen in any experiment so far. The ongoing searches for SUSY will therefore be the focus in the upcoming Chapters.

Chapter 2

Phenomenology at pp Colliders

The previous Chapter introduced the particles and couplings that have already been observed in various experiments and lead to the construction of the SM of particle physics. All the experimental data collected have given a very good understanding of how Nature works. There are however several indications, both from theory and experimental data, that the SM is not the complete picture. New theories have been constructed in order to incorporate these shortcomings of the SM, but none of them are so far confirmed experimentally. The need for more powerful and sophisticated colliders is therefore indispensable. This Chapter starts with introducing the basic concepts of high energy proton-proton collisions; in Chapter 3 the state-of-the-art proton collider, known as The Large Hadron Collider at the CERN laboratory in Geneva, is discussed.

2.1 Kinematics

The kinematics of the particles produced in pp-collisions are described by the momentum, $\mathbf{p} = (p_x, p_y, p_z)$, rest mass, m, and energy, E. The relativistic four-momentum is $P_\mu = (E, \mathbf{p})$. Defining

$$\gamma = \frac{1}{\sqrt{1-\beta^2}},$$

with $\beta = \frac{v}{c}$ gives the expressions for energy, $E = \gamma m$, and momentum, $\mathbf{p} = \boldsymbol{\beta}\gamma m$. With this we can find the famous energy-momentum formula

$$\begin{aligned} \mathbf{p}^2 &= \boldsymbol{\beta}^2\gamma^2 m^2 \\ \Rightarrow \mathbf{p}^2 + m^2 &= m^2\left(\boldsymbol{\beta}^2\gamma^2 + 1\right) \\ \Rightarrow \mathbf{p}^2 + m^2 &= m^2\gamma^2 \\ \Rightarrow \mathbf{p}^2 + m^2 &= E^2 \\ \Rightarrow E &= \sqrt{m^2 + \mathbf{p}^2}, \end{aligned} \tag{2.1}$$

where we have used that $\left(\boldsymbol{\beta}^2\gamma^2 + 1\right) = \gamma^2$. In the following we will use spherical coordinates defining ϕ as the azimuthal angle and θ as the polar angle. The coordinates

are often defined such that the z-direction is along the beam. The positive y-direction is defined as pointing upwards while the positive x-direction is towards the center of the accelerator-ring. All transverse variables are defined in the xy-plane (being transverse to the incoming beam). With these directions the azimuthal angle is the angle around the beam (Figure 2.1a) while the polar angle is the angle from the beam (Figure 2.1b). The cylindrical shape in Figure 2.1 illustrates how a particle detector will be situated around the collision point in order to cover nearly 4π solid angle. The commonly used distance, ΔR, in η-ϕ space is defined as

$$\Delta R = \sqrt{\Delta\eta^2 + \Delta\phi^2}. \tag{2.2}$$

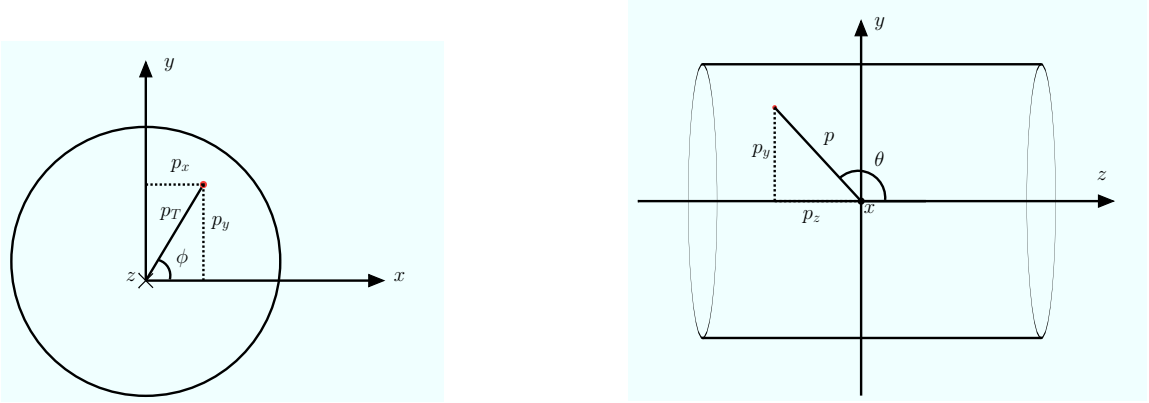

(a) The transverse plane

(b) The longitudinal plane

Figure 2.1: Spherical coordinates with azimuthal angle ϕ and polar angle θ. Figure (a) shows the xy-plane with the positive z-direction into the paper and (b) the yz-plane with the positive x-direction pointing out of the paper.

The phase space of a single particle is given by [39]

$$d\mathbf{p} = dp_x dp_y dp_z = p^2 dp d\Omega = dp_z p_{\mathrm{T}}\, dp_{\mathrm{T}}\, d\phi, \tag{2.3}$$

where p_z is the momentum projection parallel to the beam, p_T the projection transverse to the beam and Ω the solid angle. Defining the relativistic analogue of the longitudinal velocity, the rapidity y, the relativistic generalization of Eq. 2.3 becomes

$$\begin{aligned} d^4p\delta(E^2 - p^2 - m^2) = d\mathbf{p}\frac{1}{E} = p_{\mathrm{T}}\, dp_{\mathrm{T}}\, d\phi dy \quad \text{and} \\ dy = \frac{dp_z}{E} \end{aligned} \tag{2.4}$$

Knowing that $p = \sqrt{p_T^2 + p_z^2}$ and using Eq. 2.1 we can integrate Eq. 2.4 giving

$$\begin{aligned} dy &= \frac{dp_z}{\sqrt{p_z^2 + p_T^2 + m^2}} \\ \Rightarrow y &= \cosh^{-1}\left(\frac{E}{\sqrt{p_T^2 + m^2}}\right). \end{aligned}$$

For massless single particles, or if the particle masses are small with respect to the transverse momentum, we have $p_T^2 + m^2 \sim p_T^2$ with $p_{\mathrm{T}} = E \sin\theta$, leading to

$$\begin{aligned} \cosh y &= \frac{1}{\sin\theta} \\ \sinh y &= \frac{1}{\tan\theta} \\ \tanh y &= \cos\theta, \end{aligned} \tag{2.5}$$

which further can be used to get

$$e^{-y} = \tan\left(\frac{\theta}{2}\right).$$

Finally we define the pseudorapidity

$$\eta = -\ln\left[\tan\left(\frac{\theta}{2}\right)\right], \tag{2.6}$$

which in the relativistic limit used above is equal to the rapidity, y. Because the pseudorapidity does not include the particle mass and is independent on the boost it is a much used quantity in collider physics. The single particle phase space is in addition uniformly distributed in (η, ϕ) which makes it a very convenient variable when later describing the detection and identification of particles.

Two Particle System

We now look at the kinematics of a two particle system, consisting of two of the partons within the colliding protons. In the following the proton-proton center of momentum (CM) frame[1] is used. The partons have momentum $\mathbf{p_1} = x_1\mathbf{P}$ and $\mathbf{p_2} = x_2\mathbf{P}$ where $\mathbf{P}$ is the momentum of each of the protons in the proton CM frame. The variables x_1 and x_2 are the proton momentum fractions carried by each of the partons. This is sketched in Figure 2.2a. We start by finding the CM energy of the two protons, 1 and 2,

$$(P_1 + P_2)_\mu = (E_1 + E_2, \mathbf{0}) \approx (2|\mathbf{P}|, \mathbf{0}),$$

since they are moving in opposite direction to each other and we approximate their masses to be zero. The CM energy squared, s, is then given by $s = 4\mathbf{P}^2$. We now use the conservation of relativistic momentum and energy to find the mass, M^2, and momentum fraction, x, of the system containing the two initial state partons in Figure 2.2b. Again, assuming that the partons are massless and have no transverse momentum (they enter parallel to the beam), we have

$$\begin{aligned} M^2 &= (p_1 + p_2)_\mu \cdot (p_1 + p_2)^\mu \\ &\approx (e_1 + e_2)^2 - (\mathbf{p}_1 + \mathbf{p}_2)^2 \\ &= \mathbf{P}^2\left[(x_1 + x_2)^2 - (x_1 - x_2)^2\right]. \end{aligned} \tag{2.7}$$

[1] Center of momentum (CM) frame is defined as the frame where the total momentum of the system is zero.

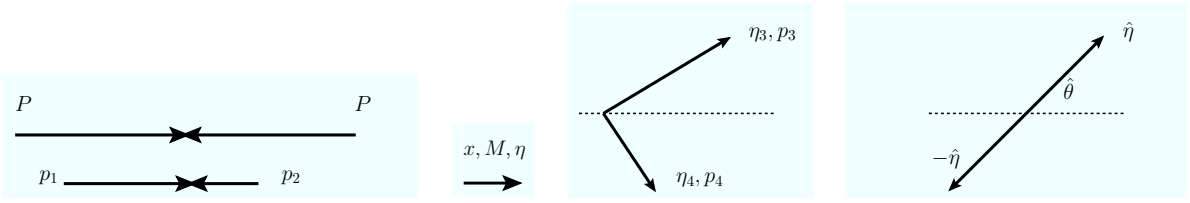

(a) (b) (c) (d)

Figure 2.2: A collision between two incoming partons with momenta $\mathbf{p_1}$ and $\mathbf{p_2}$ within the two initial protons, each having momenta $\mathbf{P}$ (a). After the collision the partons form a state of mass M and rapidity η (b). This state subsequently decays into two final state particles with four-momenta p_3, p_4 and rapidity η_3, η_4 in the proton-proton CM frame (c). The final state particles with rapidity $\pm\hat{\eta}$ and a scattering angle $\hat{\theta}$ in the CM frame of the two final state particles is shown in (d).

The momentum of the system containing the two initial state partons in Figure 2.2b is $p_z = x\mathbf{P}$, giving

$$x = \frac{p_z}{P} \approx \frac{2p_z}{\sqrt{s}}, \tag{2.8}$$

which, using a bit more algebra, result in $x_1 x_2 = \frac{M^2}{s}$ and $x_1 - x_2 = x$.

We now assume that the two body state consisting of the two initial partons with mass M and momentum fraction x decays into a two body final state consisting of two massless particles with four-momenta p_3 and p_4 pictured in Figure 2.2c. In an experiment one typically measures the pseudorapidities, η_3 and η_4, the transverse energy, E_T, and the azimuthal angle ϕ_3 and ϕ_4. Using the law of conservation of energy and momentum, we know immediately that $p_{T\,3} = p_{T\,4} = E_T$ since the transverse momentum before the decay was zero. Further we use the conservation of four-momentum

$$\begin{aligned} M^2 &= (p_3 + p_4)_\mu \cdot (p_3 + p_4)^\mu \\ &= E_3^2 + 2E_3E_4 + E_4^2 - (\mathbf{p}_3^2 + 2\mathbf{p}_3 \cdot \mathbf{p}_4 + \mathbf{p}_4^2) \\ &= 2\left(E_3E_4 - \mathbf{p}_3 \cdot \mathbf{p}_4\right) \\ &= 2\left(E_3E_4 - p_{x\,3}p_{x\,4} - p_{y\,3}p_{y\,4} - p_{z\,3}p_{z\,4}\right). \end{aligned} \tag{2.9}$$

Using

$$p_x = p_\mathrm{T}\cos\phi, \quad p_y = p_\mathrm{T}\sin\phi, \quad p_z = p_\mathrm{T}\sinh\eta, \quad \text{and} \quad E = E_T\cosh\eta$$

in Eq. 2.9 gives

$$\begin{aligned} M^2 &= 2E_T^2\cosh\eta_3\cosh\eta_4 - p_{T\,3}p_{T\,4}\left(\cos\phi_3\cos\phi_4 - \sin\phi_3\sin\phi_4 - \sinh\eta_3\sinh\eta_4\right) \\ &= 2E_T^2\left[\left(\cosh\eta_3\cosh\eta_4 - \sinh\eta_3\sinh\eta_4\right) - \left(\cos\phi_3\cos\phi_4 + \sin\phi_3\sin\phi_4\right)\right]. \end{aligned}$$

The well-known trigonometric and hyperbolic identities

$$\begin{aligned} \cosh\eta_3\cosh\eta_4 - \sinh\eta_3\sinh\eta_4 &= \cosh(\eta_3 - \eta_4) \\ \cos\phi_3\cos\phi_4 + \sin\phi_3\sin\phi_4 &= \cos(\phi_3 - \phi_4) \end{aligned}$$

give finally

$$M^2 = 2E_T^2 \left[\cosh(\eta_3 - \eta_4) - \cos(\phi_3 - \phi_4)\right]. \tag{2.10}$$

From this we can deduce another quantity which is commonly used in collider physics, the transverse mass, m_T. If we restrict Eq. 2.10 only to the plane transverse to the beam (i.e. $\theta = 90^o \Rightarrow \eta = 0$) and defining the difference in the azimuthal angle between the two particles as ϕ (i.e. $\phi_3 - \phi_4 = \phi$) we get

$$m_T = \sqrt{2E_T^2 \left[1 - \cos\phi\right]}. \tag{2.11}$$

In the final state CM frame the decay products are back to back with $\pm\hat{\eta}$ and a scattering angle $\hat{\theta}$, as sketched in Figure 2.2d. Since the pseudorapidity is additive under Lorentz transformation we get $\hat{\eta} = \eta_3 - \eta$ and $-\hat{\eta} = \eta_4 - \eta$ in this frame. Solving for $\hat{\eta}$ and η give

$$\begin{aligned} \hat{\eta} &= \frac{\eta_3 - \eta_4}{2} \\ \eta &= \frac{\eta_3 + \eta_4}{2}. \end{aligned} \tag{2.12}$$

Energy and momentum conservation requires further that each massless particle has an energy and momentum which is half of the invariant mass, $|\mathbf{p}| = M/2$, giving $p_T = E_T = (M/2)\sin\hat{\theta}$. From the measurements of E_T and the pseudorapidities, η_3 and η_4, of the two final state particles one can find the scattering angle, using the expression of $\hat{\eta}$ in Eq. 2.12 and $\tanh\hat{\eta} = \cos\hat{\theta}$ (Eq. 2.5). The momentum fractions, x_1 and x_2, of the initial partons, can be calculated from the measurements of the final state particles by [39]

$$x = \frac{2M}{\sqrt{s}}\sinh\eta = \frac{M}{\sqrt{s}}\left[e^{\eta} - e^{-\eta}\right] = x_1 - x_2, \tag{2.13}$$

finally giving

$$\begin{aligned} x_1 &= \frac{M}{\sqrt{s}}e^{\eta} \\ x_2 &= \frac{M}{\sqrt{s}}e^{-\eta}. \end{aligned}$$

2.2 Proton-Proton Interactions

The total cross-section at a proton-proton collider can be divided into the various components; elastic (el), single-diffractive (sd), double-diffractive (dd) and non-diffractive (nd) cross-sections,

$$\sigma_{\text{total}} = \sigma_{\text{el}} + \sigma_{\text{sd}} + \sigma_{\text{dd}} + \sigma_{\text{nd}}. \tag{2.14}$$

The single-, double- and non-diffractive cross-sections are all inelastic interactions leading to multi-particle final states. In the diffractive events there is no flow of colour between the

partons, but rather an exchange of colour singlet states known as *pomerons*. The non-diffractive events involve colour exchange between the partons. Neither diffractive nor elastic collisions are very interesting in high-p_{T} proton-proton collisions because they will mostly produce particles with small transverse momentum (i.e. moving along the beam pipe) and therefore be undetectable by the standard particle detectors. These events are important for luminosity measurements however, since they contribute significantly to the total proton-proton cross-section. Special detectors are used for this purpose. Events recorded when no (or a minimum) selection on the final state and momenta of the particles are imposed are often called *minimum bias* events. A sample of *minimum bias* events therefore typically contains all the components listed in Eq. 2.14. Figure 2.3 illustrates the elastic and diffractive proton-proton interactions, where there is an exchange of a pomeron, P. The X's denote the diffractive systems. The non-diffractive (inelastic)

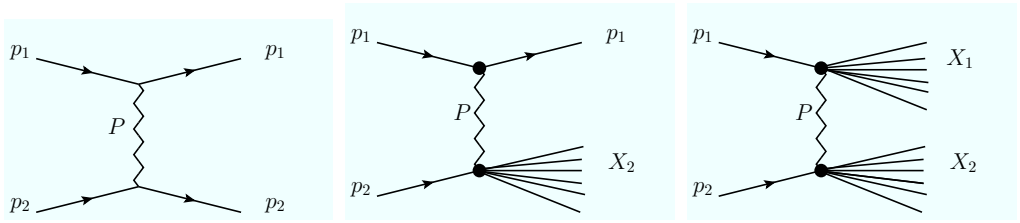

(a) Elastic (b) Single-diffractive (c) Double-diffractive

Figure 2.3: The elastic (a), single- (b) and double-diffractive (c) contributions to the total LHC proton(p_1)-proton(p_2) cross-section. The P denotes the pomeron exchanged in the interaction while X_1 and X_2 are the diffractive systems.

events are the ones of main interest for high p_{T} physics analysis and will be discussed thoroughly in the following Sections.

2.2.1 Hard Scattering Events

In high energy proton-proton collisions, like those happening at the LHC, the particles inside the protons (i.e. the partons) can be considered as being free. In this situation one can therefore treat a proton-proton collision as several incoherent collisions between the partons, where the proton-proton cross-section is the sum of the individual parton cross-sections. The main interest at hadron colliders lies in the production of heavy particles (supersymmetric particles, Higgs bosons, top, etc.) produced in non-diffractive collisions with high momentum transfer, Q^2, known as hard scattering processes. A high energy proton-proton collision is illustrated in Figure 2.4, which we can simplify by the following expression

$$A + B \rightarrow c + X, \tag{2.15}$$

where A and B are the two colliding protons, c the interesting high p_{T} object from the hard scattering process (Z boson in Figure 2.4) and X the underlying, soft products, which are mostly hadronic remnants after the hard collision. Every interaction at LHC contains a similar distribution of low transverse momentum particles, X, coming from the soft processes. As already discussed, the interesting collision can be simplified as

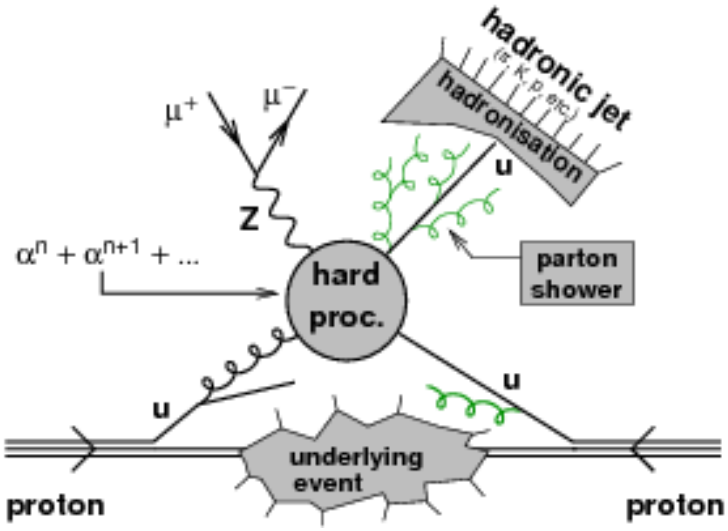

Figure 2.4: Schematic representation of a proton-proton collision, involving a quark-gluon hard scattering that leads to a final state consisting of a Z boson and a hard jet. From Ref. [40].

happening between the two partons, a and b (a gluon (curly line) and an up quark in Figure 2.4)

$$a + b \rightarrow c.$$

The probability for the two partons, a in proton A and b in proton B, to carry proton momentum fractions x_a and x_b is described by experimentally determined parton distribution functions (PDF), $f_{a/A}(x_a, Q^2)$ and $f_{b/B}(x_b, Q^2)$. The Q^2 is the squared of the momentum scale indicating the total four-momentum transfer in the collision. The proton PDFs depend on the momentum scale at which they are probed and are often measured in deep inelastic scattering of leptons against protons, where the lepton is the probe which transfers a four-momentum equals Q to the nucleon. Hadron colliders also contribute to the understanding of the PDFs, however. Summing over all the possible partons that can produce the c-state as well as over the colours of a and b the resulting cross-section for the reaction in Eq. 2.15 can be decomposed as follows [41]

$$\sigma(AB \rightarrow cX) = \sum_{a,b} C_{ab} \int dx_a\, dx_b \left[f_{a/A}(x_a) f_{b/B}(x_b) + f_{a/B}(x_a) f_{b/A}(x_b) \right] \sigma(a + b \rightarrow cX), \tag{2.16}$$

where the second term inside the brackets is valid only if $a \neq b$. The C_{ab} term contains the colour averaging factors, being 1/9, 1/24 and 1/64 for $qq/\bar{q}q$, qg and gg pairs respectively. The $\sigma(a + b \rightarrow cX)$-term is the partonic cross-section computed from the matrix element of the interaction Lagrangian of the theory summed over colour and spin.

The splitting between the hard scattering and the soft processes is called factorization. The value of the scale Q^2 which separates the hard and soft contributions is known as the *factorization scale*. The cross-sections calculated at a fixed order in perturbation theory depend on this factorization scale, but the dependence becomes weaker with increasing orders of calculation, and vanishes in the limit when all orders of perturbation theory would be used. The exact distinction between the hard scattering events and the soft events is therefore not completely as definite as in the simplified description in Eq. 2.15.

2.2.1.1 From Protons to Partons

The proton consists of two up quarks and a down quark, known as *valence* quarks. Summing up their masses one gets $\sim 6 - 12$ MeV [24]. Knowing that the mass of a proton is about 938 MeV the motion of the quarks inside the proton must be relativistic. Using Heisenberg's uncertainty principle, $\Delta x \Delta P \approx hc$, approximating the size of the proton to be $\Delta x = 1$ fm, we get

$$\Delta P \approx \frac{1.2 \cdot 10^9 \text{ eV fm}}{2\pi \text{ fm}} \approx 0.2 \text{ GeV}, \tag{2.17}$$

which means that the quarks must have a momentum of order 200 MeV, much larger than their rest mass. The quarks therefore easily radiate gluons, which again might virtually split or decay into quark-antiquark pairs, called *sea* quarks. The quark and gluon PDFs, $xf(x, Q^2)$, for $Q^2 = 10$ and 10^4 GeV^2 are shown in Figure 2.5. The valence quarks carry

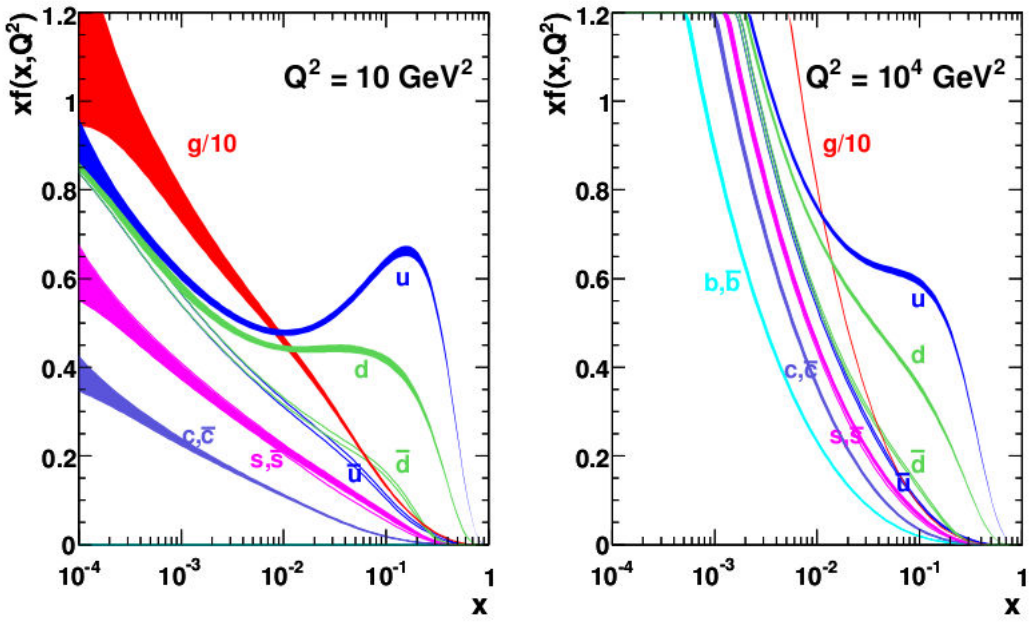

Figure 2.5: The product of the parton momentum fraction, x, and the quark or gluon probability density functions, $f(x, Q^2)$, calculated at next-to-leading order with MSTW 2008 NLO set of structure functions. The width of the curves indicate a one-sigma confidence level uncertainty. The left and right plots are for $Q^2 = 10$ GeV and 10^4 GeV respectively. From Ref. [42].

the largest fraction of proton momentum, but due to the radiation of gluons, they do not peak at $x = 1/3$, as one naively could expect. There is also a clear dependence on Q^2 when comparing the two plots in Figure 2.5. This dependence comes from the quantum corrections that contain additional powers of the coupling constants. Radiation therefore becomes more important with growing Q^2 and enhances the distribution functions at low x.

2.2.1.2 Scattering of Partons

The partons in the hard scattering process will eventually go over to other states, consisting of one or more particles. The cross-sections for these states can be calculated by using the formula in Eq. 2.16. To do this one has to use perturbation theory, however, and the results obtained including only the leading order suffer usually from large uncertainties. The need to go to higher order is therefore persistent. In order to minimize the uncertainties, calculations are often performed to next-to- or next-to-next-to leading order (NLO and NNLO). Some processes do not even occur at leading order and one is forced to go to higher orders.

Often the two parton scattering process produce a single particle which typically is one of the gauge bosons. If one of the partons is a quark and the other an antiquark they can produce a photon or a Z boson which leads to a pair of oppositely charged leptons. This process is called a Drell Yan process, pictured in Figure 2.6a.[2] A W boson can also be produced from the scattering of a down-type quark and an up-type antiquark (or vice versa). The W might subsequently decay into a lepton-antineutrino pair or a pair of quarks, as in Figure 2.6b.

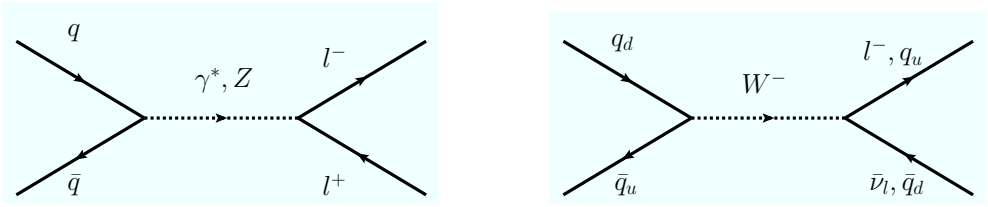

(a) Drell-Yan (b) W^-

Figure 2.6: Drell-Yan process where the quark-antiquark annihilate and leads to a pair of oppositely charged leptons (a). The graph in (b) shows a process where a down-type quark and an up-type antiquark forms a W^-, which leads to a lepton,antineutrino pair or a pair of quarks.

The dominant process at LHC leads to the production of quarks and gluons. Examples of the most important processes involving gluons, quarks and antiquarks are illustrated in Figure 2.7, 2.8 and 2.9. These are the leading order contributions only and the processes initiated by gluons dominate. Including higher order corrections would give a large number of possible Feynman graphs. Since the quarks and gluons all carry colour they could at any time radiate another quark or gluon. This makes it possible to construct processes with many quarks and gluons in the final state. The cross-section when adding more and more quarks and gluons goes drastically down, however.

Of special interest is of course the possible production of supersymmetric particles from the hard scattering. Figure 2.10, 2.11 and 2.12 show possible production processes of gluinos and squarks initiated by gluons, quarks and antiquarks respectively. Only lowest order diagrams are shown here. Figure 2.13 shows typical production mechanisms for

[2]The Z might of course also decay into a quark-antiquark pair, seen in Figure 2.8, this is not a Drell-Yan process however.

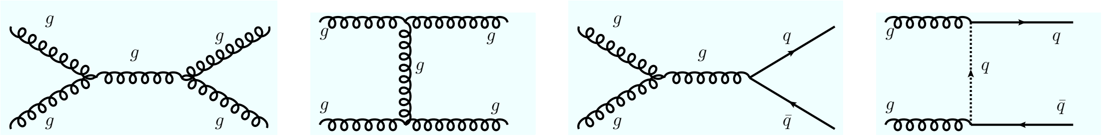

(a) (b) (c) (d)

Figure 2.7: Gluon and quark-antiquark production from gluon-gluon annihilation and fusion processes.

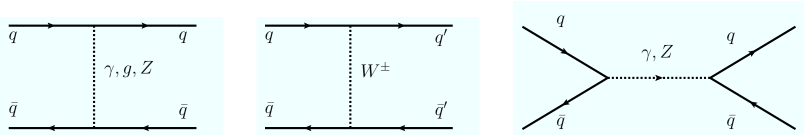

(a) (b) (c)

Figure 2.8: Quark-antiquark production from quark-antiquark scattering and annihilation

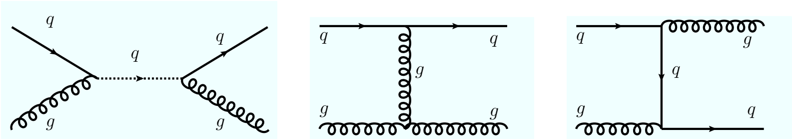

(a) (b) (c)

Figure 2.9: Gluon-quark production initiated by quark-gluon interactions.

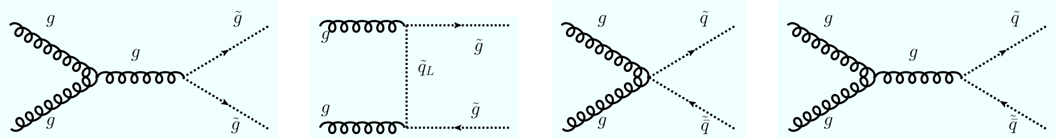

(a) (b) (c) (d)

Figure 2.10: Gluino-gluino and squark-squark production initiated by gluon processes.

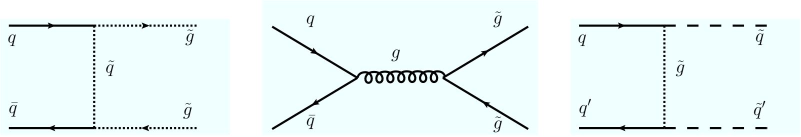

(a) (b) (c)

Figure 2.11: Gluino-gluino and squark-squark production initiated by quarks and anti-quarks.

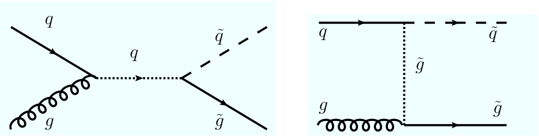

(a) (b)

Figure 2.12: Gluino-squark production initiated by quarks and gluons.

direct chargino, neutralino and slepton production through quark-antiquark annihilation.

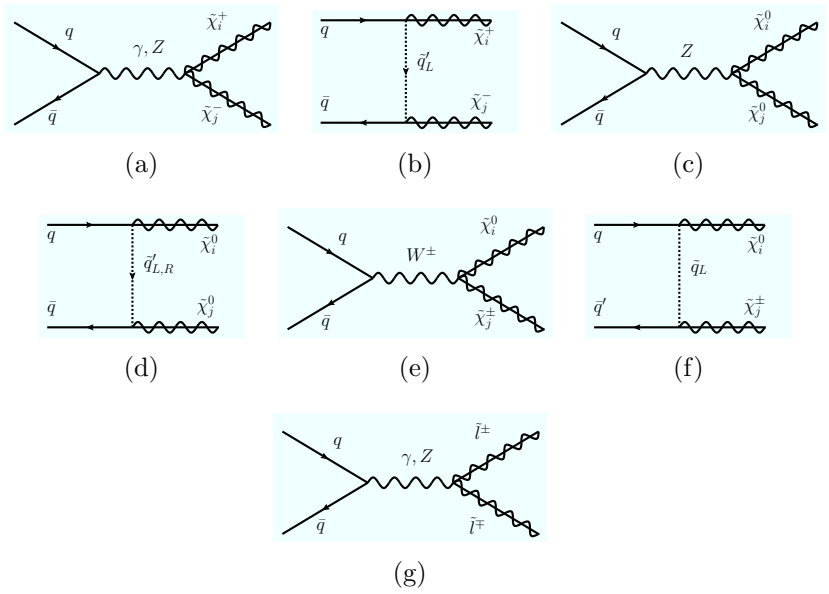

Figure 2.13: Examples of direct electroweak SUSY production from a hard scattering process. The diagrams (a-f) show production of charginos and neutralinos while the diagram in (g) depicts the direct production of a pair of sleptons.

Figure 2.14 shows the cross-section for the production of various final states in proton-proton collisions as a function of the center of mass energy. It is clear that quark and gluon production dominate the total cross-section at the LHC energies. The cross-sections of gauge or Higgs boson production are several orders of magnitude lower than for instance the $b\bar{b}$ production. Figure 2.15 shows the cross-section (in pb) for the production of supersymmetric particles as a function of the SUSY mass scale at $\sqrt{s} = 7$ TeV. Even at very small mass scales the cross-section for SUSY production is tiny compared with some of the productions in Figure 2.14. The strong production (squarks and gluinos) clearly dominates over the electroweak production in this particular SUSY model.

2.2.1.3 Hadronization

Every coloured particle eventually hadronizes when the mass scale of a process is close to the *confinement scale*, discussed in Section 1.3.2. Remember that the strong force becomes weak at short scales and stronger at large scales and if one attempts to separate gluons or quarks the binding energy will eventually go into creation of new coloured particles. As a result coloured objects cannot be separated by distances larger than ~ 1 fm (size of a proton), which means that, following the result from Eq. 2.17, hadronization occur when the mass scale of a process is of order $\Lambda_{QCD} \sim 0.2$ GeV. As already seen, at high mass scales, the processes can be calculated perturbatively and the quarks and gluons are treated as free particles. At moderate mass scales, perturbative QCD is still valid, and coloured objects radiate, producing parton showers of coloured particles. At the hadronization scale, Λ_{QCD}, the quarks and gluons subsequently organize into colourless

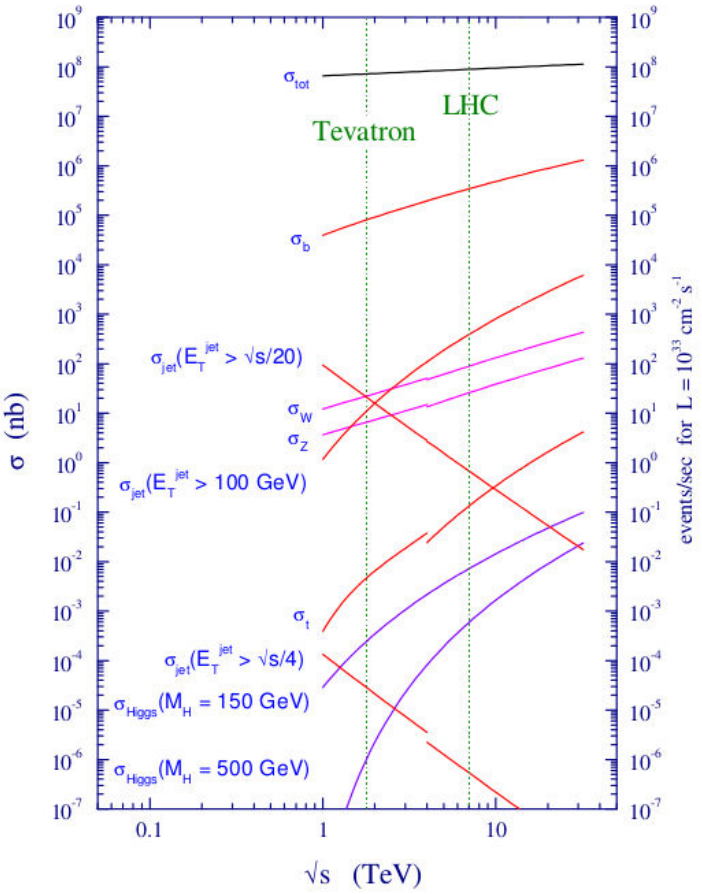

Figure 2.14: SM production cross-section as a function of center of mass energy. From Ref. [43].

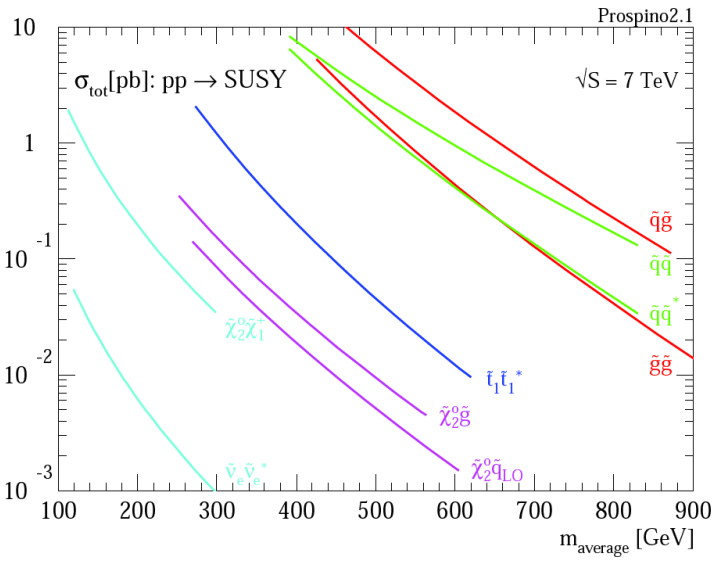

Figure 2.15: Cross-section (in pb) for supersymmetry production as a function of the SUSY mass scale, $m_{average}$, at $\sqrt{s} = 7$ TeV. From Ref. [44].

hadrons. Usually this involves the additional creation of quark-antiquark pairs from the colour force field. At this level and below, perturbative QCD is no longer applicable and hadron physics therefore needs to rely on models with free parameters that are determined experimentally. Finally, the short-lived hadrons themselves decay to lower (meta) stable mass states. The different phases of coloured particles are illustrated in Figure 2.16. In particle physics experiments like ATLAS one can only study the coloured particles by measuring them after they have hadronized. Free quarks or gluons have never been observed, one rather sees showers of hadrons in the detector. These showers are known as *jets* and will be discussed further in Chapter 3. Consider again parton c in Eq. 2.15.

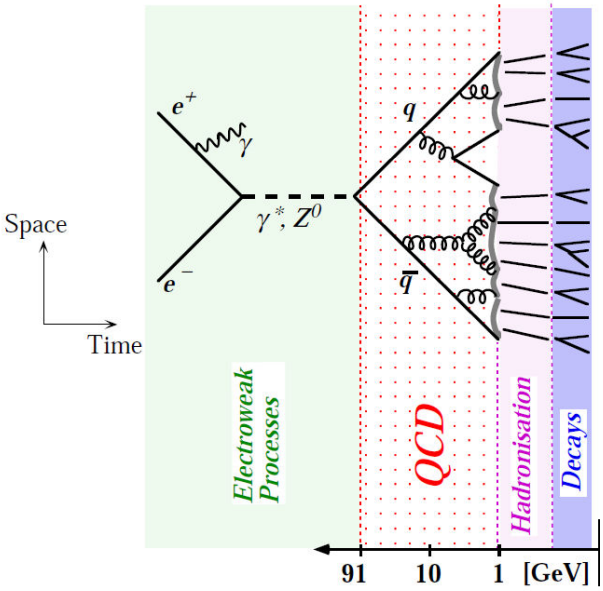

Figure 2.16: A schematic view of the evolution of coloured objects in the final state of an e^+e^- interaction. The hadronization and decay regime cannot be calculated using perturbative QCD and therefore need to rely on models with free parameters that are determined experimentally. At higher mass scales the strong force is weaker and perturbative QCD can be used. Reference [39].

It has an energy E_c, which produces a hadron, h, with energy fraction, z, of the initial parton, $z = E_h/E_c$ with $0 \leq z \leq 1$. The probability of producing h in the range z to $z + dz$ is defined as $D_c^h(z)dz$, where D_c^h is the fragmentation function. The cross-section for producing a hadron h through a parton c from the hard scattering is then given by

$$\sigma(AB \to hX) = \sum_c \int \frac{d\sigma(AB \to cX)}{dE_c} D_c^h(E_h/E_c) \frac{dE_c}{E_c},$$

where $\sigma(AB \to cX)$ is given by Eq. 2.16. Integrating only over the fragmentation function for the whole physical range of z gives the average number of hadrons, $\langle n_c^h \rangle$, in the complete jet arising from parton c

$$\langle n_c^h \rangle = \int_{z_{min}}^{1} D_c^h(z)\, dz.$$

The lower limit on z is the kinematic bound for a given parton energy; $z_{min} = m_h/E_c$. As was the case with the parton distribution functions, the fragmentation function is non-perturbative and must be constructed using models that rely on parameters obtained through fits to experimental data. There is in fact a close relation between the parton distribution functions and the fragmentation functions. The first is the probability density of finding parton c within hadron h while the latter is the probability of finding the hadron h among the fragmentation products of parton c. In Eq. 2.15 the hadron h was simply one of the protons, A or B.

Heavy Quark Hadronization

The quarks and antiquarks are most likely to form a meson when they have about the same velocity. If the hadronizing parton is a heavy quark (b- or c-quark[3]) it therefore needs to loose only a small fraction of its energy to materialize a number of light quark pairs with comparable velocities. If the heavy quarks then combine with one of these light quarks, the resulting hadron would carry a large fraction of the originally parton energy, i.e. $z \approx 1$. Their energy/momentum distribution will therefore be much harder than that of light hadrons, where z tends to peak at small values. The leptons produced in leptonic or semi-leptonic decays of heavy-flavoured hadrons have therefore usually higher momentum than the corresponding leptons from light-flavoured hadrons and thus are more likely to pass the lepton identification requirements. Typical transverse energy distributions of electrons in ATLAS are shown in Figure 2.17. In (a) the observed data is compared with the expectations from simulations. At small transverse momentum the reconstructed leptons mostly come from misidentified hadronic fakes, conversion processes and semi-leptonic decays of charm and beauty hadrons. At higher E_{T} the contributions from W, Z and γ^* become more important. In (b) only the transverse momentum of electrons passing the tightest identification requirements is shown. The bump caused by the contribution from $W$and Z is clearly visible at around 40 GeV.

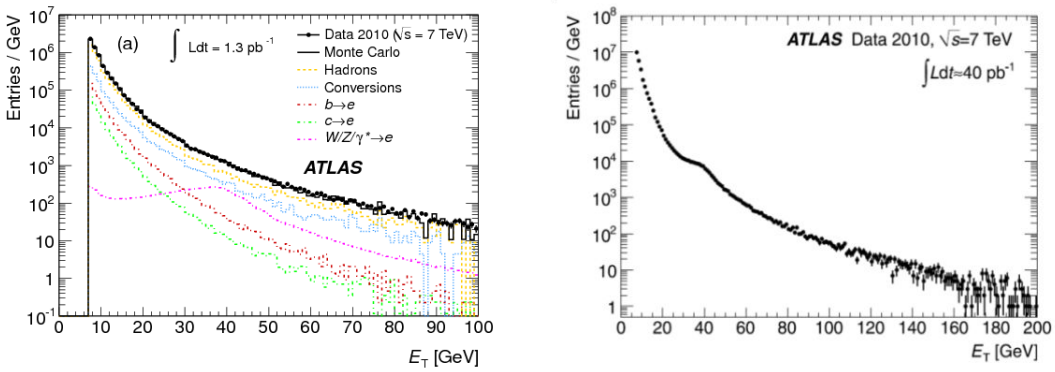

(a) From Ref. [45]. (b) From Ref. [46]

Figure 2.17: Distribution of transverse energy for electron candidates. In (a) the distribution from data is shown together with simulation of the different sources of electron production. In (b) only the data distribution for electrons passing the tightest identification criteria is shown. Here the bump caused by the contributions from W, Z and γ is clearly visible. Note that the two plots are made using different amounts of data, 1.3 pb^{-1} (a) and 40 pb^{-1} (b).

2.2.1.4 Underlying Events and Multiple Interactions

The beam remnants after a hard scattering interaction, denoted X in Eq. 2.15, will hadronize and constitute what is known as the *underlying event*. These interactions are non-perturbative processes and also need to rely on models backed up by experimental

[3]The top quark is so heavy that it decays into Wb before having a chance to hadronize.

results. Since the proton remnants move almost collinear with the incoming beams they are not fully measured by the detectors. The total momentum and energy in the longitudinal direction is therefore not possible to determine in a collision. Because of this only the energy and momentum in the transverse directions (E_{T} and p_{T}) are well defined at hadron colliders. An additional complication of the event topology is the possibility of *multiple interactions*. Multiple interactions come from the remaining quarks and gluons, after the hard scattering, which interact with each other, giving rise to additional scatterings in the event.

2.2.1.5 Initial and Final State Showers

To get a realistic description of a high energy proton-proton event at LHC one needs also to include the QCD radiation effects. There are mainly two different sources of radiation, known as *initial* and *final state radiation* (ISR and FSR respectively). As the names suggest, the ISR is radiation coming from the initial state partons while the FSR is radiation from the final state particles. The radiated particles hadronize and produce additional showers of particles in the event. It is, however, also possible to get QED radiation effects, with ISR coming from the initial quarks or antiquarks and FSR from any charged fermion (depending on the final state). There are several ways to incorporate the contribution from ISR and FSR in simulations, but the calculations often involve large uncertainties. Some of the most commonly used methods are based on matrix elements and parton showers [47].

2.3 Luminosity

After having calculated the cross-section for an interesting process at the LHC, following the discussion in Section 2.2.1, one can calculate the rate, R, of such processes when many collisions have been accumulated,

$$R = \sigma \mathscr{L},$$

where the luminosity, $\mathscr{L}$, is completely determined by the properties of the colliding beams [30]

$$\mathscr{L} = f_{\mathrm{rev}} \frac{n_b n_1 n_2}{4\pi \sigma_x \sigma_y} F(\sigma_x, \sigma_y, \sigma_s, \Phi).$$

The f_{rev} parameter is the beam revolution frequency, σ_x and σ_y are the transverse beam widths at the interaction points, n_b the number of proton bunches and n_1 and n_2 the number of protons in beam one and two respectively. The function, F, is a geometrical reduction factor due to the non-zero crossing angle at the interaction point and depends on the crossing angle, Φ, beam size and beam length (σ_s). To get the total number of expected events, N, of a certain physical process one simply takes the event rate and integrates over time

$$N = \sigma \int \mathscr{L}\, dt,$$

where $\int \mathscr{L}\, dt$ often is referred to as the *integrated luminosity*.

The design luminosity of LHC is $\mathscr{L} = 10^{34}\text{cm}^{-2}\text{sec}^{-1}$, which is very close to the current maximum value measured in ATLAS, $\mathscr{L}_{\text{max}} = 7.73 \cdot 10^{33}\text{cm}^{-2}\text{sec}^{-1}$ [48]. The total integrated luminosity collected by the ATLAS experiment since the start-up of the physics program in 2010 is more than 27 fb^{-1}, where nearly 25 fb^{-1} are used for physics.[4]

2.4 Pile-up

In order to achieve a high instantaneous luminosity the intensity of the proton beam is important. But with high intensity beams the probability of having more than one proton undergoing an inelastic interaction per bunch crossing increases. Events with several collisions from the same bunch crossing are known as pile-up events. These additional collisions have usually very small momentum transfer and are therefore characterized as minimum bias events. Figure 2.18 shows the maximum mean number of events per bunch crossing versus day during the proton-proton runs of 2010, 2011 and 2012. Figure 2.19

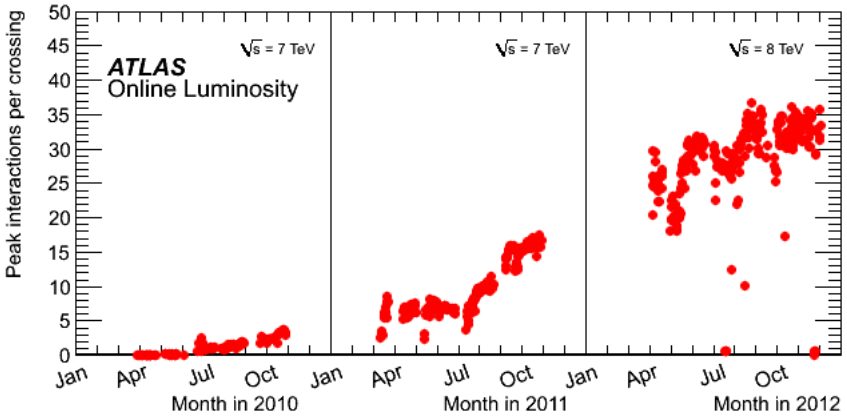

Figure 2.18: The maximum mean number of events per bunch crossing versus day during the proton-proton runs of 2010, 2011 and 2012. Ref. [48].

shows an example of an event with a Z decaying into two muons recorded by ATLAS with 20 reconstructed vertices. In 2012 over 40 vertices were recorded in one single event, which is well beyond the design of the ATLAS detector[5].

[4] $1\text{fb} = 10^{-39}\text{cm}^2$

[5] The ATLAS detector was originally designed for handling an average of 23 collisions per bunch crossing [30]

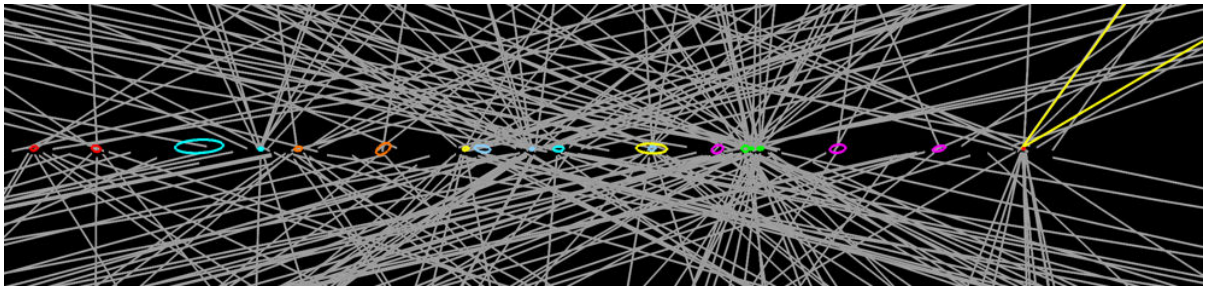

Figure 2.19: An event with a Z boson decaying into two muons (yellow tracks) with 20 reconstructed vertices. This event was recorded on September 14th and is typical for the 2011 environment. The ellipses are the reconstructed errors on the vertex positions, scaled up by a factor of 10, so that they are visible.

Chapter 3

LHC and ATLAS

3.1 CERN

CERN (Organisation européenne pour la recherche nucléaire) was founded in 1954 and is one of the largest and most respected centers of scientific research. The first proposal of building an European laboratory was made by the French physicist Louis de Broglie in 1949. In 1952 the acronym CERN was created and the location was decided to be outside Geneva on the border between Switzerland and France. This was finally ratified by the Canton of Geneva in June 1953. The CERN convention was acknowledged by 12 countries (among them Norway) later the same year. CERN officially came into being on September 29, 1954.

From the beginning in 1954 CERN has gone through many stages of experiments, accelerators and facilities. It all started with the 600 MeV Synchrocyclotron (SC) in 1957 doing mostly nuclear-oriented research. The first pure particle physics accelerator was the Proton Synchrotron (PS) with a beam energy of 28 GeV, built in 1957. Today the PS's most important task is to feed the larger accelerators with particles.

In the beginning particle collisions were studied by use of photographs from bubble chambers, among others. This was very slow, labour intensive and not very suitable for studying rare phenomena. Georges Charpak revolutionized the field of particle detection with the development of the *multiwire proportional chamber* in 1968, having a counting rate more thousands times better than the (then) existing technologies.

After a series of important measurements, discoveries and developments during the 70's and 80's, the most important being the discovery of neutral currents followed by the discovery of the W and Z bosons by the UA1 and UA2 experiments, the Large Electron Positron (LEP) collider was built to perform detailed studies of the weak bosons. This was the biggest electron-positron collider ever built[1] and did remarkable precise measurements of the electroweak theory. Among other results it was proven that there are three - and only three - generations of light neutrinos (i.e. $m_\nu < 45$ GeV). The LEP collider was closed down in 2000, and the 27 km tunnel is now used for the Large Hadron Collider

[1] A linear collider was also running at SLAC (SLC) at the Z mass (although with much smaller luminosity).

(LHC). LHC finally started up in 2008, 37 years after the first proton-proton collider in the World, the Intersecting Storage Ring (ISR), was built at CERN.

CERN has not just contributed with higher and higher energy accelerators, but has at the same time pushed technology and inventions used in many other arenas than particle physics, such as biology, radiology and medicine. On December 14, 2012 CERN was granted an observer status in the United Nation's General Assembly. CERN is also known as the place where the web was born, invented originally by Tim Berners-Lee as a way for physicists to communicate and share information with each other. CERN has also extensively contributed to the understanding of antimatter, with the first observation of antihydrogen in 1995 as a highlight.

3.2 The Large Hadron Collider

The Large Hadron Collider (LHC) is the world's largest and most powerful particle accelerator. This has been proven several times since the start-up in 2010, setting new world records of the highest energy ever achieved in proton-proton collisions, first with 7 TeV center of mass energy, and then increased to 8 TeV in 2012. The world record for beam intensity at a hadron collider held by the US Fermi National Accelerator Laboratory TeVatron was also beaten by LHC, when beams were collided with a luminosity of $4.67 \cdot 10^{32}$ cm^{-2}s^{-1} on April 22$^{\text{nd}}$, 2011.[2] Although the main focus of the LHC has been on proton-proton collisions, the machine has successfully collided lead-lead as well as lead-proton.

LHC is situated 100 m underground and consists of a 27 kilometer ring of superconducting magnets and accelerating structures. Since the LHC was built in the already existing LEP tunnel, having a radius of 4.3 km, the upper limit on the energy of the protons is limited by the maximal magnetic field possible to achieve with the current technology. The LHC was originally designed to run with 7 TeV protons, requiring a magnetic field of 8.4 Tesla. The energy of heavy ions is correspondingly limited to 5.5 TeV. In order to obtain this, the magnets need to be superconducting electromagnets operating at a temperature of -271^{o}C. A total of 1232 dipole magnets are used to bend the beams. A total of 392 quadrupole magnets are responsible of focusing the beams. Just before each collision point another type of magnet is used to squeeze the particles closer together.

The LHC is designed to have 2808 bunches with an average number of 10^{11} protons per bunch circulating in the ring at the same time. Under these conditions the protons collide at a rate of 40 MHz. However, until now the LHC has mostly run with a rate of 20 MHz. Due to the high energy and intensity achievable at the LHC, the machine serves as a perfect tool for exploring unknown phenomena which so far have been unreachable by other experiments. However, due to the large complexity of the protons, which was discussed in Chapter 2, precision measurements of for instance masses and couplings will be more challenging than at for example LEP.

[2] This record has later been beaten several times by the LHC during the pp collision runs in 2011 at $\sqrt{s} = 7$ TeV and 2012 at $\sqrt{s} = 8$ TeV with measured peak luminosities of $3.65 \cdot 10^{33}$ cm^{-2}s^{-1} [49] and $7.73 \cdot 10^{33}$ cm^{-2}s^{-1} [48] respectively.

3.3 The Accelerator Complex

The LHC is the last step in a long and complicated chain of accelerators illustrated in Figure 3.1. The protons are obtained by removing electrons from hydrogen atoms which

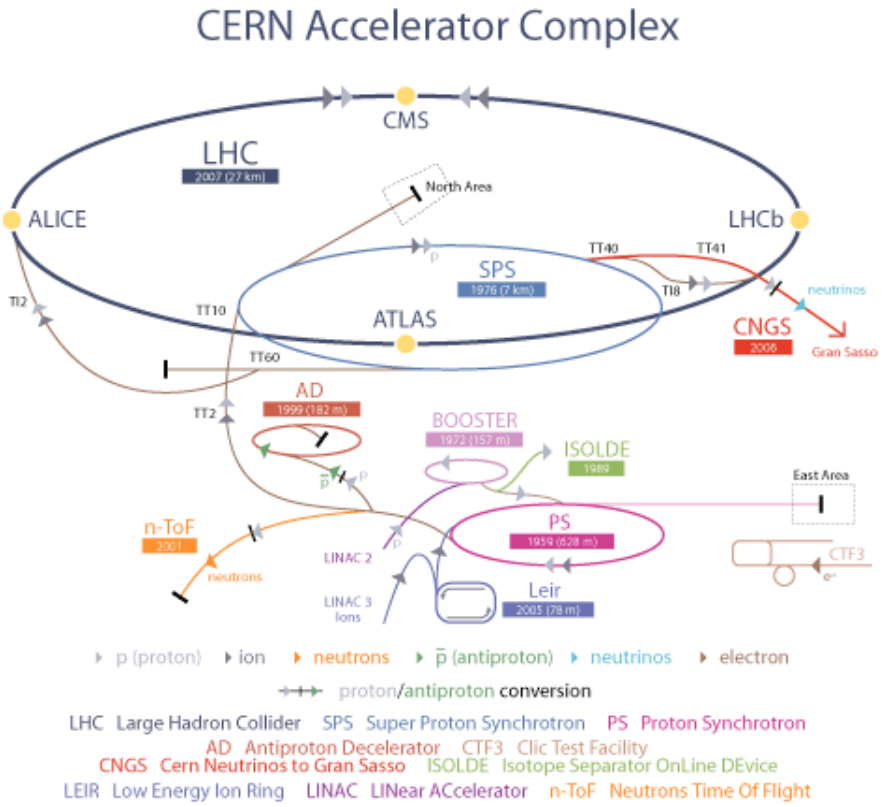

Figure 3.1: The CERN accelerator complex.

then are accelerated in a linear accelerator (LINAC2). From LINAC2 the protons are fed into the PS Booster which accelerate them up to an energy of 1.4 GeV before they are injected into the Proton Synchrotron (PS), bringing the energy up to 26 GeV. The PS creates the bunch structure finally used in the LHC, as discussed above. The final accelerator before the LHC is the Super Proton Synchrotron (SPS) which ramps the energy up to 450 GeV by use of radio frequency (RF) cavities. RF cavities are used in the LHC to accelerate the protons up to their final energy before colliding. The RF cavities, which are located at four different places around the ring, do not just accelerate the particles to the wanted energy, but help keep the protons in each bunch together, by decelerating the protons with too high energy. At nominal running it takes about 20 minutes before the desired energy is achieved. When the protons are colliding in the LHC the beams gradually loose intensity, not just due to the actual physics collisions, but also collisions with the remaining beam-gas or the beam-wall and other effects along the trajectory. A beam typically circulates in the LHC for about 10 hours.

The accelerator complex feeds not only the LHC with protons. The *CERN neutrinos to Gran Sasso* (CNGS), *neutron time-of-flight facility* (nTOF), *Antiproton Decelerator*, *Online Isotope Mass Separator* (Isolde) and the *Compact Linear Collider* (CLIC) test area make use of different parts of the accelerator complex.

3.4 The ATLAS Detector

There are four main experiments along the LHC ring. The two multi-purpose detectors ATLAS and CMS[3] are optimized for searching for new heavy particles in proton-proton collisions, but both are studying heavy ion collisions as well. The ALICE detector is mainly built for studying and exploring possible new phases of matter produced in heavy ion collisions. Finally, the LHCb experiment focuses on b-physics and measurements related to CP violation. In addition there are several smaller detectors situated close to the ATLAS and CMS experiments. These detectors are specialized in measuring the luminosity and soft proton collisions (i.e. particles that just brush past each other as the beams collide, rather than meeting head-on).

The ATLAS detector is the largest of all the detectors along the LHC ring, being about 25 m high and 44 m long. In order to capture as many as possible of the particles that are created in the collisions ATLAS is cylindrical in shape and covered with detectors in nearly 4π. A completely enclosed cylinder is not realizable since the beam pipe and various services, like cryogenics and cables, need to pass through the detector. The coverage is made as good as possible, however, with very few dead regions. The central part of the detector ($|\eta| \lesssim 2.0$) is termed *barrel* while the forward regions ($|\eta| \gtrsim 2$) are called *end-caps*. The exact division into *barrel* and *end-cap* varies between the sub-detectors. The two sides of the ATLAS detector are often referred to as the A and C sides, with the A side pointing towards Geneva Airport. A computer generated picture of the ATLAS detector is shown in Figure 3.2.

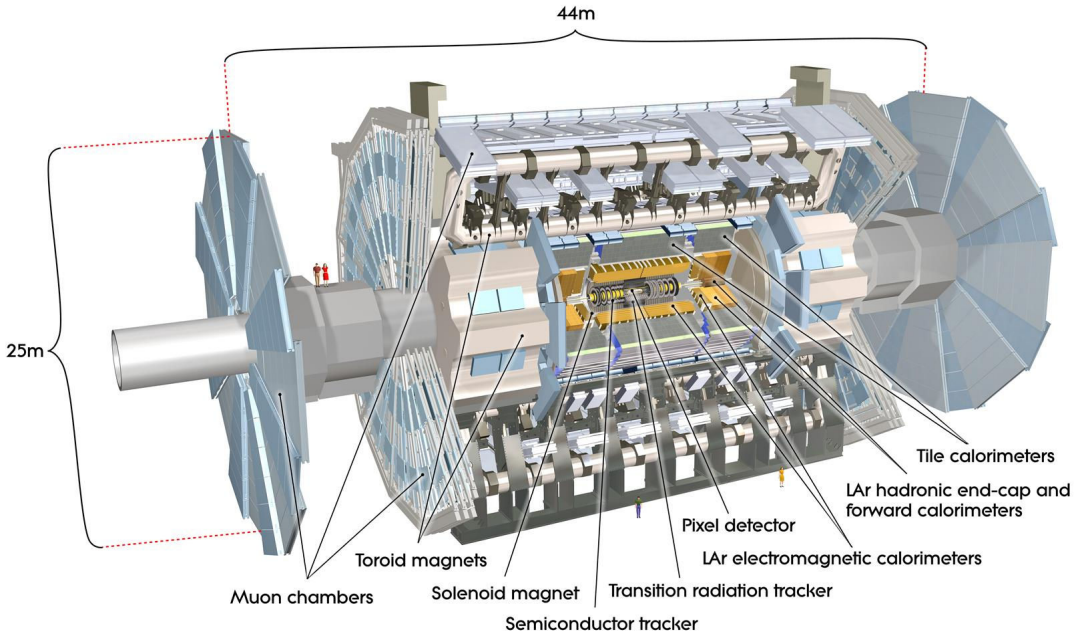

Figure 3.2: The ATLAS detector.

[3]ATLAS stands for **A** large **T**oroidal **LH**C **A**pparatu**S** while CMS stands for, the slightly more intuitive, **C**ompact **M**uon **S**olenoid.

Detector Component	Required Resolution	Coverage	
		Measurement	Trigger
Tracking	$\sigma_{p_T}/p_T = 0.05\% \, p_T \oplus 1\%$	$\lvert\eta\rvert < 2.5$	
ECal	$\sigma_E/E = 10\%/\sqrt{E} \oplus 0.7\%$	$\lvert\eta\rvert < 3.2$	$\lvert\eta\rvert < 2.5$
HCal			
barrel/end-cap	$\sigma_E/E = 50\%/\sqrt{E} \oplus 3\%$	$\lvert\eta\rvert < 3.2$	$\lvert\eta\rvert < 3.2$
forward	$\sigma_E/E = 100\%/\sqrt{E} \oplus 10\%$	$3.1 < \lvert\eta\rvert < 4.9$	$3.1 < \lvert\eta\rvert < 4.9$
MS	$\sigma_{p_T}/p_T = 10\%$ at $p_T = 1$ TeV	$\lvert\eta\rvert < 2.7$	$\lvert\eta\rvert < 2.4$

Table 3.1: Performance goals of the ATLAS detector. The symbol $\oplus$ indicates that the two numbers are added in quadrature. Numbers taken from Ref. [50].

In order to be able to detect the various types of particles and record the interesting collisions ATLAS has five main systems; an inner detector (ID), calorimeters, a muon spectrometer (MS) system, the trigger and data acquisition (DAQ) system and a magnet system. Each of these are again divided into smaller sub-systems. With this design ATLAS fulfills most of the criteria for doing a broad spectrum of detailed physic study. The ID gives efficient tracking of charged particles as well as measuring collision and decay vertices to a high precision. The ID is situated inside a magnetic field generated by a solenoid magnet allowing for accurate momentum measurements of charged particles. Excellent electron and photon identification is achieved in the Electromagnetic Calorimeters (ECal), while the Hadronic Calorimeters (HCal) make accurate hadron-jet and missing transverse energy measurements. The MS complements the ID and guarantees accurate measurements of the muon momentum also at high luminosity. The MS is situated inside a magnetic field generated by large air-core toroids allowing for momentum measurements of the muons. The trigger system ensures high acceptance for low-p_T particles, thus providing a high efficiency for most physics processes of interest at LHC.

During the long process from research and development to installation and testing of the ATLAS detectors the performance goals have been to ensure that the detector is capable of delivering high quality data sufficient for searching for new physics scenarios as well as for performing precise SM measurements, such as the top quark properties and electroweak gauge boson self-interactions. The general performance goals of ATLAS are summarized in Table 3.1. The technology and detectors needed to fulfill the performance goals are in the following sections discussed in more detail. For a complete and more comprehensive summary of the ATLAS detector and its expected performance see Ref. [50].

3.4.1 Inner Detector - ID

The layout of the ID is shown in Figure 3.3. It is contained within a 6.2 m long cylinder with a radius of $\sim$ 1.15 m. The solenoidal magnetic field which surrounds the ID has a strength of 2 T in the center. Closest to the interaction point high granularity is required because of the very high particle track density. As the distance from the interaction point

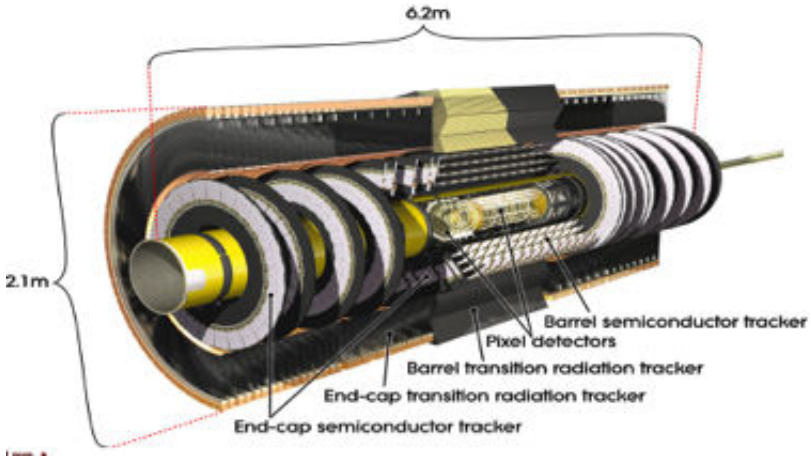

Figure 3.3: The Inner Detector

increases the particle occupancy decreases and reduced granularity detection suffices. The total number of high precision layers must be limited, however, because of the amount of material they introduce and the relatively high cost. To fulfill these requirements the ID therefore consists of three different sub-systems; the Pixel Detector, the Semiconductor Tracker (SCT) and the Transition Radiation Tracker (TRT) positioned at successively greater radii. Each of the sub-detectors contribute with precise measurements of the particle trajectory and momentum using different technologies. The innermost layers of the ID give precise information about the longitudinal (z_0) and transverse (d_0) impact parameters, defined as the the distance, parallel and transverse to the z-direction respectively, between the location of the point of closest approach of the track to the collision point. In b-tagging algorithms one often makes use of the sign of the impact parameter as well, which is based on the angle, α, between the jet and the line between the primary vertex and the point of closest approach of the track as pictured in Figure 3.4. If $\alpha < \pi/2$ the sign is positive (a) and if $\alpha > \pi/2$ the sign is negative (b). A detailed overview of the ID

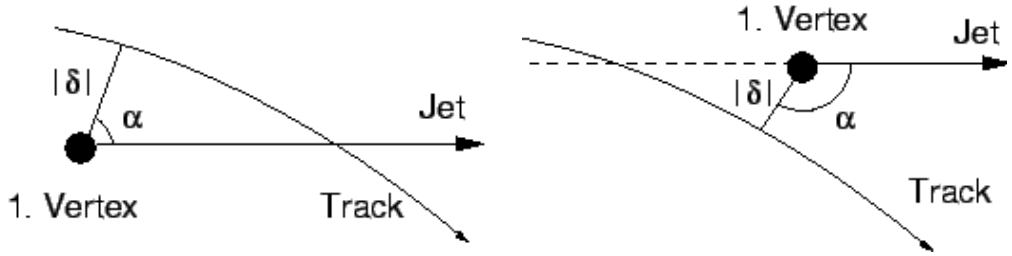

(a) Positive (b) Negative

Figure 3.4: Positive (a) and negative (b) impact parameters, $|\delta|$.

with the various components and sizes is shown in Figure 3.5.

Pixel Detector

The Pixel Detector constitute the innermost part of the ID and consists of three concentric cylinders around the beam axis and three disks perpendicular to the beam axis in each end-cap region. This gives an overall coverage of $|\eta| < 2.5$. The innermost layer of the Pixel

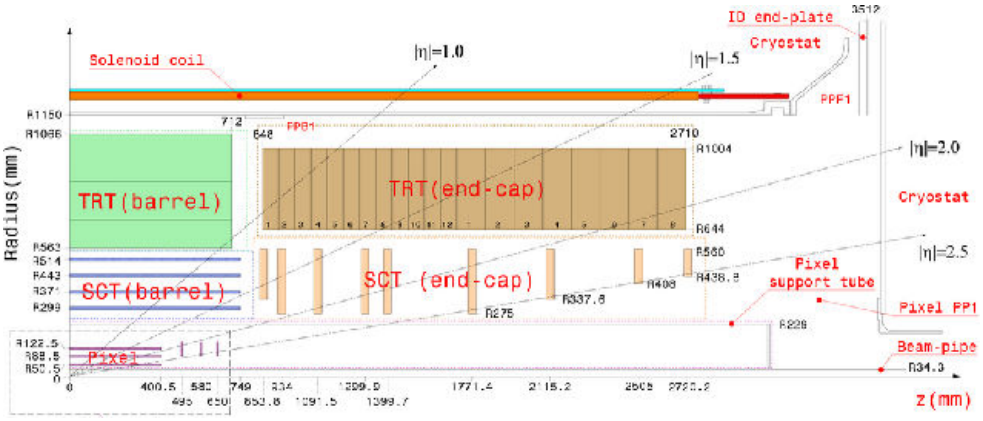

Figure 3.5: A detailed overview of one quarter of the Inner Detector showing each of the major elements with its active dimensions.

Detector, situated 50.5 mm from the beam-pipe, is called the *b-layer* because it provides impact parameter measurements and vertexing for heavy-flavour tagging. Because of the extremely high radiation close to the beam pipe the lifetime of the *b-layer* is limited and a replacement is needed after a certain amount of running.[4] Each track typically cross three pixel layers, giving an accuracy of 10 μm in R-ϕ and 115 μm in R or z [50]. To achieve such precise measurements the Pixel Detector is built up of identical sensors each having $47,232$ pixels with a size of $50 \times 400 \mu m^2$ each. The huge amount of pixels and corresponding readout channels (80.4 million) has been a major challenge with respect to the cooling and distribution of the electronics in the detector.

Semi Conducting Tracking Detector - SCT

The Pixel Detector gives an extremely high granularity detection, but the amount of material as well as the relatively high cost makes it unsuitable at larger radii. The amount of material is especially important to minimize in order to achieve accurate energy measurements in the calorimeters. Since particle density falls of with radius a slightly different design was chosen for the SCT detector. The SCT modules are made of single-sided micro-strip detectors glued back-to-back with an angular shift of 40 mrad with respect to each other (in some parts of the SCT there are four strip detectors making up one module). This allows for two dimensional position information for each hit. The strips are 80 μm apart in the barrel and between 55 and 95 μm in the end-caps. This gives a resolution of the position measurement of 580 μm in R and 17 μm in R-ϕ [50]. Like the Pixel Detector the SCT consists of one central barrel and two end-caps. The barrel is made up of 2112 modules distributed on four concentric cylinders so that four space points per track can be reconstructed. The end-cap sections on each side of the barrel has in total 1976 modules mounted on 18 disks (9 on each side). In total the SCT covers 63 m^2 with silicon micro-strip sensors distributed 40%/60% among the two end-caps and the central barrel [52]. The whole SCT provide detection for the range $|\eta| < 2.5$.

Since both the Pixel and SCT detectors suffer from high radiation damage (due to the

[4] A new Insertable B-Layer (IBL) is being installed, located on average only 34 mm from the interaction point, inside the existing *b-layer*, during the first long shutdown from 2013 to 2014 [51].

position close to the beam pipe) and large heat dissipation the modules need to be cooled down to the operating temperature of -7^oC [52]. In total the whole cooling system must remove up to 85 kW of heat from the two detectors and not have larger fluctuations than $\pm 2^0$C in order to avoid thermal shocks and cycles. The cooling used is an evaporative fluorocarbon system with C_3F_8 thin wall CuNi cooling tubes. A more detailed discussion of the SCT system follows in Chapter 4, where some work has been done by the author with respect to the running and monitoring of the detector.

Transition Radiation Tracker - TRT

The TRT is based on straw detectors, and consists of a barrel and one end-cap at each side. The barrel consists of about 52,000 straws, each being 144 cm long, installed parallel to the beam. Each straw is divided into two at $\eta = 0$, in order to reduce the occupancy, and read out at each end. In the end-caps there are about 246,000 straws, 37 cm long, arranged radially in 36 wheels, 18 on each side. The TRT is operated with a gas mixture of 70% Xe, 27% CO_2 and 3% O_2.When the charged particles pass through the TRT the gas is ionized and the charge is collected by a 30 μm diameter gold-plated tungsten wire inside each straw. On average the TRT provides about 30 (maximal 36) two-dimensional points - in the R-ϕ plane only - with 130 μm resolution over the range $|\eta| < 2$.

Transition Radiation The TRT is not only a straw drift tube tracker, but is able to detect transition radiation, which occurs when a particle travels between two media with different dielectric constants. The 73 layers of straws in the barrel, interleaved with fibres, and the 160 straw planes in the end-cap, interleaved with foils, provides the transition radiation identification of electrons in the TRT. The transition radiation is detected by absorption in the Xenon gas, which has a short absorption length for photons, yielding much larger signal amplitudes than ionizing particles. The TRT therefore runs with two thresholds, a low threshold which only detects the ionization signal and a higher threshold which detects the transition radiation. The transition radiation rate depends on the Lorentz factor, $\gamma = E/m$, of the particle. For instance a 10 GeV electron has $\gamma \sim 20,000$ while a pion with similar energy only has a $\gamma \sim 70$. The ratio of the high threshold hits to the total number of hits is therefore a powerful variable for discriminating electrons from pions.

3.4.2 Magnet System

The ATLAS magnet system consists of a central solenoid, a barrel toroid and two end-cap toroids. The solenoid magnet is located in front of the electromagnetic calorimeter and is aligned with the beam axis to minimize the amount of material the particles have to travel through. The magnet produces a 2 T axial magnetic field for the ID which is returned by the steel in the HCal. The barrel and end-cap toroids are situated outside the calorimeters and produce a magnetic field of about 0.5 T and 1 T for the barrel and end-cap regions of the Muon System, respectively.

3.4.3 Calorimeters

The ATLAS calorimeters, consisting of several different detectors with full coverage around the beam axis, are completely symmetric in ϕ, as pictured in Figure 3.6. The calorimeters at smallest radii are housed in three cryostats. The barrel cryostat contains the electromagnetic barrel calorimeter only while the two end-cap cryostats contain the hadronic end-cap calorimeter (HEC) and the forward calorimeters (FCal). All these calorimeters use liquid argon (LAr) as the active medium because of its radiation hardness and stability. Outside the LAr calorimeters are three hadronic calorimeters (denoted Tile calorimeters), one central barrel and two extended barrels. The EM calorimeters have a fine granularity ideal for precision measurements of electrons and photons. The hadronic calorimeters have coarser granularity sufficient for jet reconstruction and missing transverse energy measurements. The calorimeters cover in total the range $|\eta| < 4.9$.

The calorimeters need to efficiently stop electromagnetic and hadronic showers and limit the leakage into the muon system. The depth of the calorimeter is therefore of great importance and is usually given in radiation or interaction lengths.[5]

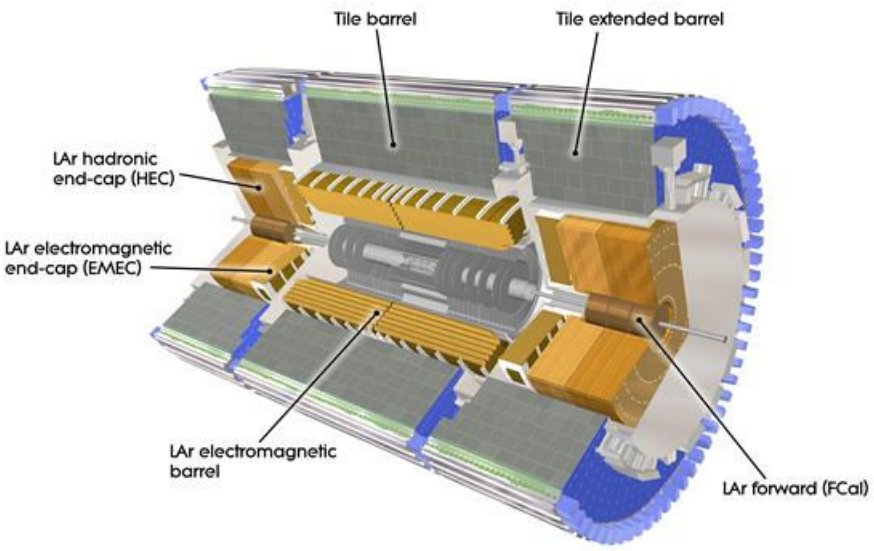

Figure 3.6: The Calorimeter system of ATLAS.

Electromagnetic Calorimeter (ECal)

The electromagnetic calorimeter is divided into a barrel part defined by $|\eta| < 1.475$ and two end-caps within $1.375 < |\eta| < 3.2$. The barrel consist of two parts bound together by a small gap of about four millimeters at $z = 0$. Each end-cap is also divided into two

[5] A *radiation length* is defined as the mean length required to reduce the energy, e, of a relativistic, electromagnetic-interacting, particle by a factor $1/e$ as it passes through matter. Correspondingly an *interaction length* is the mean length traveled by a hadronic particle before undergoing an inelastic nuclear interaction.

wheels covering different η regions. Depending on η, the total thickness of the ECal is at least 22 radiation lengths in the barrel and at least 24 in the end-caps [50]. The barrel ECal consists of 16 modules, each having three layers as shown in Figure 3.7. The first

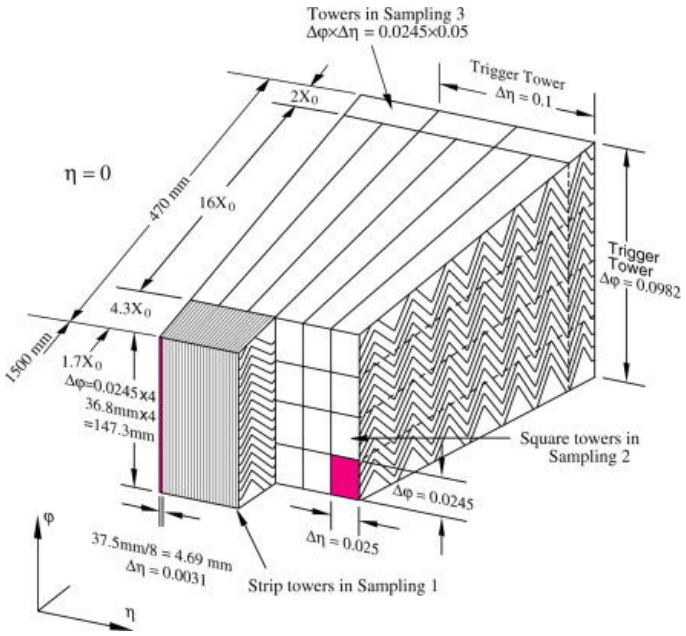

Figure 3.7: A sketch of a module in the central part of the ECal barrel. The three layers are clearly visible with the granularity in ϕ and η indicated.

layer is known as the strip layer and has a very fine granularity in η. The second layer consists of quadratic cells in the $\Delta\phi \times \Delta\eta$-plane while the third layer has cells with the same $\Delta\phi$ granularity as the second layer but twice coarser granularity in $\Delta\eta$. The exact granularity in $\Delta\phi \times \Delta\eta$ varies slightly between the central part of the barrel $|\eta| < 1.40$ and the outer part $1.40 < |\eta| < 1.475$. The end-cap wheels mainly have modules with three layers as in the barrel except for the outermost regions of the two wheels ($2.5 < |\eta| < 3.2$) which do not contain the third layer. The granularity for each layer changes with η [50]. In front of the active calorimeter, in the range $|\eta| < 1.8$, there is a pre-sampler, used to correct for the energy lost by electrons and photons upstream of the calorimeter (e.g. the ID and the solenoid).

Hadronic Calorimeters (HCal)

The HCal consists of three different systems, two of them sharing the same technology as the ECal.

The End-Cap Calorimeter (HEC) is located just outside the EM end-cap calorimeter. It consists of two wheels per end-cap, each having 32 wedge shaped modules. Each wheel is further divided into two layers consisting of copper plates interleaved with LAr gaps.

Forward Calorimeter (FCal) is integrated into the end-cap cryostats. It is approximately 10 interaction lengths deep and consists of three modules in each end-cap. The

first module is made of copper and optimized for electromagnetic measurements. The other two modules are made of tungsten and measure mainly hadronic interactions. The active medium used in the whole detector is LAr.

The Tile Calorimeter is placed directly outside the ECal. It consists of one central barrel covering the region $|\eta| < 1.0$ and two extended barrels covering $0.8 < |\eta| < 1.7$. Steel is used as absorber while the active material consists of scintillating tiles. The three components of the Tile Calorimeter are divided into 64 modules and segmented in depth into three layers. The total thickness of the detector corresponds to 9.7 interaction lengths at $\eta = 0$.

3.4.4 Muon Spectrometer - MS

The two main purposes of the MS are to measure and trigger on the muons that exit the barrel or end-cap calorimeters. It is based on deflection of charged muon tracks inside a magnetic field. In the barrel ($|\eta| < 1.4$) the magnetic field is set up by the large superconducting air-core barrel toroid while in the end-cap ($1.6 < |\eta| < 2.7$) two smaller magnets inserted into both ends of the barrel toroid generate the field. In the transition region ($1.4 < |\eta| < 1.6$) the magnetic deflection is provided by a combination of barrel and end-cap fields. Figure 3.8 shows an overview of all the components of the MS. Both barrel

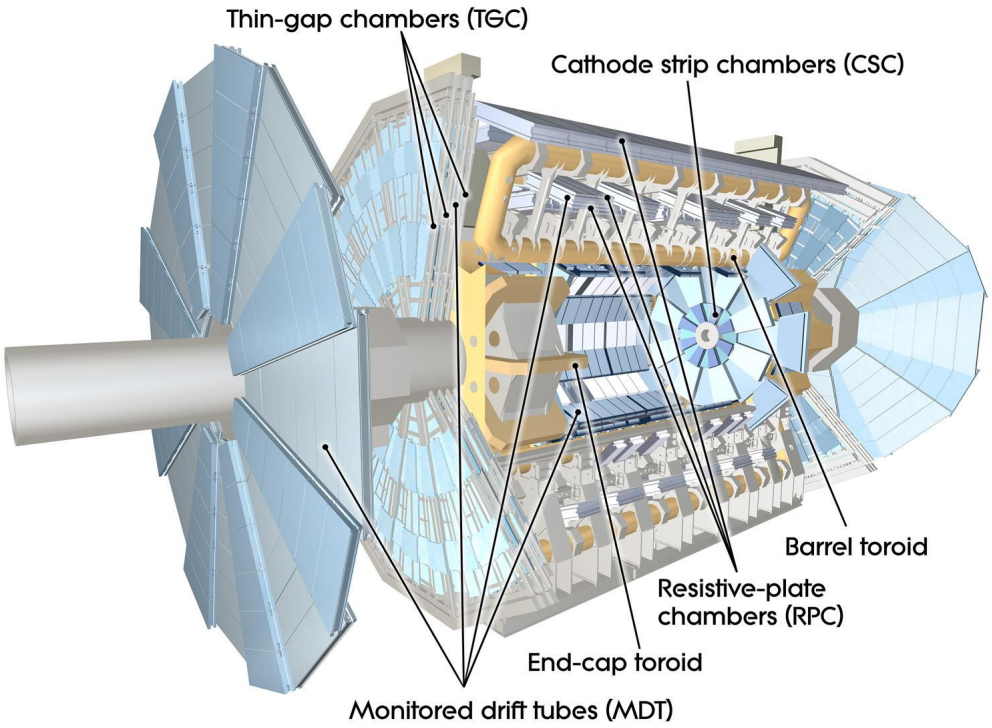

Figure 3.8: The components of the ATLAS Muon Spectrometer.

and end-caps consist of three layers which are arranged cylindrically around the beam axis in the barrel and perpendicular to the beam in the end-caps. The most precise and robust measurements of the track coordinates over a large η range are provided by the Monitored

Drift Tubes (MDTs). At larger η Cathode Strip Chambers (CSC) are responsible for the precise tracking information, having higher granularity than the barrel part because of the challenging rate and background conditions. Parts of the MS called Resistive Plate Chambers (RPCs) in the barrel and Thin Gap Chambers (TGCs) in the end-cap are used by the trigger system in order to provide bunch-crossing identification, well-defined p_T thresholds, and to measure the track coordinate in the direction orthogonal to the one determined by the MDT and CSC. Together these detectors provide trigger information in the range $|\eta| < 2.4$.

Muon Reconstruction

The identification and tracking of muons through the whole ATLAS detector is an area of intense interest in ATLAS. New algorithms have constantly been developed in order to combine the information from the various parts of the detector when trying to reconstruct muons. This has lead to a rich variety of possible muon candidates available for the analyser:

- **Standalone algorithm**: tracks from the MS extrapolated back to the interaction vertex
- **Combined algorithm**: ID tracks combined with tracks from the MS
- **Segment tagged algorithm**: ID tracks extrapolated to the MS and combined with segments reconstructed in the MS
- **Calorimeter tagged algorithms**: ID track extrapolated to the calorimeters and matched with energy deposits in the calorimeters

The various ways of identifying a muon track lead to different selections of muons [53]

- **StacoMuon Collection**: provides combined, standalone and segment tagged muons
- **MuidMuon Collection**: provides combined, standalone and segment tagged muons with a full refit of the combined ID and MS track

In addition there are several other muon collections available like MuonISR, MuonsCollection, CaloMuonCollection and MuGirlLowBetaCollection [54]. In the analyses presented in this thesis the *StacoMuon* Collection is used, as recommended by the ATLAS Muon Performance Group.

3.4.5 The ATLAS Trigger System

The huge complexity of the ATLAS detector combined with the extremely high-intensity collisions put strong requirements on the readout and data acquisition system (DAQ). As was discussed in the previous Chapter; with a bunch crossing rate of 40 MHz an interaction rate of $\sim$ 1 GHz is expected. This rate is four orders of magnitude higher than the design read-out rate of 200 Hz, which is the limit of the storage system.

The purpose of the ATLAS Trigger System is to ensure that the interesting events are kept. The system is divided into conceptually similar subsystems associated with the various subdetectors of ATLAS and has three distinct levels; Level-1 (L1, hardware), Level-2 (L2) and event filter (EF). Each level refines the decision made at the previous

level and possibly adds more requirements on the selection. The L2 and EF together constitute the High Level Trigger (HLT) which is purely software-based.

The L1 hardware trigger is implemented in custom-built electronics. It searches for signatures from possible high p_{T} muons, electrons, photons, jets and hadronically decaying τ-leptons. Events with large missing transverse energy or large transverse mass are also selected. The L1 trigger uses the information from the RPC and TGC (see Section 3.4.4) as well as from all the different calorimeters (Section 3.4.3) in order to look for these signatures. With today's design the L1 trigger can handle a rate of 75 kHz and the decision must reach the front-end electronics within 2.5 μs after the associated bunch crossing. Currently ATLAS has been running with a L1 trigger rate of 50 kHz [55]. If an event is accepted the information is passed from the front-end electronics to the Read-Out System (ROS) to be accessed by the HLT. The L1 trigger defines the regions of interest (ROIs) in the detector where possible interesting trigger objects are found.

The L2 trigger is seeded by the ROIs from L1. Based on this information L2 reduces the data to be transferred to the detector readout down to less than 3.5 kHz with an average processing time of about 40 ms. If the event is accepted the information from all ROSs are put together and assembled into a full event by the Event Builder. The last step is the EF which uses offline analysis on the fully built event to further select events down to a rate manageable for storage and offline analysis, approximately 200 Hz. The processing time of the EF is about four seconds. A schematic overview of the full ATLAS trigger chain is shown in Figure 3.9.

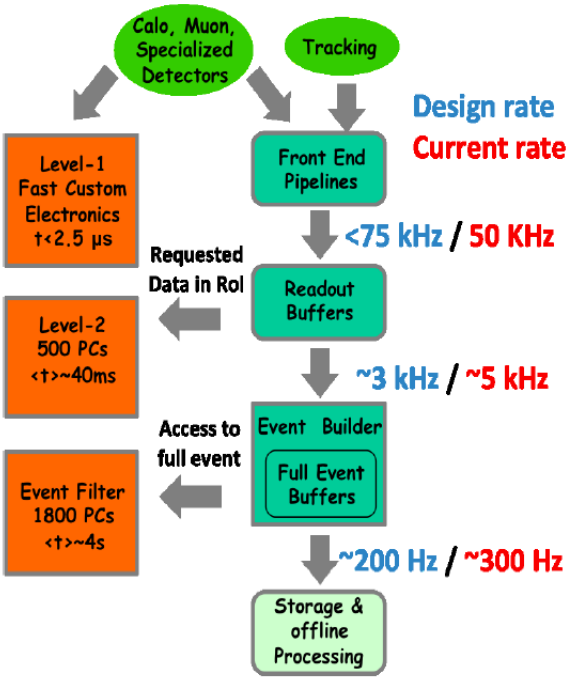

Figure 3.9: A schematic view of the ATLAS trigger system with the indicated design and actual (as of January 2012) event rates at each level. From Ref. [55].

Chapter 4

Towards 7 TeV Collision Data

After finishing the installation of all the sub-detectors, described in the previous chapter, the ATLAS detector was ready to be tested for the first time as a complete and coherent system. The first crucial step before getting ready to record 7 TeV data, however, is to ensure a safe operation of the whole detector. To be able to do this a transparent system monitoring the status of the detectors is of great importance. The Semiconductor Tracking Detector (SCT) has for many years been the main focus of the detector related activities within the Experimental Particle Physics Group (EPF) at the University of Oslo, dating back already to the first development of silicon detectors used in particle physics experiments. Since then the EPF activity within the SCT has been persistent through the building, installing, testing and commissioning of the detector. During 2008/09 the main activity of the SCT collaboration was to achieve a better understanding of the detector response, alignment and monitoring, as well as develop the tools to be used by shifters when operating the detector. This has been carried out using both data from cosmic rays and early 900 GeV collisions. The following Chapter will first discuss some of the work performed as a contribution to the operation of the SCT detector in the ATLAS and LHC environment. After this, a study of some of the first data ever recorded by ATLAS, using cosmic rays, is presented in Section 4.2. Finally, as a last important step towards the high energy collisions, studies done using the first 900 GeV collision data are discussed in Section 4.3.

4.1 SCT Operation

One of the most important tasks in a harsh environment like the LHC is to ensure that the particle detector is running under safe conditions. An unsafe running of the detector can lead to irreparable damage of the machine or cause a more rapid deterioration. The detector might then end up having a much shorter lifetime than expected, not able to deliver the amount of high quality data required by the physics analysers. Data recorded without reliable tracking information from the SCT for instance would be of no use to physicists. Anyhow, because of the enormous complexity of the SCT, there will always be modules, sensors and other electronics that do not work properly. The aim is of course

to minimize this fraction.[1] During the collision runs at 7 TeV in 2011/12, if more than 0.1% of the remaining modules were delivering data with unrecoverable problems (or no data at all), the data would be flagged as *defect*. Running with this definition the SCT delivered $\sim$ 99.5% of "good data" [56]. The high efficiency obtained was due to a very robust design of the SCT and thanks to a dedicated team doing 8 hours shifts 24/7 during operation.[2] The two main tasks for the shifters are

1. to monitor the recorded data and ensure that it looks reasonable
2. to control the detector modules and cooling system such that the detector always runs under safe conditions.

The latter task is the main purpose of the complicated Detector Control System (DCS) of the SCT.

4.1.1 SCT Detector Control System (DCS)

To ensure and control that the detector runs under safe conditions a system monitors the detector and its components. The SCT DCS provides the detector with power and cooling and protects against failure and error conditions. The DCS is divided into two subsystems, the power-supply (PS) system and the environmental monitoring and interlock system.

Power-Supply (PS) System

The largest subsystem is the PS system, which provides all voltages and control signals needed to operate an SCT module, illustrated in Figure 4.1a. Each of the 4088 modules is powered by an independent PS. There are both low voltage (LV) and high voltage (HV) supplies. The LV supplies provide all voltages needed by the Detector Module ASICs (Application Specific Integrated Circuit), the associated opto-electronics[3], temperature monitoring, module reset and clock select signals [57]. The HV provides the bias voltage needed to deplete the sensors. The LV and HV cards are installed in power-supply (PS) crates, as shown in Figure 4.1b, covering 48 modules in one crate. Each crate consists of twelve LV cards, with four channels each, and six HV cards with corresponding eight channels each. These crates are served by a common crate controller, crate PS and crate controller software. In addition to power, each module is provided with several other connections in order to be able to readout signals and to tune and control the PS. In total each module has 16 power-supplies and corresponding readout channels. To ensure safe operation of each module there are several safety mechanisms implemented in the PS system. The HV channels have an over-current and over-voltage that automatically trips the voltage if any of these parameters exceed the limits. The LV channels also have hardware protection for the analog and digital voltages and currents. If any of the channels exceeds the trip limits for a certain amount of time the LV power module is tripped. Through the DCS-DAQ-Communication (DDC) system a shifter or an expert is able to reset and power-cycle a module, in order to bring it back into a working state, after

[1] As of November 2012 0.66% of the modules, 0.09% of the chips and 0.17% of the strips are excluded from data taking [56].

[2] Which the author has taken part in.

[3] Electronic devices that interact with light.

the conditions are ensured to be safe and the cause of the problem is properly understood.

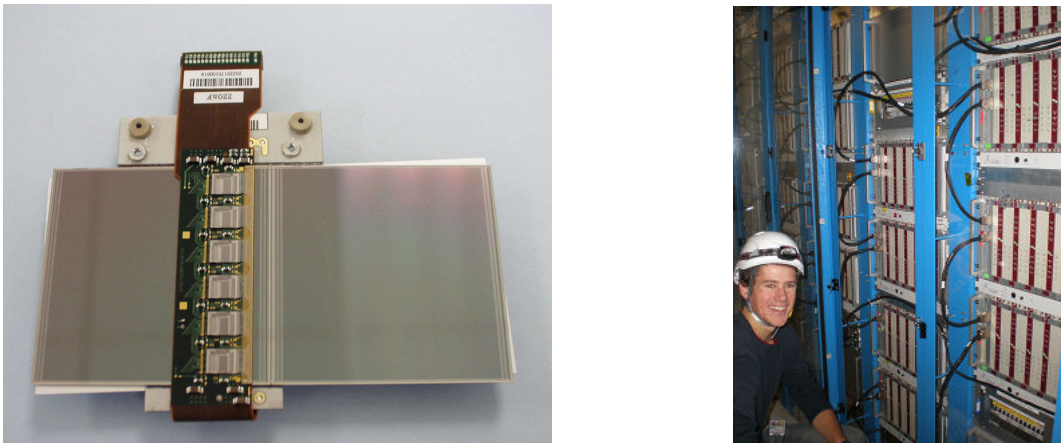

(a) (b)

Figure 4.1: An SCT barrel module (a) and me in front of one of the PS crates in the ATLAS cavern (b). You can see the HV (red bars) and LV (beige bars) cards.

The Environmental DCS and Interlock System

An environmental monitoring system is required to ensure that the SCT is running under safe conditions. There are six types of environmental sensors installed in the SCT, these are:

1. **Mechanical sensors** - measure the temperature on the carbon fiber support structure.
2. **Air sensors** - monitor the air inside the detector volume.
3. **Cooling sensors** - monitor the cooling on the outlets of the cooling pipes.
4. **Monitoring cooling sensors** - monitor the cooling near the module cooling blocks.
5. **Xeritron humidity sensors** - radiation-hard sensors monitoring the humidity inside the detector volume.
6. **Honeywell humidity sensors** - non-radiation-hard sensors monitoring the humidity inside the detector volume.

From measurements of the temperature (T) and relative humidity (RH) obtained from these sensor the dew point in ^oC can be calculated using [58]

$$T_{\text{dew-point}} = \frac{\left(\frac{\beta T}{\lambda+T} + \ln\frac{RH}{100}\right)\lambda}{\beta - \left(\frac{\beta T}{\lambda+T} + \ln\frac{RH}{100}\right)}, \tag{4.1}$$

where the constants, β and λ, are called Magnus Constants and must be determined empirically. Currently $\beta = 17.08085$ and $\lambda = 234.175$ are used in the SCT. These coefficients are valid for water in liquid phase between 0-100^oC [59].

The purpose of the interlock system is to protect the modules from overheating if cooling stops. If the interlock is triggered by high temperature on the cooling loop then

the associated power-supply channels are switched off within about 1 sec. The SCT shifter or any SCT expert can re-power the module when the conditions are again believed to be safe. The cooling sensors located close to the module cooling blocks are not part of the interlock system.

4.1.2 The Inner Detector Cooling System

The cooling of the Pixel and SCT detectors is monitored by the SCT shifter.[4] The operational temperature of the Pixel and SCT modules are -7^{o}C and there should be a stability better than $\pm 2^{o}$C in order to avoid thermal shocks and cycles.

4.1.3 Power Distributions for the SCT

About 23 kW are needed for the nominal operation of the SCT detector. The design of this system has been challenging since it should satisfy several conflicting requirements. One should minimize material in the detector, the voltage drop and the power dissipation (due to long distances) together with the costs. To satisfy these requirements the power path system from the modules to the power supplies is divided into several parts. The first part, from the modules to the patch panel (PPB1 for the barrel and PF1 for the end-cap), is done by low mass tapes (LMTs). The LMTs are made from 25 μm with Kapton and 25 μm of glue substrate with copper conductors covered by another layer of glue and Kapton. All connections needed for the modules in the detector are present on such a tape. The patch panels one (PP1) are situated just outside the detector, in the cavern, and the length of these cables are therefore between 0.7-3 m. In PP1 the LMTs are connected to a new cable which goes to the next patch panel (PP2). This distance is much longer, approximately 9 m, and very good conductors are used to minimize the voltage drop. At PP2 these cables are again connected to a new type of cables going to patch panel three (PP3), a distance of about 20 m. The last part is from PP3 to the power-supply crates which are located outside the detector cavern.

4.1.4 Scripts for Accessing the SCT Offline Database

All the information from the SCT DCS and cooling system is written to the Oracle database using the PVSS Oracle Relational Database manager [57]. The DCS data for a specific module, including voltage, temperature and current is associated with its unique offline identifier in the database. Data is written from the SCT to the database approximately every second. Several scripts have been developed by the author to be able to investigate and study some of the interesting measurements written to the database. These scripts are based on *Perl* scripts originally written by Saverio D'Auria[5], but are developed further including new functionalities as well as translated into the slightly more used programming language, *Python*. The scripts check the behavior of some specific variable during a period of time specified by the user. The script queries the Oracle database

[4] From 2012 the shifter role changed to cover the complete ID system (Pixel, SCT and TRT), including cooling.

[5] University of Glasgow (GB)

Element names	Description
HVchStat, LVchStat	high and low voltage status word (see Table 4.2)
LVchVCSI, LVchVCSV, LVchPINV, LVchPINI	optolink voltages [V] and currents [mA]
MOch_Tm0, MOch_Tm1	temperatures $[^oC]$ of the two sensors on each module (only Tm0 in endcaps)
LVretVdd, LVretVcc, LVch_Idd, LVch_Icc, LVps_Vdd, LVps_Vcc	low voltages [V] and related currents [mA] on module chips
HVchVolt, HVchCurr	high voltage PS readings of voltage [V] and current [nA]
Dew point	the dew point for a given temperature and humidity from formula in Eq. 4.1
CC Status	crate controller status word (one per crate, see Table 4.3)
hit rates coincidence (bkgA and bkgC)	see text

Table 4.1: The element names and the description of possible SCT DCS variables to be used in queries to the Oracle data base.

(through the *cx_Oracle* function in Python) and produces plots summarizing the evolution of the variable over the wanted time span. The user can also ask for specific variables within some predefined range, for instance all elements within a time interval with bias voltage above 10 V. The script then returns plots for all elements satisfying the condition. There is also a functionality to use wildcards as well as standard logical operators such as ||, && and > in the queries. These scripts can be run on any lxplus machine at CERN with access to the Oracle database. The variables that can be checked using these scripts are specified in Table 4.1 with their element name and a description.

Hit Rates Coincidence

The Beam Condition Monitor (BCM) has two detectors situated ±184 m from the collision point along the z-direction and approximately ±4.2 in pseudorapidity. These detectors measure the hit rates and coincidences of hits. When the hits are symmetric around the expected interaction time they are likely to come from the collisions. For beam induced backgrounds, such as beam gas, beam halo and scraping [60], the hits are shifted, since the particles reach the detector on the incoming beam side earlier then at the interaction point. The bkgA corresponds to a particle passing through ATLAS from C to A and correspondingly bkgC is a particle passing through ATLAS from A to C. The hit rate is measured in Hertz and corresponds to the rate of particles that are out-of-time.

Bit #	Status Word		
	Low Voltage (LV)		**High Voltage (HV)**
7	LV output ON		Over Voltage Trip
6	LV output standby		Over Current Trip
5	if bit 5 == 0:	if bit 5 == 1 (failure):	Persistent Parity Error
4	Vpin or Vcsel Volt Limit	LV OverVoltage	ramping in progress
3	Module Temp Warning	LV OverCurrent	Channel masked off by card controller
2	Open Temp Sensor 1	Module Temp Trip	Master/Slave communication error
1	Open Temp Sensor 0	Communic Err on Vdd	Current Probe Resistor MSB
0	Clock Select Set	Communic Err on Vcc	Current Probe Resistor LSB

Table 4.2: The status words for the HV and LV signals. For the LV the meaning of bit 0-4 is dependent on the value of bit 5.

Hexadecimal	Status Word	Description
0x0	OFF	HV/LV channel is OFF
0x1	ON	HV/LV channel is ON
0x2	Stand By	HV/LV channel is STANDBY
0x3	Manual	HV/LV channel is value set by an expert
0x4	Mask OFF	HV/LV channel is masked off
0x5	Mask ON	HV/LV channel is masked on
0x6	Hard Reset	
0xA	Hardware Trip	hardware trip actioned by HV/LV channel firmware
0xB	Software Trip	software trip actioned by crate controller firmware
0xC	Card latch	LV card has overheated and turned itself off
0xD	Mismatch	monitored values do not match commanded ones
0xE	UNKNOWN	HV/LV channel is not responding

Table 4.3: The hexadecimals corresponding to the different status words for the crate controller along with a description. Note that the *card latch* is valid only for the LV channel.

High and Low Voltage Status

The possible states of the HV and LV channels are stored in 8-bit variables and the meaning of each bit is listed in Table 4.2.

Crate Controller (CC) Status

The crate controller status is also stored in an 8 bit variable where the first 4 bits are for the high voltage while the latter 4 are for the low voltage channel. For more information on how to retrieve the information stored in bits see Appendix D.

Element name	Valid range min	Valid range max	Unit
CC Status		-	
MOch_Tm0	−12	28	^0C
HVchStat		-	
LVchStat		-	
Dew	−90	10	^0C
TEMP	−20	25	^0C
SURFACETEMP	−2	80	^0C
LVchPINI	0.05	0.9	Ampere
ATLASHITRATESDATA.COINCIDENCES.BKG	−10	5000	Hz

Table 4.4: Whenever a measurement is found to be outside the valid range a plot is produced showing the trend for the last 8 hours. For the HV, LV and Crate Controller status a message is printed according to Table 4.2 and Table 4.3 if any of the bits are set.

4.1.4.1 SCT DCS Cron Job Script

In order for the shifters to get an easily accessible summary of the DCS system at the end of his/her shift, a script that checks if any of the elements listed in Table 4.1 are outside a predefined range, is made. The valid range for each of the elements that are checked can be found in Table 4.4. For the HV, LV and Crate Controller status a message is printed according to Table 4.2 and 4.3 if any of the bits are set. A cron job, set up at the ATLAS Point 1 server, runs the script 45 minutes before the end of every shift (i.e. 06:15, 14:15 and 22:15). The script produces a web page with a list of the elements that were found to be outside the valid range in the last 8 h period. The web page contains links to plots for the non-valid elements as well as earlier produced web pages (currently the web pages are stored for one month before they are deleted). The web pages are accessible outside CERN[6] (with a password) as well as from a separate icon on the ID shifter computer in the ATLAS Control Room. Two examples of plots produced by the script, showing the hit rate and dew point, are found in Figure 4.2a and b respectively. An example of a complete web page is shown in Figure 4.3. More information on the cron job and the running on the ATLAS P1 web servers can be found in Ref. [61].

[6] https://atlasop.cern.ch/sct/SCT_daily_check_public.html

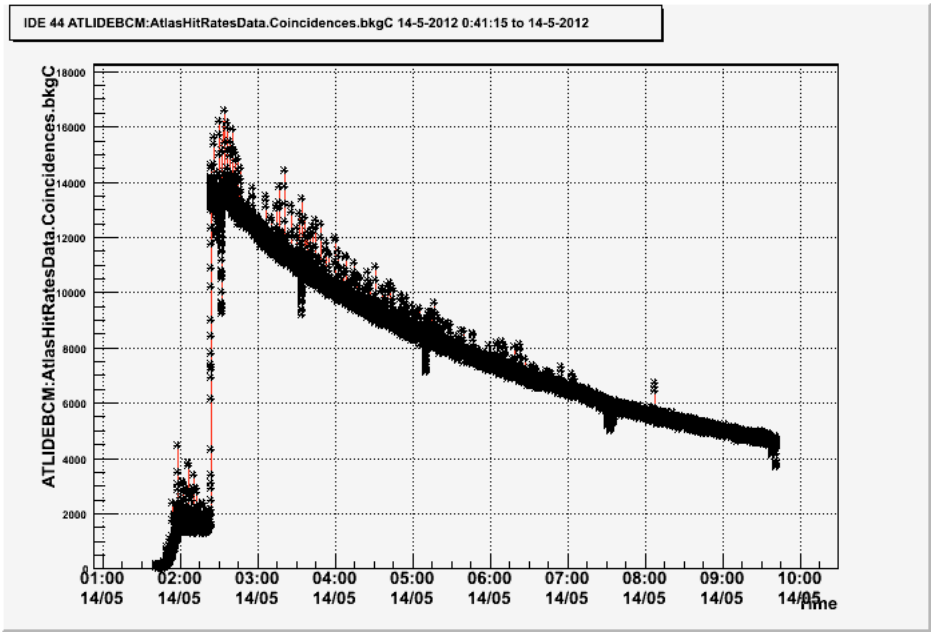

(a)Eight hours trend of the hit rate

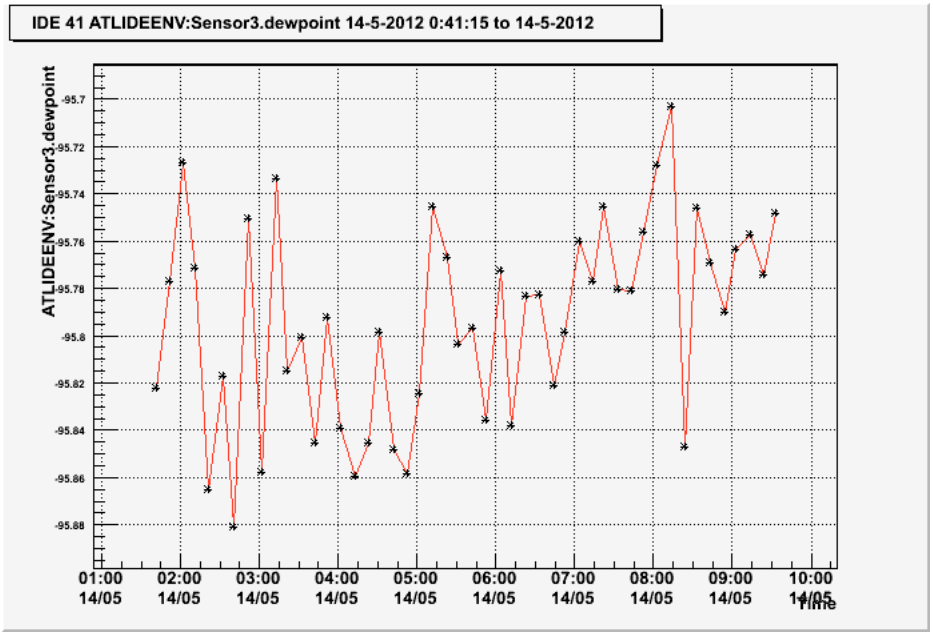

(b)Eight hours trend of the dew point

Figure 4.2: Plots showing the last 8 hours of the hit rate (a) and dew point (b) for the SCT, obtained by querying the Oracle offline data base.

Data Base report SCT check
for last 480 minutes from Sun Nov 25 06:15:04 CEST 2012

Check on TM0 From 24-11-2012 21:15:4 To: 25-11-2012 5:15:4 UTC. Valid Range used: [-12,28]
Check on HVCHSTAT From 24-11-2012 21:15:4 To: 25-11-2012 5:15:4 UTC. Valid Range used: [0,60]
Check on .STATE From 24-11-2012 21:15:4 To: 25-11-2012 5:15:4 UTC. Valid Range used: [0,60]
Check on SURFACETEMP From 24-11-2012 21:15:4 To: 25-11-2012 5:15:4 UTC. Valid Range used: [-2,80]
Check on LVCHPINI From 24-11-2012 21:15:4 To: 25-11-2012 5:15:4 UTC. Valid Range used: [0,0]
Check on TEMP From 24-11-2012 21:15:4 To: 25-11-2012 5:15:4 UTC. Valid Range used: [-20,25]
Check on ATLASHITRATESDATA.COINCIDENCES.BKG From 24-11-2012 21:15:4 To: 25-11-2012 5:15:4 UTC. Valid Range used: [-10,5000]
Check on LVCHSTAT From 24-11-2012 21:15:4 To: 25-11-2012 5:15:4 UTC. Valid Range used: [32,32]
Check on .DEWPOINT From 24-11-2012 21:15:4 To: 25-11-2012 5:15:4 UTC. Valid Range used: [-90,10]

TM0:
.....none

HVCHSTAT:
.....none

.STATE:
ATLSCTUSEPS1:Crate11.Channel39.State 20220281000018 177 25-11-2012 00:50:26:038 bl HV Software Trip LV ON

SURFACETEMP:
ATLIDEEVCOOL:endcap1_15.temperature_v.Read IDE/EVCOOL/SCT/EndcapA/Q1/loop147/heater/SurfaceTemp 0.771 -2.704

LVCHPINI:
.....none

TEMP:
.....none

ATLASHITRATESDATA.COINCIDENCES.BKG:
ATLIDEBCM:AtlasHitRatesData.Coincidences.bkgA IDE/BCM/AtlasHitRatesData/Coincidences/BackgroundA/RatePerSec 33362 0
ATLIDEBCM:AtlasHitRatesData.Coincidences.bkgC IDE/BCM/AtlasHitRatesData/Coincidences/BackgroundC/RatePerSec 57182 0

LVCHSTAT:
.....none

.DEWPOINT:
ATLIDEENV:Sensor1.dewpoint IDE/ENV/SideC/SCTBarrel/Q2/HSP/Honeywell/Dewpoint 14.491 14.385

Number of elements checked: 9
Total Number of Results Found: 5 (including multiple instances)

Note: multiple instances of the same LV trip no longer appear in the above list.

List of archived reports

List of known problems: IDE/ENV/SideC/Flange/Q2/Inner/Honeywell/Dewpoint
EndCapC/Disk4/Q1/TempSensor1/Mech
EndCapC/Cylinder/Q4/TempSensor5/Mcool
EndcapC/Disk7/Q1/Loop174/Pipe/TempSensor2
EndCapA/Cylinder/Q4/HumiSensor2/HW
EndCapA/Cylinder/Q1/TempSensor3/Mcool
IDE/ENV/SideC/SCTBarrel/Q2/HSPBarrelHex/Honeywell/Dewpoint

Atlas SCT DCS
Last modified: Sun Nov 25 06:15:04 CEST 2012

Figure 4.3: An example of the web page produced 45 min before the end of each ID shift.

4.2 Study of Cosmic Ray Data

The recording of cosmic ray data before the start-up of the LHC made it possible, for the first time, to study the performance of the overall ATLAS detector in finding, identifying and reconstructing muons, electrons and jets. This Section presents a study of the first real (i.e. not simulation) electrons in the cosmic ray data recorded between December 2008 and late 2009 [62, 63].

Studies on the cosmic ray data was a very important challenge for ATLAS in order to test the full analysis chain. Everything from the recording of data to the running of the analysis code on the grid[7] were tested. Important measurements of the alignment and material budget were also performed, and helped getting a good understanding of the detector before collisions started. The work on cosmic ray data also helped the analysers getting used to retrieve, understand and study real data.

4.2.1 Cosmic Rays

Cosmic rays are usually referred to as being either primary or secondary. The primary cosmic rays are those originally produced in various astrophysical processes while the secondary rays are produced by the interaction of the primary cosmic rays with the Earth's atmosphere. The secondary cosmic rays, and their decay products, are therefore the ones observed at the surface of the Earth.

Primary cosmic rays are highly energetic charged particles and nuclei bombarding the Earth from all directions. The main source of high energy cosmic rays hitting the Earth's atmosphere is believed to be protons and light nuclei originating mainly from outside the Solar System, and which are accelerated to very high velocities when going through remnants of supernovas. These cosmic rays typically have energies between 100 MeV and 10 TeV and are known as galactic cosmic rays [64]. The exact origin of these cosmic rays is however not yet perfectly understood. There are also other sources of primary cosmic rays, such as nuclei emitted in solar flares or ionization processes from the interaction between the interstellar gas and the solar winds. These have typically lower energies compared with the galactic cosmic rays. The most energetic type of primary cosmic rays, with energies above 1000 TeV, are known as the extragalactic cosmic rays, being extremely rare, with only a few hits per square meter expected at the surface of the Earth per year [64]. Therefore, little is known about their origin.

When the high energy cosmic rays hit the Earth's atmosphere they interact with the atoms and produce secondary cosmic rays, consisting typically of neutrons, protons and pions. The pions decay quickly, producing muons, neutrinos or photons. Most of the secondary particles reaching the Earth's surface are in fact muons and neutrinos and can therefore be studied by particle detectors at ground level.[8] The photons from the pion decay typically lead to large electromagnetic showers of electrons, positrons and photons which also can be measured by experiments at the surface of the Earth.

[7] The World-Wide LHC Computing Grid (WLCG) is used when physicists run their analysis-code on data from any of the LHC experiments.

[8] Or even 100 m under ground where ATLAS is located.

4.2.2 Particles from Cosmic Rays in ATLAS

As already discussed, ATLAS is situated 100 m underground and does not really serve as an optimal detector for studying particles from cosmic rays. Nevertheless, the fact that few particles survive all the way down to ATLAS is an advantage if aiming at studying neutrino properties. Neutrinos interact very weakly with ordinary matter and are not affected by having to penetrate through 100 m of rock and concrete. Unfortunately ATLAS is not able to detect neutrinos directly[9] so the main interest for ATLAS is therefore the muons from cosmic rays.

4.2.3 Electrons from Cosmic Ray Muons

Electrons can be produced in several ways from cosmic muons. Depending on the production mechanism the electrons leave different signatures in the detector, as sketched in Figure 4.4. One way to produce electrons is through muon decay-in-flight, $\mu \rightarrow e\nu_e\nu_\mu$. The muon decays totally independent of the distribution of material in the detector, and it can in principle happen everywhere inside the detector. A typical decay in flight event is sketched in Figure 4.4a. Muons might also interact with the detector material. This can in some cases lead to production of a photon through muon bremsstrahlung which again converts into an electron-positron pair (Figure 4.4c). The muon might also ionize atoms in the material. As a result highly energetic delta electrons can be ejected (Figure 4.4b). The cross-sections for the latter two production mechanisms are larger by a factor 4 and 80 respectively compared to the decay-in-flight cross section [63]. Because of this, electrons are in most cases expected to be produced in the more dense parts of the detector (i.e. typically inside the ID or between the ID and the electromagnetic calorimeter at $1 < |\eta| < 2$) and deposit their energy in the bottom half of the calorimeter. If the electron is produced before the muon has penetrated the upper half of the calorimeter the electron will never reach the ID and thus will not be reconstructed. In Figure 4.4d the muon emits a photon through bremsstrahlung which does not convert into an electron-positron pair within the ID volume. The photon only leaves a cluster in the lower part of the EM calorimeter. This cluster might then wrongly be matched with the muon track and lead to an event with signature similar to that of delta electrons. These candidates are denoted as fake electrons.

As already stated, delta electrons are the main source of electrons initiated by cosmic ray muons. They are defined as signal electrons in the following. The other processes are defined as backgrounds. Looking at Figure 4.4 we define the **signal sample** by requiring at least two ID tracks, one reconstructed electron in the bottom half of the detector and at least one reconstructed muon. The **background sample** is defined using the same cuts, except requiring exactly one ID track. This means that a possible decay-in-flight event would be regarded as background, but as already discussed, the rate for this is expected to be very small.

[9] In collision events however the missing transverse energy can be used as an identification of neutrinos (or any other undetectable particle), since the total transverse energy is conserved in every collision. Such an approach is of course not possible in cosmic ray events. There are however several other detectors around the world situated deep under ground, water or ice that are specialized in measuring neutrinos, like IceCube, Super-Kamiokande and ANTARES.

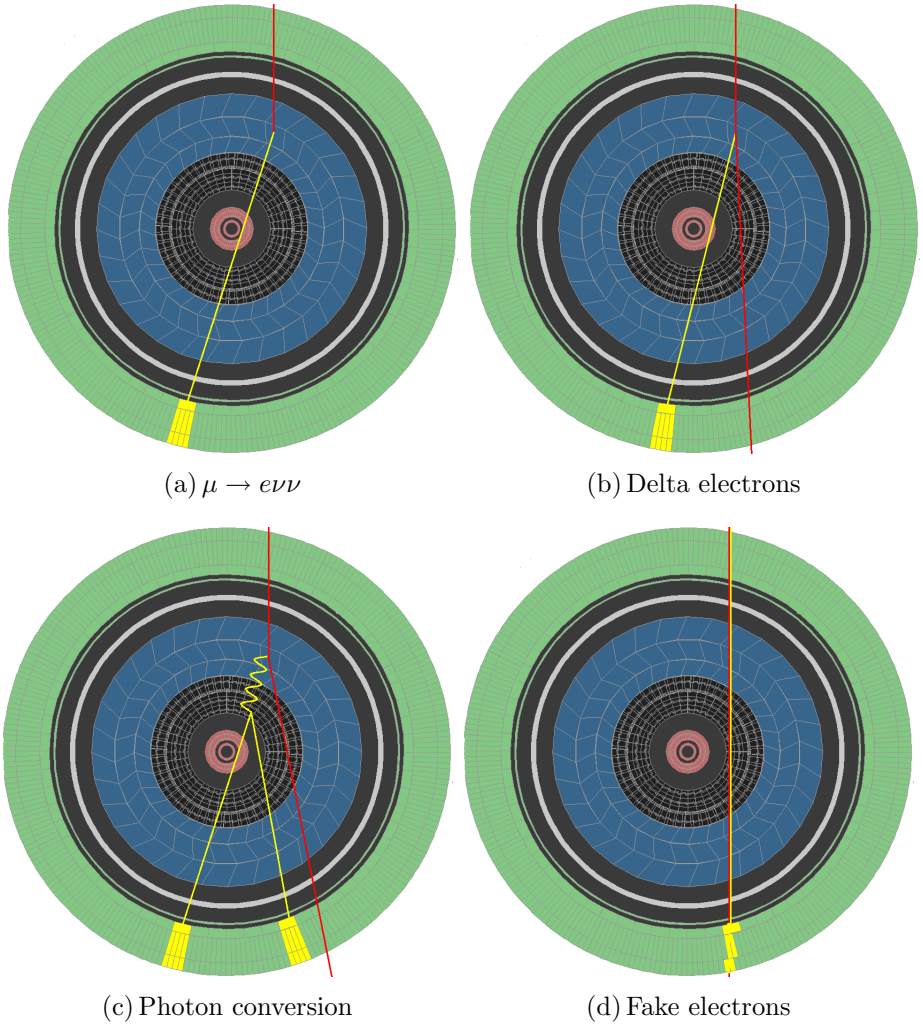

(a) $\mu \rightarrow e\nu\nu$ (b) Delta electrons

(c) Photon conversion (d) Fake electrons

Figure 4.4: Illustrations of the possible signature of different processes producing real electrons from a cosmic muon (a, b and c). In (d) a muon mimicking the signature of an electron, leading to a fake electron, is sketched. Muons are indicated by red lines, electrons with straight yellow lines and photons with curly yellow lines. The detector parts which are sketched are (from outer to inner): the electromagnetic calorimeter, the solenoid, the TRT, SCT and Pixel.

Project tag	Reprocessing tag	# of events	ATHENA release
data08_cosmag	r653	3,729,486	14.5.2.4
data08_cosmag	r653_r792	3,725,315	15.3.1.20
data09_cos	r733	10,041,312	15.2.0.11
data09_cos	f165	3,961,021	AtlasTier0-15.5.2.5
mc09_valid	r848	1,270,405	15.3.1.7

Table 4.5: Cosmic ray data used to study the first electrons observed in ATLAS. The data correspond to about 20 million events recorded in 2008 and 2009 with both of the magnets turned on. The reprocessing tag and ATHENA releases used for the various datasets are also listed. In addition a sample of about 1 million events of simulated cosmic events was used. All the data is recorded with both magnets on, even though the project tag of the 2009 data does not indicate this explicitly, as for the 2008 data.

Table 4.5 lists the data and MC used in the study of electrons from cosmic rays in ATLAS. The data is required to have been recorded with both magnets running at nominal field strength, and only runs with more than 500,000 events were included. The events are required to be picked up by the *IDCosmic* stream, meaning that every event is triggered by any L1 trigger where the L2 track trigger for cosmics [65] has found a track either in the silicon detectors or in the TRT. In the end a total of about 20 million events were used.

4.2.4 Particle Reconstruction

Cosmic ray events are significantly different from collision events because the tracks do not originate from the center of the detector, but cross the full detector from top to bottom at a random time. For the detector parts making use of the drift time (i.e. Muon Drift Tubes and the Transition Radiation Tracker (TRT)) the resolution decreases significantly if not properly corrected for, since the arrival of a cosmic muon is, obviously not, synchronized with the LHC bunch clock. A correction is therefore performed on an event by event basis using all measurements on the cosmic muon track [66].

The standard track reconstruction in the ID also needs to be significantly adjusted to incorporate tracks with an arbitrary impact with the z-axis and which cross both halves of the detector [67].

In these studies the muon candidates stored in the *StacoMuonCollection* are used, as defined in Section 3.4.4.

All electron candidates of the *ElectronAODCollection* were considered. These are electrons reconstructed by either the cluster-based or the track-based egamma algorithms [68]. The track-based algorithm starts from a good quality track and extrapolates it to the second layer of the calorimeter. A cluster is then built by summing over all energy entries within a 3×7 cell window. The cluster-based algorithm starts from a cluster which is matched with an ID track within a certain $\Delta\eta$ and $\Delta\phi$ of the cluster. For tracks only reconstructed by the TRT the matching in η is skipped.

4.2.5 Particle Identification

Because cosmic events are very different from ordinary collision events some of the standard electron identification cuts [68] need to be modified. The same division into loose, medium and tight selections, giving better and better rejection against background electrons, is preserved, but some of the cuts are completely removed or moved from the medium to the tight definition. All cuts used in the analysis of cosmic ray data are listed in Table 4.6. The loose cuts follow the standard loose definition used in collision data, which are discussed in more detail in Section 6.3.1. Since the electron tracks often do not cross the ID, or only parts of it, the requirements on the number of SCT and Pixel hits are removed from the medium definition. The matching between the cluster and track is only done in the ϕ-plane since TRT-only tracks contain axial hit information only. The distributions of the variables used in the definition of loose, medium and tight, as given in Table 4.6, are shown in Figure 4.5, 4.6-4.8 and 4.9 respectively. The plots show cosmic ray data from three different periods of data taking along with MC. There is an overall good agreement between the various periods and MC for most of the distributions. The ratio of the number of high to low threshold TRT hits, f_{HT}, in Figure 4.9b stands out however, where we see that the data taken during summer 2009 differ significantly from the rest. This is caused by the fact that the TRT was running with the Fast-OR trigger which requires lower high threshold settings and thereby giving much more high threshold hits [70].

4.2.6 Electrons from Cosmic Rays in ATLAS

Table 4.7 shows the total number of electron candidates (i.e. directly from the *ElectronAODCollection*) in the various data periods together with the number of candidates in the signal and background region. The number of electrons in each of the three categories; loose, medium and tight is also listed. It is clear from Table 4.7 that most of the electron candidates belong to the background category, which is dominated by electrons from muon bremsstrahlung. Only a small fraction falls inside the signal sample, believed to be dominated by electrons from muon ionization processes. As expected, the identification criteria reduce the number of events in the background sample to a large extent. For the signal sample a smaller fraction of the events are removed by tightening the identification criteria. In order to study the signal sample, the two variables used in defining the tight identification criteria are investigated further. Figure 4.10 shows the cluster energy divided by the track momentum, E/p, for electron candidates passing the medium cuts inside the signal (a) and background (b) samples. For the signal electrons there is a clear rise in the distribution around one, expected for the ionization electrons. In the background plot the distribution falls off and no enhancement around one is seen. The other variable used in the tight identification is the ratio of high to low threshold TRT hits, f_{HT}. This distribution is shown in Figure 4.11 for medium electron candidates for the signal (a) and background sample (b). Again the signal electron candidates differ as they tend to have a relatively broad distribution while the background falls off quite rapidly at higher values of f_{HT}. From the discussion above it is clear that the E/p and f_{HT} both seem to serve as very efficient variables in order to discriminate signal electron candidates from background. A 2D distribution of all medium electron candidates in the E/p versus f_{HT} plane is shown in Figure 4.12. As expected the signal electron candi-

Type	Description	Cut	Name
Loose selection			
Hadronic leakage	Ratio of E_T in the first layer of the hadronic calorimeter to E_T of the EM cluster (used over the range $\|\eta\| < 0.8$ and $\|\eta\| > 1.37$)	< 0.025	R_{had1}
Middle layer of EM calorimeter	Ratio of the energy in 3×7 cells over the energy in 7×7 cells in the ECal, centered at the electron cluster position	> 0.750	R_η
	Lateral width of the shower	< 0.0150	$w_{\eta 2}$
Modified medium selection (includes loose)			
Track-cluster matching	$\Delta\phi$ between the cluster position and the extrapolated track	> -0.02 and < 0.02	$\Delta\phi$
First sampling of EM calorimeter	Fraction of energy deposited in the first sampling of the ECal	> 0.005	f_1
	Total shower width	< 4	w_{tot}
	Difference between energy summed over ±3 strips and ±1 strip around the hottest strip in the first sampling divided by the energy summed over ±1 strip	> 0.6	$f_{(\pm 3,\pm 1)}$
	The fraction of energy in the second hottest strip	< 0.25	R_{max2}
	The difference between the energy in the second hottest strip and the energy on the strip with the minimal energy between the 1$^{\text{st}}$ and 2$^{\text{nd}}$ highest energy strips	$< 0.15\ GeV$	ΔE
	Lateral shower width in three strips around the hottest strip	< 0.80	$w_{\eta 1}$
Modified tight selection (includes medium and loose)			
Track-cluster	Ratio of cluster energy over track momentum	< 0.8 and > 2.5	E/p
TRT	Ratio of the number of high to low threshold TRT hits	η dep.	f_{HT}

Table 4.6: Definition of cuts applied in defining *loose*, *medium* and *tight* electron identification used in the analysis of cosmic ray data from 2008 and 2009. Some of the cuts vary with η of the electrons. Further details about the cuts can be found in Ref. [69].

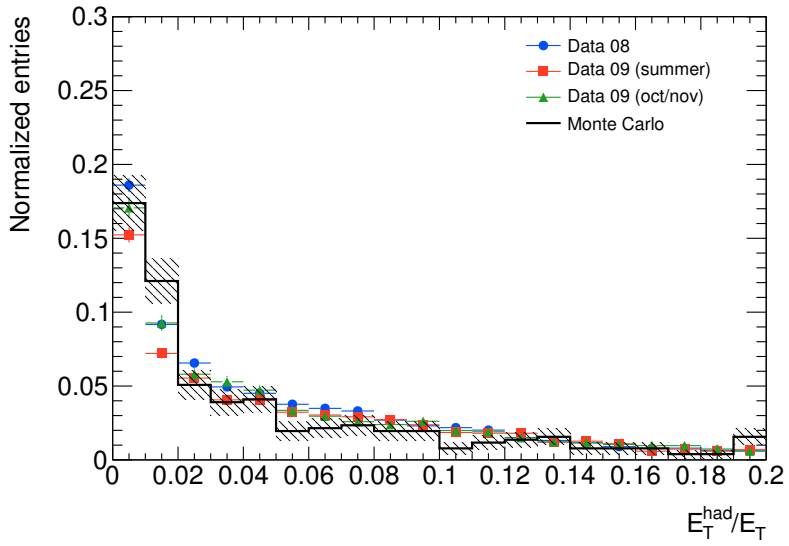

(a) $R_{\mathrm{had1}}(< 0.025)$

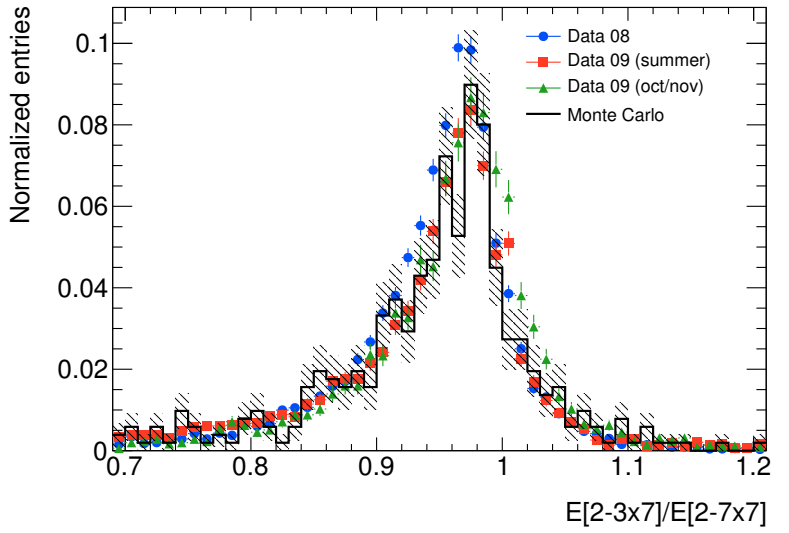

(b) $R_{\eta}(> 0.750)$

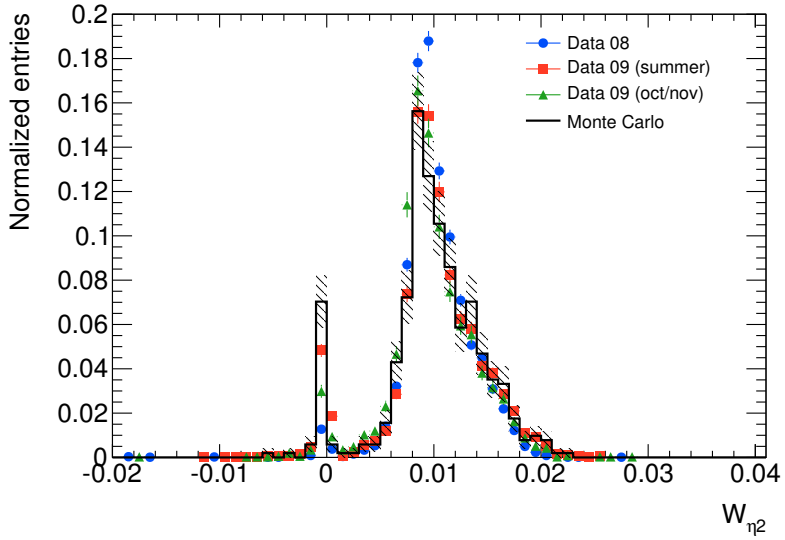

(c) $w_{\eta 2}(< 0.0150)$

Figure 4.5: The variables used in the **loose** electron definition defined in Table 4.6.

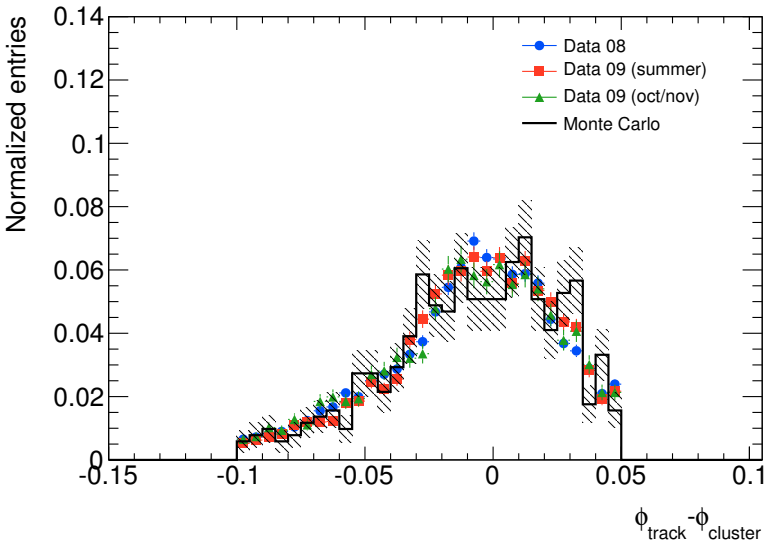

(a) $\Delta\phi(> -0.02 \text{ and } < 0.02)$

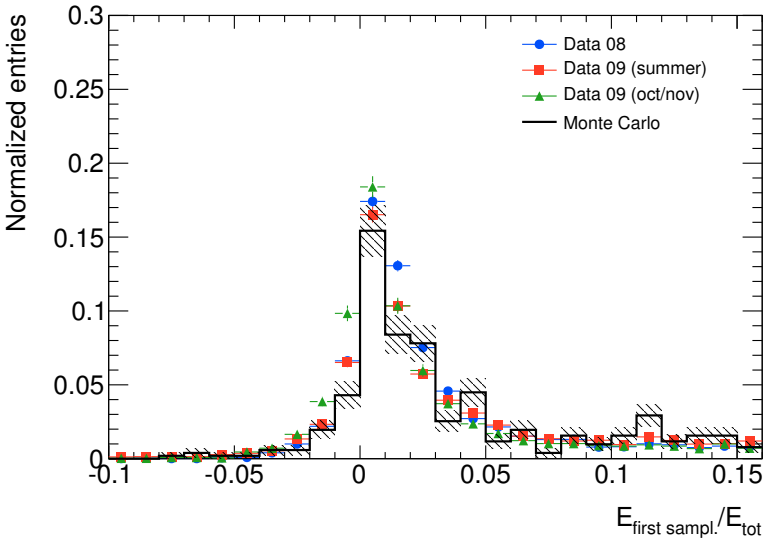

(b) $f_1(> 0.005)$

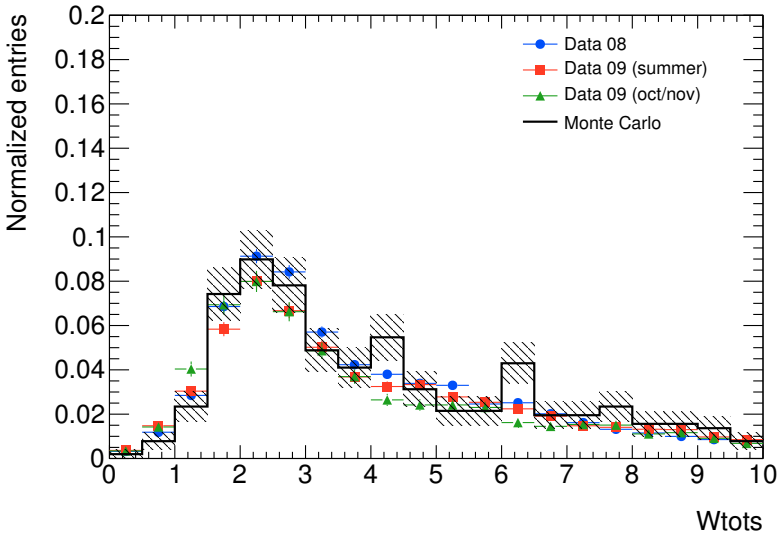

(c) $W_{tots}(< 4)$

Figure 4.6: Some of the the variables used in the **medium** electron definition in Table 4.6.

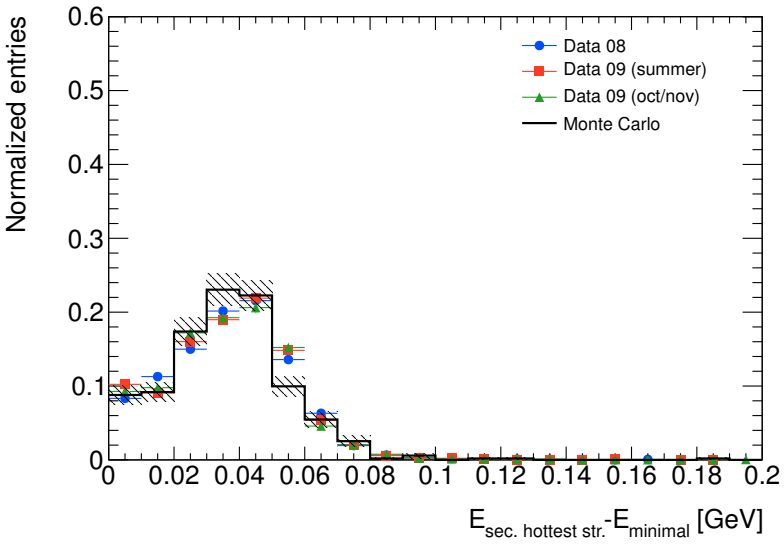

(a) $\Delta E (< 0.15)$

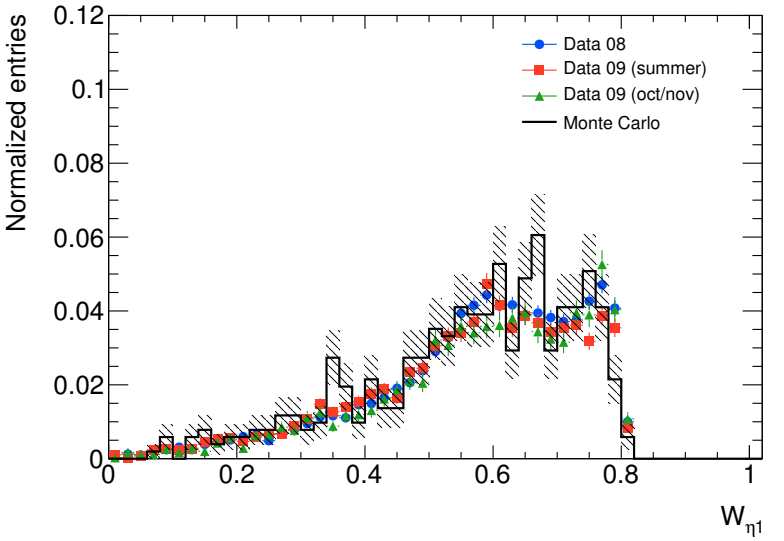

(b) $w_{\eta 1} (< 0.8)$

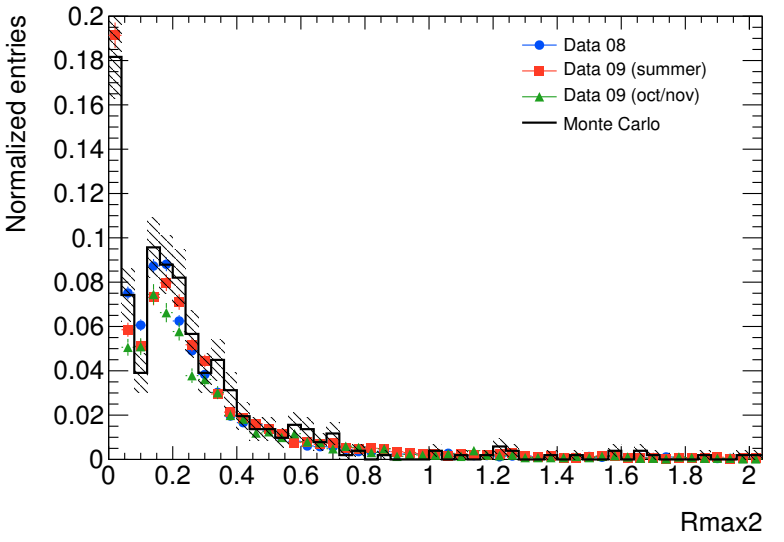

(c) $R_{max2} (< 0.25)$

Figure 4.7: Some of the the variables used in the **medium** electron definition in Table 4.6.

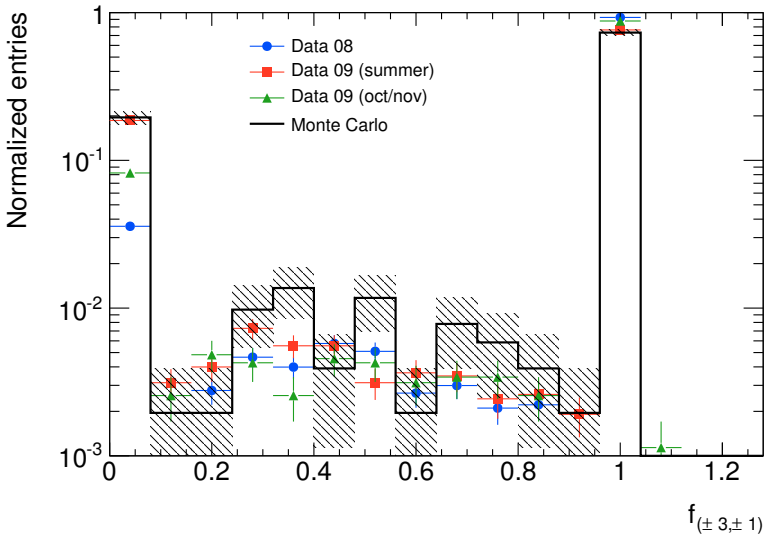

(a) $f_{(\pm 3,\pm 1)} (> 0.6)$

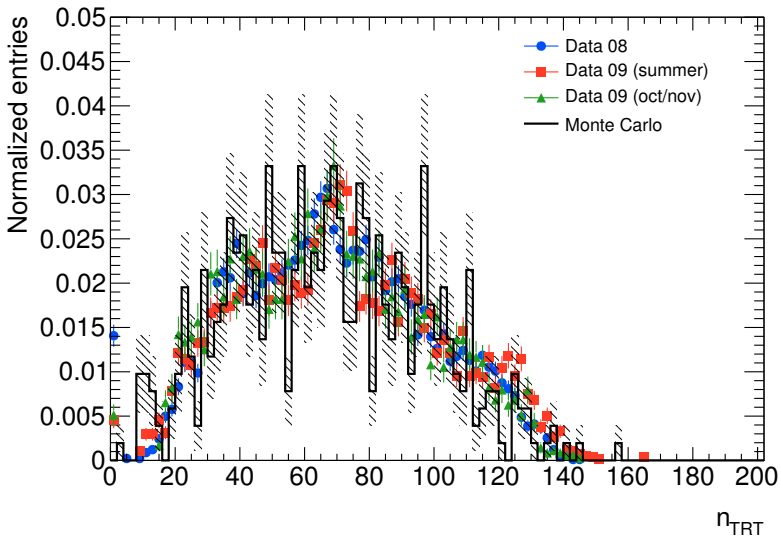

(b) $n_{TRT} (> 19)$

Figure 4.8: Some of the variables used in the **medium** electron definition in Table 4.6.

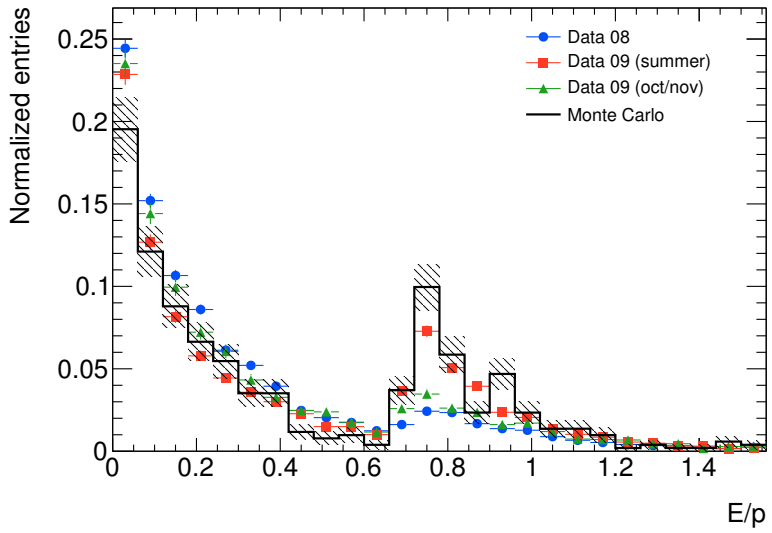

(a) $E/p(< 0.8$ and $> 2.5)$

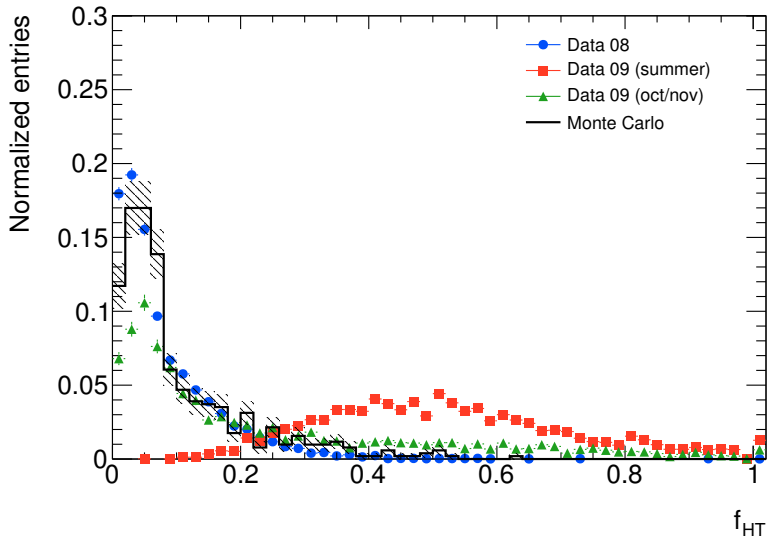

(b) $f_{HT}(\eta$ dep.)

Figure 4.9: The variables used in the **tight** electron definition.

Sample	all	loose	medium	tight
data08 (r653)				
Total # of $e^{\pm}$ candidates	14464	6187	151	6
Signal	985	530	6	3
Background	9507	4313	10	3
data08 (r653_r792)				
Total # of $e^{\pm}$ candidates	8387	4276	95	70
Signal	1447	915	62	45
Background	6679	3197	24	18
Summer 2009				
Total # of $e^{\pm}$ candidates	4450	2512	178	56
Signal	1035	675	57	31
Background	3088	1707	101	19
Autumn 2009				
Total # of $e^{\pm}$ candidates	4182	2146	472	75
Signal	556	351	84	36
Background	3392	1670	352	30

Table 4.7: Table showing the number of electron candidates in the various periods of cosmic ray data taking. The total number of electrons from the *ElectronAODCollection* and the number of electrons passing signal and background cuts are shown for the three different identification criteria, loose, medium and tight.

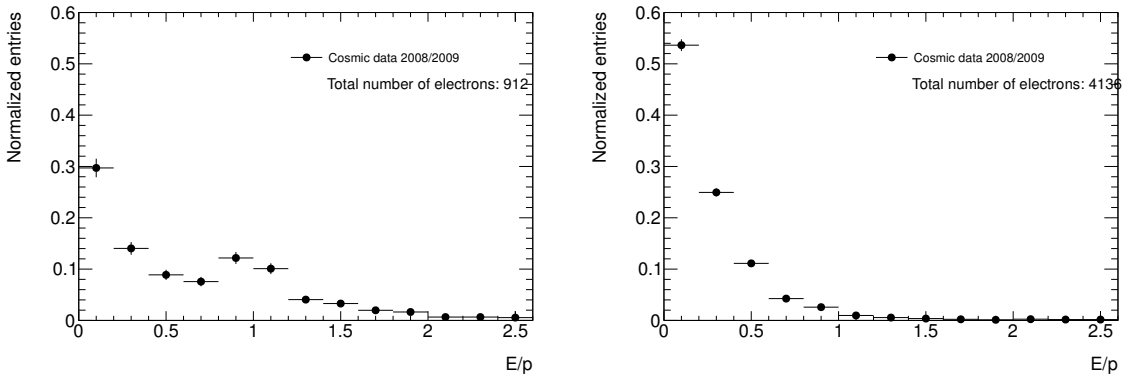

(a) Signal (b) Background

Figure 4.10: Cluster energy divided by the track momentum for all medium electron candidates in the signal (a) and background (b) categories.

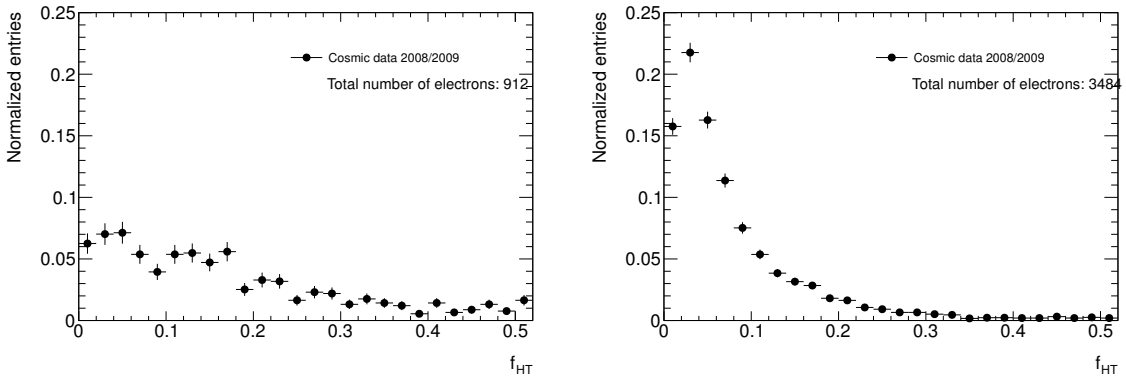

(a) Signal (b) Background

Figure 4.11: The distribution of the ratio of high to low threshold TRT hits for all medium electron candidates in the signal (a) and background (b) categories.

dates are mostly found within the blue rectangle, defining the tight region. Note that the runs taken during summer 2009 are omitted from this plot, since the TRT was running with the FAST-OR trigger, resulting in many more high threshold hits, as discussed in Section 4.2.5.

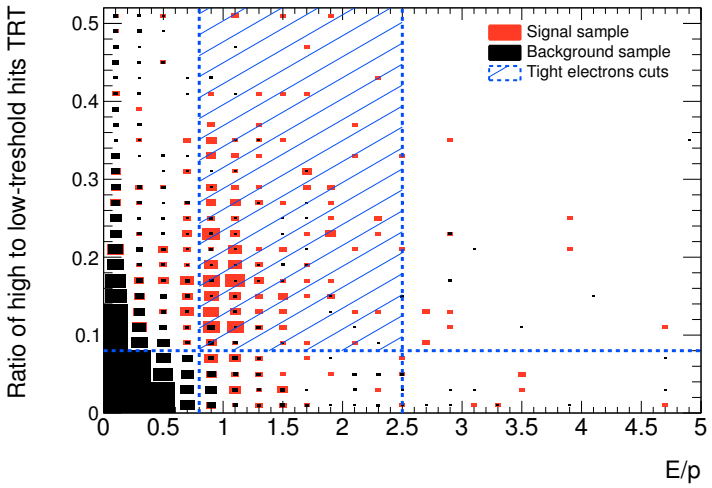

Figure 4.12: The cluster energy divided by the track momentum against the ratio of high to low threshold TRT hits for all medium electron candidates. The blue rectangle indicates the cuts used in the tight definition.

4.2.7 Inner Detector Resolution for Electron Tracks

The electron tracks found in cosmic ray data can also be used to study the resolution of the Inner Detector. All ID tracks matched with the track of an electron in the *ElectronAODCollection* are studied. Only events where the track traverses both the upper and lower part of the ID are used. In these events the track is split in two using the *InDetTrackSplittingTool*. This tool splits a track into an upper and lower part. The hits

corresponding to each of these tracks are then used in a refitting, producing two new separate tracks, one having $\phi > 0$ and the other $\phi < 0$. By comparing the impact parameters, z_0 and d_0, defined in Section 3.4.1, of the two tracks with respect to the original track[10] one can study the resolution of the ID. The difference of the transverse and longitudinal impact parameters of the two tracks are shown in Figure 4.13a and b respectively. As expected, the distributions are centered around zero with a certain width. These results show that the ID is able to reconstruct the origin of two tracks having the same coordinates in the xz-plane at $y = 0$ with a precision of $\sim$ 0.2-0.3 mm and $\sim$ 0.35-0.40 mm in the transverse and longitudinal direction respectively. This is something that will become more important when turning to the study of collision data in a moment. Then it becomes crucial to be able to properly reconstruct the various tracks back to the vertex from where they originated. Although the split ID tracks in cosmic events might behave differently than typical tracks from collisions one gets a first glimpse of the ability and precision of the ID.

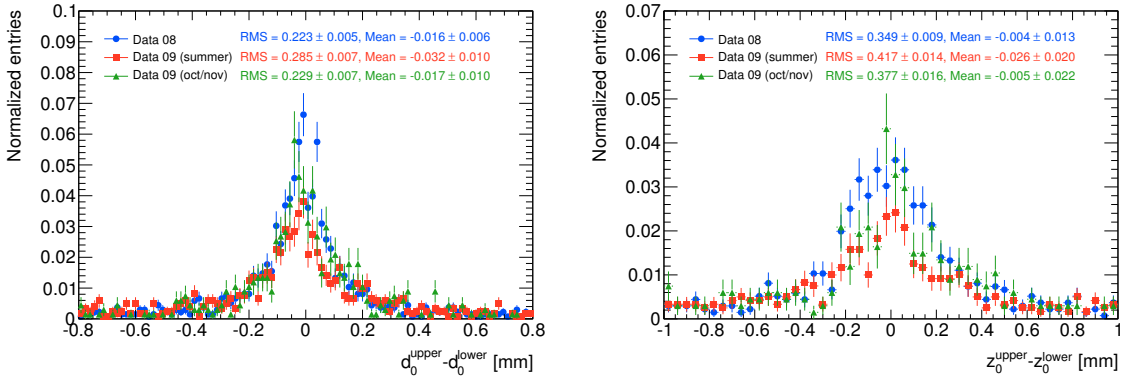

(a) $d_0^{upper} - d_0^{lower}$ in mm

(b) $z_0^{upper} - z_0^{lower}$ in mm

Figure 4.13: The differences in mm between the transverse (a) and longitudinal (b) impact parameters of the upper and lower ID tracks.

4.2.8 Concluding Remarks

The study on cosmic rays gave a unique possibility of an early testing and commissioning of the whole ATLAS detector after it was finished, installed and closed. Although cosmic events differ significantly from collision events they served as an important first step towards getting ready for collision data, not just concerning the understanding of the detector and the physics objects, but also understanding the triggers, distribution and management of the data as well as shift procedures and running the analysis on grid. My main contribution to the cosmic ray data analysis was devoted to the understanding of the electron identification variables. Some of the work discussed above was presented for the ATLAS Egamma Performance Group on December 14, 2009 [71].

[10] The impact parameters can of course not be measured with respect to the collision point. Instead, the point where the original track, before the splitting, crossed the z-axis is used.

4.3 Study of 900 GeV Collision Data

During a few weeks in December 2009, LHC was colliding protons at a center of mass energy of 900 GeV. The collisions were recorded by the ATLAS detector and were the first data we had at hand from LHC taken under stable conditions. This opened up the possibility to do some basic analysis on real collision data before the 7 TeV collisions would start in 2010. The 900 GeV collisions were much more suited to fully commission the detector than the cosmic data and gave also an unique opportunity to perform *pp* measurements at a new energy. A complete and more comprehensive overview of the electron and photon studies done with the 900 GeV data, summarised below, can be found in Ref. [72].

4.3.1 Data and Monte Carlo Samples

The events used in this analysis come from 13 runs recorded from December 6 to December 14 in 2009. The events were triggered by the Minimum Bias Trigger Scintillators (MBTS) and recorded under LHC stable beam conditions. To protect against beam backgrounds and cosmics, additional timing requirements were also applied. Only events where the solenoidal field was at its nominal value and the tracker, electromagnetic and hadronic calorimeter recorded data with high quality were used. Table 4.8 gives an overview of the runs and corresponding luminosity blocks that were included in the final analysis satisfying the requirements outlined above. This corresponds to a total of 384, 186 events, a total integrated luminosity of about $9\mu b^{-1}$.[11]

Run #	141749	141811	142149	142154	142165	142166	142171
LB (from-to)	19-100	126-165	65-87	22-35	134-257	38-96	217-229

Run #	142174	142189	142191	142193	142195	142383
LB (from-to)	8-48	140-147	7-36 141-234	33-153	11-54	260-283

Table 4.8: The run numbers with corresponding luminosity blocks (LB) from the 900 GeV collision data used in the study of electrons.

The MC sample with ID 105001 was used in the analysis, containing 10^7 non-diffractive minimum bias events generated with Pythia, using the ATLAS tune [73] and passed through the full ATLAS simulation and reconstruction software. In MC the *egammaMCTruthClassifier* [74] is used to identify the true type and origin of the electrons.

4.3.2 Electron Identification

All electron candidates with a transverse energy, $E_T > 2.5$ GeV, and $|\eta_{\text{clus}}| < 2.47$ are considered. The η_{clus} is the barycenter of the cluster cells in the middle layer of the ECal.

[11] For this analysis *Athena* version 15.6.1 was used with `DESD_COLLCAND` datasets having tag `r988_p62`.

In the following the *barrel region* is defined as the range $|\eta_{\text{clus}}| < 1.37$ while the *end-cap region* is defined as $1.52 < |\eta_{\text{clus}}| < 2.47$. The crack region, $1.37 < |\eta_{\text{clus}}| < 1.52$, is excluded from the analysis because of the large amount of material situated in front of the ECal in this particular region. Similar to the study of cosmic data, the cuts used to identify electrons in 900 GeV collisions are grouped into three categories; loose, medium and tight. The exact cuts are slightly different than what was used for the cosmic analysis in Section 4.2.5, however. This is summarized in Table 4.9. Most of the cuts are optimized in bins of E_T and η_{clus}. More detailed information can be found in Ref. [68, 75].

Type	Description	Cut	Name
Loose selection			
Hadronic leakage	Ratio of E_T in the hadronic calorimeter to E_T of the EM cluster (in range $\|\eta_{\text{clus}}\| < 0.8$ and $\|\eta_{\text{clus}}\| > 1.37$)	E_T/η dep.	R_{had1}
	Ratio of E_T in the hadronic calorimeter to E_T of the EM cluster (in range $\|\eta_{\text{clus}}\| > 0.8$ and $\|\eta_{\text{clus}}\| < 1.37$)	E_T/η_{clus} dep.	R_{had}
Middle layer of EM calorimeter	Ratio in η_{clus} of cell energies in 3×7 versus 7×7 cells	E_T/η_{clus} dep.	R_η
	Lateral width of the shower	E_T/η_{clus} dep.	$w_{\eta 2}$
Medium selection (includes loose)			
First sampling of EM calorimeter	Ratio of the energy difference between the largest and 2$^{\text{nd}}$ largest energy deposits over the sum of these energies	E_T/η_{clus} dep.	E_{ratio}
	Total lateral shower width (20 strips)	E_T/η_{clus} dep.	w_{tot}
Track quality	Number of hits in Pixel detector	> 0	n_{pix}
	Number of hits in Pixel and SCT	> 6	$n_{\text{pix+SCT}}$
	Transverse impact parameter	< 5 mm	d_0
Track-cluster matching	$\Delta\eta$ between the cluster in the strip layer and the extrapolated track	E_T/η_{clus} dep.	$\Delta\eta_1$
Tight selection (includes medium and loose)			
B-layer	Number of hits in the B-layer	> 0	$n_{\text{b-layer}}$
Track-cluster matching	$\Delta\phi$ between the cluster position in the middle layer and the extrapolated track	E_T/η_{clus} dep.	$\Delta\phi_2$
	Ratio of cluster energy over track momentum	E_T/η_{clus} dep.	E/p
TRT	Ratio of the number of high-threshold hits to the total number of hits in the TRT (used for $\|\eta_{\text{clus}}\| < 2.0$)	E_T/η_{clus} dep.	f_{HT}

Table 4.9: Definition of cuts applied in defining *loose*, *medium* and *tight* electron identification used in the analysis of 900 GeV collision data from December 2009. Most of the cuts are optimized as a function of E_T and η_{clus} of the electrons. Further details about the cuts can be found in [75].

The tight selection of electrons is used to exploit the full potential of the ATLAS electron identification. It should give a good rejection against charged hadrons by using

E/p. The cut on the ratio of high threshold TRT hits, f_{HT}, distinguishes efficiently between electrons and hadrons. In order to be robust against electron conversions a hit in the b-layer (i.e. the innermost part of the Pixel detector) as well as tighter matching of the track and cluster are used. The verification of these cuts will be discussed in following section.

4.3.3 Results

Table 4.10 gives the number of electron candidates from the *ElectronAODCollection* as well as the percentage passing the cuts defining the three categories; loose, medium and tight specified in Table 4.9 for MC and data. Separate numbers for electrons in the barrel and end-cap regions are shown. The *Had* and *Elec* columns indicate the proportion of electron candidates for each of the categories that are found to be hadrons (faking electrons) and real electrons respectively. The real electrons are defined as those having *type* equal to *Bkg. electron* or *Non-Isolated*.[12] The rest is regarded as *hadrons*. The classification of electron-type and -origin is done using the *egammaMCTruthClassifier* [74] discussed in detail in Section 6.3.7. Figure 4.14 shows the fraction in percent for all *type* and *origin* combinations of all MC electrons (a), as well as those passing the loose (b), medium (c) and tight (d) cuts. All entries less than 0.1% are omitted from the plots. Clearly the most important sources of electron candidates are hadrons faking electrons and conversions. There are also contributions from Dalitz decay and decay of heavy-flavoured hadrons. The *Unknown/Non-Defined* category is believed to be light-flavoured hadrons and is grouped as hadrons in Table 4.10. For tight and medium cuts the contribution of electrons from this category is negligible however. Using the tight cuts, about 15% of the electrons seem to come from prompt decays of heavy-flavoured hadrons. With the 20 events observed in data (from Table 4.10) we therefore expect that ~ 3 electrons are of this type. For the loose and medium cuts the fractions of prompt leptons are less than 5%.

The E_T and η distributions of all electron candidates are shown in Figure 4.15. The *non-diffractive minimum bias* MC is again divided into the two main components, *hadrons* and *electrons from conversions*. Note, however, that *electrons from conversions* include all electrons having type equal to *Bkg. electron* or *Non-Isolated*. However, according to Figure 4.14a, this category contains a tiny fraction ($\sim 1\%$) of electrons from Dalitz decays and decays of heavy-flavoured hadrons. The *hadron* category contains the rest of the electrons, already shown to mainly consist of hadrons faking electrons, although with a small ($\sim 7\%$) fraction having type *unknown*. Both distributions in Figure 4.15 show a good agreement between data and MC, despite the large uncertainties expected in this kinematic regime.

In Figure 4.16 the track-cluster matching variables used in the medium and tight definitions are plotted for data and the *non-diffractive minimum bias* MC. The distribution in Figure 4.16a shows the difference in azimuthal angle between the track extrapolated to the **middle** layer of the calorimeter and the barycenter of the cell energies in this layer. Since the electrons/positrons often loose much of their energy through bremsstrahlung when

[12] The naming here might seem strange, but the tool used to classify electrons in MC is designed for use on 7 TeV data, where the electrons referred to as real in this study (from conversions, Dalitz decays and b,$c \to e$) are indeed classified as *non-isolated* or *background electrons*.

Barrel + Endcap

Selection	Data		MC	Origin	
	[#]	[%]	Total [%]	Had [%]	Elec [%]
All	880		100.0	66.9 ± 0.4	33.1 ± 0.2
Loose	410	46.6 ± 2.8	50.9 ± 0.4	59.4 ± 0.6	40.6 ± 0.5
Medium	93	10.6 ± 1.2	13.1 ± 0.2	73.5 ± 1.4	26.5 ± 0.7
Tight	20	2.3 ± 0.5	2.4 ± 0.1	62.0 ± 3.0	38.0 ± 2.2

Barrel

Selection	Data		MC	Origin	
	[#]	[%]	Total [%]	Had [%]	Elec [%]
All	558		100.0	16.2 ± 0.2	43.9 ± 0.3
Loose	264	47.3 ± 3.5	51.8 ± 0.5	66.6 ± 0.8	33.4 ± 0.6
Medium	62	11.1 ± 1.5	12.9 ± 0.2	80.5 ± 1.6	19.5 ± 0.8
Tight	9	1.6 ± 0.5	1.8 ± 0.1	50.8 ± 3.2	49.2 ± 3.2

Endcap

Selection	Data		MC	Origin	
	[#]	[%]	Total [%]	Had [%]	Elec [%]
All	322		100.0	25.6 ± 0.3	34.5 ± 0.3
Loose	146	45.3 ± 4.5	49.5 ± 0.6	47.9 ± 0.9	52.1 ± 1.0
Medium	31	9.6 ± 1.8	13.3 ± 0.3	63.0 ± 1.7	37.0 ± 1.3
Tight	11	3.4 ± 1.0	3.3 ± 0.1	71.1 ± 3.5	28.9 ± 2.2

Table 4.10: The number of electrons candidates from the *ElectronAODCollection* (*All*) and the percentage of all electrons passing the various loose, medium and tight selection criteria are shown for data and MC. For each category the relative amount of hadrons faking electrons (*Had*) and real electrons from conversions and heavy flavoured hadron decays (*Elec*) are shown. The *Total* denote electrons regardless of their origin. The numbers are also given separately for the barrel (middle) and end-cap (lower).

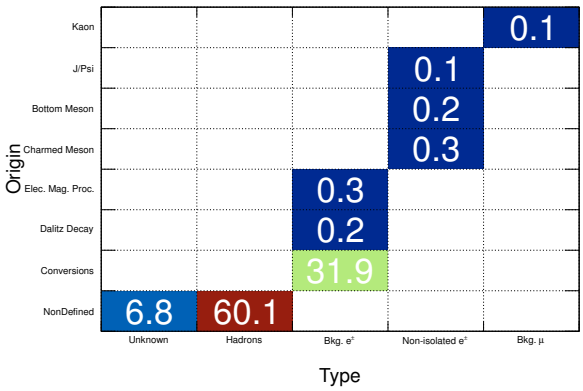

(a) All

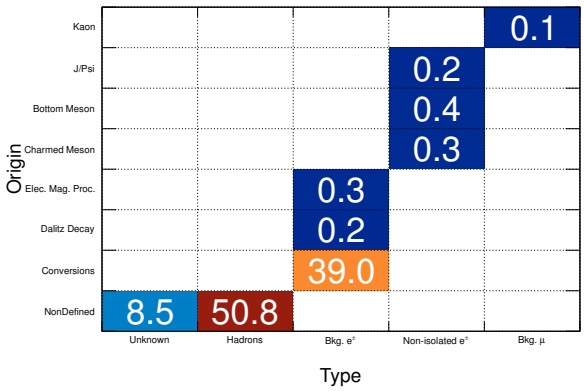

(b) Loose

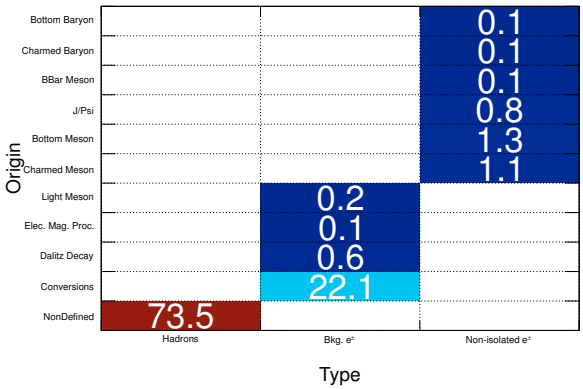

(c) Medium

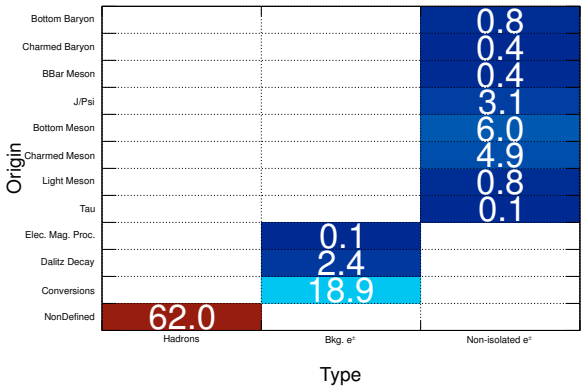

(d) Tight

Figure 4.14: The fraction in percent of electrons having specific type and origin defined by *egammaMCTruthClassifier* for all MC electrons (a) and those satisfying the different identification categories (b-d). All bins with content $< 0.1\%$ are omitted from the plots.

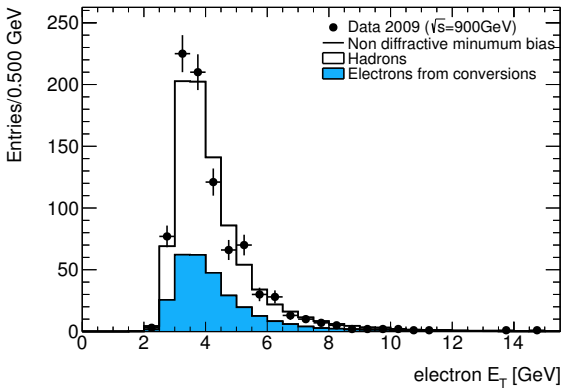

(a) E_T

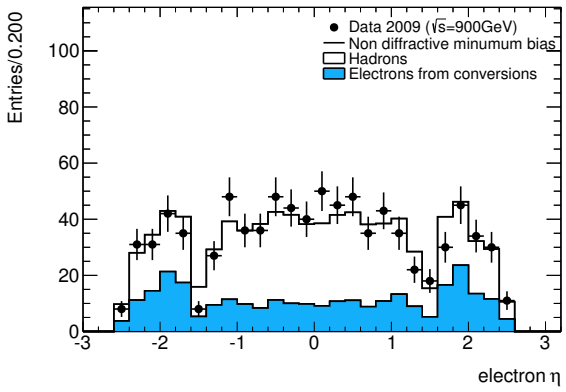

(b) η

Figure 4.15: The E_T (a) and η (b) distributions of all electron candidates in data shown together with the *non-diffractive minimum bias* MC, divided into its two main components: *hadrons* and *electrons from conversions*.

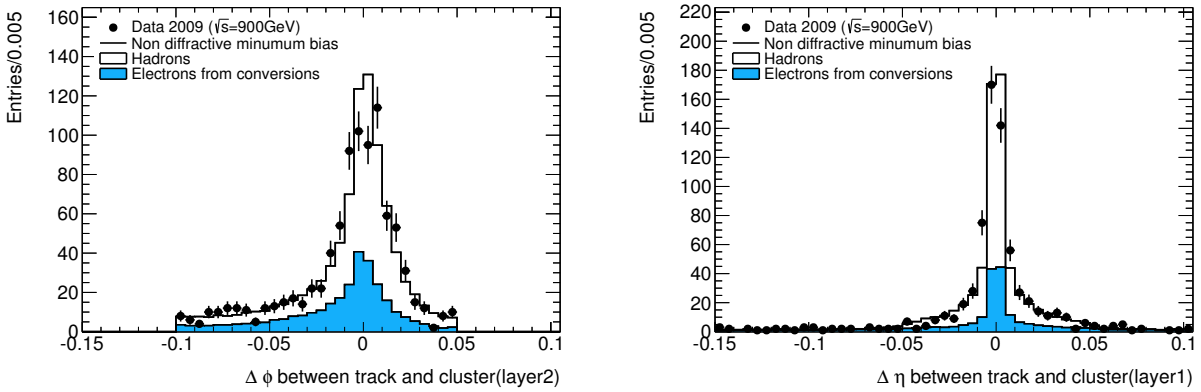

(a) $\Delta\phi_2$ (b) $\Delta\eta_1$

Figure 4.16: Distributions of the track-cluster matching variables in the ϕ (a) and η (b) directions: data vs. simulation.

going through the ID, the matching is corrected for the sign to account for the opposite curvatures of electrons and positrons. An asymmetric cut is applied in order to keep most of the candidates which then give a large negative $\Delta\phi$. The distribution in 4.16b shows the matching between the extrapolated track to the **first** layer of the calorimeter and the cell energies in this layer. In contrast with what was observed for $\Delta\phi$, the $\Delta\eta$ distribution seems to be symmetric. This is expected, since the particle trajectories are not affected by the magnetic field in the η direction.

Figure 4.17 shows four of the tracking variables used in the electron identification. In all distributions the agreement between data and simulation is surprisingly good, despite the additional material effects and reconstruction inefficiencies expected at such relatively low energies. Figure 4.17a, b and c contain the number of hits in the b-layer, in the complete Pixel detector and in the SCT respectively. As expected, the conversion electrons tend to have few hits in the innermost parts of the ID. The hadrons also have a significant amount of tracks with no hits in the silicon detectors, which might indicate that the track matching algorithm is picking up tracks from secondaries in the TRT. Figure 4.17d shows the distribution of the transverse impact parameter, d_0, of the electron track with respect to the reconstructed primary vertex. As expected, since conversions mostly happen at larger distances from the vertex, they have a much broader distribution of d_0 compared with the hadrons.

Figure 4.18 shows the E/p (a) and f_{HT} (b) distributions used in the definition of tight electrons for data and MC. Again, the agreement between data and simulation is remarkably good. In Figure 4.18a the E/p distribution is shown for all electron candidates. The MC conversion electron component is now separated into electrons having tracks with and without hits in the silicon detectors (i.e. Pixel and SCT). Tracks without silicon hits are expected to be poorly measured in the TRT, confirmed by the large tail observed at small E/p values, which exclusively consists of tracks with no silicon hits. More surprisingly, the hadrons also seem to peak around unity. This might be due to the fact that the hadrons reconstructed as electrons at these low energies deposit most of their energy in the EM calorimeter and therefore match nicely with the track momentum. The f_{HT} distribution in Figure 4.18b shows a clear difference between conversion electrons

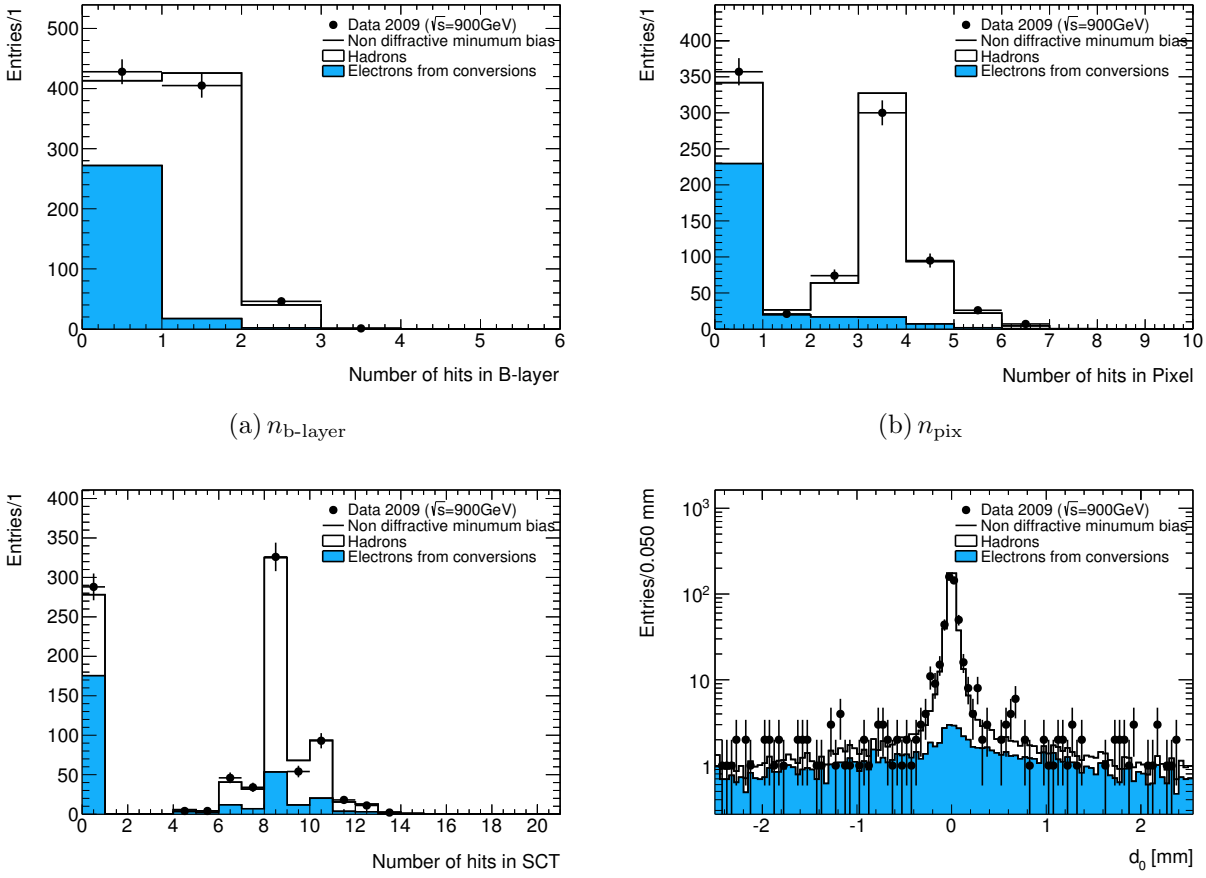

(a) $n_{\text{b-layer}}$

(b) n_{pix}

(c) n_{SCT}

(d) d_0

Figure 4.17: Distributions of tracking variables for all electron candidates: data vs. simulation. The number of hits in the various parts of the silicon detectors: the *b*-layer (a), the complete Pixel detector (b) and SCT (c), are shown together with the transverse impact parameter with respect to the reconstructed primary vertex (d). The *non-diffractive minimum bias* MC is used, divided into its two main components: *hadrons* and *electrons from conversions*.

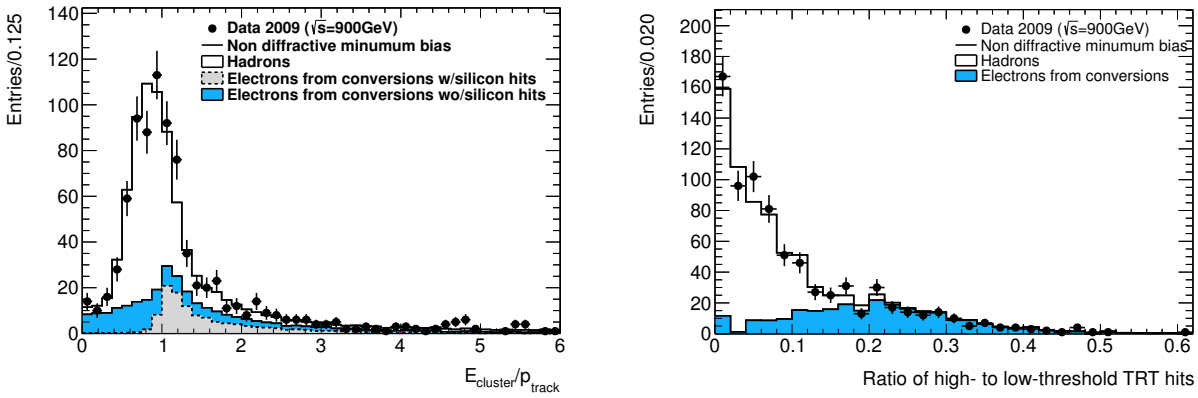

(a) E/p (b) f_{HT}

Figure 4.18: Distributions of two variables used in the tight electron identification, E/p (a) and f_{HT} (b), for all electron candidates: data vs. simulation. The *non-diffractive minimum bias* MC is used, divided into its two main components: *hadrons* and *electrons from conversions*.

and hadrons. The hadrons clearly peak at small values while the conversion electrons have a much broader distribution. Despite the fact that the transition radiation yield of electrons at these low energies is far from optimal, the TRT is able to nicely discriminate between electrons and hadrons.

4.3.4 Conclusions

The 900 GeV data recorded by ATLAS during December 2009 gave a first chance to study electrons from real collision events. A total sample of 880 electron candidates were found in the *ElectronAODCollection*, before applying any identification cuts. With these candidates the performance of the electron reconstruction and identification algorithms were studied carefully. The data and simulations were found to be in remarkable agreement, bearing in mind that the algorithms used were by no means optimized for the very low statistics and small energy. With good reasons the expectations were therefore exceptionally high for the ATLAS ID and calorimeters to perform excellently with collisions at much larger energies and intensities. ATLAS was at this stage more then ready to welcome the high energy and high intensity collisions, as will be discussed in the following chapters.

Chapter 5

Direct Gaugino and Slepton Production Signals and Backgrounds

The dominant SUSY production mechanism at the LHC depends on the masses of the sparticles. For similar masses the production cross-section of coloured sparticles (squarks and gluinos) is in general much larger than for the non-coloured (sleptons and gauginos). However, if the squarks and gluinos are much heavier than the sleptons and gauginos, the first sign of SUSY at LHC could be through direct production of sleptons and/or gauginos. In the *mSUGRA* model, discussed in Section 1.10.2.4, the breaking pattern is set and the mass difference between the coloured and non-coloured objects is not large enough to enhance direct gaugino production sufficiently. There are however several arguments for the *mSUGRA* model being too simple and giving a too limited variety of possible SUSY signatures. It is therefore interesting to look at other models and scenarios where direct gaugino and/or slepton production might be more promising channels.

In Section 5.1 and 5.2 the direct gaugino and direct slepton phenomenology of particular interest for searches requiring exactly two leptons are discussed. In Section 5.3 the various MC samples used to model the SUSY signals are presented. With the knowledge of which signals to look for, the most important SM backgrounds, and methods to best discriminate them from the signal, will be discussed in Section 5.4. Based on this a set of signal regions aimed for studying direct gaugino and slepton scenarios are constructed in Section 5.5.

5.1 Direct Gaugino Production

In proton-proton collisions gauginos are predominantly produced in pairs: $\tilde{\chi}_1^{\pm}\tilde{\chi}_2^0$, $\tilde{\chi}_1^{\pm}\tilde{\chi}_1^{\mp}$, $\tilde{\chi}_2^0\tilde{\chi}_2^0$ and $\tilde{\chi}_2^0\tilde{\chi}_1^0$, as illustrated in Figure 2.13. The cross-section depends on their masses and the exact mixing (i.e. the relative amount of **higgsino**, **wino** and **bino** as discussed in Section 1.10.2.2). Off-shell sleptons can participate in the decay of neutralinos and charginos. If the sleptons are light enough they can even be on-shell. Four particularly interesting gaugino decay channels with leptons are illustrated in Figure 5.1, where on-shell production of the intermediate sleptons maximizes the cross-section times branching ratio for final states containing leptons, therefore favouring searches involving leptons.

If the sleptons are too heavy to be produced on-shell they can still contribute to the

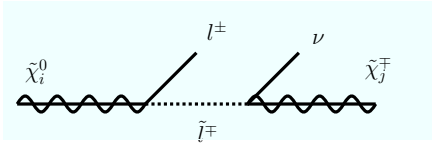

(a) $\tilde{\chi}_i^0 \to l^{\pm}\nu\tilde{\chi}_j^{\mp}$

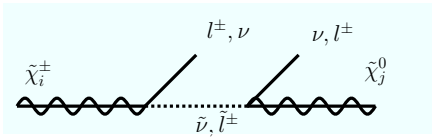

(b) $\tilde{\chi}_i^{\mp} \to l^{\pm}\nu\tilde{\chi}_j^0$

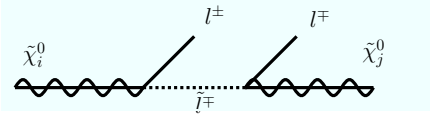

(c) $\tilde{\chi}_i^0 \to l^{\pm}\nu\tilde{\chi}_j^{\pm}$

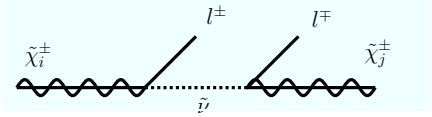

(d) $\tilde{\chi}_i^{\mp} \to l^{\pm}l^{\mp}\nu\tilde{\chi}_j^{\pm}$

Figure 5.1: The decay of charginos and neutralinos through virtual sleptons with $i > 1$, $i > j$ and l being either an electron or muon.

leptonic branching ratios as virtual particles in three-body decays. Another important consideration regarding direct gaugino models is whether or not the mass-gap between $\tilde{\chi}_2^0$ and $\tilde{\chi}_1^0$ is larger than the Z-mass. If so the $\tilde{\chi}_2^0$ could decay to Z and $\tilde{\chi}_1^0$, and thus the important vetoing of $Z \to l^{\pm}l^{\mp}$ events, to enhance the signal over SM background ratio in the analysis, will not anymore be adequate and the sensitivity of the di-lepton searches would deteriorate.

Figure 5.2 illustrates the most important decay-chains, starting with the production of a pair of gauginos and leading to final states with at least two leptons. All the diagrams involve exactly two leptons (red lines) except Figure 5.2b and g which contain three leptons. If one of the leptons fails reconstruction, however, this can give rise to final states with exactly two reconstructed leptons of either opposite-sign (OS) or same-sign (SS), depending on which of the three leptons is not reconstructed. All events feature two undetected LSPs, which like neutrinos, would contribute to the missing transverse energy (green lines). The heavier charginos may decay to neutralino and a pair of quarks (blue lines) via off-shell (or virtual) squarks. Note that in the chargino decays in Figure 5.2a and b the virtual particle might as well be a charged slepton, as illustrated in Figure 5.1b. This would then switch the position of the final state lepton and neutrino with respect to what is shown in these diagrams.

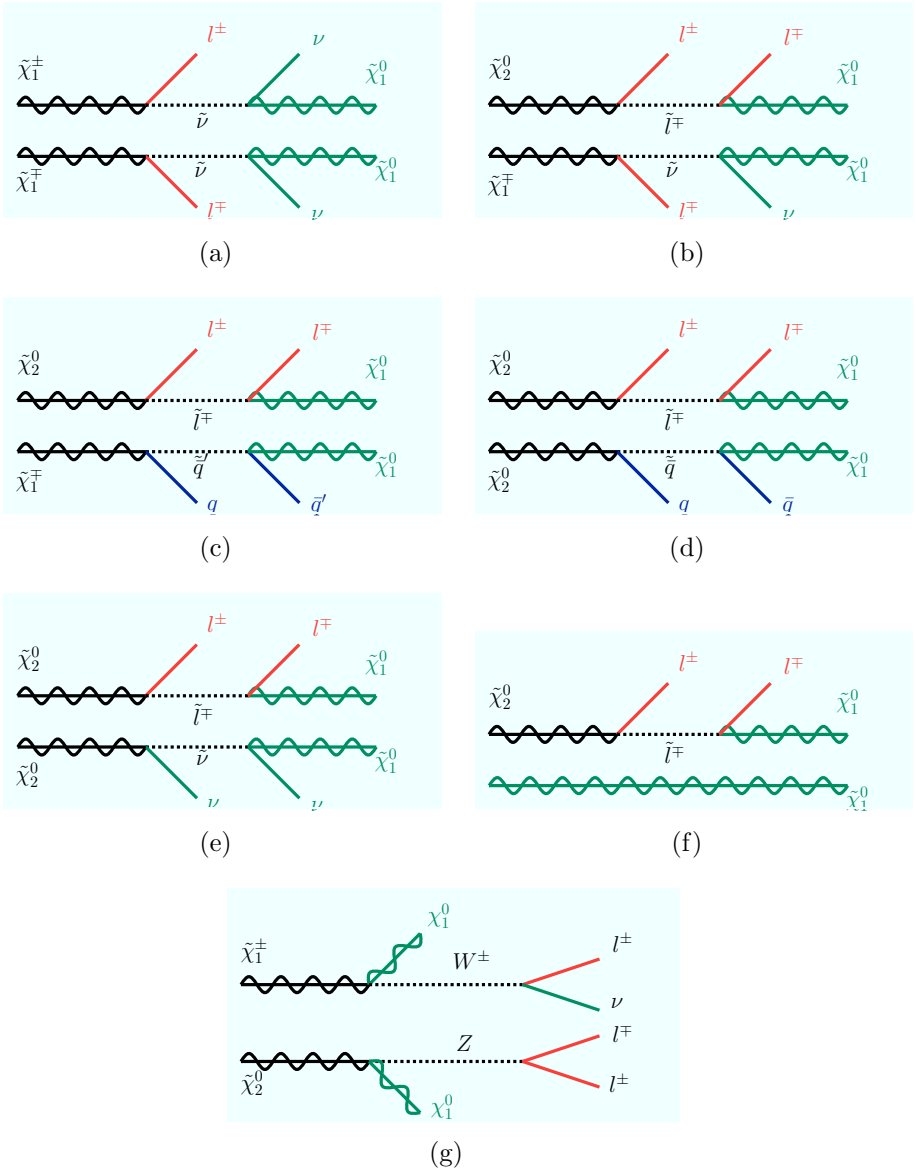

Figure 5.2: Direct gaugino production processes with at least two charged leptons.

5.2 Direct Slepton Production

Direct slepton production and decay as sketched in Figure 5.3 lead to very clean and characteristic final states. The sneutrinos can be produced in a similar way, but searches for direct sneutrino production with subsequent decays into the lightest supersymmetric particle (LSP) are difficult at the LHC as they lead to a final state without any visible particles (except for possible particles from ISR and FSR). The direct slepton production, however, with sleptons decaying into the LSP and charged leptons, would lead to final states with two OS leptons, significant missing transverse energy and no hadronic activity from the final state particles.

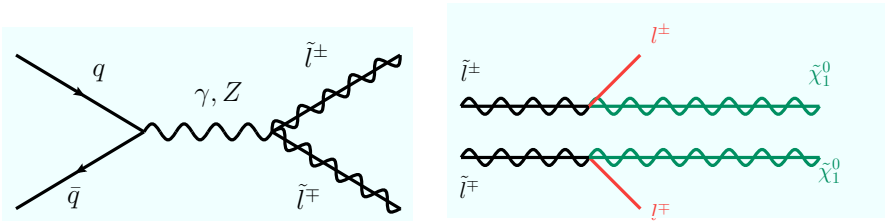

(a) $\tilde{\ell}\tilde{\ell}$ production (b) $\tilde{\ell}\tilde{\ell}$ decay

Figure 5.3: Direct slepton production (a) and decay (b) leading to a final state with exactly to oppositely charged leptons (red lines) and missing transverse energy (green lines).

5.3 SUSY Signal Grids

In order to study SUSY processes with cascades as discussed in the previous section dedicated samples including direct gaugino and slepton production are generated. Various models and methods used to generate the relevant SUSY signals are discussed in this section.

5.3.1 SUSY Simplified Models

The SUSY simplified models consist of as few particles and parameters as possible necessary to produce SUSY-like events with multileptons (i.e. final states with more than 1 lepton). This is almost the same as separately simulating each of the diagrams in Figure 5.2, with the appropriate decays. The theoretical parameter space is then strongly reduced, containing only a few sparticles and corresponding branching ratios. The results are interpreted directly as a function of the sparticle masses and given separately for each event-topology or possibly for each diagram. The results are therefore generic and can be applied to models predicting additional SM partner particles, such as the minimal (MSSM) and the next-to-minimal supersymmetric standard model (NMSSM), universal extra dimensions (UED) and Little Higgs (LH) models, believed to all have similar event topologies.

In this analysis simplified models for the direct gaugino processes leading to final states with at least two leptons are constructed. In these models the $\tilde{\chi}_1^{\pm}$ and $\tilde{\chi}_2^0$ are set to be exactly wino while the $\tilde{\chi}_1^0$ is exactly bino and all flavours of left-handed sleptons and sneutrinos are degenerate in mass. The right-handed slepton masses, however, are assumed to be out of reach for LHC. The same is valid for the squarks and gluinos, which typically have masses of a few hundred TeV in these scenarios. Two different models with an intermediate slepton are used

1. Mode A: direct production of $\tilde{\chi}_1^{\pm}\tilde{\chi}_2^0$ as in Figure 5.2b
2. Mode C: direct production of $\tilde{\chi}_1^{\pm}\tilde{\chi}_1^{\mp}$ as in Figure 5.2a

These models are chosen due to their relatively large cross-section, as shown in Figure 5.4, of order 1 pb for chargino masses of ~ 180 GeV.

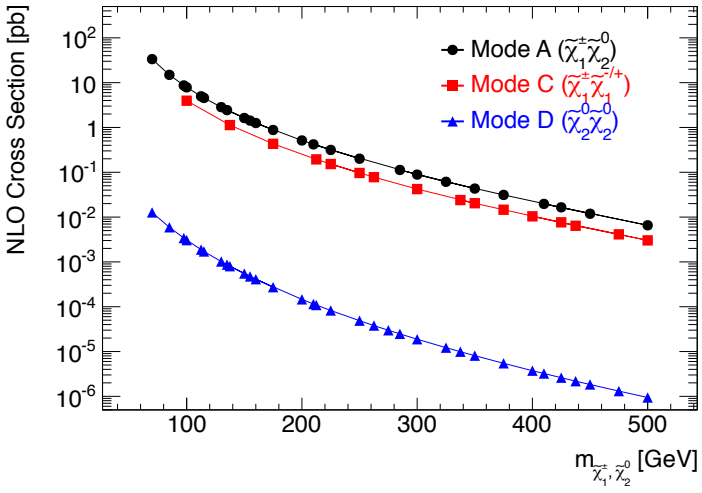

Figure 5.4: The cross-section for different direct gaugino productions modes where the $\tilde{\chi}_1^{\pm}$ has no higgsino component and the $\tilde{\chi}_2^0$ has no higgsino nor bino component. Mode D (direct production of $\tilde{\chi}_2^0\tilde{\chi}_2^0$) is not covered in this analysis because of the relatively small cross-section. Plot is taken from Ref. [76].

5.3.2 Phenomenological Minimal Supersymmetric Standard Model

The MSSM with conserved R-parity introduced in Section 1.10.2 has 105 free parameters. Adding the 19 free parameters of the SM the total number becomes 124. Even more parameters would be included with R-parity violation. Most of the MSSM parameters are in general unconstrained by experiments, the majority coming from the soft supersymmetry breaking part of the Lagrangian. Some of the parameters in SUSY are, however, constrained by experimental results from earlier searches for SUSY, mainly at LEP and TeVatron. Indirect constraints on SUSY also comes from the rate of flavour changing neutral currents (FCNC), amount of CP violation, the rate of $B_s \to \mu^+\mu^-$ and contributions to the muon anomalous magnetic moment. There are various measurements from the astrophysics community, typically from dark matter searches, which put constraints on SUSY. Despite all these constraints the freedom in the SUSY parameter space is still huge and the need for applying some simplifications when interpreting the results of SUSY searches is therefore imminent.

In the phenomenological MSSM (pMSSM) [77, 78, 79] the number of free parameters is greatly reduced. After assuming that the model is CP conserving, contains minimal flavour violation, has negligible trilinear couplings for the first and second generations

Category	Parameters	Description
Gaugino mass parameters	M_1, M_2, M_3	M_1, M_2 set the mixing between the gauginos and higgsinos while M_3 sets the gluino mass
Higgs and higgsino parameters	μ, m_A, $\tan\beta$	the parameter μ of the Higgs potential (Section 1.4.1), mass of the CP-odd Higgs (m_A, Section 1.10.2.1) and the ratio of the vacuum expectation values of the up and down parts of the Higgs field ($\tan\beta$, Eq. 1.42).
Squark mass parameters	$m_{\tilde{d}_L} = m_{\tilde{u}_L} = m_{\tilde{c}_L} = m_{\tilde{s}_L}$	left-handed 1st and 2nd gen. masses
	$m_{\tilde{t}_L} = m_{\tilde{b}_L}$	left-handed 3rd gen. masses
	$m_{\tilde{u}_R} = m_{\tilde{c}_R}$	right-handed 1st and 2nd gen. up-type masses
	$m_{\tilde{d}_R} = m_{\tilde{s}_R}$	right-handed 1st and 2nd gen. down-type masses
	$m_{\tilde{t}_R}$ and $m_{\tilde{b}_R}$	right-handed 3rd gen. masses
Slepton mass parameters	$m_{\tilde{e}_L} = m_{\tilde{\mu}_L} = m_{\tilde{\nu}_e} = m_{\tilde{\nu}_\mu}$	left-handed 1st and 2nd gen. masses
	$m_{\tilde{\tau}_L} = m_{\tilde{\nu}_\tau}$	left-handed 3rd gen. masses
	$m_{\tilde{e}_R} = m_{\tilde{\mu}_R}$	right-handed 1st and 2nd gen. masses
	$m_{\tilde{\tau}_R}$	right-handed 3rd gen. masses
Trilinear couplings	A_t, A_b and A_τ	the 3rd gen. Higgs-fermion-fermion couplings

Table 5.1: The free parameters in the pMSSM model.

and that the sfermions of the first two generations have the same mass parameters, there are only 19 free parameters left, as summarized in Table 5.1.[1]

5.3.2.1 Direct Neutralino-Chargino Grid

For the searches described in this study the masses of the squarks and gluinos are assumed to be sufficiently large so that the production of supersymmetric particles will be dominated by direct production of neutralinos, charginos and sleptons. As discussed in Section 1.10.2.2 the charginos and neutralinos are mass-eigenstates of the underlying

[1]The model is called phenomenologigal because the 19 free parameters are sufficient to cover more or less the full space of phenomenological models of the 124 parameter version of the MSSM.

gauginos and higgsinos. For the charginos ($\tilde{\chi}_1^{\pm}$,$\tilde{\chi}_2^{\pm}$) the exact mixing depends on M_2 and μ only while for neutralinos ($\tilde{\chi}_1^0$,$\tilde{\chi}_2^0$,$\tilde{\chi}_3^0$,$\tilde{\chi}_4^0$) M_1, M_2 and μ all play an important role. The phenomenology is very sensitive to the gaugino/higgsino structure of the model, which can be very different from what is typical in mSUGRA models, where the phase space is confined to a very small part of the full (M_1, M_2, μ) parameter space. In mSUGRA one typically has $M_3 : M_2 : M_1 \approx 6 : 2 : 1$ [34], which gives a very homogeneous distribution of possible neutralino/chargino phenomenologies. The specific gaugino/higgsino content of the neutralinos and charginos affects to a large extent their production cross-sections and their branching patterns. The latter is, however, also very much affected by the kinematical availability of sleptons.

The signal grids used in the analysis are defined in the (M_2, μ) space with $100 \leq M_2, \mu \leq 500$ GeV for three different values of M_1: 100, 140 and 250 GeV. All points have $\tan\beta = 6$ and $m_A = 500$ GeV. The steps in which the (M_2, μ) space is spanned vary somewhat with the value of M_1. Also, in some regions of parameter space many points are used, while in other regions the step between each point is larger. In total 336 points are generated.

Since the slepton sector of the models affects the decay patterns of the neutralinos and charginos it needs to be properly specified. In the following analysis all points have the left-handed slepton masses very high, beyond reach at the LHC. The right-handed sleptons are degenerate in mass across the generations, with the masses being exactly midway between the two lightest neutralinos. In addition the stau trilinear coupling, A_τ, is set to zero. These constraints greatly reduce the generality of the signal grids. There are for example no experimentally motivated reasons for the left-handed sleptons to be put outside reach. If also the left-handed sleptons were kinematically available for the charginos/neutralinos it would, on one hand, enhance the number of decays including leptons, but on the other hand, the neutrinos accompanying the left-handed sleptons would now also enter the decay chains, reducing the lepton yields. Making the left-handed sleptons available for the gaugino decays would complicate the situation further, with additional parameters that need to be specified.

The different pMSSM scenarios used are defined at the current scale with the sparticle spectra calculated by ISASUSY 7.80 [80]. The 336 datasets used have the sample IDs 138421-138567, 143782-143934 and 163500-164066. They all contain the string `DGemt_TB6_M12U_xxx_yyy_zzz_2L`, where `xxx`, `yyy` and `zzz` specify the value of M_1, M_2 and μ respectively. When generating the grid-points a filter requiring at least two leptons (electrons, muons and hadronic taus[2]) with transverse momentum above 7 GeV was applied. This was necessary in order to get a decent sample of events containing two leptons for each grid-point. In the analysis each sub-process (i.e. each pair of initially produced SUSY particles) was treated on its own by applying the appropriate sub-process cross-section, generator filter efficiency and number of events when scaling the distribution to the correct luminosity. The scaling therefore needs to be done on an event-by-event basis. Signal cross-sections are calculated to next-to-leading order (NLO) in the strong coupling constant using PROSPINO2 [81]. The uncertainties on the nominal cross-sections are taken from an envelope of cross-section predictions using different PDF sets and factorization and renormalization scales, as described in Ref. [82]. The event-generation and hadronization were done using Herwig [83]. In the end the events were propagated through

[2]The leptonic decays of τs are not included, thus no leptons come from the decay of τ in these models.

the ATLAS detector simulation. The cross-sections and number of generated events for each grid point is shown in Figure 5.5.

5.3.2.2 Direct Slepton Grid

Direct slepton production is known to be one of the SUSY processes with the smallest cross-sections at the LHC. Therefore, in order to be able to set limits with the available luminosity in this channel, special grids with particularly small slepton masses need to be developed. In direct slepton production one can have either charged slepton ($\tilde{\ell}^{\pm}_{\mathrm{R}}\tilde{\ell}^{\mp}_{\mathrm{R}}$, $\tilde{\ell}^{\pm}_{\mathrm{L}}\tilde{\ell}^{\mp}_{\mathrm{L}}$), sneutrino-sneutrino production ($\tilde{\nu}_{\mathrm{L}}\tilde{\nu}_{\mathrm{L}}$) or sneutrino-charged slepton production ($\tilde{\nu}_{\mathrm{L}}\ell^{\pm}_{\mathrm{L}}$) [3]. The right-handed charged slepton pair production has a significantly smaller cross-section compared with the left-handed charged slepton production. In all the grids used in this analysis only direct production of charged sleptons is covered. Moreover only the two first generations of sleptons (i.e. selectrons and smuons) are included, as their production cross-sections are completely determined by their masses, and so are model-independent. Inclusion of the staus would have contributed modestly to the signal, but would also have introduced some additional, unwanted, model dependence, since the exact position of the stau masses as well as the stau mixing angle would need to be set. By using models without the staus included, the resulting limits are conservative and robust against the model-parameters that affect the stau-sector. In fact, the combined limits from LEP [84] are even more model independent. By only setting limits on the $\tilde{\ell}^{\pm}_{\mathrm{R}}\tilde{\ell}^{\mp}_{\mathrm{R}}$ production, which is the direct slepton production process having the smallest cross-section, their limits are very conservative as well as they do not have to assume anything about the mass hierarchy between the right- and left-handed sleptons.

Another important assumption for the direct slepton model grid is that all gauginos (except the LSP, $\tilde{\chi}^0_1$) are considerably heavier than the sleptons; if not, the direct gaugino production discussed in Section 5.1 would dominate and be the most sensitive channel in searches for SUSY, given that the squarks and gluinos are still out of reach. This has also the consequence that the sleptons decay exclusively according to $\tilde{\ell}^{\pm} \rightarrow l^{\pm}\tilde{\chi}^0_1$ as in Figure 5.3. All sparticle masses other than the first two generation sleptons and the LSP masses are set to 2.5 TeV.

The slepton mass parameters generated for this grid are in the range $70 \leq m_{\tilde{\ell}} \leq 190$ GeV with corresponding LSP mass parameters of $20 \leq m_{\tilde{\chi}^0_1} \leq 160$ GeV, both in steps of 20 GeV. The value of the mass parameters used in the supersymetric Lagrangian and the physical masses of the sparticles might differ slightly. For $\tilde{\chi}^0_1$ the change between the two is negligible. For the sleptons, however, the differences are more pronounced and result in slightly different physical masses for the left- and right-handed sleptons. In the analysis the average of the left- and right-handed masses is used, since the difference is not very large, as seen in Table 5.2. The Lagrangian mass parameters are used in all plots throughout the analysis if not stated otherwise.

Since the main characteristic signature of the direct slepton channel in this analysis is the production of two high momentum (i.e. $p_T > 20/25\ GeV$) charged leptons the mass difference between the slepton and the LSP is important, as this basically sets the momentum of the produced lepton. With the current available luminosity the search for

[3] The $\tilde{\nu}_{\mathrm{L}}\tilde{\ell}^{\pm}_{\mathrm{R}}$ production is forbidden because W only couples to left-handed leptons and sleptons.

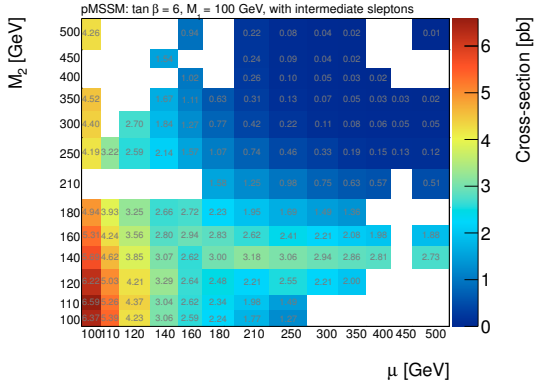

(a) Cross-section ($M_1 = 100$)

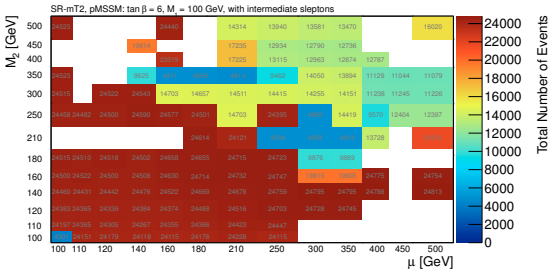

(b) Number of generated events ($M_1 = 100$)

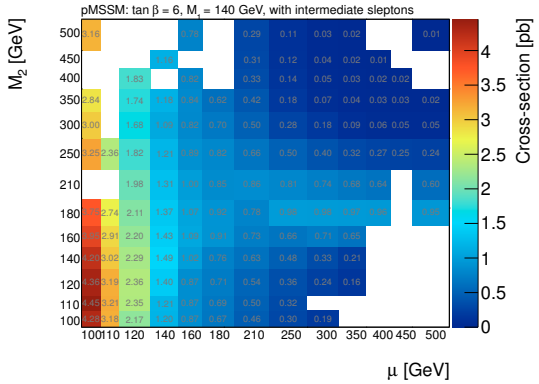

(c) Cross-section ($M_1 = 140$)

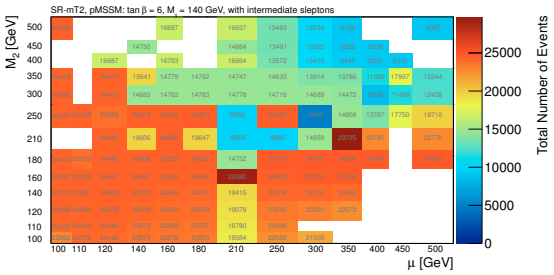

(d) Number of generated events ($M_1 = 140$)

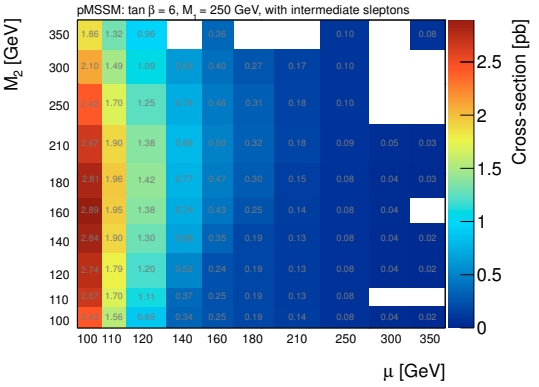

(e) Cross-section ($M_1 = 250$)

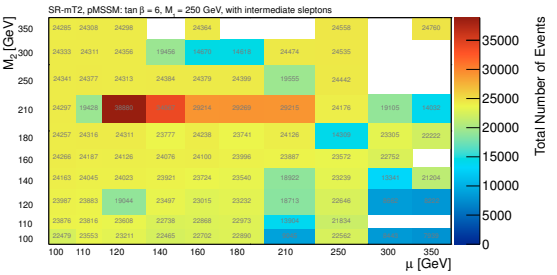

(f) Number of generated events ($M_1 = 250$)

Figure 5.5: The cross-section, in pb, (left) and the total number of generated events (right) for each of the signal points used in the direct gaugino analysis with $M_1 = 100$ GeV (top), $M_1 = 140$ GeV (middle) and $M_1 = 250$ GeV (bottom).

Lagr. mass param.	Physical mass		
$m_{\tilde{\ell}}$	$m_{\tilde{\ell}_L}$	$m_{\tilde{\ell}_R}$	$\frac{1}{2}(m_{\tilde{\ell}_L} + m_{\tilde{\ell}_R})$
70	84.2	82.4	83.3
90	101.4	100.0	100.7
110	119.5	118.2	118.9
130	138.1	137.1	137.6
150	157.1	156.2	156.6
170	176.3	175.5	175.9
190	195.7	195.0	195.3

Table 5.2: The mass parameters in the SUSY lagrangian and the corresponding physical masses of the sleptons, in GeV.

low momentum leptons would be a major challenge because of the large WW background, therefore only models with $m_{\tilde{\ell}} - m_{\tilde{\chi}_1^0} \geq 30$ GeV are generated. This results in a total of 35 generated grid-points with MC IDs in the range $[142708 - 142742]$. The files used have the string `direct_slepton_xxx_yyy`, where `xxx` and `yyy` indicate the slepton and LSP masses respectively. The event generation and the calculation of the nominal cross-sections and uncertainties are done in exactly the same way as for the direct gaugino grid discussed in Section 5.3.2.1. The resulting cross-section for the direct charged slepton production for each of the grid-points as well as the total number of generated events are shown in Figure 5.6.

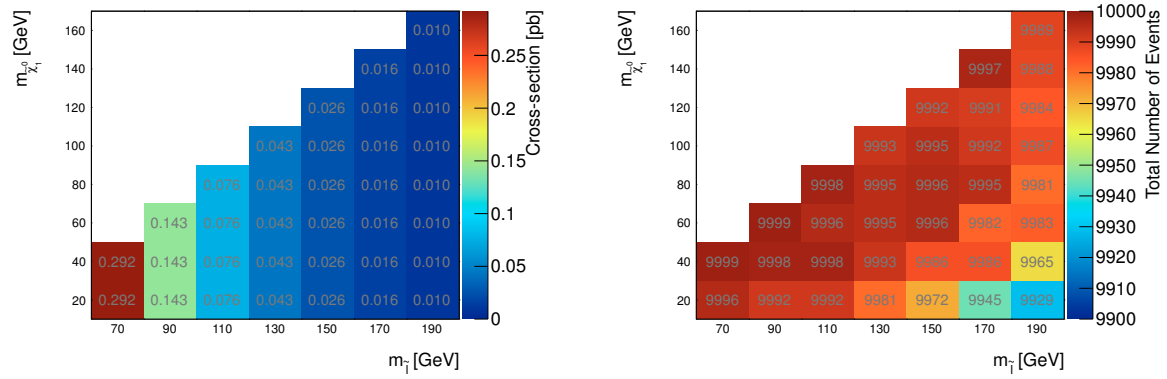

(a) Cross-section

(b) Number of generated events

Figure 5.6: The cross-section, in pb, of direct slepton production (a) and the total number of generated events (b) for each of the signal points used in the direct slepton analysis.

5.4 Standard Model Backgrounds

There are several SM processes mimicking the signal final states pictured in Figures 5.2 and 5.3 and therefore serve as important backgrounds to the SUSY analysis. The processes with the by far largest cross-section at the LHC is jet production, mainly because it

involves the strong interaction. This is therefore an important background for almost every analysis performed at the LHC. In addition, leptons from decays of W, Z and τ leptons, which in the following will be denoted as *real leptons*, also contribute significantly to the full SM background. The leptons not classified as real are called *fake leptons*, although they might literally be real, coming from decays of heavy- or light-flavoured hadrons or, in case of electrons, also from γ conversion processes. In addition *fake leptons* also include other particles that can be misinterpreted as leptons in the detector, such as pions and other jet activity.

We start by discussing the SM background arising from events with *fake leptons*, which has been a field of particular interest for the author, and move then to the discussion of the *real lepton* background.

5.4.1 Fake Leptons

Processes like W+jets, semi-leptonic $t\bar{t}$ and single top might all contain at least one *real lepton*. If a *fake lepton* is reconstructed in addition these events show up as signal events with two leptons. Events with two *real leptons*, like Z+jets, WW or leptonic $t\bar{t}$, where one lepton fails reconstruction, might also lead to di-lepton events if one *fake lepton* is reconstructed in addition. These events can be reconstructed as same-sign (SS) di-lepton events, and are therefore of particular interest since the processes giving two real SS leptons in the SM are relatively rare. Also interesting are events where both leptons are fake, typically from QCD multi-jet production, which are produced at a high rate at the LHC, as discussed in Chapter 2.

5.4.1.1 Conversions

Photons are abundantly produced in pp collisions. Here we consider those converting into a lepton-antilepton pair. Of special interest are the asymmetric conversions where one lepton carries most of the converted photon momentum, in which case the harder lepton is often seen as isolated. From the charge conjugation symmetry of electrodynamics the lepton getting most of the converted photon momentum in these events will be the lepton or antilepton with roughly the same probability. In the following we will differentiate between two main sources of conversions, namely internal and external.

A) External Conversion

External conversion stems from photons producing a lepton-antilepton pair when interacting with the material in the detector. The ratio of the probabilities for an external conversion to produce an e^+e^- pair to $\mu^+\mu^-$ pair is given by [85]

$$\frac{\mathcal{P}(\gamma \to \mu^+\mu^-)}{\mathcal{P}(\gamma \to e^+e^-)} = \mathcal{O}\left(\frac{m_e}{m_\mu}\right)^2 \sim \mathcal{O}(10^{-5}). \tag{5.1}$$

This means that external conversions are only relevant in the electron channel. This type of conversion typically happens where the material density is highest. The electron tracks

are therefore typically incomplete, with no hits in the innermost layers of the detector, thus requiring hits in the b-layer dramatically reduces the number of reconstructed electrons coming from external conversion.

Charge-Flip

One particularly important type of external conversions is known as charge-flip, since it contributes to the overall charge mis-identification of electrons in ATLAS. Charge-flip happens typically when an electron undergoes hard bremsstrahlung, followed by an asymmetric pair production, like the one shown in Figure 5.7, where the $e^{\mp}$ (dashed line) has low momentum or is not reconstructed. If the bremsstrahlung electron (the initial $e^{\mp}$) stems from a Z boson the resulting event might be reconstructed as a SS event. In 50% of the cases it is still reconstructed as an OS di-electron event, however.

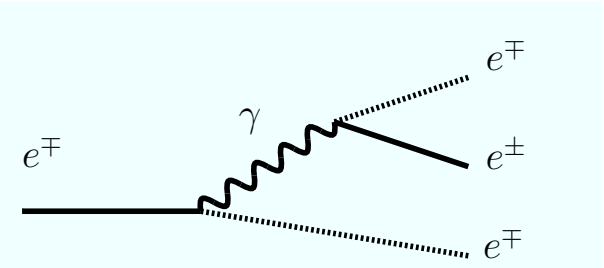

Figure 5.7: Electron undergoing hard bremsstrahlung followed by pair production. If the conversion is sufficiently asymmetric the hard electron from the photon is reconstructed. The dashed lines indicate the electrons/positrons failing reconstruction.

Leptons from Charge-Flip

Charge-flip is not very well reconstructed by the currently available MC samples. The amount of charge-flip in data is measured to be 81.3% of that in the MC [86]. This is partly caused by the somewhat different material distribution in the ATLAS detector than what is used in the simulations.[4] The charge-flip rate is therefore measured with a data-driven likelihood minimization technique using real Z events, where electrons within 10 GeV of the Z mass are selected [76]. The measured charge-flip rate as a function of η is shown in Figure 5.8. The black dots represent the charge-flip rate using truth MC to identify the $Z\rightarrow l^{\pm}l^{\mp}$ events while the red points show the charge-flip measured in data using the likelihood technique. The ratio plot at the bottom is consistent with the observed 81.3% difference between MC and data. Based on the results above, the rate of charge-flip in the MC samples used for the SUSY di-lepton searches can be estimated. A weight, w, is applied to every OS event in MC

$$w = \frac{\epsilon_1 + \epsilon_2}{(1-\epsilon_1)(1-\epsilon_2)}, \tag{5.2}$$

where $\epsilon_{1,2}$ are the probabilities for each electron to flip charge as a function of the electron's η and p_{T}. The flip rate as a function of η is retrieved using the likelihood technique

[4] The detector simulation programs are constantly updated to account for any new discrepancies found between data and MC. The main differences between data and MC in this study probably stem from the fact that the beam-pipe in reality is not centered at the (0,0) position and the fact that the density of the fluid inside the cooling pipes is somewhat different than what is used when simulating the MC [87].

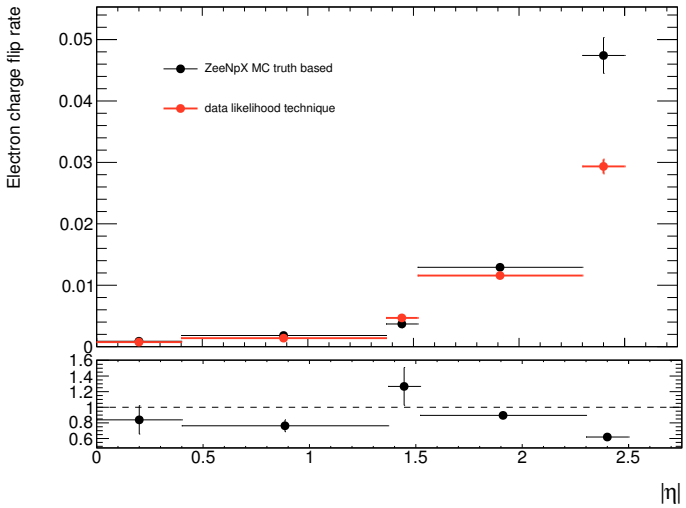

Figure 5.8: The charge-flip rate as a function of $|\eta|$ measured using MC truth (black points) and the likelihood technique using data (red points). The ratio is consistent with the 81.3% difference observed between data and MC. Plot is from Ref. [76].

(as shown in Figure 5.4.1.1) while the p_{T} dependency is found using truth MC. The denominator is due to the fact that the weight is applied to OS events only while the charge-flip probabilities are calculated using both SS and OS events. Since a small amount of energy is lost when an electron undergoes a charge-flip a small correction must be applied to the electron-p_{T} in order not to get a slightly shifted mass-peak for the Z. The corrected transverse momentum, p'_T, is given by

$$p'_T = \frac{p_{\mathrm{T}}}{1+\Delta}, \tag{5.3}$$

where Δ is a random number taken from a Gaussian distribution with mean and width both being 0.047, found to best account for the observed energy loss. If the relative charge-flip probability, $w_1/(w_1+w_2)$ is larger (smaller) than a random number drawn from a standard uniform distribution, the p_{T} of the electron with flip rate w_1 (w_2) is shifted.

A closure test using data around the Z-mass, testing the validity of weighting OS events to obtain a SS estimate, is shown in Figure 5.9a. The SS estimates using the MC truth-based η and p_{T} flip rate is clearly too large, while the method using the η-dependent data-based flip rate in Figure 5.8 together with the MC truth-based p_{T} dependent flip rate shows a much better agreement with data. This plot is made without applying the p_{T} correction, however, so the peak is somewhat shifted to the right. Another test, done using MC truth, showed that the measured flip rates were also valid for electrons from $t\bar{t}$ events in all η and p_{T} bins [76].

Figure 5.9b shows a plot of the invariant mass of all di-electron SS events in MC scaled to 4.71 fb^{-1}, with the various charge-flip contributions, estimated from OS events using the above-mentioned method. The p_{T} of each electron is also shifted, according to Eq. 5.3, before calculating the invariant mass.

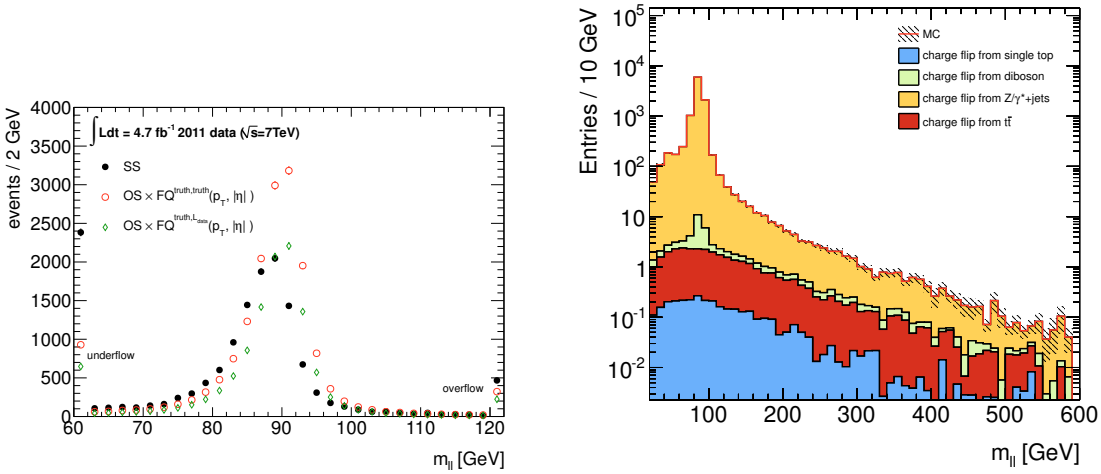

(a) Closure test

(b) m_{ll} of SS electrons

Figure 5.9: In (a) a closure test comparing the SS m_{ll} distribution in data with the corresponding distributions estimated using η dependent flip rates from MC (red circles) and those obtained from the likelihood technique (green diamonds). The plot in (b) shows the invariant mass of SS di-electrons estimated from OS events in MC.

B) Internal Conversion

In contrast to external conversion, internal conversions are not dependent on the detector material. Internal conversions therefore mostly originate from the collision vertices. Leptons produced from internal conversion may therefore leave a long track in the complete ID. Contrary to external conversions, internal conversions lead to a moderate logarithmic enhancement of e^+e^- over $\mu^+\mu^-$ pairs. For the background processes relevant for SUSY searches, the total probability for a high energy photon to undergo internal conversion is typically $\mathcal{O}(1\%)$ [85].

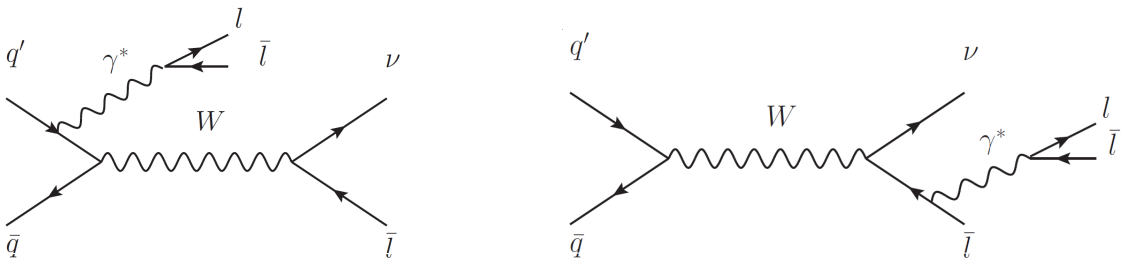

(a) photon from ISR

(b) photon from FSR

Figure 5.10: Examples of internal conversions in connection with W production. If the conversion is sufficiently asymmetric in momentum, such events may lead to two reconstructed leptons of either OS or SS in the final state.

5.4.1.2 Decays of Heavy-Flavoured Hadrons

There are many ways to produce heavy-flavoured jets (initiated by b and c quarks) in a proton-proton collision. Of special interest for studies using final states with two lep-

tons is of course when the heavy-flavoured jets are produced together with an isolated lepton. First of all; jets can deposit energy in the electromagnetic calorimeters and thus wrongly be interpreted as electrons in the detector. However, after applying the lepton and jet identification criteria and removing overlapping objects, to be discussed in detail in Chapter 6, the rate for this is expected to be very much reduced. More important are the possible leptonic and semi-leptonic decays of heavy-flavoured jets. These leptons can in some cases pass all the isolation criteria and thereby serve as a background to the di-lepton final state. Figures 5.11 and 5.12 show heavy-flavoured jets produced in association with a W and Z bosons respectively. The W can decay to a neutrino-lepton pair while the Z might decay to a pair of oppositely charged leptons. Note that the Feynman graphs shown in this and the following sections only represent a small subset of all the possible processes. Figure 5.13 illustrates the dominant processes for heavy-flavoured

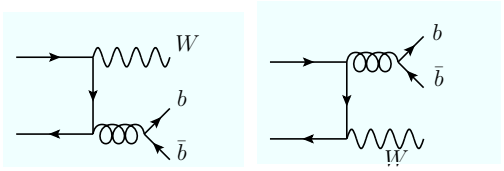

Figure 5.11: Heavy jets in association with a W boson.

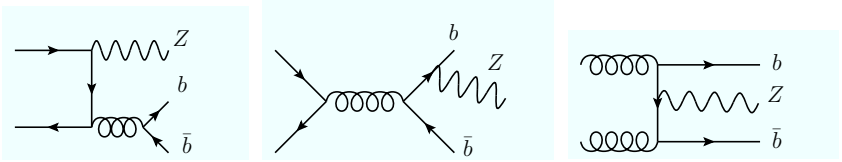

Figure 5.12: Heavy jets in association with a Z boson.

jets produced in association with a W in $t\bar{t}$ or single top events. These events can also be misinterpreted as di-lepton events, where the leptons stem from semi-leptonic b- or c-decays within the jet. Figure 5.14 shows examples of leptonic decays of heavy-flavoured hadrons. For the B-hadrons in Figure 5.14a-c as well as the Λ_b^0-baryon in Fig. 5.14e the leptonic and semi-leptonic decays account for about 10% of the total decay width. The D^+ meson in Fig. 5.14d has decay fractions into final states containing electron-neutrino or muon-neutrino pairs of 16% and 17.6% respectively. The J/Ψ in f decays to an e^+e^- or a $\mu^+\mu^-$ pair with a probability of $\sim 6\%$ to each [24].

5.4.1.3 Decays of Light-Flavoured Hadrons

The light-flavoured jets can be produced in association with W or Z bosons in the same way as shown for heavy-flavoured jets in Figure 5.11 and 5.12. This is pictured in Figure 5.15. The light-flavoured mesons also have leptonic and/or semi-leptonic decay modes, some of them exemplified in Figure 5.16. The kaon decays leptonically (a) or semi-leptonically (b) with branching fraction, $BR(K \to \mu\nu_\mu)$, of 63.5%, while $BR(K \to e\nu_e)$

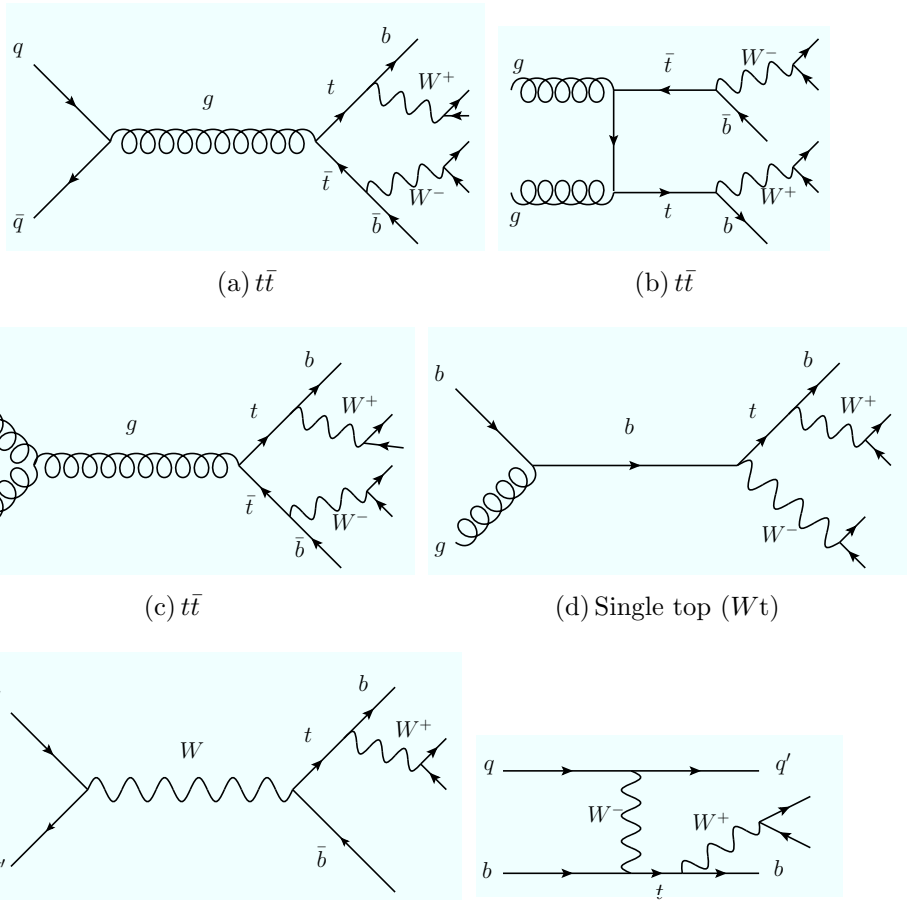

(a) $t\bar{t}$ (b) $t\bar{t}$

(c) $t\bar{t}$ (d) Single top (Wt)

(e) Single top (s-channel) (f) Single top (t-channel)

Figure 5.13: Heavy jets in $t\bar{t}$ and single top production.

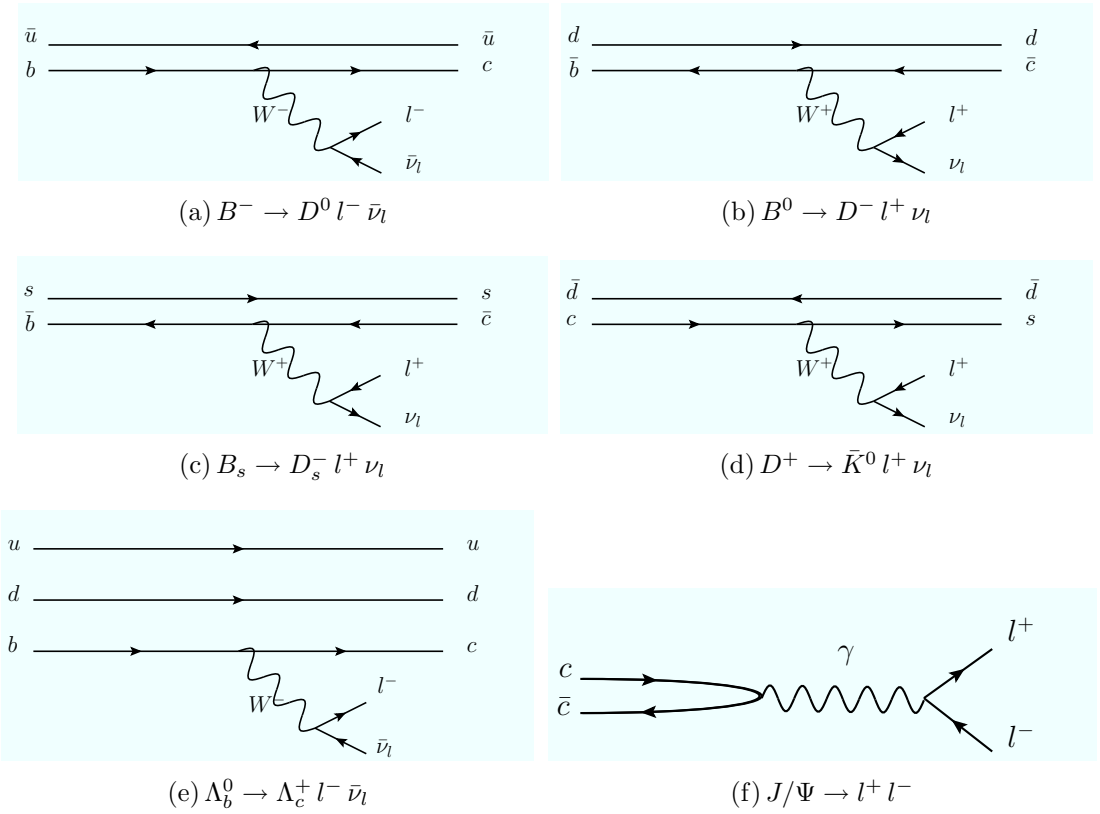

(a) $B^- \to D^0\, l^-\, \bar{\nu}_l$ (b) $B^0 \to D^-\, l^+\, \nu_l$

(c) $B_s \to D_s^-\, l^+\, \nu_l$ (d) $D^+ \to \bar{K}^0\, l^+\, \nu_l$

(e) $\Lambda_b^0 \to \Lambda_c^+\, l^-\, \bar{\nu}_l$ (f) $J/\Psi \to l^+\, l^-$

Figure 5.14: Examples of leptonic and semi-leptonic decays of heavy-flavoured hadrons.

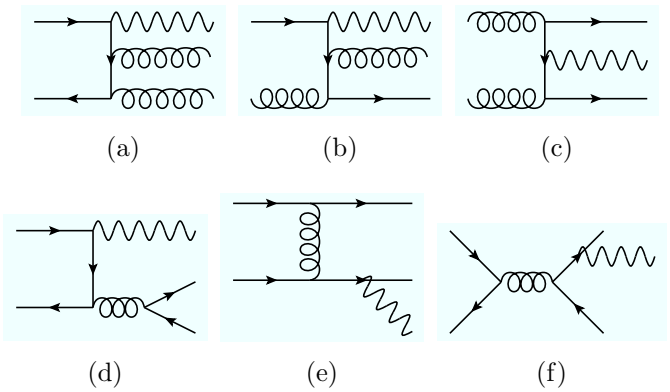

Figure 5.15: Light jets in association with a W or Z boson. The solid lines represent quarks, curly lines are for gluons while wavy lines represent W or Z bosons.

is suppressed because of the helicity structure of the W coupling [88]. For the same reason the charged pion effectively also decays solely into a $\mu\nu_\mu$-pair. The charged meson decays shown in Figure 5.16 can easily be generalized to also apply for the oppositely charged state, having the same branching fractions. The $\gamma\gamma$-decay of the neutral pion in e is completely dominating the leptonic decay (i.e. Dalitz decay) in d with branching factors of $\sim 99\%$ and $\sim 1\%$ respectively. As was discussed in Section 2.2.1.3 the p_{T} or E_{T} distribution of leptons from light-flavoured hadron decays is much softer than the leptons from heavy-flavoured hadrons. Because of this the leptons from light-flavoured jets are less probable to pass the selection criteria. The light jets are, however, produced at a much larger rate than heavy-flavoured jets and thus might still be an important background. The most important contribution to fake electrons from light-flavoured jets is in fact expected to come from jets with a leading π^0 overlapping with a charged particle. Because π^0 decays into two photons it can in addition deposit its energy in the calorimeter, giving a signature very similar that of an electron, and therefore possibly end up being reconstructed as such.

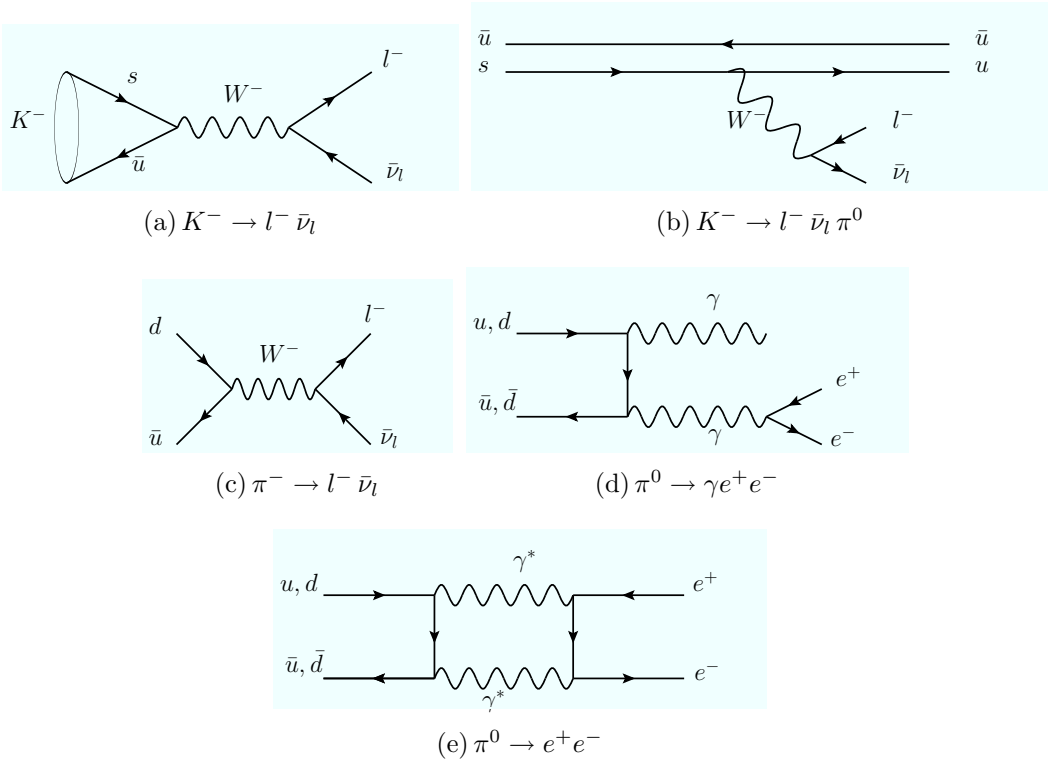

(a) $K^- \to l^- \bar{\nu}_l$ (b) $K^- \to l^- \bar{\nu}_l \pi^0$

(c) $\pi^- \to l^- \bar{\nu}_l$ (d) $\pi^0 \to \gamma e^+ e^-$

(e) $\pi^0 \to e^+ e^-$

Figure 5.16: Examples of light mesons decay leading to leptons.

5.4.2 Real Leptons

We now turn to the discussion of the SM background coming exclusively from real leptons.

5.4.2.1 Same-Sign Background

There are in general very few processes in the SM with a noticeable cross-section that can give rise to exactly two real SS leptons in the final state, and all of them suffer from relatively small cross-sections. One of the main SS processes is depicted in Figure 5.17. It is also possible to get two real SS leptons in events originally containing more than two

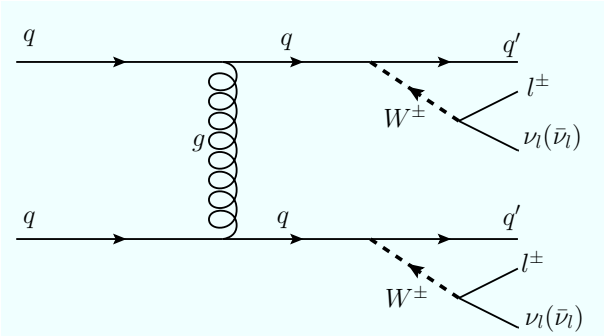

Figure 5.17: A process giving two real SS leptons.

leptons, but where one or more of the leptons have failed reconstruction (e.g. ZZ and WZ events).

5.4.2.2 Top Events

Single top and $t\bar{t}$ events are some of the most important backgrounds to the SUSY di-lepton searches. A typical $t\bar{t}$ decay is pictured in Figure 5.18a. The top quark almost solely decays into a W boson and a b-quark, where W-decays either leptonically or into quark-pairs. Depending on the decay of the two W bosons in a $t\bar{t}$ event, one can therefore get events with two OS leptons, missing transverse energy from the neutrinos and jets. If the single top is produced in association with a W, as sketched in Figure 5.18b it constitutes another important source of background for di-lepton SUSY searches.

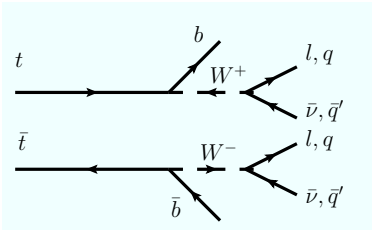

(a) $t\bar{t}$

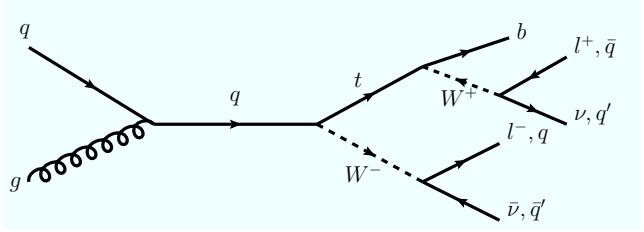

(b) single top (Wt-channel)

Figure 5.18: Diagrams for a typical $t\bar{t}$ event (a) and single top production in the Wt channel (b) giving two real leptons. Single top production through the s- and t-channels does not give two real leptons and thus an additional fake lepton is needed in order to get di-lepton final state, as pictured in Figure 5.13e and f.

Contransverse mass

The top background can be reduced by using a variable known as the *contransverse mass*, m_{CT} [89]. It is defined for two pair-produced heavy states, δ, each decaying into an invisible particle, α, and visible decay products, v_i, $i \in \{1, 2\}$

$$m_{CT}^2(v_1, v_2) = \left[E_{\mathrm{T}}(v_1) + E_{\mathrm{T}}(v_2)\right]^2 - \left[p_{\mathrm{T}}(v_1) + p_{\mathrm{T}}(v_2)\right]^2. \tag{5.4}$$

If $m(v_1) = m(v_2) = m(v)$, m_{CT} possesses an endpoint

$$m_{CT}\left[m^2(v)\right] < m_{CT}^{max}\left[m^2(v)\right] = \frac{m^2(v)}{m(\delta)} + \frac{m^2(\delta) - m^2(\alpha)}{m(\delta)}. \tag{5.5}$$

From each of the legs in a $t\bar{t}$ event one lepton and one jet are reconstructed meaning that the $v_{1,2}$ in Eq. 5.4 can be a lepton (l), a jet (j) or the aggregate product of a jet and lepton (jl). The three quantities $m_{CT}(l, l')$, $m_{CT}(j, j')$ and $m_{CT}(jl, j'l')$ are bounded from above by Eq. 5.5 after substituting (δ, α) with (W, ν), (t, W) and (t, ν) respectively. The top-tag is based on the idea that a $t\bar{t}$ should satisfy the inequality of Eq. 5.5 for all of these three contransverse mass combinations. There is however an additional complication because the exact endpoint is also dependent on the vector sum of the particles upstream of the system, p_b, for which the contransverse mass is calculated. In stead of applying a strict upper cut given by Eq. 5.5 the $m_{CT}\left[m^2(v)\right]$ is required to be [90, 91]

$$m_{CT}\left[m^2(v)\right] < m_{CT}^{max}\left[m^2(v), p_b\right] = 2\left(\frac{p_b\, p_0}{2m(\delta)} + E_0\sqrt{1 + \left(\frac{p_b}{2m(\delta)}\right)^2}\right), \tag{5.6}$$

where

$$E_0 = \frac{m^2(\delta) + m^2(\alpha) + m^2(v)}{2m(\delta)} \quad \text{and}$$
$$p_0 = \sqrt{E_0^2 - m^2(v)}.$$

After requiring the event to have a total of at least two jets (with $p_{\mathrm{T}} > 30$ GeV) and two leptons, which, added together, have a scalar sum of p_{T} above 100 GeV, the event is top-tagged if any of the following requirements below are fulfilled:

- $m_{CT}(j, j) < m_{CT}^{max}\left[jj, p_b\right]$ (code available in [92])
- $m_{CT}(l, l) < m_{CT}^{max}\left[ll, p_b\right]$ (code available in [92])
- $m_{CT}(jl, j'l')$ compatible with $t\bar{t}$ (code available in [92])
- lepton-jet invariant mass values consistent with top quark decays (i.e. $m_{j,l} < 155$ GeV and $m_{j',l'} < 155$ GeV).

By vetoing on top-tagged events the background from $t\bar{t}$ can be significantly reduced, as will be illustrated when defining the signal regions in Chapter 8

5.4.2.3 Di-Boson

Di-boson production (i.e. WW, ZZ and WZ) is another important background, especially the WW production and decay in Figure 5.19a, giving two OS leptons and missing

transverse energy (from the neutrinos), very similar to the direct slepton final state in Figure 5.3. A WZ event of Figure 5.19b might lead to three leptons. If one of them fails reconstruction this process also acts as background to the SUSY searches. The ZZ process of Figure 5.19c could also feed the final states with two leptons in addition to two jets or two neutrinos. The case with two leptons + jets would not contain any significant $E_{\mathrm{T}}^{\mathrm{miss}}$, however. In many SUSY models, where the Z does not participate in the $\tilde{\chi}_2^0$ decay, background processes involving $Z \to l^{\pm}l^{\mp}$ can be reduced by applying a cut on the invariant mass of the two leptons.

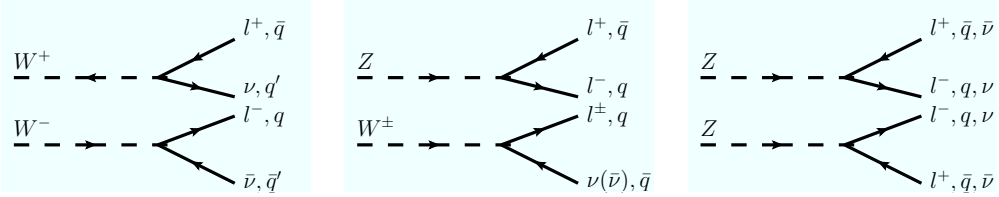

(a) (b) (c)

Figure 5.19: Diagrams for various di-boson final states leading to leptons.

5.4.2.4 Stransverse Mass

In order to further discriminate between the SM top and W backgrounds on one hand, and the SUSY signal on the other hand, a variable known as *stransverse mass*, m_{T2} [93, 94], is used. It is designed for events containing two identical decays of the same particle into a detectable and a non-detectable particle. Typical examples of such events are the direct slepton production in Figure 5.3 and the WW event in Figure 5.19a. The m_{T2} variable is defined by

$$m_{\mathrm{T2}} = \min_{\mathbf{q}_{\mathrm{T}}+\mathbf{r}_{\mathrm{T}}=\mathbf{p}_{\mathrm{T}}^{\mathrm{miss}}} \left[\max\left(m_T(\mathbf{p}_{\mathrm{T}}^{\ell_1}, \mathbf{q}_{\mathrm{T}}; m_X), m_T(\mathbf{p}_{\mathrm{T}}^{\ell_2}, \mathbf{r}_{\mathrm{T}}; m_X)\right)\right], \tag{5.7}$$

where $\mathbf{p}_{\mathrm{T}}^{\ell_1}$ and $\mathbf{p}_{\mathrm{T}}^{\ell_2}$ are the transverse momenta of the two detectable final state leptons and $\mathbf{q}_{\mathrm{T}}$ and $\mathbf{r}_{\mathrm{T}}$, satisfying $\mathbf{q}_{\mathrm{T}} + \mathbf{r}_{\mathrm{T}} = \mathbf{p}_{\mathrm{T}}^{miss}$, are the momenta of the two undetectable particles, which in SUSY events would be typically the two LSPs. The parameter m_X is free and indicates that the m_{T2} function is dependent on the hypothetical mass of these undetectable particles. The situation is even more complicated if there are more invisible particles in the event. Finally m_T denotes the well-known transverse mass defined in Eq. 2.11. The minimization in Eq. 5.7 is done for all possible decompositions of $\mathbf{p}_{\mathrm{T}}^{miss}$.

The *stransverse mass* exhibits a kinematic end-point, m_{T2}^{max}, for particles decaying into two objects, where one is detected and the other escapes (i.e. the lepton and the $\tilde{\chi}_1^0$ in slepton decays or the lepton and the neutrino in W-decays). In events containing only direct production of two sleptons with identical masses, and where each slepton decays into a lepton and an LSP, the m_{T2} distribution can take any value between 0 and

$$m_{T2}^{max} = \frac{(m_{\tilde{\ell}}^2 - m_{\tilde{\chi}_1^0}^2)}{2m_{\tilde{\ell}}} + \sqrt{\left(\frac{(m_{\tilde{\ell}}^2 - m_{\tilde{\chi}_1^0}^2)}{2m_{\tilde{\ell}}}\right)^2 + m_X}. \tag{5.8}$$

Assuming that the free parameter $m_\chi = 0$ [5] gives [95]

$$m_{T2}^{max} = \frac{(m_{\tilde{\ell}}^2 - m_{\tilde{\chi}_1^0}^2)}{m_{\tilde{\ell}}}. \tag{5.9}$$

The direct slepton searches are therefore expected to gain much sensitivity when this maximum value is larger than what is expected from WW and $t\bar{t}$ events, as the theoretical edge of the m_{T2} distribution for these events will typically fall off rapidly above the W-mass. Of course, taking into account the finite width of the W ($\Gamma_W \sim 2.1$ GeV [24]) as well as imperfections in the reconstruction, events might exceed this upper bound. A typical cut would therefore require m_{T2} to be larger than the W-mass plus a few W-widths.

5.4.2.5 W+ Jets and Z/γ^* + Jets

The W+jets will not give any final states with two real leptons. The Z/γ^*+jets, however, might act as a potential background producing two real leptons in addition to jets. This background can be greatly reduced, however, through cuts on the missing transverse energy and the invariant mass of the two leptons.

5.4.3 Cross-Sections

Figure 5.20 summarizes the cross-sections measured by the ATLAS experiment, together with the theoretical predictions, for some of the SM processes discussed above. The luminosity written in each bin indicates the amount of data used to measure each individual cross-section. Di-boson production suffers from small cross-sections compared to W+jets and Z/γ^*+jets. The $t\bar{t}$ has a somewhat larger cross-section making it a more challenging background. The measured cross-sections for W and Z/γ^* production in association with jets, together with various theoretical predictions, are shown in Figure 5.21a and b respectively. These plots illustrate that additional jets reduce the cross-sections significantly.

The cross-sections for many of the SM processes are huge compared with SUSY. However, requiring 2 leptons and some missing transverse energy reduces the SM cross-sections down to the level of 1-10 pb.

[5] This is a typical assumption of m_χ in SUSY searches since we do not know the mass of the LSP in advance and since this is approximately the mass of the only invisible particles in the SM, the neutrinos. Current limits state, however, that the lightest neutralino in R-parity conserving MSSM must have a mass above 46 GeV, assuming $\tilde{\chi}_1^0$ is the LSP [24].

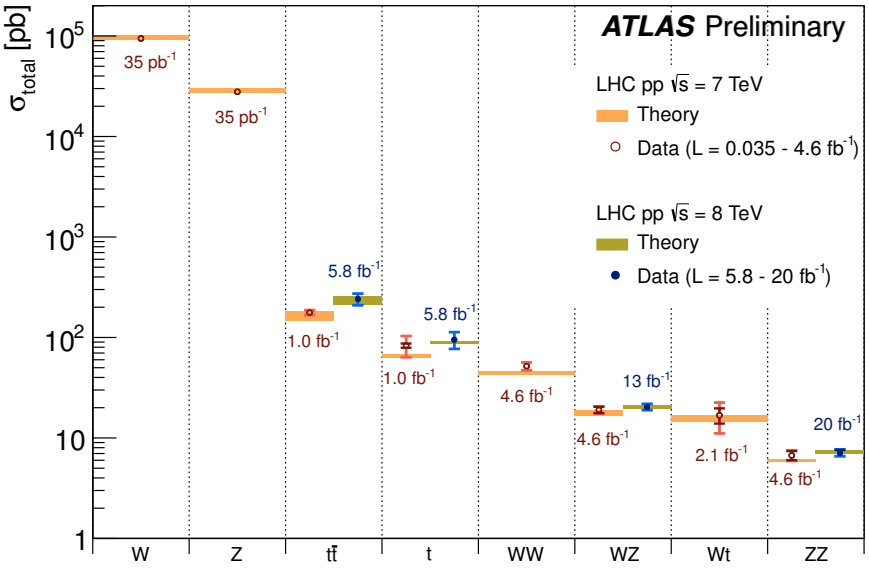

Figure 5.20: The cross-sections measured by the ATLAS experiment at 7 and 8 TeV, together with the theoretical predictions, for the SM processes which serve as important backgrounds to the di-lepton SUSY searches. Ref. [96].

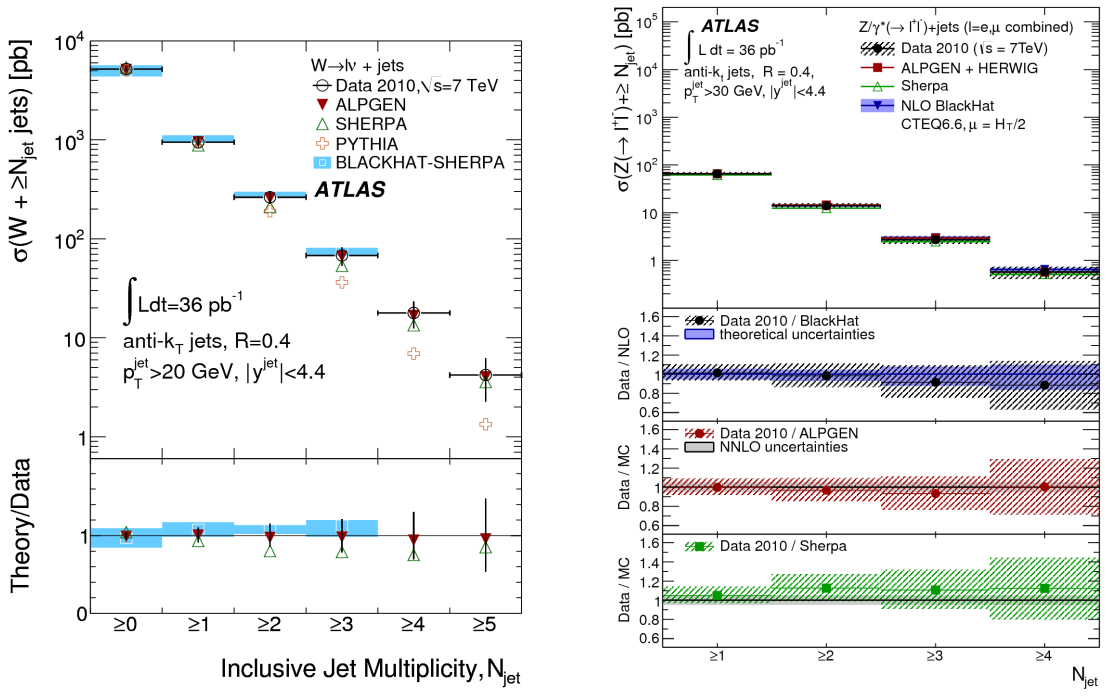

(a) W+jets. Ref. [97]

(b) Z+jets. Ref. [98]

Figure 5.21: The cross-sections measured by the ATLAS experiment along with different theoretical predictions of the W+jets (a) and Z/γ^*+jets (b) production. Only the leptonic channels of the W and Z-decays are included in these plots, thus they do not depict similar numbers as for the inclusive cross-sections in Figure 5.20.

5.5 Signal Regions

In order to cover the different scenarios in the di-lepton SUSY searches discussed in the previous Sections, four different signal regions (SR) are constructed, each targeting one or more of the diagrams in Figure 5.2 and 5.3.

1. **SR-OSjveto** requires two OS leptons of any flavour and vetoes events with any reconstructed jet. In addition a significant fraction of missing transverse energy is required. In order to enhance the signal over background ratio a veto of events with $Z \rightarrow l^{\pm}l^{\mp}$ is applied. This signal region targets the diagrams in Figure 5.2a,b,e and f
2. **SR-SSjveto** requires events with two SS leptons and significant missing transverse energy and vetoes events with any reconstructed jet. Since the leptons are required to have SS, a Z-veto is not needed. This signal region targets the diagrams in Figure 5.2b and g, where one of the leptons fails reconstruction and only the two SS leptons are measured.
3. **SR-2jets** requires two OS leptons in addition to at least two jets, of which none are tagged as b-jets, and missing transverse energy. This signal region targets the diagrams in Figure 5.2c and d. Since the two leptons stem from the same decay branch they need to be of same flavour (SF), thus only the e^+e^-- and $\mu^+\mu^-$-channels are included.
4. **SR-mT2** requires exactly two OS leptons with any flavour, missing transverse energy and Z- and jet-vetoes. In addition a cut on the m_{T2} variable is used in order to remove events from the WW-background. This signal region is especially optimized for the direct slepton diagram in Figure 5.3, but good sensitivity is also expected for the diagram in Figure 5.2a.

The exact cut values used for the various signal regions will be addressed later when discussing the optimization of signal regions in Chapter 8. Before that the details regarding the implementation of the analysis need to be described.

Chapter 6

Implementation of the Analysis

The previous Chapter discussed some interesting signal models to study when searching for supersymmetry in di-lepton final states in the direct gaugino and slepton production modes. The possible processes giving final states with at least two leptons were discussed, and signal regions specifically designed to target these final states were briefly sketched. Based on this the most important SM backgrounds were presented. In Section 6.1 and 6.2 a more detailed discussion of the exact data and MC samples to use is presented. With the appropriate samples in place the object definitions of electrons, muons, jets and missing transverse energy, based on the various recommendations from the ATLAS performance groups, are discussed in Section 6.3.1-6.3.4. Also, in order to construct an efficient and robust analysis there are several crucial points which will be described in detail in Section 6.3.5 and 6.4: (i) how to treat possible overlaps between physics objects; (ii) how to deal with the steadily increasing number of pile-up events; and (iii) how to handle and select the appropriate triggers. A more detailed study on how to classify fake and real leptons in the MC simulations is described in Section 6.3.7.

6.1 Data

The data used in this study is all what was collected of proton-proton collisions at a center of mass energy, $\sqrt{s}$, of 7 TeV, by the ATLAS detector during 2011. These are all data in the periods between B2 and M10, corresponding to collisions recorded from late March until end of October, giving a total integrated luminosity of about 5.2fb^{-1}. After requiring that all ATLAS sub-systems were working satisfactory and both magnets were turned on, the total amount of data was reduced to about 4.7fb^{-1}.[1] The uncertainty on the luminosity measurement is taken to be 3.9%, in accordance with the measurements from the ATLAS Luminosity Group [100, 101].

[1]The data quality and sub-system requirements were implemented using a so called good run list (GRL) taken from the official Data Preparation Group web page, version *data11_7TeV.periodAllYear_DetStatus-v36-pro10_CoolRunQuery-00-04-08_Susy.xml* [99]. In the analysis both the *egamma* and the *muon* streams were used.

6.2 Monte Carlo Samples

The following sections list the details of the MC samples used in the analysis in order to model the SM background and investigate systematic uncertainties, efficiencies and acceptance. For all samples the unique MC sample ID, the generator used to produce the sample, cross-sections, efficiencies and k-factors[2] are listed. The samples not used in the main analysis are indicated in gray. All other samples are used in background studies or to compute the systematic uncertainties coming from the modelling of parton showering, initial and final state radiation and the dependency on various physics generators.

In order to be able to incorporate the changing conditions with respect to pile-up and instantaneous luminosity during the data runs in 2011 every MC sample is divided into different parts having run numbers $\leq$ 184169, 186169 and 189751, meant to represent the periods from B-H, I-K and L-M respectively. The fraction of the total number of events in MC with each run number reflects the ratio of the total integrated luminosity recorded in the corresponding periods.

6.2.1 W+jets and Z/γ^*+jets

The SM backgrounds coming from W+jets and Z/γ^*+jets were discussed in Section 5.4.2.5. The samples used to model W bosons produced together with 0-5 jets are listed in Table 6.1. Table 6.2 shows the corresponding samples for the Z/γ^*+jets background, where the di-lepton invariant mass is within the range 40 GeV$< m_{ll} <$ 2000 GeV. Table 6.3 lists the corresponding low mass di-lepton samples with 10 GeV$< m_{ll} <$ 40 GeV. The samples are divided into two distinct m_{ll} ranges, otherwise the rapidly falling cross-section with increasing m_{ll} would have resulted in generated samples with very few events at high m_{ll}. All Z/γ^*+jets samples are generated with 0-5 jets. The cross-section times branching ratio into $l\nu$ or ll and k-factors are listed for all samples.

6.2.2 Di-boson

The SM background to di-lepton SUSY searches from WW, WZ and ZZ production was discussed in Section 5.4.2.3. Table 6.4 lists all the di-boson MC samples used in the analysis. In *SR-OSjveto*, *SR-SSjveto* and *SR-mT2*, the di-boson background is estimated based on the *Herwig* samples, the three uppermost samples listed in Table 6.4. In *SR-2jets*, however, the estimates are computed using the *Sherpa* samples. The reason for using another generator in this signal region, the only signal region containing jets, is that *Herwig*, unlike *Alpgen* and *Sherpa*, does not contain the proper matrix element for generating WW events with one or more jets [76]. The result using *Herwig* would thus yield an underestimation of the number of events in *SR-2jets*, as can be seen in Figure 6.1, where *Alpgen* and *Sherpa* are similar while *Herwig* differ when the number of jets is 2 or more.

[2]The k-factors are multiplied with the cross-section to account for higher order effects not included in the nominal cross-section.

Sample ID	Name	Generator	σ·BR [pb]	k-factor
107680	WenuNp0_pt20	Alpgen+Herwig,Jimmy	6.932	1.1955
107681	WenuNp1_pt20	Alpgen+Herwig,Jimmy	1.305	1.1955
107682	WenuNp2_pt20	Alpgen+Herwig,Jimmy	0.378	1.1955
107683	WenuNp3_pt20	Alpgen+Herwig,Jimmy	0.102	1.1955
107684	WenuNp4_pt20	Alpgen+Herwig,Jimmy	0.026	1.1955
107685	WenuNp5_pt20	Alpgen+Herwig,Jimmy	0.007	1.1955
107680	WmunuNp0_pt20	Alpgen+Herwig,Jimmy	6.932	1.1955
107681	WmunuNp1_pt20	Alpgen+Herwig,Jimmy	1.305	1.1955
107682	WmunuNp2_pt20	Alpgen+Herwig,Jimmy	0.378	1.1955
107683	WmunuNp3_pt20	Alpgen+Herwig,Jimmy	0.102	1.1955
107684	WmunuNp4_pt20	Alpgen+Herwig,Jimmy	0.026	1.1955
107685	WmunuNp5_pt20	Alpgen+Herwig,Jimmy	0.007	1.1955
107680	WtaunuNp0_pt20	Alpgen+Herwig,Jimmy	6.932	1.1955
107681	WtaunuNp1_pt20	Alpgen+Herwig,Jimmy	1.305	1.1955
107682	WtaunuNp2_pt20	Alpgen+Herwig,Jimmy	0.378	1.1955
107683	WtaunuNp3_pt20	Alpgen+Herwig,Jimmy	0.102	1.1955
107684	WtaunuNp4_pt20	Alpgen+Herwig,Jimmy	0.026	1.1955
107685	WtaunuNp5_pt20	Alpgen+Herwig,Jimmy	0.007	1.1955

Table 6.1: List of MC samples used to model the W+jets category, specifying the cross-section times branching ratio, k-factor (from Ref. [102]) and generators for each sample . The Npx in the names reflects the number, x, of additional jets coming from initial or final state radiation.

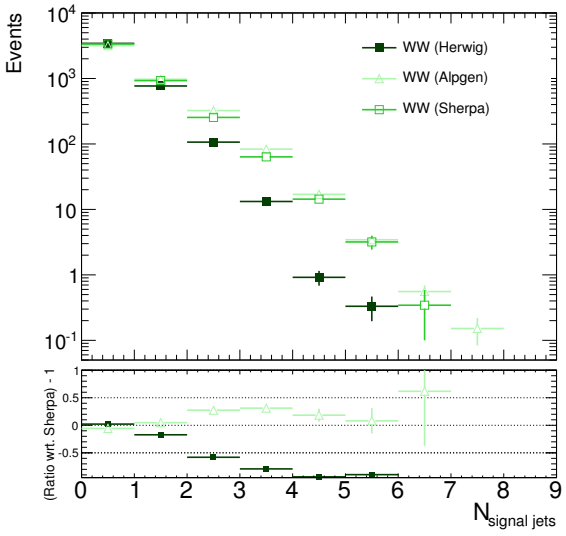

Figure 6.1: The number of signal jets as modeled by the WW MC samples generated by *Herwig*, *Alpgen* and *Sherpa* in a region requiring two leptons and $m_{ll} > 20$ GeV. The black and green points in the lower plot show the ratio between *Herwig* and *Sherpa* and *Alpgen* and *Sherpa* respectively. Both ratios are subtracted by one in order distribute them around 0. The number of events with ≥ 2 signal jets is significantly smaller in the *Herwig* sample.

Sample ID	Name	Generator	σ·BR [pb]	k-factor
107650	ZeeNp0_pt20	Alpgen+Herwig,Jimmy	0.670	1.24345
107651	ZeeNp1_pt20	Alpgen+Herwig,Jimmy	0.135	1.24345
107652	ZeeNp2_pt20	Alpgen+Herwig,Jimmy	0.041	1.24345
107653	ZeeNp3_pt20	Alpgen+Herwig,Jimmy	0.011	1.24345
107654	ZeeNp4_pt20	Alpgen+Herwig,Jimmy	0.003	1.24345
107655	ZeeNp5_pt20	Alpgen+Herwig,Jimmy	0.001	1.24345
107650	ZmumuNp0_pt20	Alpgen+Herwig,Jimmy	0.670	1.24345
107651	ZmumuNp1_pt20	Alpgen+Herwig,Jimmy	0.135	1.24345
107652	ZmumuNp2_pt20	Alpgen+Herwig,Jimmy	0.041	1.24345
107653	ZmumuNp3_pt20	Alpgen+Herwig,Jimmy	0.011	1.24345
107654	ZmumuNp4_pt20	Alpgen+Herwig,Jimmy	0.003	1.24345
107655	ZmumuNp5_pt20	Alpgen+Herwig,Jimmy	0.001	1.24345
107650	ZtautauNp0_pt20	Alpgen+Herwig,Jimmy	0.670	1.24345
107651	ZtautauNp1_pt20	Alpgen+Herwig,Jimmy	0.135	1.24345
107652	ZtautauNp2_pt20	Alpgen+Herwig,Jimmy	0.041	1.24345
107653	ZtautauNp3_pt20	Alpgen+Herwig,Jimmy	0.011	1.24345
107654	ZtautauNp4_pt20	Alpgen+Herwig,Jimmy	0.003	1.24345
107655	ZtautauNp5_pt20	Alpgen+Herwig,Jimmy	0.001	1.24345

Table 6.2: List of the MC samples used to model the Z/γ^*+jets category, specifying the cross-section times branching ratio, k-factor and generators for each sample. These samples require the di-lepton invariant mass to be within the range 40 GeV$< m_{ll} <$ 2000 GeV. The Npx in the names reflects the number, x, of additional jets coming from initial or final state radiation.

Sample ID	Name	Generator	σ BR [pb]	k-factor
116250	ZeeNp0_Mll10to40_pt20	Alpgen+Herwig/Jimmy	3054.7	1.24345
116251	ZeeNp1_Mll10to40_pt20	Alpgen+Herwig/Jimmy	84.91	1.24345
116252	ZeeNp2_Mll10to40_pt20	Alpgen+Herwig/Jimmy	41.19	1.24345
116253	ZeeNp3_Mll10to40_pt20	Alpgen+Herwig/Jimmy	8.35	1.24345
116254	ZeeNp4_Mll10to40_pt20	Alpgen+Herwig/Jimmy	1.85	1.24345
116255	ZeeNp5_Mll10to40_pt20	Alpgen+Herwig/Jimmy	0.46	1.24345
116250	ZmumuNp0_Mll10to40_pt20	Alpgen+Herwig/Jimmy	3054.9	1.24345
116251	ZmumuNp1_Mll10to40_pt20	Alpgen+Herwig/Jimmy	84.78	1.24345
116252	ZmumuNp2_Mll10to40_pt20	Alpgen+Herwig/Jimmy	41.13	1.24345
116253	ZmumuNp3_Mll10to40_pt20	Alpgen+Herwig/Jimmy	8.34	1.24345
116254	ZmumuNp4_Mll10to40_pt20	Alpgen+Herwig/Jimmy	1.87	1.24345
116255	ZmumuNp5_Mll10to40_pt20	Alpgen+Herwig/Jimmy	0.46	1.24345
116250	ZtautauNp0_Mll10to40_pt20	Alpgen+Herwig/Jimmy	3054.8	1.24345
116251	ZtautauNp1_Mll10to40_pt20	Alpgen+Herwig/Jimmy	84.88	1.24345
116252	ZtautauNp2_Mll10to40_pt20	Alpgen+Herwig/Jimmy	41.28	1.24345
116253	ZtautauNp3_Mll10to40_pt20	Alpgen+Herwig/Jimmy	8.35	1.24345
116254	ZtautauNp4_Mll10to40_pt20	Alpgen+Herwig/Jimmy	1.83	1.24345
116255	ZtautauNp5_Mll10to40_pt20	Alpgen+Herwig/Jimmy	0.46	1.24345

Table 6.3: Same information as in Table 6.2 for $10 < m_{ll} < 40$ GeV.

Sample ID	Name	Generator	σ [pb]	k-factor	eff
105985	WW	Herwig	29.6	1.48	0.388
105987	WZ	Herwig	11.23	1.70	0.310
105986	ZZ	Herwig	4.60	1.35	0.212
107100	WWlnulnuNp0	Alpgen+Herwig	2.094900	1.251	1.0
107101	WWlnulnuNp1	Alpgen+Herwig	0.995880	1.251	1.0
107102	WWlnulnuNp2	Alpgen+Herwig	0.440980	1.251	1.0
107103	WWlnulnuNp3	Alpgen+Herwig	0.229160	1.251	1.0
107104	WZincllNp0	Alpgen+Herwig	0.672190	1.28	1.0
107105	WZincllNp1	Alpgen+Herwig	0.413610	1.28	1.0
107106	WZincllNp2	Alpgen+Herwig	0.218390	1.28	1.0
107107	WZincllNp3	Alpgen+Herwig	0.127950	1.28	1.0
107108	ZZincllNp0	Alpgen+Herwig	0.509590	1.3	1.0
107109	ZZincllNp1	Alpgen+Herwig	0.230700	1.3	1.0
107110	ZZincllNp2	Alpgen+Herwig	0.087417	1.3	1.0
107111	ZZincllNp3	Alpgen+Herwig	0.038714	1.3	1.0
126892	CT10_llnunu_WW	Sherpa	3.6690	1.09	1.0
126893	CT10_lllnu_WZ	Sherpa	6.2579	1.08	1.0
126894	CT10_llll_ZZ	Sherpa	4.6244	1.14	1.0
126895	CT10_llnunu_ZZ	Sherpa	0.33788	1.17	1.0

Table 6.4: List of di-boson MC samples specifying cross-section, k-factor, efficiency (from Ref. [102]) and generators used for each sample.

6.2.3 Top samples

Table 6.5 shows the various MC samples used for the $t\bar{t}$ background. The cross-section has been calculated at approximate NNLO in QCD with Hathor 1.2 [103] using the MSTW2008 90% CL NNLO Parton Distribution Function (PDF) sets [104]. These PDFs incorporate PDF+α_S uncertainties, according to the MSTW prescription [105], added in quadrature to the scale uncertainty and cross checked with the NLO+NNLL calculation of Cacciari et al. [106] as implemented in Top++ 1.0 [107]. Table 6.6 shows the samples used for the simulation of single top. The cross-sections are taken from Refs. [108, 109, 110] for the t-, s- and Wt -channel respectively. The simulated mass of the top quark is 172.5 GeV. For the single top the *MC@NLO+Herwig* samples are used for the s- and Wt-channels while the *Acer-Pythia* samples are used for the t-channel, simply because there are problems with additional unphysical jets from the Herwig shower in the *MC@NLO+Herwig* samples in this particular channel.

Sample ID	Name	Generator	$\varepsilon \cdot \sigma$ [pb]	k-factor	process
105861	T1	Powheg+Pythia	80.07	1.131	Not all had.
117941	T0	Powheg+Pythia	67.36	1.132	All had.
105860	TTbar	Powheg+Herwig	80.85	1.120	Not all had.
105204	TTbar	MC@NLO+Herwig	79.01	1.146	All had.
105200	TTbar	MC@NLO+Herwig	66.48	1.146	Not all had.
117209	TTbar morePS	AcerMC+Pythia	61.96	1.462	Not all had.
117211	TTbar morePS	AcerMC+Pythia	52.03	1.465	All had.
117210	TTbar lessPS	AcerMC+Pythia	61.65	1.469	Not all had.
117212	TTbar lessPS	AcerMC+Pythia	51.76	1.472	All had.

Table 6.5: List of MC samples used to model the $t\bar{t}$ background, specifying cross-section times efficiency, k-factor and generators for each sample. The decay of the produced W is also indicated by the *All had.* or *Not all had.*, corresponding to events were both W bosons decay hadronically and events where at most one of the W bosons decays into quarks, respectively.

6.2.4 QCD samples

The QCD MC samples are believed not to give a very good description of leptons coming from QCD-processes. The MC samples are therefore not used directly in the analysis, but rather serve as a cross-check when trying to estimate the fake lepton background using a data-driven method, as will be discussed in Chapter 7. There are several MC samples available aiming at giving the best description of leptons coming from decays of hadrons: the ones considered in this analysis are listed in Table 6.8. The uppermost samples ($105009 \leq$ Sample ID ≤ 105017) do not contain any specific filter on leptons and are therefore not very well suited for the current analysis, since the statistics becomes extremely small once leptons are required in the analysis. The remaining samples in

Sample ID	Name	Generator	$\varepsilon \cdot \sigma$ [pb]	k-factor	decay
117360	st_tc_enu	AcerMC+Pythia	8.06	0.865	$e\nu$ (t-ch.)
117361	st_tc_munu	AcerMC+Pythia	8.06	0.865	$\mu\nu$ (t-ch.)
117362	st_tc_taunu	AcerMC+Pythia	8.05	0.866	$\tau\nu$ (t-ch.)
108343	st_sc_enu	MC@NLO+Jimmy	0.47	1.064	$e\nu$ (s-ch.)
108344	st_sc_munu	MC@NLO+Jimmy	0.47	1.064	$\mu\nu$ (s-ch.)
108345	st_sc_taunu	MC@NLO+Jimmy	0.47	1.064	$\tau\nu$ (s-ch.)
108346	st_Wt	MC@NLO+Jimmy	14.59	1.079	inclusive
108340	st_sc_enu	AcerMC+Pythia	0.47	1.064	$e\nu$ (t-ch.)
108341	st_sc_munu	AcerMC+Pythia	0.47	1.064	$\mu\nu$ (t-ch.)
108342	st_sc_taunu	AcerMC+Pythia	0.47	1.064	$\tau\nu$ (t-ch.)
105500	st_Wt	AcerMC+Pythia	14.79	1.064	inclusive
117219	st_tc_enu morePS	AcerMC+Pythia	6.97	–	$e\nu$ (t-ch.)
117221	st_tc_munu morePS	AcerMC+Pythia	6.97	–	$\mu\nu$ (t-ch.)
117223	st_tc_taunu morePS	AcerMC+Pythia	6.97	–	$\tau\nu$ (t-ch.)
117220	st_tc_enu lessPS	AcerMC+Pythia	6.97	–	$e\nu$ (t-ch.)
117222	st_tc_munu lessPS	AcerMC+Pythia	6.97	–	$\mu\nu$ (t-ch.)
117224	st_tc_taunu lessPS	AcerMC+Pythia	6.97	–	$\tau\nu$ (t-ch.)
117213	st_sc_enu morePS	AcerMC+Pythia	0.5	–	$e\nu$ (s-ch.)
117215	st_sc_munu morePS	AcerMC+Pythia	0.5	–	$\mu\nu$ (s-ch.)
117217	st_sc_taunu morePS	AcerMC+Pythia	0.5	–	$\tau\nu$ (s-ch.)
117214	st_sc_enu lessPS	AcerMC+Pythia	0.5	–	$e\nu$ (s-ch.)
117216	st_sc_munu lessPS	AcerMC+Pythia	0.5	–	$\mu\nu$ (s-ch.)
117218	st_sc_taunu lessPS	AcerMC+Pythia	0.5	–	$\tau\nu$ (s-ch.)
117245	st_Wt morePS	AcerMC+Pythia	15.74	–	inclusive
117245	st_Wt lessPS	AcerMC+Pythia	15.74	–	inclusive

Table 6.6: List of MC samples used to model the single top background, specifying the cross-sections times efficiency, k-factor and generators for each sample. The k-factor is included in the ε when not specified in the table. The decay of the W in each sample is indicated in the rightmost column.

Table 6.8, however, do contain a lepton filter, either using the *MultiElectronFilter*[3] or *MultiMuonFilter*[4] for requiring electrons or muons respectively. The details about the lepton-requirements in each sample are found in the rightmost column of the Table. For the samples with a name containing JX the X refers to the simulated p_{T} range of the di-jet system in the event, summarized in Table 6.7. Such a splitting into distinct p_{T} ranges is required since the cross-section falls off drastically with increasing p_{T} . For the lepton-filtered samples not all of the J0-J8 samples exist, in these cases the last sample includes p_{T} up to the maximum value.

Name →	J0	J1	J2	J3	J4	J5	J6	J7	J8
p_{T} range [GeV]	8-17	17-35	35-70	70-140	140-280	280-560	560-1120	1120-2240	2240 →

Table 6.7: The division into p_{T} ranges for each of the Pythia JX QCD samples.

PythiaB samples Since the heavy-flavour jets are believed to constitute the largest source of fake leptons from jets, specific samples enhanced in heavy-flavour production are produced. These are the samples listed at the bottom of Table 6.8, simulated using the *PythiaB* generator [111]. The *PythiaB* framework provides an interface to *Pythia6* allowing to speed up and simplify the simulations of heavy-flavour events. In *PythiaB* one has the flexibility to turn on and off specific decay channels, apply selection cuts at several levels of the computation and define the b-production parameters. In the *PythiaB* samples only events containing b- and c-quarks are generated. The detailed cuts on the jets and leptons for the various samples are listed in Table 6.9. For the $\mu\mu$ and $e\mu$ samples the internal *PythiaB* filter can select the two final state leptons directly. In the ee-channel, however, the external *MultiElectronFilter* must be applied instead, to ensure that there are always at least two electrons in the final state. The filter-efficiency for getting di-electron final states when generated from single-electron filtered *PythiaB* generation is about 0.006.[5]. Since the PythiaB samples are filtered on b- and c-jets at the event-generator level, the fake lepton contribution from light jets, for instance K and π decays, as shown in Figure 5.16, might be underestimated.

[3] http://alxr.usatlas.bnl.gov/lxr-stb6/source/atlas/Generators/GeneratorFilters/GeneratorFilters/MultiElectronFilter.h

[4] http://alxr.usatlas.bnl.gov/lxr-stb6/source/atlas/Generators/GeneratorFilters/GeneratorFilters/MultiMuonFilter.h

[5] The job option used to make the *mu10e10X* sample can be found here: http://alxr.usatlas.bnl.gov/lxr-stb6/source/atlas/Generators/MC11JobOptions/share/MC11.105759.PythiaB_e10e10X.py

Sample ID	Name	Generator	σ [pb]	ε	comments
105009	J0	Pythia	12030000000.0	1.	
105010	J1	Pythia	807266000.0	1.	
105011	J2	Pythia	48048000.0	1.	
105012	J3	Pythia	2192900.0	1.	
105013	J4	Pythia	87701.0	1.	
105014	J5	Pythia	2350.1	1.	
105015	J6	Pythia	33.61	1.	
105016	J7	Pythia	0.13744	1.	
105017	J8	Pythia	0.000006	1.	
109276	muJ0	Pythia	9860500000.000	0.000069	
109277	muJ1	Pythia	678010000.000	0.001147	
109278	muJ2	Pythia	40965000.000	0.005351	$== 1\mu$
109279	muJ3	Pythia	2193100.000	0.012951	$p_T > 8$ GeV
109280	muJ4	Pythia	87680.000	0.022100	$\lvert\eta\rvert < 3.0$
109281	muJ5	Pythia	2348.900	0.030094	
109282	muJ6	Pythia	33.592	0.033558	
109270	elJ0	Pythia	12032000000.0	0.000074	
109271	elJ1	Pythia	806980000.0	0.001232	≥ 1 elec.
109272	elJ2	Pythia	48036000.0	0.006189	$p_T > 8$ GeV
109273	elJ3	Pythia	2535600.0	0.016974	$\lvert\eta\rvert < 3.0$
109274	elJ4	Pythia	99614.0	0.034734	
105802	JF17	Pythia	1368200000.0	0.067266	$E_T^{\text{jet}} > 17$ GeV
105807	JF35	Pythia	64446000.0	0.125170	$E_T^{\text{jet}} > 35$ GeV
108405	bbmu15X	PythiaB	84700.0	1.	
106059	ccmu15X	PythiaB	31630.0	1.	
108326	bbe15X	PythiaB	84680.0	1.	
108327	cce15X	PythiaB	30930.0	1.	see Table 6.9
105757	mu10mu10X	PythiaB	2435.0	1.	
105758	mu10e10X	PythiaB	4380.0	1.	
105759	e10e10X	PythiaB	1228.0	1.	

Table 6.8: The list of all QCD-samples studied in the current analysis. None of the samples are used in the final analysis, however, but rather as a cross-check for the data-driven procedure and results of the fake lepton estimation. The rightmost column gives the specifications on the required lepton(s) when applicable. The NLO cross-section for di-jet production is partially known, but the uncertainties from the missing higher order corrections are still large, and thus the leading order cross-section is used, with large uncertainties, for these samples. Consequently the k-factors are all set to unity and therefore omitted from the table.

Name	jets			lep1			lep2		
	fl.	p_T	$\|\eta\|$	fl.	p_T	$\|\eta\|$	fl.	p_T	$\|\eta\|$
mu10mu10X	b/c	> 15 GeV	< 4.5	μ	> 10 GeV	< 2.5	μ	> 10 GeV	< 2.5
mu10e10X	b/c	> 15 GeV	< 4.5	μ	> 10 GeV	< 2.5	e	> 10 GeV	< 2.5
e10e10X	b/c	> 15 GeV	< 4.5	e	> 10 GeV	< 2.5	e	(see text)	(see text)
bbmu15X	b	> 18 GeV	< 4.5	μ	> 15 GeV	< 2.5	-	-	-
ccmu15X	c	> 18 GeV	< 4.5	μ	> 15 GeV	< 2.5	-	-	-
bbe15X	b	> 18 GeV	< 4.5	e	> 15 GeV	< 2.5	-	-	-
cce15X	c	> 18 GeV	< 4.5	e	> 15 GeV	< 2.5	-	-	-

Table 6.9: The QCD samples enhanced in b- and c-quark production as indicated in column two. These samples are required to contain one or two leptons with various p_{T} and η cuts in addition to jets in every event.

6.3 Physics Object Definitions

With all the data and necessary MC samples in place the exact definitions of electrons, muons, jets and missing transverse energy are discussed in the following Sections. These definitions follow mostly the recommendations of the ATLAS performance groups. During the development of the analysis a specific tool, *SUSYTools* [112], was developed within the *ATLAS SUSY Group*. The tool serves as an interface to many of the code snippets, *C++* classes, bug fixes and implementations of other important input from the performance groups and thus extensively used by most of the analyses looking for SUSY within the ATLAS experiment. Throughout this analysis version *00-00-67* of *SUSYTools* is used[6], but alternative implementations by myself are cross-checked against the output from *SUSYTools*.

6.3.1 Electrons

The variables ϕ and η of an electron are computed using the track parameters if the track has more than 4 hits in the silicon detectors; if not, the cluster information is used. The transverse energy, E_T, of the electrons is defined as $E_{cluster}/cosh(\eta)$. In MC an additional smearing procedure is applied to the electron energy, while in data a corresponding scaling of the energy is performed. These procedures correct for discrepancies between electron energy scale and resolution in data and MC. The scaling is applied using the `egammaSFclass` in the package `egammaAnalysisUtils-00-02-76` is used. The electron is further required to have $E_T > 10$ GeV and $|\eta| < 2.47$ and should be reconstructed with a cluster-based algorithm (i.e. `el_author`$= 1$ or 3) [46]. In order to reject bad quality clusters or fake clusters originating from problematic regions in the calorimeter, an additional requirement is added to the electrons. This is done by checking the `egammaPID::BADCLUSTERELECTRON`

[6]Note that for the publication *Search for direct slepton and gaugino production in final states with two leptons and missing transverse momentum with the ATLAS detector in pp collisions at* $\sqrt{s} = 7$ *TeV* [12] version *00-00-63* of *SUSYTools* was used.

bit against the `el_OQ` variable available in the SUSY D3PD's[7]. This ensures that problematic cells are not used to build the electron-clusters [113]. Baseline electrons are required to satisfy the *mediumPP*[8] identification requirements. The signal electrons are in addition required to pass the *tightPP* requirements. The exact definitions of *mediumPP* and *tightPP* are summarized in Table 6.10. The signal electrons are also required to be isolated, i.e. the p_T sum of tracks above 1 GeV within a cone of size $\Delta R < 0.2$ around each electron is required to be less than 10% of the electron's momentum. All cuts defining the baseline and signal electrons are summarized in Table 6.11. In MC a multiplicative weight for each selected electron is applied to the overall MC event weight in order to correct for differences in efficiency between data and MC, stemming from both the identification efficiency and reconstruction and track-quality efficiency. The weights are determined by using the package `egammaAnalysisUtils-00-02-76`.

6.3.2 Muons

Muons are reconstructed using an algorithm which combines a track reconstructed in the Muon Spectrometer (MS) with its corresponding track in the Inner Detector (ID) [50]. In this analysis the *StacoMuonCollection* is used, as defined in Section 3.4.4. The ID track is required to have $n^{\text{hits}}_{b-layer} > 0$ unless the track passes through an un-instrumented or dead area of the *b*-layer. The track is further required to have $n^{\text{hits}}_{\text{Pixel}} > 1$, $n^{\text{hits}}_{\text{SCT}} > 5$ and $n^{\text{holes}}_{\text{Pixel+SCT}} < 3$.[9] For the Pixel and SCT any dead sensor along the track is also counted as a hit. A successful extension of the ID track into the TRT is also required. This is ensured by requiring $n^{\text{hits+outliers}}_{TRT} > 5$ and $n^{\text{outliers}}_{TRT} < 0.9 \cdot n^{\text{hits+outliers}}_{TRT}$.[10] Finally the acceptance cuts of $p_T > 10$ GeV and $|\eta| < 2.4$ are applied to both baseline and signal muons. Signal muons are required to be isolated, i.e. if the sum of p_T of all tracks in a cone of $\Delta R < 0.2$ is less than 1.8 GeV. Table 6.12 summarizes the cuts used to identify muons. In MC the muon p_T is smeared using the package `MuonMomentumCorrections-00-05-03`. This is in order to correct for differences in the scale and resolution of the muon energy in data and MC. Multiplicative event weights are also obtained for each muon in MC using the `MuonEfficiencyCorrections-01-01-03`. This should correct for the differences in the muon reconstruction efficiency observed between data and MC.

[7] Derived Physics Data (D3PD) is the format of ATLAS data and MC simulations used in the analysis. D3PDs are basically skimmed (i.e. removing of uninteresting events) and slimmed (i.e. removing of unnecessary variables) ROOT nTuples produced from the original `pool.root` format, known as ESDs (Event Summary Data) or AODs (Analysis Object Data).

[8] The PP refers to ++ which indicates that this definition of *medium* contains additional cuts compared with what was used earlier.

[9] A hole is an expected measurement, given the track trajectory, which has not been assigned to the track. This can typically stem from material interactions, inefficiencies in the the silicon or problems with the pattern recognition. Inactive modules, however, are not included in the definition of holes.

[10] An outlier is a hit not included in the final determination of the track parameters because the χ^2 contribution was too high.

Type	Description	Cut	Name
LoosePP selection			
Acceptance	η of electron	< 2.47	η
Hadronic leakage	Ratio of E_T in the first layer of the hadronic calorimeter to E_T of the EM cluster (used over the range $\lvert\eta\rvert < 0.8$ and $\lvert\eta\rvert > 1.37$)	η/p_T dep.	R_{had1}
	Ratio of E_T in the hadronic calorimeter to E_T of the EM cluster (used over the range $\lvert\eta\rvert > 0.8$ and $\lvert\eta\rvert < 1.37$)	η/p_T dep.	R_{had}
Middle layer of EM calorimeter	Ratio of the energy in 3×7 cells over the energy in 7×7 cells centered at the electron cluster position	η/p_T dep.	R_η
	Lateral width of the shower	η/p_T dep.	$w_{\eta 2}$
EM calorimeter	Ratio of the energy difference between the largest and second largest energy deposits in the cluster over the sum of these energies	η/p_T dep.	E_{ratio}
Strip layer	Total shower width	η/p_T dep.	w_{tot}
Track-quality	Number of total hits in the pixel and SCT detectors (including outliers)	≥ 7	n_{Si}
Track-cluster matching	$\Delta\eta$ between the cluster position in the strip layer and the extrapolated track	< 0.015	$\Delta\eta$
MediumPP selection (includes loosePP requirements)			
Track-quality	Number of hits in the pixel detector (including outliers)	$\lvert\eta\rvert \leq 2.01 : > 0$, $\lvert\eta\rvert > 2.01 : > 1$	n_{pixel}
	Number of hits in b-layer (including outliers)	$\lvert\eta\rvert \leq 2.01 : > 0$, $\lvert\eta\rvert > 2.01 : \geq 0$	n_{BL}
	Transverse impact parameter	$<$ 5 mm	d_0
Track-cluster matching	$\Delta\eta$ between the cluster position in the strip layer and the extrapolated track	< 0.005	$\Delta\eta$
TRT	Ratio of the number of high-threshold hits to the total number of hits in the TRT	η dep.	f_{HT}
EM calorimeter	Tighter shower shapes for $\lvert\eta\rvert > 2.01$	η dep.	-
TightPP selection (includes mediumPP requirements)			
EM calorimeter	Tighter or similar cuts on the shower shapes as used for mediumPP	η/p_T dep.	-
Track-cluster matching	$\Delta\phi$ between the cluster position in the middle layer and the extrapolated track	$\lvert\eta\rvert \leq 0.8 : [-0.03, 0.015]$, $\lvert\eta\rvert > 0.8 : [-0.04, 0.015]$	$\Delta\phi$
	Ratio of the cluster energy to the track momentum	η/p_T dep.	E/p
Track-quality	Tighter transverse impact parameter requirement	$<$ 1 mm	d_0
	Number of hits in the b-layer (including outliers)	≥ 1 (all $\lvert\eta\rvert$)	n_{BL}
Conversions	Veto electron candidates matched to reconstructed photon conversions		

Table 6.10: Definition of cuts applied defining *loosePP*, *mediumPP* and *tightPP* electron identification. Some of the cuts vary with η and/or p_T of the electrons. Further details can be found in [114, 115, 116] for loose, medium and tight, respectively.

Variable	Baseline	Signal
p_T	> 10 GeV	> 10 GeV
$\|\eta\|$	< 2.47	< 2.47
quality	$mediumPP$	$tightPP$
author	1 or 3	1 or 3
$p_T cone20/p_T$	-	< 0.1

Table 6.11: Cuts used in defining the baseline and signal electrons in the analysis.

Variable	Baseline	Signal
p_T	> 10 GeV	> 10 GeV
$\|\eta\|$	< 2.4	< 2.4
$p_T cone20$	-	< 1.8 GeV
track-quality cuts	see text	

Table 6.12: Cuts used in defining the baseline and signal muons in the analysis.

6.3.3 Jets

Jets are reconstructed using the anti-k_t jet algorithm[11] using the distance parameter $R = 0.4$ and topological clusters[12] as input. The p_T of the jets are determined at the electromagnetic scale and then calibrated to account for the non-compensating nature of the calorimeter [120]. Baseline jets are required to have $p_T > 20$ GeV and $|\eta| < 4.9$, while signal jets should have $p_T > 30$ GeV and $|\eta| < 2.5$ in addition to a cut on the jet vertex fraction, $JVF > 0.75$. The latter ensures a selection of jets insensitive to uncorrelated soft collisions occurring in events with pile-up.[13]

[11] The anti-k_t algorithm is built upon the ideas of the k_t algorithm, which in each event loops over a set of objects, initially referred to as *protojets*, and measures the distance, d_{ij}, between object i and j. The *protojets* are defined by their azimuthal angle, ϕ, pseudorapidity, η, and transverse energy, k_t. The distance is given by $d_{ij} = min(k_{ti}^2, k_{tj}^2)\Delta R_{ij}^2/R^2$, with $\Delta R_{ij} = (y_i - y_j)^2 + (\phi_i - \phi_j)^2$. A distance, $d_{iB} = k_{ti}^2$, between each object and the beam direction, B, is also measured. If the smallest of the two measured distances is d_{ij} the *protojets* i and j are combined into a new *protojet*. If the smallest distance is between the *protojet* and the beam direction, *protojet* i is defined as a jet. This procedure continues until there are no more *protojets* in the event [117]. The anti-k_t algorithm differs in the respect that it measures the distance between the *protojets* in a different way, switching the k_{ti}^2-terms with the inverse; k_{ti}^{-2}. The anti-k_t algorithm is shown to perform very well, and has therefore become the standard jet algorithm in ATLAS. [118]

[12] The topological clusters are constructed by starting with a seed cell in the calorimeter and then clustering together neighbouring cells which have a signal significantly above the expected noise. [119]

[13] JVF refers to the fraction of tracks, matched to the jet, that comes from the identified primary vertex. $JVF = 0$ indicates that none of the tracks come from the primary vertex (i.e. the jet is likely to come from pile-up collisions). If $JVF = 1$ all tracks come from the primary vertex, thus the jet is from the hard scattering. Typically a continuous distributions of JVF between 0 and 1 is expected in data. If $JVF = -1$ it means that the jet has no matched tracks or that it is reconstructed from calorimeter cells falling outside the fiducial tracking region. [121]

b-jets

To identify *b*-jets, impact parameter and vertex taggers, exploiting the long life-time of weak *b*- and *c*-hadron decays inside *b*-jets, are combined in order to achieve the best performance. The impact parameter algorithms use the measured signed transverse (d_0) and longitudinal (z_0) impact parameters of the tracks, as defined in 3.4.1. Together with the uncertainties on the impact parameter measurements themselves, σ_{d_o} and σ_{z_o}, the signed impact parameter significances, d_0/σ_{d_0}, z_0/σ_{z_0}, are constructed. These variables give more weight to tracks measured precisely.

One of the *b*-tagging algorithms, $IP3D$, uses a likelihood ratio technique where the measured signed impact parameter significances are compared to pre-defined distributions of the *b*- and light jet hypotheses obtained from MC simulations. Another type of algorithm, $SV1$, exploiting the properties of secondary vertices, is used to further increase the discrimination between *b*-jets and light jets. The algorithm tries to build vertices out of all two-track pairs inside a jet, using only tracks which are far enough from the primary vertex. After the vertices compatible with V^0 [14] and material interactions are rejected the remaining two-track vertices are combined into a single inclusive vertex, removing always the worst track until the χ^2 of the vertex fit is good. The properties of the vertex are then further investigated by measuring: i) the invariant mass of all tracks associated to it; ii) the ratio of the sum of the energies of the tracks in the vertex to the sum of all tracks in the jet; and iii) the total number of two-track vertices. These variables are then combined into the $SV1$ tagger using a likelihood ratio technique.

A fairly new and related algorithm is the *JetFitter*. The decay of *b*-hadrons involves the decay of a *b*-quark preferably producing a *c*-quark due to the electroweak interaction ($|V_{cb}|^2 \gg |V_{ub}|^2$). The typical topology of a *b*-jet seen in the detector therefore involves a decay chain with two vertices, one from each of the *b*- and *c*-decays. In the *JetFitter* algorithm one assumes that the *b*- and *c*-hadrons lie on the same line defined by the *b*-hadron flight path, identified using a Kalman filter. All tracks are then fitted under the hypothesis that each of them represents a single vertex along this line. The tracks are then clustered into a number of vertices along the *b*-hadron flight axis, all having at least one track. The discrimination between *b*-, *c*- and light jets is then based on a likelihood ratio using similar variables as for the $SV1$ tagger, in addition to the flight length significance of the vertices, which is the vertex position divided by the error of the displaced vertex [122].

In this analysis *b*-jets are defined as jets with `JetFitterCombNN` > -1.25. This *b*-tagging algorithm is a combination of the JetFitter and IP3D algorithms described above using a neural network (NN) approach. The b-tagging requirement leads to a b-tagging efficiency of 80% and a mis-identification rate for light-quark/gluon jets of less than 1%. These values were obtained using $t\bar{t}$ MC. In order to account for small discrepancies in the b-tagging performance observed in data with respect to MC, scale factors are applied to the events where *b*-jets are required (or vetoed). These scale factors are obtained using the `BTagCalib` package within `SUSYTools-00-00-67` and are obtained based on the same five complementary methods as for the 2010 data, but updated using the 2011 data. Three

[14] Generic term of heavy unstable particles decaying into pairs of charged particles, whose tracks together form a characteristic V-structure in the ID. The name V^0 was given to the first strange particles observed to decay into two particles ($K^0 \to \pi^+\pi^-$ and $\Lambda^0 \to p\pi^-$).

of these methods use $t\bar{t}$ events while two use a sample of jets containing muons [123].

Table 6.13 summarizes the identification of baseline and signal jets (and b-jets) used in the analysis.

Variable	Baseline	Signal
p_T	> 20 GeV	> 30 GeV
$\|\eta\|$	< 4.9	< 2.5
JVF	-	> 0.75
b-jets (in addition to jet-requirements)		
`JetFitterCombNN`	> -1.25	> -1.25

Table 6.13: Cuts used in defining the baseline and signal jets in the analysis.

6.3.4 Missing Transverse Energy

The missing transverse energy, $E_{\mathrm{T}}^{\mathrm{miss}}$, is an important variable in searches for RPV SUSY. It is reconstructed based on the *Simplified20_RefFinal* algorithm and includes contributions from energy deposits in the calorimeters and muons reconstructed in the Muon Spectrometer. Any muon reconstructed from an ID track (i.e. *Segment tagged* muons, see Section 3.4.4) is also used in the $E_{\mathrm{T}}^{\mathrm{miss}}$ calculation in order to cover muons not reconstructed by the MS. The calorimeter cells used are calibrated to their associated physics object in the order: electrons, photons, hadronic taus, jets (with $p_{\mathrm{T}} > 20$ GeV) and muons. To account for soft jets, with $p_{\mathrm{T}} < 20$ GeV, cells in clusters associated to jets with 7 GeV$< p_{\mathrm{T}} <$ 20 GeV are added. Cells not associated to any object are taken into account in the $E_T^{\mathrm{miss,CellOut}}$ term. The transverse momenta of tracks, with $p_{\mathrm{T}} > 400$ MeV and passing the track-quality criteria such as number of hits and χ^2 of the track fit, which do not reach or seed any cluster in the calorimeter are added to $E_T^{\mathrm{miss,CellOut}}$ [124]. The term from the soft jets with $p_{\mathrm{T}} < 20$ GeV together with the $E_T^{\mathrm{miss,CellOut}}$ form what is known as the *soft terms* in the $E_{\mathrm{T}}^{\mathrm{miss}}$ calculation.

In the end the $E_{\mathrm{T}}^{\mathrm{miss}}$ is equal to the modulus of the vector sum of the transverse energy/momentum of the above-mentioned components. The $E_{\mathrm{T}}^{\mathrm{miss}}$ is calculated separately in the central, end-cap and forward regions of the detector. After summing up these contributions the $E_{\mathrm{T}}^{\mathrm{miss}}$ is corrected for muons passing the baseline selection in Table 6.12, by subtracting their p_{T}. In the following analysis a slightly different version of the missing transverse energy is used, known as the *relative missing transverse energy*, $E_{\mathrm{T}}^{\mathrm{miss,rel}}$,

$$E_{\mathrm{T}}^{\mathrm{miss,rel}} = \begin{cases} E_{\mathrm{T}}^{\mathrm{miss}} & \text{if } \Delta\phi_{E_{\mathrm{T}}^{\mathrm{miss}},(\ell,j)} \geq \pi/2 \\ E_{\mathrm{T}}^{\mathrm{miss}} \times \sin \Delta\phi_{E_{\mathrm{T}}^{\mathrm{miss}},(\ell,j)} & \text{if } \Delta\phi_{E_{\mathrm{T}}^{\mathrm{miss}},(\ell,j)} < \pi/2 \end{cases}, \tag{6.1}$$

where $\Delta\phi_{\ell,j}$ is the azimuthal angle between the direction of $\vec{E}_{\mathrm{T}}^{\mathrm{miss}}$ and that of the nearest signal jet or lepton. This means that in an event where the momentum of the nearest jet or lepton is badly reconstructed, such that it is aligned with the direction of $\vec{E}_{\mathrm{T}}^{\mathrm{miss}}$, only the

$E_{\mathrm{T}}^{\mathrm{miss}}$ component perpendicular to that object is considered. This might worsen the $E_{\mathrm{T}}^{\mathrm{miss}}$ resolution in events with only real $E_{\mathrm{T}}^{\mathrm{miss}}$, but it reduces significantly the instrumental $E_{\mathrm{T}}^{\mathrm{miss}}$ in processes such as $Z/\gamma^* \to ee, \mu\mu$. The use of $E_{\mathrm{T}}^{\mathrm{miss,rel}}$ was first introduced in Ref. [125] in order to reduce the false $E_{\mathrm{T}}^{\mathrm{miss}}$ contribution arising from mis-measurements of the jet and lepton energies. It also reduces the real $E_{\mathrm{T}}^{\mathrm{miss}}$ contribution in $Z \to \tau\tau$ event (i.e. from neutrinos), since the neutrino from a semi-leptonic τ-decay is parallel to the momenta of the lepton.

The $E_{\mathrm{T}}^{\mathrm{miss}}$ is computed with the `MissingETUtility-01-00-06` package. This package provides methods for incorporating the rescaled and/or smeared p_T of the objects into the $E_{\mathrm{T}}^{\mathrm{miss}}$ calculation, as well as methods for propagating the systematic uncertainties on these corrections through the calculation.

6.3.5 Event Criteria

In addition to the requirement of good runs list (GRL) provided by the SUSY group, as already discussed in Section 6.1, events are checked for noise. Events with noise bursts and/or data integrity errors in the LAr Calorimeters are rejected. This is checked by requiring the *larError* variable in the D3PD's to be different from zero.

In order to avoid that the same object is included several times in the baseline selection, a set of overlap removals between the baseline objects are applied in the following order:

1. if $\Delta R(e_1, e_2) < 0.1$: remove the electron with the smallest E_T^{cluster}
2. if $\Delta R(jet, e) < 0.2$: remove the jet
3. if $\Delta R(jet, e) < 0.4$: remove the electron
4. if $\Delta R(jet, \mu) < 0.4$: remove the muon
5. if $\Delta R(e, \mu) < 0.1$: remove both the muon and the electron

The event is further required not to contain any jets with $p_T > 20$ GeV failing the jet quality criteria *Loose*. This cut protects against fake jets reconstructed from noise in the calorimeter electronics and jets not stemming from the proton-proton collision but rather from cosmic rays or beam-induced backgrounds [126].

In order to remove events where the muon is likely to come from cosmic rays the transverse and longitudinal impact parameters with respect to the primary vertex for each baseline muon in the event are checked. This is done after the overlap removal in order to not include muons from heavy-flavour decays. If the muon has $|z_0| > 1$ mm and $|d_0| > 0.2$ mm it is tagged as a cosmic muon and the event is rejected. A rejection of events containing *bad* muons, defined as a baseline muon before overlap removal which has $\sigma(q/p)/|q/p| > 0.04$, where $\sigma(q/p)$ is the uncertainty on the q/p measurement, is applied.

The event is rejected if the primary vertex does not have at least 5 tracks or if the invariant mass of the two baseline leptons is less than 20 GeV.

The events left after applying all of the above-mentioned criteria and requiring exactly two baseline leptons is referred to as the **baseline selection**.

6.3.6 Pile-up re-Weighting

The MC samples used in the analyses are usually produced before all the data is collected and it is therefore difficult to foresee the average number of interactions per bunch crossing, $\langle\mu\rangle$, present in the data. The MC is generated with some specific pile-up conditions, but the distribution of $\langle\mu\rangle$ might differ significantly from the one in data. Luckily the range of $\langle\mu\rangle$ in data and simulation is in most cases quite similar, which means that the distribution in MC only needs to be re-weighted. The weights, wgt_i^{pu}, are calculated for every event in MC having a particular value of $\langle\mu\rangle = x$ in MC period p (indicated by the run number as discussed in Section 6.2), by

$$wgt_i^{pu}(x,p) = \frac{\mathscr{L}_i(x,p)}{\mathscr{L}} \frac{N}{N_i(x,p)}. \tag{6.2}$$

The integrated luminosity of events having $\langle\mu\rangle = x$ in the data period corresponding to p is denoted $\mathscr{L}_i$ while $\mathscr{L}$ is the total integrated luminosity in the complete dataset. The number of events in MC having $\langle\mu\rangle = x$ in period p is N_i and N is the total number of events in the MC sample. In a few cases the $\langle\mu\rangle$ in data is particularly low or particularly high and might lie just out of reach of the MC $\langle\mu\rangle$-distribution (i.e. there are zero events with this number of $\langle\mu\rangle$ in the available MC, and a weight can not be found). This is however found to happen for only a tiny fraction, $\sim 0.018\%$, of the events in this analysis and are therefore still kept. The part of the total luminosity in data with values of $\langle\mu\rangle$ not found in the MC sample causes the sum of the weights over all $\langle\mu\rangle$ and periods present in the MC samples, to not sum to unity. This means that the number of events in MC (with only generator weights applied) will be different compared to the number of events after the pile-up re-weighting is done. This is taken into account when scaling the MC to the correct luminosity.

All the events are re-weighted on an event-by-event basis using the `PileUpReweighting-00-02-05` package with the option `SetUnrepresentedDataAction(2)` to still keep events in data with a $\langle\mu\rangle$ outside the MC range. In this analysis the $\langle\mu\rangle$ distribution used to obtain the event weight is taken from the *egamma* stream, but since the luminosity blocks used in the *egamma* and *muons* stream are identical, the same weights can be applied to both streams.

6.3.7 Real and Fake Leptons in MC

In MC the information about the true origin of any lepton is available through the `MCTruthClassifierTool` [74]. This tool groups leptons into 23 different categories according to their true origin. This is extremely handy when for instance studying possible differences between the various sources of fake leptons (i.e. leptons from conversion processes or decay of light- and heavy-flavoured hadrons). These categories can in most cases be easily identified using the `origin` variable, estimated with the `MCTruthClassifierTool`, and available in all D3PDs. Throughout this analysis the grouping of leptons will follow the scheme outlined in Table 6.14, in accordance with what was discussed in Section 5.4. Real leptons are identified as those coming from W, Z and τ decays. A separate *top* origin is however also found in the real category, but these are nothing else than leptons

code	origin	category
5	conversions	conversions
9	τ	Real
10	top	
12	W boson	
13	Z boson	
25	c-meson	Heavy
26	b-meson	
27	$c\bar{c}$-meson	
28	J/ψ	
29	$b\bar{b}$-meson	
32	c-baryon	
33	b-baryon	
23	light-meson	Light
24	s-meson	
30	light-baryon	
31	s-baryon	
34	π	
35	K	
0	not-matched	undefined
6	Dalitz decays	Other
7	el.mag. processes	
11	quark weak decay	
...	the rest	

Table 6.14: The classification of fake and real leptons with the *origin* variable from the `MCTruthClassifierTool`.

from the decay of a W originating from the decay of a top quark. All hadrons containing b and c quarks are classified as heavy while the remaining hadrons are classified as *light*. A small part of the leptons come from other processes, grouped in the *other* category in Table 6.14. The last category is *undefined*, which contains leptons where the origin information is absent. Figure 6.2 shows the origin of electrons (a) and muons (b), removing those categorized as real, in all events after the baseline selection. For electrons the fraction categorized as *undefined* is $\sim 8\%$ while the *other* category makes up $\sim 3\%$, dominated by Dalitz decays. Most electrons, i.e. $\sim 89\%$, seem to stem from heavy-flavoured hadrons (i.e. b- and c-jets) and conversions. Electrons from light-flavoured jets constitutes only 0.1%. For muons the heavy-flavoured part is totally dominating, making up $\sim 99.4\%$ of the total amount of fake muons. The remaining categories are all less than 0.5%. The MC samples used to model the QCD component are the electron and muon filtered PythiaB samples, *e10e10X* and *mu10mu10X* respectively, defined in Table 6.9. Since the PythiaB samples are enhanced in b- and c-jet production, the light-flavoured component might be somewhat underestimated, which will be further discussed in the following chapters.

For muons the *undefined* category can safely be neglected, while for electrons it might be useful to study it a bit closer. By using the available MC truth information one can identify the mother of the electrons, by looping backwards to the initial proton through all the decay vertices which lead to the final state electron. Figure 6.3 shows the `pdgID` [24] of the mother of all the electrons classified as *undefined* in Figure 6.2. In many cases the `pdgID` of the mother is 91 or 92, which are IDs used by specific MC generators when simulating the hadronization processes, and thus are not physical particles. In these cases the mother of the electron is defined as the particle stemming from the vertex in the previous step, prior to the vertex containing the particle with `pdgID` 91 or 92. Doing this the mother often, $\sim$ 10-15%, ends up being either a down (`pdgID` = 1) or up (`pdgID` = 2) quark, which might indicate that these electrons come from some initial state radiation

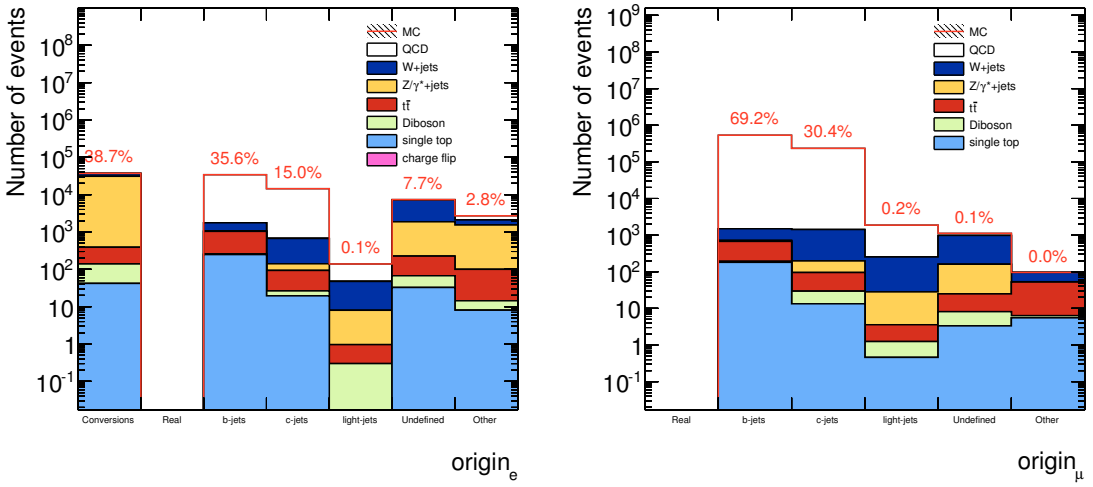

(a) Electrons (b) Muons

Figure 6.2: The origin of non-real (i.e. not in the *real* category in Table 6.14) electrons (a) and muons (b) in all di-lepton events after the baseline selection. The distributions are normalized to 4.71 fb^{-1}.

process of the initial partons. Otherwise the mother is distributed mainly among $\rho(770)^0$

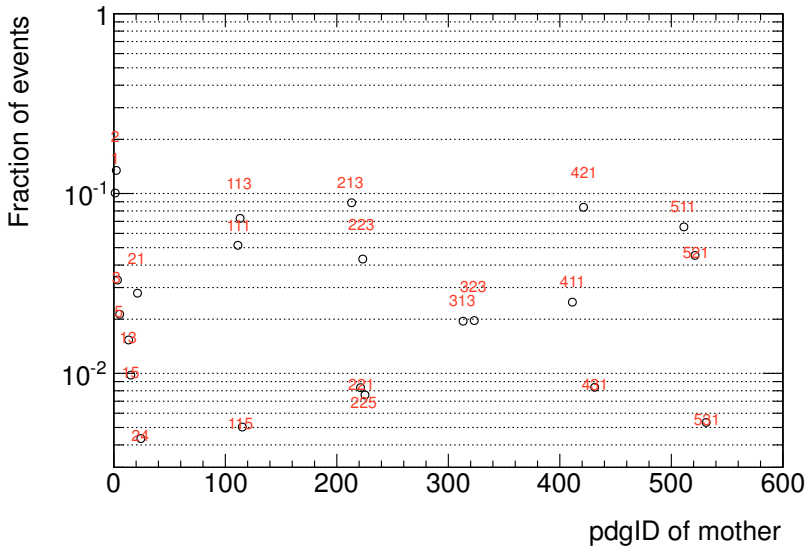

Figure 6.3: The `pdgID` (also written in red text) of the mother of the *undefined* electrons.

(ID = 113), π^0 (`pdgID` = 111), $\rho(770)^+$ (`pdgID` = 213), D^0 (`pdgID` = 421) and B^0 (`pdgID` = 511) all constituting 5-10% of the total amount of *undefined* electrons. The $\rho(770)^0$ and D^0 might both decay into electrons. The π^0 might also decay into electrons through Dalitz decays, but since this is a separate category in the *origin* variable these are probably pi-zeros faking electrons. This might be the case with $\rho(770)^+$ as well, which does not have any possibilities of decaying into leptons. Since the *undefined* category seems to be a conglomerate of different sources of electrons they are kept separated from the other categories in the further analysis; they are however included in the umbrella word *fake* which also contains leptons in the heavy, light and conversion categories (i.e. everything

Period	Single		Double	
	Trigger	Offline p_T threshold	Trigger	Offline p_T threshold
	Electron			
A-J	`e20_medium`	25 GeV	`2e12_medium`	17 GeV
K	`e22_medium`	25 GeV	`2e12T_medium`	17 GeV
L-M	`e22vh_medium1`	25 GeV	`2e12Tvh_medium`	17 GeV
	Muon			
A-I	`mu_18`	20 GeV	`2mu10_loose`	12 GeV
J-M	`mu_18_medium`	20 GeV	`2mu10_loose`	12 GeV
	Electron-Muon			
A-M	-	-	`e10_medium_mu6`	15 GeV (e)/8 GeV (μ)

Table 6.15: The triggers used in the analysis for the different channels and data periods. The corresponding offline cut on the lepton p_T for each trigger is indicated.

except the *real* and *other* categories).

6.4 Triggers

Different triggers, summarized in Table 6.15, are used in order to optimize the efficiency for different p_T ranges and for the various data periods and channels. Events in the ee- and $\mu\mu$-channels use combinations of the single- and di-lepton triggers. Events in the $e\mu$-channel are triggered either by the single-electron or single-muon triggers or by the electron-muon trigger, `e10_medium_mu6`. The triggers used are the lowest un-prescaled triggers available in each period.

6.4.1 Trigger Efficiencies

The goal is to maximize the efficiency in the parameter space defined by the transverse momenta of the two leptons in the event. This can be achieved by OR-ing the various triggers in Table 6.15. In order to do this, conditional probabilities of single- and di-lepton triggers need to be calculated. This becomes rather challenging when all possible combinations of the triggers are included. Instead, the most efficient trigger is used in disjoint regions of parameter space as illustrated in Figure 6.4. One exception is for the $\mu\mu$-channel, where the single-muon trigger only reaches an efficiency of about 80%. The gain in OR-ing the single-muon trigger with the di-muon trigger is therefore too large to be dropped.

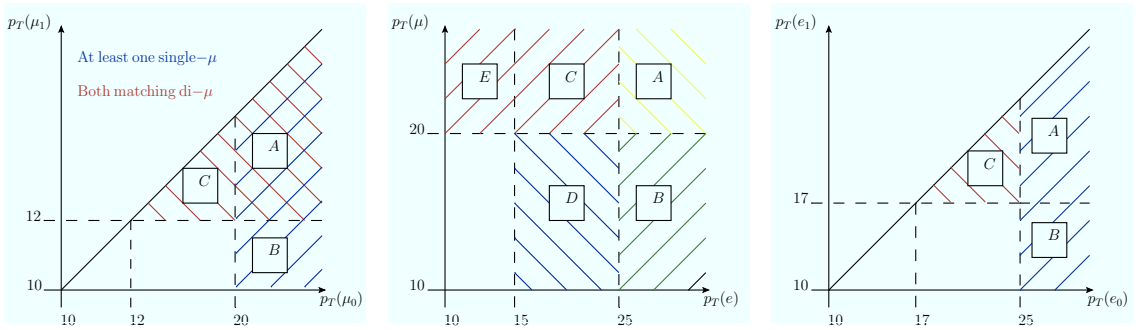

(a) $\mu\mu$ (b) $e\mu$ (c) ee

Figure 6.4: The different triggers used in the various parts of the parameter space defined by the transverse momentum of the two leptons.

6.4.1.1 Di-Muon Channel

Two different types of muon trigger efficiencies are measured. They are called absolute and conditional efficiencies and are defined as

$$\varepsilon_{\text{absolute}} = \frac{n^{\mu}_{\text{off,trig}}}{n^{\mu}_{\text{off}}} \tag{6.3}$$

$$\varepsilon_{\text{conditional}} = \frac{n^{\mu}_{\text{off,trig A!B}}}{n^{\mu}_{\text{off,trig !B}}}, \tag{6.4}$$

where $n^{\mu}_{\text{off,trig}}$ is the number of offline muons matched to a trigger-object associated with the appropriate data period trigger and n^{μ}_{off} is the total number of offline muons. Further, $n^{\mu}_{\text{off,trig A!B}}$ is the number of muons matched with a trigger-object associated to trigger A but not with any trigger-object associated with trigger B. Accordingly $n^{\mu}_{\text{off,trig !B}}$ is number of offline muons not matched to any muon trigger-object associated to trigger B. The absolute efficiencies are calculated for the single-muon triggers, while the conditional efficiencies are calculated for the di-muon and electron-muon triggers, using `2mu10_loose` and `mu6` respectively as trigger A in Eq. 6.4.

The efficiencies are measured in data using the tag-and-probe method requiring events with a Z-decay containing at least two OS muons passing the baseline selection in Table 6.12 (except the p_T cut) and satisfying $|m_{\mu\mu} - m_Z| < 10$ GeV were used to measure the efficiency. The events are taken from the data period of interest selected from the *Muons* stream and required to have passed the corresponding single-muon triggers in Table 6.15. One of the two muons is required to match one of the muon trigger-objects associated with the the trigger of interest. An offline muon is matched with a muon trigger-object if ΔR between at most one trigger-object and the offline muon is < 0.15 and there are no other offline leptons within $\Delta R < 0.15$ of this trigger-object. The tag muon is defined as the muon matching the trigger-object. The other muon in the event is used as the probe. Each event is processed twice since both muons might pass the criteria to be the tag muon. The absolute trigger efficiencies are determined by checking for a trigger match on the probe muon. The conditional efficiencies are also measured using the probe muons. Figure 6.5a shows the efficiency for the `mu18_medium` trigger illustrating the steep increase (i.e. turn-on) of the efficiency around the p_{T} threshold of 20 GeV.

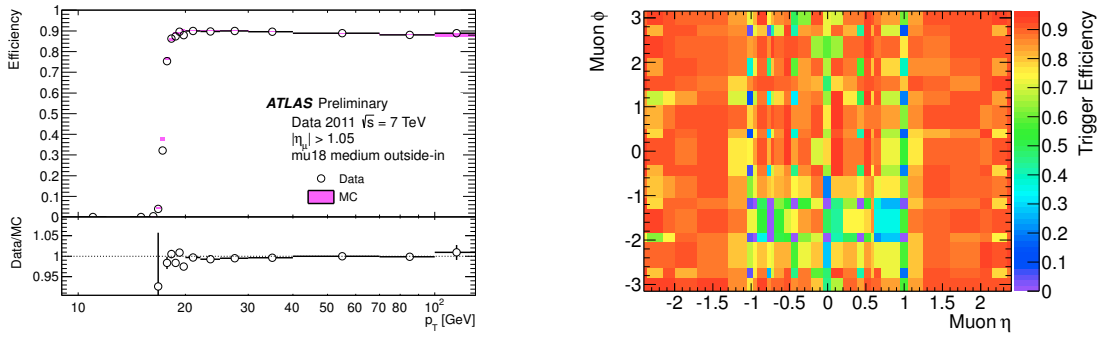

(a) Ref. [127] (b) Ref. [76]

Figure 6.5: The left plot shows the efficiency of the `mu18_medium` as a function of the offline muon p_{T}. The right plot shows the trigger efficiencies for muons with $p_{\mathrm{T}} > 20$ GeV as a function of η and ϕ for the same trigger.

Since only muons from Z-decays, which are expected to mostly have high p_{T}, are used in the tag and probe method this might lead to a significant bias of the trigger efficiencies towards higher p_{T}. In order to avoid this, only muons with a momentum of > 2 GeV above the threshold are considered in the matching procedure. Muons with a smaller p_T are given an efficiency of 0. The trigger efficiencies are determined as a function of the muon p_T, η and ϕ simultaneously in order to minimize a bias from the fact that only muons from Z-decays are used in the tag and probe method, which do not necessarily match completely the kinematics of any other sample. Since in each event the offline muon either passes or fails the trigger we can construct a probability density function from the binomial distribution

$$p(\varepsilon) = \binom{n_{\mathrm{off}}}{n_{\mathrm{off,trig}}} \varepsilon^{n_{\mathrm{off,trig}}} (1-\varepsilon)^{n_{\mathrm{off}} - n_{\mathrm{off,trig}}}. \tag{6.5}$$

The efficiency is then taken as the ε which maximizes this function. The uncertainty is calculated using the smallest interval which covers 68%. In case of enough statistics and efficiencies sufficiently different from 0 and 1, a Gaussian approximation can be used to get the uncertainties, $\Delta\varepsilon$, found to be 1.2% for the single- and di-muon triggers.

In order to gain sensitivity an OR-ing of the single- and di-muon triggers are used in events where the leading muon has $p_T^{\mu} > 20$ GeV (region A in Figure 6.4a), thus requiring the calculation of the conditional single- to di-muon trigger probability according to Eq. 6.4. Eventually, this brings the trigger efficiency in region A from about 80% to more than 90%. If both muons have $p_T < 20$ GeV the di-muon trigger is used alone (region C). Finally, if the leading muon has $p_T > 20$ GeV and the other muon $p_T < 12$ GeV (region B) only the single-muon trigger is used.

The trigger efficiencies for muons above the trigger thresholds depend on both η and ϕ. In the barrel the efficiencies reach a maximum of about 90% while in the end-caps they are somewhat lower, reaching a maximum of $\sim 70\%$. The trigger efficiency as a function of η and ϕ found for the `mu18_medium` trigger for muons with $p_{\mathrm{T}} > 20$ GeV are shown in Figure 6.5b.

6.4.1.2 Electron-Muon Channel

The different triggers used in the $e\mu$-channel are shown in Figure 6.4b. When $p_T^e > 25$ GeV and/or $p_T^\mu > 20$ GeV the single-electron and/or single-muon triggers are used (regions A,B,C and E). When $p_T^e < 25$ GeV and $p_T^\mu < 20$ GeV (region A) the electron-muon trigger is used. To determine the efficiencies of the $e\mu$ trigger, the conditional efficiency in Eq. 6.4 is used.

6.4.1.3 Di-Electron Channel

The various triggers used in the different p_{T} ranges in the electron channel is shown in Figure 6.4c. To determine the trigger efficiencies and corresponding uncertainties for these triggers the tag-and-probe method is used, requiring at least one pair of OS electrons passing the signal electron cuts in Table 6.11 and having an invariant mass of 10 GeV within the Z peak. The tag electron is required to be within $\Delta R < 0.02$ of one of the electron trigger-objects associated to the lowest available un-prescaled trigger. The probe electron is then matched to the electron trigger-object from the trigger of interest using the same $\Delta R < 0.02$ requirement. The efficiencies are measured in bins of $|\eta|$[15], and for each $|\eta|$-bin the efficiency is calculated as a function of p_T. In the range with $p_T > 60$ GeV statistics is limited and the results are therefore extrapolated to higher values from the efficiencies found within the range $30 < p_T < 60$ GeV. The trigger efficiencies for electrons with p_{T} above the trigger threshold reach a maximum of $> 95\%$ in all $|\eta|$-bins except for $|\eta| > 2.37$, where the maximum is found to be $\sim 90\%$. The efficiencies calculated for electrons passing the *tightPP* and *mediumPP* identification criteria are also found to agree very well and any observed deviation is incorporated in the systematic uncertainties. Figure 6.6 depicts the trigger efficiencies as a function of p_{T} for the `e12_medium` trigger when either *tightPP* (blue triangles) or *mediumPP* (red squares) electrons are used as the tag.

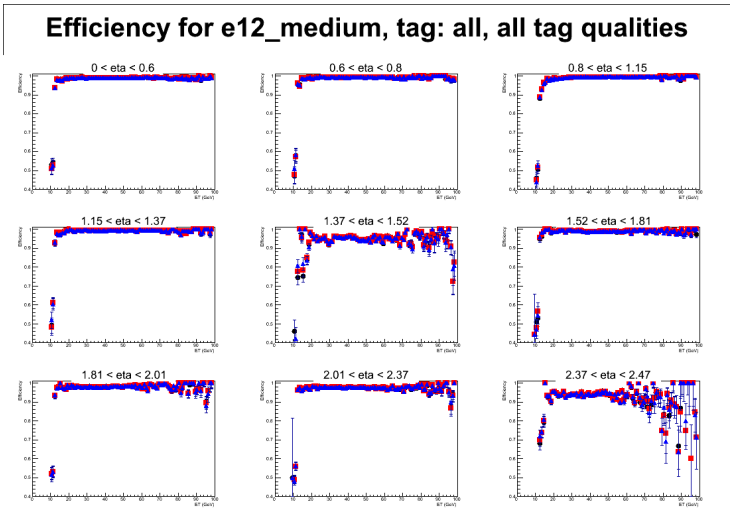

Figure 6.6: The trigger efficiencies for the `e12_medium` trigger as functions of p_{T} in various η bins. The red squares show the efficiencies when the tag is required to pass *mediumPP* and the blue triangles when the tag is required to pass *tightPP* identification criteria.

Several other sources of systematic uncertainties are investigated: changing the trigger used for the tag electron, varying the mass window (m_{ee} from ± 8 to ± 14 GeV of the Z-

[15] $[0, 0.6]$, $\langle 0.6, 0.8]$, $\langle 0.8, 1.15]$, $\langle 1.15, 1.37]$, $\langle 1.37, 1.52]$, $\langle 1.52, 1.81]$, $\langle 1.81, 2.01]$, $\langle 2.01, 2.37]$, $\langle 1.37, 2.47]$

peak), dependence on pile-up, changing the ΔR cut to 0.015, changing the algorithms for obtaining the p_T and η, using either the values directly from the D3PDs or the ones described in Section 6.3.1. The effect of changing the size of the background sidebands was also studied. The sidebands are the regions on either side of the Z-peak, expected to be highly contaminated by background, and can therefore be used to estimate the expected background within the signal region. The effect on the measured efficiencies was studied using sidebands of both 8 and 15 GeV. The variation of the efficiencies on the run period was also investigated. The systematic uncertainty is found to be quite similar amongst all the triggers in Table 6.15 and is set to 1% for $|\eta| < 1.5$ and 1.5% for $|\eta| > 1.5$ [76].

6.4.2 Trigger re-Weighting

To account for the limited acceptance of the triggers in MC, the events are weighted using trigger weights derived from the data-driven efficiencies. Unlike in data, the events in MC are therefore not required to pass any trigger. The weights correspond instead to the probability that a signal or baseline lepton passed one of the triggers. Weights for all combinations of single- and di-lepton triggers need to be calculated. The probability for an event, with a certain number of leptons, $n_{\text{lep}} = n_{el} + n_{\mu}$, and where the trigger efficiency for the i^{th} lepton is measured to be ε_i, to pass the single-lepton trigger, $1L$, is given by

$$p(1L) = 1 - \prod_{m=1}^{n_{\mu}} (1 - \varepsilon_m^{\mu}) \prod_{e=1}^{n_{el}} (1 - \varepsilon_e^{el}). \tag{6.6}$$

Correspondingly, the probability for an event to pass the di-lepton trigger, $2L$, is

$$p(2L) = 1 - \prod_{k=1}^{n_{\text{lep}}} (1 - \varepsilon_k^{\text{lep}}) \sum_{k=1}^{n_{\text{lep}}} \varepsilon_k^{\text{lep}} \prod_{j=1, j\neq k}^{n_{\text{lep}}} (1 - \varepsilon_j^{\text{lep}}), \tag{6.7}$$

given that the efficiency of a di-lepton trigger can be modelled as the product of the efficiencies of a single-lepton trigger with the same threshold. This is found to be a good approximation in all channels [76].

The trigger efficiencies, uncertainties and weights are all implemented using the `DGTrigger Reweight-00-00-11` package [128] which in turn uses the `ReweightUtils-00-02-06` package [129]. The division of the events in the MC samples into different parts, to reflect the various run periods in data, as discussed in Section 6.2, is again used to define the set of triggers in Table 6.15 to use in the re-weighting procedure. The p_{T} of the two leptons define further, according to Figure 6.4 and the discussion in Section 6.4.1, if the weights should be retrieved from the single- or di-lepton triggers. First the efficiencies are calculated by retrieving two histograms, depending on the p_{T} , η and ϕ of the two leptons, one for the numerator and one for the denominator in Eq. 6.3 and 6.4. These efficiencies are then used in Eq. 6.6 or 6.7 to calculate the final event weight. In order to avoid the turn-on region for the triggers, all leptons are required to have a p_{T} above the threshold, given in Table 6.15, for the trigger in use.

6.4.3 Trigger Matching

In the analysis only signal and baseline leptons are added to the selection of events for which a trigger weight is calculated. There might be leptons, not passing the baseline cuts, but having fired one of the triggers. This would lead to MC weights that are smaller than the absolute probability of an event to be selected by the trigger. This is, however, compensated by applying a trigger matching in data. A match, similar to the one used in Section 6.4.1, between at least one (two) of the leptons in the event associated to the single-lepton (di-lepton) trigger is required. The leptons are again required to have a p_{T} above the threshold in Table 6.15. If none of the leptons have a trigger match the event is rejected.

6.5 Concluding Remarks

In Chapter 5 the measured cross-sections at the LHC for the relevant SM processes, expected to constitute the main backgrounds to di-lepton SUSY searches, were discussed. Some of the SM processes with the highest real lepton production rates (i.e. W+jets, Z/γ^*+jets, di-boson and top), have cross-sections between 10 and 10^5 pb. The cross-sections of the SUSY models that were discussed in Section 5.3, on the other hand, vary typically from very small values to $\sim$ 1-3 pb. A study of appropriate methods and cuts to use in order to efficiently reject the backgrounds culminated into a set of four different signal regions. In the current chapter the samples used to model the SM backgrounds, how to identify the physics objects and all the other ingredients needed to develop a robust analysis were studied. Having this in place the expected reduction of the SM backgrounds, obtained after applying the baseline selection, discussed above, can be deduced. The distribution in Figure 6.7a shows the cross-section times acceptance as a function of $E_{\mathrm{T}}^{\mathrm{miss,rel}}$ for the SM backgrounds requiring the baseline selection and two electrons of any sign. By applying an additional $E_{\mathrm{T}}^{\mathrm{miss,rel}}$ cut of for example > 80 GeV the SM backgrounds are reduced to less than 1 pb, with $t\bar{t}$ being the dominant, and are of the same order as what is expected for some SUSY scenarios, as depicted in Figure 6.7b.

There is, however, one important background component left to discuss, namely the possible backgrounds stemming from QCD processes, which are produced at an enormously high rate ($> 10^8$ pb!) at the LHC, and which are not properly modelled in the MC. Chapter 7 is devoted to the study of the backgrounds from QCD processes, before moving to the final part of the analysis in Chapter 8.

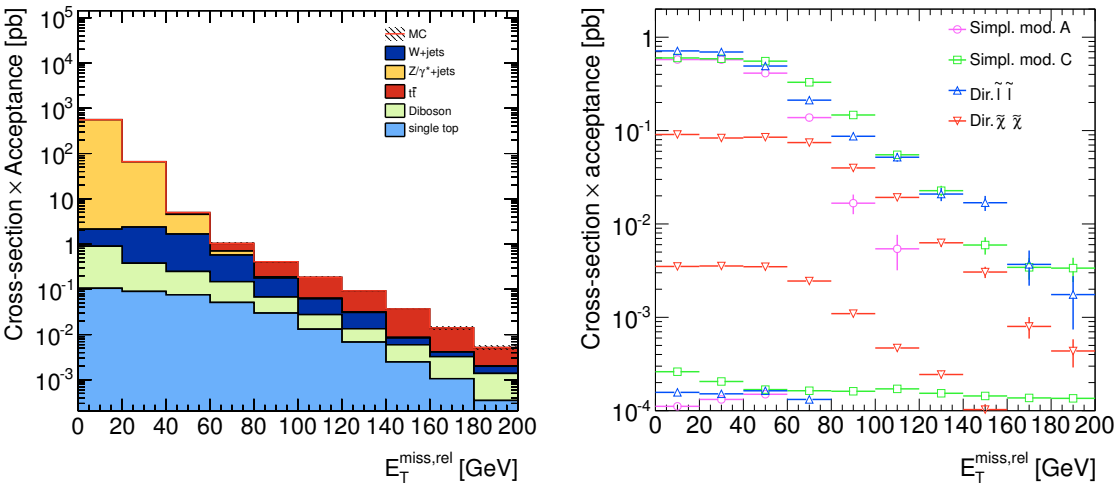

Figure 6.7: The cross-section times acceptance as a function of $E_{\mathrm{T}}^{\mathrm{miss,rel}}$ for the SM backgrounds (a) and SUSY signals (b), after applying the baseline selection with two electrons. For each SUSY signal model the scenarios with the highest and lowest cross-sections times acceptance are shown.

Chapter 7

Matrix Method

The main method used to estimate the contribution of fake leptons from QCD and conversion processes is known as the *Matrix Method* (MM) [130]. The MM uses two sets of lepton identification criteria, the standard set used in the final analysis (called *tight*) and a looser one (called *loose*), where some of the standard lepton criteria are removed or relaxed. The exact discriminating cuts used typically depend on the exact lepton definitions and on the kind of study performed.

Let T denote leptons passing the tight identification criteria and L leptons that at least pass the loose criteria, named *inclusive loose*. Leptons passing loose but **not** tight are called *exclusive loose*, denoted l. Figure 7.1 illustrates the classification of leptons used in the MM. All the observed events containing two inclusive loose leptons are counted,

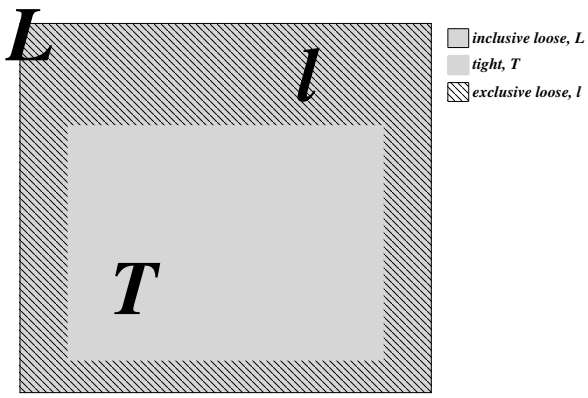

Figure 7.1: A schematic view of the lepton categorization used in the MM. L denotes all leptons that pass the loose criteria, T all leptons passing both loose and tight and l leptons passing loose but **not** tight.

ordered in p_{T}, and classified into four different categories, N_{TT}, N_{Tl}, N_{lT} and N_{ll}, where the first letter indicates the lepton with the highest p_{T}. In addition two probabilities, r and f, are defined: r is the probability that a real lepton passing the loose identification criteria also passes the tight and f the corresponding probability for a fake lepton that passes loose to also pass tight. If the event contains two leptons of opposite flavour ($e\mu$ or μe) four probabilities are needed, since the electron and muon probabilities are in general different. Using p_{T} or η dependent efficiencies demands also four different efficiencies since the two leptons often have different values of p_{T} and η and thus different efficiencies. The probabilities are therefore r_1, r_2, f_1 and f_2 where the subscripts, 1 and 2, indicate the hardest and second hardest lepton respectively. From these inputs the number of events

with two real (N_{LL}^{RR}), one real and one fake (N_{LL}^{RF} and N_{LL}^{FR}) and two fake (N_{LL}^{FF}) leptons can be estimated by inverting the following matrix

$$\begin{bmatrix} N_{TT} \\ N_{Tl} \\ N_{lT} \\ N_{ll} \end{bmatrix} = \begin{bmatrix} r_1 r_2 & r_1 f_2 & f_1 r_2 & f_1 f_2 \\ r_1(1-r_2) & r_1(1-f_2) & f_1(1-r_2) & f_1(1-f_2) \\ (1-r_1)r_2 & (1-r_1)f_2 & (1-f_1)r_2 & (1-f_1)f_2 \\ (1-r_1)(1-r_2) & (1-r_1)(1-f_2) & (1-f_1)(1-r_2) & (1-f_1)(1-f_2) \end{bmatrix} \begin{bmatrix} N_{LL}^{RR} \\ N_{LL}^{RF} \\ N_{LL}^{FR} \\ N_{LL}^{FF} \end{bmatrix}, \quad (7.1)$$

obtaining

$$N_{LL}^{RR} = (1-f_1)(1-f_2)N_{TT} - [f_2(1-f_1)]\,N_{Tl} - [f_1(1-f_2)]\,N_{lT} + f_1 f_2 N_{ll} \quad (7.2)$$
$$N_{LL}^{RF} = -(1-f_1)(1-r_2)N_{TT} + [r_2(1-f_1)]\,N_{Tl} + [f_1(1-r_2)]\,N_{lT} + f_1 r_2 N_{ll} \quad (7.3)$$
$$N_{LL}^{RF} = -(1-f_2)(1-r_1)N_{TT} + [f_2(1-r_1)]\,N_{Tl} + [r_1(1-f_2)]\,N_{lT} + f_2 r_1 N_{ll} \quad (7.4)$$
$$N_{LL}^{FF} = (1-r_1)(1-r_2)N_{TT} - [r_2(1-r_1)]\,N_{Tl} - [r_1(1-r_2)]\,N_{lT} + r_1 r_2 N_{ll}. \quad (7.5)$$

These are the expected number of events with two, one and zero real leptons in a sample of two inclusive loose leptons (therefore LL subscript). Since the analysis searching for new physics in the di-lepton channel is requiring two tight leptons in the final state these numbers need to be translated into the corresponding yields for a sample containing two tight leptons. This is performed by multiplying Eq. 7.2 - 7.5 by the appropriate probabilities

$$N_{TT}^{RR} = r_1 r_2 N_{LL}^{RR} \quad (7.6)$$
$$N_{TT}^{RF} = r_1 f_2 N_{LL}^{RF} \quad (7.7)$$
$$N_{TT}^{FR} = f_1 r_2 N_{LL}^{FR} \quad (7.8)$$
$$N_{TT}^{FF} = f_1 f_2 N_{LL}^{FF}. \quad (7.9)$$

7.1 Determination of r and f

The efficiencies r and f are in general measured in data using control samples enriched in either real or fake leptons. The key issue in selecting these control regions is to ensure that they are kinematically compatible with the signal region where the background is to be estimated. The real-efficiency is typically estimated from a real $Z \to l^{\pm}l^{\mp}$ control sample while the choice of control region for measuring the fake-efficiency is more dependent on the analysis and exact definition of the signal region used.

Once appropriate control regions are found there are in general various ways of calculating the resulting efficiencies. Two of the methods are described below.

In **Method 1**, the *tag-and-probe method*, one loops through a sample of events with exactly two inclusive loose leptons. First the hardest lepton is tagged while the other lepton is acting as the probe and checked whether it passes tight or not. The procedure is then repeated on the same event, but now tagging the softest and probing the hardest lepton whether it is tight. There are now several possibilities of how to choose the requirements on the tag in each iteration. It can either be tight (T), exclusive loose (l) or

any of the two; i.e. just inclusive loose (L), leading to three different ways of measuring the efficiency.

Eq. 7.10: When the tag is required to pass the tight criteria . The numerator is the number of times the probe passes tight while the denominator is the total number of times a tight tag is found

$$\varepsilon^{1lep}_{TT/TL} = \frac{2 \cdot N_{TT}}{N_{Tl} + N_{lT} + 2 \cdot N_{TT}} \tag{7.10}$$

Eq. 7.11: When the tag is required to be exclusive loose. The numerator is the number of times the probe passes tight while the denominator is the total number of times an exclusive loose tag is found

$$\varepsilon^{1lep}_{lT/lL} = \frac{N_{lT} + N_{Tl}}{N_{lL} + N_{Ll} + 2 \cdot N_{ll}} \tag{7.11}$$

Eq. 7.12: When the tag is required to be inclusive loose. The numerator is the number of times the probe passes tight while the denominator is the total number of times an inclusive loose tag is found (i.e. all events times two, since all leptons pass loose by definition).

$$\varepsilon^{1lep}_{LT/LL} = \frac{2 \cdot N_{TT} + N_{Tl} + N_{lT}}{2\left(N_{ll} + N_{Tl} + N_{lT} + N_{TT}\right)} \tag{7.12}$$

The ε^{1lep} represent the r or f in the matrix in Eq. 7.1. These possible ways of measuring the probabilities differ in fact only in the limit of small statistics, given a completely pure control region, where the quality of one lepton is uncorrelated with that of the other lepton in the event. This is certainly not the case in the control regions selected in data, thus the above-mentioned efficiencies would select different sub-categories or type of events inside the control regions, and possibly lead to different efficiencies. In the analysis presented in this thesis the differences are found to be small, however, and the efficiency in Eq. 7.12 is therefore used, as this method includes all events in the denominator and thus maximize the statistics. To find the efficiencies as a function of some kinematic variable, like η or p_{T} , one histogram for the numerator and one for the denominator used in constructing the efficiencies are filled using η or p_{T} of the probe lepton. Then, to get the final efficiency, the two histograms are divided by each other, bin-by-bin, in the end.

Method 2 simply counts the occurrence frequency of each event type in an appropriate di-lepton control region, resulting in eight counts: N_{TT}, N_{TL}, N_{LT}, N_{Tl}, N_{lT}, N_{lL}, N_{Ll} and N_{LL} (some being subsets of the others). From these counts similar ratios as in the list above are built

$$\varepsilon^{2lep}_{TT/TL} = \frac{N_{TT}}{N_{TL} + N_{LT}} \tag{7.13}$$

$$\varepsilon^{2lep}_{lT/lL} = \frac{N_{lT} + N_{Tl}}{N_{lL} + N_{Ll}} \tag{7.14}$$

$$\varepsilon^{2lep}_{LT/LL} = \frac{N_{LT} + N_{TL}}{N_{LL}}, \tag{7.15}$$

Efficiency	$N = 100$		$N = 1000$		$N = 100000$	
	Method1	Method2	Method1	Method2	Method1	Method2
$\varepsilon^{1lep}_{TT/TL}$	0.333 ± 0.047	0.333 ± 0.056	0.280 ± 0.014	0.280 ± 0.017	0.277 ± 0.001	0.277 ± 0.002
$\varepsilon^{1lep}_{lT/lL}$	0.247 ± 0.043	0.247 ± 0.050	0.293 ± 0.014	0.293 ± 0.015	0.282 ± 0.001	0.282 ± 0.002
$\varepsilon^{1lep}_{LT/LL}$	0.270 ± 0.044	0.258 ± 0.047	0.289 ± 0.014	0.291 ± 0.014	0.280 ± 0.001	0.281 ± 0.001

Table 7.1: Table illustrating the three different efficiencies calculated using Method 1 and Method 2 with different numbers of generated toy events.

but since these correspond to event counts (i.e. di-lepton efficiencies) they need to be translated into single-lepton efficiencies. Assuming infinite statistics and $\varepsilon^{2lep} = \left(\varepsilon^{1lep}\right)^2$ gives

$$\varepsilon^{2lep}_{TT/TL} = \frac{N_{TT}}{N_{TL}} = \frac{N_{TT}}{N_{Tl} + N_{lT} + N_{TT}} \approx \frac{\left(\varepsilon^{1lep}_{TT/TL}\right)^2}{2\varepsilon^{1lep}_{TT/TL}\left(1 - \varepsilon^{1lep}_{TT/TL}\right) + \left(\varepsilon^{1lep}_{TT/TL}\right)^2}$$

$$\varepsilon^{2lep}_{lT/lL} = \frac{(N_{lT} + N_{Tl})}{N_{lL}} = \frac{N_{lT} + N_{Tl}}{N_{ll} + N_{lT} + N_{Tl}} \approx \frac{2\left(1 - \varepsilon^{1lep}_{lT/lL}\right)\varepsilon^{1lep}_{lT/lL}}{\left(1 - \varepsilon^{1lep}_{lT/lL}\right)^2 + 2\left(1 - \varepsilon^{1lep}_{lT/lL}\right)\varepsilon^{1lep}_{lT/lL}}$$

$$\varepsilon^{2lep}_{LT/LL} = \frac{N_{LT}}{N_{LL}} = \frac{N_{Tl} + N_{lT} + N_{TT}}{N_{ll} + N_{Tl} + N_{lT} + N_{TT}} \approx \frac{2\varepsilon^{1lep}_{LT/LL}\left(1 - \varepsilon^{1lep}_{LT/LL}\right) + \left(\varepsilon^{1lep}_{LT/LL}\right)^2}{\left(1 - \varepsilon^{1lep}_{LT/LL}\right)^2 + 2\varepsilon^{1lep}_{LT/LL}\left(1 - \varepsilon^{1lep}_{LT/LL}\right) + \left(\varepsilon^{1lep}_{LT/LL}\right)^2}.$$

Solving for the ε^{1lep} efficiencies gives

$$\varepsilon^{1lep}_{TT/TL} = \frac{2\varepsilon^{2lep}_{TT/TL}}{1 + \varepsilon^{2lep}_{TT/TL}} \tag{7.16}$$

$$\varepsilon^{1lep}_{lT/lL} = \frac{\varepsilon^{2lep}_{lT/lL}}{2 - \varepsilon^{2lep}_{lT/lL}} \tag{7.17}$$

$$\varepsilon^{1lep}_{LT/LL} = 1 - \sqrt{1 - \varepsilon^{2lep}_{TL/LL}}. \tag{7.18}$$

The two methods, 1 and 2, are shown to give the same result in the limit of large statistics. However, Method 1 gives better statistics with the same number of events as in Method 2, since both leptons are used in every event. This is illustrated in Table 7.1, which shows the three efficiencies calculated using Method 1 and Method 2 with different numbers, N, of generated toy events. The true efficiency for loose to pass tight is set to 0.28. Twice per event (to simulate events with two leptons) this efficiency is checked against a random number from a standard uniform distribution. If the efficiency is larger than the random number the loose passed tight, otherwise not. This would typically generate events of the various types, lT, ll, TT, etc. and make it possible to test all of the different efficiencies discussed above.

Since all the methods and efficiencies are shown to give the same result when the statistics are large the preference is to use Method 1 with the efficiency in Eq. 7.12.

Obviously, in single-lepton regions, the simple counting of the number of events with inclusive loose, N_L, and tight leptons, N_T, is used. The efficiency then is simply

$$\varepsilon^{1lep} = \frac{N_T}{N_L}.$$

7.1.1 Combining Different Efficiencies

The fake-efficiencies of fake leptons from different sources, decay of light- and heavy-flavoured hadrons and conversions, have in general different dependencies on p_{T} , η and possibly other variables. This can be taken into account by combining several fake-efficiencies into one global fake-efficiency to be used in the matrix in Eq. 7.1,

$$f_{total}(p_{\mathrm{T}}\,,\eta) = \sum_i f_i(p_{\mathrm{T}}\,,\eta) w_i(p_{\mathrm{T}}\,,\eta) s_i(p_{\mathrm{T}}\,,\eta), \tag{7.19}$$

where i goes over the different fake types considered, having efficiencies f_i. The weight, w_i, reflects the relative amount of each fake type in the signal region. The scale factor, s_i, is applied to account for possible differences between the fake-efficiency extracted from data and that from MC. All these quantities are evaluated as a function of p_{T} and/or η.

For the real-efficiency one usually uses the p_{T} and/or η dependent efficiency extracted from the $Z \rightarrow l^{\pm}l^{\mp}$ control region, since all real leptons behave quite similar to the leptons from Z.

Once the real- and fake-efficiencies are measured, the MM can be used on an event-by-event basis in the actual analysis. For each event in the signal region where one wants to estimate the fake lepton background the real- and fake-efficiencies of each lepton are extracted from histograms, as function of η and/or p_{T} . The event is then classified to be either TT, Tl, lT or ll, setting the corresponding count, N_{TT}, N_{Tl}, N_{lT} or N_{ll}, to one, and the others to zero. The estimations using Eq. 7.6-7.9 are then interpreted as an event weight, one for each of the categories RR, RF, FR and FF. These event weights are stored in ROOT nTuples and can be used to plot the final distributions (for instance $E_{\mathrm{T}}^{\mathrm{miss}}$) in the signal region, with the estimated background from the MM.

7.1.2 Uncertainty Calculation

The real- and fake-efficiencies used in the MM are often computed from control regions with limited statistics and thus have a non-negligible statistical uncertainty. The total number of TT, Tl, lT and ll events entering the matrix inversion are also subject to statistical uncertainties. In addition there are possibly several different sources of systematic uncertainties on the real- and fake-efficiencies, coming from analysis-specific features. The calculation of the total uncertainty on the final estimated numbers needs to properly include and combine the various sources of uncertainties. Errors are estimated following the procedure sketched below. The nominal real- and fake-efficiencies used in estimating the fake lepton background in the final analysis are denoted r_{nom} and f_{nom} respectively. All the other efficiencies referred to below are only used in the uncertainty calculations.

To compute the error on the final estimates coming from the statistical uncertainties on the real- and fake-efficiencies, the matrix inversion is repeated using a new set of real- and fake-efficiencies

$$r_{stat.up/down} = r_{nom} \pm \sigma(r_{nom}) \text{ and} \tag{7.20}$$
$$f_{stat.up/down} = f_{nom} \pm \sigma(f_{nom}), \tag{7.21}$$

where $\sigma(r_{nom})$ and $\sigma(f_{nom})$ are the statistical uncertainties on r and f respectively. This gives a maximal upward/downward estimate, $N_{stat.\,up}(est.)/N_{stat.\,down}(est.)$, due to the statistical uncertainty on r and f. The final statistical uncertainty on the estimate is then found by taking the average between the upward and downward estimates

$$\sigma_{stat\,r,f}(est.) = \frac{N_{stat.\,up}(est.) - N_{stat.\,down}(est.)}{2}. \tag{7.22}$$

The errors on the final estimates coming from the systematic uncertainty on r and f are calculated in a similar way as the statistical error

$$r_{syst.up/down} = r_{nom} \pm \sigma_{syst}(r_{nom}) \text{ and}$$
$$f_{syst.up/down} = f_{nom} \pm \sigma_{syst}(f_{nom}),$$

where $\sigma_{syst}(r_{nom})$ and $\sigma_{syst}(f_{nom})$ are the systematic uncertainties on r and f respectively. This gives the maximal upward/downward shifts, $N_{syst.\,up/down}(est.)$, on the estimate due to the systematic uncertainty on r and f. The final systematic uncertainty on the estimate is found by using Eq 7.22, switching $N_{stat.\,up}(est.)$ and $N_{stat.\,down}(est.)$ with the corresponding upward and downward systematic estimates.

The part of the total uncertainty coming from the statistical error on N_{TT}, N_{Tl}, N_{lT} or N_{ll}, $\sigma_{stat\,N_{TT,Tl,lT,ll}}(est.)$, is computed simply by taking the sum of the squares of the weights for all events in the region where we want to estimate the fake lepton background. That is in fact just the error obtained directly from the histograms containing the fake lepton estimates.

The final total error on the estimate, $\sigma_{total}(est.)$, is found by

$$\sigma_{total}(est.) = \sqrt{\sigma^2_{stat\,r,f}(est.) + \sigma^2_{stat\,N_{TT,Tl,lT,ll}}(est.) + \sigma^2_{syst}(est.)}. \tag{7.23}$$

7.2 Matrix Method Applied to the di-Lepton SUSY Search

The Experimental Particle Physics Group at the University of Oslo has been involved in the ATLAS SUSY 2-lepton and 3-lepton subgroups. PhD student Maiken Pedersen and I were the main responsible for estimating the fake lepton backgrounds in both the 1 fb^{-1} and 4.71 fb^{-1} published di-lepton SUSY searches [11, 12]. We also did a cross-check of the fake lepton studies in the published 35 pb^{-1} note [86].[1] We applied the MM for all

[1]The corresponding ATLAS internal notes for the 35 pb^{-1}, 1 fb^{-1} and 4.71 fb^{-1} published searches can be found in Refs. [91], [131] and [76] respectively.

di-lepton flavour and sign combinations: ee, $e\mu$, $\mu\mu$; opposite-sign (OS) and same-sign (SS). The work was done in close collaboration with the ATLAS SUSY di-lepton group. In this thesis the work related to the analysis using 4.71 fb^{-1} of data is presented.

During the development of the analysis, the object definitions and the various recommendations as well as the trigger and pile-up conditions were constantly changing. In order to fulfill many of the tough conference and publication deadlines the study on the fake lepton backgrounds had to be done in parallel with the changing conditions. Some of the background studies were therefore performed with a somewhat smaller dataset and with different definitions compared to what was used for the final results, as described in detail in Section 6.3 and 6.4. In addition, since Maiken and I were the only ones working on the fake lepton background estimation, and in order to ensure quality assurance of reproducing all results, the necessity to cross-check each other's work was crucial. The sections about the MM in [76, 131] are therefore a combination of Maiken's and my own studies, always cross-checked by the other person. As a continuation of the electron studies performed with early ATLAS data presented in Chapter 4, I concentrated mostly on the studies related to electrons while Maiken worked mostly on muon-related issues. In the following sections, some of the plots are taken directly from the internal note [76]. In some cases new figures or tables are made with the most up-to-date analysis, and the exact numbers might therefore differ slightly from what is published; the conclusions and final results of the MM studies remain unchanged, however.

The first step in the MM is to find proper control regions where the fake- and real-efficiencies can be determined. The control regions used in computing the fake-efficiency are typically regions where we expect a large contamination of heavy- and light-flavoured jets, and very few real leptons from processes involving Z, γ, W and τ. A separate region dominated by electrons from conversions allows us to measure the fake-efficiency of converted electrons. The real-efficiency is measured from a $Z \to l^{\pm}l^{\mp}$ region. A detailed discussion of the various control regions follows.

7.2.1 QCD Fake-Efficiencies from Data Control Regions

We start by constructing control regions to extract the fake-efficiency for leptons stemming from heavy- and light-flavoured hadron decays. Both single- and di-lepton control regions as well as a dedicated tag-and-probe region, enhanced in leptons from b- and c-decays, are investigated.

7.2.1.1 Single- and di-Lepton Regions

Both single- and di-lepton control regions are investigated in order to measure the fake-efficiency. The single-lepton regions are advantageous because of large statistics whereas the di-lepton same-sign (SS) regions have less SM backgrounds. The fake-composition differs however, so studying both regions is important for completeness and for extracting some systematic uncertainties.

For the single-lepton regions, real leptons, especially from W-decays, but also from Z-decays if one of the leptons fails reconstruction, are believed to be the most challenging real

lepton backgrounds. First, in order not to overlap with the signal regions, an upper cut on $E_{\mathrm{T}}^{\mathrm{miss,rel}}$ is applied for all single-lepton control regions. Another effective discriminating variable for reducing the real lepton contributions is the angular separation between the $E_{\mathrm{T}}^{\mathrm{miss}}$ and the lepton,

$$\Delta\phi_{E_{\mathrm{T}}^{\mathrm{miss}},l} = \phi(\mathrm{lepton}) - \phi(E_{\mathrm{T}}^{\mathrm{miss}}),$$

plotted in Figure 7.2 for events with exactly one signal muon and $E_{\mathrm{T}}^{\mathrm{miss,rel}} < 30$ GeV. As expected, the W+jets and Z/γ^*+jets clearly peak at high values of $|\Delta\phi_{E_{\mathrm{T}}^{\mathrm{miss}},l}|$, while

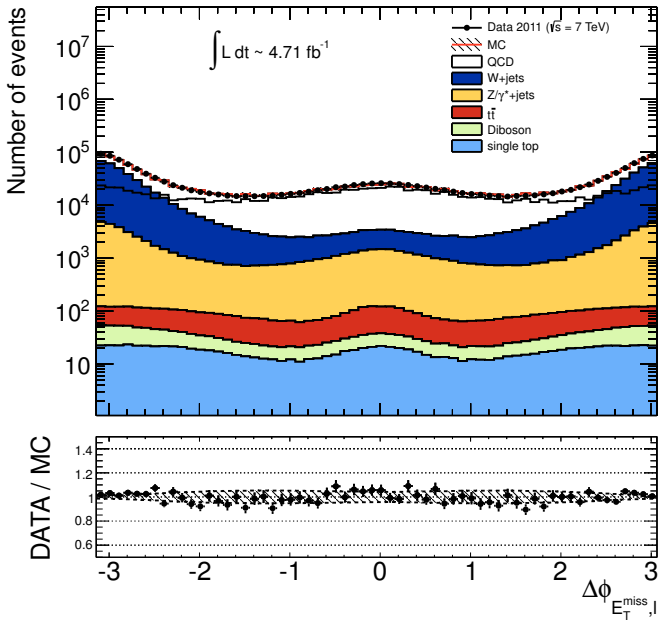

Figure 7.2: The variable $\Delta\phi_{E_{\mathrm{T}}^{\mathrm{miss}},l}$ for events with exactly one signal muon and $E_{\mathrm{T}}^{\mathrm{miss,rel}} < 30$ GeV. The SM MC samples, using the PythiaB sample (*bbmu15X*) to model the QCD, are stacked together. The QCD is also plotted on top of the stacked MC to better illustrate its dependency.

the other processes, especially QCD, show a much flatter behaviour. This is therefore a powerful variable to reduce the contribution of real leptons in the single-lepton control regions.

For the di-lepton regions the two leptons are always required to have SS in order to suppress real leptons coming from Z-decays. The charge-flip processes, however, contribute significantly to the sample of SS di-electrons, thus an additional Z-veto would be efficient to further suppress this background. An upper cut on $E_{\mathrm{T}}^{\mathrm{miss,rel}}$ is applied in the di-lepton regions to avoid overlap with the signal regions.

As will become clearer when studying the real efficiencies in Section 7.2.5, the MC simulation is proven to have a fairly good description of real leptons. MC can therefore be relied on to statistically subtract the expected contribution from real leptons in the data control regions, using the classification of real leptons shown in Table 6.14. After subtraction the QCD data control regions are supposed to be totally dominated by fake leptons coming from decays of heavy- and light-flavoured hadrons. The relatively good knowledge about the amount of real leptons polluting the control regions makes it possible to measure how pure the data control regions are with respect to fake leptons. Purity is defined as

$$\mathrm{purity}_{\text{fake leptons}} = \frac{N_{\mathrm{data}} - N_{\text{real lepton MC}}}{N_{\mathrm{data}}} \sim \frac{N_{\text{fake leptons}}}{N_{\mathrm{data}}}. \tag{7.24}$$

The larger the purity is the less real leptons are expected to enter the control region, and the smaller is the number of real leptons needed to be subtracted, and thus the resulting uncertainties are reduced.

Tables 7.2 and 7.3 summarize the fake-efficiencies and purities for electrons and muons, respectively, for a few selected single-lepton (upper) and SS di-lepton (lower) regions. The number of events used when calculating the fake-efficiencies are shown as N_T and N_L. For the single-lepton regions these numbers correspond simply to the number of tight and inclusive loose leptons respectively. For the di-lepton regions however these are the numerator and denominator of the $\varepsilon^{1lep}_{LT/LL}$ efficiency in Eq. 7.12. The purities are denoted with T and L, corresponding to the purity in the N_T and N_L samples, respectively. The numbers are shown both before and after real lepton subtraction. When subtracting the real leptons a 5% uncertainty on the cross-section is applied. This in turn is added in quadrature with the statistical uncertainty. The errors before subtraction are purely statistical.

Region	Before Subtraction			After Subtraction		Cuts
	f_{data} [%]	(N_T, N_L)	purity(T,L) [%]	$f_{data}^{MCsub.}$ [%]	(N_T, N_L)	
	single-electron regions					
1L-R01	27.51±0.06	(137060,635273)	72.94,77.96	23.06±1.55	(106853,463340)	$E_{\mathrm{T}}^{\mathrm{miss,rel}} < 20$ GeV
1L-R03	27.21±0.08	(79689,372548)	73.36,78.71	22.95±1.48	(62721,273285)	$E_{\mathrm{T}}^{\mathrm{miss,rel}} < 20$ GeV, $\lvert\Delta\phi_{E_{\mathrm{T}}^{\mathrm{miss}},l}\rvert < 0.5$
1L-R07	31.21±0.06	(216205,908857)	66.28,63.84	22.91±3.08	(138032,602422)	$E_{\mathrm{T}}^{\mathrm{miss,rel}} < 30$ GeV
1L-R09	30.36±0.07	(123962,532302)	67.58,66.00	22.75±2.79	(81819,359722)	$E_{\mathrm{T}}^{\mathrm{miss,rel}} < 30$ GeV, $\lvert\Delta\phi_{E_{\mathrm{T}}^{\mathrm{miss}},l}\rvert < 0.5$
	di-electron regions					
2L-R03	35.54±0.14	(40334,113486)	75.27,45.97	21.70±4.51	(18541, 85426)	$E_{\mathrm{T}}^{\mathrm{miss,rel}} < 30$ GeV
2L-R04	35.85±0.13	(46683,130213)	74.18,44.91	21.70±4.76	(20964, 96591)	$E_{\mathrm{T}}^{\mathrm{miss,rel}} < 60$ GeV
2L-R06	29.10±0.17	(20622, 70872)	90.07,74.53	24.08±1.48	(15370, 63831)	$E_{\mathrm{T}}^{\mathrm{miss,rel}} < 20$ GeV, Z-veto
2L-R07	28.99±0.15	(27130, 93574)	89.73,73.63	23.79±1.55	(19976, 83965)	$E_{\mathrm{T}}^{\mathrm{miss,rel}} < 30$ GeV, Z-veto

Table 7.2: A selection of single- (upper) and SS di-electron (lower) fake lepton control regions.

The single-electron regions of Table 7.2 all have quite similar fake-efficiencies before subtraction, ranging from 27.2-30.4%. The purity lies between 64-78% and increases when tightening the $E_{\mathrm{T}}^{\mathrm{miss,rel}}$ cut. The fake-efficiency decreases to about 23% after subtraction of real leptons, as expected, since the latter have a significantly higher fake-efficiency than leptons from QCD processes. After the subtraction the various fake-efficiencies retrieved from the different regions are consistent within uncertainties. Further, the fake-efficiencies measured in the SS di-electron regions differ significantly whether or not an additional Z-veto is applied. This is reflected in the purity which increases from ~ 46 and $\sim 75\%$ to ~ 74 and $\sim 89\%$, for the samples L and T respectively, after applying the Z-veto. This comes from the fact that several Z events are present also in the SS region because of the charge-flip process discussed in Section 5.4.1.1. After subtraction the fake-efficiency decreases to about 24% for the regions with a Z-veto and around 22% for the regions without. The uncertainties are however quite large for the regions without the Z-veto because of the relatively large number of subtracted events. The statistics is in general

Region	Before Subtraction			After Subtraction		Cuts
	f_{data} [%]	(N_T, N_L)	purity(T,L) [%]	$f_{data}^{MCsub.}$ [%]	(N_T, N_L)	
	single-muon regions					
1L-R01	51.67±0.08	(190947,560524)	84.84,60.68	47.63±1.37	(162000,340150)	$E_{\mathrm{T}}^{\mathrm{miss,rel}} < 20$ GeV
1L-R03	50.67±0.11	(109248,324870)	86.13,61.63	47.00±1.24	(94093,200215)	$E_{\mathrm{T}}^{\mathrm{miss,rel}} < 20$ GeV $\lvert\Delta\phi_{E_{\mathrm{T}}^{\mathrm{miss}},l}\rvert < 0.5$
1L-R07	55.37±0.07	(286786,804764)	71.08,53.89	47.01±3.12	(203860,433687)	$E_{\mathrm{T}}^{\mathrm{miss,rel}} < 30$ GeV
1L-R09	53.61±0.09	(162270,464942)	73.78,55.80	46.15±2.72	(119719,259423)	$E_{\mathrm{T}}^{\mathrm{miss,rel}} < 30$ GeV, $\lvert\Delta\phi_{E_{\mathrm{T}}^{\mathrm{miss}},l}\rvert < 0.5$
	di-muon regions					
2L-R03	51.29±0.18	(40727, 79411)	99.36,99.67	51.13±0.18	(40468, 79148)	$E_{\mathrm{T}}^{\mathrm{miss,rel}} < 30$ GeV
2L-R04	51.19±0.17	(43669, 85303)	98.45,99.18	50.82±0.21	(42994, 84602)	$E_{\mathrm{T}}^{\mathrm{miss,rel}} < 60$ GeV
2L-R06	51.77±0.20	(33669, 65041)	99.65,99.82	51.68±0.20	(33551, 64924)	$E_{\mathrm{T}}^{\mathrm{miss,rel}} < 20$ GeV, Z-veto
2L-R07	51.32±0.18	(40109, 78159)	99.41,99.70	51.17±0.18	(39874, 77921)	$E_{\mathrm{T}}^{\mathrm{miss,rel}} < 30$ GeV, Z-veto

Table 7.3: A selection of single- (upper) and SS di-muon (lower) fake lepton control regions.

much smaller than for the corresponding single-lepton regions.

The single-muon regions in the upper part of Table 7.3 give higher fake-efficiencies, ranging from 50-54%. This variation in fake-efficiencies can be understood from the different purity measured when applying $E_{\mathrm{T}}^{\mathrm{miss,rel}} < 20$ GeV or $E_{\mathrm{T}}^{\mathrm{miss,rel}} < 30$ GeV. The purity increases significantly, from about 54% and 74% in L and T, respectively, to about 61% and 85%, when tightening the $E_{\mathrm{T}}^{\mathrm{miss,rel}}$ cut. This results in lower fake-efficiencies. The effect of applying the additional $|\Delta\phi_{E_{\mathrm{T}}^{\mathrm{miss}},l}| < 0.5$ cut is small, increasing the purity only by a few percent. After subtraction, all regions lead to a fake-efficiency of about 47%, although with larger uncertainties from the subtraction procedure.

For the SS di-muon control regions the purity is very high and the contamination of real leptons is negligible. The fake-efficiencies before and after subtraction are thus almost identical, all being about 51%. As expected, since the charge-flip process is highly suppressed for muons, the additional Z-veto has basically no effect.

The choice of the control regions to study in more detail is a compromise between stability (i.e. no strong dependencies of the fake-efficiency on p_{T} , $E_{\mathrm{T}}^{\mathrm{miss,rel}}$, η, etc.), purity and statistics. High purity means the region is less dependent on subtraction and the corresponding uncertainties are smaller. For the SS di-electron control regions a Z-veto drastically increases the purity. In order to maintain a large number of events in the control region an upper cut on $E_{\mathrm{T}}^{\mathrm{miss,rel}}$ of < 30 GeV is applied, defined as region *2L-R07* in Table 7.2. For muons the Z-veto is not necessary, and only a cut on $E_{\mathrm{T}}^{\mathrm{miss,rel}} < 30$ GeV is used, corresponding to region *2L-R03* in Table 7.3. For the single-lepton regions the purity is relatively high already when using the $E_{\mathrm{T}}^{\mathrm{miss,rel}} < 20$ GeV cut only. Adding an additional $|\Delta\phi_{E_{\mathrm{T}}^{\mathrm{miss}},l}| < 0.5$ increases the purity slightly, but in order to keep consistency with the di-lepton regions we choose to use region *1L-R07* requiring $E_{\mathrm{T}}^{\mathrm{miss,rel}} < 30$ GeV for both electrons and muons.

Figure 7.3 shows the p_{T} distribution of inclusive loose electrons (upper) and muons (lower) in the chosen single- (left) and di-lepton (right) control regions discussed above

and shaded in gray in Tables 7.2 and 7.3. The figures show the full 4.71 fb^{-1} data together with all the important real lepton MC samples, as listed in Section 6.2, i.e. without the QCD samples. The discrepancy between data and the sum of MC is interpreted as the fake lepton contribution. Since the single-lepton trigger weights used in MC are only available above the trigger thresholds, being 25 and 20 GeV for electrons and muons, respectively, the 10-20 GeV bins in MC in Figure 7.3a and c are empty. In the electron channel the number of MC events in the 20-30 GeV is also slightly reduced due to this. We expect the real leptons to constitute a very small fraction of the total number of events in the lowest p_{T} bins so the impact on the subtraction procedure is, however, weak. For the single-lepton regions in Figure 7.3a and c the fraction of fake leptons at

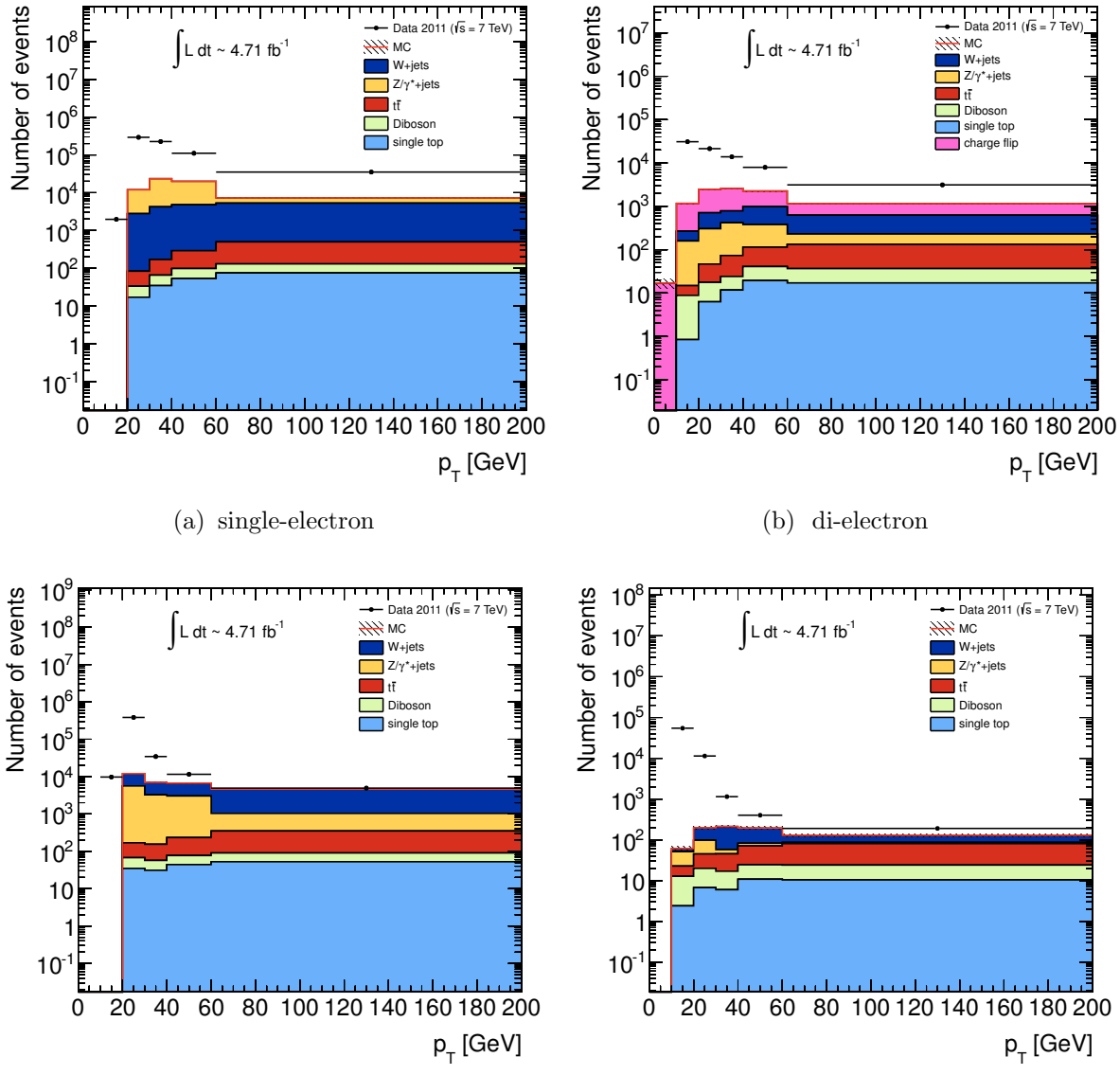

(a) single-electron

(b) di-electron

(c) single-muon

(d) di-muon

Figure 7.3: The transverse momenta of inclusive loose electrons (upper) and muons (lower) for data and the real lepton SM backgrounds in the selected single- (left) and di-lepton (right) fake control region indicated by a gray colour in Table 7.2 and 7.3.

low p_{T} is large; the real lepton MC, almost exclusively from W+jets and Z/γ^*+jets, only

constitutes about 3-4% of the total number of data events in the 20-30 GeV bin. At higher p_{T}, however, real leptons become much more important. In the di-muon channel the real leptons constitute about 93% of the data in the 60-200 GeV bin, mainly from W+jets events. In the single-electron channel the fraction of real leptons at high p_{T} is much smaller, being only about 20% in the highest bin, also mainly from W+jets events. Integrated over the complete p_{T} range the amount of real leptons is only about 7% in the single-muon channel while it is about 9% in the single-electron channel, as seen from the purity in Tables 7.3 and 7.2 respectively.

The di-lepton distributions in Figures 7.3b and d show the same predominance of fake leptons at low p_{T} as in the single-lepton control regions, with real lepton background estimated to be about 2% and $\sim 10\%$ in the 20-30 GeV bin for the $\mu\mu$- and ee-channels respectively. The main difference between the di-electron and di-muon channel comes from the charge-flip component which is the dominant source of real leptons in the di-electron region. Towards higher p_{T} the relative fraction of real leptons grows. For the 60-200 GeV bin in the di-muon region 70% of the data is explained by real lepton MC, with equal fractions coming from the W+jets and $t\bar{t}$ backgrounds. In the electron channel the real lepton contribution is about 40% in the highest bin, with roughly equal amounts coming from W+jets and charge-flip events. For the complete p_{T} range the fraction of real leptons in the di-muon channel is only about 1% while it is significantly higher, $\sim 12\%$, in the di-electron channel.

After having studied the composition, average fake-efficiencies and purity of the various control region it is time to look closer at the dependency of the fake-efficiencies as a function of some important lepton variables.

Fake-Efficiency Dependency

Figure 7.4 shows the fake-efficiencies obtained from the selected single- (left) and di-lepton (right) control regions for electrons (upper) and muons (lower). The fake-efficiency is shown both prior to the subtraction, in black, and after subtracting the real lepton MC from the data, indicated by the red markers. Note that for muons the highest bins are missing after subtraction as there are simply no events left. This in turn leads to a lack of data-driven fake-efficiency prediction above a certain value of p_{T}. The impact of the subtraction is, as expected from the discussion in the previous section, most visible in the high p_{T} bins. In the di-electron region the average fake-efficiency decreases from ~ 33 to $\sim 29\%$ while the average muon fake-efficiency is nearly insensitive, with a slight change from ~ 50.5 to $\sim 49.5\%$. In the single-lepton regions the subtraction has a somewhat bigger effect: The average electron fake-efficiency decreases from ~ 31 to $\sim 22\%$ while for muons it goes from ~ 55 to $\sim 47\%$. In both cases the distributions tend to be flatter after the subtraction is applied, indicating that the real leptons contribute significantly to the fake-efficiencies at high p_{T} before subtraction. It should be noted, however, that the uncertainty on the subtraction at high p_{T}, especially in the di-lepton regions, but also in the single-muon region, becomes very large due to the fact that we are subtracting close to 100% of the events. Figure 7.3 already gave a hint that the high p_{T} regions would lead to uncertain information about the fake leptons, since it is in most cases dominated by real leptons from W, Z/γ^* and $t\bar{t}$.

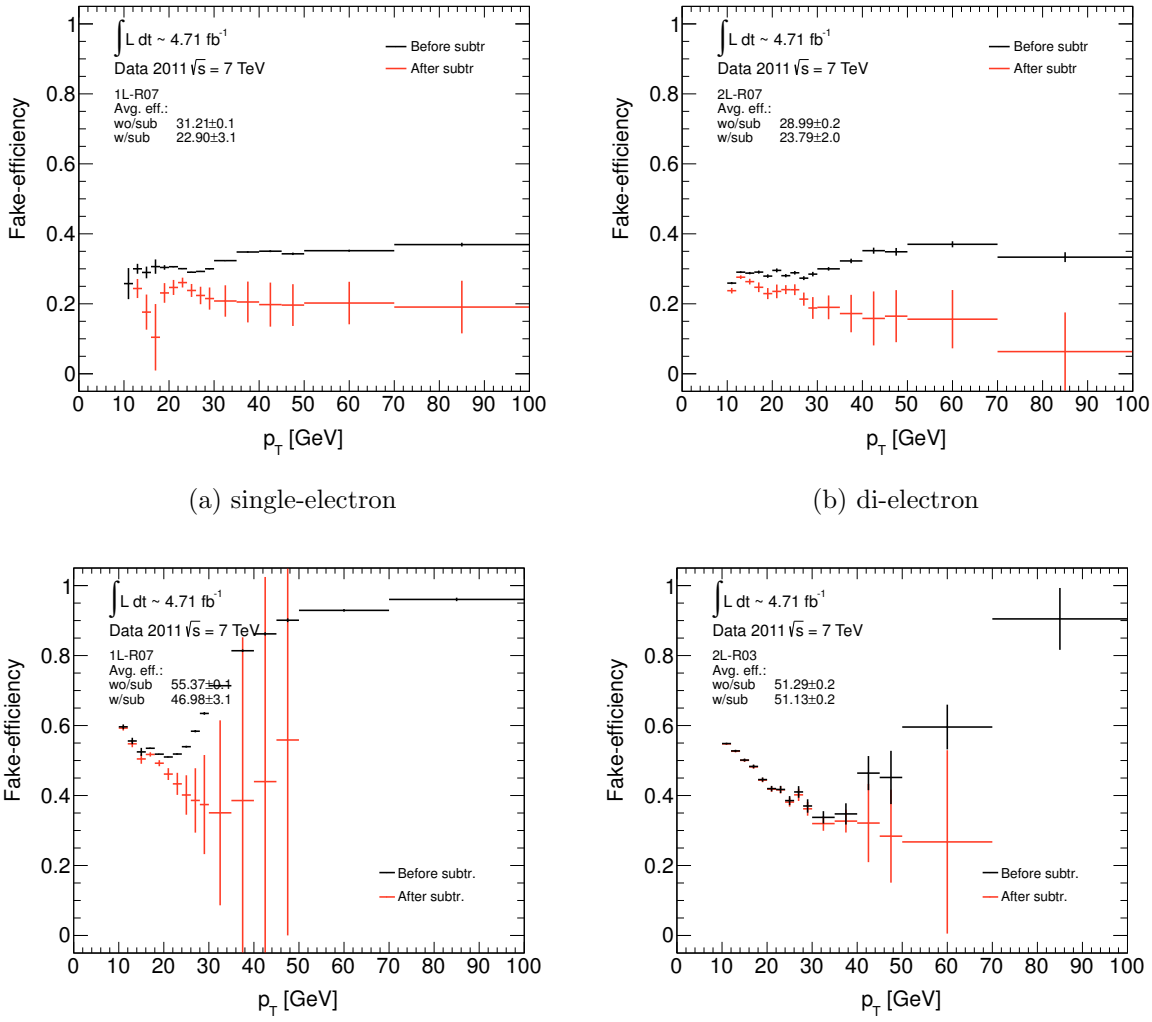

(a) single-electron

(b) di-electron

(c) single-muon

(d) di-muon

Figure 7.4: Fake-efficiency for electrons (upper) and muons (lower) versus p_{T} before (black) and after (red) MC subtraction of real leptons. The left two plots are for the single-lepton control regions while the right plots show the di-lepton control regions.

Figure 7.4 clearly points to the fact that the single- and di-lepton regions show a somewhat different dependency on p_{T} , and that their average fake-efficiencies differ. Figure 7.5 shows the ratio between the fake-efficiencies from the di-lepton and single-lepton control regions as a function of p_{T} for electrons (a) and muons (b). The fake-efficiencies are obtained after real lepton subtraction. There are some clear deviations from unity, although in the range with the smallest uncertainties (i.e. $20 < p_{\mathrm{T}} < 40$ GeV) the ratio seems to be quite flat and close to 1. The best fit, assuming a constant ratio over the complete p_{T} range, gave 0.96 ± 0.03 and 1.12 ± 0.004 for electrons and muons respectively. In the analysis the ratio is approximated to be unity and the observed deviations, being ± 4 % and ± 12 % for electrons and muons respectively, are incorporated in the final systematic uncertainty.

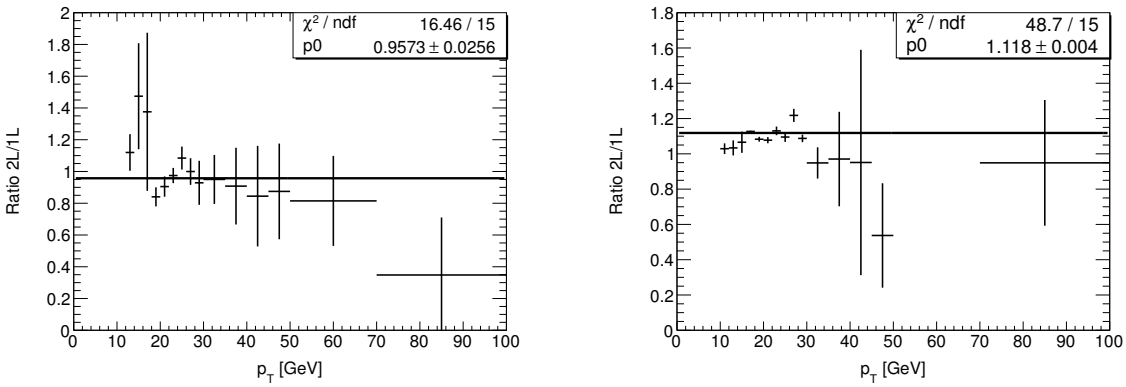

(a) electrons (b) muons

Figure 7.5: The fake-efficiency from the di-lepton control region divided by the corresponding fake-efficiency from the single-lepton control region for electrons (a) and muons (b). The horizontal line shows the best fit under the assumption of a constant ratio.

The fake-efficiencies as functions of η are shown in Figure 7.6, both before and after the subtraction of real leptons. The subtraction seems to be independent of η as it causes a constant decrease in the fake-efficiency over the complete η range. As expected, the η dependency in the muon channel is relatively small compared with the p_{T} dependency. In the electron channel, however, the dependency is more pronounced with smaller efficiencies at high $|\eta|$ and in the region between the barrel and end-cap of the ECal ($1.37 < |\eta| < 1.52$). The effect of including the η dependency (in addition to the p_{T} dependency) of the fake-efficiency is illustrated in Table 7.4, showing the fake lepton estimates in OS and SS di-electron regions with $E_{\mathrm{T}}^{\mathrm{miss,rel}} > 100$ GeV. The fake-efficiencies are taken from the *2L-R07* region before subtraction and both p_{T}-only and 2D $p_{\mathrm{T}}+\eta$ dependencies are investigated. The absolute and relative differences between the two estimates are also shown. The small effect, only of about 0.2%, indicates that the inclusion of an additional η dependency has a negligible effect on the final estimates. As expected the statistical uncertainties increase when including the η dependency. As clearly seen in Figure 7.6, the η dependency of the muon fake-efficiency is even smaller than for electrons, thus only the p_{T} dependency is used for all channels, ee, $e\mu$ and $\mu\mu$, in the following studies.

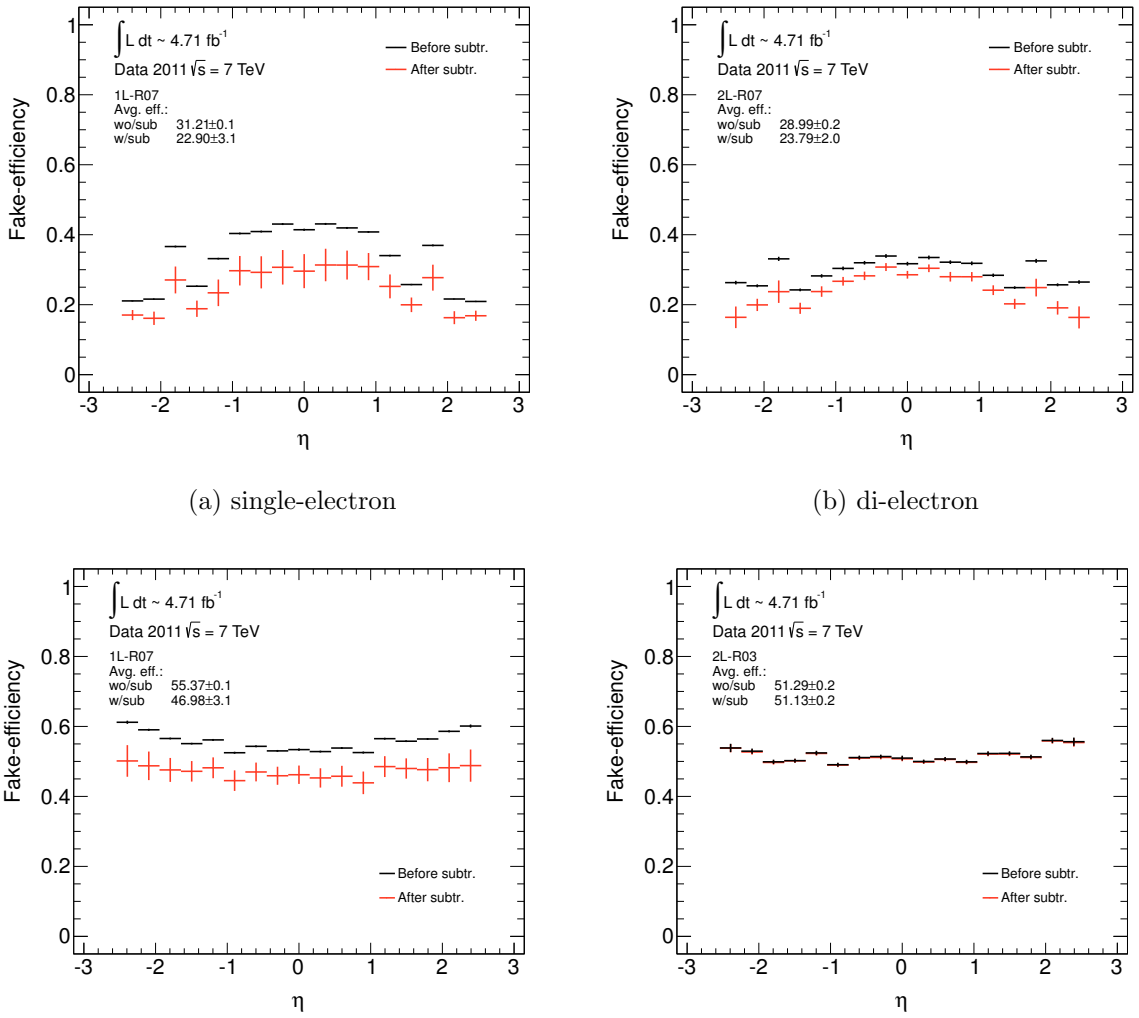

(a) single-electron

(b) di-electron

(c) single-muon

(d) di-muon

Figure 7.6: Fake-efficiency for electrons (upper) and muons (lower) versus η before (black) and after (red) MC subtraction of real leptons. The left two plots are for the single-lepton control regions while the right plots show the di-lepton control regions.

	SS + $E_{\mathrm{T}}^{\mathrm{miss,rel}}$> 100 GeV	OS + $E_{\mathrm{T}}^{\mathrm{miss,rel}}$> 100 GeV
	ee	*ee*
p_{T} dep.	34.2 ± 9.0	62.3 ± 18.1
p_{T} +η dep.	34.1 ± 10.0	62.2 ± 24.1
max diff. (%)	0.077 (0.22%)	0.121 (0.19%)

Table 7.4: The fake lepton estimates in the OS and SS di-electron regions with $E_{\mathrm{T}}^{\mathrm{miss,rel}}$> 100 GeV using the p_{T} dependent and p_{T} +η dependent fake-efficiencies from the *2L-R07* control region in the full 4.71 fb^{-1}dataset.

7.2.1.2 $b\bar{b}$ Control Region

Since we expect leptons from the decay of heavy-flavoured jets to be the most important source of fake leptons, these are studied more carefully using a dedicated region enhanced in $b\bar{b}$ events. This region also serves as an important cross-check against the single- and di-lepton regions discussed above. The $b\bar{b}$ control region is defined by requiring the following [132]:

1. exactly one baseline **tag** muon (according to Table 6.12) before overlap removal
2. exactly one baseline **probe** muon/electron (according to Tables 6.12/6.11)
3. the **tag** muon to be within 0.4 in ΔR to a b-jet
4. the **probe** lepton (muon/electron) to be separated from any jet by > 1.0 in ΔR
5. $E_{\mathrm{T}}^{\mathrm{miss,rel}} < 40$ GeV
6. transverse mass of the **probe** lepton-$E_{\mathrm{T}}^{\mathrm{miss,rel}}$ to be less than 40 GeV
7. exactly one b-jet in the event
8. appropriate triggers
   - 8a) for **probe** electrons: require *emu-trigger* to have fired
   - 8b) for **probe** muons: require *di-muon trigger* to have fired

The tag muon is ensured to come from a reconstructed b-jet, and would, in the ordinary analysis, have been removed by the overlap removal, according to the discussion in Section 6.3.5. Therefore, in order to get a probe lepton which is not removed by the overlap removal it needs to be separated from any jet, as described above. By assuming that one of the b-jets in these $b\bar{b}$ events is unreconstructed, the requirement of exactly one b-jet is important. If there would have been more b-jets in the event, this would have indicated that the probe lepton does not come from the second b-jet. Figure 7.7 shows this type of event topology.

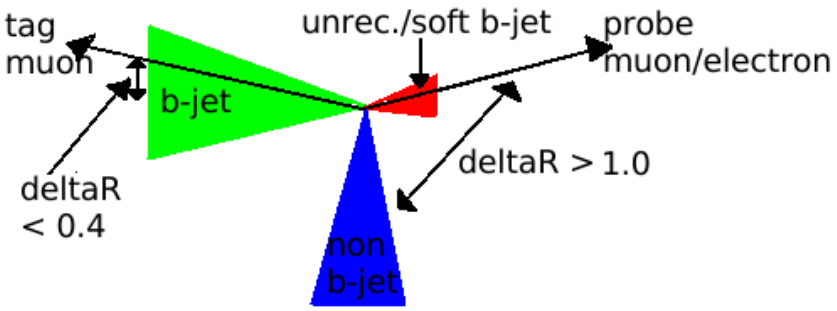

Figure 7.7: A drawing of the event topology in the $b\bar{b}$ tag-and-probe control region.

Figure 7.8 shows the p_{T} distribution of the inclusive loose probe electrons (a) and muons (b) in all events passing the cuts above. The real lepton MC is plotted together with the full 4.71 fb^{-1} dataset. The discrepancy between data and MC is again interpreted as fake leptons coming from QCD-processes, which clearly seem to be the dominant contribution. At high p_{T} , however, especially for muons, the contamination of real leptons from Z/γ^*+jets becomes important.

To be able to study the $b\bar{b}$ control region in more detail an attempt to describe the QCD-component, using various MC samples, has been performed. The p_{T} distribution of the probe electrons and muons using the di-lepton filtered *PythiaB* samples, *mu10e10X*

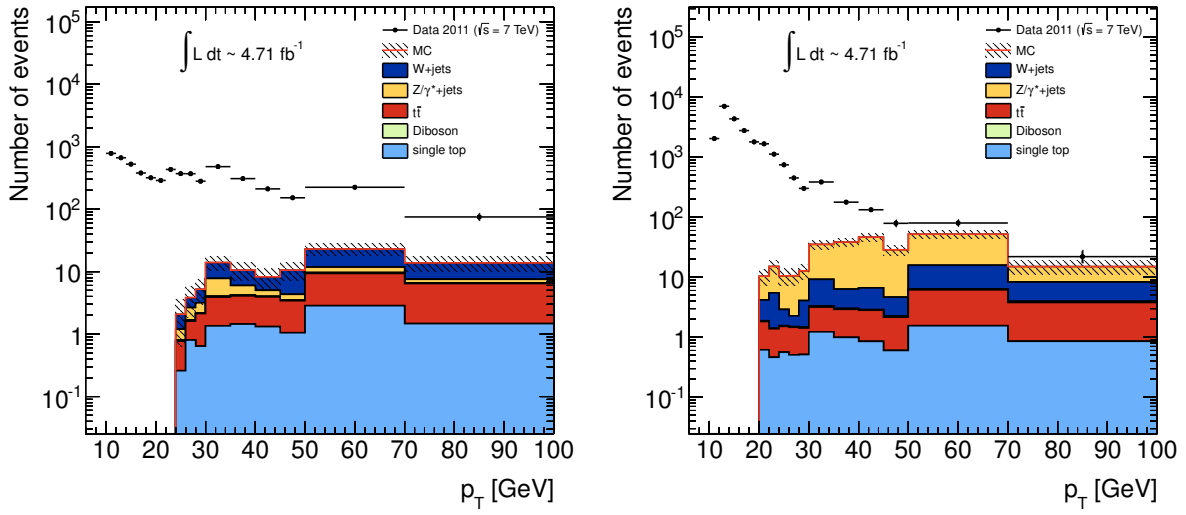

(a) electrons (b) muons

Figure 7.8: The transverse momentum of inclusive loose probe electrons (a) and muons (b) for data and real lepton SM backgrounds in the $b\bar{b}$ tag-and-probe control region.

and *mu10mu10X* for electrons and muons respectively are depicted in Figure 7.9a and b.[2] For muons the agreement between data and MC is quite good. Truth information can

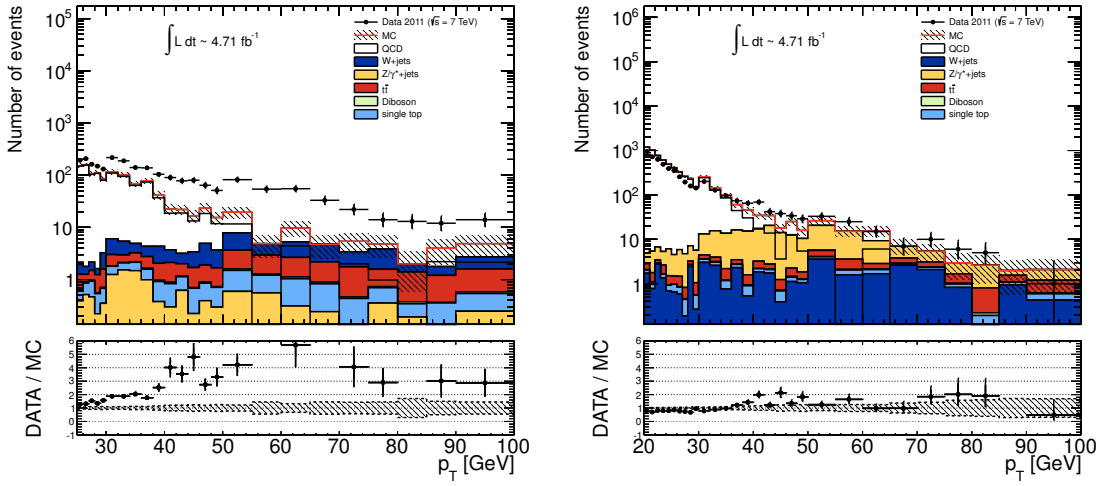

(a) PythiaB (mu10e10X) (b) PythiaB (mu10mu10X)

Figure 7.9: The momentum of all inclusive loose electrons (a) and muons (b) in the $b\bar{b}$ tag-and-probe fake control region using the PythiaB samples to model the QCD component.

therefore be trusted in order to get a better understanding of the exact composition of fake muons in the $b\bar{b}$ control region. For electrons, however, the agreement between data and MC is not particularly good and the truth studies are therefore less reliable. Nevertheless, Figure 7.10 shows the origin of all probe electrons (a) and muons (b) in the $b\bar{b}$ tag-and-probe control region. It is clear that the region seems to be totally dominated by leptons

[2] Attempts using the other QCD MC samples (presented in Section 6.2.4) to describe data in the fake lepton control regions are summarized in Section A.1 of Appendix A.

from b-jets, constituting 73 and 91% in the electron and muon channel, respectively. In the electron channel there are also some contributions from real leptons (14%) and c-jets (10%), while for muons the real leptons and leptons from c-jets only comprise about 4 and 5%, respectively. The fraction of leptons coming from light jets is small in both channels. Note however that the leptons from decay of light-flavoured hadrons are underestimated, since the MC used to describe the QCD component only involves b- and c-jet production. According to MC the fake electrons from conversions only constitutes 1% of the total, thus this component is also definitely underestimated in the PythiaB MC sample. The discrepancies observed in the electron channel, in contrast to the relatively good agreement observed in the muon channel, illustrated in Figure 7.9, are therefore understood to come from the two missing components: light-flavoured QCD and conversion processes. These sources of fake leptons play a negligible role in the muon channel, however, and thus the PythiaB sample succeeds very well in describing the data. A more detailed discussion on how to tackle the missing components of the fake electrons will follow in Section 7.2.4.

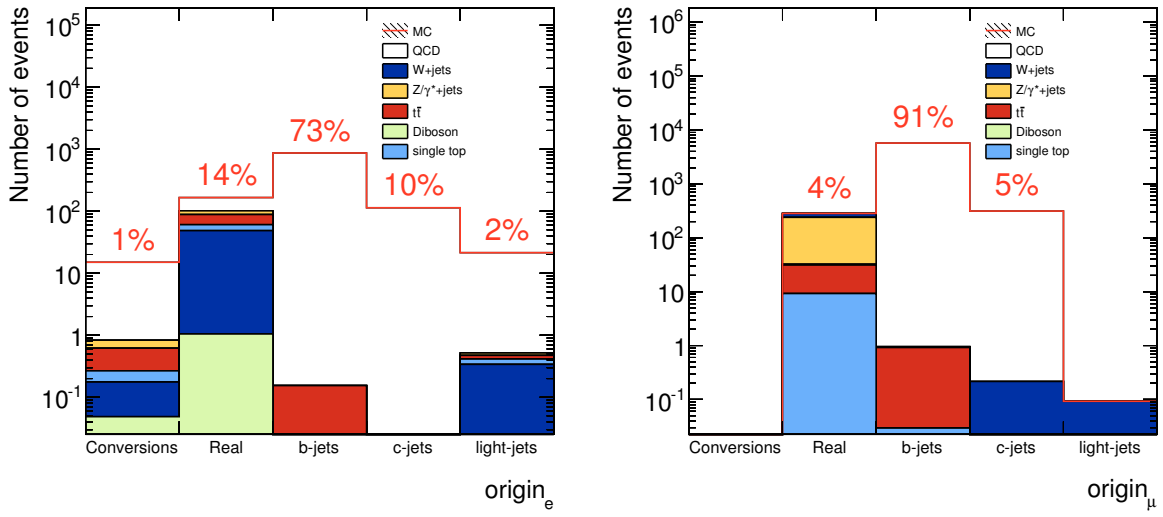

(a) electrons (b) muons

Figure 7.10: Origin of the inclusive loose probe electrons (left) and muons (right) in the $b\bar{b}$ tag-and-probe control region. For the QCD component the di-lepton filtered PythiaB samples, *mu10e10X* and *mu10mu10X*, for electrons and muons respectively, are used.

Fake-Efficiency Dependency

Figure 7.11 shows the fake-efficiency as a function of p_{T} for electrons (a) and muons (b) using the $b\bar{b}$ tag-and-probe control region. Since this region already consists of mostly leptons from decays of heavy-flavoured jets no subtraction of real lepton MC is performed. The average fake-efficiencies are ~ 28 and $\sim 44\%$ for electrons and muons respectively. The p_{T} dependencies show a similar behaviour as in the single- and di-lepton control regions, but since the $b\bar{b}$ region is highly contaminated by fake leptons no rise in the fake-efficiency at high p_{T} is present. Comparing the integrated fake-efficiencies in Figure 7.11 with the average of the fake-efficiencies from the selected single- and di-lepton control regions in Table 7.2 and 7.3, being 23.4 and 49.1%, the differences are found to be $\sim \pm 20\%$

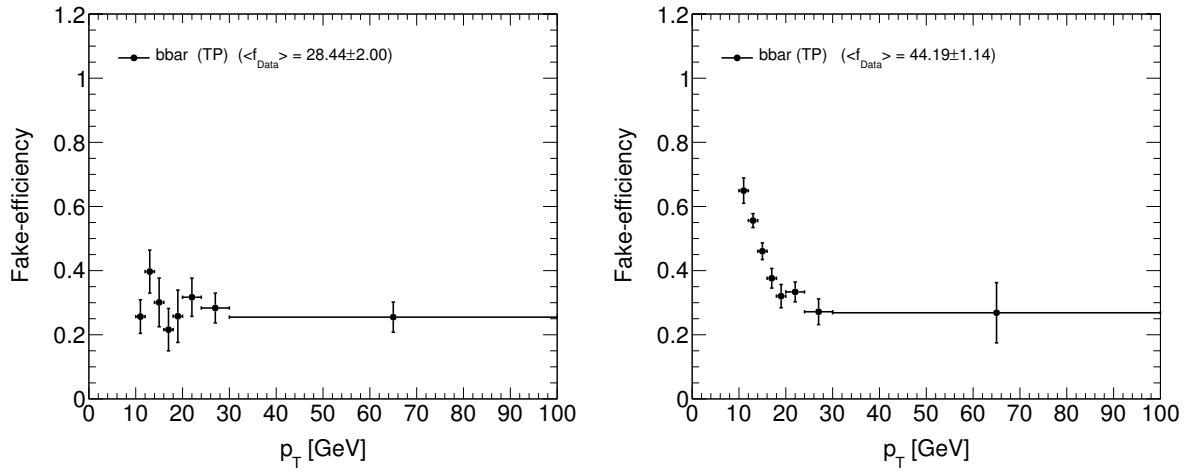

(a) electrons (b) muons

Figure 7.11: The fake-efficiency as a function of p_{T} for electrons (left) and muons (right) using the $b\bar{b}$ tag-and-probe (TP) control region.

in the electron channel and ±10% for muons. These deviations are added to the final systematic uncertainty on the fake-efficiencies.

7.2.1.3 Effects on the Fake-Efficiency From Sign and Flavour of the Leptons

The signal regions discussed in Section 5.4, where the fake lepton estimates are eventually performed, deal with both OS and SS as well as same flavour (SF) and different flavour (DF) di-lepton combinations. The compatibility between the fake-efficiencies extracted from control regions requiring SS or OS in combination with both SF and DF di-leptons has therefore been studied. Two new control regions are defined in which $e\mu$-events with either OS or SS are selected and $E_{\mathrm{T}}^{\mathrm{miss,rel}} < 30$ GeV is required. The single-electrons or muons in these events are then used to calculate the corresponding fake-efficiency. Figure 7.12a and c show the ratio between the fake-efficiencies from the $e\mu$ SS di-lepton region versus the fake-efficiency from the ee and $\mu\mu$ SS di-lepton regions, respectively. Any significant deviations from unity in these plots would indicate that the fake-efficiency varies whether or not there is an additional lepton of different flavour in the event. Figure 7.12b and d show similar ratios between the electron and muon fake-efficiencies respectively, obtained from OS $e\mu$ and SS $e\mu$ events. In all cases the ratios in the most reliable range, $12 < p_{\mathrm{T}} < 35$ GeV, are rather flat with a small overall shift of $\sim 10\%$ above (below) unity for electrons (muons). For p_{T} above ~ 35 GeV uncertainties are too large for any claims to be made. The effect on the fake-efficiency if extracted from a SF/DF or SS/OS region does not seem to be very large in the electron nor in the muon channel. The 10% effect is therefore simply included in the systematic uncertainty when performing the final estimates.

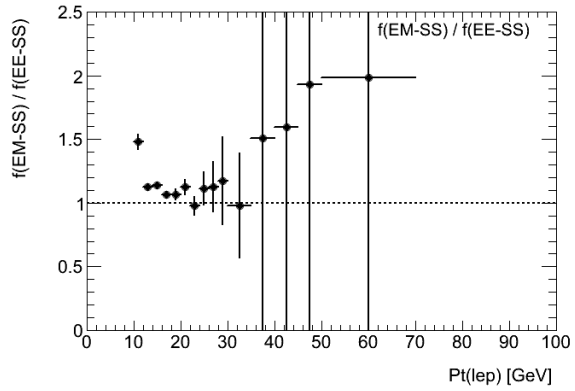

(a) $e\mu$ vs. ee for electrons

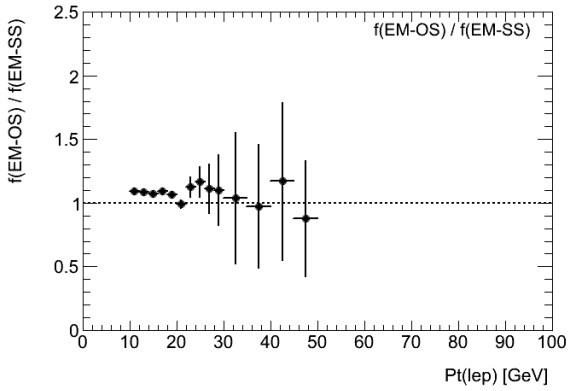

(b) OS vs. SS for electrons

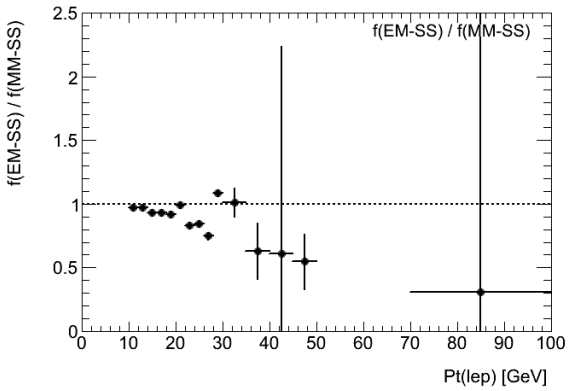

(c) $e\mu$ vs. $\mu\mu$ for muons

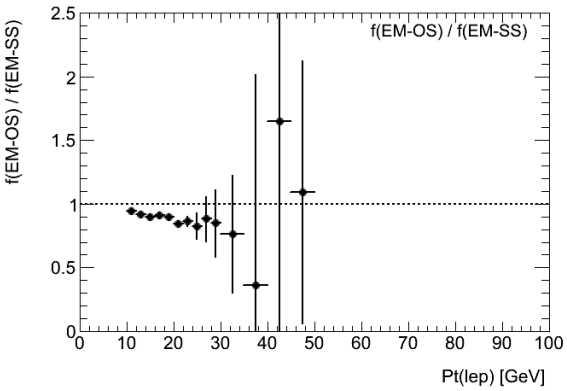

(d) OS vs. SS for muons

Figure 7.12: Left are the fake-efficiencies extracted from DF-SS regions divided by the corresponding fake-efficiencies from SF-SS region. The right plots show corresponding ratios between fake-efficiencies from the DF-OS and DF-SS regions. The upper two plots represent the electron fake-efficiencies while the bottom two plots are for the muon fake-efficiencies.

7.2.2 Fake-Efficiencies from Monte Carlo

The estimates from the MM aim at describing the fake lepton contribution in the signal regions, which all apply some adequate lower cut on $E_{\mathrm{T}}^{\mathrm{miss,rel}}$. The fake-efficiencies obtained from the low $E_{\mathrm{T}}^{\mathrm{miss,rel}}$ regions discussed in the previous sections might therefore not necessarily reflect the fake leptons we expect to populate the signal regions. Using MC truth, however, we can study the fake-efficiencies of leptons in the higher $E_{\mathrm{T}}^{\mathrm{miss,rel}}$ regions, and compare those with the ones obtained from the low $E_{\mathrm{T}}^{\mathrm{miss,rel}}$ regions in data.

The fake leptons coming from decays of heavy- and light-flavoured hadrons in QCD-events are not very well modeled in the available MC simulations. The MC samples found to best describe the QCD component are the heavy-quark filtered *PythiaB* samples, where only events containing b and c quarks are generated. The light-flavoured component are therefore underestimated, especially for electrons. The performance of the other, non heavy-filtered QCD samples (i.e. *JF17/35* and electron/muon filtered *PythiaJx* samples in Table 6.8) is, however, not particularly good. We assume that the decay of heavy-flavoured jets is the dominating part of the fake lepton contribution in QCD-events, denoted by *(HF-QCD)*, and is therefore studied in particular in the next sections. The uncertainties arising from a possibly underestimation of the light-flavoured component will be discussed later, after the final fake-efficiency used in the analysis is defined.

Figure 7.13a and b show the fake-efficiencies for electrons and muons respectively, obtained by requiring only fake leptons (i.e. leptons from conversions, heavy- and light-flavoured hadron decays) in a low $E_{\mathrm{T}}^{\mathrm{miss,rel}}< 30$ GeV region using truth MC, normalized to an integrated luminosity of 4.71 fb^{-1}. For the QCD component the *PythiaB* samples are used. The MC is split into the most important processes with the legend giving the relative amount and the average fake-efficiency for each contribution. For muons a significant difference between OS and SS events in MC is observed, especially at low $E_{\mathrm{T}}^{\mathrm{miss,rel}}$, as summarized in Section A.2 of Appendix A. Only SS events are therefore included in the muon channel, since this gave the best overall agreement with the fake-efficiencies obtained from the data control regions. For electrons the differences between OS and SS events were not significant, and are therefore combined in order to gain statistics. The fake-efficiency from the $b\bar{b}$ data control region is plotted for comparison.

For both electrons and muons the fake-efficiency in the low $E_{\mathrm{T}}^{\mathrm{miss,rel}}$ region is driven by the $b\bar{b}$ component, which makes up most of the fake lepton contribution (90 and 99% for electrons and muons respectively.). For electrons the $t\bar{t}$ and $b\bar{b}$ contributions, which we expect to behave similarly, as they are both dominated by b-jets, show a fairly good agreement. The W+jets and Z/γ^*+jets show a significant lower fake-efficiency than the one for $t\bar{t}$ and $b\bar{b}$, however. This could be understood from the fact that the W+jets and Z/γ^*+jets processes mostly consist of fake leptons from decay of light-flavoured hadrons, which we expect to have a lower fake-efficiency due to their relative soft p_{T} spectrum and corresponding smaller probability of being reconstructed compared with leptons from heavy-flavoured jets.

The agreement between the fake-efficiencies extracted from data and MC in the low $E_{\mathrm{T}}^{\mathrm{miss,rel}}$ region is investigate further. The plots in Figure 7.14a and b show the total MC fake-efficiency, for electrons and muons respectively, together with the corresponding fake-efficiency obtained from data using the $b\bar{b}$ control region. Underneath each plot the ratio of the two fake-efficiencies is plotted and fitted with a straight line in order to extract

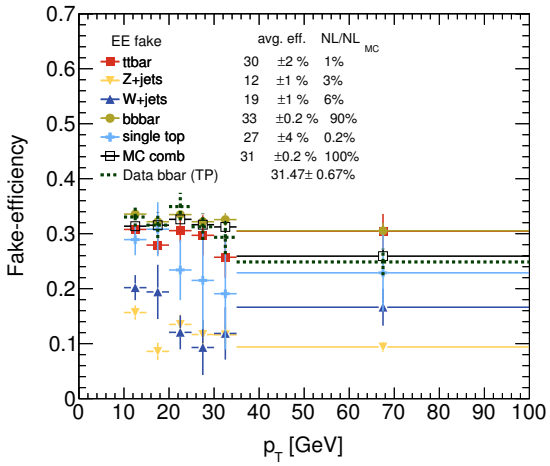

(a) ee with $E_{\mathrm{T}}^{\mathrm{miss,rel}} < 30$ GeV

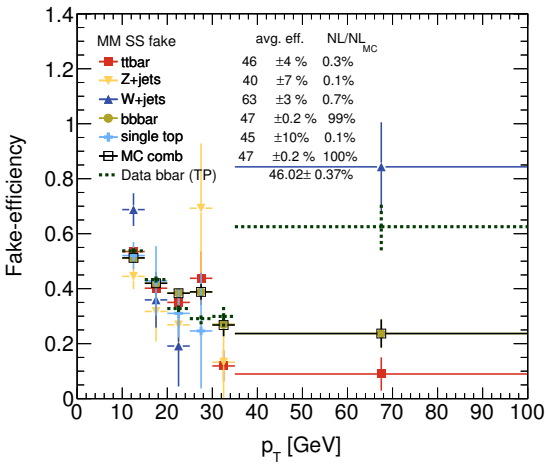

(b) $\mu\mu$ SS with $E_{\mathrm{T}}^{\mathrm{miss,rel}} < 30$ GeV

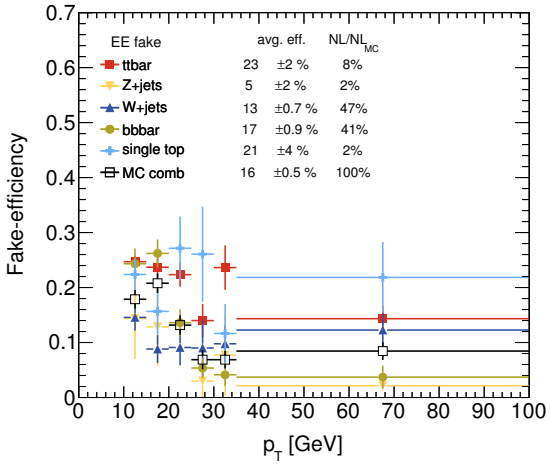

(c) ee with $40 < E_{\mathrm{T}}^{\mathrm{miss,rel}} < 100$ GeV

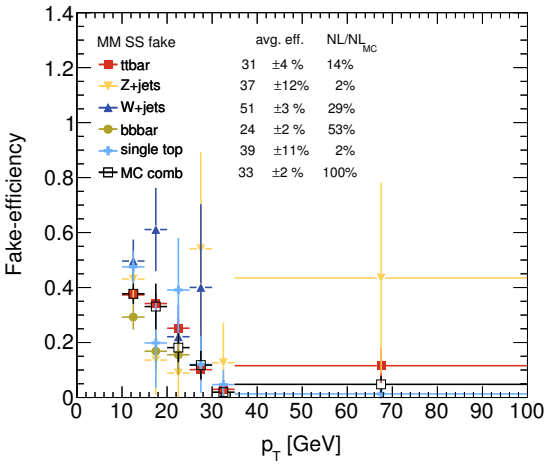

(d) $\mu\mu$ SS with $40 < E_{\mathrm{T}}^{\mathrm{miss,rel}} < 100$ GeV

Figure 7.13: The fake-efficiencies from the most important MC processes using truth are shown as coloured markers, together with the combined MC fake-efficiency in black open squares. The two left plots show the electron fake-efficiency from OS and SS ee-events while the right plots show the corresponding muon fake-efficiency in SS $\mu\mu$-events. The upper two plots show the low $E_{\mathrm{T}}^{\mathrm{miss,rel}}$ region ($E_{\mathrm{T}}^{\mathrm{miss,rel}} < 30$ GeV) while the two bottom plots are for the intermediate $E_{\mathrm{T}}^{\mathrm{miss,rel}}$ region ($40 < E_{\mathrm{T}}^{\mathrm{miss,rel}} < 100$ GeV). The legend gives the average fake-efficiency and the ratio of each MC component. The dashed black line in the upper two plots is the fake-efficiency from data in the $b\bar{b}$ tag-and-probe control region.

an overall scale factor between data and MC. The best fits, assuming a constant ratio

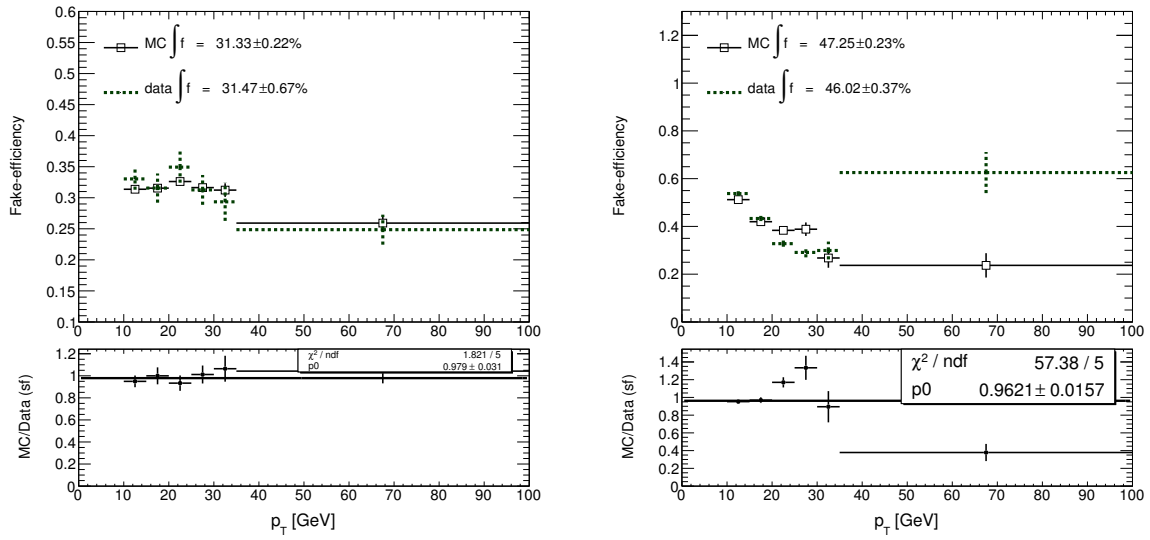

(a) electrons

(b) muons

Figure 7.14: The fake-efficiencies obtained from MC and data with the corresponding ratio between them in the $E_{\mathrm{T}}^{\mathrm{miss,rel}} < 30$ GeV region. The data fake-efficiency is taken from the $b\bar{b}$ tag-and-probe control region while the MC fake-efficiencies are as in Figure 7.13a and b.

between the fake-efficiencies from MC and data, yield 0.979 ± 0.031 and 0.9621 ± 0.0157 for electrons and muons respectively. The deviations from unity are included in the final systematic uncertainties on the fake-efficiency. It is reasonable to assume that the agreement between data and MC also holds for an intermediate $E_{\mathrm{T}}^{\mathrm{miss,rel}}$ region between 40 and 100 GeV. This is however hard to prove, since it would be difficult to construct a region dominated by fake leptons within this $E_{\mathrm{T}}^{\mathrm{miss,rel}}$ range in data.

Figures 7.13c and d show similar fake-efficiencies as in Figures 7.13a and b but for a higher $E_{\mathrm{T}}^{\mathrm{miss,rel}}$ region, $40 < E_{\mathrm{T}}^{\mathrm{miss,rel}} < 100$ GeV. Still only the SS $\mu\mu$ events are used. As expected, the contribution from other processes than $b\bar{b}$, such as $t\bar{t}$, W+jets and single top are more important in this intermediate $E_{\mathrm{T}}^{\mathrm{miss,rel}}$ region compared with the low $E_{\mathrm{T}}^{\mathrm{miss,rel}}$ region. The overall fake-efficiency is also much lower in the intermediate region, being 15.5 and 33% for electrons and muons respectively (compared with 31.3 and 47.2% in the low $E_{\mathrm{T}}^{\mathrm{miss,rel}}$ region). This is not only because of the more important light jet component from W+jets in the intermediate $E_{\mathrm{T}}^{\mathrm{miss,rel}}$ region. Each MC component exhibits in fact an intrinsic dependency on $E_{\mathrm{T}}^{\mathrm{miss,rel}}$, as shown in Figures 7.15a and b. Here the fake-efficiency is averaged over p_{T} [3] and scaled to the average MC fake-efficiency in the complete $40 < E_{\mathrm{T}}^{\mathrm{miss,rel}} < 100$ GeV range (from Figure 7.13c and d). The horizontal line at 1 therefore corresponds to the nominal fake-efficiency, and any deviation from this indicates a dependency on $E_{\mathrm{T}}^{\mathrm{miss,rel}}$. The maximum and minimum deviation from unity is included in the final systematic uncertainty on the fake-efficiency. Most pronounced is in fact the $E_{\mathrm{T}}^{\mathrm{miss,rel}}$ dependency in the $b\bar{b}$ MC, but since we expect the $t\bar{t}$ and W+jets to constitute most of the fake lepton background at high $E_{\mathrm{T}}^{\mathrm{miss,rel}}$ we only include the

[3] The $E_{\mathrm{T}}^{\mathrm{miss,rel}}$ dependency is found to be the same for all p_{T} as illustrated in Section A.3 of Appendix A.

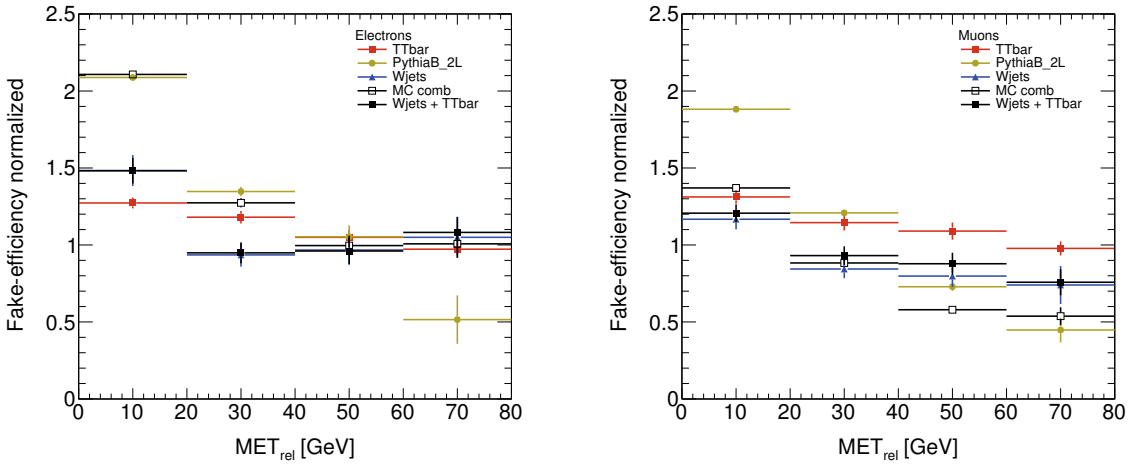

(a) ee (b) $\mu\mu$

Figure 7.15: The average fake-efficiency for the various MC samples as a function of $E_{\mathrm{T}}^{\mathrm{miss,rel}}$ scaled to the total fake-efficiency from MC in the region $40 < E_{\mathrm{T}}^{\mathrm{miss,rel}} < 100$ GeV.

dependency of these two (shown as black squares) in the systematic uncertainty. An upward systematic uncertainty of 50% (from the first bin in Figure 7.15a) was found in the electron channel, as none of the bins have a value below unity. For muons a symmetric uncertainty of ±20% (from the first and last bin in Figure 7.15b) was found.

7.2.2.1 Composition of Control Regions

In the low $E_{\mathrm{T}}^{\mathrm{miss,rel}}$ SS di-electron control regions none of the QCD MC samples succeed in describing the fake electron contribution (see Section A.1). In the low $E_{\mathrm{T}}^{\mathrm{miss,rel}}$ SS di-muon control region, however, the PythiaB di-muon filtered sample (*mu10mu10X*), succeeds in at least describing the shape of the fake muon contribution fairly well, as shown in Figure 7.16, although the normalization still seems to be off by a factor ~ 1.5. The agreement is nevertheless found to be satisfactory enough to study the composition in more detail. Obviously, a similar study for electrons would not give any reliable information.

Table 7.5 shows the various fake muon components taken from all SM MC (including the *mu10mu10X* sample) using the truth information events requiring SS muons. Shown are the total number of inclusive loose muons (N_L), the number of inclusive loose muons categorized as fakes (N_L^{fakes}, includes leptons from both light- and heavy-flavoured hadron decays) and those found to come from decays of heavy-flavoured hadrons only (N_L^{heavy}), identified according to Table 6.14. The ratio of each of these categories compared to the total number of inclusive loose muons indicates the amount of fake muons in each bin of p_{T} and in the two $E_{\mathrm{T}}^{\mathrm{miss,rel}}$ regions, below 30 GeV and between 40 GeV and 100 GeV.

For the low $E_{\mathrm{T}}^{\mathrm{miss,rel}}$ region the fake muons dominate the sample of inclusive loose leptons, with $> 90\%$ of the muons classified as fakes for $p_{\mathrm{T}} < 30$ GeV. Above 30 GeV the amount of fake muons decreases steadily down to 15% for $p_{\mathrm{T}} > 40$ GeV. The fractions of fake leptons are somewhat smaller in the intermediate $E_{\mathrm{T}}^{\mathrm{miss,rel}}$ region, ranging from 80% in the lowest p_{T}-bin to only 1% in the highest p_{T}-bin. The available statistics of fake leptons in the $p_{\mathrm{T}} \gtrsim 30$ GeV range is therefore limited. Overall the heavy-flavour

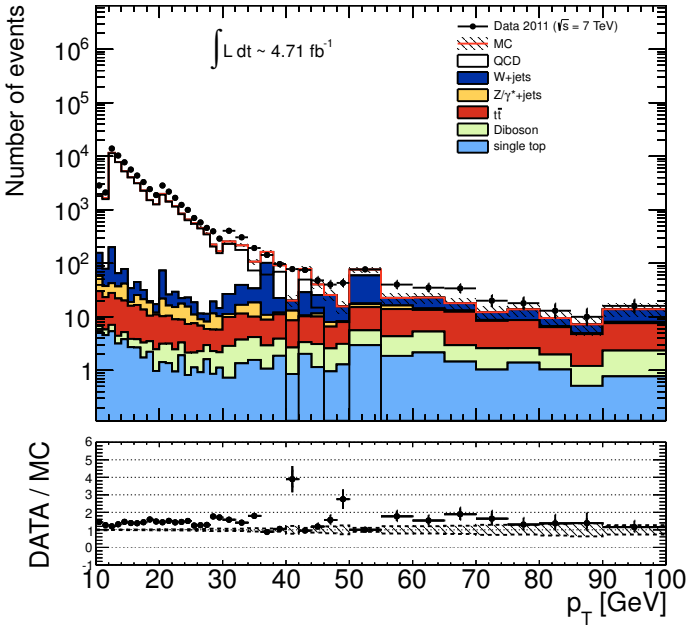

Figure 7.16: The momentum of all inclusive loose muons in the low $E_{\mathrm{T}}^{\mathrm{miss,rel}}$ SS di-muon fake control region. The PythiaB *mu10mu10X* sample is used to model the QCD. The steps at $p_{\mathrm{T}} \sim 12$ GeV and $p_{\mathrm{T}} \sim 20$ GeV in the distribution, coincide with the thresholds of the single- and di-muon triggers, as shown in Table 6.15. The steps at $p_{\mathrm{T}} \sim 30$ GeV and $p_{\mathrm{T}} \sim 50$ GeV come from the histogram binning which changes from 1 to 2 GeV and from 2 to 5 GeV at the two points respectively.

component dominates in most regions, however, at low p_{T} there seems to be a small fraction coming also from other sources; this is especially visible in the intermediate $E_{\mathrm{T}}^{\mathrm{miss,rel}}$ region.

7.2.2.2 Systematic Study of the Uncertainty from the QCD Normalization of the Heavy-Flavour Components

The final QCD fake-efficiency used in the analysis is taken from an intermediate $E_{\mathrm{T}}^{\mathrm{miss,rel}}$ region using MC truth, as already discussed in Section 7.2.2. The use of MC to extract the fake-efficiencies is justified from the relatively good agreement between data and MC in the low $E_{\mathrm{T}}^{\mathrm{miss,rel}}$ region seen in Figure 7.14. Despite this, none of the available MC samples are found to give a completely satisfactory description of the fake leptons from QCD events, and then in particular leptons from decays of heavy-flavoured jets, which seem to be the dominant source. The final fake-efficiency would possibly be sensitive to the exact amount of heavy-flavour in the intermediate $E_{\mathrm{T}}^{\mathrm{miss,rel}}$ region. The other main source of fake leptons from heavy-flavoured jets is $t\bar{t}$, and as shown in Figures 7.13c and d, the QCD heavy-flavour and $t\bar{t}$ components have slightly different average fake-efficiencies.

To evaluate the effect an upward or downward scaling of the heavy-flavour QCD component would have on the final fake-efficiency, a weighted fake-efficiency, f_{heavy}, of the $t\bar{t}$ and heavy-flavour QCD components was made, given by

$$f_{\mathrm{heavy}} = f_{\text{HF-QCD}} \cdot w_{\text{HF-QCD}} + f_{t\bar{t}} \cdot (1.0 - w_{\text{HF-QCD}}), \tag{7.25}$$

Region	$10 < p_{\mathrm{T}} < 15$ GeV				
	N_L	N_L^{fakes}	N_L^{fakes}/N_L	N_L^{heavy}	N_L^{heavy}/N_L
$E_{\mathrm{T}}^{\mathrm{miss,rel}} < 30$ GeV	40899.2	40526.3	0.99	40271.4	0.98
$40 < E_{\mathrm{T}}^{\mathrm{miss,rel}} < 100$ GeV	986.1	784.0	0.80	593.6	0.60

Region	$15 < p_{\mathrm{T}} < 20$ GeV				
	N_L	N_L^{fakes}	N_L^{fakes}/N_L	N_L^{heavy}	N_L^{heavy}/N_L
$E_{\mathrm{T}}^{\mathrm{miss,rel}} < 30$ GeV	18583.5	18241.1	0.98	18153.3	0.98
$40 < E_{\mathrm{T}}^{\mathrm{miss,rel}} < 100$ GeV	423.6	229.5	0.54	214.7	0.51

Region	$20 < p_{\mathrm{T}} < 25$ GeV				
	N_L	N_L^{fakes}	N_L^{fakes}/N_L	N_L^{heavy}	N_L^{heavy}/N_L
$E_{\mathrm{T}}^{\mathrm{miss,rel}} < 30$ GeV	8001.2	7668.0	0.96	7644.5	0.96
$40 < E_{\mathrm{T}}^{\mathrm{miss,rel}} < 100$ GeV	426.1	127.0	0.30	123.7	0.29

Region	$25 < p_{\mathrm{T}} < 30$ GeV				
	N_L	N_L^{fakes}	N_L^{fakes}/N_L	N_L^{heavy}	N_L^{heavy}/N_L
$E_{\mathrm{T}}^{\mathrm{miss,rel}} < 30$ GeV	2389.5	2156.6	0.90	2152.3	0.90
$40 < E_{\mathrm{T}}^{\mathrm{miss,rel}} < 100$ GeV	360.7	68.4	0.19	66.6	0.18

Region	$30 < p_{\mathrm{T}} < 35$ GeV				
	N_L	N_L^{fakes}	N_L^{fakes}/N_L	N_L^{heavy}	N_L^{heavy}/N_L
$E_{\mathrm{T}}^{\mathrm{miss,rel}} < 30$ GeV	903.4	622.1	0.69	616.6	0.68
$40 < E_{\mathrm{T}}^{\mathrm{miss,rel}} < 100$ GeV	219.9	52.2	0.24	52.0	0.24

Region	$35 < p_{\mathrm{T}} < 40$ GeV				
	N_L	N_L^{fakes}	N_L^{fakes}/N_L	N_L^{heavy}	N_L^{heavy}/N_L
$E_{\mathrm{T}}^{\mathrm{miss,rel}} < 30$ GeV	471.3	222.8	0.47	220.2	0.47
$40 < E_{\mathrm{T}}^{\mathrm{miss,rel}} < 100$ GeV	193.1	21.9	0.11	21.8	0.11

Region	$p_{\mathrm{T}} > 40$ GeV				
	N_L	N_L^{fakes}	N_L^{fakes}/N_L	N_L^{heavy}	N_L^{heavy}/N_L
$E_{\mathrm{T}}^{\mathrm{miss,rel}} < 30$ GeV	578.7	84.2	0.15	83.6	0.14
$40 < E_{\mathrm{T}}^{\mathrm{miss,rel}} < 100$ GeV	339.2	2.8	0.01	2.8	0.01

Table 7.5: The number of all inclusive loose muons in MC (N_L) together with those classified as fakes (N_L^{fakes}) and/or as coming from heavy-flavoured hadron decays (N_L^{heavy}) in events requiring SS muons. The ratio of each category, relative to the total number of loose leptons, is also shown. All numbers are divided into bins of p_{T} and into two separate $E_{\mathrm{T}}^{\mathrm{miss,rel}}$ regions, below 30 GeV and between 40 GeV and 100 GeV. The numbers are scaled to an integrated luminosity of 4.71 fb^{-1}.

where $f_{\text{HF-QCD}}$ and $f_{t\bar{t}}$ are the fake-efficiencies of the QCD heavy-flavour and $t\bar{t}$ components respectively, taken from Figure 7.13c and d. The weight $w_{\text{HF-QCD}}$ is the relative amount of the heavy-flavour QCD component. Table 7.6 shows the individual electron and muon fake-efficiencies from the *HF-QCD* and $t\bar{t}$ MC in the intermediate $E_{\text{T}}^{\text{miss,rel}}$ region. The last three columns contain the average fake-efficiency with the $w_{\text{HF-QCD}}$ as predicted by MC (f_{heavy}^{nom}) and the result when varying it down (f_{heavy}^{down}) or up (f_{heavy}^{up}) by a factor 2 with respect to the prediction. The factor 2 is chosen from the discrepancy seen in the ratio plot in Figure 7.16, where the MC seems to be off by a factor $\sim 1.5 - 2$. The deviations in percent from f_{heavy}^{nom} found in this study are included in the systematic uncertainty on the fake-efficiencies, found to be $^{+15}_{-5}\%$ and $^{+10}_{-5}\%$ for the di-electron and di-muon control regions respectively.

	$f_{t\bar{t}}[\%]$	$f_{\text{HF-QCD}}[\%]$	$f_{\text{heavy}}^{nom}[\%]$	$f_{heavy}^{\text{down}}[\%]$	$f_{heavy}^{\text{up}}[\%]$
ee	17.1	22.8	18.0	17.1	20.5
$\mu\mu$	31.1	23.8	25.3	24.0	28.2

Table 7.6: The first two columns give the individual electron and muon fake-efficiencies in % from the heavy-flavour $t\bar{t}$ and QCD MC, respectively, in the intermediate $E_{\text{T}}^{\text{miss,rel}}$ region, obtained from Figure 7.13c and d. The next three columns show the weighted average of the two fake-efficiencies and the result when scaling up or down the weight of the *HF-QCD* component by a factor 2.

7.2.3 Conversion Fake-Efficiencies from Data Control Regions

In the electron channel some extra studies are needed since the heavy-flavoured part has been shown to not explain the full spectra of fake electrons. The conversion component constitutes an important part of the fake electron background. In order to study the fake-efficiency for electrons from conversions a dedicated control region dominated by $Z \rightarrow \mu\mu + \gamma$ has been chosen [132]. The region requires two muons in addition to exactly one electron, coming from the conversion of a photon. The other electron from the converted photon, carrying a much smaller fraction of the photon's energy, is not reconstructed. To ensure that the three leptons are all connected with the Z-decay the invariant mass is required to be within a Z-mass window. A b-jet veto is also applied in order to suppress possible backgrounds from Z+jets, where an electron might come from a decay within a b-jet. The $t\bar{t}$ and W backgrounds are rejected by requiring the transverse mass of the electron and $E_{\text{T}}^{\text{miss}}$ to be less than 40 GeV. In order to be orthogonal to the signal regions an upper $E_{\text{T}}^{\text{miss,rel}}$ cut is used. Summarizing the discussion above, the control region is defined by requiring:

1. exactly two OS baseline muons (before overlap removal), one having $p_T > 18$ GeV
2. exactly one baseline electron
3. invariant mass of the three leptons within 80-100 GeV
4. b-jet veto
5. $E_{\text{T}}^{\text{miss,rel}} < 50$ GeV (not < 30, in order to gain some statistics)
6. invariant mass of the two muons > 20 GeV
7. transverse mass of the electron and $E_{\text{T}}^{\text{miss}}$, $m_T^{e,E_{\text{T}}^{\text{miss}}} < 40$ GeV.

Since this would give a sample enhanced in $Z\rightarrow \mu\mu+\gamma$ events, we do not expect the region to contain any charge-flip processes. The fake-efficiency obtained from this region is therefore valid for electrons stemming from other types of conversion processes.

A detailed study of the conversion control region, using MC truth, is presented in Figure 7.17, showing the origin of all inclusive loose (a) and tight (b) electrons. As

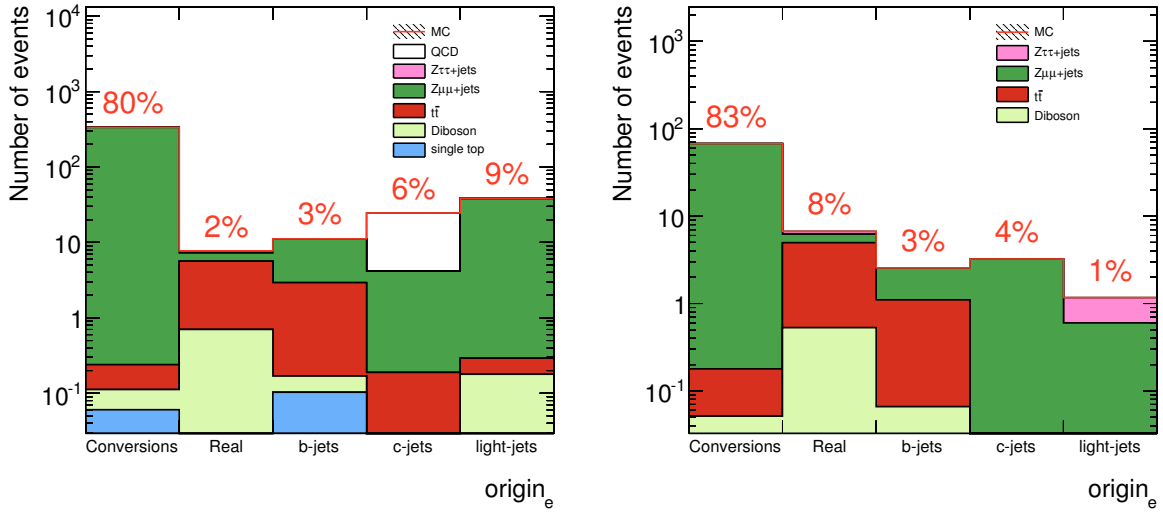

(a) inclusive loose electrons

(b) tight electrons

Figure 7.17: The origin of the inclusive loose (a) and tight (b) electrons in the conversion control region identified using truth MC. The percentage indicates the relative amount of each component.

expected the region is dominated by conversion electrons, which constitute 80 and 83% of the total number of inclusive loose and tight electrons, respectively. As expected, the $Z\rightarrow \mu\mu$ MC sample clearly dominates. From this study it is clear that the control region is highly contaminated by electrons from conversion processes. The agreement between the fake-efficiencies obtained using data and MC is therefore investigated further. Figure 7.18 shows the fake-efficiency measured using the conversion control region in data and MC. In MC, both the fake-efficiency using all leptons (black squares) or only true conversions (red squares) are shown. There is a quite good agreement between data and both of the fake-efficiencies from MC over the complete p_{T} range. The average fake-efficiencies are found to vary between 20-25%, although they all agree within the uncertainties, which for the efficiencies in MC are quite large.

7.2.4 Summary of the Fake-Efficiency Calculation

Section A.1 in Appendix A summarizes how the various QCD MC samples perform in describing the fake lepton contribution in the QCD control regions. For muons the agreement is found to be rather good in all regions using the PythiaB samples, while for electrons only the single-lepton control region revealed a fairly good description, at least of the shape of the data distribution. The overall normalization is found to still be off, with the PythiaB *bbe15X* sample underestimating and the JF17+35 samples overestimating the data, as illustrated in Figures 7.19a and b respectively. Since the fake muons are

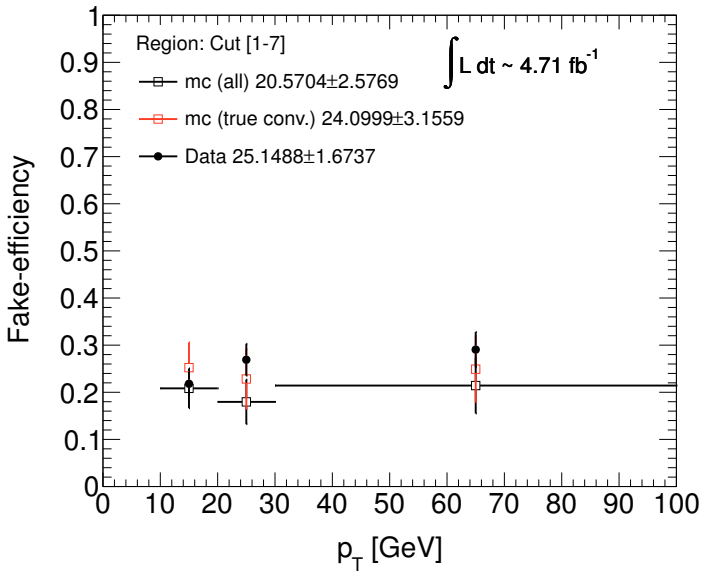

Figure 7.18: Fake-efficiency for electrons taken from the conversion control region. Squares show the fake-efficiency extracted from MC by using all electrons in the control region (black) or using truth to identify actual conversions (red). The circles show the fake-efficiency extracted from data. Errors are purely statistical.

rather well described it is obvious to think that the discrepancy in the electron channel lies in the modelling of the conversion component (which is negligible for muons) and differences in the amount of fake leptons expected from light-flavoured hadron decays in the two channels. The PythiaB samples are enhanced in b- and c-jets and therefore underestimate any light-flavoured component, which seems to be more needed for electrons than muons.

It is natural to assume that light-flavoured jets more likely can fake electrons, stemming from charged and neutral pions, than muons. It is much less probable for jets to mimic two muons, since the muon reconstruction also relies on hits in the Muon Spectrometer. The muons must therefore come from kaon or pion decays, which eventually will lead to muons having much smaller momenta than the initial jets, thus having a smaller probability of being reconstructed. In order to get muons from light-flavoured hadrons the momenta of the jets need to be much higher, making the cross-section for such processes relatively small.

The other important component is the conversion electrons which also contributes to the total fake electron composition in the QCD control regions. Figures 7.19c and d show a more detailed view of the fake electron composition for the two QCD MC samples, PythiaB *bbe15X* (c) and JF17+35 (d), for all inclusive loose electrons in the single-lepton control region. The plots reveal quite some differences in the amount of conversion in the two samples. In *bbe15X* conversion electrons are totally absent, while they comprise 45% of the fake electrons in the JF17+35 sample. As expected the heavy-flavoured part is larger in *bbe15X*, while the *undefined* component is of the same order in the two samples. Light-flavoured jets are absent in both samples indicating that the *undefined* category probably contains some light-flavoured component.

Since the MC seems to describe fake muons rather well the final fake-efficiency for

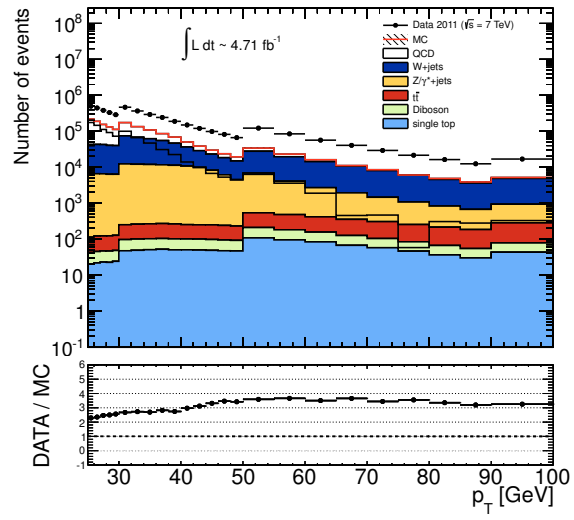

(a) PythiaB *bbe15X*

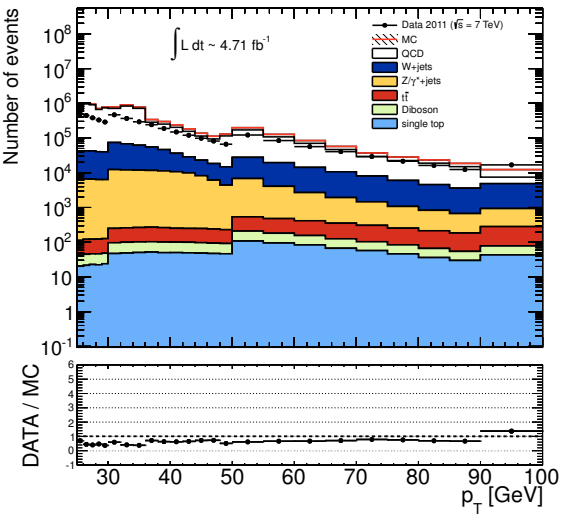

(b) JF17+35

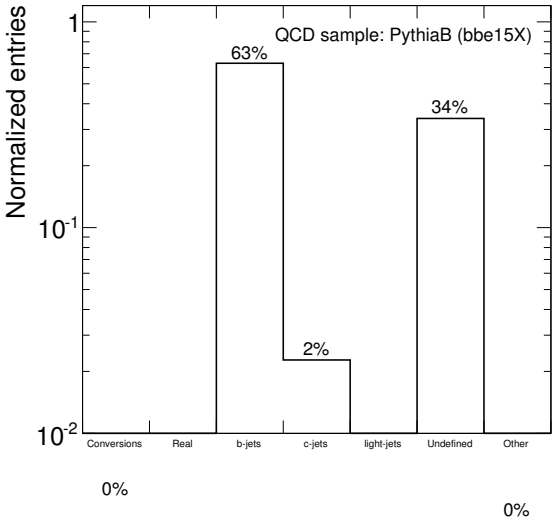

(c) PythiaB *bbe15X*

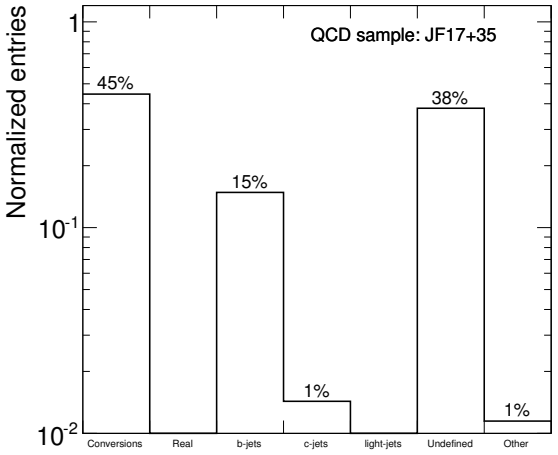

(d) JF17+35

Figure 7.19: The two upper plots show the momentum of all inclusive loose electrons in the single-lepton fake control region, *1L-R07*, using *PythiaB* (a) and *JF17+35* (b) to model the QCD component. The lower two plots show the corresponding fake electron components, only using the *PythiaB* (c) and *JF17+35* (d) MC samples.

muons will simply be extracted from an intermediate $E_{\mathrm{T}}^{\mathrm{miss,rel}}$ region in MC, as discussed in Section 7.2.2. Fake electrons, however, require a heavy-flavour QCD component, a conversion component as well as a less well defined light-flavour component. In the final analysis a weighted average of the fake-efficiency extracted from an intermediate $E_{\mathrm{T}}^{\mathrm{miss,rel}}$ region (using PythiaB samples to model the main QCD contribution) and the conversion fake-efficiency from the data control region in Section 7.2.3 are used. However, since the above discussion concluded that the light-flavoured component is somewhat underestimated in the used PythiaB samples, an additional systematic uncertainty is introduced. This is discussed in more detail when moving to the last part of the analysis in Chapter 8. First, a study of the real-efficiency needs to be performed.

7.2.5 Real-Efficiency

The other important ingredient in the MM is the real-efficiency which is measured using a Z control region (to be referred to as the real lepton control region) defined by requiring two OS leptons with an invariant mass within ± 5 GeV of the Z-mass. Figures 7.20a and b show the p_{T} of all inclusive loose leptons in the real control region for electrons and muons respectively. The ratio-plots, *data/MC*, underneath detail how data is reproduced by MC. The agreement is relatively good, especially for muons. For electrons a small discrepancy is seen at low p_{T}, probably coming from a small fake electron component and the fact that the trigger re-weighting is optimized for tight electrons while this plot includes exclusive loose electrons. Nevertheless, the regions are highly contaminated by

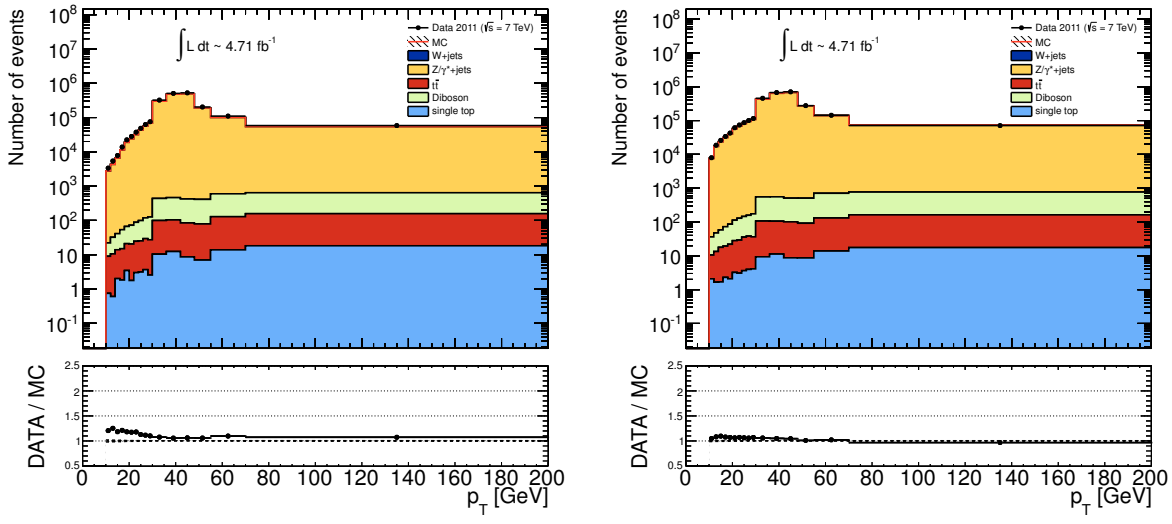

(a) electrons (b) muons

Figure 7.20: The transverse momentum of all inclusive loose electrons (left) and muons (right) from data and non-QCD SM backgrounds in events with two OS leptons having an invariant mass within ± 5 GeV of the Z-mass.

leptons from Z-decays, constituting $> 99\%$ of the total MC in both the electron and muon channel.

7.2.5.1 Real-Efficiency Dependency

The real-efficiencies are calculated in the same way as the fake-efficiencies using Method 1 and the single-lepton efficiency in Eq. 7.12. The dependencies of the real-efficiency on p_{T} and η are shown in Figure 7.21. The plots show the comparison between the real-efficiency computed from data, using the real lepton control region, and by using truth information in the $Z \rightarrow ll$ MC samples (i.e. Z+jets, WZ and ZZ). The agreement

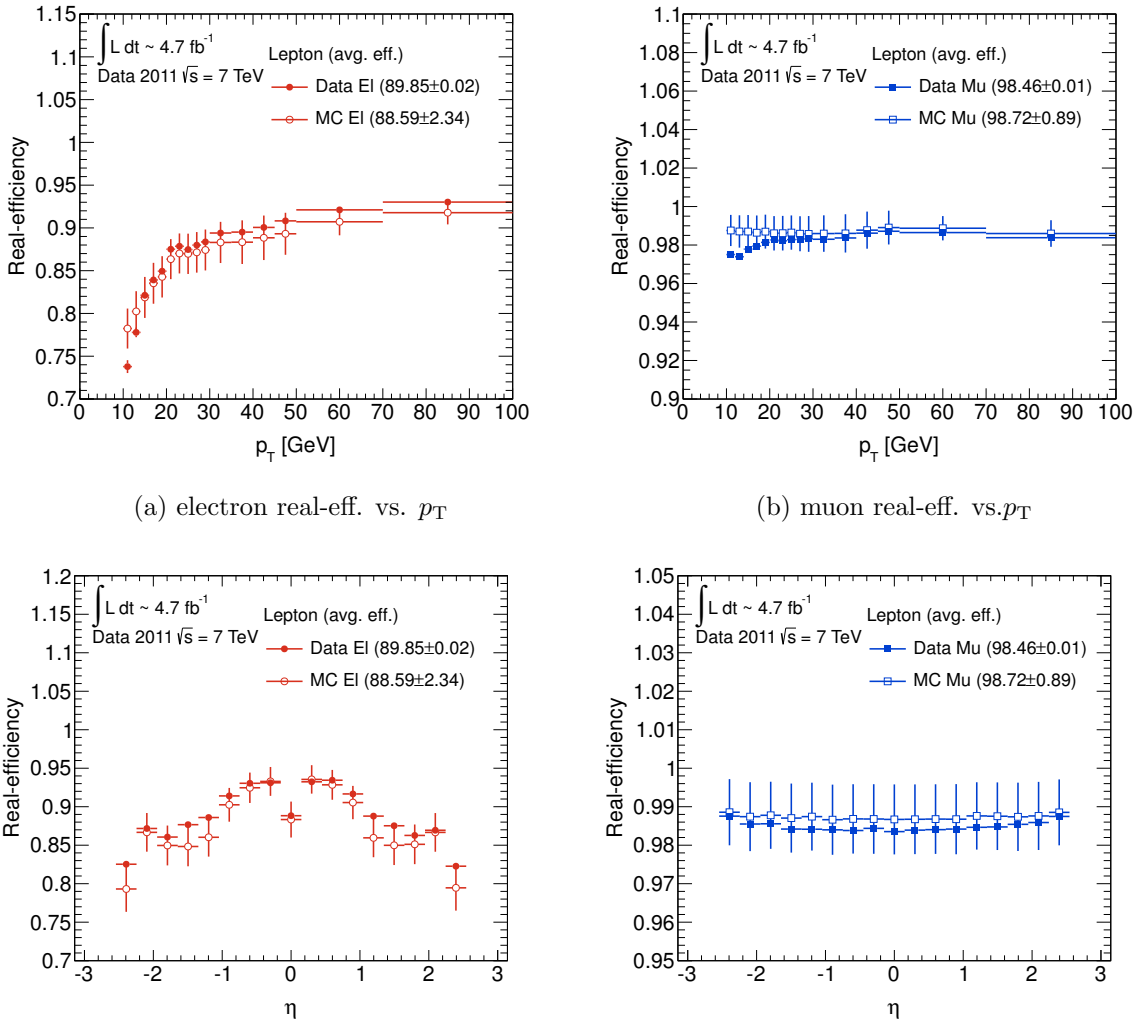

(a) electron real-eff. vs. p_{T}

(b) muon real-eff. vs.p_{T}

(c) electron real-eff. vs.η

(d) muon real-eff. vs.η

Figure 7.21: The real-efficiency for electrons and muons as function of p_{T} (upper) and η (lower). The left plots are for electrons while the right ones are for muons. Data (filled markers) is compared to MC (open markers). All errors are statistical only.

between data and MC is within uncertainties for most of the points. Small discrepancies are however observed, especially in the low p_{T} regions for muons and electrons. This can be understood from the discussion of the distributions in Figure 7.20, as there seems to be a small component missing at low p_{T} in the available MC. Small discrepancies are also observed in the η distribution for electrons, particular at high $|\eta|$. The errors in these points are however quite large. The muons show overall a very small dependency on both p_{T} and η. For the electrons, however, the dependencies are more visible. The

	SS + $E_{\mathrm{T}}^{\mathrm{miss,rel}}$> 100 GeV			OS + $E_{\mathrm{T}}^{\mathrm{miss,rel}}$> 100 GeV		
	ee	$e\mu$	$\mu\mu$	ee	$e\mu$	$\mu\mu$
p_{T} dep.	14.4 ± 3.0	20.1 ± 4.0	8.3 ± 3.0	23.7 ± 5.5	42.7 ± 7.2	9.95 ± 3.8
p_{T} +η dep.	14.4 ± 3.0	20.2 ± 4.0	8.3 ± 3.0	25.4 ± 5.5	44.0 ± 7.3	9.70 ± 3.8
max diff. (%)	0.05 (0.34%)	0.10 (0.50%)	0.04 (0.54%)	1.74 (7.37%)	1.37 (3.21%)	0.25 (2.47%)

Table 7.7: The fake lepton estimates in a SS/OS+$E_{\mathrm{T}}^{\mathrm{miss,rel}}$> 100 GeV region with and without an additional η dependency on the p_{T} dependent real-efficiency. Only statistical errors are included for the estimates.

real-efficiency rises as a function of p_{T} while the η dependency has a symmetric shape around $\eta = 0$, with lower efficiency at higher $|\eta|$ as well as close to $\eta = 0$, as to be expected from the geometry of the ATLAS ECal (described in Section 3.4.3). The p_{T} dependency is included in the computation of the final fake lepton estimates for both electrons and muons. The η dependency is however not applied since it is shown in Table 7.7 to have a minor effect on the final estimates. The table shows the estimations obtained when using a p_{T} dependency only and using a two-dimensional p_{T} +η dependency on the real-efficiency in two signal-like regions defined by requiring SS or OS together with a $E_{\mathrm{T}}^{\mathrm{miss,rel}}$> 100 GeV cut. The lowest row shows the maximal discrepancy between the largest and smallest estimation, with the relative deviation from the estimates using the p_{T} dependent real-efficiency only. The inclusion of an η dependency has a relatively small effect, $< 1\%$, for all channels in the SS region. In the OS region the effect is somewhat larger, from around 3% in the $e\mu$- and $\mu\mu$-channels to $\sim 7\%$ in the ee-channel, but the deviation is still within the statistical error on the estimate itself. The effect on the final estimates due to the omission of the η dependency of the real-efficiency can therefore safely be neglected.

The data-driven real-efficiency is extracted using a region dominated by Z-decays. The question is if real leptons from other types of processes, such as W+jets, $t\bar{t}$, di-boson or single top exhibit a different real-efficiency. In Figure 7.22 the real-efficiencies for leptons from various MC processes, using truth to identify real leptons, are shown. All processes are in quite good agreement especially at high p_{T}. At low p_{T} the statistics are quite limited for some of the samples and thus some of the discrepancies are not as dramatic as it might seem. Taking the average real-efficiencies quoted in the legends of the plots, the smallest and largest values in the electron channel, including the errors, are found to be 84.2%, for the Drell-Yan sample, and 89.2%, for single top, respectively. This gives a total relative variation of 5%, which, compared to the real-efficiency of 89.9% measured in data, accounts for a total uncertainty of about 6%. In the muon channel the real-efficiency ranges from 97%, for the $t\bar{t}$ sample, to 98.8% for the Drell-Yan sample, a total spread of 1.8%. Compared to the measured real-efficiency of 98.5% in data, this constitutes a 2% uncertainty. Both these uncertainties are included in the total systematic uncertainty on the real-efficiency.

All the ingredients of the MM, necessary to estimate the backgrounds from fake leptons, are finally in place. The last part of the SM background is settled, and it is time to go ahead and search for supersymmetry!

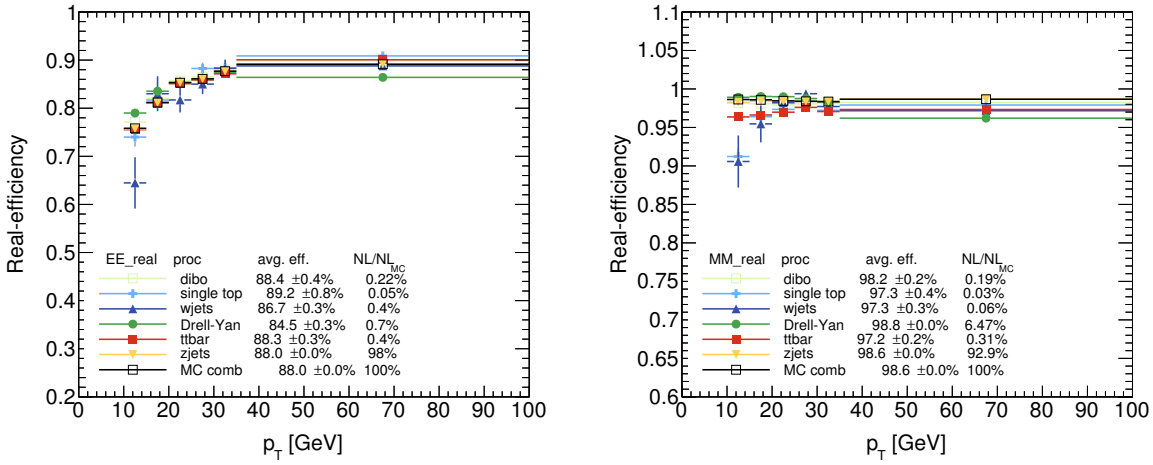

(a) electron real-eff. from MC

(b) muon real-eff. from MC

Figure 7.22: The real-efficiency for electrons (a) and muons (b) as function of p_{T} for the individual MC components as well as the sum. The legend gives the integrated real-efficiency and the relative fraction of each component separately. Errors are statistical only.

Chapter 8

Results of the Searches for Direct Gaugino and Slepton Production

In Chapter 5 the most interesting final states to consider in a search for supersymmetry requiring two leptons were discussed. This made it possible to briefly sketch the signal regions designed to target each of these final states. The signal regions were motivated by the characteristics of the final state, but at the same time kept a good rejection against the most important SM backgrounds. In Chapter 6 the samples used to model the SM backgrounds were introduced, and the exact definitions of the important objects in the analysis, electrons, muons, jets and $E_{\mathrm{T}}^{\mathrm{miss,rel}}$ were defined. A method to properly measure the background from fake leptons, which is not very well modeled in the current available MC, was studied in Chapter 7. In this chapter the exact cuts defining the signal regions are settled, by optimizing the signal to background ratio using the signal grids discussed in Section 5.3. However, to ensure a statistically reliable treatment of the results and to better understand the methods used in the signal region optimization in Section 8.2, some important statistical topics need first to be introduced in Section 8.1. With the final signal regions in place the contribution from the fake lepton background is estimated in Section 8.3. The relevant systematic uncertainties and the final background yields are summarized in Section 8.4 and 8.5 respectively, before moving to the results and interpretation of the searches in Section 8.6 and 8.7.

8.1 Probability and Statistics

Before moving to the main analysis of defining the signal regions, estimating the fake lepton background and finally interpreting the results from the full study in terms of exclusion limits, it is important to discuss the statistical tools and definitions which are commonly used in particle physics experiments. The first few subsections below introduce how to statistically interpret possible excesses, above the expected SM background, observed in data, and in case no such excesses are observed, how to set limits on the cross-section of new physics and interpret it in the various SUSY models. The procedure of optimizing the signal regions is also subject to statistical considerations and thus needs a serious and thorough treatment, to be discussed below.

8.1.1 Introduction

A particular important theorem in statistics is known as Bayes' theorem. It defines a relationship between the probability of A, $P(A)$, and B, $P(B)$, and the conditional probabilities of A given B, $P(A|B)$, and B given A, $P(B|A)$, [24]

$$P(A|B) = \frac{P(B|A)P(A)}{P(B)}, \tag{8.1}$$

where A and B are possible subsets of a sample-space S. The conditional probability $P(A|B)$ is defined

$$P(A|B) = \frac{P(B \cap A)}{P(B)}. \tag{8.2}$$

From this one can easily deduce the law of total probability

$$P(B) = \sum_i P(B|A_i)P(A_i), \tag{8.3}$$

with A_i being disjoint to each other and whose union is the entire sample space, S. In particle physics experiments the most common interpretation of the subsets of the sample-space are outcomes of each collision event. The probability $P(A)$ is assigned a value equal to the limiting frequency of occurrence of A. This interpretation forms the basis of **frequentist statistics**. The subsets of the sample-space can also be seen as statements (hypotheses) which are, from a frequentist point of view, either true or false. In **Bayesian statistics** this is however not the case. The probability, $P(A)$, is rather interpreted as the degree of belief that the hypothesis A is true. This is called subjective probability. In Bayesian statistics Bayes' theorem can simply be written

$$P(hypo|data) \propto P(data|hypo)P(hypo), \tag{8.4}$$

where *hypo* represents some hypothesis and *data* is the outcome of the experiment. The probability, $P(hypo)$, is the degree of belief in the hypothesis before performing the experiment, known as the prior probability. $P(data|hypo)$ is the probability of observing the actual outcome of an experiment given that the hypothesis is correct, also known as the likelihood. Once the prior probability is known and the experiment is carried out (i.e. the data is collected), Equation 8.4 gives the posterior probability which gives the probability of the hypothesis to be correct given the outcome of the experiment.

8.1.2 Significance

To claim that an observation is significant or not, requires a proper definition of significance. In counting-experiments, such as the one performed in this study, the outcome of the analysis is simply the number of events (or distribution) falling inside some particular signal region. Each collision recorded in ATLAS leads to an event which passes or fails the signal selection requirements. The number of events follow therefore a binomial distribution. The success probability, however, (i.e. probability of the event to pass the

selection) happens to be very small and the binomial distribution can be approximated by a Poisson distribution [133]. The probability of observing n events when ν events are expected for a specific hypothesis, H_0, is given by

$$P(n|\nu) = \frac{\nu^n}{n!}e^{-\nu}. \tag{8.5}$$

For the background-only hypothesis, ν is simply the number of background events. Let us assume that we observe a certain number of events, q_{obs}, in the experiment. If this is more than predicted by the background-only hypothesis we can calculate the p-value, p, which is the probability to actually observe at least q_{obs} events assuming only background, b,

$$p = P(n \geq q_{obs}|b) = \sum_{n=q_{obs}}^{\infty} \frac{b^n}{n!}e^{-b}. \tag{8.6}$$

Often one converts the p-value into a significance, z, in units of σ (standard deviations). For a given significance, defined as

$$z = \Phi^{-1}(1-p), \tag{8.7}$$

the upward fluctuation of a Gaussian random variable would have an upper tail with area equal to the p-value. The Φ^{-1} is the inverse of a standard Gaussian distribution. In high energy particle physics experiments an observation can be claimed to traditionally be a discovery when $z \geq 5\sigma$. This corresponds to a p-value of $2.87 \cdot 10^{-7}$ [24]. However, the credibility of such a claim relies on avoiding any biases in data selection, a proper estimation of the background and on an adequate choice of the techniques to compute the p-value.

8.1.3 Exclusion

Now that we have quantified the significance of any excess observed in a counting experiment, we have to deal with cases where no excess is seen above the expected background. In this unfortunate case the hypothesis of new physics predicted by some model can be excluded. This is done by defining another type of p-value, known as CL_{s+b} [134], which for the counting experiment is

$$CL_{s+b} = P(n \leq q_{obs}|s+b) = \sum_{n=0}^{q_{obs}} \frac{(s+b)^n}{n!}e^{-(s+b)}. \tag{8.8}$$

The CL_{s+b} is the probability to observe at most q_{obs} events in the experiment, given the signal+background hypothesis, which is excluded with a confidence level equal to $1 - CL_{s+b}$. In particle physics one often excludes a model when $CL_{s+b} \leq 5\%$. The probability to wrongly exclude a signal+background model is then 5%. A variation of the expected signal events leads to a value s_{up} which gives exactly $CL_{s+b} = 0.05$. All models giving $s \geq s_{up}$ are excluded at 95% confidence level (CL). The CL_{s+b} probability is shown in Figure 8.1a as the yellow area in case 13 events are observed and the two test statistics for background-only and signal+background hypotheses are $P(n|b)$ and $P(n|s+b)$ respectively.

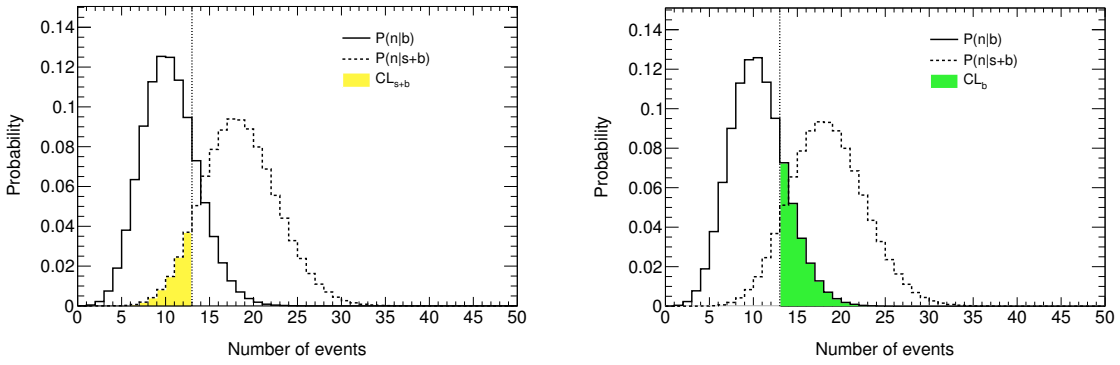

(a) CL_{s+b} (b) CL_b

Figure 8.1: The test statistics for the background-only and signal+background hypothesis. The left plots shows the p-value CL_{s+b} in yellow while the right plot illustrates the CL_b in green. The number of observed events, 13, is shown as the dashed vertical line.

8.1.3.1 Sensitive and Insensitive Searches

A limitation of CL_{s+b} is the possibility to exclude hypotheses to which one has little or no sensitivity. This typically happens when the expected number of signal events is much less than that of background. If $b >> s$ and the observed number of events has a sufficient downward fluctuation relative to $s + b$, the corresponding value of s is then excluded. Intuitively one expects the exclusion probability to go to zero, but using CL_{s+b} this probability goes in fact towards 5%. This would mean that in 5% of the experiments where $b >> s$ one would exclude a model to which one has no sensitivity! To protect against this a new p-value, CL_b, is introduced in the background-only hypothesis, defined analogous to CL_{s+b}

$$CL_b = P(n \leq q_{obs}|b) = \sum_{n=0}^{q_{obs}} \frac{b^n}{n!} e^{-(b)}. \tag{8.9}$$

The CL_b is shown as the green area in Figure 8.1b. $1 - CL_b$ differs from the p-value in Eq. 8.6 only by the inclusion or not of the observation in the full probability. The effective p-value, CL_s, used in exclusions is the ratio of the two p-values discussed above,

$$CL_s = \frac{CL_{s+b}}{CL_b}. \tag{8.10}$$

8.1.3.2 Likelihood Ratios

The quantity which evaluates how much a model A is more suited to explain the outcome of an experiment than another model B is called the test-statistic. In the previous section the number of observed events, q_{obs}, was used as test-statistic. In particle physics it has become common, instead, to use the likelihood ratio

$$Q = \frac{P(n|s+b)}{P(n|b)},$$

which using Equation 8.5 reads

$$Q = \left(1 + \frac{s}{b}\right)^n e^{-s}. \tag{8.11}$$

The p-values for exclusion, using the likelihood ratio as test statistics, observing Q_{obs}, becomes

$$CL_{s+b} = P(Q < Q_{obs}|s+b) = \sum_{Q \leq Q_{obs}} P(Q|s+b) \tag{8.12}$$

$$CL_b = P(Q < Q_{obs}|b) = \sum_{Q \leq Q_{obs}} P(Q|b). \tag{8.13}$$

In a simple counting experiment, using the likelihood ratio as test statistics would be identically to use q_{obs} as test statistics, i.e. Eq. 8.12 would be equal to Eq. 8.10. To calculate the p-values in 8.12 and 8.13, the probability distribution of the test-statistic must be known. This is usually done by generating a sufficient number of pseudo-experiments and counting how often each value of the test-statistic appears. In order to obtain both p-values we need to generate pseudo-experiments under both background-only and signal + background hypotheses. For the counting experiment, a pseudo-experiment corresponds to generating one Poisson-distributed random number with mean b or $s + b$ for the background-only or signal+background hypothesis.

The inclusion of various systematic uncertainties is crucial in the limit calculation. Systematic uncertainties are in statistics often referred to as *nuisance parameters*. One typically models the systematic uncertainty using a Gaussian distribution with a standard deviation equal to the size of the error. Then, for each pseudo-experiment, the value of each of the *nuisance parameters* are generated according to the Probability Density Functions (PDF). This, of course, alters the distribution of the test-statistics and changes the produced limits.

8.1.3.3 The Profile Likelihood Method

A commonly used method in high energy particle physics is the profile likelihood method. Let the expected outcome of an experiment, $E(n)$, be expressed by

$$E(n) = \mu s + b, \tag{8.14}$$

where s and b are the signal and background contributions respectively. The parameter μ is known as the signal-strength and from Eq. 8.14 one can easily deduce that $\mu = 0$ corresponds to the background-only hypothesis while $\mu = 1$ correspond to the signal + background hypothesis. Given the outcome of the experiment one can construct the likelihood function using Equation 8.5:

$$L(\mu, \theta) = \frac{(\mu s + b)^n}{n!} e^{-(\mu s + b)},$$

which depends on the signal strength parameter and a set of nuisance parameters, θ, included in the value b. The profile likelihood ratio, to test a hypothesized value of μ

against the alternatives following Eq. 8.10 becomes

$$\lambda(\mu) = \frac{L(\mu, \hat{\hat{\theta}})}{L(\hat{\mu}, \hat{\theta})}. \tag{8.15}$$

The numerator is the profile likelihood function with $\hat{\hat{\theta}}$ being the value of θ maximizing L for the hypothesized value of μ and thus depends on μ. The denominator is the likelihood function where $\hat{\mu}$ and $\hat{\theta}$ are the true maximum likelihood estimators. The profile likelihood ratio can therefore take values from 1, when the hypothesized μ coincides with $\hat{\mu}$ and 0 when the assumed μ is in total disagreement with $\hat{\mu}$. The first scenario corresponds to the case where the observation fits very well the hypothesis and the latter when there is a high degree of incompatibility between data and the hypothesis. The presence of the nuisance parameters typically broadens the profile likelihood and thus reflects the loss of information about μ due to systematic uncertainties.

According to Wilks' theorem the null hypothesis is defined as the case where μ totally coincides with the true value, $\hat{\mu}$. Under the null hypothesis the theorem ensures that the quantity known as the log-likelihood ratio, $t = 2\ln\lambda(\mu)$, is asymptotically distributed according to a χ^2 function with degrees of freedom equal the difference between the number of maximization parameters in the denominator and numerator of Eq. 8.15.

When scanning over many different signal models, which often is the case in searches for supersymmetry, a large number of pseudo-experiments must be generated, which computationally can be quite challenging and time consuming. There is, however, a less computationally demanding method available, based on approximating the probability distribution of the test-statistics by asymptotic formulas [135]. The approximations become in fact exact in the large sample limit, but it has been shown that accurate results are obtained even for fairly small sample-sizes. Generating pseudo-experiments is the standard method used in ATLAS searches, including the publication this thesis is based on [12]. In the following analysis, however, the asymptotic method is used and the results are cross-checked against the published limits.

8.1.4 Statistical Poisson Limits

In this analysis the statistical errors on the number of observed events, n, are the statistical Poisson limits at 68% CL. This means that the probability of observing a value larger (smaller) than the computed upper (lower) limit is 32%. The relationship between the cumulative distribution functions of the Poisson and χ^2 distributions can be used to compute the 68% confidence interval for the mean, $\langle n \rangle$, of a Poisson distribution [24]

$$\frac{1}{2}F^{-1}_{\chi^2}\left(\frac{0.32}{2}; 2n\right) \leq n \leq \frac{1}{2}F^{-1}_{\chi^2}\left(1 - \frac{0.32}{2}; 2(n+1)\right). \tag{8.16}$$

$F^{-1}_{\chi^2}(p;k)$ is the quantile function of the chi-square distribution with k degrees of freedom, specifying the value at which a randomly distributed Poisson variable will be at, or below, with a probability p. If the number of events observed is more than 1000 the Pearson's

χ^2 intervals are instead used, and the upper and lower limits on the error band are then given by

$$\sigma_{upper} = n + \sqrt{n + 0.25} + 0.5 \text{ and}$$
$$\sigma_{lower} = n - \sqrt{n + 0.25} + 0.5$$

respectively [136].

8.1.5 HistFitter

The statistical treatment for the current analysis is based on the profile likelihood method implemented using *HistFitter* [137]. This section introduces the details and the exact implementation of the limit setting procedure.

HistFitter is a package developed within the ATLAS SUSY Working Group and serves as an interface to the *HistFactory* package in ROOT. *HistFactory* is a tool to build parametrized Probability Density Functions (PDF) based on ROOT histograms organized within an XML file. The PDFs are stored in RooWorkspaces [138].

8.1.6 Implementation

The various signal regions are described by PDFs which are implemented as a collection of one-bin histograms, where each histogram holds the number of events in a specific signal region. This means that several histograms are produced for each background and signal. A separate histogram is made for the nominal counts as well as the counts including each systematic uncertainty, modeled by *nuisance parameters* that are constrained by Gaussians. The width of each constraint is specified from external input, as will be clarified in Section 8.4. The observed number of events in data is stored in one-bin histograms in a similar manner.

The PDF includes free parameters, which are scaling factors that can adjust the relative contribution of the various background and signal components.

A signal strength parameter, μ, is introduced such that $\mu = 0$ correspond to the background only hypothesis and $\mu = 1$ to the signal+background hypothesis.

The nominal numbers of events for the backgrounds and signals are fed into HistFitter by using TTrees. They contain necessary variables to specify various search signal regions. The number of observed events is also taken from a TTree by running through the data.

Each systematic uncertainty is either implemented as a separate TTree or by using event weights. TTrees are typically used for systematic uncertainties affecting the energy and/or momentum of the objects. Then, for each background, there is a separate TTree named *bkgName_systUnc* which contains exactly the same leaves as the nominal TTree, but with the variables shifted according to the systematic uncertainty. When the systematic uncertainty only affects the event weight, meaning that none of the properties of the

objects are changed, the effect is introduced by simply adding an appropriate contribution to the nominal event weight. In *HistFitter* one can specify which systematics uncertainties should be applied to which backgrounds. One can also specify different systematic uncertainties for different signal regions. For instance a signal region using a cut on b-jets will have an additional systematic uncertainty coming from the flavour tagging procedure (see Section 8.4).

When calculating model-independent upper limits on a cross-section, one uses typically a *dummy* signal model with exactly one event in the signal region.

Although only one-bin histograms are used in the calculations, the number of nuisance parameters for all systematics is rather large. This means that there are most probably multiple parameters having the same effect on the likelihood, i.e. scaling the bin up or down. The model therefore becomes ill-defined as there are many redundant parameters that are strongly correlated. In case of a multi-bin histogram there are more degrees of freedom, so having more parameters is less troublesome. The upper limit calculation is therefore performed in a two-step way.

First the correlations between all the various background systematics are computed, and the total number of background events and the corresponding total systematic uncertainty is calculated. This latter is then added in quadrature with the statistical uncertainty, giving the total background uncertainty for that region. The total error together with the total number of background events are then used when performing the final upper limit calculations. This prevents the limits from being unstable.

8.2 Signal Region Definitions

On the basis of the studies of various di-lepton final states in scenarios with direct gaugino and slepton production in Chapter 5 some appropriate signal regions, *OS-jetveto*, *SS-jetveto*, *OS-2jets* and *mT2*, were introduced in Section 5.5. In this section a more thoroughly study of the cuts used to define the four signal regions is described.

In Ref. [12, 76] the optimization of the signal regions was done before the complete 4.7 fb^{-1} of data had been collected. The exact amount of data to be used for the final analysis in the end was also not known. The optimization was therefore performed with the first 1.23 fb^{-1} of data, and before all the details regarding systematic uncertainties, trigger procedure, object definitions, analysis framework etc. were properly settled. The results of the optimization could therefore possibly have lead to slightly different cuts as the ones used in this analysis if it would have been re-done with today's knowledge and amount of data. Using the exact same data sample for optimization and justification as one plans to use for the final analysis is however not recommended as it can lead to large biases in the selection. Throughout this Section the same cuts as in the final publication are used, and the reader is referred to Refs. [12, 76] for further details about the optimization procedure. All the SM backgrounds are in the following taken from the MC simulations except the fake lepton and charge-flip backgrounds. The charge-flip contribution is estimated as described in Section 5.4.1.1. The background from fake leptons is estimated using the Matrix Method as explained in detail in Chapter 7. All distributions are normalized to an integrated luminosity of 4.71 fb^{-1}. The signal models

used are the ones discussed in Section 5.3. In all plots in the current section only the statistical uncertainty on the MC simulated backgrounds and signals are shown. This is added in quadrature with the full systematic and statistical uncertainty from the MM and charge-flip estimates.

In order to see how the cuts used in the various signal regions affect some typical SUSY scenarios a few reference points are chosen from each of the signal grids discussed in Section 5.3. The points used in the following discussion are indicated in Figure 8.2. The points are chosen such that they span the part of parameter space where some sensitivity is expected, i.e. at low to moderate masses.

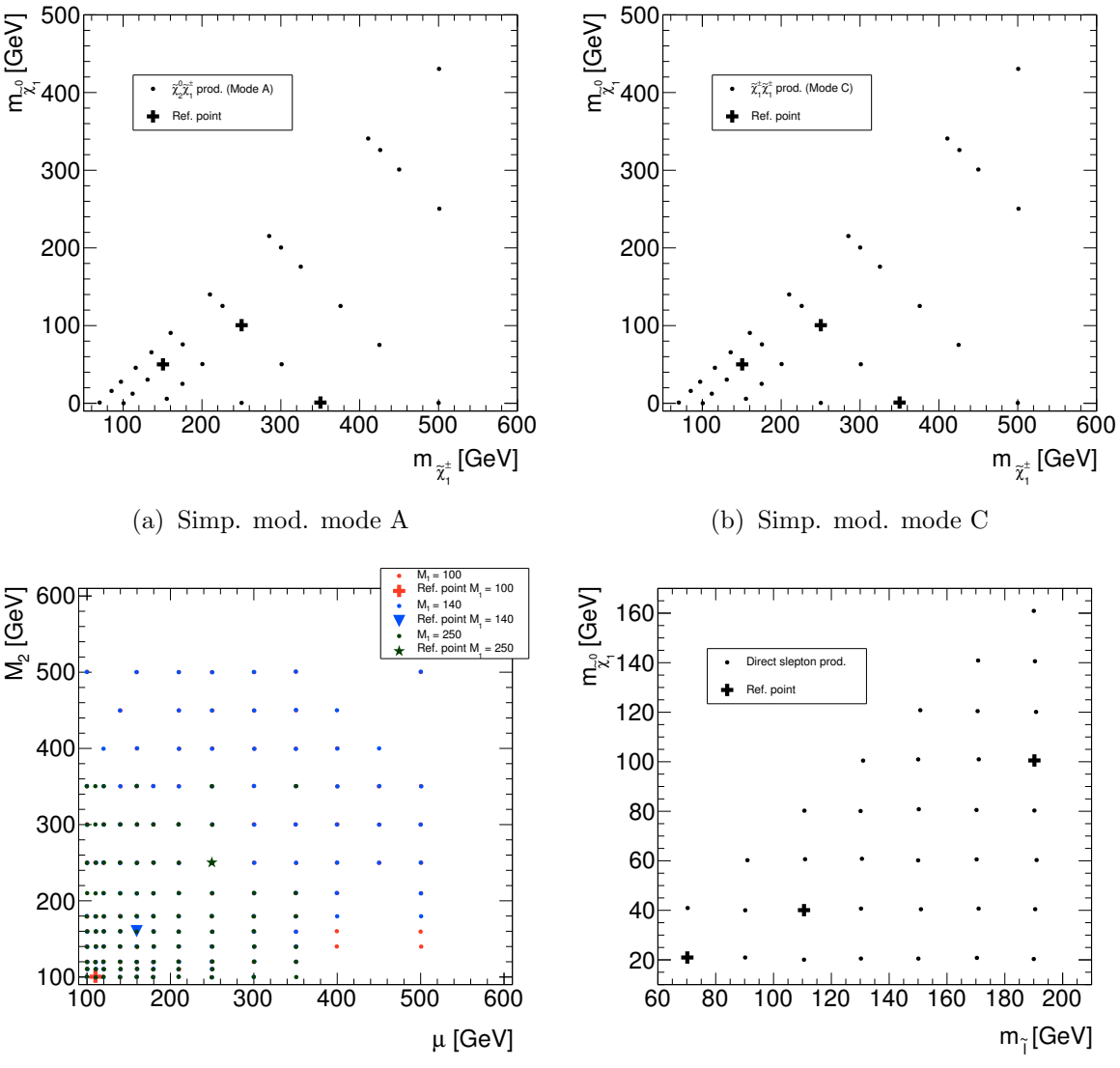

(a) Simp. mod. mode A

(b) Simp. mod. mode C

(c) Direct gaugino

(d) Direct slepton

Figure 8.2: All the generated points for the SUSY signal grids together with the reference points used as examples in the signal region justification. The following simplified models are shown; mode A (a) and C (b), the direct gaugino (c) and the direct slepton (d) pMSSM grids.

8.2.1 SR-OSjveto

Figure 8.3 shows the invariant mass distribution of the two leptons in the inclusive OS di-lepton channel allowing the leptons to have either same or different flavour (SF/DF). The total SM background is shown together with three different signal scenarios within the simplified model mode C (i.e. $\tilde{\chi}_1^{\pm}\tilde{\chi}_1^{\mp}$ production). The dominant backgrounds are

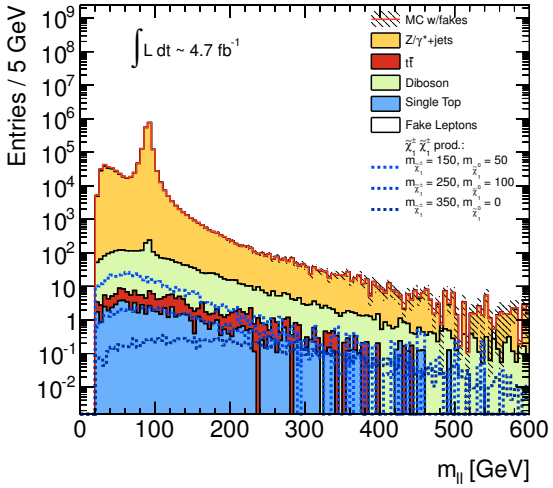

Figure 8.3: The invariant mass of two leptons in the inclusive OS channel. All SM backgrounds are shown together with three signal scenarios in the simplified model mode C grid.

clearly Z/γ^*+jets and di-boson production. Both backgrounds show a clear Z-peak, which is not present in any of the signal models. Applying a Z-veto, rejecting events with $|m_Z - m_{ll}| < 10$ GeV, is therefore very efficient in reducing the background coming from $Z \rightarrow l^{\pm}l^{\mp}$. As shown in Table 8.1 the Z/γ^*+jets and di-boson backgrounds are reduced by 80% and 55% respectively, while the signal is only reduced by around 7-10%, depending on the signal model.

According to the discussion in Section 5.5 we do not expect any jets, except from ISR and FSR, in the signal selection. The upper two plots in Figure 8.4 show the jet multiplicity and momentum of the hardest jet, $p_T^{jet\,1}$, using baseline jets. Clearly, a veto on jets will be efficient in removing background from $t\bar{t}$ and single top. The two lower plots in Figure 8.4 show the same distributions but only including the jets passing the additional signal jet requirements. The fourth column in Table 8.1 summarizes the effect of applying a veto on events containing any signal jets. As expected the $t\bar{t}$ and single top backgrounds are significantly reduced by 50 and 36%, respectively. The signal is also reduced, however, but with a somewhat smaller amount, between 26-33%, depending on the model. The $E_{\mathrm{T}}^{\mathrm{miss,rel}}$ distribution of the remaining events is shown in Figure 8.5. In order to find the optimal signal region a scan over $E_{\mathrm{T}}^{\mathrm{miss,rel}}$ from 80 GeV to 140 GeV in steps of 20 GeV is performed. The significance z in Eq. 8.7 is computed for every signal point in the simplified model mode C grid. The cut which maximized the area in the $\tilde{\chi}_1^0\tilde{\chi}_1^{\pm}$-plane for which $z > 1.64$, corresponding to a 95% confidence level exclusion, was chosen. The optimization was done using the first 1.23fb^{-1} of data and neglecting the effect of background uncertainty [76]. The optimal cut was found to be $E_{\mathrm{T}}^{\mathrm{miss,rel}} > 100$ GeV. The number of SM background events and events in three of the signal scenarios after all the cuts are applied is shown in the rightmost column in Table 8.1.

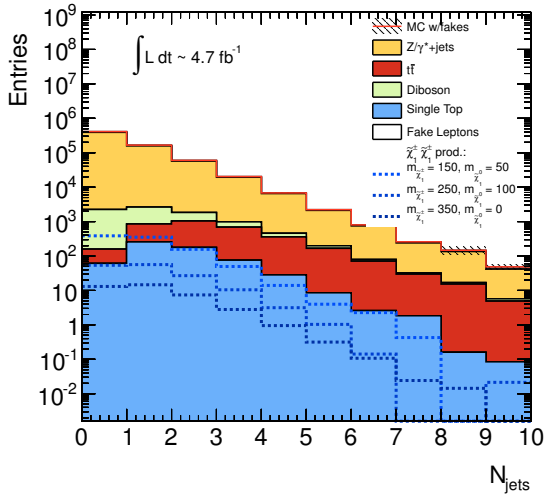

(a) $N_{\text{baseline jets}}$

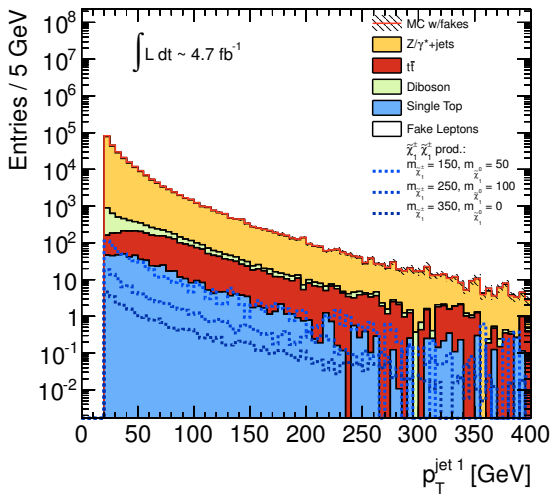

(b) $p_T^{\text{baseline jet 1}}$

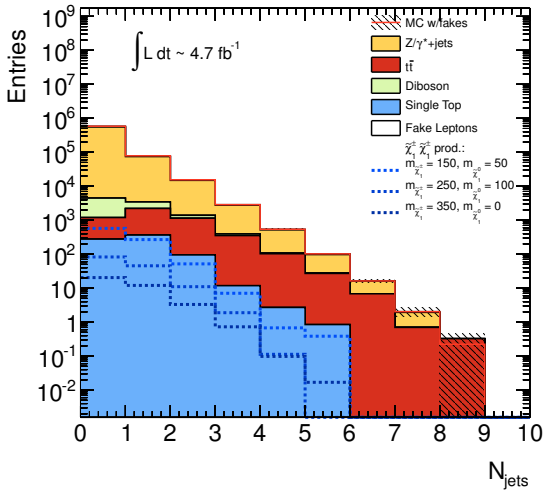

(c) $N_{\text{signal jets}}$

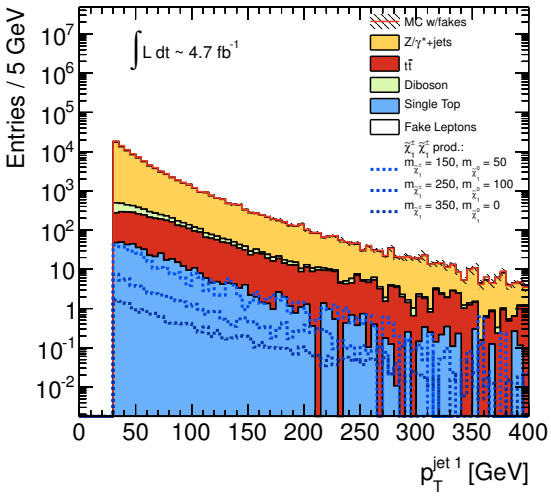

(d) $p_T^{\text{signal jet 1}}$

Figure 8.4: The upper two plots show the jet multiplicity (a) and momentum of the hardest jet (b) for the baseline jets. The lower plots (c,d) show the corresponding distributions using the signal jet selection.

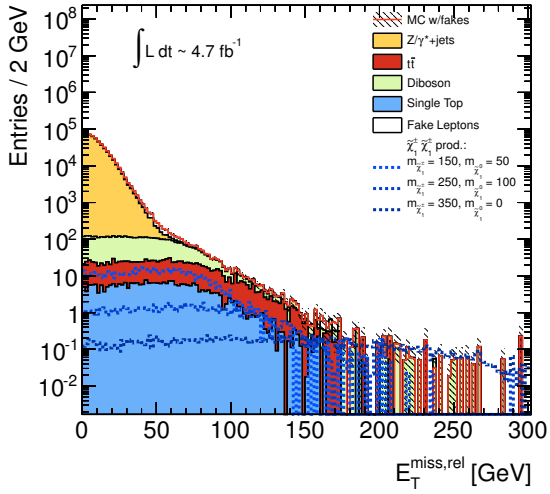

Figure 8.5: The $E_{\text{T}}^{\text{miss,rel}}$ distribution after applying a Z-veto and jet-veto in the opposite sign channel (*SR-OSjveto*).

	OS	+ Z-veto		+ jet-veto: $p_T^{jet} > 30$ GeV, $\|\eta^{jet}\| < 2.5$, JVF > 0.75		+ $E_T^{\text{miss,rel}} > 100$ GeV	
	N_{events}	N_{events}	red. [%]	N_{events}	red. [%]	N_{events}	red. [%]
Diboson	7387.0	4229.5	42.7	3262.0	55.8	48.3	99.3
Single Top	498.8	430.5	13.6	276.7	44.5	16.9	96.6
$t\bar{t}$	2181.8	1882.3	13.7	917.4	57.9	76.2	96.5
Z/γ^*+jets	3023685.4	619732.6	79.5	548120.0	81.8	0.4	99.9
Fake Leptons	36276.5	33885.9	6.5	30474.6	15.9	10.1	99.9
Total SM	3070029.5	660160.9	78.4	583050.7	81.0	152.0	99.9
$\tilde{\chi}_1^\pm\tilde{\chi}_1^\pm$ prod.							
$m(\tilde{\chi}_1^\pm,\tilde{\chi}_1^0) = (150, 50)$	904.9	773.9	14.4	573.5	36.6	20.7	97.7
$m(\tilde{\chi}_1^\pm,\tilde{\chi}_1^0) = (250, 100)$	137.6	119.2	13.3	82.6	39.9	19.7	85.6
$m(\tilde{\chi}_1^\pm,\tilde{\chi}_1^0) = (350, 0)$	32.6	30.3	6.8	20.4	37.2	12.3	62.2

Table 8.1: Number of SM background events in the inclusive SFOS channel before any additional cuts are applied (first column). The next columns show the number of events and the reduction of events in percent relative to the first column after adding more and more cuts. The lower part of the table shows the corresponding numbers for three different signal scenarios in the simplified model mode C.

8.2.2 SR-SSjveto

The same sign signal region is targeted towards final states with three leptons where one of the leptons fails reconstruction, leading to two reconstructed SS leptons

$$\tilde{\chi}_2^0\tilde{\chi}_1^\pm \rightarrow l_{rec.}^\pm l^\mp\tilde{\chi}_1^0 + l_{rec.}^\pm\nu\tilde{\chi}_1^0 \tag{8.17}$$

where *rec.* indicates the reconstructed leptons. Such decays are illustrated in Figure 5.2b and g. The final state in Figure 5.2g involves the decay of a Z into a pair of leptons, and because of the relative small branching ratio of $Z \rightarrow l^\pm l^\mp$, only 3.4% into $e^\pm e^\mp$ or $\mu^\pm\mu^\mp$, the event yield for this channel is very small and therefore omitted in the signal region optimization. A three lepton analysis would typically have a greater reach than a di-lepton analysis in these final states, but the intention is to combine the di-lepton results with the tri-lepton to achieve a 100% efficiency on the third lepton [132]. A similar table as shown in the previous section for *OSjveto* can be found in Table 8.2, with the second column giving the number of events with two SS leptons regardless of flavour. In addition to the SM background three of the signal scenarios in the simplified model mode A are also shown. As can be seen both from Table 8.2 and Figure 8.6a, showing the invariant mass distribution of two leptons for an inclusive di-lepton SS sample, the dominant background is the charge-flip and fake lepton processes. Di-boson events, especially ZZ and ZW events where one of the leptons have failed reconstruction also contribute to the total SM background. The background from charge-flip comes from the charge mis-identification of one of the leptons in the major OS backgrounds (i.e. $t\bar{t}$, WW and Z/γ^*+jets events), as shown in Figure 5.9 in Section 5.4.1.1. Since the background around the Z-peak is much smaller in the SS case a Z-veto is not applied since any lower $E_{\text{T}}^{\text{miss,rel}}$ cut removes most

	SS	+ jet-veto: $p_T^{jet} > 30$ GeV, $\|\eta^{jet}\| < 2.5$, JVF > 0.75		+ $E_T^{\text{miss,rel}} > 100$ GeV	
	N_{events}	N_{events}	red. [%]	N_{events}	red. [%]
ChargeFlip	9947.7	8575.9	13.8	0.5	100.0
Diboson	208.6	137.4	34.1	3.0	98.5
Z/γ^*+jets	2.7	2.7	0.0	0.0	100.0
Fake Leptons	17836.3	15780.2	11.5	5.9	100.0
Total SM	18047.6	15920.2	11.8	8.9	100.0
$\tilde{\chi}_2^0\tilde{\chi}_1^\pm$ prod.					
$m(\tilde{\chi}_1^\pm, \tilde{\chi}_1^0) = (150, 50)$	176.9	99.2	43.9	5.9	96.6
$m(\tilde{\chi}_1^\pm, \tilde{\chi}_1^0) = (250, 100)$	24.7	11.9	51.6	3.1	87.5
$m(\tilde{\chi}_1^\pm, \tilde{\chi}_1^0) = (350, 0)$	6.1	2.6	57.4	1.5	75.4

Table 8.2: Number of SM background events in the inclusive SS channel before any additional cuts are applied (second column). The next columns show the number of events and the reduction of events in percent relative to the second column after additional cuts. The lower part of the table show the corresponding numbers for three different signal scenarios in the simplified model mode A.

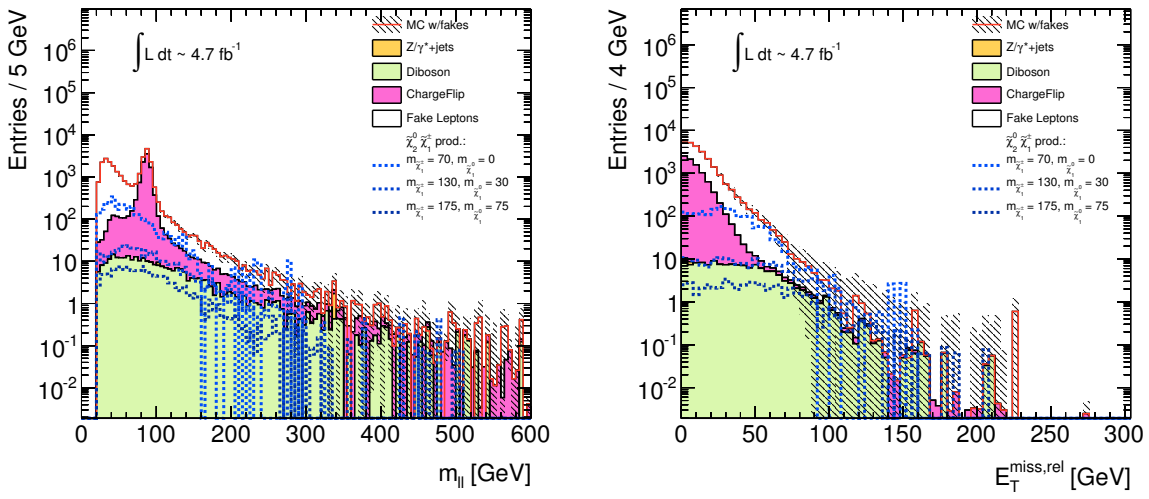

(a) m_{ll} of SS leptons

(b) $E_{\mathrm{T}}^{\mathrm{miss,rel}}$

Figure 8.6: The invariant mass distribution of the two SS leptons before applying any cuts (a) and the $E_{\mathrm{T}}^{\mathrm{miss,rel}}$ distribution after applying a jet-veto on signal jets (b).

of this background as it does not contain any real $E_{\mathrm{T}}^{\mathrm{miss,rel}}$. A veto on events containing any signal jet is used in order to suppress the background from fake leptons and $t\bar{t}$, however. The effect of applying a jet-veto can be seen in the third column in Table 8.2. The $E_{\mathrm{T}}^{\mathrm{miss,rel}}$ distribution after the jet-veto cut is shown in Figure 8.6b. Finally a scan in $E_{\mathrm{T}}^{\mathrm{miss,rel}}$ from 40 GeV to 120 GeV in steps of 20 GeV is performed. The cut which was found to maximize the area with expected $z > 1.64$ using the simplified model mode A is $E_{\mathrm{T}}^{\mathrm{miss,rel}} > 100\ GeV$ [76].

8.2.3 SR-OS2jets

The OS signal region with jets is targeted at the diagrams in Figure 5.2c and d. These processes always produce two OS leptons with same flavour, the $e\mu$-channel is therefore excluded in this signal region. These events contain at least two jets from the decay of the gauginos and squarks in addition to missing transverse energy from the lightest neutralino. The optimization is performed using the direct gaugino (DG) pMSSM grid discussed in Section 5.3.2.1. The first cut applied is the requirement of at least two signal jets. The jet multiplicity prior to the cut is shown in Figure 8.7a and the exact number of events before and after are put together in Table 8.3. Figure 8.7b shows the

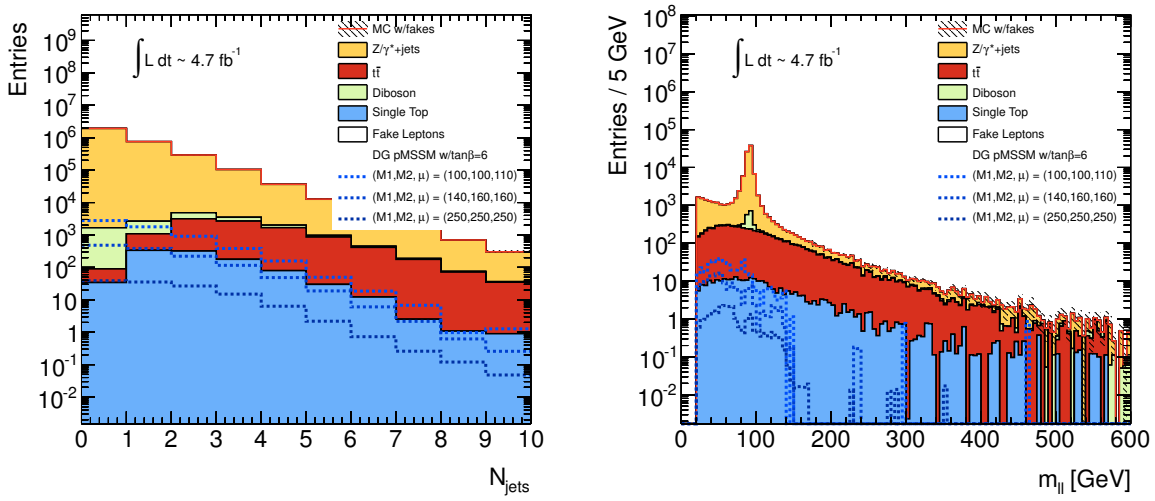

(a) $N_{\text{signal jets}}$

(b) m_{ll} of OSSF leptons

Figure 8.7: Signal jet multiplicity in events with two OSSF leptons (a) and invariant mass of two leptons after requiring two or more signal jets (b).

invariant mass distribution of the two leptons after requiring at least two signal jets. Since the leptons in the signal regions come from the decay of $\tilde{\chi}_2^0$ they do not show any enhancement around the Z-mass. The di-boson and Z/γ^*+jets backgrounds however are clearly peaked around m_Z and a Z-veto, similar to the one used for the *OS-jveto* signal region, is very efficient in removing most of these backgrounds. The most challenging background left after the Z-veto is therefore $t\bar{t}$, which typically gives events with two b-jets, in addition to two lepton-neutrino pairs from the decay of the W-bosons. The fact that these events always contain b-jets can be used to discriminate the background from the signal by applying a veto on events having any b-jet candidates, as discussed

in Section 6.3.3. Figure 8.8 shows the number of jets tagged as b-jets after requiring at least two signal jets and a Z-veto. The $t\bar{t}$ background peaks, as expected, at two b-jets

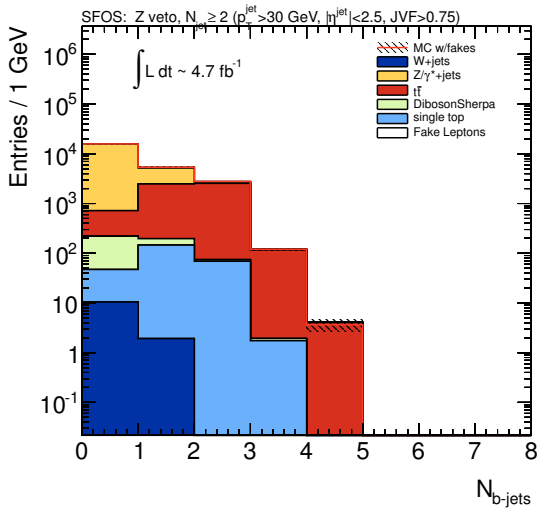

Figure 8.8: The number of b-tagged jets after requiring at least two signal jets and applying a Z-veto. All SM backgrounds together with three signal scenarios from the pMSSM direct gaugino (DG) grid are shown.

while the majority of the signal events have no b-jets. An additional veto on b-jet events is therefore applied. Table 8.3 shows that the $t\bar{t}$ background is reduced by $\sim 94\%$ after this cut. Another powerful $t\bar{t}$ discriminate is the *contransverse mass*, m_{CT}, defined in Eq. 5.4. Every di-lepton event satisfying the list of requirements given in Section 5.4.2.2 (i.e. consistent with $t\bar{t}$ kinematics) are thus removed. The $E_{\mathrm{T}}^{\mathrm{miss,rel}}$ distributions before and after the m_{CT} cut are shown in Figure 8.9a and b respectively. As can be deduced from the numbers in Table 8.3 the m_{CT} cut rejects 82% of the $t\bar{t}$ background still remaining after the jet requirement and the Z- and b-jet vetoes are applied. Since the targeted final

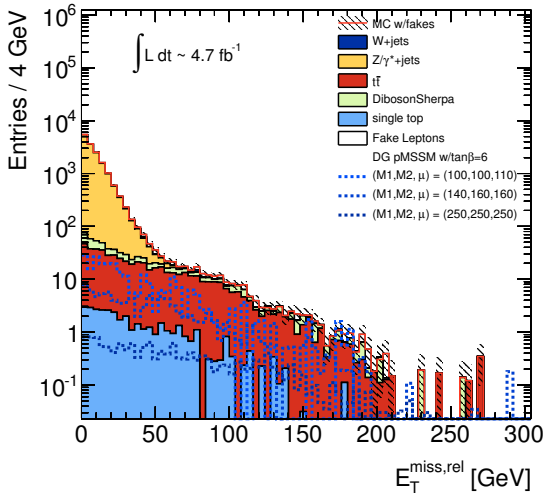

(a) $E_{\mathrm{T}}^{\mathrm{miss,rel}}$ before m_{CT}-veto

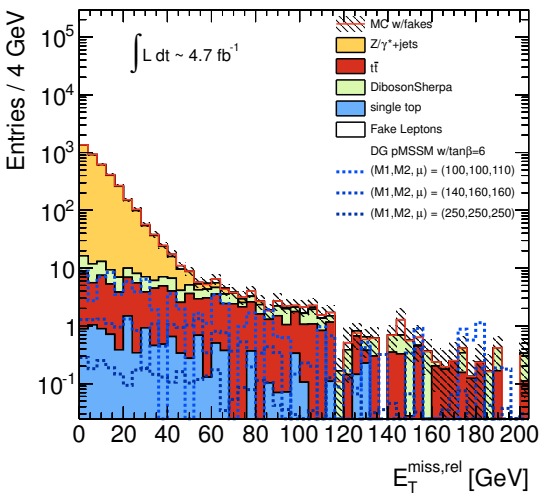

(b) $E_{\mathrm{T}}^{\mathrm{miss,rel}}$ after m_{CT}-veto

Figure 8.9: The $E_{\mathrm{T}}^{\mathrm{miss,rel}}$ distribution of all OSSF events with $N_{jet} \geq 2$ and surviving a Z-veto and b-jet veto. To the left is the $E_{\mathrm{T}}^{\mathrm{miss,rel}}$ distribution before applying the cut on m_{CT}, while the right plot shows the distribution after cutting on m_{CT}. Note the different range of the x-axis in the two plots.

states contain two LSPs we expect some $E_{\mathrm{T}}^{\mathrm{miss,rel}}$ in the event. A final scan over $E_{\mathrm{T}}^{\mathrm{miss,rel}}$

is therefore performed from 50 GeV to 100 GeV, as the statistics becomes quite limited for $E_{\mathrm{T}}^{\mathrm{miss,rel}} > 100$ GeV. As for the other signal regions the optimal cut was defined to be the one maximizing the number of signal grid points with a significance corresponding to 95% confidence level exclusion (i.e. $z > 1.64$). A $E_{\mathrm{T}}^{\mathrm{miss,rel}} > 50$ GeV cut provided the best sensitivity [76].

8.2.4 SR-mT2

The *mT2* signal region is mainly targeted at the direct slepton production processes of Figure 5.3. The cut optimization is therefore performed using the pMSSM direct slepton grid discussed in Section 5.3.2.2. Here we expect no jets, except possibly from ISR. The leptons also come exclusively from the decay of a slepton. This allows both a jet- and a Z-veto to be applied in order to remove much of the SM background. The effect of applying these two cuts is visible in Table 8.4. The corresponding $E_{\mathrm{T}}^{\mathrm{miss,rel}}$ distribution is shown in Figure 8.10a. According to Table 8.4 the dominant background, other than

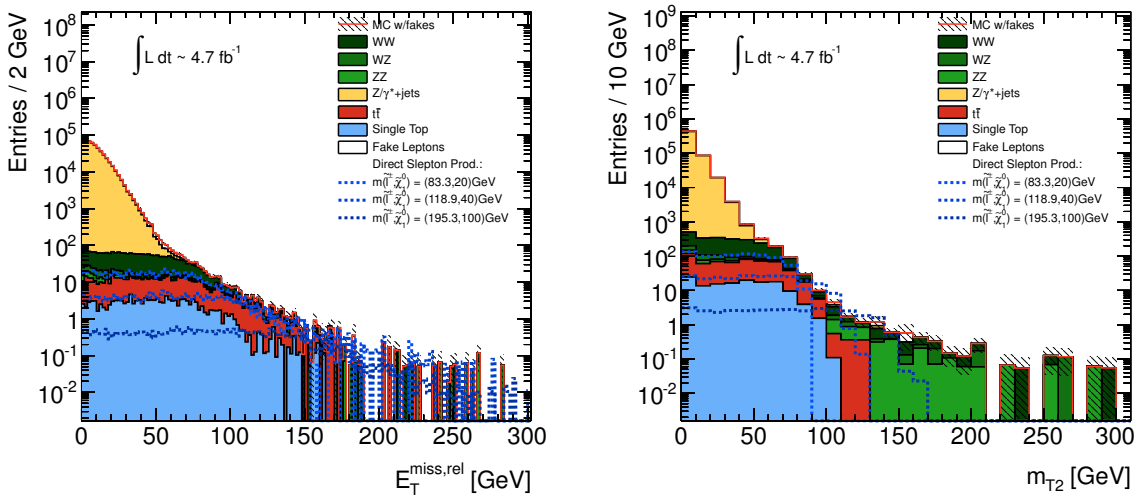

(a) $E_{\mathrm{T}}^{\mathrm{miss,rel}}$ (b) m_{T2}

Figure 8.10: The $E_{\mathrm{T}}^{\mathrm{miss,rel}}$ (a) and m_{T2} (b) distributions for the SM backgrounds along with three direct slepton signal scenarios after applying a Z- and jet-veto on all opposite sign same flavour events.

the Z/γ^*+jets, which is easily removed by an $E_{\mathrm{T}}^{\mathrm{miss,rel}}$ cut, is clearly the WW, which is expected to have a very similar event topology as the direct slepton decays. It is however possible to reduce the WW, as well as the $t\bar{t}$ backgrounds, further by using the *stransverse mass*, m_{T2}, variable defined in Section 5.4.2.4. The m_{T2} distribution after applying the Z- and jet-vetoes is shown in Figure 8.10b, where the smeared upper edge in WW events is clearly visible. The theoretically expected upper kinematic edge from Eq. 5.9 of the m_{T2} distribution for the various signal grid points is shown in Figure 8.11. This plot shows that most of the signal points do indeed have an edge larger than 90 GeV. Several different configurations of $E_{\mathrm{T}}^{\mathrm{miss,rel}}$ and m_{T2} cuts were tried in order to maximize the number of direct slepton signal points having a significance larger than 1.64. As already pointed out, an increasing m_{T2} cut removes more of the WW background and increases the sensitivity

	OSSF	$N_{jet} \geq 2$: $p_T^{jet} > 30$ GeV, $\lvert\eta^{jet}\rvert < 2.5$, JVF > 0.75		+ Z veto		+ b-jet veto		+ m_{CT}-veto		+ $E_T^{\text{miss,rel}} > 50$ GeV	
	N_{events}	N_{events}	red. [%]	N_{events}	red. [%]	N_{events}	red. [%]	N_{events}	red. [%]	N_{events}	red. [%]
DibosonSherpa	7213.1	388.7	94.6	228.6	96.8	172.4	97.6	61.7	99.1	17.4	99.8
single top	990.3	294.7	70.2	250.5	74.7	36.5	96.3	11.7	98.8	2.9	99.7
W+jets	140.3	12.4	91.2	12.4	91.2	10.4	92.6	0.0	100.0	0.0	100.0
$t\bar{t}$	9251.2	6230.4	32.7	5347.3	42.2	496.9	94.6	89.7	99.0	34.3	99.6
Z/γ^*+jets	3108875.3	91325.1	97.1	17912.5	99.4	15029.9	99.5	3826.2	99.9	6.7	100.0
fake leptons	21836.8	801.4	96.3	610.9	97.2	364.9	98.3	74.0	99.7	4.5	100.0
MCSherpa	3148306.9	99052.6	96.9	24362.1	99.2	16111.1	99.5	4063.4	99.9	65.8	100.0
DG pMSSM w/$\tan\beta = 6$											
$(M1, M2, \mu) = (100, 100, 110)$ GeV	6073.8	420.7	93.1	354.8	94.2	255.9	95.8	73.5	98.8	19.5	99.7
$(M1, M2, \mu) = (140, 160, 160)$ GeV	1273.5	148.6	88.3	131.4	89.7	99.6	92.2	21.9	98.3	9.8	99.2
$(M1, M2, \mu) = (250, 250, 250)$ GeV	124.8	23.2	81.4	19.9	84.0	15.2	87.8	4.5	96.4	2.4	98.1

Table 8.3: Number of SM background events in the OSSF channel before any additional cuts are applied (second column) and after adding more and more cuts. The *red.* column shows the reduction of events in percent after each cut relative to the events in the second column. The lower part of the table shows the corresponding numbers for three different signal scenarios in the pMSSM direct gaugino grid.

	SFOS	+ Z veto		+ jet veto: $p_T^{jet} > 30$ GeV, $\|\eta^{jet}\| < 2.5$, JVF > 0.75 + b-jet veto		+ $E_T^{\text{miss,rel}} > 40$ GeV	
	N_{events}	N_{events}	red. [%]	N_{events}	red. [%]	N_{events}	red. [%]
WW	2185.9	1888.9	13.6	1508.7	31.0	668.6	69.4
WZ	2277.5	435.1	80.9	157.8	93.1	41.8	98.2
ZZ	1677.3	258.2	84.6	83.0	95.1	25.6	98.5
Single Top	990.3	847.8	14.4	139.8	85.9	84.7	91.4
$t\bar{t}$	9258.8	7968.4	13.9	454.8	95.1	270.1	97.1
Z/γ^*+jets	3112368.9	625304.6	79.9	534480.0	82.8	1979.4	99.9
Fake Leptons	21836.8	19777.1	9.4	16743.2	23.3	563.2	97.4
Total SM	3150595.4	656480.1	79.2	553567.3	82.4	3633.5	99.9
direct slepton prod.							
$m(\tilde{\ell}, \tilde{\chi}_1^0) = (83.3, 20)$ GeV	1195.0	1025.4	14.2	821.2	31.3	466.4	61.0
$m(\tilde{\ell}, \tilde{\chi}_1^0) = (118.9, 40)$ GeV	355.9	320.5	10.0	242.6	31.8	166.2	53.3
$m(\tilde{\ell}, \tilde{\chi}_1^0) = (195.3, 100)$ GeV	54.0	49.9	7.7	35.9	33.6	27.6	48.9

Table 8.4: Number of SM background events in the OSSF channel before any additional cuts are applied (second column) and after adding additional cuts. The *red.* column is the reduction of events in percent after each cut relative to the events in the second column. The lower part of the table shows the corresponding numbers for three different signal scenarios in the direct slepton grid.

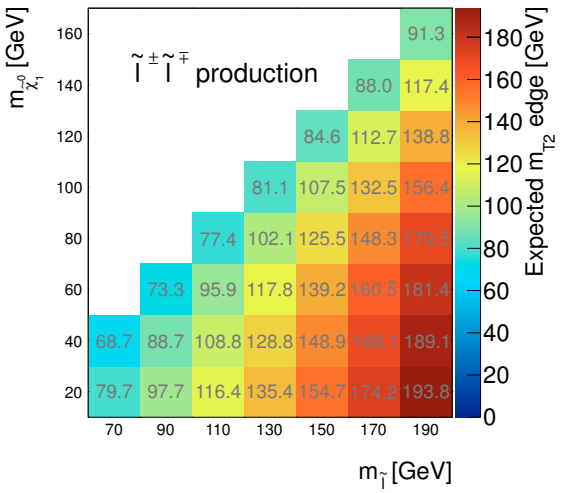

Figure 8.11: The expected edge of the m_{T2} distribution in the direct slepton grid assuming $m_\chi = 0$ (calculated using Eq. 5.9). The physical slepton masses are used in the calculation (see Table 5.2).

Name	Sign		Flavour			Z-veto	N_{jets}	b-jet veto	m_{CT}-veto	$E_{\mathrm{T}}^{\mathrm{miss,rel}}$	m_{T2}
	OS	SS	ee	$\mu\mu$	$e\mu$						
OSjveto	✓	✗	✓	✓	✓	✓	$= 0$	✗	✗	> 100 GeV	✗
SSjveto	✗	✓	✓	✓	✓	✗	$= 0$	✗	✗	> 100 GeV	✗
OS2jets	✓	✗	✓	✓	✗	✓	≥ 2	✓	✓	> 50 GeV	✗
MT2	✓	✗	✓	✓	✗ †	✓	$= 0$	✗	✗	> 40 GeV	> 90 GeV

† When using the *MT2* signal region to set limits on the direct gaugino production the $e\mu$ channel is also included.

Table 8.5: The definitions of the signal regions used in the final analysis.

for large mass splittings between the slepton and the LSP. These models typically have small cross-sections and a large background rejection is therefore crucial. On the other hand, a high m_{T2} cut would decrease the sensitivity for signal models having small values of $m_{\tilde{\ell}} - m_{\tilde{\chi}_1^0}$ (i.e. along the diagonal in Figure 8.11). The best compromise between being sensitive to models with both large and small mass splittings has been found to be when requiring $E_{\mathrm{T}}^{\mathrm{miss,rel}} > 40$ GeV and $m_{T2} > 90$ GeV [76].

Despite the fact that the *mT2* signal region has been developed and optimized for direct slepton production it can also be a very sensitive region for direct gaugino production, for instance processes like in Figure 5.2a. In Ref. [76] the optimization of the *mT2* signal region especially targeted at direct gaugino production was not performed, however. The *mT2* signal region was nevertheless included when calculating the limits in the direct gaugino production grids, simply using the cuts optimized within the direct slepton grid as discussed above. The only difference was the inclusion of the $e\mu$-channel, which obviously, by studying Figure 5.2a, would contribute to the signal final states in the direct gaugino scenario.

8.2.5 Summary

Table 8.5 finally summarizes the cuts used for each of the signal regions in the analysis, as presented in the previous Section.

In many of the signal regions used as examples in Tables 8.1-8.4 a quite large fraction of the events are rejected. It might seem that many of the cuts used to remove the SM backgrounds are too hard and reject also most of the signal. The optimization is, however, performed such that a maximal number of the signal grid points exhibit an expected significance which is larger than the 95% CL limit of 1.64. In some cases, hard cuts might favour one part of the phase space while other parts suffer dramatically. A more refined analysis could therefore have been performed by designing several signal regions targeting at different parts of the same signal grid. Would it for instance have been beneficial to use several versions of the *mT2* signal region by changing the m_{T2} cut? This would optimize for both scenarios having large and small mass splittings between the slepton and the LSP. This is in fact done in the most recent update of this analysis using 20 fb^{-1} of data at $\sqrt{s} = 8$ TeV [139].

In the original optimization of the signal regions referred to in the publication [76] the fake lepton background was assumed to constitute the part missing after applying

all the relevant MC simulation samples.[1] In the above discussion, however, the fake lepton background was estimated using the MM, as discussed in Chapter 7, with the final weighted fake-efficiencies to be discussed in more detail in Section 8.3.

8.3 Fake Lepton Background in the Signal Regions

In order to estimate the fake lepton background in the signal regions we need to use the proper real- and fake-efficiencies as discussed in Section 7.2.5 and 7.2.2 respectively. In the following sections the final fake-efficiency to be used in the analysis is established based on the definition of the signal regions. The final validation of the estimates in signal-like regions is studied at the end.

8.3.1 Final Weighted Fake-Efficiencies

The final fake-efficiencies to be used in the analysis are weighted combinations of the QCD and conversion components for electrons. For muons the conversion contribution is neglected and only the QCD-part is treated. Since all signal regions require at least $E_{\mathrm{T}}^{\mathrm{miss,rel}}$ above 40 GeV the fake-efficiency for the fake leptons coming from QCD processes is taken from a region with $40 < E_{\mathrm{T}}^{\mathrm{miss,rel}} < 100$ GeV, as discussed in Section 7.2.2. This is motivated by the fact that the dependency of the fake-efficiency on $E_{\mathrm{T}}^{\mathrm{miss,rel}}$ was shown to be relatively large, with a significantly lower fake-efficiency in the intermediate $E_{\mathrm{T}}^{\mathrm{miss,rel}}$ region compared with the $E_{\mathrm{T}}^{\mathrm{miss,rel}} < 30$ GeV region, illustrated in Figure 7.15. Using a fake-efficiency from a low $E_{\mathrm{T}}^{\mathrm{miss,rel}}$ region would therefore not necessarily yield good estimates for the signal regions considered.

8.3.1.1 Electron Fake-Efficiency

Following the general form in Eq. 7.19 we construct

$$f^{e}_{final}(p_{\mathrm{T}}) = \sum_{i \in QCD,conv.} f^{e}_{i}(p_{\mathrm{T}}) w^{e}_{i}(p_{\mathrm{T}}) s^{e}_{i}(p_{\mathrm{T}}), \tag{8.18}$$

where $f^{e}_{QCD}(p_{\mathrm{T}})$ and $f^{e}_{conv.}(p_{\mathrm{T}})$ are the fake-efficiencies for electrons from QCD processes in Figure 7.13c and conversion electrons in Figure 7.18 respectively. The $s^{e}_{QCD}(p_{\mathrm{T}})$ is the scale factor to account for possible differences between the fake-efficiencies for QCD obtained from data and MC, which is, from Figure 7.14a, found to be 0.979 ± 0.031 in the low $E_{\mathrm{T}}^{\mathrm{miss,rel}}$ region. This scale factor is further assumed to be valid for all $E_{\mathrm{T}}^{\mathrm{miss,rel}}$ values. Since the scale factor is quite close to unity over the complete p_{T} range it is approximated to 1 in Eq. 8.18. For the conversion fake-efficiency the differences between data and MC are found to be negligible and thus $s^{e}_{conv.}(p_{\mathrm{T}})$ is set equal to 1.

The weights, $w^{e}_{i}(p_{\mathrm{T}})$, indicate the relative amount of each of the two contributions to the total fake-efficiency. The weights are calculated by constructing regions similar

[1] The estimates of the fake lepton from the MM were not yet available at the time when the signal region optimization was performed.

to the signal regions where we want to estimate the fake lepton contribution. For the *2jets* and *mT2* signal regions the statistics are too low to obtain any reliable scale factors, so we assume that these signal regions have similar composition to the *OSjveto* and *SSjveto* regions. We would, however, expect the conversion component to be slightly more important in the *SR-2jets* region because of the veto on b-jets and m_{CT}, which strongly suppress $t\bar{t}$. Also, since the charge-flip component is estimated using a different method the *SR-SSjveto* is not expected to contain more conversion electrons than *SR-OSjveto*. The final region used to extract the weights for electrons is therefore defined by requiring OS di-electron events in addition to a jet-veto. The weights are shown in Figure 8.12.

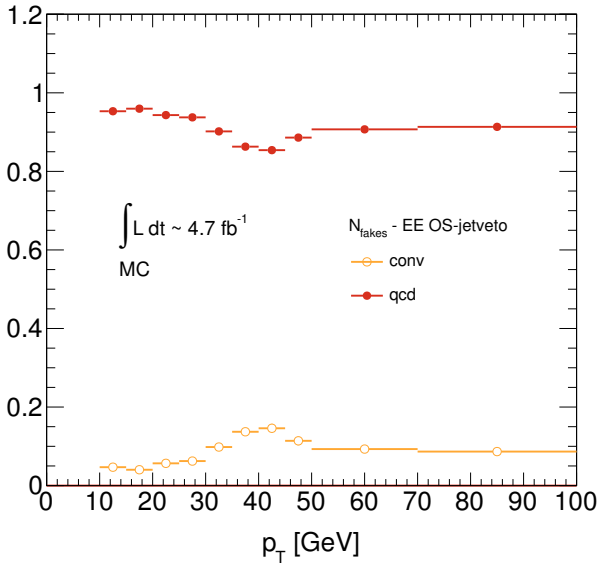

Figure 8.12: The p_{T} dependent weights used in the weighted electron fake-efficiency. Orange open circles are conversions, red closed circles are QCD. Weights are extracted within a di-electron OS sample after applying the jet-veto.

The conversion component is found to be relatively small and does not have a big impact on the final fake-efficiency, $f^{e}_{final}(p_{\mathrm{T}})$, plotted in Figure 8.13a. The figure shows the two individual fake-efficiency components, from QCD and conversions, together with the final weighted fake-efficiency. The error bars on the points indicate the statistical error, while the shaded area shows the full systematic uncertainty, to be summarized in Section 8.4.3

8.3.1.2 Muon Fake-Efficiency

For muons the conversion component is neglected as it is highly suppressed by the relatively large muon mass. The final fake-efficiency becomes merely

$$f^{\mu}_{final}(p_{\mathrm{T}}) = f^{\mu}_{QCD}(p_{\mathrm{T}})w^{\mu}_{QCD}(p_{\mathrm{T}})s^{\mu}_{QCD}(p_{\mathrm{T}}). \tag{8.19}$$

The QCD fake-efficiency, $f^{\mu}_{QCD}(p_{\mathrm{T}})$, is taken from Figure 7.13c. As was done in the electron case the scale factor, $w^{\mu}_{QCD}(p_{\mathrm{T}})$ coming from the differences between data and MC, shown to be 0.9621 ± 0.0157 in Figure 7.14b, is set to 1 and instead included in the systematic uncertainty. The final fake-efficiency for muons, $f^{\mu}_{final}(p_{\mathrm{T}})$ is shown in 8.13b. The error bars on the points indicate the statistical error, while the shaded area shows the full systematic uncertainty.

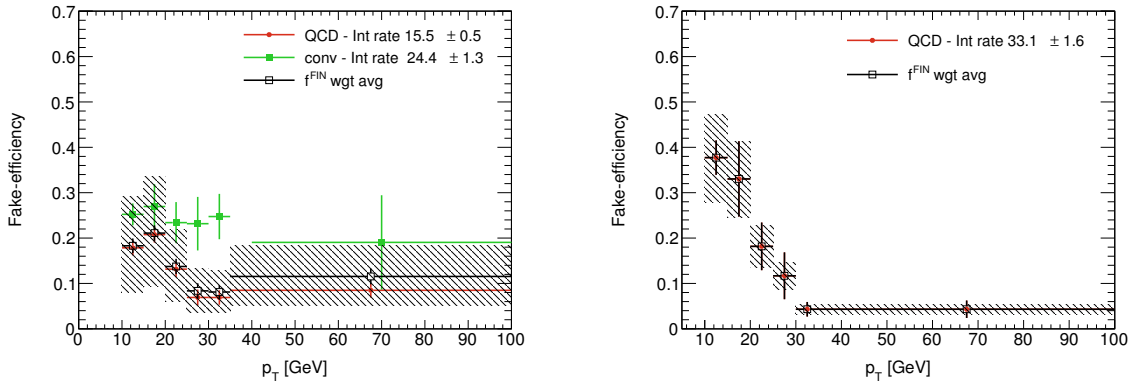

(a) Fake-efficiency for electrons

(b) Fake-efficiency for muons

Figure 8.13: The final fake-efficiencies for electrons (a) and muons (b). For electrons the fake-efficiency is a weighted average of the data-driven conversion fake-efficiency (green) and the semi-data driven QCD fake-efficiency (red closed circles). The hashed area shows the total upward and downward systematic uncertainties used. The error bars on the points are purely statistical. The last bin includes overflow.

8.3.2 Uncertainty on the Final Fake-Efficiencies from Light- and Heavy-Flavoured Jets

As discussed in Section 7.2.2.1 we have a relatively poor description of the fake leptons coming from decays of light-flavoured jets in the available QCD MC. A study has therefore been performed by varying the relative amount of fake leptons from light-flavoured jets with respect to the contribution from heavy-flavoured jets. The light-flavoured fake-efficiency is taken from the a 40 $< E_{\mathrm{T}}^{\mathrm{miss,rel}} <$ 100 GeV region using MC truth to identify light-flavoured jets. The main sources are from the Z/γ^{*}+jets and W+jets processes. We used truth MC to identify the two components. Figure 8.14 shows how the final electron fake-efficiency (black dashed line) changes when scaling up the amount of light-flavour (and a corresponding downscaling of the heavy-flavour, such that the sum of light and heavy is always equal to one). The amount of light-flavour is scaled up by 20%, 40%, 60% or 80%. The numbers in each bin show the maximum change in percent from the nominal. When scaling up the light-flavour part the errors increase since the fake-efficiency for the light-flavour component is computed with relatively limited statistics. This is especially visible in the highest bin, where all points are in fact consistent within errors. Based on this we assign a $^{+\,0}_{-50}$ % systematic uncertainty on the electron fake-efficiency. For muons the light-flavoured component is very small in the intermediate $E_{\mathrm{T}}^{\mathrm{miss,rel}}$ region, as seen from the numbers in Table 7.5. Only in $p_{\mathrm{T}} < 20$ there is a small, $\sim 2\%$, contribution from light-flavoured jets. It is, however, not sufficient for performing a similar study as with electrons and thus the effect from any light-flavoured component in the muon channel is neglected.

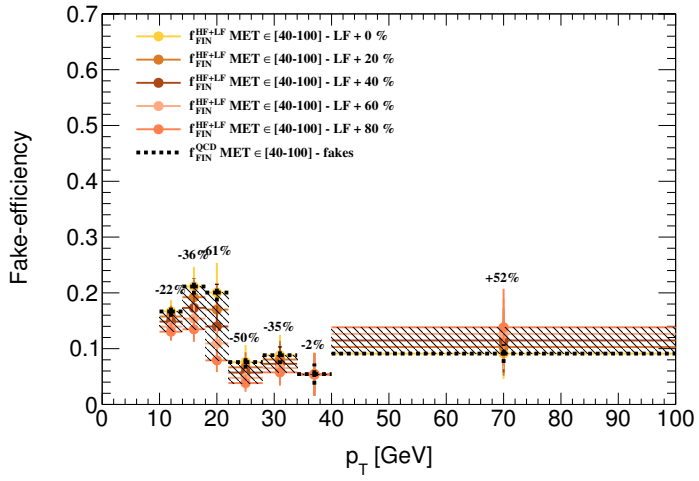

Figure 8.14: The black dashed points show the nominal QCD electron fake-efficiency. The other coloured points show how the fake-efficiency is altered when scaling up the light-flavour component by 20-80%. The numbers printed for each bin is the maximal change in percent from the nominal value.

8.3.3 Overlap Between Fake Lepton Estimates and Charge-Flip

In SS di-electron events both the MM and the method of estimating the charge-flip contribution, introduced in Section 5.4.1.1, are used. The MM method might, however, include some of the events already described by the charge-flip estimates and thus lead to an overlap between the two methods. Figure 8.15 shows the invariant mass of SS di-electron events in the full 2011 dataset where most of the SS events in MC are estimated from OS events according to the charge-flip method. The electron p_{T} distribution is shifted to account for the energy-loss when undergoing a charge-flip. The total fake lepton contribution obtained using the MM is shown as a white histogram.

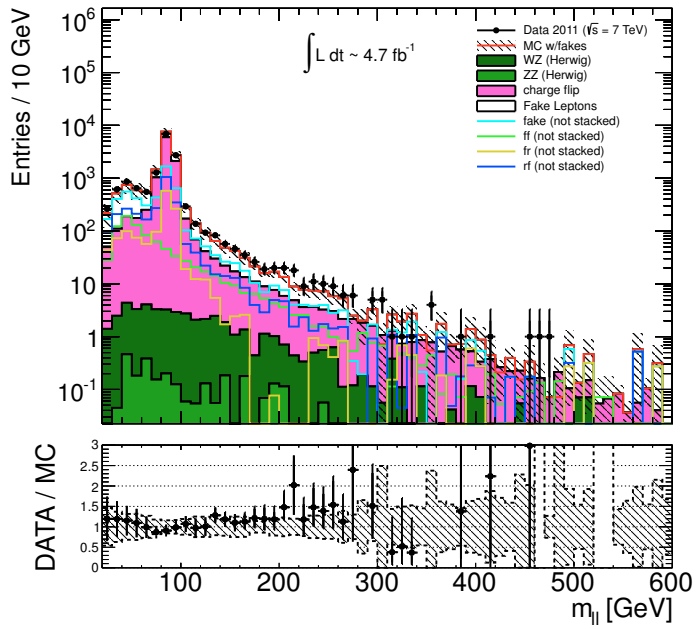

Figure 8.15: The invariant mass of SS di-electrons. Each of the estimated components, rf, fr and ff, of the fake lepton contribution is also plotted together with the total fake lepton and the charge-flip estimates.

Figure 8.15 shows a slight overestimate of SS events around the Z-mass. This can be understood from looking at the fr and rf components from the fake lepton estimates, which both exhibit a clear enhancement around 90 GeV. This means that the MM must pick up some fraction of charge-flip events. Table 8.6 shows the estimated number of

charge-flip events together with the number of fake leptons, as estimated from the MM for SS di-electron events with m_{ll} within 10 GeV of the Z-mass. The small amount of events coming from di-boson MC is also included. Comparing the sum of all these contributions to the total number of data events an overestimate of 7% is found. However, comparing

Table 8.6: The predicted and observed number of events in SS di-electron having m_{ll} within 10 GeV of the Z-mass. The prediction overshoots the data by 7%.

Contribution	N_{events}
Data	9647 ± 98.22
MC simulation	6.67 ± 0.64
Total charge-flip	8054.94 ± 12.81
Fake leptons	2320.80 ± 28.20
Predicted	10382.41 ± 30.98
Discrepancy (%)	734 (7.1%)

with the total systematic and statistical uncertainties of 10% from the charge-flip method in Table 8.7 this overlap is not significant. Furthermore, the charge-flip only comprises about 13% of the total background in the *SSjveto* signal region. The overlap between

Table 8.7: The number of events with statistical and systematic uncertainties predicted in the *SSjveto* signal region using the MC simulation and the charge-flip and fake lepton estimates.

Contribution	N_{events} ± stat. ± syst.
Data	2
MC simulation	0.746 ± 0.207 ± 0.100
charge-flip	0.540 ± 0.034 ± 0.045
di-boson	0.325 ± 0.020 ± 0.029
$t\bar{t}$	0.164 ± 0.025 ± 0.011
single top	0.038 ± 0.009 ± 0.003
Z/γ^*+jets	0.013 ± 0.008 ± 0.001
fake leptons	2.920 ± 0.893 ± 1.102
Total predicted	4.206 ± 0.917 ± 1.105

the charge-flip and fake lepton estimates is therefore neglected throughout the remaining analysis.

8.3.4 Detailed Fake Contribution in Full $E_{\mathrm{T}}^{\mathrm{miss,rel}}$ Signal Regions

With all the signal regions properly defined it is now possible to study the detailed contribution from the various fake sources, i.e. heavy- and light-flavoured hadron decays and conversion electrons, using truth information in the available MC samples. Table 8.8 shows the fake contributions in four signal regions before applying the $E_{\mathrm{T}}^{\mathrm{miss,rel}}$ cut. In order to have sufficient statistics the m_{T2} cut is also removed from *SR-mT2*. The fake contributions are also divided into fake leptons coming from decays of heavy- and light-flavoured jets, as well as conversions for the ee- and $e\mu$-channels. The PythiaB di-lepton filtered samples are used to model the QCD component. The relative amount of each fake type is given in percent. In the $\mu\mu$ and $e\mu$-channels the heavy-flavour component

ee-channel	Tot fakes	Heavy		Light		Conv	
Region	N_L	N_L	[%]	N_L	[%]	N_L	[%]
SR-jveto′	88323.68	75110.27	85.04	5282.68	5.98	7930.73	8.98
SR-SSjveto′	78748.50	50251.31	63.81	18493.44	23.48	10003.76	12.70
SR-2jets′	145.70	25.23	17.31	54.86	37.65	65.61	45.03
SR-mT2-L1′	160598.65	122764.82	76.44	23455.28	14.60	14378.54	8.95

$\mu\mu$-channel	Tot fakes	Heavy		Light	
Region	N_L	N_L	[%]	N_L	[%]
SR-jveto′	427346.97	404385.88	94.63	22961.06	5.37
SR-SSjveto′	86048.05	85849.58	99.77	198.47	0.23
SR-2jets′	3810.70	3795.86	99.61	14.83	0.39
SR-mT2-L1′	513339.44	490190.08	95.49	23149.32	4.51

$e\mu$-channel	Tot fakes	Heavy		Light		Conv	
Region	N_L	N_L	[%]	N_L	[%]	N_L	[%]
SR-jveto′	3989389.65	3800325.57	95.26	133979.26	3.36	55085.05	1.38
SR-SSjveto′	1321171.63	1143133.19	86.52	121788.51	9.22	56249.88	4.26
SR-mT2-L1′	5306817.01	4941782.18	93.12	255623.06	4.82	109412.36	2.06

Table 8.8: Total number of inclusive loose (N_L) fake leptons and the relative amount of each type (heavy, light and conversions (only in ee and $e\mu$-channel)) for all signal regions, before the $E_{\mathrm{T}}^{\mathrm{miss,rel}}$ cut (indicated by a ′), in the di-electron (upper), di-muon (middle) and electron-muon (lower) channels. The *L1* in *SR-mT2-L1′* refers to the fact that the cut on m_{T2} is also removed. The *SR-2jets* does not include the $e\mu$ channel and is therefore omitted from the lower table. Numbers are from Ref. [76].

seems to totally dominate the fake lepton contribution in all signal regions. For the ee-channel the heavy-flavour contribution is also dominating, except in *SR-2jets*, where the light-flavoured and conversion components lead. This can be understood from the large suppression of $t\bar{t}$ after applying the veto on events with b-jets and the *contransverse mass*, m_{CT}.

With the fake lepton and charge-flip estimates as well as the MC simulations and data in place it is time to finally validate the results from the MM.

8.3.5 Validation Plots

In order to validate the fake lepton estimates and investigate further the agreement between data and the predictions, including the result from the MM, specific signal-like regions are constructed. The final fake-efficiency for electrons used in the MM is totally dominated by the fake-efficiency from QCD processes, while it is the **only** component included for muons. Since the QCD fake-efficiency from the $E_{\mathrm{T}}^{\mathrm{miss,rel}} < 30$ GeV region is shown to significantly differ from the one at intermediate $E_{\mathrm{T}}^{\mathrm{miss,rel}}$ (i.e. $40 < E_{\mathrm{T}}^{\mathrm{miss,rel}} < 100$), the fake lepton contribution at low $E_{\mathrm{T}}^{\mathrm{miss,rel}}$ is not expected to be properly estimated. The validation regions therefore all include a cut on $E_{\mathrm{T}}^{\mathrm{miss,rel}} > 40$ GeV. In order to have a validation region sufficiently separated from *SR-mT2*[2], another region with an additional Z-veto and $m_{T2} \leq 90$ GeV cut was used. The three regions used are

(i) OS di-lepton + $E_{\mathrm{T}}^{\mathrm{miss,rel}} > 40$ GeV
(ii) OS di-lepton + $E_{\mathrm{T}}^{\mathrm{miss,rel}} > 40$ GeV, Z-veto and $m_{T2} \leq 90$ GeV
(iii) SS di-lepton + $E_{\mathrm{T}}^{\mathrm{miss,rel}} > 40$ GeV.

Figure 8.16 shows the estimates in the OS $\mu\mu$-channel for validation region (i) as a function of $E_{\mathrm{T}}^{\mathrm{miss,rel}}$ (a), invariant mass of the two muons (b) and p_{T} of the leading (c) and sub-leading (d) muons. In the plots the fake estimation is divided into the various components, rf, fr, ff and their sum, denoted as $fake$. The white histogram shows the total fake lepton contribution stacked together with the other SM real lepton backgrounds from MC. Figure 8.17 depicts similar plots for OS $e\mu$ in validation region (ii) while Figure 8.18 shows plots for SS ee in validation region (iii). The agreement between data and MC is quite good, meaning that the MM is able to predict the fake lepton background in signal-like regions. The errors on the data-counts are statistical Poisson limits calculated as described in Section 8.1.4. The hatched band reflects the statistical uncertainty on the MC simulations, added in quadrature with the full uncertainty from the MM, summarized in Section 8.4.3.

[2]Which requires exactly $E_{\mathrm{T}}^{\mathrm{miss,rel}} > 40$ GeV.

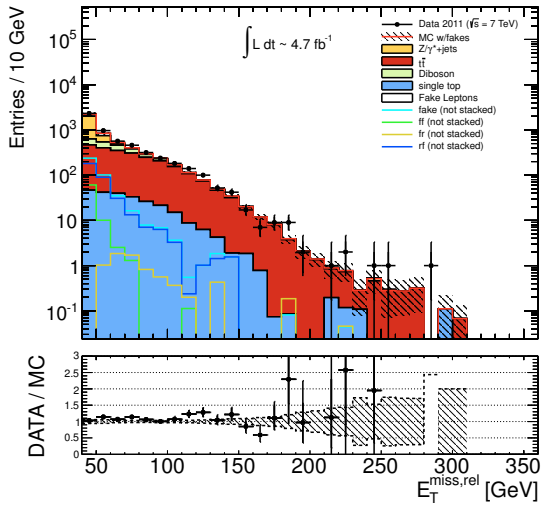

(a) $E_{\mathrm{T}}^{\mathrm{miss,rel}}$

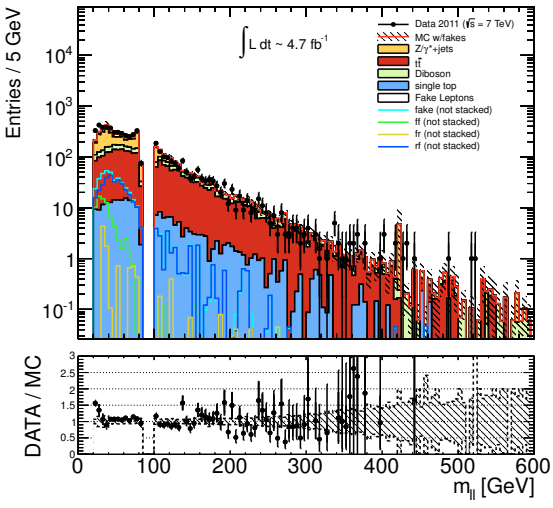

(b) m_{ll}

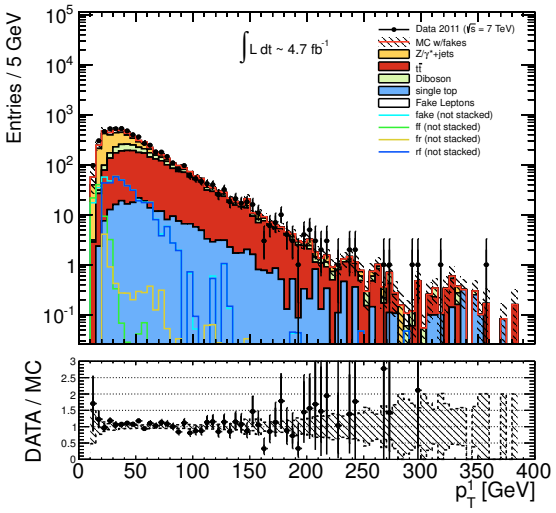

(c) $p_T^{lep,1}$

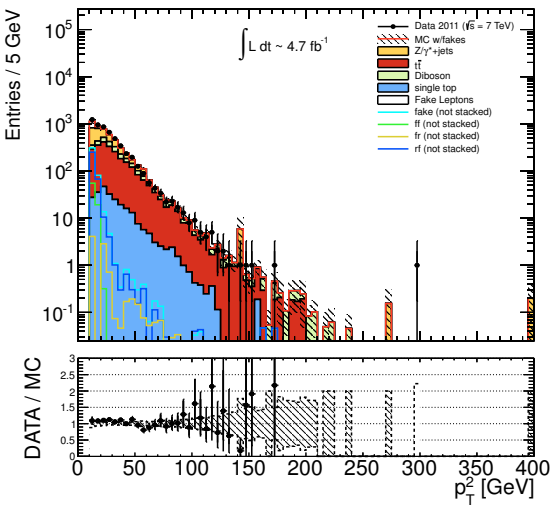

(d) $p_T^{lep,2}$

Figure 8.16: Fake lepton estimation in the OS $\mu\mu$-channel together with real lepton MC and data in validation region (ii). The sum of the various components contributing to the total fake lepton estimate, rf, fr, ff, is denoted as $fake$.

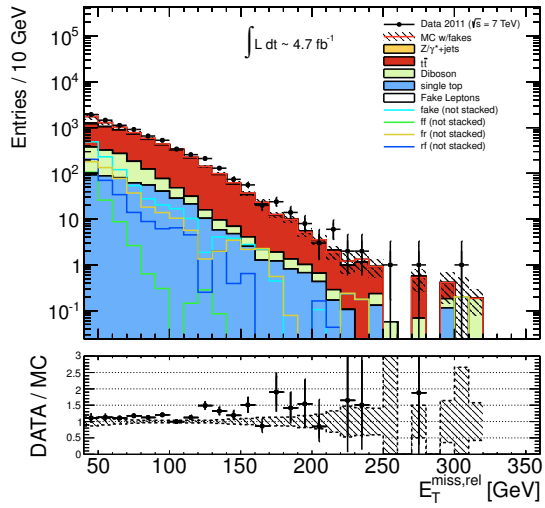

(a) $E_{\mathrm{T}}^{\mathrm{miss,rel}}$

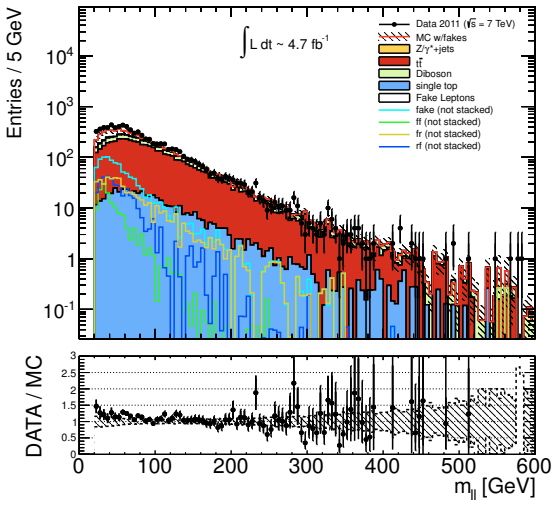

(b) m_{ll}

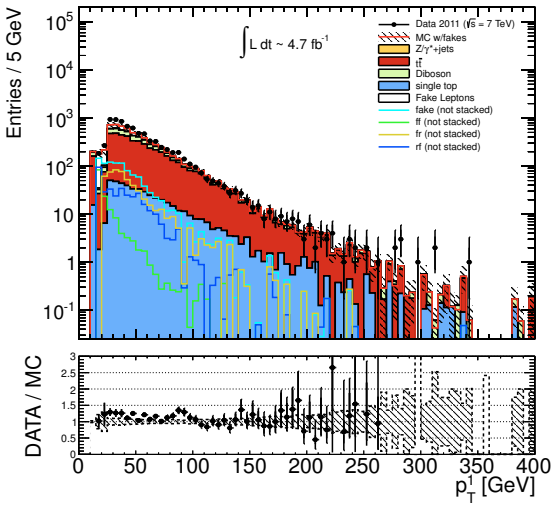

(c) $p_T^{lep,1}$

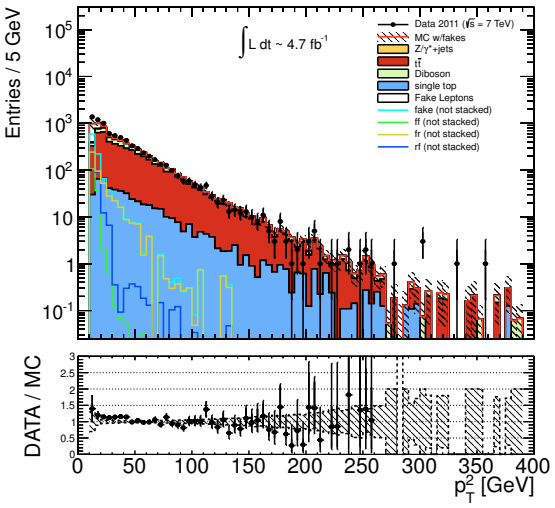

(d) $p_T^{lep,2}$

Figure 8.17: Fake lepton estimation in the OS $e\mu$-channel together with real lepton MC and data in validation region (i). The sum of the various components contributing to the total fake lepton estimate, rf, fr, ff, is denoted as $fake$.

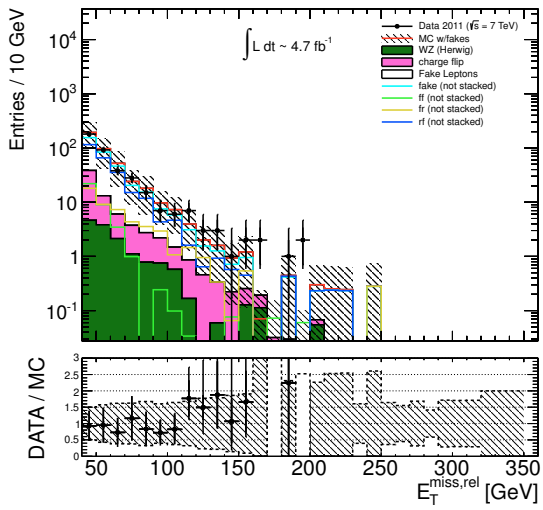

(a) $E_{\mathrm{T}}^{\mathrm{miss,rel}}$

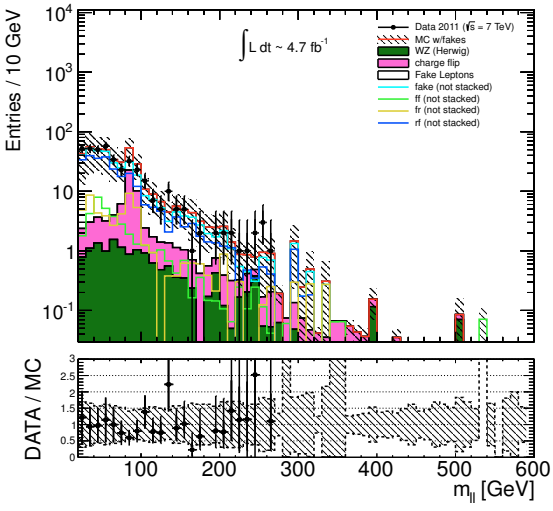

(b) m_{ll}

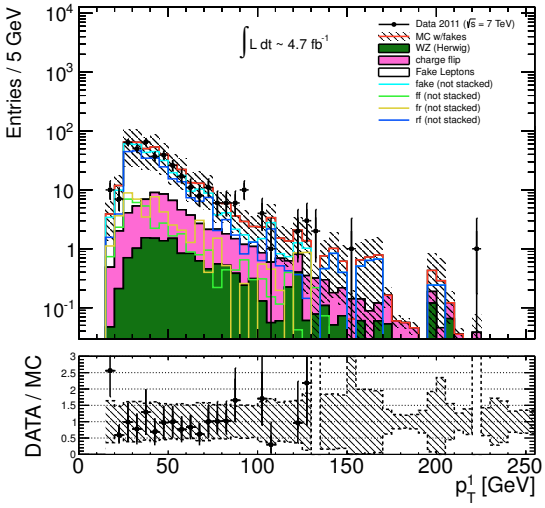

(c) $p_T^{lep,1}$

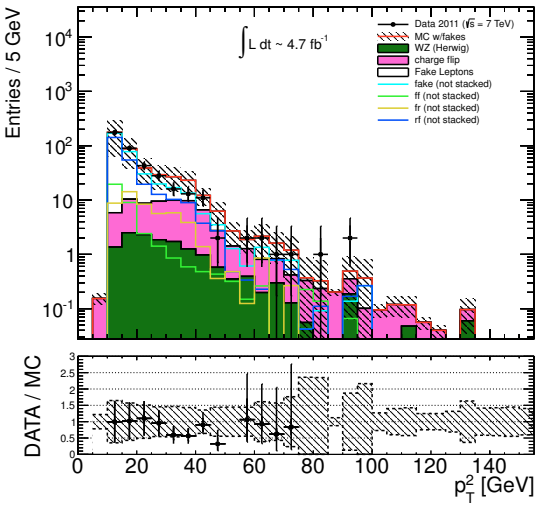

(d) $p_T^{lep,2}$

Figure 8.18: Fake lepton estimation in the SS ee-channel together with real lepton MC and data in validation region (iii). The sum of the various components contributing to the total fake lepton estimate, rf, fr, ff, is denoted as $fake$.

8.4 Systematic Uncertainties

This Section deals with systematic uncertainties from various effects stemming from MC simulations and from the methods used to estimate the fake lepton and charge-flip backgrounds. Most of the uncertainties coming from the MC simulations are applied following recommendations from the ATLAS performance groups.

8.4.1 Uncertainties from the MC Simulation

The systematic uncertainties related to various parameters and variables entering the MC generation and simulation are discussed in the following. The impact of each systematic uncertainty with the various signal regions is detailed in Table 8.11 at the end of this Section.

Cross-Section Uncertainties are summarized in Table 8.9 for various processes involved in producing the MC samples presented in Section 6.2 together with the nominal cross-sections.

Sample	Nominal [pb]	Upw. unc.	Downw. unc.	Reference(s)
W+jets, Z/γ^*+jets	Table 6.1,6.2,6.3	5.0%	5.0%	[140]
$t\bar{t}$	167	9.80%	10.70%	[103]
WW, ZZ	17,1.3	5.0%	5.0%	[140, 102]
WZ	5.9	7.0%	7.0%	[140, 102]
single top (t-channel)	20.9	37.7%	25.0%	[141]
single top (s-channel)	1.50	40.0%	36.0%	[141]
single top (Wt-channel)	15.7	7.40%	7.70%	[141]

Table 8.9: Upward and downward systematic uncertainties on the cross-sections used to generate the different MC samples.

Jet Energy Scale (JES) Uncertainty is an asymmetric uncertainty coming from the up- and down-scaling of the jet energy scale. The uncertainty is evaluated using the `MultijetJESUncertaintyProvider` which provides uncertainties on the jet energy scale as a function of jet p_T and η using the package `JetUncertainties-00-05-10`. This tool takes into account uncertainties both due to pile-up and nearby jets. When evaluating the impact of the jet energy scale systematic uncertainty, estimates obtained using the nominal jet energy scale corrections are compared with estimates after applying the additional correction retrieved by using the `MultijetJESUncertaintyProvider` tool.

Jet Energy Resolution (JER) Uncertainty is applied by smearing the jet energy according to a Gaussian distribution with mean one and a standard deviation given by

a p_T dependent resolution function [142]. The systematic uncertainty is implemented using `JetResolution-01-00-00`. The impact of this uncertainty on the final analysis is evaluated in the same way as for the JES uncertainty.

B-tagging Uncertainty is applied in accordance with the 80% working point of the `JetFitterCombNN`-tagger using the `BTagCalibrations.root` file from April 2011 provided with `SUSYTools-00-00-67`. The systematic uncertainties were obtained by investigating the impact various effects had on the method used to calculate the efficiency of the b-tagging algorithm in data, briefly discussed in Section 6.3.3. Some of the studied were the pile-up, differences with respect to the modeling of b-hadrons in data and MC, jet energy scale, differences between data and simulations of the p_{T} for the muons used in the study as well as other known differences between data and MC [123].

Electron and Muon Efficiency Uncertainty stems from the electron and muon efficiency-weights discussed in Section 6.3.1 and 6.3.2 respectively. They are calculated using the same packages as for obtaining the weights (i.e. `egammaAnalysisUtils-00-02-76` and `MuonEfficiencyCorrections-01-01-03`). The estimates using the nominal scale factors are then compared to the results using the nominal plus an upward or downward systematic effect.

Electron Resolution and Scale Uncertainties are the systematic uncertainties from the electron energy resolution and the uncertainty due to the up- or down-scaling of the electron energy-scale. They are obtained using the appropriate functions in the `egammaAnalysisUtils-00-02-76` package, as described in Section 6.3.1. The impact of these uncertainties are evaluated by comparing the nominal estimates with those scaled up or down by the smearing or energy-scale systematic uncertainty providers.

Uncertainties on the Muon Momentum Components from the MS and ID are the systematic uncertainties arising from variations of the muon momentum of the MS and ID components. They are calculated using the `MuonMomentumCorrections-00-05-03` package. The impact of this uncertainty is obtained by comparing the nominal estimates with the up/down scaling of the muon momentum from the MS and ID.

Trigger re-weighting Uncertainty is a per event uncertainty of $\pm 1.5\%$ to the trigger weights for both electrons and muons. The systematic uncertainty is applied by simply adding/subtracting 1.5%, added in quadrature with the statistical uncertainty, to the nominal weight. In the $e\mu$-channel this is done separately on the electron and muon weights. For most p_T and η values 1.5% is conservative. The details on how the systematic uncertainty on the trigger weights were obtained is discussed in Section 6.4.1.

Factorization and Renormalization Scale Uncertainties are applied to the Z/γ^*+ jets and $W+$jets Alpgen samples as an additional uncertainty on the cross-section by varying the factorization and renormalization scales. This is implemented using the

`ScaleVariatioReweighter` in `SUSYTools-00-00-67`. The scale uncertainties for $t\bar{t}$ and single top are included in the uncertainty on the cross-section.

Uncertainties from Parton Showering and ISR/FSR are studied for the $t\bar{t}$ and single top samples using the corresponding *morePS*/*lessPS* Acer samples (listed in Tables 6.5 and 6.6 for $t\bar{t}$ and single top respectively). The final uncertainty is defined by taking the event yields in each of the two sample types (N_{morePS}, N_{lessPS}) and calculate $(N_{\text{morePS}} - N_{\text{lessPS}})/2$. This relative uncertainty is then applied to the estimates obtained using the nominal $t\bar{t}$ (PowHeg+Pythia) and single top (MCAtNlo for the s-channel and Wt and AcerMC for the t-channel) samples.

Generator Uncertainties are studied by comparing the nominal samples with the corresponding samples produced using other generators. For $t\bar{t}$ this is done by comparing the *PowHeg+Herwig* and *MC@NLO* samples with the nominal *PowHeg+Pythia* samples through

$$\sigma_{\text{PowHeg+Pyth.}} = \max\left(\frac{N_{\text{PowHeg+Pyth.}} - N_{\text{PowHeg+Jimmy}}}{N_{\text{PowHeg+Pyth.}}}, \frac{N_{\text{PowHeg+Pyth.}} - N_{\text{MC@NLO}}}{N_{\text{PowHeg+Pyth.}}}\right). \tag{8.20}$$

A similar approach is followed for the single top backgrounds, thus only for the Wt- and s-channels since the *MC@NLO* samples for the t-channel can not be trusted (see Section 6.2.3). The generator systematic uncertainties are calculated for the WW, WZ and ZZ samples, comparing the *Alpgen* and *Sherpa* generators with *Herwig*. The final error on the *Herwig* sample is then given as

$$\sigma_{\text{Herwig}} = \max\left(\frac{N_{\text{Herwig}} - N_{\text{Alpgen}}}{N_{\text{Herwig}}}, \frac{N_{\text{Herwig}} - N_{\text{Sherpa}}}{N_{\text{Herwig}}}\right). \tag{8.21}$$

For the *OS-2jets* signal region the generator uncertainty is calculated with respect to the *Sherpa* samples (as these are the ones which best describe the di-boson background, as discussed in Section 6.2.2) and thus *Herwig* needs to be switched with *Sherpa* in Eq. 8.21.

Uncertainty on the Missing Transverse Energy is computed by propagating the effect of the relevant systematic uncertainties discussed above through the calculation of the missing transverse energy. This results in slightly different values of the $E_{\text{T}}^{\text{miss}}$, depending on which uncertainty is considered. An extra 5% systematic uncertainty is applied to the magnitude of the soft terms (see Section 6.3.4) that go into the $E_{\text{T}}^{\text{miss}}$ calculation. Also, a resolution uncertainty, depending on the $\sum E_T$ in the event, is used to smear the magnitude of the soft terms.

8.4.2 Uncertainties from the Charge-Flip Estimates

The systematic uncertainty from charge-flip events is calculated by using an upward and downward shift on the nominal charge-flip probabilities. The flip rates with the corresponding errors are shown in Figure 8.19.

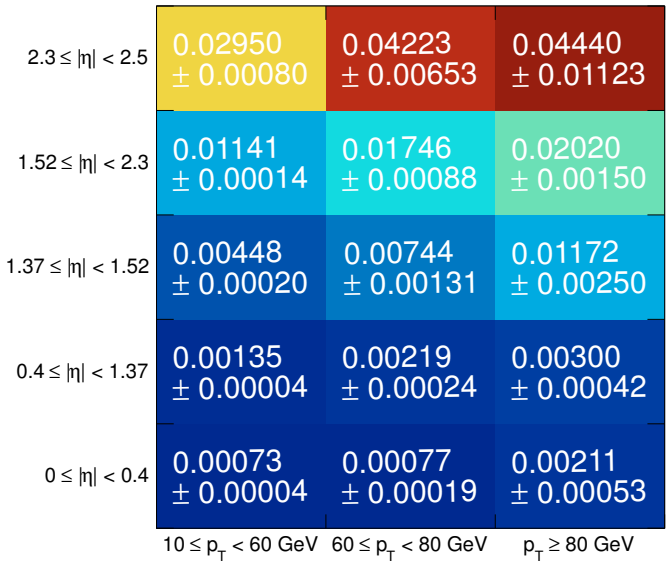

Figure 8.19: The charge-flip probability for leptons as a function of p_{T} and η. The errors shown are used when computing the systematic uncertainty on the final charge-flip estimates.

8.4.3 Uncertainties from the Fake Lepton Estimates

Table 8.10 summarizes the various systematic uncertainties considered in the MM and which have been discussed in Chapter 7 and Section 8.3. A reference to the exact section discussing the relevant uncertainty is quoted, in addition to figures or tables where present.

8.4.4 Final Systematic Uncertainties in Signal Regions

All the systematic uncertainties presented above were implemented in the analysis as discussed in Section 8.1.6. Table 8.11 shows the final systematic uncertainties in all four signal regions including all channels except for *SR-2jets*, where the $e\mu$ channel is omitted. The numbers in bold indicate the largest contribution to the total systematic uncertainty for each region.

Description	Sec.	Fig.	Tab.	e[%]	μ[%]
Systematic uncertainties on the fake-efficiency					
1. Effect of composition on the determination of the QCD MC-based fake-efficiency, f.					
a) Uncertainty on the heavy-flavour fake-efficiency due to QCD normalization.	7.2.2.2	-	7.6	$^{+15}_{-5}$	$^{+10}_{-5}$
c) Uncertainty on the combined fake-efficiency due to normalization of light-flavour component and overall QCD normalization.	8.3.2	8.14	-	$^{+0}_{-50}$	neg.
d) $E_{\mathrm{T}}^{\mathrm{miss,rel}}$ dependency (from MC).	7.2.2	7.15	-	$^{+50}_{-0}$	± 20
b) Difference in fake-efficiency for OS or SS events (from MC).	A.2	A.4	-	$^{+10}_{-0}$	± 5
2. Uncertainty of the fake-efficiencies measured in data.					
a) Difference in fake-efficiencies between $b\bar{b}$ and single- and di-lepton CR's.	7.2.1.2	-	-	± 20	± 10
b) Differences in the fake-efficiencies between single-and di-lepton CR's.	7.2.1.1	7.5	-	± 4	± 12
4. The Data-MC comparisons, and items that affect the agreement.					
a) Scale factors measured between data and MC for the QCD component.	7.2.2	7.14	-	$^{+2}_{-0}$	$^{+4}_{-0}$
b) Scale factors measured between data and MC for the conversion component.	7.2.3	7.18	-	neg.	-
c) Effect of lepton and event wise scale factors applied in MC (e.g. trigger weights or cross-section uncertainties) on the data-MC agreement in the point above.	8.4.1	-	-	± 2	neg.
Sum				$^{+57}_{-54}$	$^{+28}_{-26}$
Systematic uncertainties on the real-efficiency					
1. Differences in real-efficiency depending on process (W, Z, di-boson or top).	7.2.5.1	7.22	-	± 6	± 2

Table 8.10: Full table of systematic uncertainties for the electron and muon fake- and real-efficiencies including references to the sections where studies are performed and the relevant tables and/or figures where present. A *"neg"*. indicates that the uncertainty is negligible.

Systematics	Uncertainties in inclusive channel			
	SR-OSjveto	SR-SSjveto	SR-2jets	SR-mT2
jet energy resolution (JER)	±10.88	±0.03	±3.60	±1.51
jet energy scale (JES)	±13.21	±0.03	±2.19	±1.46
electron resolution	±0.18	±0.00	±0.22	±0.11
electron scale	±0.06	±0.00	±0.21	±0.92
electron weights	±2.57	±0.05	±0.93	±0.38
muon ID momentum comp.	±0.05	±0.00	±0.06	±0.03
Muon Spectrometer momentum comp.	±0.24	±0.06	±0.51	±0.25
muon scale	±0.01	±0.00	±0.16	±0.86
muon weights	±0.42	±0.01	±0.20	±0.09
soft terms in $E_{\mathrm{T}}^{\mathrm{miss,rel}}$ calc.	±1.31	±0.06	±0.11	±0.11
syst. from Matrix Method	±2.56	**±1.68**	±2.11	±1.14
trigger weights	±2.88	±0.06	±1.20	±0.55
pile-up	±1.05	±0.08	±0.27	±0.31
luminosity	±0.15	±0.00	±0.09	±0.03
diboson MC generators	±6.77	±0.46	±9.73	±0.00
single top MC generators	±13.00	±0.00	±2.22	±1.72
$t\bar{t}$ MC generators	±3.05	±0.00	±0.69	±0.20
single top MC ISR/FSR	±0.51	±0.00	±0.09	±0.09
$t\bar{t}$ MC ISR/FSR	**±32.77**	±0.00	**±14.39**	±0.00
Z/γ^* MC reweighting scale	±0.10	±0.00	±2.25	±0.30
Z/γ^* MC factorisation scale	±0.05	±0.00	±0.91	±0.13
cross section	±11.22	±0.21	±5.04	**±2.08**
luminosity	±0.15	±0.00	±0.09	±0.03
total systematic	±41.74	±1.76	±19.06	±5.58
Total ± (stat.) ± (syst)	$152.0 \pm 4.8 \pm 41.74$	$9.4 \pm 1.5 \pm 1.76$	$65.8 \pm 3.2 \pm 19.06$	$32.5 \pm 2.1 \pm 5.58$

Table 8.11: The total systematic uncertainty in the various signal regions including all relevant channels. The total number of events together with the full statistical and systematic uncertainty is summarized in the last row.

8.5 Full SM Background Composition in the Signal Regions

In Section 8.3.5 the fake lepton and charge-flip estimates were shown, together with the real lepton contribution from the MC simulations, to give a satisfactory description of data in some chosen validation regions. All the various parts of the analysis are now in place to have a closer look at the expected SM backgrounds, broken down into the various components, for each of the signal regions. This allows to better understand the relative impact of each background on the final result. Table 8.12 summarizes the background in each of the signal regions for the ee- (upper), $e\mu$- (middle) and $\mu\mu$-channels (lower). The errors are statistical only. The di-boson contribution is split into its three components, WW, WZ and ZZ. For the *OSjveto* and *OS2jets* signal regions $t\bar{t}$ is the dominant background followed by the di-bosons, particularly WW. In the ee- and $\mu\mu$-channels there are, in addition, non-negligible contributions from ZZ. In the *SSjveto* signal region the SM real lepton background is negligible, as expected, with only a small contribution from WZ[3]. The dominant background is the one coming from fake leptons. In the ee- and $e\mu$-channels there is a non-negligible component from charge-flip events. It should be noticed that the W+jets contribution from MC is totally absent in all 3 tables, since these events (with one real lepton) are estimated from the rf and fr components of the MM.

The yields in Table 8.12 differ somewhat from the published numbers in [76]. This comes not only from the slightly newer *SUSYTools* version used in the current analysis, but also from the fact that some of the SM backgrounds in the publication were estimated using techniques based on data. This is the case for $t\bar{t}$ in all signal regions, WW in the *SR-OSjveto* and the Z/γ^*, WZ and ZZ background in the SF signal regions. The fake lepton and charge-flip backgrounds were estimated in the same way as detailed in this thesis.

8.5.1 Data to Monte Carlo Comparison in Signal and Support Regions

In this section some distributions including the full 4.71 fb^{-1} dataset together with all the SM backgrounds after applying some additional cuts on the baseline selection are shown. In Section 8.5.1.1 some relevant distributions, such as $E_{\mathrm{T}}^{\mathrm{miss,rel}}$, m_{ll} and N_{jet}, are plotted for some selected signal-like regions. In Section 8.5.1.2 the $E_{\mathrm{T}}^{\mathrm{miss,rel}}$ distributions for the *OSjveto*, *SSjveto* and *2jets* signal regions are shown, prior to the final $E_{\mathrm{T}}^{\mathrm{miss,rel}}$ cut. For the *mT2* signal region the m_{T2} distribution is shown after the cut on $E_{\mathrm{T}}^{\mathrm{miss,rel}}$ is applied.

The error bars on the data points are statistical Poisson limits calculated as discussed in Section 8.1.4, while the hatched area reflects the full statistical uncertainty on the MC simulations added in quadrature with the uncertainty on the fake-estimates. The systematic uncertainties from the MC simulations discussed in Section 8.4.1 are, however, not included in these plots. In the bottom histograms in each figure the data yields are

[3]This process gives SS events in cases where the lepton from the Z-decay, having opposite sign to that of the lepton from the W-decay, is not reconstructed.

ee channel	SR-OSjveto	SR-SSjveto	SR-2jets	SR-mT2
Z/γ^*+jets	0.20 ± 0.20	0.00 ± 0.00	2.28 ± 0.66	0.36 ± 0.26
WW	7.63 ± 0.67	0.00 ± 0.00	6.61 ± 1.08	1.94 ± 0.35
WZ	1.45 ± 0.30	0.75 ± 0.21	0.78 ± 0.28	1.27 ± 0.28
ZZ	3.24 ± 0.46	0.00 ± 0.00	0.11 ± 0.04	2.48 ± 0.40
diboson	12.32 ± 0.87	0.75 ± 0.21	7.50 ± 1.11	5.69 ± 0.60
$t\bar{t}$	14.45 ± 1.62	0.00 ± 0.00	15.58 ± 1.68	2.18 ± 0.63
single top	4.27 ± 0.78	0.00 ± 0.00	1.38 ± 0.47	0.80 ± 0.33
charge flip	0.00 ± 0.00	0.54 ± 0.03	0.00 ± 0.00	0.00 ± 0.00
fake leptons	2.78 ± 1.15	2.92 ± 0.89	3.11 ± 1.34	1.37 ± 0.67
total SM	34.03 ± 2.31	4.04 ± 0.92	29.86 ± 2.55	10.40 ± 1.17

$e\mu$ channel	SR-OSjveto	SR-SSjveto	SR-mT2
WW	17.96 ± 1.02	0.00 ± 0.00	4.34 ± 0.52
WZ	1.59 ± 0.31	1.46 ± 0.30	0.32 ± 0.14
ZZ	0.22 ± 0.11	0.05 ± 0.05	0.06 ± 0.06
diboson	19.77 ± 1.07	1.51 ± 0.31	4.72 ± 0.54
$t\bar{t}$	37.84 ± 2.61	0.00 ± 0.00	4.72 ± 0.95
single top	8.32 ± 1.08	0.00 ± 0.00	0.68 ± 0.35
charge flip	0.00 ± 0.00	0.17 ± 0.01	0.00 ± 0.00
fake leptons	7.07 ± 1.64	2.41 ± 0.82	1.13 ± 0.60
total SM	73.00 ± 3.44	4.10 ± 0.88	11.25 ± 1.29

$\mu\mu$ channel	SR-OSjveto	SR-SSjveto	SR-2jets	SR-mT2
Z/γ^*+jets	0.23 ± 0.23	0.00 ± 0.00	4.35 ± 0.99	0.55 ± 0.36
WW	11.48 ± 0.80	0.00 ± 0.00	7.50 ± 1.10	3.74 ± 0.46
WZ	2.05 ± 0.34	0.78 ± 0.21	1.43 ± 0.38	1.18 ± 0.26
ZZ	2.71 ± 0.40	0.00 ± 0.00	0.31 ± 0.06	1.54 ± 0.30
diboson	16.24 ± 0.96	0.78 ± 0.21	9.25 ± 1.16	6.46 ± 0.62
$t\bar{t}$	23.93 ± 1.99	0.00 ± 0.00	18.16 ± 1.78	3.03 ± 0.73
single top	4.29 ± 0.77	0.00 ± 0.00	1.37 ± 0.50	0.85 ± 0.32
fake leptons	0.24 ± 0.63	0.56 ± 0.60	1.44 ± 1.21	−0.02 ± 0.01
total SM	44.94 ± 2.43	1.34 ± 0.63	34.57 ± 2.69	10.88 ± 1.07

Table 8.12: The SM backgrounds broken down into the various components for each of the signal regions in the three channels, ee (top), $e\mu$ (center) and $\mu\mu$ (bottom). The number are normalized to an integrated luminosity of 4.71 fb^{-1}.

divided by the SM backgrounds in each bin, in order to better illustrate any deviation of MC from data.

8.5.1.1 Signal-Like Regions

The plots in Figure 8.20 show the m_{ll} distribution for OS ee (a), $\mu\mu$ (b) and $e\mu$ (c) pairs after requiring a jet-veto in addition to $E_{\mathrm{T}}^{\mathrm{miss,rel}} > 100$ GeV. The statistics is quite limited, but the agreement between data and MC is within the errors. As already pointed out the di-boson and top backgrounds are dominating.

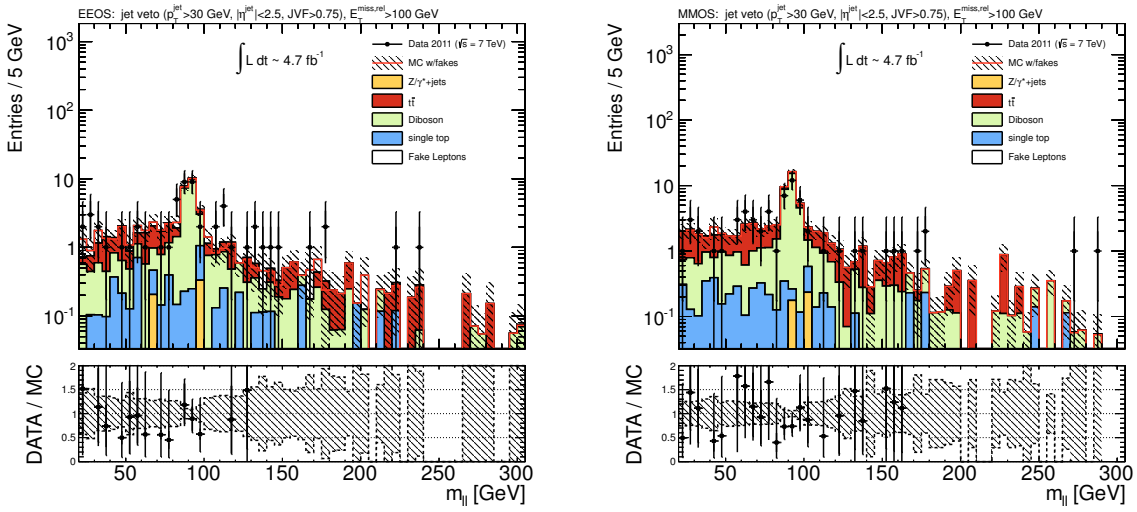

(a) OS-ee

(b) OS-$\mu\mu$

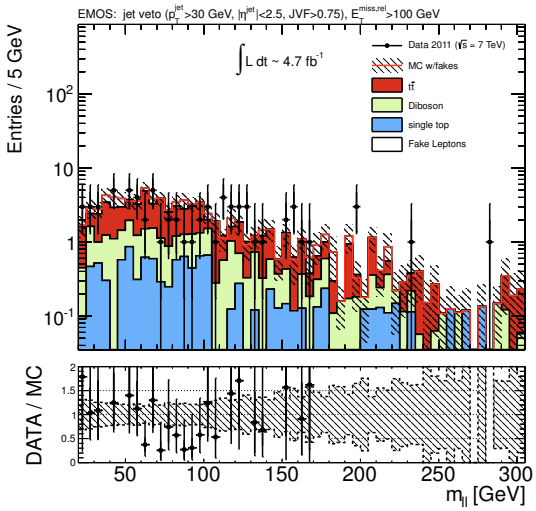

(c) OS-$e\mu$

Figure 8.20: The m_{ll} distribution for OS ee (a), $\mu\mu$ (b) and $e\mu$ (c) pairs in events requiring a jet-veto and $E_{\mathrm{T}}^{\mathrm{miss,rel}} > 100$ GeV.

Figure 8.21 presents the distributions of the number of signal jets in events with SS ee (a), $\mu\mu$ (b) and $e\mu$ (c) pairs without any further cuts besides the ones defining the baseline selection. The fake lepton and charge-flip backgrounds are dominating and thus

the errors are quite large due to the relatively large uncertainty on the fake estimates. The only significant background from the MC simulations comes from di-boson processes, in particular WZ and ZZ. Despite the relatively large errors, the agreement between data and MC is found to be very good.

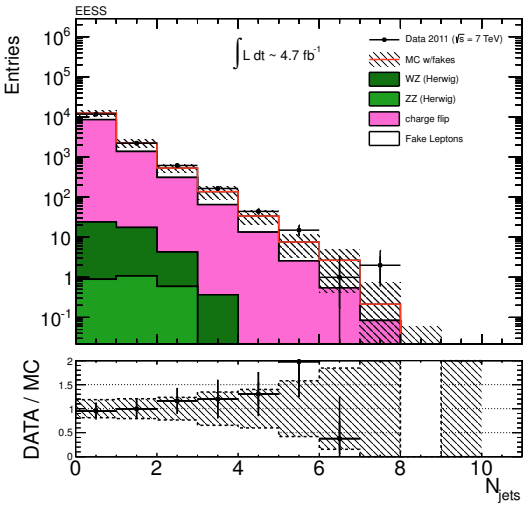

(a) SS-ee

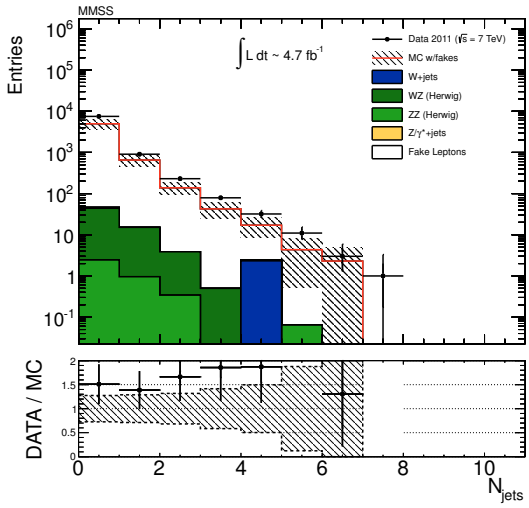

(b) SS-$\mu\mu$

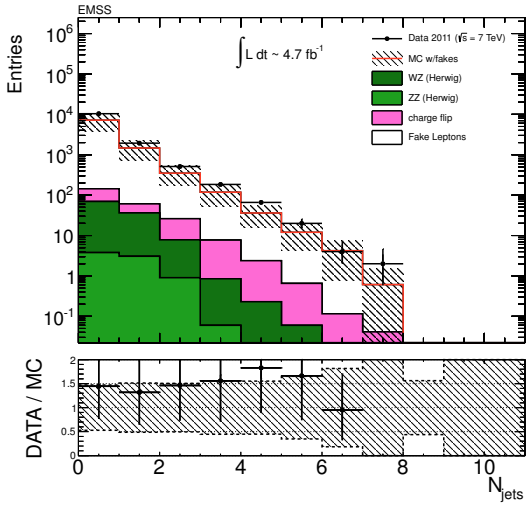

(c) SS-$e\mu$

Figure 8.21: The signal jet multiplicity for all events with SS ee (a), $\mu\mu$ (b) and $e\mu$ (c) pairs passing the baseline selection.

Figure 8.22 shows the m_{ll} distributions for OS ee (a) and $\mu\mu$ (b) events with two or more signal jets requiring additional vetoes on b-jets and the *contransverse* mass, m_{CT}. The $t\bar{t}$ background is quite small as expected after applying the vetoes on b-jets and m_{CT}. The dominating background is clearly the Z/γ^*+jets. The agreement between data and MC is relatively good in both distributions. In all these plots the *Sherpa* samples are used to model the di-boson background, as discussed in Section 6.2.2.

Figures 8.23 and 8.24 illustrate the m_{ll} and $E_{\mathrm{T}}^{\mathrm{miss,rel}}$ distributions, respectively, for OS ee (a), $\mu\mu$ (b) and $e\mu$ (c) events after requiring a Z-veto (not for the m_{ll} plots in Fig.

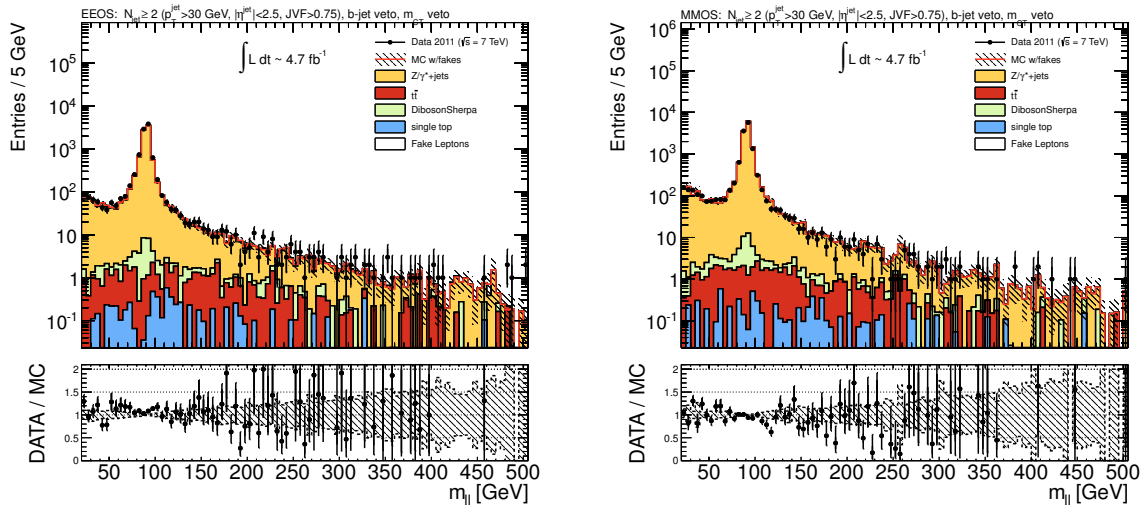

(a) OS-ee (b) OS-$\mu\mu$

Figure 8.22: The m_{ll} distributions in events with OS ee (a) or $\mu\mu$ (b) pairs requiring $N_{jet} >= 2$ and applying vetoes on b-jets and m_{CT}. The $e\mu$-channel is omitted since the *OS2jets* signal regions does not include it.

8.23) and a jet-veto in addition to $E_{\mathrm{T}}^{\mathrm{miss,rel}} > 40$ GeV. The agreement between data and the prediction is good. In the $e\mu$-channel the Z/γ^*+jets is as expected very small and the fake lepton estimates are relatively important, especially towards smaller values of m_{ll} and $E_{\mathrm{T}}^{\mathrm{miss,rel}}$. In the ee- and $\mu\mu$-channels the fake lepton background plays a less important role as the Z/γ^*+jets make up most of the background in these regions, some discrepancies are, however, seen in these channels for small values of m_{ll}.

8.5.1.2 Plots for the Signal Regions

Figures 8.25, 8.26 and 8.27 show the $E_{\mathrm{T}}^{\mathrm{miss,rel}}$ distributions for the relevant channels in the *OSjveto*, *SSjveto* and *2jets* signal regions, respectively, after all cuts are applied except the final cut on $E_{\mathrm{T}}^{\mathrm{miss,rel}}$. Figure 8.28 shows the distribution of m_{T2} for the *mT2* signal region after the $E_{\mathrm{T}}^{\mathrm{miss,rel}} > 40$ GeV cut and before the final $m_{T2} > 90$ GeV cut is applied.

The agreement between data and MC is found to be relatively good in most plots. Some deviations are seen, however, especially at low $E_{\mathrm{T}}^{\mathrm{miss,rel}}$. This is however as expected, since, as already pointed out in Chapter 7, the fake-efficiency does not properly reflect the leptons in $E_{\mathrm{T}}^{\mathrm{miss,rel}} < 40$ GeV region. In the *SSjveto* signal region the background from fake leptons is the dominant. In most of the other regions the fake lepton contribution is less prominent, except in the $e\mu$-channel where it is more important, especially at low $E_{\mathrm{T}}^{\mathrm{miss,rel}}$ or m_{T2}. Since the systematic uncertainties from the SM MC simulations are not included in these plots some of the deviations observed between data and MC are expected to be covered when adding the full uncertainty (listed in Table 8.11 for the 4 signal regions).

From the studies in this section, by looking at various distributions, the SM predictions seem to describe the observed data rather well for all variables in all signal regions. Any significant deviation above the SM background could have indicated the presence of some new physics, especially at high $E_{\mathrm{T}}^{\mathrm{miss,rel}}$ and m_{T2} values. Since no excesses are

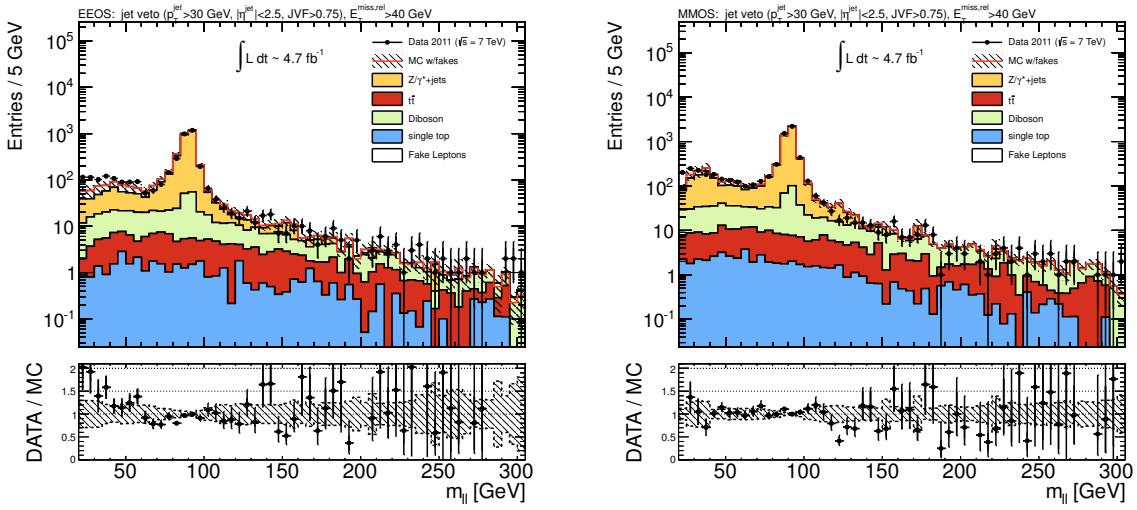

(a) OS-ee

(b) OS-$\mu\mu$

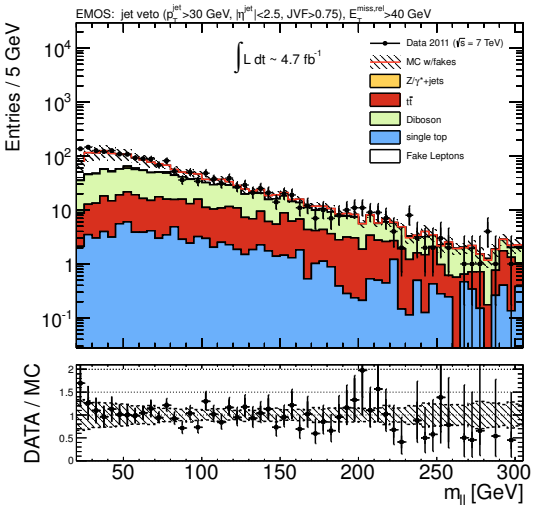

(c) OS-$e\mu$

Figure 8.23: The m_{ll} distribution for OS ee (a), $\mu\mu$ (b) and $e\mu$ (c) pairs in events requiring a jet-veto and $E_{\mathrm{T}}^{\mathrm{miss,rel}} > 40$ GeV.

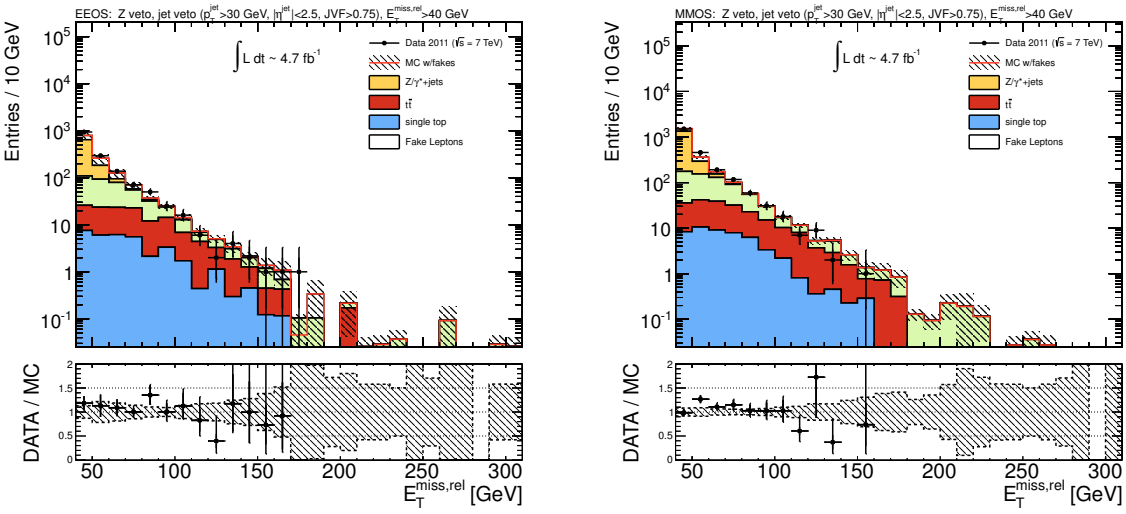

(a) OS-ee (b) OS-$\mu\mu$

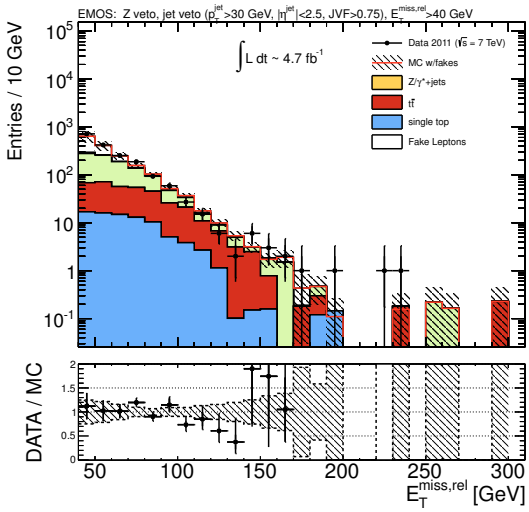

(c) OS-$e\mu$

Figure 8.24: The $E_{\mathrm{T}}^{\mathrm{miss,rel}}$ distribution for OS ee (a), $\mu\mu$ (b) and $e\mu$ (c) pairs in events requiring Z- and jet-vetoes.

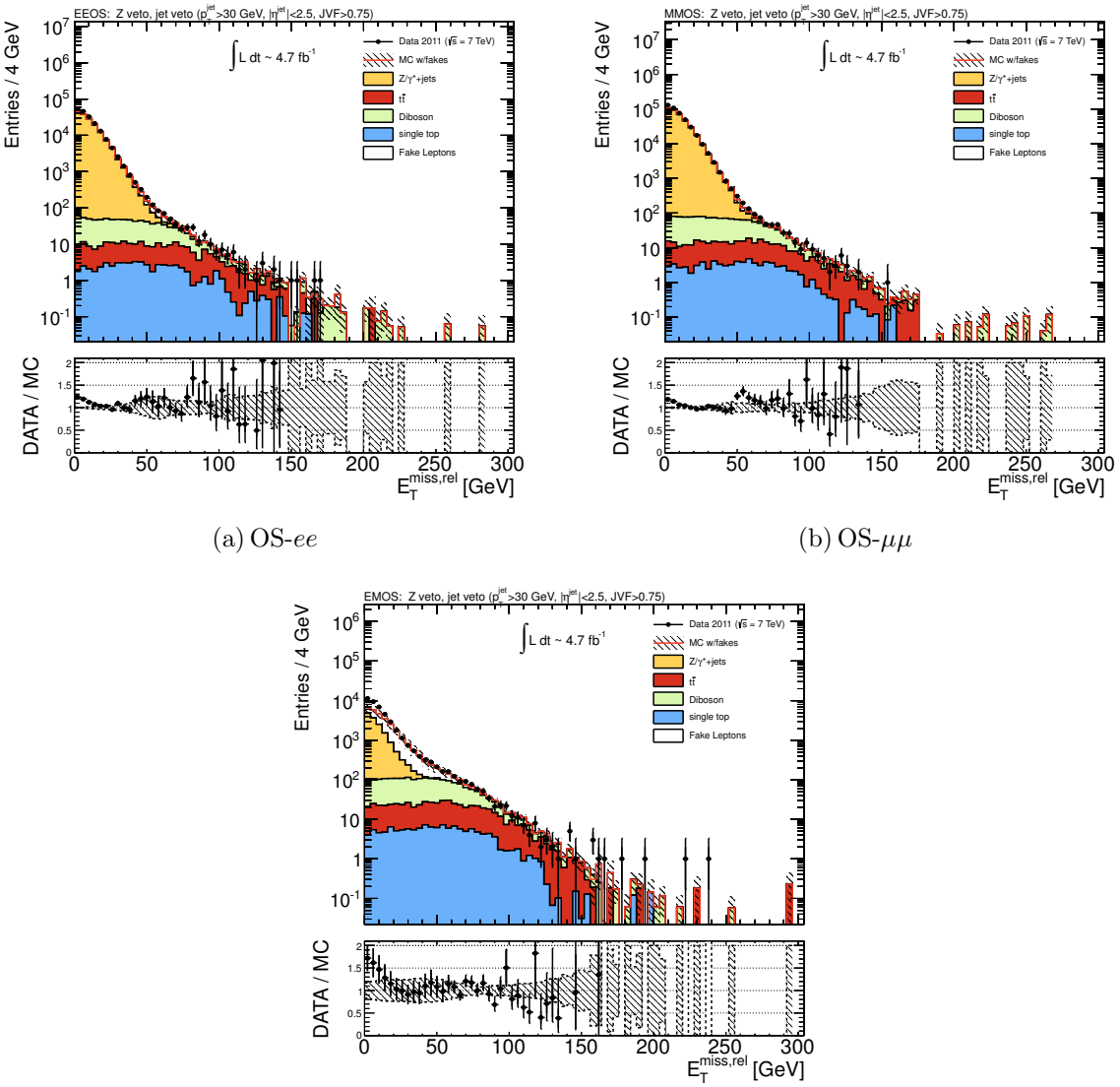

(a) OS-ee (b) OS-$\mu\mu$

(c) OS-$e\mu$

Figure 8.25: The $E_{\mathrm{T}}^{\mathrm{miss,rel}}$ distribution for OS ee (a), $\mu\mu$ (b) and $e\mu$ (c) pairs in the *OSjveto* signal region. A cut on $E_{\mathrm{T}}^{\mathrm{miss,rel}}$ > 100 GeV defines the signal region.

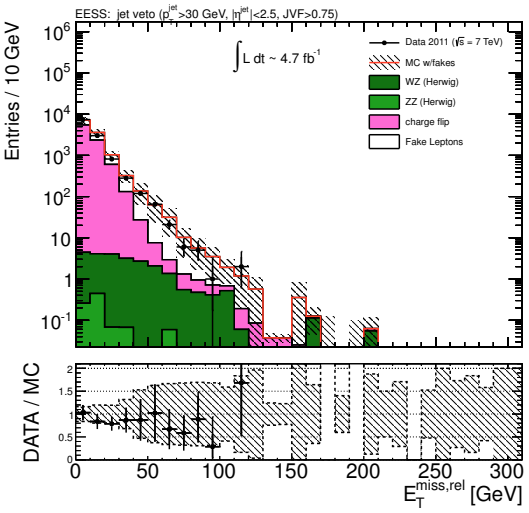

(a) SS-ee

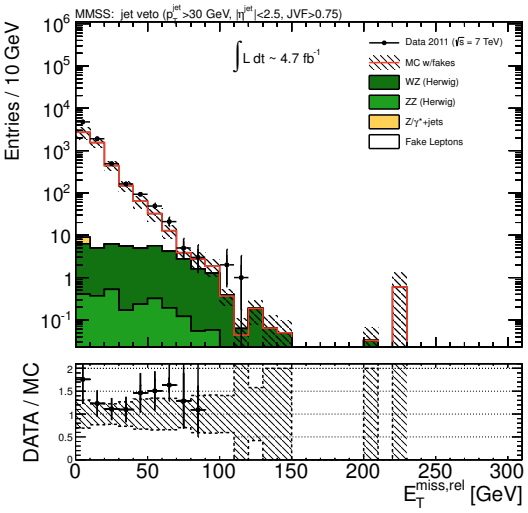

(b) SS-$\mu\mu$

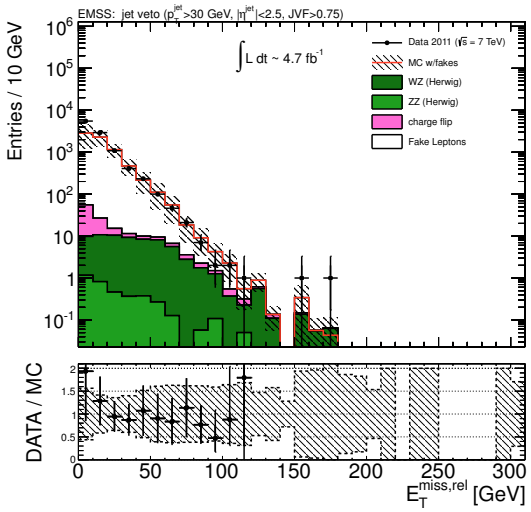

(c) SS-$e\mu$

Figure 8.26: The $E_{\mathrm{T}}^{\mathrm{miss,rel}}$ distribution for SS ee (a), $\mu\mu$ (b) and $e\mu$ (c) pairs in the *SSjveto* signal region. A final cut on $E_{\mathrm{T}}^{\mathrm{miss,rel}} > 100$ GeV defines the signal region.

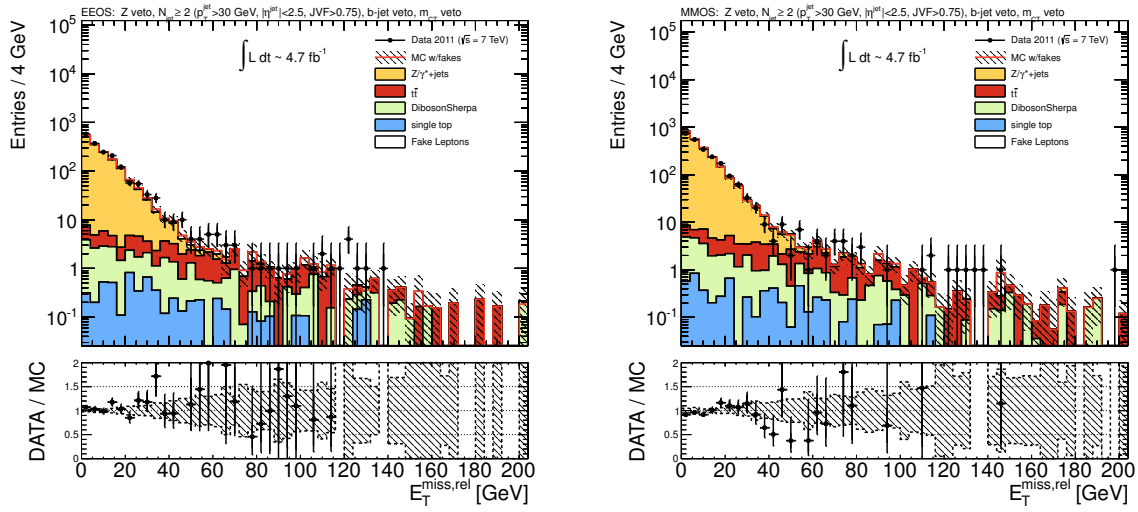

(a) OS-ee (b) OS-$\mu\mu$

Figure 8.27: The $E_{\mathrm{T}}^{\mathrm{miss,rel}}$ distribution for OS ee (a) and $\mu\mu$ (b) pairs in the *2jets* signal region. A final cut on $E_{\mathrm{T}}^{\mathrm{miss,rel}} > 50$ GeV defines the signal region.

found, however, the results can be used to set upper limits on the visible cross-section for processes involving new physics scenarios. The results can also be used to exclude certain regions of the parameter space of interesting SUSY models. This will be discussed in the following sections.

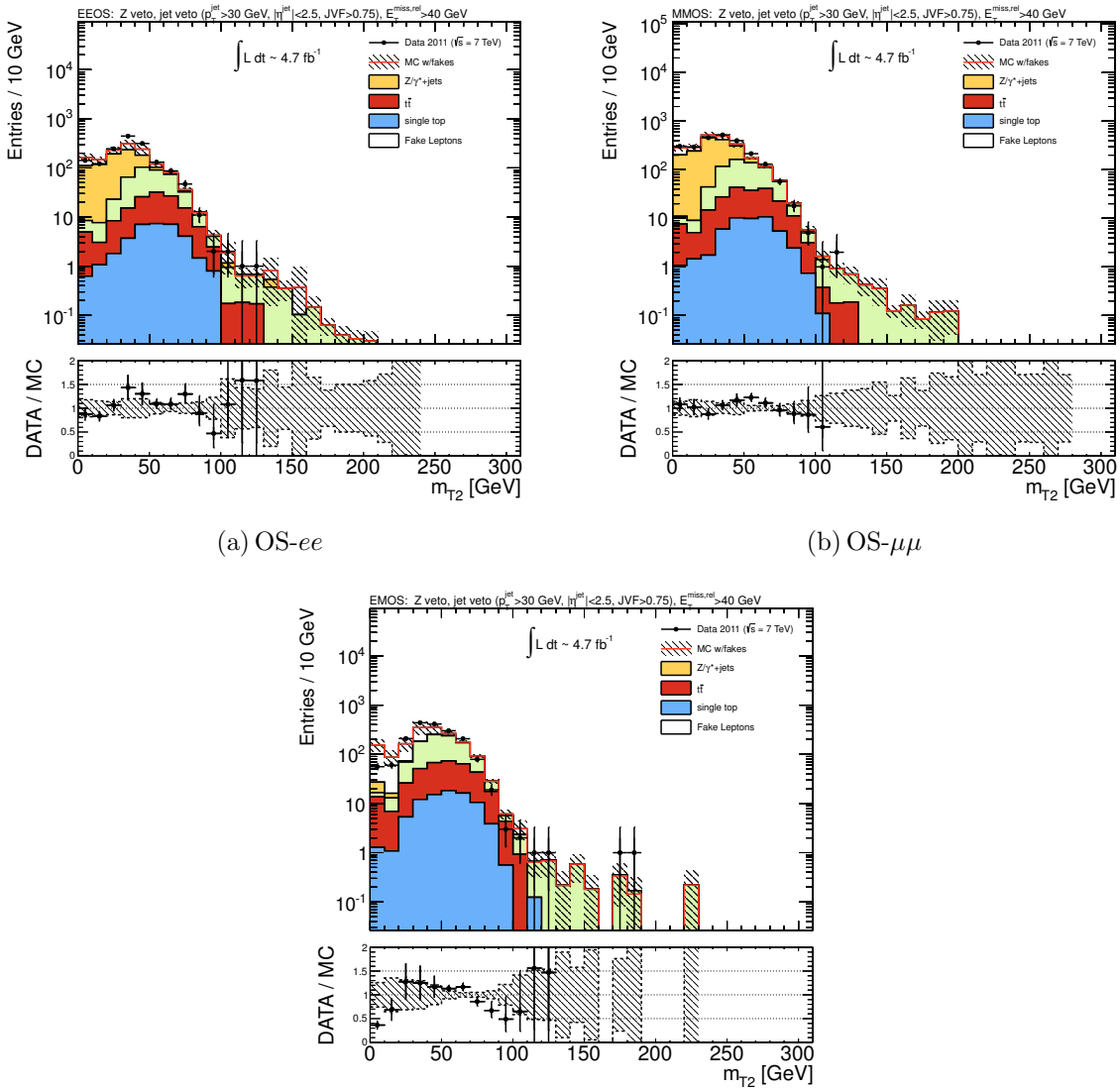

(a) OS-ee

(b) OS-$\mu\mu$

(c) OS-$e\mu$

Figure 8.28: The m_{T2} distribution for OS ee (a), $\mu\mu$ (b) and $e\mu$ (c) pairs in the $mT2$ signal region. A final cut on $m_{T2} > 90$ GeV defines the signal region.

8.6 Upper Limits on the Cross-Section for New Physics

With the fake lepton estimates, the SM MC backgrounds and the systematic uncertainties in place, the final numbers in each signal region can be computed. Table 8.6 shows the number of observed events together with the various SM backgrounds

Together with the number of events in each signal region the total statistical and systematic errors are shown, as the first and second error respectively. The statistical errors are taken from the sum of squares of the weights for each event in the signal region. The systematic uncertainty is computed using HistFitter as described in Section 8.1.5 and takes into all possible correlations between sources, backgrounds and channels. All the systematic uncertainties listed in Section 8.4 are included.

Also quoted are the observed and expected 95% confidence limits on the effective cross-section for signal-like SUSY events in the signal regions, $\sigma^{obs(exp)}$. The error on the expected limit is computed by taking the $\pm 1\sigma$ band around the expected limit. All limits are computed using the *HistFitter* tool running with asymptotics and using the profile likelihood method discussed in Section 8.1.3.3.

SROSjveto

	$e^{\pm}e^{\mp}$	$e^{\pm}\mu^{\mp}$	$\mu^{\pm}\mu^{\mp}$	all
Diboson	$12.3 \pm 0.9 \pm 2.1$	$19.8 \pm 1.1 \pm 12.0$	$16.2 \pm 1.0 \pm 4.8$	$48.3 \pm 1.7 \pm 7.6$
$t\bar{t}$	$14.5 \pm 1.6 \pm 6.7$	$37.8 \pm 2.6 \pm 17.1$	$23.9 \pm 2.0 \pm 11.1$	$76.2 \pm 3.6 \pm 36.3$
Single Top	$4.3 \pm 0.8 \pm 3.4$	$8.3 \pm 1.1 \pm 6.6$	$4.3 \pm 0.8 \pm 3.3$	$16.9 \pm 1.5 \pm 13.3$
Fake Leptons	$2.8 \pm 1.2 \pm 1.5$	$7.1 \pm 1.8 \pm 2.0$	$0.2 \pm 0.6 \pm 0.4$	$10.1 \pm 2.2 \pm 2.6$
Z/γ^*+jets	$0.2 \pm 0.2 \pm 0.1$	$0.0 \pm 0.0 \pm 0.0$	$0.2 \pm 0.2 \pm 0.1$	$0.4 \pm 0.3 \pm 0.3$
Total	$34.0 \pm 2.3 \pm 7.9$	$73.0 \pm 3.5 \pm 22.0$	$44.9 \pm 2.4 \pm 12.5$	$152.0 \pm 4.8 \pm 41.7$
Data	33	65	37	135
$\sigma^{obs(exp)}$[fb]	4.11 ($4.2^{+1.5}_{-1.0}$)	7.71 ($8.3^{+2.5}_{-1.9}$)	4.39 ($5.1^{+1.7}_{-1.3}$)	13.28 ($15^{+4.2}_{-3.4}$)

SRSSjveto

	$e^{\pm}e^{\pm}$	$e^{\pm}\mu^{\pm}$	$\mu^{\pm}\mu^{\pm}$	all
Diboson	$0.7 \pm 0.2 \pm 0.1$	$1.5 \pm 0.3 \pm 0.9$	$0.8 \pm 0.2 \pm 0.2$	$3.0 \pm 0.4 \pm 0.5$
ChargeFlip	$0.5 \pm 0.0 \pm 0.1$	$0.1 \pm 0.0 \pm 0.0$	$0.0 \pm 0.0 \pm 0.0$	$0.4 \pm 0.0 \pm 0.0$
Fake Leptons	$2.9 \pm 0.9 \pm 1.1$	$2.4 \pm 0.9 \pm 1.0$	$0.6 \pm 0.6 \pm 0.6$	$5.9 \pm 1.4 \pm 1.7$
Total	$4.2 \pm 0.9 \pm 1.1$	$4.0 \pm 0.9 \pm 1.4$	$1.3 \pm 0.6 \pm 0.6$	$9.4 \pm 1.5 \pm 1.8$
Data	2	5	3	10
$\sigma^{obs(exp)}$[fb]	0.84 ($1.1^{+0.6}_{-0.4}$)	1.46 ($1.3^{+0.6}_{-0.4}$)	1.27 ($0.9^{+0.5}_{-0.3}$)	1.84 ($1.7^{+0.8}_{-0.5}$)

SR2jets

	$e^{\pm}e^{\mp}$	$e^{\pm}\mu^{\mp}$	$\mu^{\pm}\mu^{\mp}$	all
Diboson	$7.8 \pm 0.4 \pm 4.5$	-	$9.6 \pm 0.5 \pm 6.3$	$17.4 \pm 0.6 \pm 9.9$
$t\bar{t}$	$15.7 \pm 1.7 \pm 6.9$	-	$18.5 \pm 1.8 \pm 8.3$	$34.3 \pm 2.5 \pm 14.9$
DrellYan	$0.2 \pm 0.2 \pm 0.0$	-	$0.3 \pm 0.3 \pm 1.1$	$0.5 \pm 0.4 \pm 1.1$
Single Top	$1.4 \pm 0.5 \pm 1.1$	-	$1.4 \pm 0.5 \pm 1.1$	$2.9 \pm 0.7 \pm 2.2$
Fake Leptons	$3.1 \pm 0.7 \pm 1.7$	-	$1.4 \pm 1.1 \pm 1.2$	$4.5 \pm 1.4 \pm 2.1$
Z/γ^*+jets	$2.1 \pm 0.7 \pm 1.0$	-	$4.1 \pm 1.0 \pm 1.9$	$6.2 \pm 1.2 \pm 2.7$
Total	$30.4 \pm 2.1 \pm 8.5$	-	$35.4 \pm 2.4 \pm 10.7$	$65.8 \pm 3.2 \pm 19.1$
Data	40	-	39	79
$\sigma^{obs(exp)}$[fb]	6.04 ($4.6^{+1.7}_{-1.3}$)	-	5.59 ($5.1^{+1.8}_{-1.3}$)	10.38 ($8.6^{+2.9}_{-2.2}$)

SRmT2

	$e^{\pm}e^{\mp}$	$e^{\pm}\mu^{\mp}$	$\mu^{\pm}\mu^{\mp}$	SF	all
Diboson	$5.7 \pm 0.6 \pm 0.5$	$4.7 \pm 0.5 \pm 0.5$	$6.5 \pm 0.6 \pm 0.4$	$12.1 \pm 0.9 \pm 0.8$	$16.9 \pm 1.0 \pm 1.2$
$t\bar{t}$	$2.2 \pm 0.6 \pm 1.1$	$4.7 \pm 0.9 \pm 2.0$	$3.0 \pm 0.7 \pm 1.3$	$5.2 \pm 1.0 \pm 2.4$	$9.9 \pm 1.4 \pm 4.3$
Single Top	$0.8 \pm 0.3 \pm 0.9$	$0.7 \pm 0.3 \pm 0.6$	$0.8 \pm 0.3 \pm 0.7$	$1.6 \pm 0.5 \pm 1.4$	$2.3 \pm 0.6 \pm 1.8$
Fake Leptons	$1.4 \pm 0.7 \pm 0.9$	$1.1 \pm 0.6 \pm 0.8$	$0.0 \pm 0.0 \pm 0.0$	$1.3 \pm 0.7 \pm 0.9$	$2.5 \pm 0.9 \pm 1.1$
Z/γ^*+jets	$0.4 \pm 0.3 \pm 0.1$	$0.0 \pm 0.0 \pm 0.0$	$0.6 \pm 0.4 \pm 0.4$	$0.9 \pm 0.5 \pm 0.5$	$0.9 \pm 0.5 \pm 0.5$
Total	$10.4 \pm 1.2 \pm 1.7$	$11.3 \pm 1.3 \pm 2.3$	$10.9 \pm 1.1 \pm 1.6$	$21.3 \pm 1.6 \pm 3.0$	$32.5 \pm 2.1 \pm 5.6$
Data	6	9	8	14	23
$\sigma^{obs(exp)}$[fb]	1.12 ($1.7^{+0.8}_{-0.5}$)	1.56 ($1.9^{+0.8}_{-0.5}$)	1.33 ($1.7^{+0.8}_{-0.5}$)	1.57 ($2.4^{+1.0}_{-0.7}$)	2.08 ($3.1^{+1.3}_{-0.9}$)

Table 8.13: Table summarizing all the various SM backgrounds. The number of events observed in each signal region for the full 4.7 fb^{-1} 2011 dataset and the observed (expected) 95% CL limits, $\sigma^{obs(exp)}$, on the effective cross-sections are quoted.

8.7 Interpretation in SUSY Models

Since no excess was found in any of the channels in Section 8.6 the observations and background expectations are used to exclude regions in parameter space of various SUSY signal grids. The exclusion limits are calculated using the *HistFitter* package.

All the relevant flavour channels are combined when computing the limits. Only the SF channel of the *SR-mT2* is used, however, when interpreting the results in the direct slepton signal grid, since we do not expect any mixing of flavours in these models. All channels are included when using *SR-mT2* in the simplified models and direct gaugino grids, however.

Table 8.14 summarizes the results for each signal region used when computing the limits presented in this section. The $\sigma^{obs(exp)}$ are the numbers used in the final limit

Num: Name	1: *OSjveto*	2: *SSjveto*	3: *2jets*	4: *mT2*	
Channels	OSSF+OSDF	SSSF+SSDF	OSSF	OSSF+OSDF	OSSF
Cuts	jet-veto Z-veto $E_{\mathrm{T}}^{\mathrm{miss,rel}} > 100$ GeV	jet-veto $E_{\mathrm{T}}^{\mathrm{miss,rel}} > 100$ GeV	≥ 2 jets b-jet veto m_{CT}-veto Z-veto	jet-veto Z-veto $E_{\mathrm{T}}^{\mathrm{miss,rel}} > 40$ GeV $m_{T2} > 90$ GeV	
Total SM	$152.0 \pm 4.8 \pm 41.7$	$9.4 \pm 1.5 \pm 1.8$	$65.8 \pm 3.2 \pm 19.1$	$32.5 \pm 2.1 \pm 5.6$	$21.3 \pm 1.6 \pm 3.0$
Data	135	10	79	23	14
$\sigma^{obs(exp)}$[fb]	$13.28\ (15^{+4.2}_{-3.4})$	$1.84\ (1.7^{+0.8}_{-0.5})$	$10.38\ (8.6^{+2.9}_{-2.2})$	$2.08\ (3.1^{+1.3}_{-0.9})$	$1.57\ (2.4^{+1.0}_{-0.7})$

Table 8.14: A remainder of the cuts used for the various signal regions as well as the relevant numbers used in the final limit setting.

setting. For example, in the *OSjveto* signal region, any model predicting more than 13.28 fb $\cdot$ 4.71 fb^{-1}= 62.5 events would be excluded. The error bands on the computed limits reflect then the uncertainty on the excluded cross-sections from Table 8.14.

8.7.1 pMSSM Direct Gaugino Grid

The phenomenological MSSM (pMSSM) direct gaugino grid is used to set limits in the plane of the M_2 and μ parameters, described in Section 5.3.2. Three different values of M_1 are considered while $\tan\beta = 6$ and $M_A = 500$ GeV are held constant. The left plots in Figures 8.29, 8.30, 8.31 show the final exclusion limits with $M_1 = 100$, 140 and 250 GeV respectively. In all plots the excluded regions from the current limit on the chargino mass from LEP2 is shown. The rightmost plot in each figure indicates the signal region with the best expected sensitivity used in computing the limits. The most sensitive region for all values of M_1 is, with a few exceptions, the *mT2* signal region. All the computed limits significantly extend the results from LEP.

For $M_1 = 100$ GeV values of μ between 100 GeV and 500 GeV are excluded for $150 \lesssim M_2 \lesssim 230$ GeV while μ values up to ~ 180 GeV are excluded for the complete M_2 range.

For $M_1 = 140$, μ values up to ~ 200 GeV are excluded for the complete M_2 range, even better exclusion for μ is achieved towards larger values of M_2. However, the uncer-

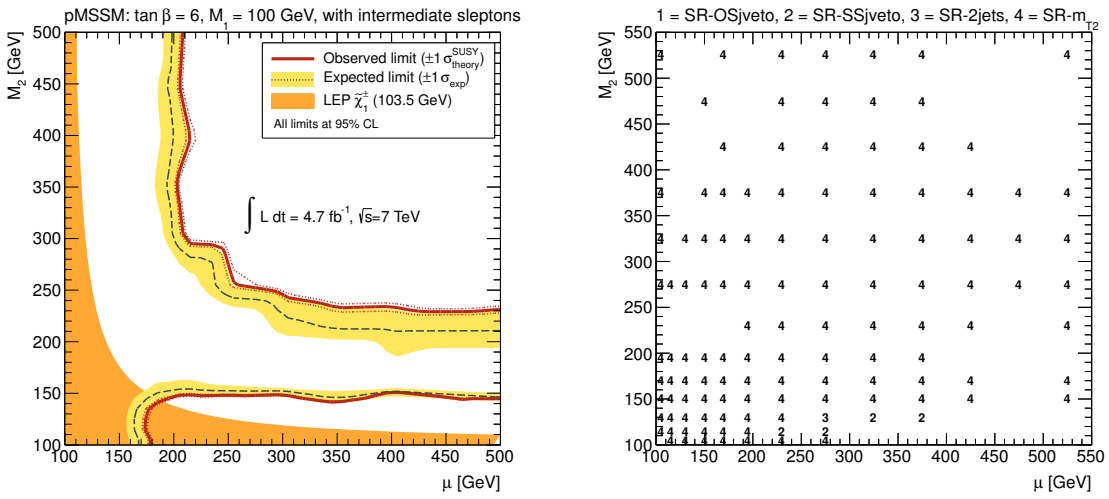

(a) Exclusion in μ-M_2 plane

(b) SR with best sensitivity

Figure 8.29: The 95% exclusion limit in the plane of the M_2 and μ parameters with $M_1 = 100$ GeV, $\tan\beta = 6$ and $m_A = 500$ GeV of the pMSSM direct gaugino model grid together with the LEP2 chargino limit (a). For each point the signal region giving the best expected sensitivity is shown (b).

tainties on both the observed and expected limits increase significantly in this part of the parameter space. Similar to the model with $M_1 = 100$, μ values between 350 GeV and 500 GeV are excluded for $200 \lesssim M_2 \lesssim 240$ GeV.

The exclusion limits for $M_1 = 250$ are significantly weaker than for the models with $M_1 = \{100,140\}$ GeV. Only a small part of the parameter space, defined by $100 \lesssim M_2 \lesssim 290$ GeV and $100 \lesssim \mu \lesssim 270$ GeV, is excluded in this model.

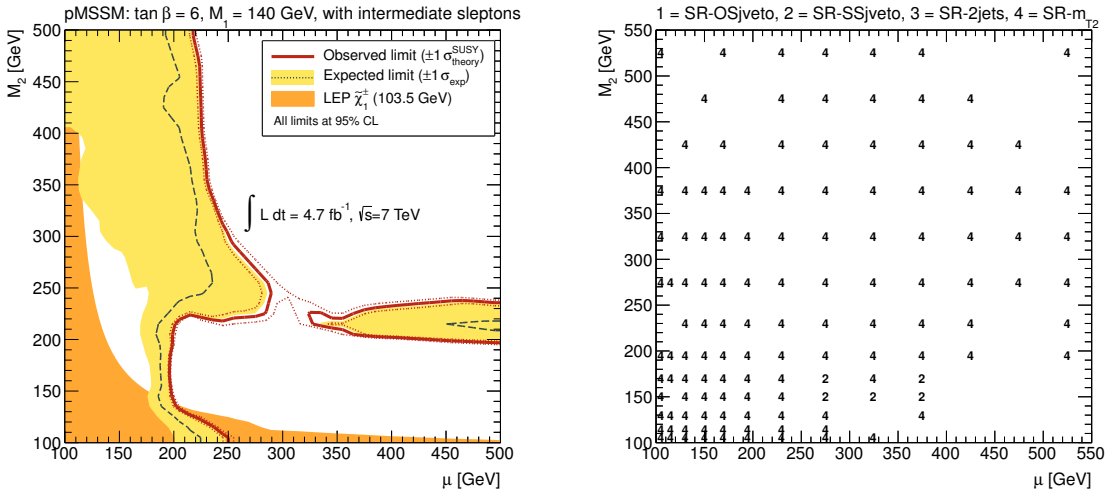

(a) Exclusion in μ-M_2 plane

(b) SR with best sensitivity

Figure 8.30: The 95% exclusion limit in the plane of the M_2 and μ parameters with $M_1 = 140$ GeV, $\tan\beta = 6$ and $m_A = 500$ GeV of the pMSSM direct gaugino model grid together with the LEP2 chargino limit (a). For each point the signal region giving the best expected sensitivity is shown (b).

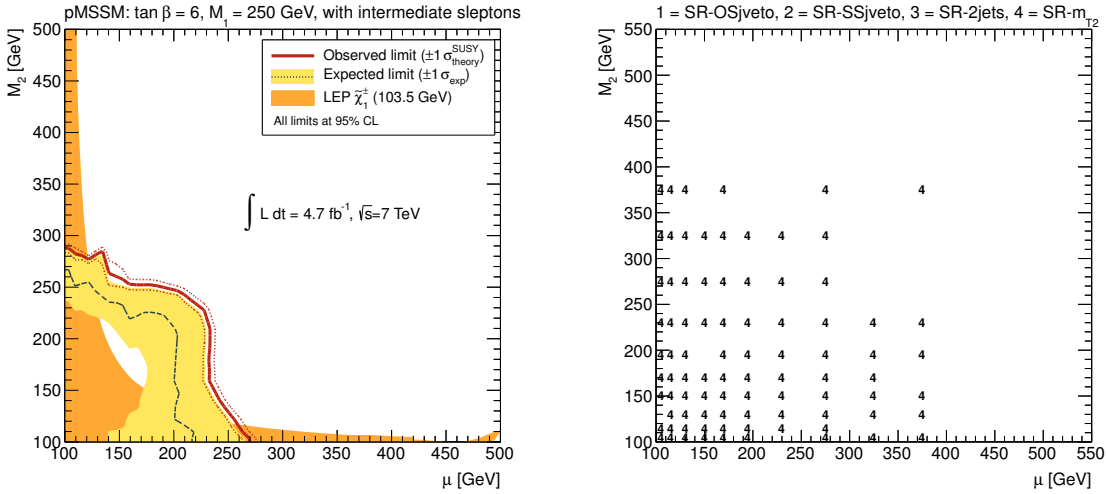

(a) Exclusion in μ-M_2 plane

(b) SR with best sensitivity

Figure 8.31: The 95% exclusion limit in the plane of the M_2 and μ parameters with $M_1 = 250$ GeV, $\tan\beta = 6$ and $m_A = 500$ GeV of the pMSSM direct gaugino model grid together with the LEP2 chargino limit (a). For each point the signal region giving the best expected sensitivity is shown (b).

8.7.2 pMSSM Direct Slepton Grid

The direct slepton grid discussed in Section 5.3.2.2 is used to set limits in the plane of the slepton and lightest neutralino masses shown in Figure 8.32. Only the dedicated slepton signal region, *SR-mT2*, requiring leptons of same flavour, is used to set the limits. The physical masses of the sleptons, from Table 5.2, are used. The difference between the mass parameters and the physical LSP mass is neglected. Shown in orange is the excluded part of parameter space from the limit on the mass of the right-handed smuon from LEP [84]. The dashed line indicates the line where $m_{\tilde{\chi}_1^0} = m_{\tilde{\ell}}$. Slepton masses between 95 and 200 GeV for a 20 GeV $\tilde{\chi}_1^0$ are excluded at 95% confidence level. The excluded range of slepton masses decreases for larger $\tilde{\chi}_1^0$ masses.

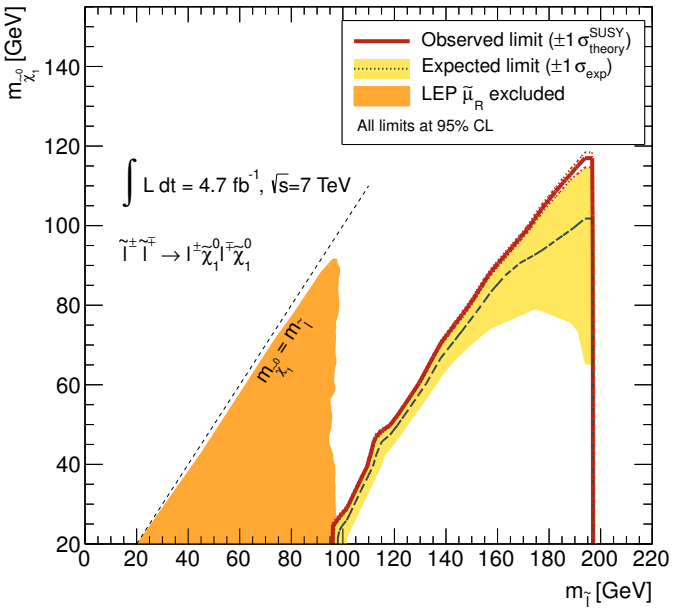

Figure 8.32: The 95% exclusion limit in the plane of the slepton and lightest neutralino masses. Only the same flavour channel is included for the *mT2* signal region when computing the limits.

8.7.2.1 Deviations from the Published Limits

The exclusion limits in Figure 8.32 are significantly better than the ones published in the study using 4.71 fb^{-1} of data at $\sqrt{s} = 7$ TeV [12]. This is due to the fact that the published limits are made performing a flavour-blind analysis, with a signal region including both the ee and $\mu\mu$ channels, but where one searches for a single lepton flavour only, thus the resulting exclusion limits are much weaker. The result of doing a flavour blind analysis with the analysis presented here is shown in Figure 8.33. The significant degradation of the excluded limits, comparing with Figure 8.32, is clearly visible.

For the limits computed in this thesis the slepton grid should definitely have been extended for slepton masses above 190 GeV, as the limit shown in Figure 8.32 exhibits

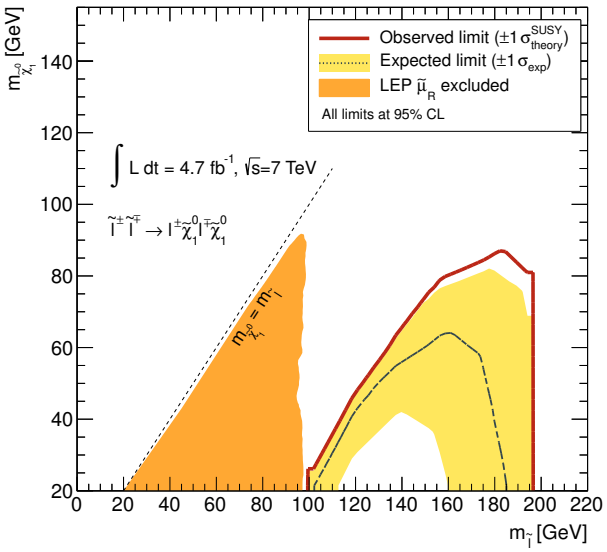

Figure 8.33: Exclusion limits in the direct slepton grid using a flavour-blind analysis.

an unnatural cutoff at $m_{\tilde{\ell}} \approx 190$ GeV. A new analysis has already been carried out in the direct slepton channel, however, using the full $\sqrt{s} = 8$ TeV 2012 data sample [139] and where the grid has been drastically extended both in the $m_{\tilde{\chi}_1^0}$ and $m_{\tilde{\ell}}$ masses. The limits presented in [12] are therefore ousted.

8.7.3 Simplified Models

The SUSY Simplified Models were discussed in detail in Section 5.3.1. The current section summarizes the result of the analysis interpreted in the simplified models Mode A and C with intermediate sleptons, the models to which we are sensitive. Mode A includes the direct production of $\tilde{\chi}_1^{\pm}\tilde{\chi}_2^0$, giving typical cascades as pictured in Figure 5.2b. Mode C governs direct production of $\tilde{\chi}_1^{\pm}\tilde{\chi}_1^{\mp}$ and gives final states as shown in Figures 5.2a. The final 95% exclusion limits are shown in Figure 8.34 and 8.35 for Mode A and C respectively. Also shown are the signal regions with the best expected sensitivity, used to set the limit, for each of the grid points. For Mode A the *SR-mT2* has best sensitivity while for Mode C *SR-mT2* dominates at high masses while *SR-OSjveto* dominates at smaller masses.

Chargino masses of 80-250 GeV and 120-360 GeV are excluded for a $\tilde{\chi}_1^0$-mass of 10 GeV in Mode A and C respectively. The range of excluded chargino masses decreases with increasing $\tilde{\chi}_1^0$-mass. No sensitivity is found for $\tilde{\chi}_1^0$-mass above 100 and 150 GeV in Mode A and C respectively.

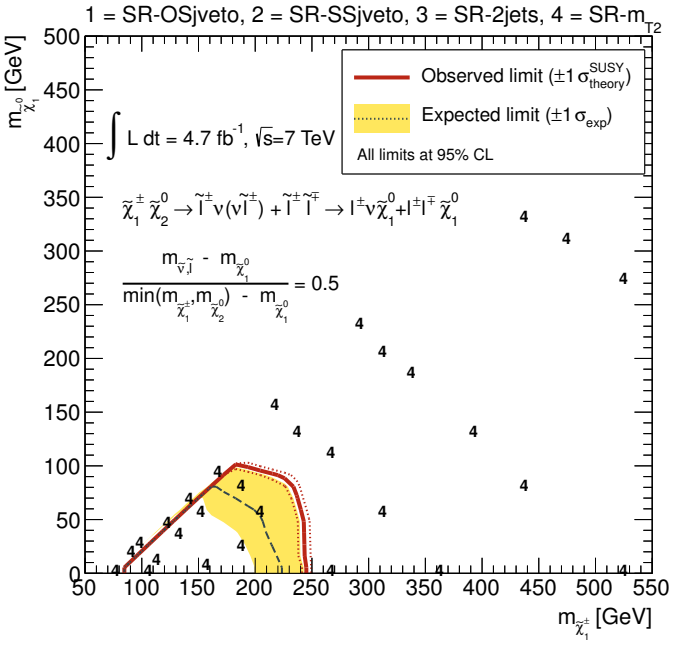

Figure 8.34: The 95% exclusion limit in the plane of lightest neutralino and chargino masses in the simplified model, Mode A with sleptons. The signal regions with the best expected sensitivity are also shown.

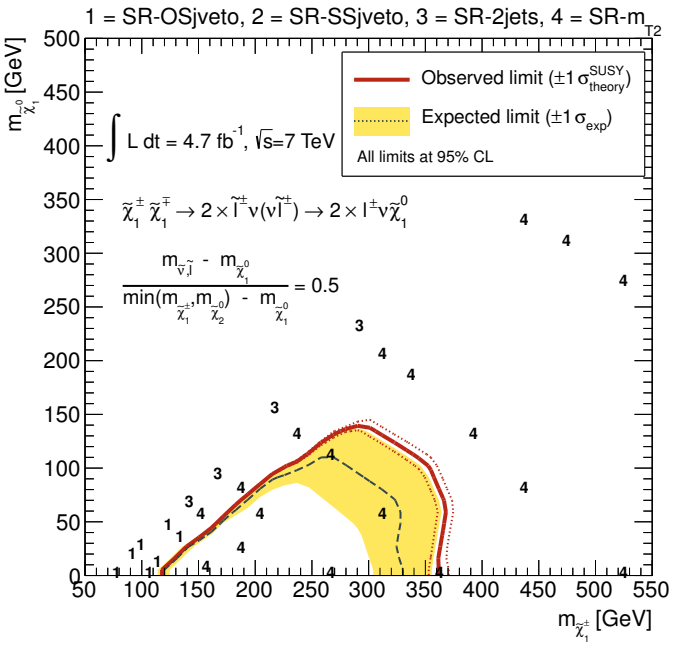

Figure 8.35: The 95% exclusion limit in the plane of lightest neutralino and chargino masses in the simplified model, Mode C with sleptons. The signal regions with the best expected sensitivity are also shown.

Summary and Conclusions

September 19, 2008, around the same time as the research programme for this thesis was put down, the LHC experienced the infamous magnet quench, leaving the LHC machine non-operational for more than one year. Every physicist at CERN that had prepared him/herself and very much looked forward to analyse the first collision data ever to be recorded by any of the particle detectors at the LHC were taken by surprise. It did not just mean a one year delay for the collision data to arrive, but also realizing that the LHC, with the current design, was not able to run at the vowed center of mass energy of $\sqrt{s} = 14$ TeV. In fact, a reduction to half of the design energy, $\sqrt{s} = 7$ TeV, was finally agreed upon to be the best compromise between ensuring a safe running of the LHC machine while still being able to explore new energy domains. This completely new scene of the LHC staged an impressive turnaround of all analysers, now having to deal with less data at a lower energy. The energy would, however, still be almost four times higher than any collider experiment ever had achieved before!

In this thesis a quick MC study of the search for a light Higgs, decaying into $b\bar{b}$, and produced in cascade decays of supersymmetric particles within the MSSM was presented in Appendix B. This study was originally started out in 2006 and constituted the main subject of my master thesis [143], carried out at the time when the LHC was expected to deliver massive amounts of data at 14 TeV already from 2008. The implications of the 19/9 incident forced a re-evaluation of the physics potential for this analysis, knowing that the LHC would deliver less data at a lower energy. However, after realizing that there would not be any real collision data to analyse before the end of 2009 the crave after getting to grips with the processing, distribution, reconstruction and analysis software of the ATLAS data was imminent. The arrival of cosmic ray data recorded by the ATLAS detector during 2008 and 2009 was therefore a first glimpse of the data handling and what could be expected from the performance of the ATLAS detector. A study of some of the first electrons ever recorded by ATLAS were presented in Chapter 4 and the detector proved already then to be in a very good shape, despite the fact that cosmic ray data is far from what the detector is designed for. Even more impressive was the agreement of the data and expectations for the electron studies performed with the $\sqrt{s} = 900$ GeV data recorded in December 2009, presented in Chapter 4 and documented in [72]. Last but not least, these early studies of real data gave a unique chance of getting familiar with the full chain of ATLAS data, from the recording to the use of ATLAS software and running the final analysis on the grid. Like a top athlete, after spending four years preparing for an Olympic competition, physicists world wide working within one of the LHC experiments were extremely focused and prepared for the start of a new era of particle physics experiments, and the arrival of $\sqrt{s} = 7$ TeV data!

The main part of this thesis has been devoted to the search for supersymmetry in the direct gaugino and slepton production channel requiring final states with two leptons using the $\sqrt{s} = 7$ TeV data recorded during 2010/11. Three studies were performed during the period of almost constant data taking of the ATLAS detector between 2010 and 2012, only interrupted by small breaks over Christmas, heavy ion runs and because of various technical stops due to maintenance. Separate studies were carried out and published in [86, 11, 12] using 35 pb^{-1}, 1 fb^{-1} and 4.71 fb^{-1} of data respectively. The particle physics group in Oslo contributed significantly to these publications, especially PhD student Maiken Pedersen and myself were responsible for the development of the methods used in estimating the fake lepton background, defined as leptons coming from decay of heavy- and light-flavoured hadrons and conversion processes. The importance of developing methods for estimating this background is indispensable due to the imprecise modelling of these processes in the available MC simulations. As more and more data were collected the analysis got more and more refined and the work presented in Chapters 6-8 are therefore devoted to the most up-to-date analysis, of the complete 2011 dataset. No excess of events above the SM was observed in any of the signal regions, and the results were therefore used to exclude regions of parameter space in various SUSY models, as presented in Chapter 5 and 8. In scenarios where directly produced sleptons decay into $\tilde{\chi}_1^0$ and an electron or muon, slepton masses between 95 and 200 GeV for a 20 GeV $\tilde{\chi}_1^0$ are excluded at 95% confidence level (CL). In scenarios with direct production of wino-like charginos decaying through an on-shell charged slepton, chargino masses of 120-360 GeV are excluded for a $\tilde{\chi}_1^0$-mass of 10 GeV. Limits have been set in the μ-M_2 plane within the pMSSM direct gaugino model with $M_1 = 100, 140, 250$, $\tan\beta = 6$ and $M_A = 500$ GeV. In addition model independent upper limits have been set on the cross-section for new physics at 95% CL using several different signal regions.

At the time of writing (June 2013) an updated and refined version of the analysis presented in this thesis, with four times the integrated luminosity and including data taken in 2012 at $\sqrt{s} = 8$ TeV, has been presented at recent conferences [139]. The fake lepton estimation was carried out along the lines described in this thesis and applied also to the $\sqrt{s} = 8$ TeV data. Still no hints of any new physics are made, but the excluded parts of the parameter space have been extended, squeezing the available room for the existence of SUSY particles at LHC energies.

The running of the LHC is now stopped for the first planned long shutdown (LS1). When LHC will be back in the beginning of 2015 it will be stronger and more robust, able to approach the designed energy of $\sqrt{s} = 14$ TeV with an instantaneous luminosity higher than ever achieved before. The current plan is to collect 75-100 fb^{-1} of data in the period between 2015 and 2018 [144]. In the even more distant future, about 10 years from now, the start-up of the High Luminosity LHC (HL-LHC) will probably take place with the ambitious goal to collect up to 3000 fb^{-1} of luminosity at 14 TeV. This will then significantly extend the current limits for searches for new physics and in particular SUSY [145]. We all hope (and expect) of course that SUSY will be discovered long before that. If so the HL-LHC will be a sparticle factory, enabling us to do numerous interesting measurements on the new super partners. From a particle physicist's point of view the prospects of a bright and enlightening future does indeed seem to be more impending than ever.

Appendices

Appendix A

Additional Checks Regarding the Estimation of Fake Leptons

The current Appendix summarizes some additional checks and studies regarding the Matrix Method (MM) and the study of fake leptons. Section A.1 gives an overview of how well the various QCD MC samples are in describing the fake lepton contribution in the control regions used in the MM. Section A.2 summarizes the effects on the fake-efficiency from the sign of the leptons, OS or SS, in the low ($E_{\mathrm{T}}^{\mathrm{miss,rel}} < 30$ GeV) and intermediate ($40 < E_{\mathrm{T}}^{\mathrm{miss,rel}} < 100$ GeV) $E_{\mathrm{T}}^{\mathrm{miss,rel}}$ control regions in MC. The last Section, A.3, discusses the $E_{\mathrm{T}}^{\mathrm{miss,rel}}$ dependency of the fake-efficiency for various p_{T} ranges.

A.1 QCD MC Samples Used in the Study of Fake Leptons

In the current Section various MC samples, trying to describe the fake leptons from QCD processes, are tested in order to best describe the data in the QCD control regions. Three different samples are investigated: (i) the lepton filtered PythiaB samples; (ii) the single-lepton filtered Jx Pythia samples; and (iii) the JF17+JF35 samples.The details regarding these samples are summarized in Table 6.8.

Figure A.1, A.2 and A.3 show the transverse momentum of all inclusive loose leptons in the selected single-lepton, di-lepton and $b\bar{b}$ tag-and-probe control regions respectively, described in Section 7.2.1.1 and 7.2.1.2. The upper plots are for electrons while the lower plots are for muons. For each control region and lepton flavour the performance of the three different QCD MC samples are shown. The plots show, from left to right: the PythiaB, lepton filtered Jx Pythia and JF17+JF35 samples. The PythiaB samples in Table 6.9 to actually use are the ones which achieve the best agreement between data and MC. This is indicated in the plot-captions. Underneath each plot the ratio data/MC is plotted in order to better investigate the overall (dis)agreement between data and MC. Note also that there are in some cases, especially for the Jx and JF17/35 samples, some bins that have an artificially large value while the neighbouring bins are empty or much smaller. This comes from the relatively large scale factors, > 1000 for some of the samples,

needed when normalizing to the total integrated luminosity of 4.71 fb^{-1}. For the single-lepton and $b\bar{b}$ tag-and-probe control regions we suffer from the fact that we do not have trigger-weights for single-electrons with $p_{\mathrm{T}} < 25$ GeV and single-muons with $p_{\mathrm{T}} < 20$ GeV.

For the single-electron control regions the JF17+JF35 samples (Fig. A.1c) are the best, as expected since these samples require exactly one electron. The two other QCD samples in Fig. A.1a and b, for the PythiaB and Jx samples respectively, the shape of the distribution is relatively well described although the scaling seems to be off by a factor between 2 and 4. For the single-muon control regions all samples do a fairly good job, but the discrepancy between data and MC increases for $p_{\mathrm{T}} < 30$ GeV, especially in Figure A.1e.

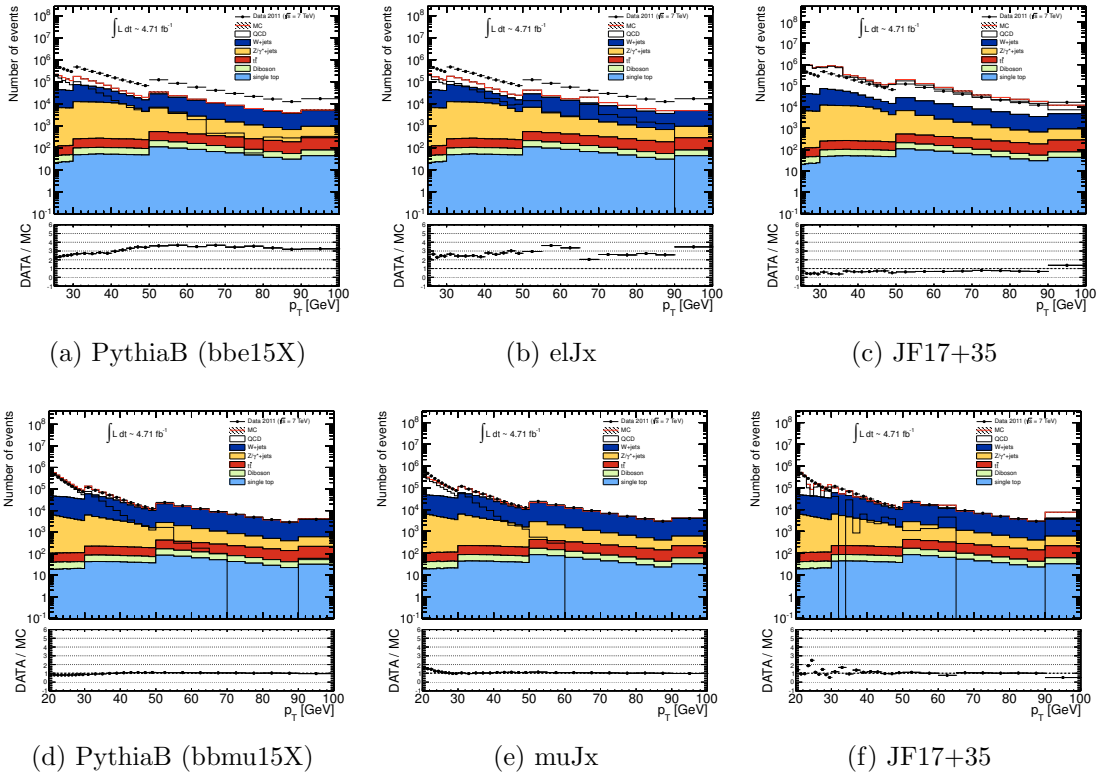

(a) PythiaB (bbe15X) (b) elJx (c) JF17+35

(d) PythiaB (bbmu15X) (e) muJx (f) JF17+35

Figure A.1: The momentum of all inclusive loose electrons (upper) and muons (lower) in the single-lepton fake control regions (shaded gray in Table 7.2 and 7.3). The discontinuities (or steps) seen at $p_{\mathrm{T}} \sim 30$ GeV and $p_{\mathrm{T}} \sim 50$ GeV in the distributions come from the histogram binning which changes from 1 to 2 GeV and from 2 to 5 GeV at the two points respectively.

None of the QCD samples are able to describe the p_{T} distribution (alone) of electrons in the di-electron control region, shown in Figure A.2a-c. For muons the di-muon filtered PythiaB sample, mu10mu10X, in Figure A.2d describes the shape of the data distribution fairly well, although with a factor ~ 1.5 off.

In the $b\bar{b}$ tag-and-probe regions, as expected, the PythiaB QCD samples seems to give the best agreement between data and MC. For electrons, in Figure A.3a, the discrepancy is still significant, especially at high p_{T} . For muons in Figure A.3d, however, the agreement between data and MC is remarkably good.

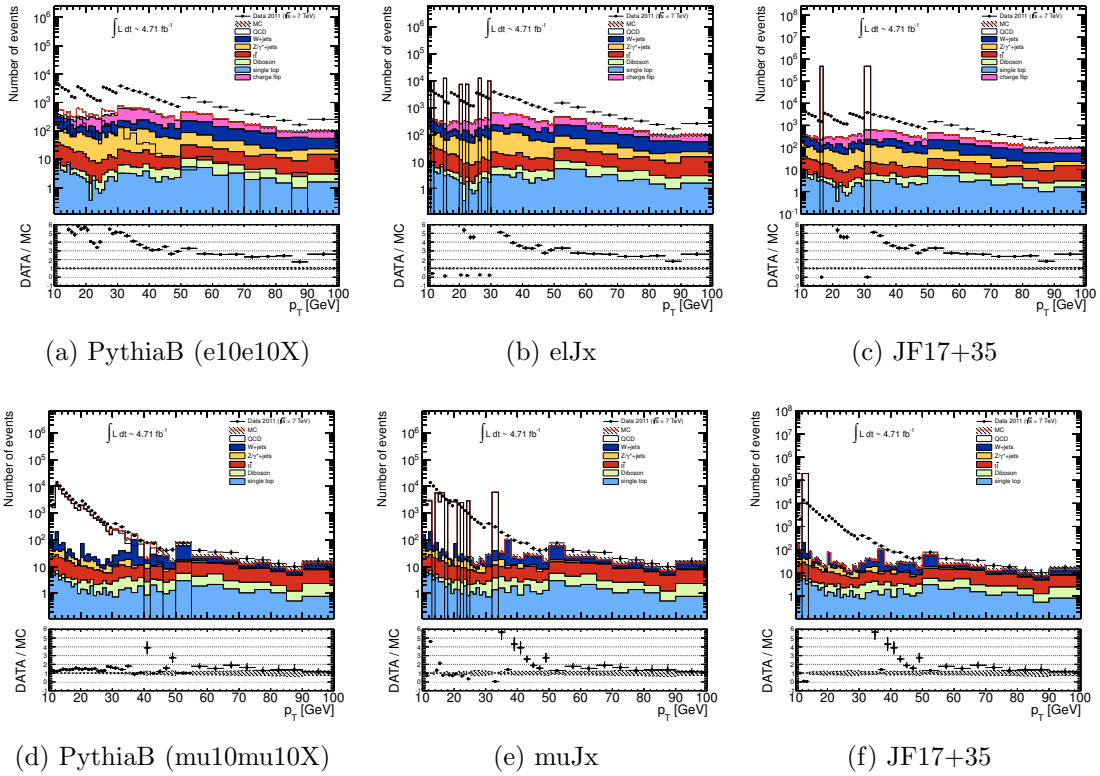

(a) PythiaB (e10e10X) (b) elJx (c) JF17+35

(d) PythiaB (mu10mu10X) (e) muJx (f) JF17+35

Figure A.2: The momentum of all inclusive loose electrons (upper) and muons (lower) in the di-lepton fake control regions (shaded gray in Table 7.2 and 7.3). In these distributions several discontinuities (or steps) are seen. The steps at $p_{\mathrm{T}} \sim 15$ GeV and $p_{\mathrm{T}} \sim 25$ GeV for electrons and $p_{\mathrm{T}} \sim 12$ GeV and $p_{\mathrm{T}} \sim 20$ GeV for muons, coincide with the thresholds of the single- and di-lepton triggers, as shown in Table 6.15. The steps at $p_{\mathrm{T}} \sim 30$ GeV and $p_{\mathrm{T}} \sim 50$ GeV for both electron and muons come from the histogram binning which changes from 1 to 2 GeV and from 2 to 5 GeV at the two points respectively.

Overall the QCD MC samples, especially PythiaB, describe the fake lepton contribution fairly well in all control regions for muons. For electrons, however, the disagreements are in some cases quite large. This is because of a missing component from conversions and an underestimation of leptons from decays of light-flavoured hadrons, as these are not included in the PythiaB sample. A further discussion of how to improve the agreement in the electron channel is found in the summary of the fake-efficiency studies in Section 7.2.4.

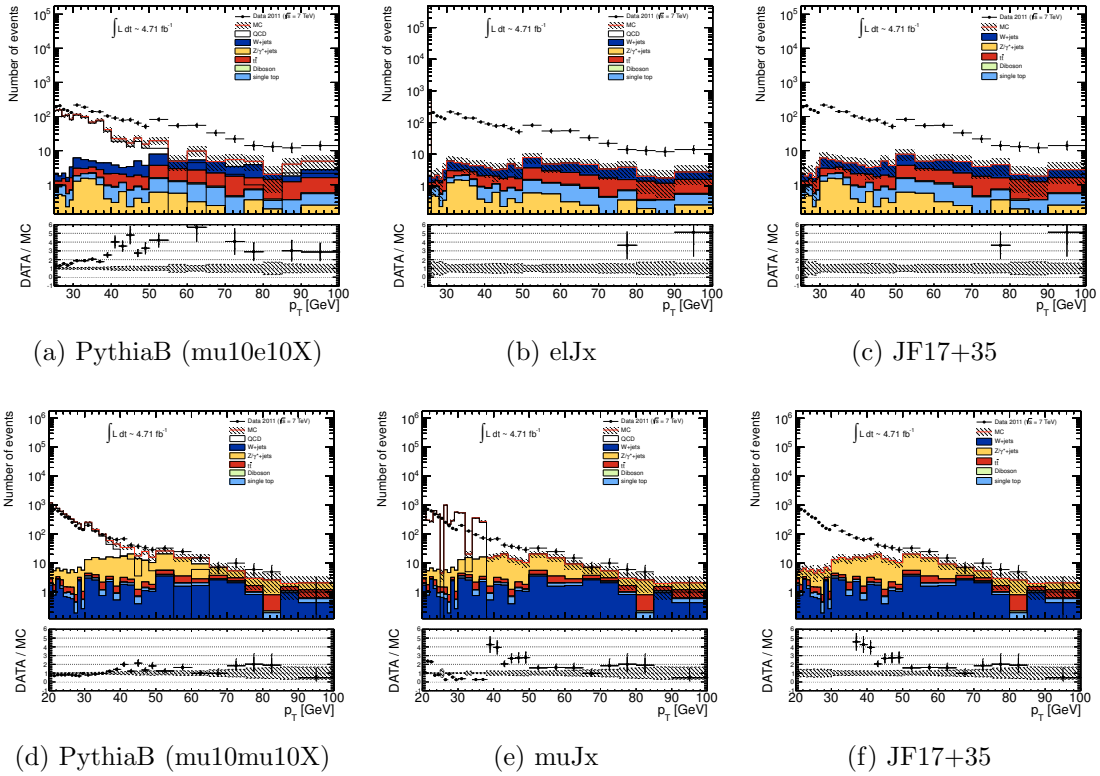

(a) PythiaB (mu10e10X) (b) elJx (c) JF17+35

(d) PythiaB (mu10mu10X) (e) muJx (f) JF17+35

Figure A.3: The momentum of all inclusive loose electrons (upper) and muons (lower) in the $b\bar{b}$ tag-and-probe fake control regions discussed in Section 7.2.1.2. The steps at $p_{\mathrm{T}} \sim 30$ GeV and $p_{\mathrm{T}} \sim 50$ GeV seen in the Figures above are less pronounced in these distributions due to smaller statistics. The discontinuities are, however, seen in some of the plots and comes from the histogram binning which changes from 1 to 2 GeV and from 2 to 5 GeV at the two p_{T}-points.

A.2 Effects on the Fake-Efficiency from Charge of the Leptons

By using MC truth to identify fake leptons, as discussed in Section 6.3.7, possible differences between fake-efficiencies in OS and SS events can be investigated. In data we are limited to only study SS events in the SF channels (ee, $\mu\mu$), discussed in Section 7.2.1.1, in order to obtain a region dominated by fake leptons. By selecting only fake leptons in MC, both OS and SS events can be studied, however, regardless of the flavour composition. Figure A.4a and b show the ratios between the fake-efficiencies obtained from SS and OS di-electron and di-muon regions respectively in a low $E_{\mathrm{T}}^{\mathrm{miss,rel}}$ region ($E_{\mathrm{T}}^{\mathrm{miss,rel}} < 30$ GeV). Figure A.4c and d show the corresponding ratios for the intermediate $E_{\mathrm{T}}^{\mathrm{miss,rel}}$ region ($40 < E_{\mathrm{T}}^{\mathrm{miss,rel}} < 100$ GeV). The dashed lines indicate the best fit to the points, assuming a constant ratio throughout the p_{T} range, except for the low $E_{\mathrm{T}}^{\mathrm{miss,rel}}$region for muons where a first order polynomial is used. The fit parameters are given in the legends. For electrons the ratios are close to unity in both $E_{\mathrm{T}}^{\mathrm{miss,rel}}$ regions. For muons, however, there is a significant difference between the SS and OS fake-efficiencies in the low $E_{\mathrm{T}}^{\mathrm{miss,rel}}$ region. For the intermediate $E_{\mathrm{T}}^{\mathrm{miss,rel}}$ region the differences are much less prominent.

The differences between the OS and SS fake-efficiencies are included in the final sys-

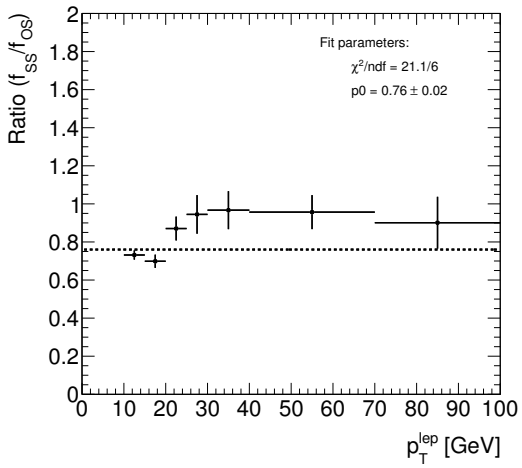

(a) ee SS/OS for $E_{\mathrm{T}}^{\mathrm{miss,rel}} < 30$ GeV

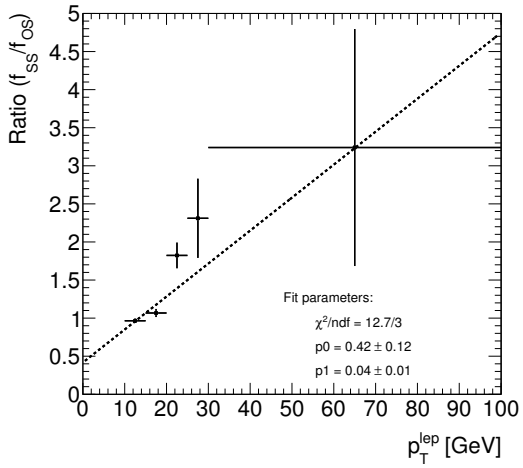

(b) $\mu\mu$ SS/OS for $E_{\mathrm{T}}^{\mathrm{miss,rel}} < 30$ GeV

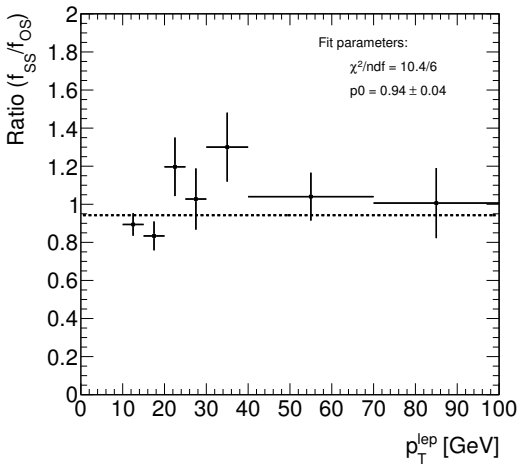

(c) ee SS/OS for $40 < E_{\mathrm{T}}^{\mathrm{miss,rel}} < 100$ GeV

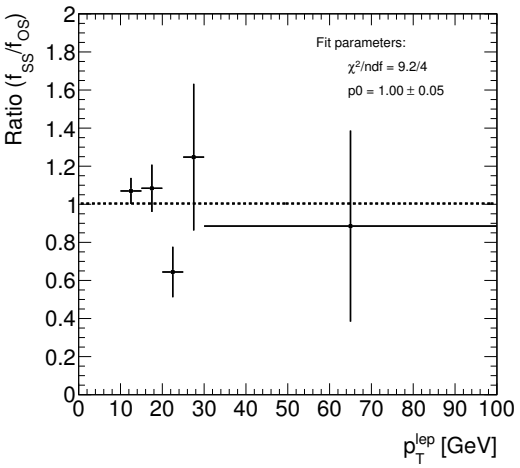

(d) $\mu\mu$ SS/OS for $40 < E_{\mathrm{T}}^{\mathrm{miss,rel}} < 100$ GeV

Figure A.4: The left and right plots show the ratios between the fake-efficiencies obtained using truth MC to identify fake leptons in SS and OS di-electron and di-muon events respectively. The two upper plots are for the low $E_{\mathrm{T}}^{\mathrm{miss,rel}}$ region while the lower ones are for the intermediate $E_{\mathrm{T}}^{\mathrm{miss,rel}}$ region. The dashed lines show the best fit to the data points using a 0^{th} order (in a,c and d) and 1^{st} order (in b) polynomial.

tematic uncertainty on the fake lepton estimates. However, since the final QCD fake-efficiency is taken from the intermediate $E_{\mathrm{T}}^{\mathrm{miss,rel}}$ region, as discussed in Section 7.2.2, we only include the deviations seen in Figure A.4c and d. The corresponding fitted ratios are 0.94 ± 0.04 for electrons and 1.00 ± 0.05 for muons. Both OS an SS events are used in the computation of the fake-efficiency for electrons, but the vast majority still comes from OS events and thus the systematic effect in Figure A.4c is reversed with respect to the fit. A 10% *upward* uncertainty is therefore added for electrons. For muons we measure the fake-efficiency from SS events, thus the difference is added as a symmetric ±5% systematic uncertainty.

A.3 $E_{\mathrm{T}}^{\mathrm{miss,rel}}$ Dependency of the Fake-Efficiency

Figure A.5 and A.6 show how the fake-efficiency, for electron and muons respectively, depends on $E_{\mathrm{T}}^{\mathrm{miss,rel}}$ in four different p_{T} ranges, $0 < p_{\mathrm{T}} < 20$ GeV, $20 \leq p_{\mathrm{T}} < 40$ GeV, $40 \leq p_{\mathrm{T}} < 60$ GeV and $p_{\mathrm{T}} \geq 60$ GeV. The efficiencies are taken from MC, using truth to identify fake leptons, and divided into the various SM processes. The fake-efficiencies in each p_{T} range are normalized to the average fake-efficiency in the current p_{T} bin, integrated over the full $E_{\mathrm{T}}^{\mathrm{miss,rel}}$ region, in order to better illustrate the dependencies. The statistics is in some cases quite limited, so the focus should be on the most important processes (i.e. $t\bar{t}$ and PythiaB). The fake-efficiencies for electrons in Figure A.5a-d decrease steadily from about 0.35 in the $0 < E_{\mathrm{T}}^{\mathrm{miss,rel}} < 20$ GeV bin to 0.15-0.2 in the bin with $E_{\mathrm{T}}^{\mathrm{miss,rel}} \geq 60$ GeV[1] for all p_{T} ranges with sufficient statistics. For muons in Figure A.6a-d the statistics is much worse, since only the SS channel is used (see Appendix A.2), but an overall trend of a decreasing fake-efficiency as a function of $E_{\mathrm{T}}^{\mathrm{miss,rel}}$ can be seen, however with some discrepancies seen for example in the $0 < E_{\mathrm{T}}^{\mathrm{miss,rel}} <$ 20-bin for the lowest p_{T} range. Nevertheless; since the dependency seems to be quite similar across p_{T}-bins the full p_{T} range can be combined, in order to gain statistics, when studying the full $E_{\mathrm{T}}^{\mathrm{miss,rel}}$ dependency in Section 7.2.2.

[1] The highest bin includes the overflow.

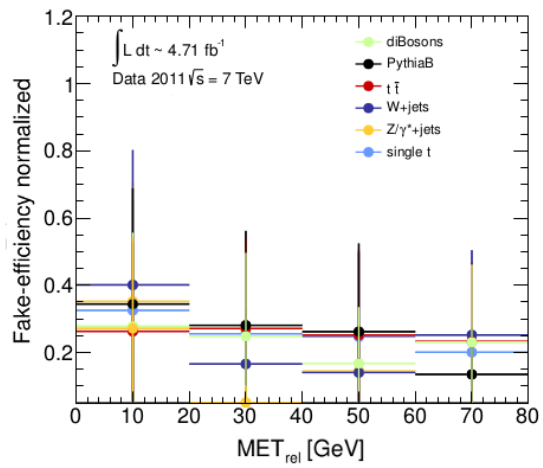

(a) $0 < p_{\mathrm{T}} < 20$ GeV

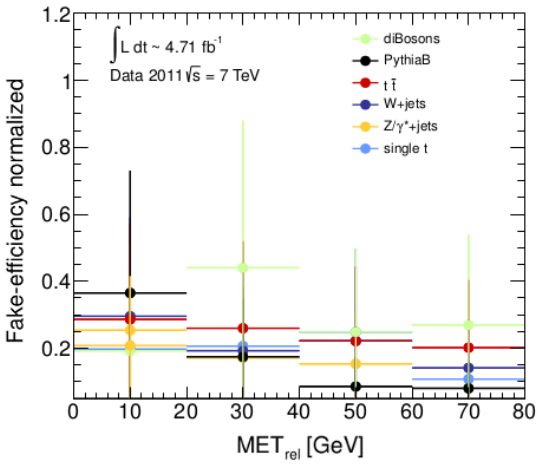

(b) $20 \leq p_{\mathrm{T}} < 40$ GeV

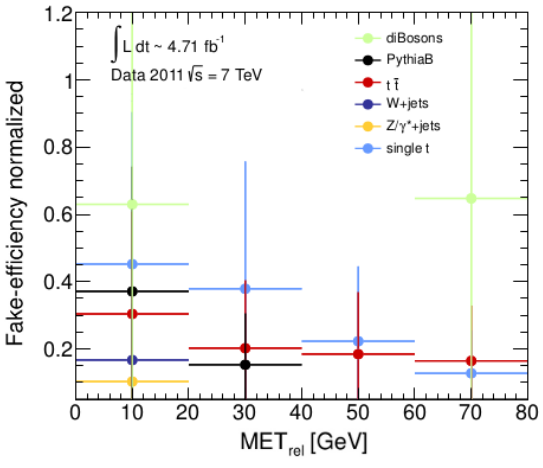

(c) $40 \leq p_{\mathrm{T}} < 60$ GeV

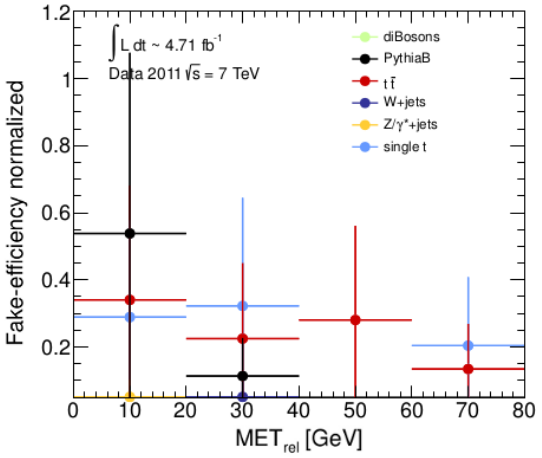

(d) $p_{\mathrm{T}} \geq 60$ GeV

Figure A.5: The fake-efficiency for electrons, using MC truth to identify fakes, as a function of $E_{\mathrm{T}}^{\mathrm{miss,rel}}$ in different p_{T} bins. The fake-efficiency for each process is normalized to the average fake-efficiency, over the complete $E_{\mathrm{T}}^{\mathrm{miss,rel}}$ range, for that p_{T} region.

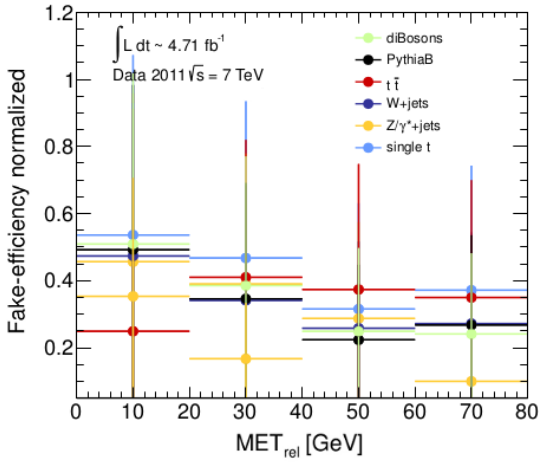

(a) $0 < p_{\mathrm{T}} < 20$ GeV

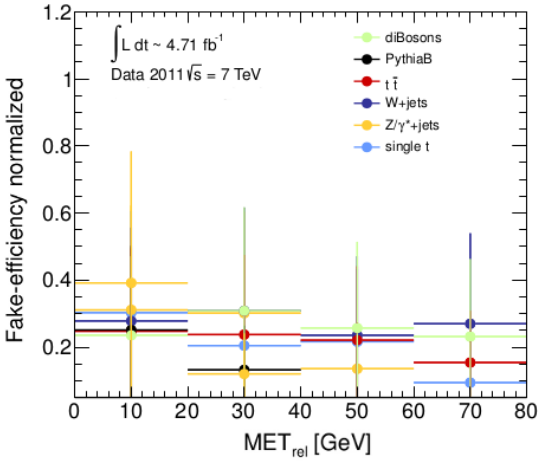

(b) $20 \leq p_{\mathrm{T}} < 40$ GeV

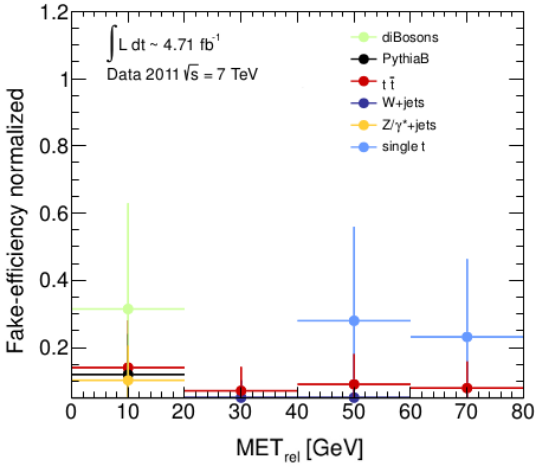

(c) $40 \leq p_{\mathrm{T}} < 60$ GeV

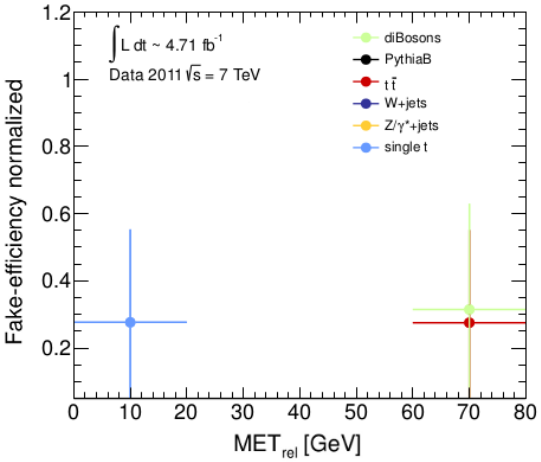

(d) $p_{\mathrm{T}} \geq 60$ GeV

Figure A.6: The fake-efficiency for muons, using MC truth to identify fakes, as a function of $E_{\mathrm{T}}^{\mathrm{miss,rel}}$ in different p_{T} bins. The fake-efficiency for each process is normalized to the average fake-efficiency, over the complete $E_{\mathrm{T}}^{\mathrm{miss,rel}}$ range, for that p_{T} region.

Appendix B

Phenomenology Study of a Light Supersymmetric Higgs at $\sqrt{s} = 7$ TeV

In my master thesis [143] I studied the prospect of finding the lightest Minimal Supersymmetric Standard Model (MSSM) Higgs boson, h^0, produced in cascades of supersymmetric particles and decaying into $b\bar{b}$, as shown in Figure B.1. In the MSSM, discussed

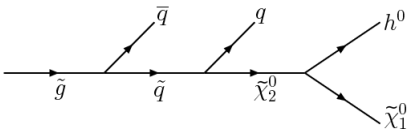

Figure B.1: A typical cascade of SUSY particles with the subsequent production of the lightest MSSM Higgs boson.

in Section 1.10.2, the mass of the lightest supersymmetric Higgs is predicted to be small (< 135 GeV, including higher order corrections) and the decay into $b\bar{b}$ is therefore dominant, between 50-80% depending on the mass. The main advantage of searching within models of R-parity conserving SUSY is that it allows $E_{\mathrm{T}}^{\mathrm{miss}}$ to be used as a discriminating variable and thus removes much of the otherwise dominant QCD background. Another important feature with such cascades is that they often lead to several high p_{T} jets, which can be used to efficiently reject many of the SM backgrounds. There has, however, not been very much focus on this channel within the ATLAS SUSY Working Groups nor in the Higgs Working Groups. The channel was studied in the CSC analysis, published by ATLAS in 2008 [68], using a dedicated mSUGRA signal scenario, SU9[1], with enhanced h^0 production. For 10 fb^{-1} at $\sqrt{s} = 14$ TeV the signal significance, $S/\sqrt{B}$, was found to be about 14.

Since mSUGRA does not give a very flexible or wide variety in phenomenologies, as discussed in Chapter 5, this model is not necessarily optimal for producing interesting

[1]Throughout this study some of the ATLAS benchmark scenarios within the mSUGRA model used in the CSC analysis [68] are used or referred to. These points were made such that the predicted cosmological relic density of neutralinos was consistent with the observed density of cold dark matter. As this happens in only restricted regions of parameter space the phenomenological variety of these models is quite limited. The benchmark models referred to in this appendix, defined by using the parameters of the mSUGRA model introduced in Section 1.10.2.4, are: The *bulk region*, SU3: $m_0 = 100$ GeV, $m_{1/2} = 300$ GeV, $A_0 = -300$ GeV, $\tan\beta = 6$ and $\mu > 0$; the *low mass point*, SU4: $m_0 = 200$ GeV, $m_{1/2} = 160$ GeV, $A_0 = -400$ GeV, $\tan\beta = 10$ and $\mu > 0$; and the *Higgs enhanced*, SU9: $m_0 = 300$ GeV, $m_{1/2} = 425$ GeV, $A_0 = 20$ GeV, $\tan\beta = 20$ and $\mu > 0$.

SUSY scenarios for Higgs searches in cascade decays. In the beginning of my PhD, and as a continuation of my master project, I started to look at other interesting SUSY scenarios, outside the mSUGRA framework, where the Higgs production could be enhanced. The study was done before any collision data had been collected, primarily to look at the prospect of finding a light MSSM Higgs decaying into $b\bar{b}$ in the early ATLAS data, i.e. ~ 1 fb^{-1} at 7 TeV. The study was not continued on real data, however, since the $h^0 \rightarrow b\bar{b}$ study did not really fit with the focusing on searches for new physics in di- and multi-lepton final states within the Experimental Particle Physics Group at UiO. My results and conclusions were presented in a workshop arranged by Higgs Working Group 5[2] at the Joint Institute For Nuclear Research (JINST) in Dubna, Russia, May 2010 [146].

B.1 Interesting Scenarios

The production of the lightest MSSM Higgs from the decay of SUSY particles mostly happens through $\tilde{\chi}_2^0 \rightarrow \tilde{\chi}_1^0 h^0$. The exact branching ratio of this decay depends on the bino, wino and higgsino components of the $\tilde{\chi}_2^0$ as well as whether the decays into slepton-lepton or sneutrino-neutrino pairs are kinematically allowed or not. It is also possible to construct models where the heavier neutralinos or charginos can decay into h^0, but this is not studied here. The SUSY model framework used in the following study is the MSSM24, with 24 free parameters [147], quite similar to the 19 parameters in the pMSSM listed in Table 5.1.

When generating an MSSM24 signal point one can freely choose the M_1, M_2 and μ parameters, which roughly sets the mass of the $\tilde{\chi}_1^0$, $\tilde{\chi}_2^0$ and $\tilde{g}$ respectively. An increasing value of M_2 makes $\tilde{\chi}_2^0$ more wino-like and thus increases the branching ratio of $\tilde{\chi}_2^0 \rightarrow \tilde{\chi}_1^0 h^0$ as illustrated in Figure B.2, showing the relative branching ratios of $\tilde{\chi}_2^0$ as a function of M_2. A clear enhancement of the decay into $\tilde{\chi}_1^0 h^0$ ($N1{+}h$) is seen at higher values of M_2.

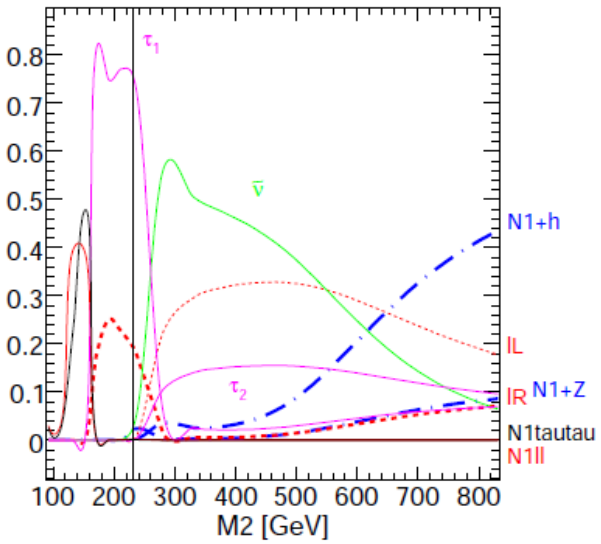

Figure B.2: The relative branching ratio of $\tilde{\chi}_2^0$ as a function of the M_2 parameter of the MSSM24 model. The decay into $\tilde{\chi}_1^0 h^0$ ($N1{+}h$) increases at higher M_2. The black vertical line indicates the value of M_2 in the SU3 benchmark point [68] which is obviously not very suitable for Higgs studies. The lL and lR represent the decays into left- and right-handed sleptons respectively, $N1ll$ into a neutralino and two leptons ($\tau^+\tau^-$ is shown separately) and $N1{+}Z$ is into a neutralino and a Z.

Based on the knowledge about how the decay of $\tilde{\chi}_2^0$ behaves as a function of the

[2]The Higgs sub-group dedicated to searches for SM or SUSY Higgs decaying to $b\bar{b}$, searches for charged Higgs and other exotic Higgs-models.

input parameters, three typical h^0-enhanced SUSY scenarios, each targeted at one of the three Feynman graphs illustrated in Figure B.3, were studied further. The various

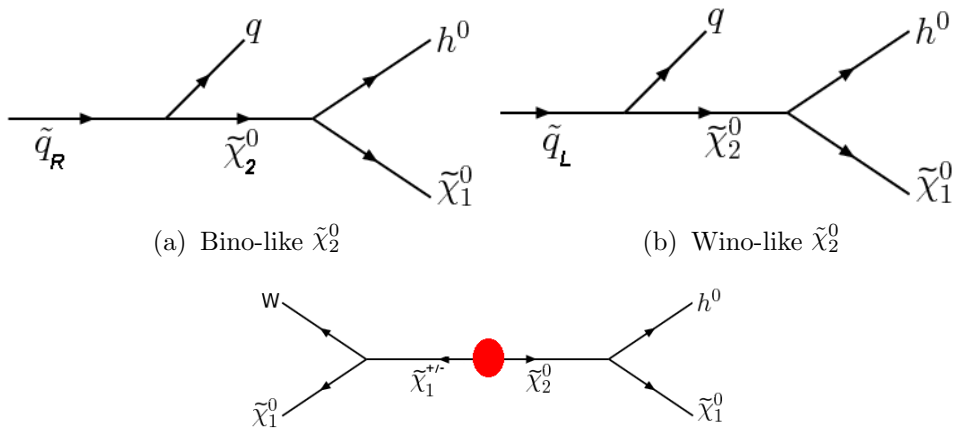

(a) Bino-like $\tilde{\chi}_2^0$ (b) Wino-like $\tilde{\chi}_2^0$

(c) Direct Gaugino

Figure B.3: Three different SUSY cascades leading to the production of h^0. The red blob in (c) represents the typical production of gauginos shown in Figure 2.13.

sparticle masses and parameters for each of the three SUSY models constructed are listed in Table B.1.

B.1.0.1 Bino-like $\tilde{\chi}_2^0$ - Strong Production

A typical decay of a bino-like $\tilde{\chi}_2^0$ is illustrated in Figure B.3a. The masses of the right-handed squarks are set to 500 GeV while the other squarks and gluinos have masses > 500 GeV. The sleptons are much heavier, making them inaccessible for the $\tilde{\chi}_2^0$ decay. In addition the stop and sbottom masses are put high such that b-production, other than the $b\bar{b}$ from h^0-decays, is minimized. The branching ratio of a right-handed squark decay to $\tilde{\chi}_2^0$ and a quark is about 99% in this scenario. The caveat with this model is the relatively large branching ratio of 70% for $\tilde{\chi}_2^0 \rightarrow \tilde{\chi}_1^{\pm} W$ compared to only 30% for $\tilde{\chi}_2^0 \rightarrow \tilde{\chi}_1^0 h^0$.

B.1.0.2 Wino-like $\tilde{\chi}_2^0$ - Strong Production

A scenario with a wino-like $\tilde{\chi}_2^0$ typically contains cascades as in Figure B.3b which leads to an identical final state as in Figure B.3a. The only difference is that the production now starts with a $\tilde{q}_{\mathrm{L}}$ whose mass is forced to be smaller than that of the $\tilde{q}_{\mathrm{R}}$. The $\tilde{q}_{\mathrm{L}}$ might also decay to a $\tilde{\chi}_1^{\pm}$ and a quark, which in this model has a branching ratio of 66%, to be compared with the 33% into $\tilde{\chi}_1^0$ and h^0.

B.1.0.3 Direct Gaugino - Electroweak Production

The lightest Higgs boson can also be produced through cascades stemming from direct electroweak production of gauginos as in Figure B.3c. The squark masses are then put to $\sim$ 1 TeV while the $\tilde{\chi}_1^0$ and $\tilde{\chi}_2^0$ masses are relatively small in order to increase the

Parameter	Scenario		
	Bino-like $\tilde{\chi}_2^0$	Wino-like $\tilde{\chi}_2^0$	Direct Gaugino
m_{h^0} [GeV]	106	110	107
$m_{\tilde{g}}$ [GeV]	550	400	1200
Left-Handed Squarks			
$m_{\tilde{u}_\mathrm{L}}, m_{\tilde{d}_\mathrm{L}}, m_{\tilde{c}_\mathrm{L}}, m_{\tilde{s}_\mathrm{L}}$ [GeV]	600	350	1000
Right-Handed Squarks			
$m_{\tilde{u}_\mathrm{R}}, m_{\tilde{d}_\mathrm{R}}, m_{\tilde{c}_\mathrm{R}}, m_{\tilde{s}_\mathrm{R}}$ [GeV]	500	450	1300
Left-Handed Sleptons			
$m_{\tilde{e}_\mathrm{L}}, m_{\tilde{\nu}_e}, m_{\tilde{\mu}_\mathrm{L}}, m_{\tilde{\nu}_\mu}$ [GeV]	900	900	1000
Right-Handed Sleptons			
$m_{\tilde{e}_\mathrm{R}}, m_{\tilde{\mu}_\mathrm{R}}$ [GeV]	900	900	1000
Third gen. sfermions			
$m_{\tilde{t}_1}$ [GeV]	1001	1002	1184
$m_{\tilde{t}_2}$ [GeV]	1018	1017	1231
$m_{\tilde{b}_1}$ [GeV]	997	987	1189
$m_{\tilde{b}_2}$ [GeV]	1005	1015	1212
$m_{\tilde{\tau}_1}$ [GeV]	898	891	992
$m_{\tilde{\tau}_2}$ [GeV]	904	911	1010
Other Parameters			
μ [GeV]	600	1000	2000
m_{H_A} [GeV]	800	400	300
M_1 [GeV]	480	110	46
M_2 [GeV]	360	300	160
$\tan\beta$	5	10	5
Neutralinos			
$m_{\tilde{\chi}_1^0}$ [GeV]	344	109	46
$m_{\tilde{\chi}_2^0}$ [GeV]	472	297	158
$m_{\tilde{\chi}_3^0}$ [GeV]	603	1003	2001
$m_{\tilde{\chi}_4^0}$ [GeV]	626	1007	2003
Charginos			
$m_{\tilde{\chi}_1^\pm}$ [GeV]	345	297	158
$m_{\tilde{\chi}_2^\pm}$ [GeV]	619	1007	2003

Table B.1: The masses of most of the sparticles together with some of the parameters for the three h^0-enhanced scenarios within the MSSM24 SUSY model.

cross-section for direct gaugino production, as illustrated in Figure 2.13. The $\tilde{\chi}_2^0$ is 100% wino-like such that it almost exclusively (branching ratio of 98%) decays into $\tilde{\chi}_1^0$ and h^0. The dominant direct production of gauginos in this model is $\tilde{\chi}_1^{\pm}\tilde{\chi}_2^0$, leading typically to a W and $\tilde{\chi}_1^0$ from the other branch, since the branching ratio of $\tilde{\chi}_1^{\pm}\rightarrow W\tilde{\chi}_1^0$ is 100%. Theoretically, in cases with $\tilde{\chi}_2^0\tilde{\chi}_2^0$ production, both legs can contain a Higgs, giving two $b\bar{b}$ pairs in the final state. However, in the particular model studied here this has a negligible cross-section however. Since the squarks and gluinos are much heavier than the gauginos this scenario will not have any jet production, except the ones possibly coming from the W-decay and ISR/FSR.

B.2 Sensitivity Study

Since the strong production bino- and wino-like scenarios in Figures B.3a and b give very similar final states only the wino-like scenario is studied further, since the analysis targeting at the bino-like models will be very similar. By using the mSUGRA benchmark point SU4 [68], modifying it slightly such that the branching ratio of $\tilde{\chi}_2^0\rightarrow\tilde{\chi}_1^0h^0$ is maximized, a similar analysis to the one developed in [143] can be applied. The direct gaugino channel is, however, very different and a separate analysis is performed.

B.2.1 Technicalities

To generate proton-proton collisions at 7 TeV within the SUSY scenarios discussed above, ISAJET 7.80, which incorporates ISASUSY, designed to evaluate branching ratios for the MSSM, is used [148]. The corresponding event simulation and reconstruction are done using the ATLFAST II [149, 150] package within ATHENA release 14. The LO and NLO cross-sections are calculated using Prospino2 [151, 152, 153, 154, 81]. For each sample a total of 5000 events are generated.

B.2.2 Modified SU4

Table B.2 shows some of the most important parameters of the modified SU4 model used. The slepton masses are all set high in order to avoid the decay of $\tilde{\chi}_2^0$ into sleptons. The third generation squark masses are also increased in order to minimize the production of b-quarks other than from the decay of h^0. The 1$^{\text{st}}$ and 2$^{\text{nd}}$ generation squark masses are unchanged compared to SU4, however. Finally, the $\tilde{\chi}_2^0$ is set mostly wino-like, giving a branching ratio of 90% for $\tilde{\chi}_2^0\rightarrow\tilde{\chi}_1^0h^0$. The LO cross-section for this model was calculated to be 21.61 pb at $\sqrt{s} = 7$ TeV. A total of 10386 h^0-boson events were generated at truth level corresponding to 1 fb^{-1}. Assuming $BR(h^0 \rightarrow b\bar{b}) = 85\%$ and a b-tagging efficiency of 50% per b-jet, a total of about 2207 h^0-bosons would be reconstructed in 1 fb^{-1} of data. In the Higgs-enhanced benchmark scenario, SU9, which was studied in the ATLAS CSC book [68], the expected number of events containing h^0 in 1 fb^{-1} of data collected at 7 TeV, doing the same rough estimates as for the modified SU4 above, is about 12. A similar analysis was performed on the modified SU4 model and the unchanged SU9 model by requiring ≥ 2 b-jets, $E_{\text{T}}^{\text{miss}} > 200$ GeV and ≥ 2 additional jets with transverse momentum

Parameter	Modified SU4
$m_{\tilde{q}_L}$	420
$m_{\tilde{q}_R}$	520
$m_{\tilde{q}^3_L}$	1000
$m_{\tilde{g}}$	408
$m_{\tilde{\ell}_L}$,$m_{\tilde{\ell}_R}$	900
$m_{\tilde{\chi}^0_1}$	100
$m_{\tilde{\chi}^0_2}$	220
$m_{\tilde{\chi}^\pm_1}$	220
m_{h^0}	110
m_{A^0}	400
$\tan\beta$	10
μ	1000

Table B.2: The most important masses and parameters of the modified SU4 model, based on the SU4 benchmark scenario in [68], but changed slightly to maximize the branching ratio of $\tilde{\chi}^0_2 \rightarrow \tilde{\chi}^0_1 h^0$.

larger than 100 and 50 GeV for the hardest and second hardest jets, respectively. For the SU9 scenario an additional cut on the effective mass, $M_{\text{eff}} > 800$ GeV[3] is used in order to further reject the SM backgrounds. This is not needed for the modified SU4, however, as the signal to background ratio is already sufficiently good, as depicted in Figure B.4, showing the invariant mass distributions of two b-jets after applying the cuts above. The plots illustrate clearly that the SU9 benchmark point is far from the most optimal scenario for light Higgs studies. The modified SU4 scenario indicates that there are indeed possibilities for discovering a light MSSM Higgs with the early ~ 1 fb^{-1} of ATLAS data at 7 TeV.

B.2.3 Direct Gaugino

A SUSY model targeting direct gaugino production and subsequent production of h^0 as in Figure B.3c is constructed optimizing its parameters to enhance direct gaugino cross-section and production of h^0. The resulting sparticle parameters are shown in the rightmost column of Table B.1. Again 5000 events are generated and the LO cross-section calculated to be 1.53 pb at $\sqrt{s} = 7$ TeV, giving a total of 987 h^0 events for 1 fb^{-1} at truth level. Assuming $BR(h^0 \rightarrow b\bar{b}) = 85$ % and a 50% b-tagging efficiency per jet, the expected number of reconstructed h^0 events is found to be 215. Direct production of $\tilde{\chi}^\pm_1\tilde{\chi}^0_2$ totally dominates, giving typically events with two LSPs, h^0 and a W. Since the LSP is relatively light in this scenario, being only 46 GeV[4], a cut on $E_{\text{T}}^{\text{miss}}$ is less powerful in rejecting the SM backgrounds. In addition, since jets only stem from hadronic decays

[3]The effective mass is defined as the sum of the p_{T} of the three hardest jet added with the scalar sum of the selected leptons and the $E_{\text{T}}^{\text{miss}}$ in the event.

[4]Identical to the lower limit excluded at that time [24].

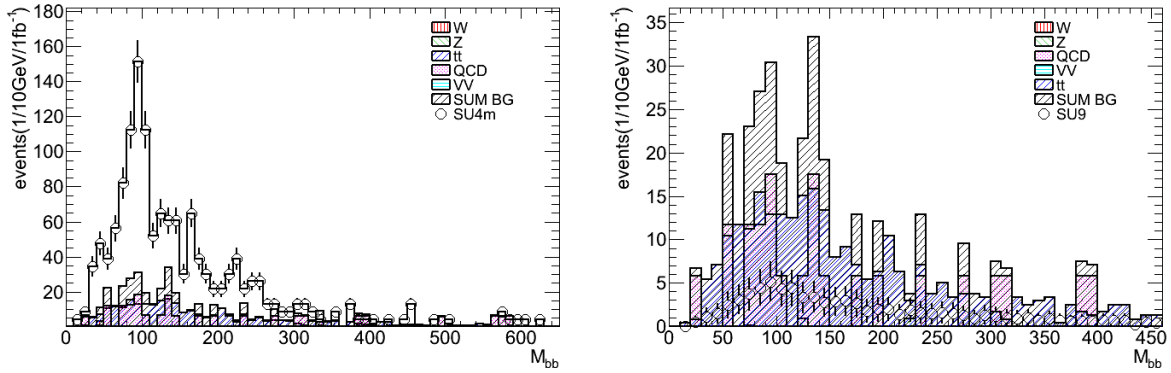

(a) Modified SU4 (b) SU9

Figure B.4: The invariant mass distributions of two b-jets in the modified SU4 (a) and SU9 (b) after requiring $\geq 2b$-jets, $E_{\mathrm{T}}^{\mathrm{miss}} > 200$ GeV and ≥ 2 additional jets with transverse momentum larger than 100 and 50 GeV for the hardest and second hardest jets, respectively. In the SU9 model an additional cut on $M_{\mathrm{eff}} > 800$ GeV is used. Both plots correspond to 1 fb^{-1} at 7 TeV.

of the W and ISR/FSR in this scenario, the high p_{T} jet requirement is also not very well suited for background rejection. This makes it quite challenging to efficiently remove the SM backgrounds. This is illustrated in Figure B.5, showing the distributions of $E_{\mathrm{T}}^{\mathrm{miss}}$ and the p_{T} of the hardest jet for the direct gaugino SUSY model and the SM backgrounds. The production mechanism in Figure B.3c is in fact more similar to events with a Higgs

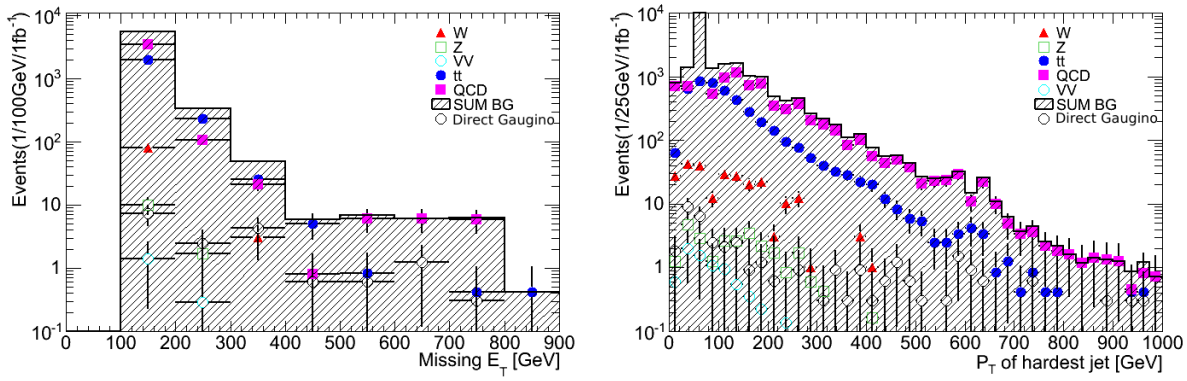

(a) $E_{\mathrm{T}}^{\mathrm{miss}}$ (b) $p_T^{jet\,1}$

Figure B.5: The left and right plots show the distribution of $E_{\mathrm{T}}^{\mathrm{miss}}$ and p_{T} of the hardest jet respectively for the direct gaugino SUSY scenario together with the SM backgrounds. Neither of these variables seems to be very efficient in reducing the SM background.

boson produced in association with a W [155]. Therefore, a typical WH analysis is probably more sensitive to these SUSY scenarios than an ordinary SUSY analysis, as a more thorough treatment of the SM backgrounds has to be carried out. An interpretation of this analysis in a direct gaugino model could however be interesting, as one might gain some sensitivity in specific SUSY models.

B.3 Conclusions

Searches for a Higgs boson decaying into $b\bar{b}$ is particularly challenging due to the enormous QCD background at LHC, making the dominant production mechanisms such as gluon-gluon, WW and ZZ fusion very difficult. Detailed studies of a SM Higgs boson, H, decaying into $b\bar{b}$ have been performed in channels where H is produced in association with a vector boson [155], however, so far with relatively low sensitivity. Another possibly interesting scenario is the production of the lightest MSSM Higgs boson through cascades of SUSY particles. This channel has so far not been very well studied within ATLAS. A MC study at 14 TeV was however done for the CSC analysis [68], giving a significance, $S/\sqrt{B}$, of 14 with an integrated luminosity of 10 fb^{-1} using the h^0-enhanced mSUGRA benchmark region, SU9. The degradation of the collision energy from 14 TeV to 7 TeV (later 8 TeV) had quite some impact on this analysis, as shown in the study outlined in this Appendix, which showed little sensitivity for the SU9 benchmark point at 1 fb^{-1}. It is however possible to construct more optimized models using the MSSM24 SUSY framework [147]. To increase the cross-section the masses of some of the sparticles need to be set relatively low, however, and might therefore, after the SUSY analysis carried out on the available data, already have been excluded.

Another possibly interesting model was investigated within the direct production of gauginos. Little sensitivity in standard SUSY searches, requiring high p_{T} jets and large $E_{\mathrm{T}}^{\mathrm{miss}}$, was found. The searches in a channel with associated production of Higgs with a W can however have some sensitivity in these models, but has so far only governed the searches for a SM Higgs boson.

No further studies of the MSSM Higgs boson in SUSY cascades were performed with the real data. A closer study would now need to be carried out, taking into account all the new limits on the various sparticle masses from other SUSY analyses, in order to reveal if one still can gain sensitivity from a study of $h^0 \rightarrow b\bar{b}$ in some specific SUSY models. Also, the recent discovery of what seems to be the Higgs boson has put even stronger constraints on the lightest MSSM Higgs. The new scalar particle discovered at the LHC at a mass of 126 GeV puts additional constraints on this channel. Decays to ZZ, $WW$and $\gamma\gamma$ are established and found compatible with the SM predictions. Decays to $b\bar{b}$ and $\tau\tau$ are not yet established, however. For the lightest MSSM Higgs the decay widths into the SM particles are dependent on the values of the parameters of the SUSY model. For instance the decays into the down type fermions are enhanced with an increasing value of $\tan\beta$, which again affects the other decay channels [32].

Appendix C

Outreach

A crucial and indispensable task for everyone working within research at a university or any other institution is to make their field understandable and attractive for teachers, pupils, students and journalists. The future of any field of research depends on how well one succeeds in making it interesting and available for the coming generations. In order to make complicated research topics available and interesting for a broader audience one needs to greatly simplify the concepts and ideas of the field, but at the same time be correct and precise. In my opinion this is the most difficult challenge in any outreach activity, but also what makes it so interesting.

Along with my own research project and the analysis of ATLAS data presented in this thesis I have gotten several opportunities to speak to journalists, students and teachers about particle physics. This is something I have found very meaningful, but also quite challenging. Since particle physics consists of many phenomena, which for most people are totally unknown and might be inaccessible in the beginning, the need to find good and understandable ways of describing them is an extra difficult task. A summary of some of the most important contributions, ranging from ordinary presentations for student and articles in Norwegian newspapers to arranging the International Masterclass in Particle Physics, are outlined in this Appendix.

C.1 School Presentations

The Department of Physics at the University of Oslo (UiO) welcomes several times a year high school students to visit some of the labs, do experiments and listen to presentations about various research topics. The field of CERN-related particle physics has, since the start-up of LHC, gotten quite some attention in the media and has therefore been a natural part of the lecture program for the visiting students. This has given me and my colleagues at the Group of Experimental Particle Physics (EPF) the opportunity to speak about our research to young students at several occasions. Since the LHC experiments at CERN the past three years have recorded more and more data and done better and better measurements the presentations have constantly been updated with the newest results, and the the focus and content of my presentations have therefore evolved quite a lot throughout the years. Some of my presentations are listed below.

- *Jakten på Higgs, antimaterie og Big bang* (En.: *The Hunt for Higgs, antimatter and the Big Bang*), presentation for high-school students visiting UiO, Oslo, May 29, 2012.
- *Partikkelfysikk på CERN* (En.: *Particle Physics at CERN*), presentation held for high school students 17 times in the period from September 12, 2008 to May 25, 2012.
- *Svarte hull og partikler - i en og samme maskin* (En.: *Black Holes and Particles - all in the Same Machine*), presentation held at *Åpen Dag*[1] at UiO March 10, 2011.

C.2 "Ungforsk" and Various other Outreach Related Activities

In connection with an event called *Ungforsk*[2] in 2012 I held, together with a colleague from the Group of Nuclear and Energy Physics, a show with the title *Fra strålebehandling til Supernovaer*[3]. *Ungforsk* is an annual event where pupils, mostly from the lower secondary school, come to the Faculty of Mathematics and Natural Sciences at UiO to follow several natural science related presentations and shows. By giving young children the opportunity to experience research at a close range, the idea is to inspire and recruit them to the natural sciences. In 2012 *Ungforsk* was arranged for the 15$^{\text{th}}$ time in cooperation with many of the research institutes around Oslo. A total of 3600 pupils from schools all around Oslo and the surrounding areas participated in *Ungforsk* 2012, distributed over two days. Our show presented some highlights from each of our research fields and we also did experiments, putting balloons and fruits into liquid nitrogen. The frozen fruit was later used to explain the differences between ordinary collisions, i.e. crashing frozen strawberries against the wall, and the particle collisions at the LHC. In the first example you only get broken pieces of strawberries out of the collision while in a particle physics collision, due to Einsteins' $E = mc^2$, you get fruits (or particles) which did not exist before the collision, as illustrated in Figure C.1.

I have also participated in various other events trying to spread enthusiasm and inform about physics and in particular experimental particle physics at CERN by holding presentations or writing articles. A selection of the most important contributions is listed below:

- Stand at the *Particle Physics Exhibition* at *Åpen Dag* at University of Oslo, March 08, 2012;
- Article about the LHC and CERN; *Kjører partikkelkrasj i lysets hastighet* (En.: *Crashing Particles at the Speed of Light*), article in *VG HELG*[4] March 13, 2010;
- *Engler, demoner og vitenskapsmenn* (En.: *Angels, Demons and Scientists*) a chronicle in VG related to the premiere of the Angels & Demons movie May 26, 2009;
- A 10 minutes presentation, *Forskning på antimaterie...og enda rarere ting ved LHC* (En.: *Study of AntiMatter... and even Stranger Things at the LHC*), about CERN

[1] A day where all students, attending their last year at high school, come and visit UiO.
[2] http://www.ungforsk.com/Hjem/tabid/2189/Default.aspx
[3] En.: *From Radiotherapy to Supernovas*
[4] VG is one of the most sold newspapers in Norway.

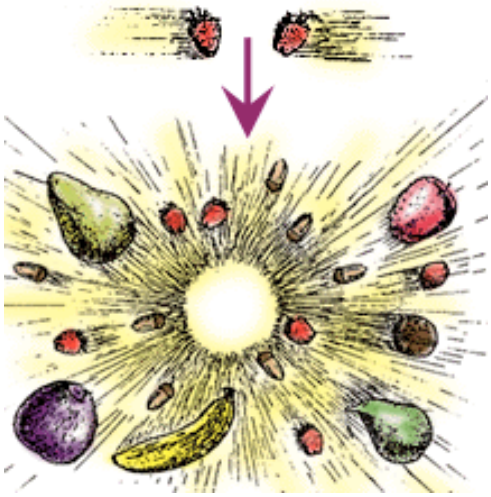

Figure C.1: To the left are two strawberries meant to imitate the proton-bunches in a particle physics collision at the LHC. What happens in a proton-proton collision is analogous to getting all kinds of new fruit (bananas, nuts, plums etc.) from the collision of two strawberries, in contradiction with what most students intuitively would expect. The right photo shows me when demonstrating a particle collision, with the creation of a variety of new particles, here illustrated by the Particle Zoo plushies (http://www.particlezoo.net/). Photo: Hilde Lynnebakken.

and the LHC experiment, in connection with the press screening of Angels & Demons at *Filmens Hus* in Oslo;

- *De vokter LHC* (En.: *Watching the LHC*), article at *forskning.no*[5] February 2010.

C.3 Masterclass in Particle Physics

The Masterclass in Particle Physics is an event gathering about 10,000 high school students from more than 30 countries (37 in 2013) every year. The Masterclasses were arranged for the first time in 2005, in connection with the World Year of Physics and the Einstein jubilee, originally based on an idea from England, which already had established a similar event. Masterclass in particle physics is arranged such that students can come to their local university or research center and attend lectures about particle physics and the LHC experiments at CERN, held by the local researchers. Afterwards the students do their own measurements by studying real data from any of the experiments at the LHC; CMS, ATLAS, ALICE or LHCb[6]. Before the start-up of LHC, data from the Large Electron-Positron (LEP) experiment at CERN was analyzed. At the end of the day all the participating institutes of that day join together in a video conference, to discuss the results and experiences from working as particle physicists for one day.

The Masterclass in Particle Physics has been arranged by the Experimental Particle Physics Group at the Physics Department at UiO every year since the beginning in 2005. The number of students has varied between $\sim$ 100 to more than 200. The students stay

[5]Online newspaper presenting national and international research.

[6]Exercises using data from LHCb are not yet started, but will hopefully start up in 2014.

at the department for the whole day and follow an extensive program divided into three parts with lectures, measurements and a video conference.

The Lectures

The day typically starts with two lectures. The first covers particle physics in general and the Standard Model, including the Higgs boson. Theories beyond the SM, including Supersymmetry or new interactions mediated by new gauge bosons W' and Z' are also introduced. In the next lecture the concepts of particle physics experiments, like LHC (or LEP detectors), are introduced. A careful treatment of the particle detection within the particle detectors is covered, as these are important concepts for the students needed to later perform the measurements. Below are the presentations given by me at the Masterclasses at UiO:

- *Å forstå tid, rom, stoff og energi* (En.: *Understanding Time, Space and Matter*), presentation at the *International Masterclass* February 18, 2010 and March 15, 2011;
- *Akseleratorer og detektorer* (En.: *Accelerators and Detectors*), presentation at the *International Masterclass* March 9, 2012 and March 15, 2013.

The Measurement

After the lectures the students are divided into smaller groups to typically work 2 by 2 in the various computer labs at the University. In the last few years the measurement[7] has been to identify short-lived particles decaying into di-electrons, di-muons, di-photons or four-leptons ($ee\mu\mu$, $eeee$ and $\mu\mu\mu\mu$) making use of the invariant mass technique. Since the start-up of the LHC, real collision data from the ATLAS detector has been used in these exercises. The di-lepton events contain events with both J/Ψ, Υ and Z bosons. In addition, MC simulations of Z' decaying into pairs of leptons have been added to the dataset, without the students knowing it. This in order to simulate for the students how new and unknown particles might appear, unexpectedly, in the analysis. The reaction from the students has often been that they believe they have done something wrong when they obtain an invariant mass of about 1 TeV from a pair of electrons or muons. The di-photon and four-lepton events have been selected from the 2011 data by applying similar cuts as in the corresponding Higgs analysis.

Each group analyses 50 events, containing a mixture of the event-types mentioned above. The students calculate then the invariant mass of the identified di-lepton, di-photon or four-lepton in every event. The tool used is Hypatia[8], which is based on the *Atlantis* event display for ATLAS [156]. A typical event is displayed in Figure C.2. In Hypatia selected leptons or photons are entered into a table where the invariant mass of two and/or four entered particles is automatically calculated (upper window in Figure C.2). The students select tracks for further investigation (middle right window in Figure C.2) or cut on the various track parameters, such as the p_{T} or the number of hits in any of

[7] *Z-path*: http://atlas.physicsmasterclasses.org/en/zpath.htm
[8] **Hy**brid **P**upil's **A**nalysis **T**ool for **I**nteractions in **A**tlas, http://hypatia.phys.uoa.gr/

the tracking detectors (lower right window C.2). A more comprehensive overview of the measurements will soon be found in the PhD thesis of Maiken Pedersen.

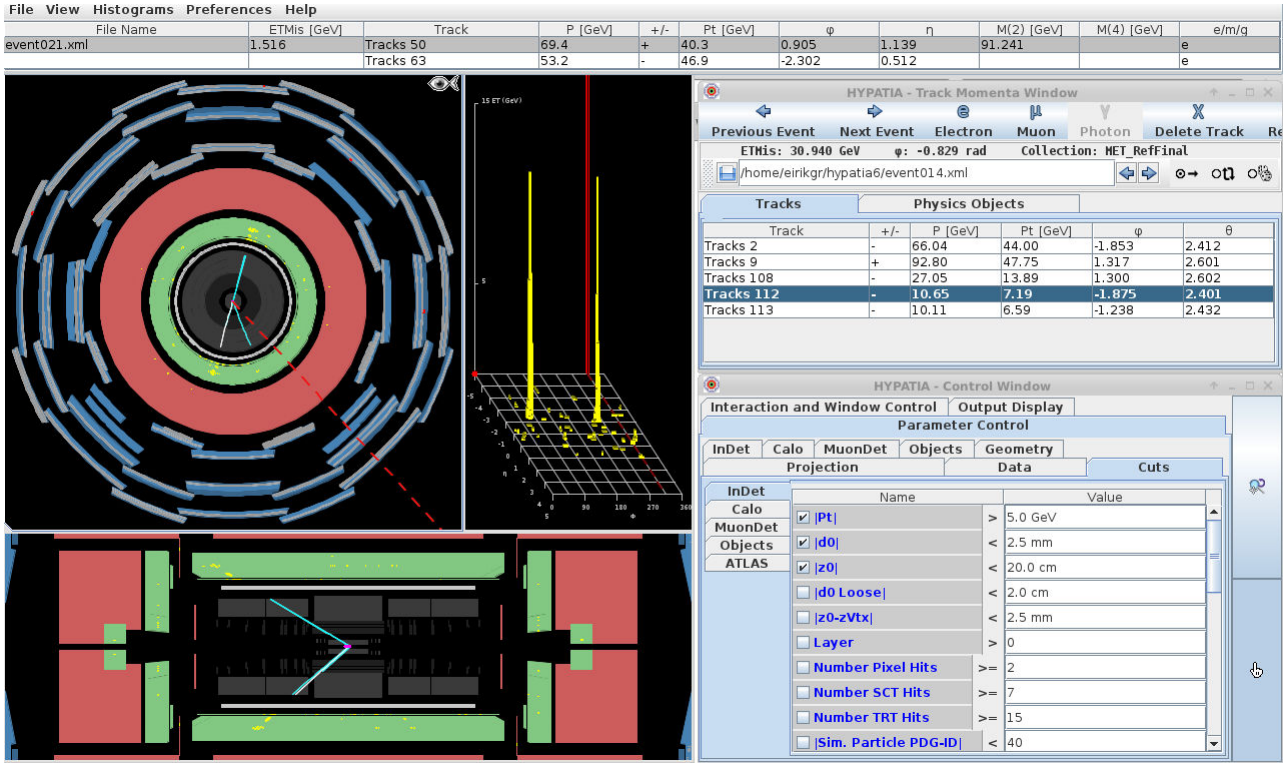

Figure C.2: A typical event, as seen by the students, with all the cutting tools and the invariant mass table. This event shows two electrons where the two electrons' invariant mass (91.2 GeV) strongly suggests that these come from a Z-decay.

After the students have gone through the events and filled a table with invariant masses, which is converted to a long list of events giving the event type (di-lepton, di-photon or four-leptons) and the corresponding value of the invariant mass, it is uploaded to a plotting tool, *OPloT*[9]. The students can then look at the invariant mass distributions. The di-lepton distributions feature a clear Z-peak and some other resonances. Since each group only analyses relatively few events, the statistics is quite limited. *OPloT* has, however, the feature to automatically combine the results from each group into a common institute result. These are then discussed locally at each institute before the video conference. The results obtained by various institutes are combined, as shown in Figure C.3, and compared with the official ATLAS publications of $H \to \gamma\gamma$ and $H \to ZZ^{(*)} \to llll$ and other di-lepton resonances at the video conference.

The Video Conference

The video conference concludes the day, where the participating institutes join together in a meeting chaired by some representatives from CERN. Two students from each institute

[9] http://cernmasterclass.uio.no/

summarise their results followed by the discussion of the combined results. A question session follows, where students can challenge the moderators about life at CERN. Finally a quiz about LHC and CERN closes the day.

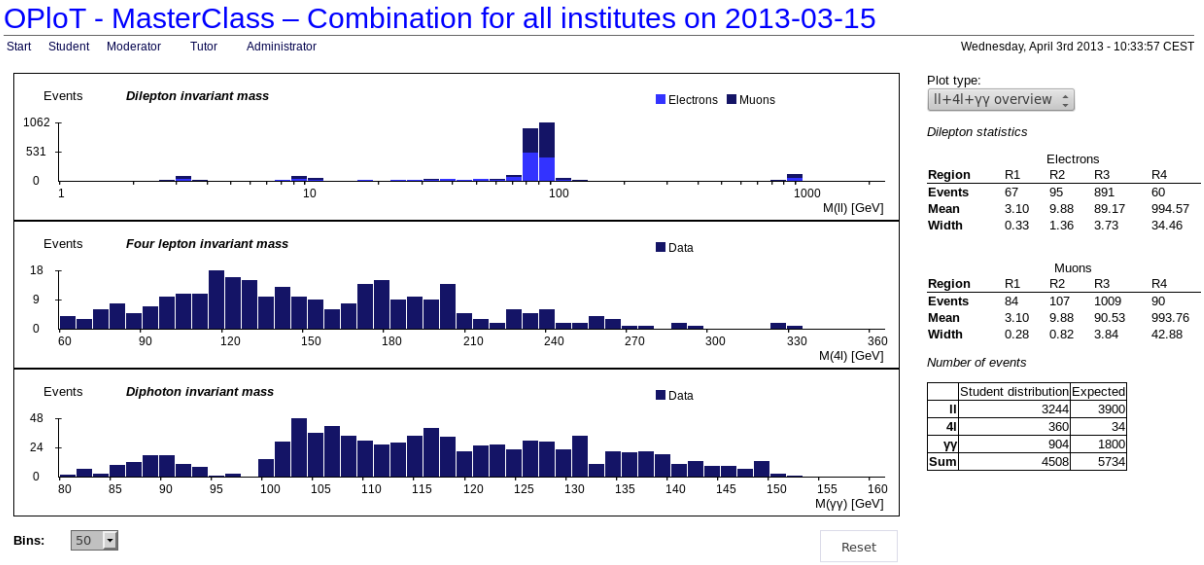

Figure C.3: The combined results from all the participating institutes (Grenoble subatomic physics and cosmology laboratory, Humboldt University of Berlin, Nikhef (Amsterdam) and University of Oslo) in the International Masterclass March 15, 2013. The Figure shows the di-lepton (upper), four-lepton (middle) and di-photon (lower) invariant mass distributions discussed at the video conference.

C.4 Physics Olympiad

Together with Carl Angell (professor at the University Of Oslo) I was the leader for the Norwegian delegation to the 41st International Physics Olympiad in Zagreb, Croatia, held from July 17 to 25, 2010.[10] The Norwegian team got one *honourable mention* and one bronze medal! From 2008 to 2013 I have every year given presentations about particle physics for the Norwegian finalists in the qualification for the International Physics Olympiads.

[10] http://ipho2010.hfd.hr/tekst.php?id=21

Appendix D

Binary Operators

The possibility to use bits to store information is a powerful tool in all programming languages. To identify electrons for instance, there is one variable, often referred to as *isEM*, storing the value of 32 different properties for an electron. By applying various logical bit-operations, discussed below, on this variable the quality of every electron can easily be deciphered. My qualification task gave me the opportunity to look carefully at this possibility of storing information. I eventually learned how to use this[1], as a lot of the information about the current condition and state of the SCT detector happened to be stored in bits. With the present Appendix, I would like to share my enthusiasm, hoping that it can be a stepping stone to others who want to start exploring the power of bit-operations.

D.1 Binary System

Bits (contraction of *binary digits*) are used in computers to store information and can take the two values, 1 or 0. Eight bits combine into what is more commonly known as a *byte*. In many cases it is preferable to save information using every bit of a variable, which often can store 4, 8, 16, 32 or 64 bits, depending on the type of the variable. Each bit is then typically assigned to some set of requirements, and the value of the bit then reflects if these requirements are fulfilled or not (true/false). There are several bit-operations available in most computer languages, making it possible for the user to decode the value of each bit of two variables, x and y:

[1] In addition I also had to learn the fantastic, but not very much used, programming language known as *Perl*, but that is another story...

$x\&y$ each bit of the output is 1 if the corresponding bit of x AND of y is 1, otherwise it is 0

$x|y$ each bit of the output is 0 if the corresponding bit of x AND of y is 0, otherwise it is 1

$\tilde{}x$ returns the complement of x (i.e. the number returned by switching each 1 to a 0 and each 0 to a 1)

$x\hat{}y$ each bit of the output is the same as the bit in x if the corresponding bit in y is 0, and it is the complement of the bit in x if the corresponding bit in y is 1

According to this, in order to for example pick out the first 4 and last 4 bits in an 8-bit variable, x, and store them in y_1 and y_2 respectively one could do

$$y_1 = x\&240$$
$$y_2 = x\&15$$

since the binary representations of 240 and 15 are 11110000 and 00001111 respectively.

The bits are counted from right to left, so that in an 8-bit variable, the rightmost bit is 0 an the leftmost bit is 7. Given the binary representation of a few convenient Arabic numbers presented in Table D.1, one can check if the bits 0-7 have value 1 or 0 using the logic presented in Table D.2

Arabic	1	2	4	8	16	32	64	128
binary	00000001	00000010	00000100	00001000	00010000	00100000	01000000	10000000

Table D.1: The binary representation of some handy Arabic numbers. Multiplying the Arabic number with two moves the non-zero element one step to the left.

bit #	bit_0	bit_1	bit_2	bit_3	bit_4	bit_5	bit_6	bit_7
logic	$x\&1$	$x\&2$	$x\&4$	$x\&8$	$x\&16$	$x\&32$	$x\&64$	$x\&128$

Table D.2: Logic to retrieve each bit of an eight bit variable, x.

D.2 Hexadecimals

Hexadecimal is a base 16 system also widely used to represent numbers in computers. One usually uses the numbers 1-9 to represent the values zero to nine and the letters A-F (a-f) to represent the numbers ten to fifteen. A $0x$ is often put in front of a hexadecimal number to distinguish it from ordinary numbers (or even words). For example the hexadecimal number $0x2F$ is

$$2 \cdot 16^1 + 15 \cdot 16^0 = 47$$

using the Arabic numerals. Each hexadecimal digit represents four binary digits, also known as a *nibble*. So, to represent the hexadecimal number $0x2F$ above, one would need 8 bits giving $0x2F = 00101111$.

List of Figures

List of Tables

Bibliography

[1] F. Englert and R. Brout, *Broken Symmetry and the Mass of Gauge Vector Mesons*, Phys. Rev. Lett. **13** (1964) 321–323. http://link.aps.org/doi/10.1103/PhysRevLett.13.321.

[2] P. Higgs, *Broken symmetries, massless particles and gauge fields*, Physics Letters **12** no. 2, (1964) 132 – 133. http://www.sciencedirect.com/science/article/pii/0031916364911369.

[3] P. W. Higgs, *Broken Symmetries and the Masses of Gauge Bosons*, Phys. Rev. Lett. **13** (1964) 508–509. http://link.aps.org/doi/10.1103/PhysRevLett.13.508.

[4] G. S. Guralnik, C. R. Hagen, and T. W. B. Kibble, *Global Conservation Laws and Massless Particles*, Phys. Rev. Lett. **13** (1964) 585–587. http://link.aps.org/doi/10.1103/PhysRevLett.13.585.

[5] P. W. Higgs, *Spontaneous Symmetry Breakdown without Massless Bosons*, Phys. Rev. **145** (1966) 1156–1163. http://link.aps.org/doi/10.1103/PhysRev.145.1156.

[6] T. W. B. Kibble, *Symmetry Breaking in Non-Abelian Gauge Theories*, Phys. Rev. **155** (1967) 1554–1561. http://link.aps.org/doi/10.1103/PhysRev.155.1554.

[7] M. Banner et al., *Observation of single isolated electrons of high transverse momentum in events with missing transverse energy at the CERN pp collider*, Physics Letters B **122** no. 5-6, (1983) 476 – 485. http://www.sciencedirect.com/science/article/pii/0370269383916052.

[8] UA1 Collaboration, G. Arnison et al., *Experimental Observation of Isolated Large Transverse Energy Electrons with Associated Missing Energy at* $\sqrt{s} = 540$ *GeV*, Phys.Lett. **B122** (1983) 103–116.

[9] ATLAS Collaboration, G. Aad et al., *Observation of a new particle in the search for the Standard Model Higgs boson with the ATLAS detector at the LHC*, Physics Letters B **716** no. 1, (2012) 1 – 29. http://www.sciencedirect.com/science/article/pii/S037026931200857X.

[10] CMS Collaboration, S. Chatrchyan et al., *Observation of a new boson at a mass of 125 GeV with the CMS experiment at the LHC*, Physics Letters B **716** no. 1, (2012) 30 – 61. http://www.sciencedirect.com/science/article/pii/S0370269312008581.

[11] ATLAS Collaboration, G. Aad et al., *Searches for supersymmetry with the ATLAS detector using final states with two leptons and missing transverse momentum in proton-proton collisions*, Physics Letters B **709** no. 3, (2012) 137 – 157. http://www.sciencedirect.com/science/article/pii/S0370269312001177.

[12] ATLAS Collaboration, G. Aad et al., *Search for direct slepton and gaugino production in final states with two leptons and missing transverse momentum with the ATLAS detector in pp collisions at* $\sqrt{s} = 7$ *TeV.*, Physics Letters B **718** no. 3, (2013) 879 – 901. http://www.sciencedirect.com/science/article/pii/S0370269312012245.

[13] OPERA Collaboration, T. Adam et al., *Measurement of the neutrino velocity with the OPERA detector in the CNGS beam*, JHEP **1210** (2012) 093, arXiv:1109.4897 [hep-ex].

[14] F. Halzen and A. Martin, *Quarks and Leptons: An Introductory Course in Modern Particle Physics*. John Wiley & Sons, Inc., 1984.

[15] J. H. Christenson, J. W. Cronin, V. L. Fitch, and R. Turlay, *Evidence for the* 2π *Decay of the* K_2^0 *Meson*, Phys. Rev. Lett. **13** (1964) 138–140. http://link.aps.org/doi/10.1103/PhysRevLett.13.138.

[16] CPLEAR Collaboration Collaboration, L. Alvarez-Gaume, C. Kounnas, S. Lola, and P. Pavlopoulos, *Direct T violation measurements and T odd effects in decay experiments*, arXiv:hep-ph/9903458 [hep-ph].

[17] S. L. Glashow, *Partial-symmetries of weak interactions*, Nuclear Physics **22** no. 4, (1961) 579 – 588. http://www.sciencedirect.com/science/article/pii/0029558261904692.

[18] S. Weinberg, *A Model of Leptons*, Phys. Rev. Lett. **19** (1967) 1264–1266. http://link.aps.org/doi/10.1103/PhysRevLett.19.1264.

[19] A. Salam, *in Elementary Particle Theory, Proc. 8th Nobel Symp., ed. N. Svartholm (Wiley-Interscience, New York, 1968)*,.

[20] Gargamelle Neutrino Collaboration, F. Hasert et al., *Observation of Neutrino Like Interactions Without Muon Or Electron in the Gargamelle Neutrino Experiment*, Phys.Lett. **B46** (1973) 138–140.

[21] F. Hasert et al., *Search for elastic muon-neutrino electron scattering*, Physics Letters B **46** no. 1, (1973) 121 – 124. http://www.sciencedirect.com/science/article/pii/0370269373904942.

[22] M. Kobayashi and T. Maskawa, *CP-Violation in the Renormalizable Theory of Weak Interaction*, Progress of Theoretical Physics **49** no. 2, (1973) 652–657. http://ptp.ipap.jp/link?PTP/49/652/.

[23] N. Cabibbo, *Unitary Symmetry and Leptonic Decays*, Phys. Rev. Lett. **10** (1963) 531–533. http://link.aps.org/doi/10.1103/PhysRevLett.10.531.

[24] J. Beringer et al., *Particle Data Group*, Phys. Rev. D86 010001 (2012). http://pdg.lbl.gov/.

[25] J. Goldstone, *Field theories with "Superconductor" solutions*, Il Nuovo Cimento **19** no. 1, (1961) 154–164. http://dx.doi.org/10.1007/BF02812722.

[26] T. W. B. Kibble, *Englert-Brout-Higgs-Guralnik-Hagen-Kibble mechanism*, Scholarpedia **4** no. 1, (2009) 6441. http://www.scholarpedia.org/article/Englert-Brout-Higgs-Guralnik-Hagen-Kibble_mechanism.

[27] G.-Z. Liu and G. Cheng, *Extension of the Anderson-Higgs mechanism*, Phys. Rev. B **65** (2002) 132513. http://link.aps.org/doi/10.1103/PhysRevB.65.132513.

[28] F. Close, *The Infinity Puzzle: Quantum Field Theory and the Hunt for an Orderly Universe*. Oxford University Press, 2011.

[29] I. Gogoladze, B. He, and Q. Shafi, *New fermions at the LHC and mass of the Higgs boson*, Physics Letters B **690** no. 5, (2010) 495 – 500. http://www.sciencedirect.com/science/article/pii/S0370269310006921.

[30] ATLAS Collaboration, *ATLAS: Detector and physics performance technical design report. Volume 1*,. http://atlas.web.cern.ch/Atlas/GROUPS/PHYSICS/TDR/access.html.

[31] ATLAS Collaboration, *ATLAS: Detector and physics performance technical design report. Volume 2*,. http://atlas.web.cern.ch/Atlas/GROUPS/PHYSICS/TDR/access.html.

[32] A. Djouadi, *The anatomy of electroweak symmetry breaking Tome II: The Higgs bosons in the Minimal Supersymmetric Model*, Physics Reports **459** no. 1-6, (2008) 1 – 241. http://www.sciencedirect.com/science/article/pii/S0370157307004346.

[33] H. Baer and X. Tata, *Weak Scale Supersymmetry, From Superfields to Scattering Events*. Cambridge University Press, 2006.

[34] S. P. Martin, *A Supersymmetry Primer*, (1997), arXiv:hep-ph/9709356 [hep-ph].

[35] I. J. Aitchison, *Supersymmetry and the MSSM: An Elementary introduction*, arXiv:hep-ph/0505105 [hep-ph].

[36] ATLAS Collaboration, G. Aad et al., *Search for a heavy narrow resonance decaying to e mu, e tau, or mu tau with the ATLAS detector in $\sqrt{s} = 7$ TeV pp collisions at the LHC*, arXiv:1212.1272 [hep-ex].

[37] D. Chung et al., *The soft supersymmetry-breaking Lagrangian: theory and applications*, Physics Reports **407** no. 1-3, (2005) 1 – 203. http://www.sciencedirect.com/science/article/pii/S0370157304004466.

[38] M. E. Peskin, *Beyond the standard model*, arXiv:hep-ph/9705479 [hep-ph].

[39] D. Green, *High Pt Physics at Hadron Colliders*. Cambridge University Press, 2005.

[40] J. M. Butterworth, G. Dissertori, and G. P. Salam, *Hard Processes in Proton-Proton Collisions at the Large Hadron Collider*, arXiv:1202.0583 [hep-ex].

[41] V. Barger and R. Phillips, *Collider physics*. Addison-Wesley, 1991.

[42] A. Martin, W. Stirling, R. Thorne, and G. Watt, *Parton distributions for the LHC*, The European Physical Journal C **63** (2009) 189–285. http://dx.doi.org/10.1140/epjc/s10052-009-1072-5.

[43] J. M. Campbell, J. W. Huston, and W. J. Stirling, *Hard interactions of quarks and gluons: a primer for LHC physics*, Reports on Progress in Physics **70** no. 1, (2007) 89. http://stacks.iop.org/0034-4885/70/i=1/a=R02.

[44] T. Plehn, "Supersymmetry at the LHC." http://www.thphys.uni-heidelberg.de/~plehn/includes/talks/2010/psi_10.pdf [online; accessed 11-june-2013]. Slides from talk given at PSI Colloquium, October 7, 2010, Switzerland.

[45] ATLAS Collaboration, G. Aad et al., *Measurements of the electron and muon inclusive cross-sections in proton-proton collisions at* $\sqrt{s} = 7$ *TeV with the ATLAS detector*, Physics Letters B **707** no. 5, (2012) 438 – 458. http://www.sciencedirect.com/science/article/pii/S037026931101522X.

[46] ATLAS Collaboration, G. Aad et al., *Electron performance measurements with the ATLAS detector using the 2010 LHC proton-proton collision data*, The European Physical Journal C - Particles and Fields **72** (2012) 1–46. http://dx.doi.org/10.1140/epjc/s10052-012-1909-1.

[47] F. Ambroglini et al., *Proceedings of the Workshop on Monte Carlo's, Physics and Simulations at the LHC PART I*, arXiv:0902.0293 [hep-ph].

[48] LuminosityPublicResults Twiki [online; accessed 11-june-2013]. https://atlas.web.cern.ch/Atlas/GROUPS/DATAPREPARATION/PublicPlots/2012/DataSummary/figs/peakLumiByFill.png.

[49] LuminosityPublicResults Twiki [online; accessed 11-june-2013]. https://atlas.web.cern.ch/Atlas/GROUPS/DATAPREPARATION/PublicPlots/2011/DataSummary/figs/peakLumiByFill.png.

[50] ATLAS Collaboration, G. Aad et al., *The ATLAS Experiment at the CERN Large Hadron Collider*, JINST **3** (2008) S08003.

[51] M. Capeans et al., *ATLAS Insertable B-Layer Technical Design Report*, CERN-LHCC-2010-013. ATLAS-TDR-019 (LHCC Public Document), CERN, Geneva, Sep, 2010. https://cds.cern.ch/record/1291633.

[52] Z. Dolezal, *The ATLAS Semiconductor Tracker 2013 design and status of construction*, Nuclear Physics B - Proceedings Supplements **150** no. 0, (2006) 128 – 131. http://www.sciencedirect.com/science/article/pii/S092056320500825X.

[53] S. Hassani et al., *A muon identification and combined reconstruction procedure for the ATLAS detector at the LHC using the (MUONBOY, STACO, MuTag) reconstruction packages*, Nuclear Instruments and Methods in Physics Research Section A: Accelerators, Spectrometers, Detectors and Associated Equipment **572**

no. 1, (2007) 77 – 79.
http://www.sciencedirect.com/science/article/pii/S0168900206019863.

[54] B. Resende, *Muon identification algorithms in ATLAS*, ATL-PHYS-PROC-2009-113, CERN, Geneva, Sep, 2009. https://cds.cern.ch/record/1209632.

[55] C. Gabaldon, *Performance of the ATLAS Trigger System*, Journal of Instrumentation **7** no. 01, (2012) C01092. http://stacks.iop.org/1748-0221/7/i=01/a=C01092.

[56] S. D'Auria, *The ATLAS semiconductor tracker: operations and performance*, ATL-INDET-PROC-2012-027, CERN, Geneva, Nov, 2012. https://cds.cern.ch/record/1494558?ln=no.

[57] A. Sfyrla et al., *The Detector Control System for the ATLAS Semiconductor Tracker Assembly Phase*, Nuclear Science, IEEE Transactions on **52** no. 4, (2005) 938 – 943.

[58] "Shtxx application note dew-point calculation [online; accessed 11-june-2013]." http://irtfweb.ifa.hawaii.edu/~tcs3/tcs3/Misc/Dewpoint_Calculation_Humidity_Sensor_E.pdf.

[59] SctEnvSoftware Twiki (ATLAS Internal) [online; accessed 11-june-2013]. https://twiki.cern.ch/twiki/bin/viewauth/Atlas/SctEnvSoftware.

[60] ATLAS Collaboration, *Non-collision backgrounds as measured by the ATLAS detector during the 2010 proton-proton run*, ATLAS-CONF-2011-137 (ATLAS Internal), CERN, Geneva, Sep, 2011. http://cds.cern.ch/record/1383840.

[61] E. Gramstad, "Python scripts for checking the SCT DCS (ATLAS Internal) [online; accessed 11-june-2013]." https://indico.cern.ch/getFile.py/access?contribId=4&resId=0&materialId=slides&confId=197512. Slides from a talk given at SCT operations weekly, June 27, 2012, CERN, Switzerland.

[62] "Search for electrons from ionisation in 2008 cosmic-ray data (ATLAS Internal) [online; accessed 11-june-2013]." ElectronGammaApprovedCosmicPlots Twiki, 2008. https://twiki.cern.ch/twiki/pub/AtlasPublic/ElectronGammaApprovedCosmicPlots/Cosmic_electrons_Final.pdf.

[63] J. Kraus, C. Schmitt, and E. Von Toerne, *First observation of electrons in the ATLAS detector*, ATL-COM-PHYS-2009-564 (ATLAS Internal), CERN, Geneva, Oct, 2009. https://cds.cern.ch/record/1211560.

[64] S. Swordy, *The Energy Spectra and Anisotropies of Cosmic Rays*, Space Science Reviews **99** no. 1-4, (2001) 85–94. http://dx.doi.org/10.1023/A%3A1013828611730.

[65] S. Fratina, *Approval Request for Cosmic Plots: Level 2 Track Trigger Efficiency in 2008 Cosmic Data*, ATL-COM-DAQ-2009-016, CERN, Geneva, Mar, 2009. https://cds.cern.ch/record/1166539.

[66] E. Abat, A. Abdesselam, et al., *Combined performance tests before installation of the ATLAS Semiconductor and Transition Radiation Tracking Detectors*, Journal of Instrumentation **3** no. 08, (2008) P08003. http://stacks.iop.org/1748-0221/3/i=08/a=P08003.

[67] C. Schmitt, *Commissioning of the ATLAS reconstruction software with first data*, ATL-SOFT-PROC-2008-004. ATL-COM-SOFT-2008-020, CERN, Geneva, Nov, 2008. https://cds.cern.ch/record/1141221. Deadline: November 30th 2008.

[68] G. Aad et al., *Expected performance of the ATLAS experiment: detector, trigger and physics*. CERN, Geneva, 2009. arXiv:0901.0512 [hep-ex].

[69] "Cut details for cosmic electrons." https://svnweb.cern.ch/trac/atlasoff/browser/Reconstruction/egamma/egammaPIDTools/trunk/python/egammaElectronCutIDToolBase.py. [Online; accessed 11-June-2013].

[70] S. Fratina et al. ATL-INDET-PUB-2009-002, CERN, Geneva, Dec, 2009. http://cds.cern.ch/record/1229213.

[71] E. Gramstad, "Cosmic with 2008 and 2009 data." https://indico.cern.ch/conferenceOtherViews.py?view=standard&confId=48799. Slides from a talk given at egamma phone conference, December 14, 2009, CERN, Switzerland (ATLAS Internal) [Online; accessed 11-June-2013].

[72] H. Abreu, E. Gramstad, et al., *Electron and photon reconstruction and identification results from ATLAS at 900 GeV*, ATL-COM-PHYS-2010-172 (ATLAS Internal), CERN, Geneva, Apr, 2010. https://cds.cern.ch/record/1256613.

[73] ATLAS Collaboration, *ATLAS Monte Carlo tunes for MC09*, ATL-PHYS-PUB-2010-002, CERN, Geneva, Mar, 2010. https://cds.cern.ch/record/1247375.

[74] "MCTruthClassifier Twiki (ATLAS Internal) [online; accessed 11-june-2013]." https://twiki.cern.ch/twiki/bin/viewauth/AtlasProtected/MCTruthClassifier.

[75] "Cut details for 900 gev electrons." https://svnweb.cern.ch/trac/atlasoff/browser/Reconstruction/egamma/egammaPIDTools/tags/egammaPIDTools-00-00-75/python/egammaElectronCutIDToolBase.py. [Online; accessed 11-June-2013].

[76] I. Santoyo Castillo, B. Gjelsten, E. Gramstad, F. Ould-Saada, M. Pedersen, et al., *Searching for direct gaugino production and direct slepton production with two leptons and missing transverse momentum at* $\sqrt{s} = 7$ *TeV*, ATL-COM-PHYS-2011-1721 (ATLAS Internal), CERN, Geneva, Dec, 2011. https://cds.cern.ch/record/1408807.

[77] S. S. AbdusSalam, B. C. Allanach, F. Quevedo, F. Feroz, and M. Hobson, *Fitting the phenomenological MSSM*, Phys. Rev. D **81** (2010) 095012. http://link.aps.org/doi/10.1103/PhysRevD.81.095012.

[78] C. F. Berger, J. S. Gainer, J. L. Hewett, and T. G. Rizzo, *Supersymmetry without prejudice*, Journal of High Energy Physics **2009** no. 02, (2009) 023. http://stacks.iop.org/1126-6708/2009/i=02/a=023.

[79] A. Djouadi, J.-L. Kneur, and G. Moultaka, *SuSpect: A Fortran code for the Supersymmetric and Higgs particle spectrum in the MSSM*, Computer Physics Communications **176** no. 6, (2007) 426 – 455. http://www.sciencedirect.com/science/article/pii/S001046550600419X.

[80] F. E. Paige, S. D. Protopopescu, H. Baer, and X. Tata, *ISAJET 7.69: A Monte Carlo event generator for pp, anti-p p, and e+e- reactions*, arXiv:hep-ph/0312045 [hep-ph].

[81] W. Beenakker, R. Hopker, M. Spira, and P. Zerwas, *Squark and gluino production at hadron colliders*, Nucl.Phys. **B492** (1997) 51–103, arXiv:hep-ph/9610490 [hep-ph].

[82] M. Kramer, A. Kulesza, R. van der Leeuw, M. Mangano, S. Padhi, et al., *Supersymmetry production cross sections in pp collisions at* $\sqrt{s} = 7$ *TeV*, arXiv:1206.2892 [hep-ph].

[83] G. Corcella et al., *HERWIG 6: an event generator for hadron emission reactions with interfering gluons (including supersymmetric processes)*, Journal of High Energy Physics **2001** no. 01, (2001) 010. http://stacks.iop.org/1126-6708/2001/i=01/a=010.

[84] LEP2 SUSY Working Group, "Combined lep selectron/smuon/stau results, 183-208 GeV." http://lepsusy.web.cern.ch/lepsusy/www/sleptons_summer04/slep_final.html, 2004. [Online; accessed 11-June-2013].

[85] R. C. Gray, C. Kilic, M. Park, S. Somalwar, and S. Thomas, *Backgrounds To Higgs Boson Searches from Asymmetric Internal Conversion*, arXiv:1110.1368 [hep-ph].

[86] ATLAS Collaboration, G. Aad et al., *Search for supersymmetric particles in events with lepton pairs and large missing transverse momentum in* $\sqrt{s} = 7$ *TeV proton-proton collisions with the ATLAS experiment*, Eur.Phys.J. **C71** (2011) 1682, arXiv:1103.6214 [hep-ex].

[87] ATLAS Collaboration, *A study of the material in the ATLAS inner detector using secondary hadronic interactions*, Journal of Instrumentation **7** no. 01, (2012) P01013. http://stacks.iop.org/1748-0221/7/i=01/a=P01013.

[88] B. Povh, K. Rith, C. Scholz, and F. Zetsche, *Particles and nuclei : an introduction to the physical concepts*. Springer, 4th ed., 2004.

[89] D. R. Tovey, *On measuring the masses of pair-produced semi-invisibly decaying particles at hadron colliders*, Journal of High Energy Physics **2008** no. 04, (2008) 034. http://stacks.iop.org/1126-6708/2008/i=04/a=034.

[90] G. Polesello and D. Tovey, *Supersymmetric particle mass measurement with the boost-corrected contransverse mass*, Journal of High Energy Physics **2010** (2010) 1–33. http://dx.doi.org/10.1007/JHEP03%282010%29030.

[91] ATLAS Collaboration, *SUSY searches with dileptons and high missing transverse momentum*, ATL-PHYS-INT-2011-030 (ATLAS Internal), CERN, Geneva, Apr, 2011. https://cds.cern.ch/record/1341811.

[92] SUSY di-lepton group (Rick Ueno), "m_{CT} tagger code snippet." https://twiki.cern.ch/twiki/pub/AtlasProtected/SUSYTwoLeptonMoriond2012/mct_tagger_snippet.txt, 2011. (ATLAS Internal) [Online; accessed 07-May-2013].

[93] C. Lester and D. Summers, *Measuring masses of semi-invisibly decaying particles pair produced at hadron colliders*, Phys.Lett. **B463** (1999) 99–103, arXiv:hep-ph/9906349 [hep-ph].

[94] A. Barr, C. Lester, and P. Stephens, *m(T2): The Truth behind the glamour*, J.Phys. **G29** (2003) 2343–2363, arXiv:hep-ph/0304226 [hep-ph].

[95] W. S. Cho, K. Choi, Y. G. Kim, and C. B. Park, *Transverse Mass for Pairs of Gluinos*, Phys. Rev. Lett. **100** (2008) 171801. http://link.aps.org/doi/10.1103/PhysRevLett.100.171801.

[96] J. Barreiro Guimaraes da Costa, *Summary plot of electroweak cross section measurements for Moriond Electroweak 2013*, ATL-COM-PHYS-2013-237 (ATLA Internal), CERN, Geneva, Feb, 2013. https://cds.cern.ch/record/1519717.

[97] ATLAS Collaboration, G. Aad et al., *Study of jets produced in association with a W boson in pp collisions at $\sqrt{s} = 7$TeV with the ATLAS detector*, Phys. Rev. D **85** (2012) 092002. http://link.aps.org/doi/10.1103/PhysRevD.85.092002.

[98] ATLAS Collaboration, G. Aad et al., *Measurement of the production cross section for Z/γ^* in association with jets in pp collisions at $\sqrt{s} = 7$TeV with the ATLAS detector*, Phys. Rev. D **85** (2012) 032009. http://link.aps.org/doi/10.1103/PhysRevD.85.032009.

[99] "Good Run List for 2011 data." http://atlasdqm.web.cern.ch/atlasdqm/grlgen/Archive/Susy/Susy_v01/data11_7TeV.periodAllYear_DetStatus-v36-pro10_CoolRunQuery-00-04-08_Susy.xml. [Online; accessed 11-June-2013].

[100] ATLAS Collaboration, *Luminosity Determination in pp Collisions at $\sqrt{s} = 7$ TeV Using the ATLAS Detector at the LHC*, Eur.Phys.J. **C71** (2011) 1630, arXiv:1101.2185 [hep-ex].

[101] *Luminosity Determination in pp Collisions at $\sqrt{s} = 7$ TeV using the ATLAS Detector in 2011*, ATLAS-CONF-2011-116, CERN, Geneva, Aug, 2011. https://cds.cern.ch/record/1376384.

[102] J. Butterworth et al., *Single Boson and Diboson Production Cross Sections in pp Collisions at $\sqrt{s} = 7$ TeV*, ATL-COM-PHYS-2010-695 (ATLAS Internal), CERN, Geneva, Aug, 2010. https://cds.cern.ch/record/1287902.

[103] M. Aliev, H. Lacker, U. Langenfeld, S. Moch, P. Uwer, and M. Wiedermann, *HATHOR - HAdronic Top and Heavy quarks crOss section calculatoR*, Computer Physics Communications **182** no. 4, (2011) 1034 – 1046, arXiv:1007.1327 [hep-ph]. http://www.sciencedirect.com/science/article/pii/S0010465510005333.

[104] A. Martin, W. Stirling, R. Thorne, and G. Watt, *Parton distributions for the LHC*, The European Physical Journal C **63** no. 2, (2009) 189–285. http://dx.doi.org/10.1140/epjc/s10052-009-1072-5.

[105] A. Martin, W. Stirling, R. Thorne, and G. Watt, *Uncertainties on α_S in global PDF analyses and implications for predicted hadronic cross sections*, The European Physical Journal C **64** no. 4, (2009) 653–680. http://dx.doi.org/10.1140/epjc/s10052-009-1164-2.

[106] M. Cacciari and others, *Top-pair production at hadron colliders with next-to-next-to-leading logarithmic soft-gluon resummation*, arXiv:1111.5869 [hep-ph].

[107] M. Czakon and A. Mitov, *Top++: a program for the calculation of the top-pair cross-section at hadron colliders*, arXiv:1112.5675 [hep-ph].

[108] N. Kidonakis, *Next-to-next-to-leading-order collinear and soft gluon corrections for t-channel single top quark production*, Phys. Rev. D **83** (2011) 091503. http://link.aps.org/doi/10.1103/PhysRevD.83.091503.

[109] N. Kidonakis, *Next-to-next-to-leading logarithm resummation for s-channel single top quark production*, Phys. Rev. D **81** (2010) 054028. http://link.aps.org/doi/10.1103/PhysRevD.81.054028.

[110] N. Kidonakis, *Two-loop soft anomalous dimensions for single top quark associated production with a W^- or H^-*, Phys. Rev. D **82** (2010) 054018. http://link.aps.org/doi/10.1103/PhysRevD.82.054018.

[111] M. Smizanska, *PythiaB an interface to Pythia6 dedicated to simulation of beauty events*, ATL-COM-PHYS-2003-038 (ATLAS Internal), CERN, Geneva, 2003. https://cds.cern.ch/record/681440.

[112] "SUSY Tools source code." https://svnweb.cern.ch/trac/atlasoff/browser/PhysicsAnalysis/SUSYPhys/SUSYTools. [Online; accessed 11-June-2013].

[113] "Object quality flag and bitmasks definitions for egamma objects." https://twiki.cern.ch/twiki/bin/viewauth/AtlasProtected/LArCleaningAndObjectQuality#Usage_on_D3PD. ATLAS Internal [Online; accessed 11-June-2013].

[114] "Cut details for loose electrons." https://svnweb.cern.ch/trac/atlasoff/browser/Reconstruction/egamma/egammaPIDTools/trunk/python/egammaLooseElectronCutIDToolBase.py. [Online; accessed 11-June-2013].

[115] "Cut details for medium electrons." https://svnweb.cern.ch/trac/atlasoff/browser/Reconstruction/egamma/egammaPIDTools/trunk/python/egammaMediumElectronCutIDToolBase.py. [Online; accessed 11-June-2013].

[116] "Cut details for tight electrons." https://svnweb.cern.ch/trac/atlasoff/browser/Reconstruction/egamma/egammaPIDTools/trunk/python/egammaTightElectronCutIDToolBase.py. [Online; accessed 11-June-2013].

[117] S. D. Ellis and D. E. Soper, *Successive combination jet algorithm for hadron collisions*, Phys. Rev. D **48** (1993) 3160–3166. http://link.aps.org/doi/10.1103/PhysRevD.48.3160.

[118] M. Cacciari, G. Salam, and G. Soyez, *The anti-kt jet clustering algorithm*, JHEP **0804** (2008) 063, arXiv:0802.1189.

[119] W. Lampl et al., *Calorimeter Clustering Algorithms: Description and Performance*, ATL-LARG-PUB-2008-002. ATL-COM-LARG-2008-003, CERN, Geneva, Apr, 2008. https://cds.cern.ch/record/1099735.

[120] ATLAS Collaboration, *Jet energy scale and its systematic uncertainty in proton-proton collisions at $\sqrt{s} = 7$ TeV in ATLAS 2010 data*, ATLAS-CONF-2011-032, CERN, Geneva, Mar, 2011. https://cds.cern.ch/record/1337782.

[121] D. W. Miller, A. Schwartzman, and D. Su, *Pile-up jet energy scale corrections using the jet-vertex fraction method*, ATL-PHYS-INT-2009-090 (ATLAS Internal), CERN, Geneva, Sep, 2009. https://cds.cern.ch/record/1206864.

[122] G. Piacquadio and C. Weiser, *A new inclusive secondary vertex algorithm for b-jet tagging in ATLAS*, Journal of Physics: Conference Series **119** no. 3, (2008) 032032. http://stacks.iop.org/1742-6596/119/i=3/a=032032.

[123] ATLAS Collaboration, G. Aad et al., *Calibrating the b-Tag Efficiency and Mistag Rate in $35pb^{-1}$ of Data with the ATLAS Detector*, ATLAS-CONF-2011-089, CERN, Geneva, Jun, 2011. https://cds.cern.ch/record/1356198.

[124] ATLAS Collaboration, G. Aad et al., *Performance of missing transverse momentum reconstruction in proton-proton collisions at $\sqrt{s} = 7$ TeV with ATLAS*, The European Physical Journal C - Particles and Fields **72** (2012) 1–35. http://dx.doi.org/10.1140/epjc/s10052-011-1844-6.

[125] ATLAS Collaboration, G. Aad et al., *Measurement of the WW production cross section in proton-proton collisions at $\sqrt{s} = 7$ TeV with the ATLAS detector*, ATLAS-CONF-2011-015, CERN, Geneva, Mar, 2011. https://cds.cern.ch/record/1334877.

[126] ATLAS Collaboration, G. Aad et al., *Selection of jets produced in proton-proton collisions with the ATLAS detector using 2011 data*, ATLAS-CONF-2012-020, CERN, Geneva, Mar, 2012. https://cds.cern.ch/record/1430034.

[127] *Performance of the ATLAS muon trigger in 2011*, ATLAS-CONF-2012-099, CERN, Geneva, Jul, 2012. https://cds.cern.ch/record/1462601.

[128] "Trigger Reweighting Software." https://svnweb.cern.ch/trac/atlasgrp/browser/Institutes/UCIrvine/btoggers/DGTriggerReweight/tags/DGTriggerReweight-00-00-11. (ATLAS Internal) [Online; accessed 11-June-2013].

[129] M. Hamer, C. Hensel, F. Kohn, and A. Quadt, *Measurement of Trigger Efficiencies from Data and their Application in Physics Analyses*, ATL-COM-DAQ-2011-083 (ATLAS Internal), CERN, Geneva, Sep, 2011. https://cds.cern.ch/record/1381241.

[130] ATLAS Collaboration, G. Aad et al., *Measurement of the top quark-pair production cross section with ATLAS in pp collisions at* $\sqrt{s} = 7$ *TeV*, The European Physical Journal C **71** (2011) 1–36. http://dx.doi.org/10.1140/epjc/s10052-011-1577-6.

[131] A. Alonso, B. Kile Gjelsten, E. Gramstad, F. Ould-Saada, M. Pedersen, et al., *Searching for Supersymmetry with two leptons and missing transverse momentum at* $\sqrt{s} = 7$ *TeV*, ATL-PHYS-INT-2011-091 (ATLAS Internal), CERN, Geneva, Nov, 2011. https://cds.cern.ch/record/1398592.

[132] L. S. Ancu, B. K. Gjelsten, K. Pajchel, et al., *SUSY Searches in the Final States with Three Leptons and Missing Transverse Momentum at ATLAS (Direct Gaugino support note for multileptons)*, ATL-PHYS-INT-2012-059 (ATLAS Internal), CERN, Geneva, Sep, 2012. https://cds.cern.ch/record/1482141.

[133] P. K. Sinervo, *Signal Significance in Particle Physics*,. http://arxiv.org/abs/hep-ex/0208005v1.

[134] A. L. Read, *Presentation of search results: the* CL_s *technique*, Journal of Physics G: Nuclear and Particle Physics **28** no. 10, (2002) 2693. http://stacks.iop.org/0954-3899/28/i=10/a=313.

[135] G. Cowan, K. Cranmer, E. Gross, and O. Vitells, *Asymptotic formulae for likelihood-based tests of new physics*, European Physical Journal C **71** (2011) 1554, arXiv:1007.1727 [physics.data-an].

[136] J. G. Heinrich, "Coverage of Error Bars for Poisson Data." http://www-cdf.fnal.gov/physics/statistics/notes/cdf6438_coverage.pdf, May, 2003. [Online; accessed 11-June-2013].

[137] "HistFitter Twiki." https://twiki.cern.ch/twiki/bin/viewauth/AtlasProtected/SusyFitter. [Online; accessed 11-June-2013].

[138] K. Cranmer, G. Lewis, L. Moneta, A. Shibata, and W. Verkerke, *HistFactory: A tool for creating statistical models for use with RooFit and RooStats.*, CERN-OPEN-2012-016, New York U., New York, Jan, 2012. https://cds.cern.ch/record/1456844.

[139] ATLAS Collaboration, *Search for direct-slepton and direct-chargino production in final states with two opposite-sign leptons, missing transverse momentum and no jets in* $20fb^{-1}$ *of pp collisions at* $\sqrt{(s)} = 8$ *TeV with the ATLAS detector*, ATLAS-CONF-2013-049, CERN, Geneva, May, 2013. https://cds.cern.ch/record/1547565.

[140] https://twiki.cern.ch/twiki/bin/viewauth/AtlasProtected/BackgroundStudies#Common_systematic_uncertainties. (ATLAS Internal) [Online; accessed 11-June-2013].

[141] https://twiki.cern.ch/twiki/bin/viewauth/AtlasProtected/TopMC11#MC11_Common_Conventions. (ATLAS Internal) [Online; accessed 11-June-2013].

[142] ATLAS Collaboration, G. Aad et al., *Jet energy resolution and selection efficiency relative to track jets from in-situ techniques with the ATLAS Detector Using Proton-Proton Collisions at a Center of Mass Energy* $\sqrt{s} = 7$ *TeV*, ATLAS-CONF-2010-054, CERN, Geneva, Jul, 2010. https://cds.cern.ch/record/1281311.

[143] E. Gramstad, *Search for the lightest MSSM Higgs boson in cascades of supersymmetric particles in ATLAS*, Master's thesis, Department of Physics, University of Oslo, Oslo, 2008. https://www.duo.uio.no/bitstream/handle/10852/11205/Gramstad_v2.pdf?sequence=2.

[144] *Letter of Intent for the Phase-I Upgrade of the ATLAS Experiment*, CERN-LHCC-2011-012. LHCC-I-020, CERN, Geneva, Nov, 2011. https://cds.cern.ch/record/1402470.

[145] A. Barr et al., *Searches for Supersymmetry at the high luminosity LHC with the ATLAS Detector*, ATL-PHYS-PUB-2013-002, CERN, Geneva, Feb, 2013. https://cds.cern.ch/record/1512933.

[146] E. Gramstad, "MSSM h→bb." ATLAS HSG5 meeting at JINR (Dubna), 2010. https://indico.cern.ch/conferenceDisplay.py?confId=83611. (ATLAS Internal).

[147] A. Salam and S. S., *The Full 24-Parameter MSSM Exploration*, AIP Conf.Proc. **1078** (2009) 297–299, arXiv:0809.0284 [hep-ph].

[148] H. Baer, F. Paige, S. Protopopescu, and X. Tata, "A monte carlo event generator for pp, $p\bar{p}$ and e^+e^- interactions." http://www.nhn.ou.edu/~isajet/isajet783.ps. ATLAS Internal [Online; accessed 11-June-2013].

[149] AtlfastII Twiki:. https://twiki.cern.ch/twiki/bin/viewauth/Atlas/AtlfastII. [Online; accessed 11-June-2013].

[150] E. Torró Pastor, D. Côté, and X. Portell Bueso, *Validation of the ATLFAST-II package for the simulation of supersymmetry events*, ATL-COM-PHYS-2011-1181 (ATLAS Internal), CERN, Geneva, Sep, 2011. https://cds.cern.ch/record/1379479.

[151] T. Plehn, *Measuring the MSSM Lagrangean*, Czech.J.Phys. **55** (2005) B213–B220, arXiv:hep-ph/0410063 [hep-ph].

[152] M. Spira, *Higgs and SUSY particle production at hadron colliders*, arXiv:hep-ph/0211145 [hep-ph].

[153] W. Beenakker, M. Klasen, M. Krämer, T. Plehn, M. Spira, and P. M. Zerwas, *Production of Charginos, Neutralinos, and Sleptons at Hadron Colliders*, Phys. Rev. Lett. **83** (1999) 3780–3783, arXiv:hep-ph/9906298 [hep-ph]. http://link.aps.org/doi/10.1103/PhysRevLett.83.3780.

[154] W. Beenakker, M. Kramer, T. Plehn, M. Spira, and P. Zerwas, *Stop production at hadron colliders*, Nucl.Phys. **B515** (1998) 3–14, arXiv:hep-ph/9710451 [hep-ph].

[155] ATLAS Collaboration, G. Aad et al., *Search for the Standard Model Higgs boson produced in association with a vector boson and decaying to a b-quark pair with the ATLAS detector*, Physics Letters B **718** no. 2, (2012) 369 – 390. http://www.sciencedirect.com/science/article/pii/S0370269312011276.

[156] "Atlas event display for atlas." http://www.hep.ucl.ac.uk/atlas/atlantis/.